Edited by
Wolfgang Schattke, Michel A. Van Hove

WILEY-VCH

Solid-State Photoemission and Related Methods

Theory and Experiment

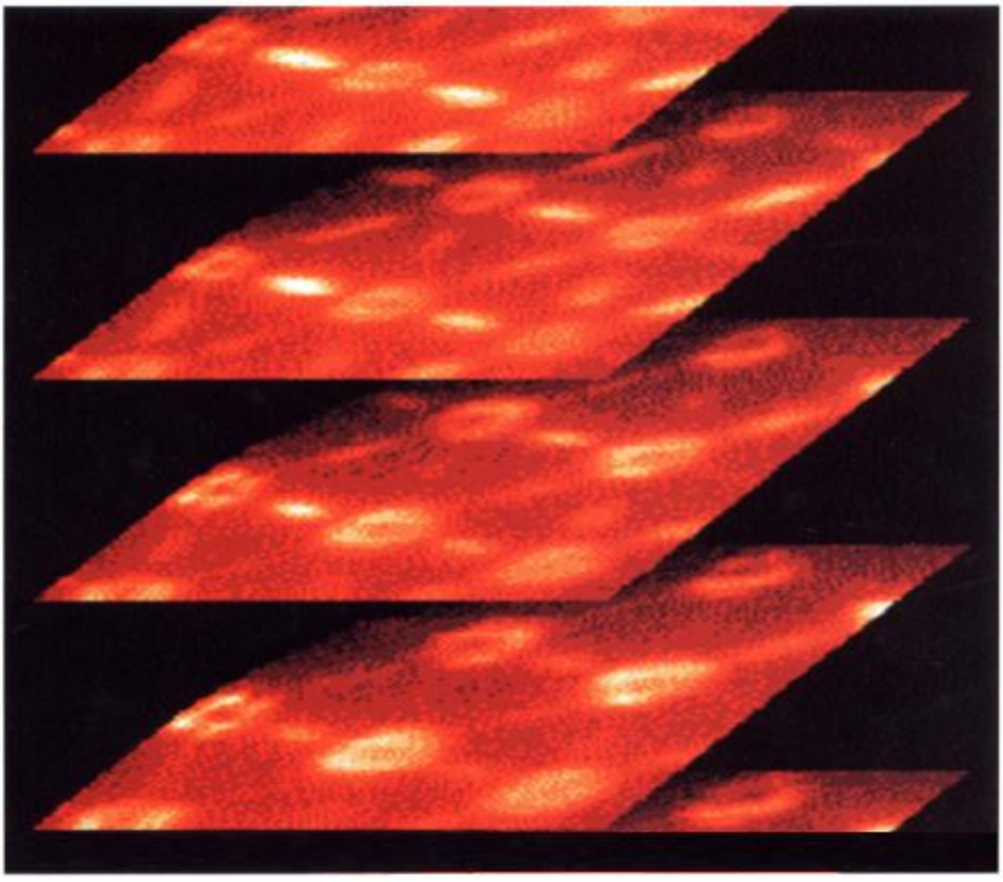

Wolfgang Schattke, Michel A. Van Hove (Eds.)

Solid-State Photoemission and Related Methods

Theory and Experiment

Wolfgang Schattke, Michel A. Van Hove (Eds.)

Solid-State Photoemission and Related Methods

Theory and Experiment

WILEY-VCH GmbH & Co. KGaA

Editors
Prof. Wolfgang Schattke
Universität Kiel, Germany
schattke@tp.cau.de

Prof. Michel A. Van Hove
Lawrence Berkeley National Laboratory, USA
VanHove@lbl.gov

Library of Congress Card No.: applied for
British Library Cataloging-in-Publication Data:
A catalogue record for this book is available from the British Library

Bibliographic information published by Die Deutsche Bibliothek
Die Deutsche Bibliothek lists this publication in the Deutsche Nationalbibliografie; detailed bibliographic data is available in the Internet at <http://dnb.ddb.de>.

Cover Picture
Photoelectron angular distributions of 1T-$TiTe_2$ taken at 100 eV photon energy (showing the momentum resolved electronic structure over several Brillouin zones). Top sheet: Fermi level. Sheets to higher binding energies separated by 100 meV.

Printed in the Federal Republic of Germany
Printed on acid-free paper

Composition Uwe Krieg, Berlin
Printing Strauss Offsetdruck GmbH, Mörlenbach
Bookbinding Litges & Dopf Buchbinderei GmbH, Heppenheim

ISBN 3-527-40334-5

Preface

The objective of this volume is to provide a comprehensive review of the state and progress of solid-state photoemission, including closely-related methods, both from a theoretical and from an experimental point of view. This material should be of particular interest to a wide range of theoretical and experimental physicists, materials scientists, and chemists, from graduate students to experts, dealing especially with surfaces and other nanostructures.

Many excellent treatments of major aspects of this field have appeared in the last decade: we mention in particular Inglesfield and Plummer's 1992 review article[1], which focused on the fundamental principles of valence-level angle-resolved photoemission, and the 1995 book by Hüfner[2], which adopted a more experimental perspective.

This field has continued to grow at a fast pace on many fronts, greatly expanding its capabilities and achievements. We thus felt that it was necessary and timely to bring together diverse developments in a single monograph, in an attempt to provide a degree of up-to-date completeness of the current state of the art.

Given that photoemission is intimately tied to ground and excited electronic states, this book starts with an exposition of contemporary theory of such states. It then provides a unified overview of the theoretical principles of core and valence photoemission. This is then followed by a much more thorough treatment of the theory of core level photoemission.

Turning to valence photoemission, a chapter is devoted to valence bands and VUV spectra, while another addresses actual development of spatial imaging of valence levels besides the traditional spectroscopic analysis. The very important application to the study of magnetic materials is covered in the following chapter. In the subsequent chapter, recent progress towards a compact photoemission program based on an all-electron ab-initio representation is described in the context of band structure theory.

Several very exciting novel developments with two-particle spectroscopies and their inherent access to many-particle properties such as lifetime and correlation are introduced in three separate chapters dealing with: time-resolved two-photon photoemission; low-energy (e,2e) spectroscopy; and one-photon two-electron transitions at surfaces.

The book next shifts the attention toward the use of core levels, in particular for surface structure determination. For that purpose, an overview of the known structures of surfaces is offered, being fundamental to many surface processes, including photoemission itself.

---

[1] J. E. Inglesfield and E. W. Plummer, *The physics of photoemission* in S. D. Kevan (ed.) *Angle-resolved photoemission*, (Elsevier 1992)

[2] S. Hüfner, *Photoelectron spectroscopy* in Springer Series in Solid State Sciences, Vol. 82 (Springer, Berlin 1995)

This is followed by a very recent application of core-level angle resolved photoelectron spectroscopy to surface structural analysis; its implications for the valence band structure are also discussed. Then, new holographic approaches to obtaining surface structure are addressed.

Several related methods of surface analysis are covered next. One is X-ray absorption fine structure and its derivative techniques. Another is the use of X-rays and their properties in photoemission and X-ray emission. Finally, developments in low-energy electron diffraction are addressed in the last chapter, covering the important issue of surface vibrations.

Wolfgang Schattke and *Michel A. Van Hove, Editors*

August 2003

In memoriam Lars Hedin (1930–2002)

Tragically, soon after completing his chapter for this Handbook, Professor Lars Hedin passed away.

Lars was born in 1930 and raised in Örebro, Sweden. He met and within one year married his lifetime companion Hillevi in 1953. They now have three daughters and six grandchildren. His higher education was at the Royal Institute of Technology in Stockholm, Uppsala University, and finally Chalmers University of Technology in Gothenburg, from which he obtained his Ph.D. in 1965. He then became Professor of Physics at Linköping University (1970–71), and subsequently at Lund University (1971–95), where he spent most of his career. During his years in Lund, he made extended visits to Stanford, Nijmegen, and Yokohama. He was head of a theory group at the Max Planck Institute in Stuttgart from 1994-98, at which time he returned to Lund as Professor Emeritus, and continued to maintain an active research program until his death. Beyond this, Lars was an editor of Solid State Communications (1971–90), played a leading role in the organization of the International Conferences on Vacuum Ultraviolet Radiation Physics (1977–92), and was a member of many other committees and editorial boards in Sweden and abroad.

The field of condensed matter theory has been enriched by Lars' many outstanding and fundamental contributions over the last half century. He is responsible for various important advances, particularly in the theory of interacting electron systems. These began in the 1960s, the fascinating period during which many of the analytical tools of many body theory were being developed. His contributions took place in parallel with the development of various powerful spectroscopic tools for studying complex electronic systems, and Lars provided crucial insights for linking theory with experiment, as illustrated in his chapter for this Handbook. His theoretical developments demonstrate his unique ability to combine mathematical rigor and physical intuition within formal analytical frameworks which he designed. A multitude of scientific milestones testify to his profound impact. In particular, Lars' theories paved the way for a quantitative understanding of electronic excitations, in particular in photoemission and X-ray absorption spectra. These theories provide the basis for many calculations of electronic structure and for a quantitative understanding of experimental investigations that now dominate the science of the microscopic world.

Those who personally know him will agree that Lars combined a most friendly and engaging personality with an exacting scientific attitude that made him a great researcher, teacher, and friend. We are most grateful for having received Lars' manuscript in time for inclusion in this Handbook. It reflects most of the topics he was devoted to, especially in the last few years of his very productive life. As such it represents one of his last scientific achievements, and it also provides a solid foundation for many of the topics covered in the Handbook. By dedicating this Handbook to Lars Hedin, we hope to show how very much alive his influence will remain within the scientific community.

Wolfgang Schattke and *Michel A. Van Hove*

Contents

List of contributors

- *R.C. Albers*

  Theoretical Division
  Los Alamos National Laboratory
  Los Alamos
  NM 87545
  USA

- *K.N. Altmann*

  Department of Physics and SRC
  University of Wisconsin Madison
  1150 University Ave.
  Madison, WI 53706-1390
  USA

- *A.L. Ankudinov*

  Department of Physics
  University of Washington
  Seattle
  WA 98195-1560
  USA

- *Ryoji Asahi*

  Toyota Central R&D Labs., Inc.
  Nagakute
  Aichi 480-1192
  Japan

- *I. Bartoš*

  Institute of Physics
  Academy of Sciences of the Czech Republic
  Cukrovarnická 10
  162 53 Prague 6
  Czech Republic
  e-mail: bartos@fzu.cz

- *J. Berakdar*

  Max-Planck-Institut für Mikrostrukturphysik
  Weinberg 2
  D-06120 Halle (Saale)
  Germany
  e-mail: jber@mpi-halle.mpg.de

- *P. Bruno*

  Max-Planck-Institut für Mikrostrukturphysik
  Weinberg 2
  D-06120 Halle (Saale)
  Germany

- *Alessandra Continenza*

  Istituto Nazionale di Fisica della Materia and
  Università dell'Aquila
  L'Aquila
  Italy

- *Hiroshi Daimon*

  Graduate School of Materials Science
  Nara Institute of Science and Technology
  8916-5 Takayama, Ikoma, Nara
  630-0192 Japan
  e-mail: daimon@ms.aist-nara.ac.jp

- *R. Díez Muiño*

  Donostia International Physics Center
  (DIPC)
  Paseo Manuel de Lardizabal 4,
  20018 San Sebastián, Spain
  e-mail: wabdimur@sq.ehu.es

- *Charles S. Fadley*

  Department of Physics
  University of California Davis
  Davis, CA 95616 USA

  and

  Materials Sciences Division
  Lawrence Berkeley National Laboratory
  Berkeley CA 94720 USA
  e-mail: fadley@lbl.gov

- *Thomas Fauster*

  Lehrstuhl für Festkörperphysik
  Universität Erlangen-Nürnberg
  Staudtstr. 7
  D-91058 Erlangen
  Germany
  e-mail: fauster@fkp.physik.uni-erlangen.de

- *R. Feder*

  Theoretische Festkörperphysik
  Universität Duisburg
  D-47048 Duisburg
  Germany
  e-mail: feder@dagobert.uni-duisburg.de

- *N. Fominykh*

  Max-Planck-Institut für Mikrostrukturphysik
  Weinberg 2
  D-06120 Halle (Saale)
  Germany

- *A.J. Freeman*

  Department of Physics and Astronomy
  Northwestern University
  Evanston, Il
  e-mail: art@pluto.phys.nwu.edu

- *F.J. García de Abajo*

  Centro Mixto CSIC-UPV/EHU,
  Apartado 1072,
  20080 San Sebastián, Spain

  and

  Donostia International Physics Center
  (DIPC)
  Paseo Manuel de Lardizabal 4,
  20018 San Sebastián, Spain
  e-mail: jga@sc.ehu.es

- *H. Gollisch*

  Theoretische Festkörperphysik
  Universität Duisburg
  D-47048 Duisburg
  Germany

- *R.J. Harder*

  Department of Physics and Laboratory for Surface Studies
  University of Wisconsin-Milwaukee
  P. O. Box 413
  Milwaukee, WI 53201
  USA

- *Lars Hedin*

  Dept. of Physics
  University of Lund
  Sölvegatan 14A, 22362 Lund,
  Sweden

  and

  MPI-FKF
  Heisenbergstrasse 1
  D-70569 Stuttgart
  Germany

- *J. Henk*

  Max-Planck-Institut für Mikrostrukturphysik
  Weinberg 2
  D-06120 Halle (Saale)
  Germany

- *F.U. Hillebrecht*

  Max-Planck-Institut für Mikrostrukturphysik
  Weinberg 2
  D-06120 Halle (Saale)
  Germany

- *Franz J. Himpsel*

  Department of Physics
  University of Wisconsin Madison
  1150 University Ave.
  Madison, WI 53706-1390
  USA
  e-mail: fhimpsel@facstaff.wisc.edu

- *Lutz Kipp*

  Institut für Experimentelle und Angewandte Physik
  Christian-Albrechts-Universität
  Leibnizstraße 19
  D-24098 Kiel
  Germany
  e-mail: kipp@physik.uni-kiel.de

- *J. Kirschner*

  Max-Planck-Institut für Mikrostrukturphysik
  Weinberg 2
  D-06120 Halle (Saale)
  Germany

- *E.E. Krasovskii*

  Institut für Theoretische Physik und Astrophysik
  Christian-Albrechts-Universität
  Leibnizstr.15
  D-24098 Kiel
  Germany
  e-mail: krasovsk@tp.cau.de

- *J. Landskron*

  Department of Earth and Environmental Sciences
  Section Crystallography
  University of Munich
  Theresienstr. 41
  80333 Munich
  Germany

- *N. Mannella*

  Materials Sciences Division and Advanced Light Source
  Lawrence Berkeley National Laboratory
  Berkeley, CA 94720
  USA
  e-mail: norman@electron.lbl.gov

  and

  Department of Physics
  University of California
  Davis, CA 95616, USA

- *Fumihiko Matsui*

  Graduate School of Materials Science
  Nara Institute of Science and Technology
  8916-5 Takayama, Ikoma, Nara
  630-0192 Japan

- *Wolfgang Moritz*

  Department of Earth and Environmental Sciences
  Section Crystallography
  University of Munich
  Theresienstr. 41
  80333 Munich
  Germany
  e-mail:
  Wolfgang.Moritz@lrz.uni-muenchen.de

- *A. Morozov*

  Max-Planck-Institut für Mikrostrukturphysik
  Weinberg 2
  D-06120 Halle (Saale)
  Germany

- *Bongjin Simon Mun*

  Materials Sciences Division and Advanced Light Source
  Lawrence Berkeley National Laboratory
  Berkeley CA 94720
  USA

- *J.J. Rehr*

  Department of Physics
  University of Washington
  Seattle
  WA 98195-1560
  USA
  e-mail: jjr@leonardo.phys.washington.edu

- *Kai Roßnagel*

  Institut für Experimentelle und Angewandte Physik
  Christian-Albrechts-Universität
  Leibnizstraße 19
  D-24098 Kiel
  Germany
  e-mail: rossnagel@physik.uni-kiel.de

- *Kazuyuki Sakamoto*

  Department of Physic
  Graduate School of Science
  Tohoku University
  Sendai, 980-8578, Japan
  e-mail: sakamoto@surface.phys.tohoku.ac.jp

- *D.K. Saldin*

  Department of Physics and Laboratory for Surface Studies
  University of Wisconsin-Milwaukee
  P. O. Box 413
  Milwaukee, WI 53201
  USA
  e-mail: dksaldin@uwm.edu

- *S. Samarin*

  Max-Planck-Institut für Mikrostrukturphysik
  Weinberg 2
  D-06120 Halle (Saale)
  Germany

- *Wolfgang Schattke*

  Institut für Theoretische Physik und Astrophysik
  Christian-Albrechts-Universität
  Leibnizstr. 15
  D-24098 Kiel
  Germany
  e-mail: schattke@tp.cau.de

- *Michael Skibowski*

  Institut für Experimentelle und Angewandte Physik
  Christian-Albrechts-Universität
  Leibnizstraße 19
  D-24098 Kiel
  Germany

- *Michel A. Van Hove*

  Materials Sciences Division and Advanced Light Source
  Lawrence Berkeley National Laboratory
  Berkeley, CA 94720
  USA
  e-mail: vanhove@lbl.gov

  and

  Department of Physics
  University of California at Davis
  Davis, CA 95616
  USA

- *Ruqian Wu*

  Department of Physics and Astronomy
  University of California
  Irvine
  CA 92697-4575

- *See-Hun Yang*

  IBM Almaden Research Center
  San Jose, CA 95120 USA
  e-mail: shyang@electron.lbl.gov

Solid-State Photoemission and Related Methods
Wolfgang Schattke, Michel A. Van Hove (Eds.)

1 Electronic structure theory for ground and excited state properties of materials

Arthur J. Freeman, Ryoji Asahi, Alessandra Continenza, and Ruqian Wu

1.1 Introduction

It is now well recognized that recent major advances in the quantitative computation of ground-state properties in solids are essentially related to the development of density-functional theory (DFT) in the local density approximation (LDA) and the local spin density approximation (LSDA). [1, 2] These efficient approximation schemes give the electronic ground-state energy and density distribution as a function of the position of the atomic nuclei, which in turn determine the molecular and crystal structure and give the forces acting on the atomic nuclei when they are not at their equilibrium positions. The LDA (or LSDA) has been widely used to solve problems in atomic, molecular, and condensed matter physics, such as phase transitions, vibration spectra, chemical reactions, and magnetic properties.

Recent advances in experimental techniques such as X-ray absorption and inverse photoemission strongly require understanding of unoccupied states by first-principles calculations in addition to the occupied states. Although excitation properties are outside the domain of DFT, LDA eigenvalues have been frequently interpreted as quasiparticle states. This is because LDA is so widely used and much easier to perform than full many-body theories. In practice, LDA band structures successfully give an account of experiment including some excitation properties, *e.g.*, photoemission spectra of metals. This procedure, however, is certainly not valid for all the eigenvalues and excitation properties.

One of the major problems in describing excitation properties is that the LDA gives a substantial underestimate of the band gap in semiconductors and insulators, typically by 40–50% in comparison with experiment. This problem, the so-called band gap problem, is so serious when considering fundamental properties in semiconductors for instance, that it has been intensively discussed over 20 years. A complication of the problem comes from the difficulty to access an exact form of the exchange-correlation functional or the corresponding exchange-correlation potential in the Kohn Sham (KS) scheme.

Several attempts have been undertaken to set up alternatives to LDA in order to improve LDA and to extend its applicability to excitation properties. These can be divided into mainly two groups. One is to obtain the quasiparticle energies, which directly correspond to the excitation energies of a many-body Dyson equation, by the perturbation expansion of the self-energy. A comprehensive discussion including a more realistic approximation, known as the GW approximation, to the self-energy was given by Hedin [3]. Another theoretical approach in going beyond LDA is to attempt to find better energy functionals by modeling the exchange-correlation hole but still within DFT framework; this includes the self-interaction correction

Solid-State Photoemission and Related Methods: Theory and Experiment. Edited by Wolfgang Schattke, Michel A. Van Hove

ISBN: 3-527-40334-5

(SIC), [4] the LDA+U, [5] and the optimized effective potential (OEP) method, [6–8] the generalized density functional theory, [9–11] and the generalized Kohn-Sham (GKS) scheme with the screened-exchange LDA method [12, 13] (sX-LDA).

The simplification of the GW calculation, called the model GW method, [14, 15] is one way to reduce the numerical effort of the GW calculations. Although the accuracy should be limited by the neglect of local-field effects and dynamic screening, the results for various nonmagnetic semiconductors [14] and for transition metal oxides [15–18], give mostly good agreement with experiment and the results of full GW calculations. While the method gives self-consistent eigenvalues and wavefunctions with respect to the perturbed self-energy corrections, the reliability of the total energy, and therefore of the ground states obtained, has not been established.

The applicability of the SIC and the LDA+U approaches is relatively limited to the particular systems where localized states are involved. The LDA+U works reasonably well for the Mott-Hubbard insulators or rare-earth metal compounds, where the partially filled $3d$ or $4f$ bands are split by the Coulomb interaction, forming the upper and lower Hubbard bands. The SIC also describes the Mott-Hubbard insulators and the $3d$ monoxides. However, these methods fail to give satisfactory results for more itinerant systems; in particular, the SIC does not yield good band gaps of sp semiconductors, *e.g.*, Si and Ge. [19]

The basic idea of the OEP method was proposed [6] by Sharp and Horton in 1953, showing the way to obtain a local exchange potential exactly from the Hartree-Fock potential. The method was revised to improve the LDA description. Kotani [7] used the OEP with the correlation energy in the random-phase approximation (RPA) and presented results for Cu, Fe, Co, Ni, Si, and MnO. The results for metals are very close to those of LDA, and a good agreement with experiment is obtained for MnO. However, the band gap of Si is improved by only 0.2 eV. Städele *et al.* suggested [8] that a main effect for improvement of the band gap by the OEP method is a self-interaction reduction, not including the discontinuity of the exchange-correlation potential which is supposed to be dominant for Si. [20]

The screened-exchange LDA method (sX-LDA) was first proposed [12] by Bylander and Kleinman in order to obtain a better band gap. Seidl *et al.*showed [13] that the method is actually described in the framework of the generalized Kohn-Sham scheme (GKS), and that the discontinuity of the exchange-correlation potential is introduced through the nonlocal screened potential. Encouraging results for the band gaps, structural properties, and optical properties were demonstrated for several bulk semiconductor materials. [12, 13, 21–23] The method was also applied to surface and superlattice. [24] The advantages of the sX-LDA over the GW calculations are that it is much less computationally demanding, and that it permits the self-consistent determination of ground-state properties.

In this chapter, after a short introduction to density functional theory and its most precise implementation via the full-potential linearized augmented plane wave (FLAPW) method, we present a brief discussion on the general aspects of the band gap problem and its prescriptions, theoretical frameworks of the model GW and the sX-LDA are presented. The former is derived from the quasiparticle picture through the GW approximation, and the latter is introduced as a particular case of the generalized KS scheme. These two methods have a capability to obtain self-consistent properties including band gaps in a wide range of semiconductors. Moreover, rather light computational demands allows us to implement them into an all-electron methods, the FLAPW method. The applications of these method are also demonstrated in the case of semiconductor and magnetic properties.

1.2 Density functional theory and the FLAPW method

1.2.1 Introduction

The full-potential spin-polarized linear augmented plane wave (FLAPW) method is considered to be the most accurate electronic structure calculation scheme. It has its origin in the augmented plane wave (APW) method introduced by Slater [25] (details about this method can also be found in Ref. [26]). In this approach, real space is partitioned into spherical regions around atoms ("muffin-tins" or "atomic spheres") and interstitial regions between the spheres. Computationally, the APW method is demanding since the basis functions are energy dependent and the eigenvalue problem non-linear. The subsequent linearization of the APW method (LAPW) [27, 28], where the energy dependence is removed by selecting a fixed set of suitable muffin-tin radial functions and their energy derivatives, represented an important development. In the full-potential (F)LAPW method there is no shape approximation for either the charge density or the potential, and all electrons are treated in the self-consistent process; the core electrons are treated fully relativistically and the valence electrons are treated semi-relativistically. Further details can be found in original papers [29, 30] and in recent reviews [31, 32].

Aside from the early important introduction of a total energy capability [33], recent improvements and extensions to the present FLAPW calculation scheme include: (i) evaluation of forces on the atoms, which affords automatic optimization of the atomic geometry [34–36], (ii) methodological developments resulting in significant speed-ups [37], (iii) spin-orbit coupling affording calculation of magnetic properties, namely, magnetocrystalline anisotropy (MCA), surface magneto-optic Kerr effect (SMOKE), and magnetic circular X-ray dichroism (MCD), (iv) optical properties, (v) the option of several different exchange-correlation functionals, i.e., the local density approximation (LDA) and the generalized gradient approximation (GGA) and (vi) the treatment of excited states via screened exchange (sX), as well as model GW treatments, and (vii) the calculation of vibrational frequencies. A very recent and important break-through is the successful implementation of a parallelized version of the code.

1.2.2 Density-functional theory

The FLAPW method employs density-functional theory (DFT), introduced by Hohenberg and Kohn [38] and Kohn and Sham [39]. The underlying theorem (Hohenberg-Kohn-Sham theorem) on which this theory rests is that the total energy, E, of an atomistic system can be expressed as a functional of its electron density, ρ, namely, $E = E[\rho]$, that E is at its minimum for the ground-state density, and is stationary with respect to first-order variations in the density.

Typically, the Born-Oppenheimer approximation [40] is employed which assumes that the motion of the nuclei are negligible with respect to that of electrons. This implies that the electronic structure is calculated for a given atomic geometry; the nuclei are then moved according to classical mechanics.

The Kohn-Sham equations

To obtain the ground-state density, the variational principle is applied with respect to the one-particle wave functions:

$$\left[(-\hbar^2/2m)\nabla^2 + V_{eff}(\mathbf{r})\right]\psi_i(\mathbf{r}) = \varepsilon_i\psi_i(\mathbf{r}), \tag{1.1}$$

where

$$V_{eff}(\mathbf{r}) = V_C(\mathbf{r}) + \mu_{xc}[\rho(\mathbf{r})] \tag{1.2}$$

is the effective potential and ε_i the effective one-electron eigenvalues. Equations (1.1) are the "Kohn-Sham equations" and the solutions, $\psi_i(\mathbf{r})$, form an orthonormal set,
i.e., $\int \psi_i^*(\mathbf{r})\psi_j(\mathbf{r})\, d\mathbf{r} = \delta_{ij}$. The Coulomb or electrostatic potential is given as:

$$V_C(\mathbf{r}) = -e^2 \sum_\alpha \frac{Z_\alpha}{|\mathbf{r} - \mathbf{R}_\alpha|} + e^2 \int \frac{\rho(\mathbf{r}')}{|\mathbf{r} - \mathbf{r}'|} d\mathbf{r}' \tag{1.3}$$

which can also be calculated using Poisson's equation, i.e.,

$$\nabla^2 V_C(\mathbf{r}) = -4\pi e^2 q(\mathbf{r}) \quad , \tag{1.4}$$

where $q(\mathbf{r})$ represents the electronic charge distribution *and* the positive point charges at position $\mathbf{R}_\alpha$. The exchange-correlation potential is given by

$$\mu_{xc} = \partial E_{xc}[\rho]/\partial\rho \quad . \tag{1.5}$$

Because the exchange-correlation potential (and energy) are not known, approximations have to be made.

Spin-polarized density functional theory

The generalization of density-functional theory to spin-polarized systems has been made within the local spin density approximation (LSD) [41, 42]. The important quantity, in addition to the electron density $\rho(\mathbf{r})$, is the spin density $\sigma(\mathbf{r})$ which is the density difference between the spin-up and spin-down configurations, i.e., $\sigma(\mathbf{r}) = \rho_\uparrow(\mathbf{r}) - \rho_\downarrow(\mathbf{r})$; the total density being given by $\rho(\mathbf{r}) = \rho_\uparrow(\mathbf{r}) + \rho_\downarrow(\mathbf{r})$. Because the exchange-correlation potential for spin-up and spin-down electrons is in general different, the spin-polarized form of the Kohn-Sham equations are:

$$\left[(-\hbar^2/2m)\nabla^2 + V^\sigma_{eff}(\mathbf{r})\right]\psi^\sigma_i(\mathbf{r}) = \varepsilon^\sigma_i\psi^\sigma_i(\mathbf{r}), \quad \text{where}\, \sigma = \uparrow \text{ or } \downarrow \quad , \tag{1.6}$$

and

$$V^\sigma_{eff}(\mathbf{r}) = V_C(\mathbf{r}) + \mu^\sigma_{xc}[\rho(\mathbf{r}), \sigma(\mathbf{r})] \quad . \tag{1.7}$$

Thus there are two sets of single-particle wave functions, one for spin-up (or "majority") electrons and one for spin-down ("minority") electrons, each with corresponding one-electron eigenvalues.

Exchange-correlation functions

Local-density approximation (LDA) A very successful and widely used approximation for the exchange-correlation energy is the local-density approximation (LDA). Here the exchange-correlation energy is assumed to depend only on the local electron density of each volume element $d\mathbf{r}$:

$$E_{xc}[\rho] \approx \int \rho(\mathbf{r})\varepsilon_{xc}[\rho(\mathbf{r})]d\mathbf{r} \quad . \tag{1.8}$$

$\varepsilon_{xc}[\rho]$ is the exchange-correlation energy per electron of a *homogeneous* electron gas and is expressed as an analytic function of the electron density, as is the exchange-correlation potential, μ_{xc}. There are various forms of the LDA in the literature; we refer to those of Hedin-Lunqvist [43] and Wigner (non-spin-polarized forms), and Barth-Hedin [41] (spin-polarized form) since they are the ones implemented in the present FLAPW program version.

Generalized gradient approximation (GGA) In recent years, the generalized gradient approximation (GGA) is being considered as a possible improvement over the LDA. The GGA has been found to generally improve the description of total energies, ionization energies, and electron affinities of atoms, atomization energies of molecules [44–46] and some solid state properties [47–50]. Adsorption energies of adparticles on surfaces are also reported to be improved [51, 52] as are reaction energies [53, 54]. Furthermore, the GGA leads to significantly better activation energy barriers for H_2 dissociation [55, 56] and also the relative stability of structural phases appears to be better described for magnetic [57] and non-magnetic systems [58, 59].

There are a number of GGA approaches in the literature. The generic form of the GGA exchange-correlation energy may be written as:

$$E_{xc}^{\mathrm{GGA}}[\rho] = \int \rho(\mathbf{r})\varepsilon_{xc}^{\mathrm{GGA}}\big(\rho(\mathbf{r}), \nabla\rho(\mathbf{r})\big)\, d\mathbf{r} \tag{1.9}$$

so that it depends locally on the electronic density $\rho(\mathbf{r})$ and its gradient.

The GGA developed by Perdew and Wang (PW) [44] is derived essentially from first principles, combining the gradient expansions of the exchange and correlation holes of a non-uniform electron gas with real-space truncations to enforce constraints imposed by properties of the physical exchange-correlation hole. The GGA developed by Becke and Perdew [60] on the other hand relies on fitted parameters. In the present program version of the FLAPW program the GGA implemented is that proposed by Perdew, Burke and Ernzerhof (PBE) [61]. This functional is regarded to be conceptually more concise than the PW GGA but appears to yield very similar results [62].

1.2.3 The FLAPW basis-set

In the FLAPW method, in bulk material, real space is partitioned into spherical regions around atoms ("muffin-tins" or "atomic spheres") and interstitial regions between the spheres. In the spherical region, the basis functions are products of radial functions and spherical harmonics, and in the interstitial region plane waves are used. For the film geometry, there is a number

of atomic layers surrounded by vacuum, thus in addition to spherical and interstitial regions, one defines a vacuum region, which starts at $\pm D/2$ and ends at $\pm\tilde{D}/2$ (see Fig. 1.1), where the wave functions are products of two-dimensional (2D) plane waves and z-dependent functions which are solutions of the one-dimensional Schrödinger equation of the (x, y)-averaged potential in the vacuum region.

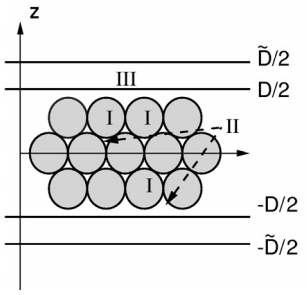

Figure 1.1: Geometry for a film calculation showing division of space in a film geometry.

Specifically, the FLAPW one-particle wave functions in the film geometry are:

$$\psi_i(\mathbf{r}, \mathbf{k}_\parallel) = \sum_j c_{ij}\phi(\mathbf{r}, \mathbf{K}_j); \quad \mathbf{K}_j = \mathbf{k}^\parallel + \mathbf{G}_j \quad , \tag{1.10}$$

where $\mathbf{k}^\parallel$ is an arbitrary vector of the 2D BZ and $\mathbf{G}_j$ is a three-dimensional (3D) reciprocal lattice vector (in the z-direction an artificial periodicity between the boundaries at $\pm\tilde{D}/2$ is imposed). The basis functions are:

$$\phi(\mathbf{r}, \mathbf{K}_j) = \begin{cases} \Omega^{-1/2} e^{i\mathbf{K}_j \cdot \mathbf{r}} & \text{interstitial} \\ \sum_{lm}[A^\alpha_{lm}(\mathbf{K}_j)u_l(E^\alpha_l, r_\alpha) + B^\alpha_{lm}(\mathbf{K}_j)\dot{u}_l(E^\alpha_l, r_\alpha)]Y_{lm}(\hat{r}_\alpha) & \text{sphere} \\ \sum_q [A_q(\mathbf{K}_j)u_{\mathbf{k}q}(E_\nu, z) + B_q(\mathbf{K}_j)\dot{u}_{\mathbf{k}q}(E_\nu, z)]e^{i(\mathbf{k}^\parallel + \mathbf{K}^\parallel_q)\cdot\mathbf{r}} & \text{vacuum} \end{cases} \tag{1.11}$$

The Coulomb potential $V(\mathbf{r})$ is obtained by solving Poisson's equation in each of the three regions. At infinity the potential is gauged equal to zero in the case of the film geometry. The effective single-particle potential is constructed by adding the exchange-correlation potential, which is determined by the charge density in real space and transformation of it into each representation. The core electrons are treated fully relativistically and are updated at each iteration using a scheme for *free* atoms (only the spherical part of the potential is used). The valence electrons are expanded in a variational basis set and are treated scalar-relativistically.

1.3 Electronic structure theory for excited states

1.3.1 Band gaps and derivative discontinuities

The band gap is rigorously defined as the difference between the lowest conduction-band energy and the highest valence-band energy: the latter is the energy required to remove an electron from the insulating N-particle ground state to infinity, *i.e.*, the ionization potential, I;

the former is obtained by adding an electron to the insulating N-particle ground state, *i.e.*, the electron affinity, A. Thus the exact band gap is defined in terms of the total energy of the M-particle system, $E(M)$, and the chemical potential, $\mu(M)$, as

$$\begin{aligned} E_g &= I - A && (1.12)\\ &= E(N-1) - E(N) - (E(N) - E(N+1)) && (1.13)\\ &= -\mu(N-\delta) + \mu(N+\delta), && (1.14) \end{aligned}$$

where we used the definition of the chemical potential,

$$\mu(N) = \frac{\partial E(N)}{\partial N}. \quad (1.15)$$

On the other hand, the ground-state total energy in DFT satisfies the variational principle formulation subjected to the constraint, $\int d\mathbf{r}\, n(\mathbf{r}) = N$, with a Lagrangian multiplier μ';

$$\frac{\delta}{\delta n}\left(E_0[n] - \mu' \int d\mathbf{r}\, n(\mathbf{r}) \right) = 0, \quad (1.16)$$

or

$$\frac{\delta E_0[n]}{\delta n(\mathbf{r})} = \mu'. \quad (1.17)$$

Actually μ' is exactly μ since [63]

$$\begin{aligned} \mu(N+\delta)\,\delta &= E_0[n_{N+\delta}] - E_0[n_N] \\ &= \int d\mathbf{r}\ \left.\frac{\delta E_0[n]}{\delta n(\mathbf{r})}\right|_{N+\delta} (n_{N+\delta}(\mathbf{r}) - n_N(\mathbf{r})) \\ &= \int d\mathbf{r}\, \mu'(N)\ \{n_{N+\delta}(\mathbf{r}) - n_N(\mathbf{r})\} \\ &= \mu'(N)\,\delta. \end{aligned} \quad (1.18)$$

From Eqs. (1.14) and (1.17) the band gap is expressed as

$$E_g = \left[\left.\frac{\delta E_0[n]}{\delta n(\mathbf{r})}\right|_{N+\delta} - \left.\frac{\delta E_0[n]}{\delta n(\mathbf{r})}\right|_{N-\delta} \right]_{n=n_0}, \quad (1.19)$$

i.e., the band gap is rigorously determined by derivatives of the total energy functional with respect to the *ground-state* density, $n_0(\mathbf{r})$.

Now we consider the KS scheme, [2], expressing the total energy functional in terms of the non-interacting kinetic energy functional $T_s[n]$,

$$E_0[n] = T_s[n] + \int d\mathbf{r}\, v_{\rm eff}(\mathbf{r})\, n(\mathbf{r}), \quad (1.20)$$

where $v_{\rm eff}(\mathbf{r})$ is the effective local potential. The band gap in this case comes only from the discontinuity of the $\delta T_s[n]/\delta n(\mathbf{r})$. In other words, the band gap is exactly evaluated in terms

of the difference of the eigenvalues in the non-interacting system. Thus we can write a KS gap as

$$E_g^{KS} = \left[\left. \frac{\delta T_s[n]}{\delta n(\mathbf{r})} \right|_{N+\delta} - \left. \frac{\delta T_s[n]}{\delta n(\mathbf{r})} \right|_{N-\delta} \right]_{n=n_0} \tag{1.21}$$

$$= \epsilon_{N+1}^{KS} - \epsilon_N^{KS}. \tag{1.22}$$

The origin of the derivative discontinuity of the kinetic energy is, of course, just the finite change of the highest occupied orbital which may occur when the electron number increases by an integer. The question here is whether the effective potential, $v_{\rm eff}(\mathbf{r})$, obtained with the LDA would yield the exact KS gap. One answer can be found in the results [20] of Godby *et al.* They evaluated the local exchange-correlation potential generated from the GW self energy, which is assumed to be close to the exact effective potential, and concluded that the LDA band gap agrees very closely with the true KS gap, at least in Si.

The main source of the band gap problem is hidden in the previous KS scheme using the effective external potential $v_{\rm eff}(\mathbf{r})$. Actually, exact DFT yields another derivative discontinuity from the exchange-correlation energy functional $E_{xc}[n]$;

$$\begin{aligned} E_g &= \epsilon_{N+1}^{KS} - \epsilon_N^{KS} \\ &\quad + \left[\left. \frac{\delta E_{xc}[n]}{\delta n(\mathbf{r})} \right|_{N+\delta} - \left. \frac{\delta E_{xc}[n]}{\delta n(\mathbf{r})} \right|_{N-\delta} \right]_{n=n_0} \\ &= E_g^{KS} + \Delta_{xc}, \end{aligned} \tag{1.23}$$

where Δ_{xc} is the derivative discontinuity of the exchange-correlation energy or the discontinuity of the exchange-correlation potential. The existence of Δ_{xc} in insulators has been shown by an analysis taking the limit $\mathbf{r} \to \infty$, [64] by the two-plane-wave model, [65] and by a finite one-dimensional model. [66] The derivative discontinuity of the exchange energy has a similar origin to that of the kinetic energy; the highest occupied orbital of the Fock potential may have a finite change through the gap. However, that of the correlation energy is more complicated, and not well understood.

Note that while the band gap is not correctly evaluated from the KS eigenvalues, the center of the gap relative to the vacuum level, ϵ_m, is accurately obtained; [67]

$$\begin{aligned} \epsilon_m &= -\frac{1}{2}[I + A] \\ &= \frac{1}{2}[\epsilon_{N+1}^{KS} + \epsilon_N^{KS}]. \end{aligned} \tag{1.24}$$

In particular for metals, from the continuity condition, $I = A$, we have

$$\Phi = I = A = -\epsilon_N^{KS} \tag{1.25}$$

where Φ is the work function.

One way to describe the band gap is to construct the self-energy operator given the ground-state density, and to solve a quasiparticle Dyson equation. On the other hand, it has been suggested [65, 68] that if the potential of the band theory includes the nonlocality and energy dependence, as in the self-energy, the eigenvalues could describe the accurate band gap.

1.3.2 Band gaps and nonlocal potentials

Göling and Levy showed [69] that the discontinuity of the exchange-correlation potential with respect to particle number is related to the difference between local and nonlocal treatments of the exchange-correlation potential. In the KS scheme, the many-body N-electron ground state, $|\Psi(N)\rangle$, is equivalent with a single Slater determinant of the KS orbitals in the ground-state N-electron system, $|\Phi(N)\rangle = |\{\psi_i\}\rangle$, which is the solution of the non-interacting Schrödinger equation,

$$(\hat{T} + \hat{V}_{\text{eff}})|\Phi(N)\rangle = E|\Phi(N)\rangle, \tag{1.26}$$

and yields the ground-state density, $n(\mathbf{r})$. Accordingly, we can assume the zeroth order many-body (N+1)- and (N-1)-electron states in terms of the Slater determinant of the KS orbitals to be

$$\begin{aligned} |\Psi(N+1)\rangle &\simeq |\Phi(N+1)\rangle, \\ |\Psi(N-1)\rangle &\simeq |\Phi(N-1)\rangle. \end{aligned} \tag{1.27}$$

Expressing the Hamiltonian using $\hat{V}_{\text{eff}} = \hat{W}_s + \hat{V}_{xc} + \hat{V}$,

$$\begin{aligned} \hat{H} &= \hat{T} + \hat{V} + \hat{W}_c \\ &= \hat{T} + \hat{V}_{\text{eff}} + \left[\{\hat{W}_c - \hat{W}_s\} - \hat{V}_{xc}\right], \end{aligned} \tag{1.28}$$

where $\hat{W}_s$, $\hat{V}_{xc}$, $\hat{V}$ and $\hat{W}_c$ are the energy operators corresponding to the Hartree, the exchange-correlation, the external, and Coulomb potentials, respectively, the band gap E_g is thus evaluated up to the first order as follows:

$$\begin{aligned} E_g &= E(N+1) - E(N) - [E(N) - E(N-1)] \\ &= \langle\Phi(N+1)|\hat{H}|\Phi(N+1)\rangle - \langle\Phi(N)|\hat{H}|\Phi(N)\rangle \\ &\quad - \left[\langle\Phi(N)|\hat{H}|\Phi(N)\rangle - \langle\Phi(N-1)|\hat{H}|\Phi(N-1)\rangle\right] \\ &\simeq \epsilon^{KS}_{N+1}[n] - \epsilon^{KS}_{N}[n] \\ &\quad + \langle\psi_{N+1}|\hat{v}^{NL}_x[n] - \hat{v}^{L}_x[n]|\psi_{N+1}\rangle - \langle\psi_N|\hat{v}^{NL}_x[n] - \hat{v}^{L}_x[n]|\psi_N\rangle. \\ &= E^{KS}_g + \Delta_x \end{aligned} \tag{1.29}$$

where $\hat{v}^{NL}_x$ and $\hat{v}^{L}_x$ are nonlocal and local exchange potentials, and correlation terms are neglected since those are higher order with respect to e^2. Equations (1.23) and (1.29) thus suggest

$$\begin{aligned} \Delta_{xc} &\simeq \langle\psi_{N+1}|\hat{v}^{NL}_{xc}[n] - \hat{v}^{L}_{xc}[n]|\psi_{N+1}\rangle \\ &\quad - \langle\psi_N|\hat{v}^{NL}_{xc}[n] - \hat{v}^{L}_{xc}[n]|\psi_N\rangle, \end{aligned} \tag{1.30}$$

i.e., the discontinuity of the exchange-correlation potential would be described by difference between the nonlocal and the local exchange-correlation potential energies. This consequence is one of the foundations of the sX-LDA method we describe in Sec. 1.3.4.

1.3.3 Quasiparticle calculations

The GW approximation

Hedin [3] derived a set of coupled equations to solve the quasiparticle equation. The lowest expansion of the self-energy is called GW approximation, representing the Green's function G times the screened interaction W. The detailed derivation is given in Ref. [3]. Here we will make clear the concept of the quasiparticle spectrum.

The amplitudes f_s and the energies e_s are defined in terms of the one particle annihilation operator, ψ, as

$$\begin{aligned} \langle N-1, v|\psi(x)|N, 0\rangle &= f_v(x)\theta(\mu - e_v), \\ e_v &= E_N - E_{N-1,v} + i\delta, \\ \langle N, 0|\psi(x)|N+1, c\rangle &= f_c(x)\theta(e_c - \mu), \\ e_c &= E_{N+1,c} - E_N - i\delta. \end{aligned} \tag{1.31}$$

The energies e_s are interpreted as the change in the total energy when a particle in the state s is added to or removed from the N-particle system. In particular, fundamental energy gap E_g in a semiconductor is, by definition, directly given by the difference between two quasiparticle energies:

$$E_g = [E_{N+1,c} - E_N] - [E_N - E_{N-1,v}] = e_c - e_v, \tag{1.32}$$

where e_c and e_v are the quasiparticle energies at the bottom of the conduction band and the top of the valence band, respectively. This point is in contrast with the LDA eigenvalues for which Eq. (1.32) is generally not valid except in the vicinity of the Fermi energy.

The Green's function is expressed using Eq. (1.31) as

$$\begin{aligned} G(x, x'; e) &= -i\langle N|T[\psi(x,t)\psi^+(x',t')]|N\rangle \\ &= \sum_s \frac{f_s(x) f_s^*(x')}{e - e_s}, \end{aligned} \tag{1.33}$$

here T is the time-ordering operator. Constructing the equation of motion for the Green's function, we get the eigenvalue equation for the quasiparticle:

$$[e - h(x) - v(x)]\, f(x) - \int \Sigma(x, x''; e) f(x'')\, dx'' = 0. \tag{1.34}$$

Now quasiparticle states $f(x)$ and energies e are obtained as the solutions of Eq. (1.34). The self-energy Σ in the GW approximation equals to iGW. One can compare it with the Kohn-Sham equation in LDA,

$$\left[e^{\mathrm{LDA}} - h(x) - v(x)\right] \phi(x) - v_{xc}(x)\phi(x) = 0, \tag{1.35}$$

where the exchange-correlation potential $v_{xc}(x)$ is derived by DFT-LDA in the N-particle system, and e^{LDA} and $\phi(x)$ are the eigenvalues and the eigenfunction of LDA. Since both

Eqs. (1.34) and (1.35) give the same ground-state charge density, $f(x)$ and $\phi(x)$ are not expected to be so different, although they are exactly identical only in the non-interacting electron system. So the quasiparticle energies can be formulated in terms of the LDA eigenvalues and eigenfunctions, invoking perturbation theory, as

$$\begin{aligned} e_s &= e_s^{\mathrm{LDA}} + \langle\phi_s|\Sigma(e_s) - v_{xc}|\phi_s\rangle + O\left((\Sigma(e_s) - v_{xc})^2\right) \\ &\approx e_s^{\mathrm{LDA}} - \langle\phi_s|v_{xc}|\phi_s\rangle + \langle\phi_s|\Sigma(e_s)|\phi_s\rangle \\ &\quad +(e_s - e_s^{\mathrm{LDA}})\langle\phi_s|\left(\frac{\partial\Sigma}{\partial e}\right)_{e_s^{\mathrm{LDA}}}|\phi_s\rangle. \end{aligned} \tag{1.36}$$

This procedure yields up to the first order,

$$e_s = e_s^{\mathrm{LDA}} + \frac{\langle\phi_s|\Sigma(e_s^{\mathrm{LDA}}) - v_{xc}|\phi_s\rangle}{1 - \left(\frac{\partial\Sigma}{\partial e}\right)_{e_s^{\mathrm{LDA}}}}. \tag{1.37}$$

One of the major computational efforts in self-energy calculations is to calculate the screened interaction. The physical features of W are well known; the imaginary part of W is characterized by a strong peak corresponding to a plasmon excitation at the plasmon frequency. Thus, the simplest form of the so-called plasmon-pole approximation is given by [70]

$$\mathrm{Im}\,\epsilon^{-1}(\mathbf{q},\omega) = A_{\mathbf{q}}\delta(\omega - \omega_{\mathbf{q}}). \tag{1.38}$$

The two parameters $A_{\mathbf{q}}$ and $\omega_{\mathbf{q}}$ are determined from the sum rules. In the case of the electron gas, this is strictly true in the long wave length limit. For finite $\mathbf{q}$, the spectrum also contains particle-hole excitations at lower energies. Since the imaginary part of the self-energy is assume to be zero except at the plasmon-poles, the life-time of the quasiparticles cannot be calculated. Nevertheless, the plasmon-pole approximation has been widely applied for bulk semiconductors, and the results for s-p electron systems are generally good. [71]

The GW calculations have been performed for many semiconductors and insulators by a number of authors, giving good agreement with experiment, typically within an error of 0.1 eV. The results are summarized in recent reviews. [72, 73]

While the GW approximation has shown a lot of successful results, there are some restrictions to its applications. First, the large computational demands restrict it to simple crystal systems. Second, although it is possible in principle to calculate the total energy from the Green's function, it is by no means clear that the resulting total energies would be accurate. The second point comes from the fact that the formalism and the approximation of the GW approximation is not directly supported by the variational principle for the total energy in contrast with DFT-LDA, and that it is difficult to estimate the errors in the GW approximation itself and in the dielectric function included in W with the complicated cancellations that exist among them. Finally, the self-consistent GW has not given successful results and remaines an open question how to find suitable vertex corrections. [72]

The model GW method

The model GW method [14, 15] (sometimes called as LDA+$\delta\Sigma_{COHSEX}$) is considered to be one of the simplifications of the GW approximation. Gygi *et al.* proposed [14] to focus

on the discrepancy in the self-energy between metals and semiconductors. The self-energy is then rewritten into two terms:

$$\begin{aligned}\Sigma(\mathbf{r},\mathbf{r}';e) &= i\int G(\mathbf{r},\mathbf{r}';e+e')W^{\mathrm{IEG}}(\mathbf{r},\mathbf{r}';e')\,de' \\ &\quad +i\int G(\mathbf{r},\mathbf{r}';e+e')\delta W^{\mathrm{IEG}}(\mathbf{r},\mathbf{r}';e')\,de'. \end{aligned} \tag{1.39}$$

The first term on the right-hand side of Eq. (1.39) is the self-energy of a metallic inhomogeneous electron gas, and can be approximated by the LDA expression, $v_{xc}(\mathbf{r})\delta(\mathbf{r}-\mathbf{r}')$.

The main contribution of the difference in the screened interactions, δW, comes from the different screening behavior in the long wave length region from the metallic one. The screened interactions for metals [74], semiconductors [75], and zero-gap semiconductor [76] are asymptoticly expressed as,

$$\begin{aligned}\left[\epsilon_M(q)q^2\right]^{-1} &\overset{q\to 0}{\longrightarrow} \left[q^2+k_{TF}^2\right]^{-1} && \text{(metal)} \\ \left[\epsilon_{SC}(q)q^2\right]^{-1} &\overset{q\to 0}{\longrightarrow} \left[\epsilon(0)q^2\right]^{-1} && \text{(semiconductor)} \\ \left[\epsilon_{SM}(q)q^2\right]^{-1} &\overset{q\to 0}{\longrightarrow} q^{-1} && \text{(zero-gap semiconductor)} \end{aligned} \tag{1.40}$$

where k_{TF} is the Thomas-Fermi wavevector and $\epsilon(0)$ is the dielectric constant of the semiconductor. In metals, the screened interaction decreases rapidly for $|\mathbf{r}-\mathbf{r}'| > k_{TF}^{-1}$, but in semiconductors, it decreases as $[\epsilon(0)|\mathbf{r}-\mathbf{r}'|]^{-1}$ for large $|\mathbf{r}-\mathbf{r}'|$ due to the incompleteness of the screening in semiconductors.

Focusing on the above point, it is assumed that δW depends only on $|\mathbf{r}-\mathbf{r}'|$, which is strictly valid only when $|\mathbf{r}-\mathbf{r}'| \to \infty$. It has also been shown numerically that in semiconductors the local field effects become negligible when $|\mathbf{r}-\mathbf{r}'|$ exceeds the interatomic distance. [71] Furthermore, the energy dependence of δW can be neglected since the excitation energies around the gap are much smaller than the plasmon frequency, as seen in the plasmon-pole approximation. The correction term of the self-energy to the LDA is therefore approximated in the following form:

$$\delta\Sigma(\mathbf{r},\mathbf{r}') = -\rho(\mathbf{r},\mathbf{r}')\delta W(|\mathbf{r}-\mathbf{r}'|) + \delta\Sigma_{\mathrm{COH}}, \tag{1.41}$$

where the first term is the screened exchange contribution and $\rho(\mathbf{r},\mathbf{r}')$ is the two-particle density matrix. The second term of Eq. (1.41) is given as

$$\delta\Sigma_{\mathrm{COH}} = \frac{\Omega}{2(2\pi)^3}\int d\mathbf{r}\,\delta W(\mathbf{r}), \tag{1.42}$$

which shifts all eigenvalues by the same constant. The Fourier component of δW is given by

$$\delta\widetilde{W}(q) = \frac{4\pi}{\Omega q^2}\left[\epsilon_{SC}^{-1}(q) - \epsilon_M^{-1}(q)\right], \tag{1.43}$$

where $\epsilon_{SC}^{-1}(q)$ is the diagonal part of the inverse static dielectric matrix of the semiconductor and $\epsilon_M^{-1}(q)$ is that of the metal.

Table 1.1: Energy gaps at L, Γ, and X, measured from the top of the valence band, and valence band width (VBW) of Si, Ge, InSb, GaAs in eV calculated by FLAPW within LDA (FLAPW), model GW using the FLAPW implementation (mGW-FLAPW), model GW using the pseudopotential (mGW-PP), the sX-LDA using the FLAPW implementation (sX-FLAPW), and the sX-LDA using the pseudopotential (sX-PP), which are compared with experiment (Expt). The results of FLAPW and sX-FLAPW are taken from Ref. [21], those of mGW-FLAPW are taken from Ref. [78], those of mGW-PP are taken from Ref. [14] with spin-orbit effects added, and those of sX-PP and Expt are taken from Ref. [13] and references therein.

		L	Γ	X	VBW
Si	FLAPW	1.40	2.48	0.58	12.08
	mGW-FLAPW	2.30	3.40	1.53	12.66
	mGW-PP	2.10	3.21	1.33	
	sX-FLAPW	2.17	3.22	1.30	12.61
	sX-PP	2.18	3.37	1.55	12.47
	Expt	1.65$\pm$ 0.01	3.05, 3.4	1.25	12.5$\pm$ 0.6
		2.1, 2.4$\pm$ 0.15			
Ge	FLAPW	-0.04	-0.27	0.58	12.92
	mGW-FLAPW	0.63	0.32	1.36	13.58
	mGW-PP	0.55	0.27	1.24	
	sX-FLAPW	0.68	0.63	1.22	13.65
	sX-PP	0.66	0.28	1.45	13.41
	Expt	0.74	0.89	1.3$\pm$ 0.2	12.6, 12.9$\pm$ 0.3
InSb	FLAPW	0.12	-0.72	0.99	11.01
	mGW-FLAPW	0.65	-0.47	1.56	11.67
	sX-FLAPW	0.82	0.18	1.55	11.57
	sX-PP	1.02	0.21	1.82	11.02
	Expt		0.24	1.79	11.7, 11.2
GaAs	FLAPW	0.78	0.21	1.29	12.89
	mGW-FLAPW	1.57	0.96	2.20	13.62
	mGW-PP	1.67	1.11	2.22	
	sX-FLAPW	1.64	1.19	2.01	13.70
	sX-PP	1.70	1.11	2.35	13.40
	Expt	1.81	1.52	1.98	13.1

Applications of the model GW method

Gygi *et al.* implemented the model GW method with the pseudopotential method (mGW-PP) and tested for simple semiconductors, [14] and Massidda *et al.* implemented it with the FLAPW basis (mGW-FLAPW) and applied to several transition metal oxides. [15–18]

While good agreement with experiment for diamond, Si, and GaP is demonstrated. a relatively large discrepancy from experiment still remains in the band gaps at Γ for Ge, InSb, GaAs as seen in Table 1.1. [14, 78] The accuracy for these materials should be limited by the neglect of local-field effects and dynamic screening.

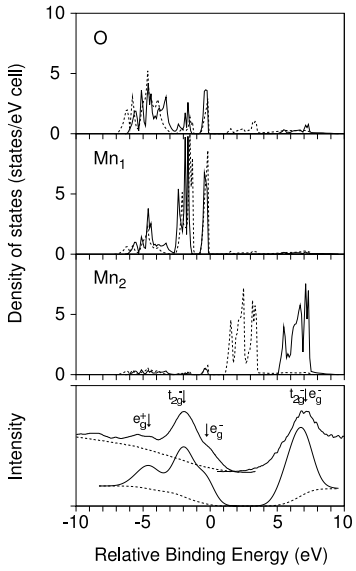

Figure 1.2: Partial densities of spin-up states of antiferromagnetic MnO. Top panel: the total O $2p$ projection into the O spheres. Second and third panels: d projection into the two inequivalent Mn spheres. Solid (dashed) lines correspond to the model GW (LSDA) calculations. Bottom panel, upper curves: inverse photoemission spectrum (Ref. [79]) and difference between the on- and off-resonance photoemission spectra (Ref. [80]), representing the Mn $3d$ contribution. Lower curves: GW d-projected DOS into both Mn spheres. (Taken from Ref. [15]).

On the other hand, for the systems which involve correlated d electrons, model GW generally exhibits good results. The densities of states of antiferromagnetic MnO calculated with LSDA and model GW are shown in Fig. 1.2 [15]. Significant improvement, upon going from LSDA to the model GW, and in particular, good agreement with photoemission spectra [79, 80] are demonstrated. The band gap and magnetic moment of the model GW, 4.2 eV and 4.52 μ_B, can be compared with the experimental values, 3.8–4.2 eV and 4.58–4.79 μ_B, which are also improved over the LSDA results, 1.0 eV and 4.29 μ_B, respectively.

The band structure of antiferromagnetic NiO is compared with experimental angle-resolved photoemission (ARPES) data as shown in Fig. 1.3.

An agreement of the model GW band dispersion with the ARPES data is in overall good agreement with and much better than that of the LSDA results. The bandgaps calculated by model GW and LSDA are 3.7 eV and 0.3 eV, respectively, which compared with experiment, 4.0–4.3 eV. The importance to include self-consistently self-energy corrections in transition-metal oxides, due to large changes in the wave functions, is emphasized.

The above results demonstrate the capability of the model GW method to calculate strongly correlated systems. As expected, however, the method can not explain the high-binding-energy satellite observed in photoemission. [15, 18] This requires going beyond the GW approximation where a vertex correction, *e.g.*, ladder diagrams, should be included. [77]

1.3.4 Density functional theory using non-local functionals

The generalized Kohn-Sham scheme and the sX-LDA method

The KS scheme employed the non-interacting energy functional, $T_s[n]$, instead of the Hohenberg-Kohn functional, [1] $F_{HK}[n]$, by introducing the effective potential, $v_{\rm eff}(\mathbf{r})$, as seen in Eq. (1.20). However the choice of the energy functional is rather arbitrary. One can consider

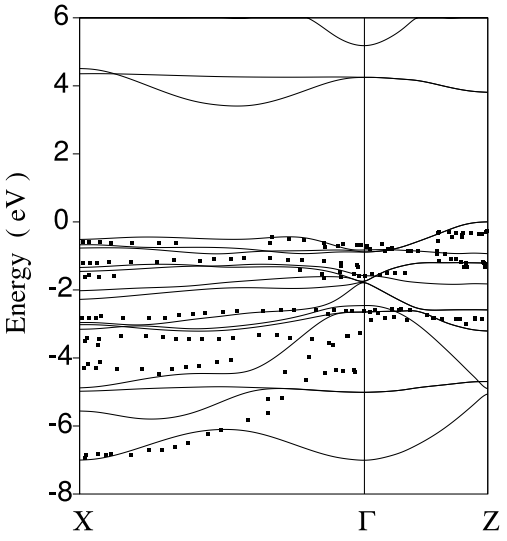

Figure 1.3: Model GW self-consistent band structure of NiO, compared with the APRES data. (Taken from Ref. [18]) and references therein.

the model system or the energy functional in which some part of the electron-electron interaction is taken into account. Seidl *et al.* generalized [13] the KS scheme (GKS scheme) for some energy functional, $F_s[n]$, chosen with a correction energy function, $R_s[n]$, so that

$$F_{HK}[n] = T[n] + W_s[n] + E_{xc}[n] = F_s[n] + R_s[n]. \tag{1.44}$$

A main extension for $F_s[n]$ is that it can include some part of the interacting energy functional as well as the non-interacting one. In order to guarantee the existence of self-consistent single particle equations, the interaction should be represented by the density and/or a single Slater determinant $\Phi = \{\psi\}$. The total energy is given as

$$E_0[n] \quad = \quad F_s[\{\psi\}, n] + R_s[n(\{\psi\})] + \int d\mathbf{r}\, v(\mathbf{r})\, n(\{\psi\}, \mathbf{r}) \tag{1.45}$$

and the corresponding single-particle equations (GKS equations) are

$$\hat{O}_s[\{\psi\}]\psi_j + v_R\psi_j + v\psi_j = \epsilon_j\psi_j, \tag{1.46}$$

where $\hat{O}_s[\{\psi\}]$ may depend on the orbitals, and

$$v_R(\mathbf{r}) = \frac{\delta R_s[n]}{\delta n(\mathbf{r})}. \tag{1.47}$$

Whether the density constructed from ψ_j is v-representable and equals the true density remains a question as in the KS scheme; the method, however, has an advantage that a suitable choice of F_s can result in R_s being small compared to the total energy.

The sX-LDA method was first proposed [12] by Bylander and Kleinman (who called the method the modified LDA) in order to describe a better band gap. Seidl *et al.* showed that the method can be actually described in the GKS framework. Using Eq. (1.44), the choices of F_s

and R_s in the sX-LDA method are given by

$$\begin{aligned} F_s^{sx}[\{\psi\},n] &= T^{sx}[n] + W_s[n] + E_x^{sx}[\{\psi\}], \quad (1.48) \\ R_s^{sx}[n] &= T[n] - T^{sx}[n] + E_{xc}[n] - E_x^{sx}[n] \\ &\simeq E_{xc}^{\rm LDA}[n] - E_x^{sx}[n]. \quad (1.49) \end{aligned}$$

Here $E_{xc}^{\rm LDA}[n]$ is the exchange-correlation energy expression in LDA, and we assumed $T^{sx}[n] \simeq T[n]$. The functional R_s^{sx} is constructed so that the accuracy of the total energy in the sX-LDA is as good as that in the LDA. The single-particle equation, Eq. (1.46), is obtained as

$$\left[\frac{-\hbar^2}{2\,m_{\rm e}}\nabla^2 + v_{\rm eff}(\mathbf{r})\right]\,\psi_i(\mathbf{r}) + \int d\mathbf{r}'\,v_{sx}^{NL}(\mathbf{r},\mathbf{r}')\psi_i(\mathbf{r}') - v_{sx}^{L}(\mathbf{r})\psi_i(\mathbf{r}) = \epsilon_i^{sx}\,\psi_i(\mathbf{r}), \quad (1.50)$$

where $v_{\rm eff}(\mathbf{r})$ is the effective potential formulated by LDA, and $v_{sx}^{NL}(\mathbf{r},\mathbf{r}')$ and $v_{sx}^{L}(\mathbf{r})$ are nonlocal and local screened exchange potentials. The virtue of this method is that the sX-LDA eigenvalues can describe the discontinuity of the exchange-correlation potential for the band gaps; from Eq. (1.50) we obtain

$$\begin{aligned} E_g^{sx} &= \epsilon_{N+1}^{sx}[n] - \epsilon_N^{sx}[n] \\ &\simeq \epsilon_{N+1}^{\rm LDA}[n] - \epsilon_N^{\rm LDA}[n] \\ &\quad + \langle\psi_{N+1}|\hat{v}_{sx}^{NL} - \hat{v}_{sx}^{L}|\psi_{N+1}\rangle - \langle\psi_N|\hat{v}_{sx}^{NL} - \hat{v}_{sx}^{L}|\psi_N\rangle. \\ &\simeq E_g, \quad (1.51) \end{aligned}$$

where we used the consequence of Eqs. (1.23) and Eq. (1.30). Therefore the sX-LDA is a promising method which can realize accurate ground-state total energies, ground-state charge densities, and band gaps. Note that even though the sX-LDA is expected to have good band gaps, it does not mean that all the sX-LDA eigenvalues correspond to the quasiparticle energies. The meaning of the sX-LDA eigenvalues is still nothing but Lagrange parameters as in the LDA. However, providing that the LDA can yield the excited states with a certain accuracy except the band gap, we expect equivalent or better results for the sX-LDA eigenvalues in the excited states.

Implementation of the sX-LDA method

In the sX-LDA, a GKS equation is written invoking perturbation theory as

$$(\hat{h}^{\rm LDA} + \Delta\hat{v}_{sx})|i\rangle = \epsilon_i^{sx}|i\rangle, \quad (1.52)$$

where

$$\Delta\hat{v}_{sx} = \hat{v}_{sx}^{\rm NL} - \hat{v}_{sx}^{L}. \quad (1.53)$$

Here $\hat{h}^{\rm LDA}$ is the LDA Hamiltonian, $\hat{v}_{sx}^{\rm NL}$ the nonlocal screened Fock exchange operator, $\hat{v}_{sx}^{L}$ the corresponding local one, and $|i\rangle$ are the eigenkets of the sX-LDA. The screened Fock exchange operator is given as

$$v_{sx}^{\rm NL}(\mathbf{r},\mathbf{r}') = -\sum_j^{\rm occ} W(\mathbf{r},\mathbf{r}')\langle\mathbf{r}|j\rangle\langle j|\mathbf{r}'\rangle. \quad (1.54)$$

Employing the simple Thomas-Fermi screening for $\Delta\hat{v}_{sx}$, we have the screened interaction in the form

$$W(r) = \frac{e^{-k_{\rm TF}r}}{r}, \tag{1.55}$$

and the corresponding local potentials, [81]

$$v_{sx}^{L}[\rho(\mathbf{r})] = -2\left(\frac{3}{\pi}\rho(\mathbf{r})\right)^{1/3} F(\gamma), \tag{1.56}$$

$$F(\gamma) = 1 - \frac{4}{3}\gamma \arctan\frac{2}{\gamma} - \frac{\gamma^2}{6}\left[1 - \left(\frac{\gamma^2}{4} + 3\right)\ln\left(1 + \frac{4}{\gamma^2}\right)\right]. \tag{1.57}$$

Here $\gamma = k_{\rm TF}/q_F$, where $k_{\rm TF}$ is a Thomas-Fermi screening wave vector, $k_{\rm TF}^2 = 4q_F/\pi$, and $q_F = (3\pi^2\bar{\rho})^{1/3}$ is a Fermi wave vector corresponding to the average density $\bar{\rho}$. It needs to be emphasized that, as discussed in Ref. [12], it is assumed that the *local* screened exchange density functional has the same dependence on the local density as the LDA exchange functional, so that γ has no dependence on $\rho(\mathbf{r})$ and q_F depends only on $\bar{\rho}$.

Now let's consider the case of films or superlattices (FLM/SL). [24] The essential difference between the FLM/SL and the bulk is that the linear response for the FLM/SL, $\chi(\mathbf{r}, \mathbf{r}')$, is spatially non-uniform, necessitating a translationally non-invariant response function in the z direction, whereas the response function in the form $\chi(\mathbf{r} - \mathbf{r}')$ is used for the bulk; in other words, we need to include local field effects in the z direction. In the GW calculations, the response function and the corresponding screened interaction are directly calculated by the random-phase approximation (RPA). Instead of its heavy evaluation, we employ a rather simple but reasonable nonlocal response function as

$$\chi(\mathbf{r_1}, \mathbf{r_2}) = \chi\left(r_{12}; \rho_{12}\right), \tag{1.58}$$

where

$$\rho_{12} = \frac{\rho(z_1) + \rho(z_2)}{2}, \tag{1.59}$$

i.e., the response function depends on an intermediate density between planar-averaged densities, $\rho(z_1)$ and $\rho(z_2)$, and the distance of the two positions $r_{12} = |\mathbf{r_1} - \mathbf{r_2}|$. Apparently, in a homogeneous system, Eq. (1.58) is reduced to the response function which depends only on a constant average density over the solid, *i.e.*, the approximation used in sX-LDA for bulk. Equation (1.58) was applied to calculations for the H_2 molecule [82] and for a surface energy [83], which give reasonable improvement over the results using the homogeneous form.

Corresponding Thomas-Fermi screening function for FLM/SL is given by

$$W(r_{12}; z_1, z_2) = \frac{e^{-k_{\rm FS}(z_1, z_2)\, r_{12}}}{r_{12}}, \tag{1.60}$$

where the *nonlocal* Thomas-Fermi wave vector $k_{\rm FS}$ is defined by

$$[k_{\rm FS}(z_1, z_2)]^2 = \frac{4}{\pi}(3\pi^2\rho_{12})^{1/3}. \tag{1.61}$$

For a local screened potential, we use Eq. (1.56) but assume that γ depends on $\rho(z)$, and keep it independent of $\rho(\mathbf{r})$. With this particular choice of screening function, a Fourier component of Eq. (1.60) is given as

$$\begin{aligned}\widetilde{W}(\mathbf{q}_{\rm xy}; z_1, z_2) &= \frac{1}{A}\int d\mathbf{r}_{\rm xy}\, W(r_{12}; z_1, z_2) e^{-i\mathbf{q}_{\rm xy}\cdot\mathbf{r}_{\rm xy}} \\ &= \frac{2\pi}{A}\int_{d_{12}}^{\infty} dr\, J_0\left(q_{\rm xy}\sqrt{r^2 - d_{12}^2}\right) e^{-k_{\rm FS}(z_1,z_2)\, r}, \end{aligned} \tag{1.62}$$

where $\mathbf{q}_{\rm xy}$ is a two dimensional wave vector, $d_{12} = |z_1 - z_2|$, A is the area of the unit cell, and J_0 is the zeroth order Bessel function.

We solve the secular equation, (1.52), self-consistently in a second variational way; the sX-LDA Bloch states $|i\rangle$ are expanded in terms of the FLAPW basis set $|n\rangle$ as

$$|i\rangle = \sum_n |n\rangle\langle n|i\rangle. \tag{1.63}$$

Starting from the LDA results calculated by the usual FLAPW procedure, we construct perturbation matrix elements. [24, 84] After diagonalization, the new eigenfunctions obtained are used to update the screened Fock exchange operator in the following iteration until the charge densities and eigenfunctions satisfy self-consistency.

Applications of the sX-LDA method

We here present some of the results calculated by the sX-LDA method implemented with the FLAPW basis (sX-FLAPW).

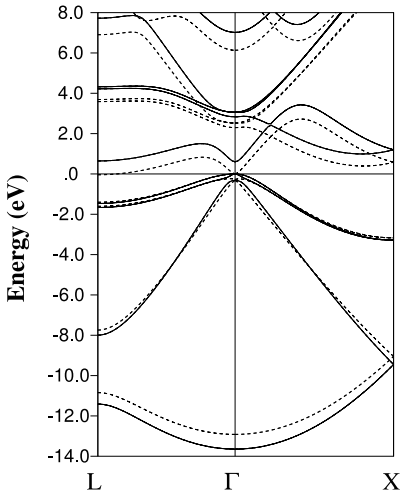

Figure 1.4: Self-consistent band structure of Ge by the sX-LDA method (solid line) and LDA (dashed line). (Taken from Ref. [21]).

The calculated sX-FLAPW band structure for cubic Ge is shown in Fig. 1.4 in comparison with the band structure within LDA results. [21] Even erroneous *negative* band gaps at the Γ and L points obtained by LDA are now corrected by the sX-LDA method. In Table 1.1, the

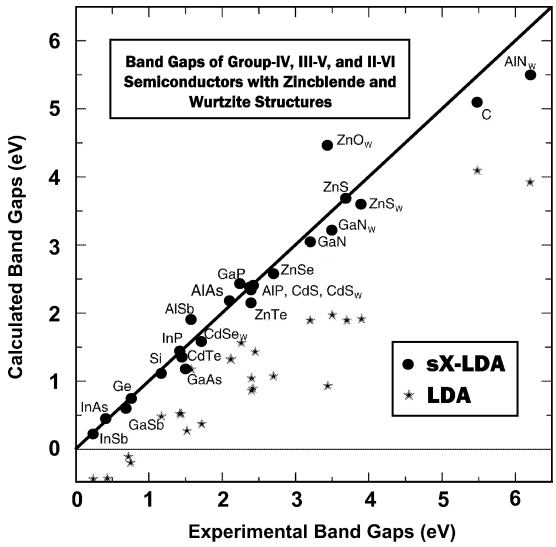

Figure 1.5: Calculated v.s. experimental energy-band gaps for 24 elemental and binary semiconductors. Results from sX-FLAPW calculations are shown as solid circles. Values obtained within LDA are represented as stars. (Taken from Ref. [23])

calculated band gaps and valence band widths (VBW) of cubic semiconductors are summarized, in comparison with the sX-LDA results obtained using the plane-wave pseudopotential method (sX-PP), [13] and with experiment. The improvement of the band gaps by the sX-LDA method is clearly shown for all materials, and agreement with experiment is good. Although the FLAPW results give a larger discrepancy of the band gaps from experiment than the more approximate plane-wave pseudopotential method, [13] the corrected sX-LDA results, sX-FLAPW and sX-PP, show overall agreement with each other; the sX-FLAPW results are closer to experiment at the Γ point in Ge and at the X point in GaAs than the sX-PP results.

Fundamental band gaps for several semiconductors are calculated as shown in Fig. 1.5. [23] Typical deviations between experimental values and sX-FLAPW predictions are a few tenths of 1 eV. A systematic investigation of effective masses reveals a similar picture, namely, that sX-FLAPW improves the overall agreement with experiment [85–88], as shown in Table 1.2. [23] In particular, the performance of sX-FLAPW in predicting m_c^Γ is rather remarkable. Nevertheless, in some cases involving flat bands, significant discrepancies remain (*e.g.*, m_l^X of GaAs and m_t^X of GaSb).

The sX-LDA results generally overestimate the valence band width while the LDA results give better agreement with experiment as seen in Table 1.1. Engel [89] proposed a screening function that is possibly better than the traditional Thomas-Fermi function. The new screened interaction, W_2, is given by

$$W_2(q) = \frac{4\pi}{\Omega q^2}\Theta(q - k_s), \tag{1.64}$$

Table 1.2: Computed and measured effective masses (conduction masses: m_c, longitudinal and transverse conduction masses: m_l and m_t, heavy hole and light hole masses: m_{hh} and m_{lh}). For InAs, effective density of states masses are defined as: $m^L = [16 m_l^L \, (m_t^L)^2]^{1/3}$ and $m^X = [9 m_l^X \, (m_t^X)^2]^{1/3}$. (Taken from Ref. [23])

		LDA	sX-FLAPW	Exp.
GaAs	m_c^Γ	0.011	0.055	0.067[a], 0.063[b]
	m_l^L	1.749	1.870	1.9[b]
	m_t^L	0.099	0.126	0.075[b]
	m_l^X	-0.978	-0.973	1.98[c], 1.9[b]
	m_t^X	0.272	0.275	0.3[c],0.19[b]
	m_{hh}^Γ	0.312	0.323	0.45[c], 0.51[b]
	m_{lh}^Γ	0.105	0.091	0.085[c], 0.082[b]
GaSb	m_c^Γ	0.066[e]	0.014	0.0412[a]
	m_l^L	0.080	0.014	
	m_t^L	1.745	1.714	0.95[b]
	m_l^X	0.095	0.123	0.11[b]
	m_t^X	-0.721	-0.626	1.51[b]
	m_{hh}^Γ	0.954[e]	0.691	0.28[a], 0.22[b]
InP	m_c^Γ	0.019	0.089	0.0765[a], 0.079[d], 0.081[d]
	m_t^L	0.145	0.180	0.25[b]
	m_t^X	0.402	0.392	0.32[b]
	$m_{hh}^\Gamma(001)$	0.415	0.456	0.56[a], 0.52[d], 0.61[d]
	$m_{hh}^\Gamma(111)$	1.011	1.032	0.60[a], 0.95[d], 0.63
	$m_{lh}^\Gamma(001)$	0.165	0.172	0.12[a], 0.104[d], 0.118[d], 0.089[b]
InAs	$m_c^\Gamma(100)$	0.094[e]	0.022	0.0231[a]
	$m_c^\Gamma(111)$	0.112[e]	0.021	
	m^L	0.862	0.821	0.29[b]
	m^X	1.367	1.254	0.64[b]
	m_{hh}^Γ	0.353[e]	0.388	0.41[b]
	m_{lh}^Γ	0.046[e]	0.025	0.026[b]

[a] Reference [85] [b] Reference [86]
[c] Reference [87] [d] Reference [88]
[e] A proper assignment of valence and conduction bands is hampered by the incorrect band overlap in the LDA.

where $\Theta(q - k_s)$ is a step function with a cutoff, k_s. In this case, the corresponding local field factor behaves quite similar to that obtained by quantum Monte Carlo simulations [90] in predicting that the higher density region contributes to the narrowing of the band width – in contrast with the consistently larger band width (compared with LDA) that is obtained for the Thomas-Fermi function in the whole density region. There is, however, difficulty in implementing this newly proposed screening function; since the minimum cutoff parameter k_s in W_2 is placed at about $0.9 q_F$ where the contribution is large, the result is very sensitive to the choice of the cutoff, and because of this, a small number of special k-points does not give a smooth band structure over the Brillouin zone.

The sX-FLAPW implementation for films, *i.e.*, Eq. (1.60), was applied to calculations of the 2x1 reconstruction surface of Si(100). [24] The band structures of the Si(100)2x1 surface and bulk Si along the [010] direction on the SBZ calculated by the sX-FLAPW methods, compared with angle-resolved photoemission data, [91] are presented in Fig. 1.6. In order to put the bulk band structure together with the film band structure, the Si $1s$ core level in the sixth layer from the surface was used as a reference, which showed a good convergence within 0.05 eV between the fifth and the sixth layers. In this way, the absolute value of the valence band maximum measured from the vacuum level, *i.e.*, the ionization energy, was evaluated to be 5.35 eV, in good agreement with an experimental value of 5.15$\pm$0.08 eV. [92]

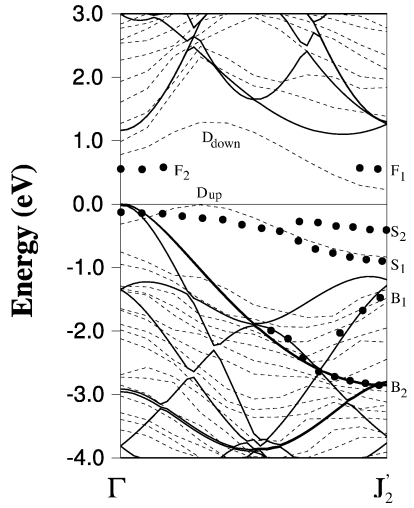

Figure 1.6: Self-consistent band structures in the [010] direction for the Si(100)2x1 surface calculated by the $film$ sX-FLAPW method (dashed lines), and for the bulk Si band structure projected into the 2x1 surface Brillouin zone calculated by the $bulk$ sX-FLAPW method. Filled circles (labeled F, S, and B) represent the experimental data taken from Ref. [91]. The valence-band maximum of bulk Si is set to be zero.

The occupied surface states ($D_{\rm up}$) calculated by sX-FLAPW show good agreement with the experimental dispersion S_1 in Fig. 1.6. Good agreement between experimentally observed occupied structures, B_1 and B_2, and the present folded bulk bands indicates that both structures come from the bulk resonance states. While the FLAPW calculations give a metallic surface with the negative $D_{\rm down}$ state at J', the sX-FLAPW calculations give a semiconducting surface which is observed in experiment. Focusing on the corrections at Γ where both LDA results agree with each other, we found that the $D_{\rm down}$ states of sX-FLAPW are lower in energy than those of the GW approximation using the RPA dielectric matrix [93] by about 0.2 eV, but are quantitatively comparable with those of the GW method using the model dielectric function (with $\epsilon_\infty = 10.0$) proposed by Hybertsen and Louie. [94] Note that the sX-FLAPW method has an obvious advantage over the above model dielectric function; the latter needs to calculate or assume the dielectric constant $\epsilon_\infty(\mathbf{r})$ which significantly changes in space at surfaces. [95]

Recently the sX-FLAPW method was also applied to describe band offsets in the strained InAs/InSb superlattices [24] and the Burnstein-Moss shift in a transparent conducting material, [96] In-doped CdO.

1.4 Application to semiconductor materials

In this section, we discuss how *ab-initio* electronic structure calculations can give important insights to designing novel materials suited to fit specific requirements for semiconductor device applications. Understanding the electronic properties of a given material is, in fact, the basis for the full comprehension of its thermal, transport and electric properties; thus, band structure calculations provide a powerful tool to explore real complex materials, – providing valuable information such as density of states, energy level transitions and carrier effective masses. In the following, we focus on semiconductors as intrinsic materials as well as fundamental constituents of more complex engineered materials, such as heterostructures and interfaces.

1.4.1 Bulk semiconductor materials

Ordered ternary systems, based on III-V semiconductors, constitute an important class of new materials of relevant scientific interest, whose structural, electronic and transport properties can be properly tuned, as a function of the constituent materials, alternating layer widths, strain or doping. The flexibility of their electronic properties has thus opened new perspectives in the technological field: superstructures and heterojunctions have recently been proposed as fundamental components in many applications, such as laser diodes, infrared detectors and non-linear optical devices [97].

In the following, we focus on the properties of ternary and quaternary [98] III-V semiconductor alloys that have been the subject of many experimental [99] and theoretical [100] studies. For example, it has been shown that the efficiency of thermophotovoltaic devices depends strongly on carrier diffusion lengths, which is related to the carrier effective mass and electron–hole pair lifetime. Both the effective mass and carrier lifetime are greatly affected by details of the band structure. With an aim at meeting specific technological requirements, our work focuses on understanding key chemical and structural effects which influence critical points in the conduction band of III-V alloys. Thus, we studied ordered $In_xGa_{1-x}X$ systems (with $x = \frac{1}{4}, \frac{3}{4}$ and X = As, Sb), which are promising materials for thermo–photovoltaic (TPV) devices. Moreover, we focus on the luzonite structure and in particular on the $\overline{\Gamma} - \overline{\Gamma}$ and $\overline{\Gamma} - \overline{L}$ transitions (the overbar denoting electronic states of ternary compounds), which can play a key role in determining the carrier lifetime in these materials.

Since the widely used density functional theory (DFT) in the local density approximation (LDA) [101] gives unphysical negative band gaps and incorrect excitation energies for these compounds, we use the screened-exchange LDA (sX-LDA) approach [102] to obtain quasiparticle energies within our FLAPW method [103]. This scheme goes beyond DFT by modelling the exchange hole within a non-local scheme [104] and is discussed in detail in Sect.III D above.

We recall that carriers in conduction side band valleys (*e.g.* those at L and X) in III-V semiconductors have much higher effective masses than those in the primary valley (Γ), because the band curvature at Γ is steeper. It follows that valence band electrons that are excited into these valleys will have relatively short diffusion lengths and, thus, will have a low probability of being collected at the leads of a TPV device. Moreover, carriers originally in the conduction band minimum at Γ may also be scattered into the L or X side valleys by

non-radiative processes, such as Auger or scattering due to impurities and alloy disorder. In essence, then, these indirect transitions are a loss mechanism competing with the direct $\Gamma - \Gamma$ transition. As a consequence, in addition to the $\overline{\Gamma} - \overline{\Gamma}$ ($E^{\overline{\Gamma}-\overline{\Gamma}}$) and $\overline{\Gamma} - \overline{L}$ gaps ($E^{\overline{\Gamma}-\overline{L}}$), it is particularly important to examine the so called "$\overline{\Gamma} - \overline{L}$ separation", $\Delta E^{\overline{\Gamma}-\overline{L}} = E^{\overline{\Gamma}-\overline{L}} - E^{\overline{\Gamma}-\overline{\Gamma}}$.

We examine [105] III-V ternary compounds based on InAs and InSb, alloyed with Ga at different concentrations and study the behaviour of the transitions of interest (namely $\overline{\Gamma} - \overline{\Gamma}$ and $\overline{\Gamma} - \overline{L}$) as well as the previously defined $\overline{\Gamma} - \overline{L}$ separation, as a function of volume and Ga concentration. In the calculations, we use experimental lattice constants [106] (the FLAPW calculated values [107] are within 0.5 $\%$ of experiment) for the binary compounds while the equilibrium lattice constants for the ternaries, $A_x\, B_{1-x}\, C$, were chosen according to Vegard's rule: $a_{Vegard} = (x)\, a_{AC} + (1-x)\, a_{BC}$. More details regarding the calculation can be found in Ref. [105] and are not repeated here.

As well-known, band folding in superstructures can cause a repulsion due to the coupling of two binary states of different symmetries folded onto states of the same symmetry in the ternary system. As a result, we find an appreciable reduction of the direct band gap in going from the average band gap to the luzonite calculated value.

If we concentrate on the $\overline{\Gamma} - \overline{\Gamma}$ and $\overline{\Gamma} - \overline{L}$ transitions [105], obtained within self-consistent sX-LDA (spin-orbit included) as a function of the cubic lattice constant, we note a dramatic volume effect on the direct energy gap: in all the systems considered, variations of the lattice constant of $\pm$ 4 $\%$ can change the band gap by as much as 0.7–0.8 eV. On the other hand, the effect of pressure on the $\overline{\Gamma} - \overline{L}$ transition is less evident (around 0.3 eV for changes of $\pm$ 4$\%$ in the lattice constant) [105]. In all the structures, the trend is almost perfectly linear, leading to a smaller band gap as the lattice constant is increased. Most remarkably, the compounds at different Ga concentrations follow the same trend: upon expansion of the lattice, the direct and indirect energy band gaps diminish with a slope af approximately -1.6 eV/a.u. and -0.5 eV/a.u., respectively. It is therefore possible to tune the transition energies by varying the lattice constant.

The $\overline{\Gamma} - \overline{L}$ separation as a function of volume for all systems considered is shown in Fig. 1.7: the energy separation is found to increase in all the systems. We recall that two major effects determine energy band gaps in III-V semiconductors: *(i)* the splitting of bonding and anti–bonding states (valence band and conduction band) due to chemical interactions between anion s, p states and cation s, p states and *(ii)* the width of each band. As cations and anions are brought into closer contact and reduce the lattice parameter, the splitting between bonding and anti–bonding states increases. At the same time, both the valence and the conduction bands are broadened due to the increased overlap of the wave functions. This second effect tends to close the band gap and to drive the system towards a metallic state. As it turns out, the splitting of the bonding–antibonding states prevails and one observes a band gap that widens with decreasing lattice parameter. Moreover, the volume dependence of the direct gap as well as the indirect gap is fairly independent of the specific chemical nature of the cation in the III-V semiconductors investigated in this study.

The $\overline{\Gamma} - \overline{L}$ separation is determined by an energy difference within a band and therefore depends primarily on the width of the conduction band, *i.e.* on the overlap of the states forming the conduction band. Since cationic s and p states dominate the conduction band, the width of the conduction band is related to the nature and distance of the cations. For typical Ga–Ga

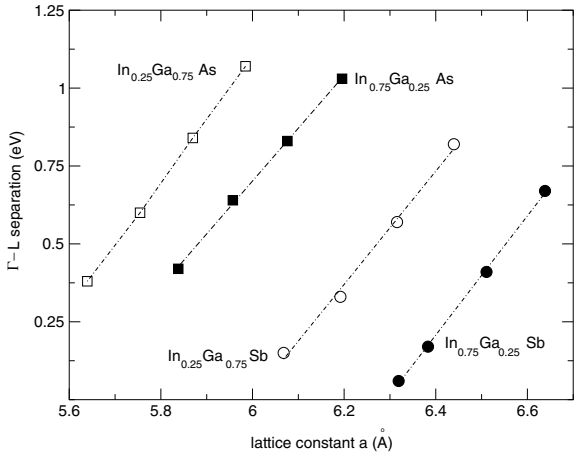

Figure 1.7: sX-LDA $\overline{\Gamma} - \overline{L}$ separation (in eV) for the luzonite structures as a function of the cubic lattice constant (in Å): Ga–rich InGaAs (empty squares); In–rich InGaAs (filled squares); Ga–rich InGaSb (empty circles); In–rich InGaSb (filled circles).

and Ga–In equilibrium spacings in III-V semiconductors, the Ga and In wave functions are quite similar and size effects prevail over chemical effects.

The dependence of the characteristic transitions on anion substitution (Sb versus As) is more complex. A complete study would of course imply the examination of disordered alloys: however, we can study the trend as a function of composition in ordered structures, considering only five different compositions: x = 0 and 1 (binary compounds), x = 0.25, x = 0.5 (CuAu system) and x = 0.75 (luzonite structures).

In Fig. 1.8 (a), the sX-LDA values for the direct transitions in InGaAs (circles) and InGaSb (stars) respectively, are shown together with a parabolic fit. The trend of the direct band gap versus composition is well represented by a parabolic behaviour, so that both As and Sb based compounds show an appreciable deviation from linearity ("bowing" [105]), mainly due to ordering effects. Moreover, the energy range that the direct gap can span is larger in As-based than in Sb-based compounds; therefore, InGaAs systems appear to be more suitable for band gap tuning purposes.

We show in Fig. 1.8 (b), the composition dependence of sX-LDA energy values for the first and second conduction band states at $\overline{L}$ (with respect to the valence band maximum) in InGaAs systems. As a result of the different composition–dependent character of the states involved [105], the strongest reduction in the $\overline{\Gamma} - \overline{L}$ transition is obtained for In-rich systems.

Our results can be summarized as follows: (*i*) both the direct band $\overline{\Gamma} - \overline{\Gamma}$ and indirect $\overline{\Gamma} - \overline{L}$ band gap decrease linearly as the lattice parameter is increased; (*ii*) the reduction is two times faster for the direct than for the indirect band gap; (*iii*) the slope of this linear behaviour is nearly independent of the chemical composition;(*iv*) the direct band gap shows a parabolic dependence on the ternary concentration with a non-negligible bowing parameter (*i.e.* about 1 eV). Therefore, pressure as well as composition can be used as valid tools to

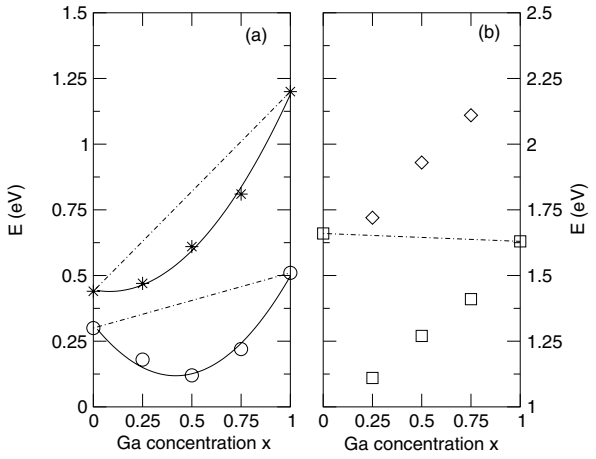

Figure 1.8: (a) sX-LDA direct band gaps (in eV) for InGaAs (circles) and InGaSb (stars) systems versus Ga concentration (the dot-dashed line shows a linear average of the direct band gaps in the binaries). (b) sX-LDA lowest (squares) and second-lowest (diamonds) indirect band gaps at $\overline{L}$ in InGaAs systems (the dot-dashed line shows a linear average of the indirect band gap in the binaries).

vary the transitions considered; in particular, due to the symmetry properties of the ternary luzonites, In-rich systems show a strong reduction of the $\overline{\Gamma} - \overline{L}$ transition, compared to the linear average of the $\Gamma - L$ band gaps in binaries. Finally, As-based systems are predicted to have larger $\overline{\Gamma} - \overline{L}$ gaps than Sb-based luzonites and therefore seem to be more promising for achieving high carrier mobilities in TPV device applications.

1.4.2 Semiconductor/semiconductor interfaces

Particular attention has been devoted to the electronic properties of interfaces between two semiconductors. The relevant quantity in this case is the relative position of the band gap which determines the potential steps (the so-called "valence band offset" (VBO) and "conduction band offset") that the different charge carriers (holes and electrons) have to overcome to allow conductivity across the interface. The relative alignment of the potential in the two materials in contact is determined by some intrinsic bulk properties (i.e. the position of the conduction and valence band with respect to the vacuum level) and by the charge rearrangement at the interface.

One important area is the determination of the valence band offset and its dependence on strain and growth conditions. As example, we consider homopolar isovalent heterostructures and in particular III-V superlattices (SLs), namely the common-anion system GaSb/InSb (lattice mismatch of 5.7 %) and the common-cation system InAs/InSb (lattice mismatch of 6.4 %), and concentrate on the effect of ordering direction and strain conditions determined by pseudomorphic growth on a given substrate [108]. The dependence of the VBO on the strain at an

Table 1.3: Interface term ($\Delta\ b$), strained bulk term ($\Delta\ E_b$) and valence band offset ($\Delta\ E_v$) for elastically relaxed $(GaSb)_3/(InSb)_3$ and $(InAs)_3/(InSb)_3$ -average substrate- superlattices as a function of the ordering direction. The suffix *nr* (*r*) denotes scalar-relativistic (relativistic) treatment. Energy differences (in eV) are considered positive if the level relative to the InSb layer is higher in energy with respect to the GaSb (InAs) layer in the common-anion (common-cation) system.

		$\Delta\ b$	$\Delta\ E_b^{(nr)}$	$\Delta\ E_b^{(r)}$	$\Delta\ E_v^{(nr)}$	$\Delta\ E_v^{(r)}$
$(GaSb)_3/(InSb)_3$	[001]	$+0.19$	-0.21	-0.12	-0.02	$+0.07$
	[111]	$+0.29$	-0.27	-0.13	$+0.02$	$+0.16$
$(InAs)_3/(InSb)_3$	[001]	$+0.07$	$+0.27$	$+0.47$	$+0.34$	$+0.54$
	[111]	$+0.17$	$+0.30$	$+0.51$	$+0.47$	$+0.68$

AC/BC junction is examined in different strain conditions: (i) pseudomorphic growth of a BC epilayer on an AC substrate; (ii) "free standing mode", equivalent to a system grown on an $A_{0.5}B_{0.5}C$ substrate ("Av. subs."); and (iii) pseudomorphic growth of an AC epilayer on a BC substrate.

On the other hand, the dependence of the VBO on the ordering direction is studied through a comparison of the [001] and [111] ordered SLs grown on a fixed substrate with average lattice constant, but different crystallographic orientations. This choice of the substrate, and the consequent lattice relaxation, lead to a small difference (about 1.4 $\%$) between the lattice constants of the binary constituents along the [001] and [111] growth direction. In analogy with the common experimental approach followed in photoemission measurements, we evaluate the VBO using core electron binding energies as reference levels [109]. We consider the $1s$-levels of the common atom C (*i.e.* Sb in the common-anion system and In in the common-cation system); other choices of core levels for different atoms would produce a VBO value differing from those reported here by at most 0.06 eV, which has thus to be considered as our numerical uncertainty.

The calculation of the VBO, $\Delta\ E_v$, is done according to the usual expression [109]:

$$\Delta\ E_v\ =\ \Delta\ b + \Delta\ E_b \tag{1.65}$$

where the interface term $\Delta\ b$ indicates the relative core level alignment of the two C atoms at opposite sides of the interface (one belonging to the AC side and the other to the BC side), while $\Delta\ E_b$ indicates the binding energy difference (relative to the valence band maximum (VBM)) of the same core levels evaluated in the binary constituents, opportunely strained to reproduce the elastic conditions of the SL. Table 1.3 lists the contributions due to the interface ($\Delta\ b$) and to the strained bulks ($\Delta\ E_b$) and the resulting values of the VBOs ($\Delta\ E_v$) as a function of the ordering direction; the superscripts (nr) and (r) indicate respectively the non-relativistic and relativistic (*i.e.* spin-orbit coupling treated in a perturbative approach) calculations.

We note that the first contribution ($\Delta\ b$) is seen to be sensitive to the crystallographic ordering (the two values for [001] and [111] growth axis differ by 0.1 eV), while the second contribution to the VBO ($\Delta\ E_b$) is almost uninfluenced by the ordering direction. Overall, we do not observe a marked dependence of the VBO on the crystallographic ordering at the

Table 1.4: Interface term ($\Delta\, b$), strained bulk term ($\Delta\, E_b$) and valence band offset ($\Delta\, E_v$) for $(GaSb)_3/(InSb)_3$ and $(InAs)_3/(InSb)_3$ [001] superlattices as a function of the substrate lattice parameter. Energy differences (in eV) are considered positive if the level relative to the InSb layer is higher in energy with respect to the GaSb (InAs) layer in the common-anion (common-cation) system.

		$\Delta\, b$	$\Delta\, E_b^{(nr)}$	$\Delta\, E_b^{(r)}$	$\Delta\, E_v^{(nr)}$	$\Delta\, E_v^{(r)}$
$(GaSb)_3/(InSb)_3$	GaSb-subs.	$+0.20$	$+0.10$	$+0.14$	$+0.30$	$+0.34$
	Av. subs.	$+0.19$	-0.21	-0.12	-0.02	$+0.07$
	InSb-subs.	$+0.18$	-0.47	-0.34	-0.29	-0.16
$(InAs)_3/(InSb)_3$	InAs-subs.	$+0.09$	$+0.65$	$+0.79$	$+0.74$	$+0.88$
	Av. subs.	$+0.07$	$+0.27$	$+0.47$	$+0.34$	$+0.54$
	InSb-subs.	$+0.05$	-0.04	$+0.18$	$+0.01$	$+0.22$

interface. Since it is well-known, for lattice matched structures [110, 111], that the band line-up is independent of interface orientation, the VBO change we find in going from the [001] to the [111] ordered SLs has to be related only to the appreciable mismatch which causes a different relaxation of the interface bond-lengths.

Let us now look at the role of the mismatch in determining the band line-up. Our results for [001] systems [108] with different pseudomorphic growth conditions are shown in Table 1.4. Note that the interface term $\Delta\, b$ is very similar in the same SL grown on the three different substrates, implying that the charge readjustment at the interface is almost independent of strain conditions. On the other hand, the $\Delta\, E_b$ term (*i.e.* the bulk contribution to the VBO) varies dramatically, showing that the core level binding energies in the strained binary suffer an appreciable change when growing the SL on different substrates. In fact, the energy of the topmost valence level (and hence the binding energy E_b) is determined by the interplay of the spin-orbit coupling and the non-cubic "crystal field" [112]. In particular, the second of these two effects is critically dependent on strain conditions, and is thus the origin of the large difference between the $\Delta\, E_b$ in Table 1.4. Furthermore, the clear trend shown by the VBO as a function of the substrate lattice constant is remarkable: the smaller the a_{sub}, the more the InSb topmost valence level is raised with respect to the VBM of the other SL constituent. Figure 1.9 illustrates the linear dependence of the VBO on the lattice parameter for the common-anion case (the results for common-cation are similar and hence not shown) and reports other theoretical results [110, 113–116]. Thus, GaSb/InSb and InAs/InSb SLs provide a good opportunity for VBO tuning: a range of about 0.5 eV for common-anion and of 0.7 eV for common-cation systems is covered by varying the strain conditions determined by the substrate.

In summary, our results indicate that under the same strain conditions, the ordering direction has quite a small effect on the band line-up. On the other hand, a much more important effect is due to pseudomorphic growth on different substrates: the high tunability of the VBO is evidenced by its linear decreasing trend as the substrate lattice constant is increased, mainly due to the bulk contribution to the band line-up.

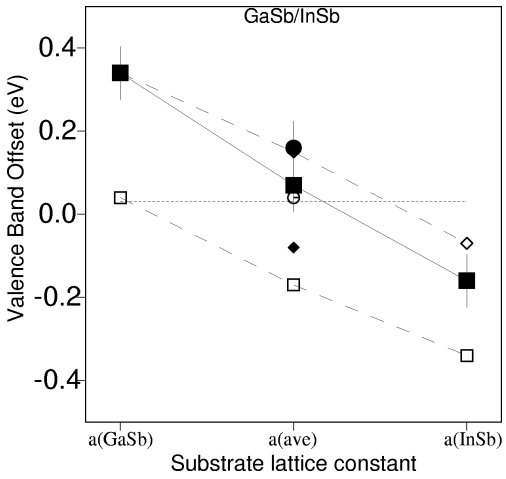

Figure 1.9: Valence band offset (in eV) for GaSb-InSb SLs as a function of the substrate lattice parameter. Our results (together with their error bars) are evidenced by filled squares ([001] SLs) or filled circles ([111] SLs) and solid line. The dotted line shows the behaviour of unstrained GaSb and InSb. Empty squares: Ref. [114]; empty diamonds: Ref. [113]; filled diamond: Ref. [116]; empty circles: Ref. [115].

1.4.3 Semiconductor/metal interfaces

GaN has certainly been one of the most studied compounds in the last few years, mainly because of both its interesting optical properties and remarkable thermal stability, which render this semiconductor particularly suitable for important technological applications. As is well-known, however, device performances depend on good metallic contacts and so the study of Schottky barrier heights (SBH) in GaN/metal systems is of great relevance: as an example, the performance of GaN–based laser diodes is still limited by the difficulty in making low resistance ohmic contacts. In this regard, surface reactivity and the presence of interface states are also seen to play a relevant role in Schottky barrier formation.

We investigated the GaN/Al system, which is considered to be a *reactive* interface due to the Ga–Al exchange reaction driven by AlN formation at the immediate interface; we studied the ideal interface [117], as well as the effects on the interface properties of some defects (such as atomic swap and $Ga_xAl_{1-x}N$ intralayers [118]) at the initial stages of SBH formation [119].

We here describe results of ab-initio calculations for GaN/M interfaces (with M = Ag, Au) [120] which are considered to be non–reactive [121] and compare the results (such as metal induced gap states (MIGS) and SBH) with those obtained for GaN/Al, in order to understand the dependence of the relevant electronic properties on the deposited metal. The interest in studying noble metal contacts resides in understanding the effect of the d states on the Fermi level position, which has been thought to be relevant in the case of GaAs/metal interfaces [122].

By comparing the partial density of states for the GaN/Al interface with the GaN/Au or GaN/Ag systems [120], we find that the main differences are found on the metal induced gap states which are seen to affect mainly the first layer close to the interface on both sides. The reason for this behavior is that in GaN/Au, the Au $3d$ states are occupied and interact strongly with the N p states, which are also filled. As a result, the antibonding states rise in energy above the semiconductor VBM and form peaks at around 1.5 eV, just in proximity to the Fermi level. Such features, present in the PDOS of the interface N and Au atoms [120], completely disappear on atoms far from the junction inside GaN and are absent in the GaN/Al case.

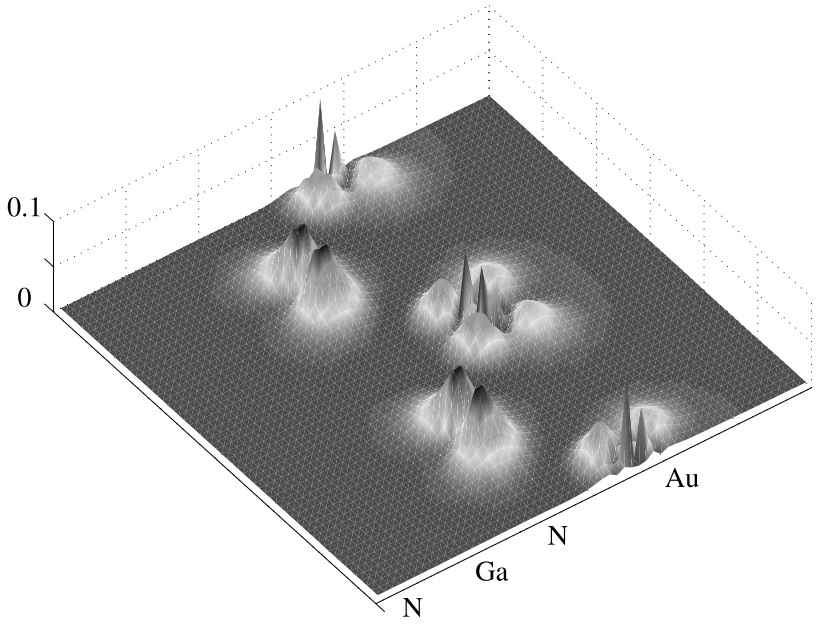

Figure 1.10: 3D plot of the GaN/Au MIGS charge density due to the DOS peak in proximity to E_F projected on a plane which cuts the N–Au interface bond. Values on the z-axis in electrons/cell.

The spatial location of the charge density corresponding to the peak around E_F is shown in Fig.1.10: these states, which have a clear anti–bonding character between N and Au, are mainly localized in the interface region with a resonant behavior inside the Au region (not shown) and a negligible charge density in the GaN region. A similar situation occurs in the GaN/Ag system (not shown) and was also reported for a [110] GaAs/Ag interface [122].

To calculate the values of the SBH, we adopt the usual procedure [109, 123] which takes core levels as reference energies. In analogy with the semiconductor heterostructures considered in the previous section, the potential discontinuity can be expressed as the sum of two terms: $\Phi_B = \Delta\, b + \Delta\, E_b$, where $\Delta\, b$ and $\Delta\, E_b$ denote an *interface* and *bulk* contribution, respectively. We evaluate $\Delta\, b$ by taking the difference of Ga $1s$ and the noble–metal $1s$ core levels energies in the superlattice: $\Delta\, b = E_{1s}^{Ga} - E_{1s}^{NM}$. On the other hand, the *bulk* contribution can be evaluated from separate calculations for bulk GaN and noble–metal, calculating binding energies differences referred to the Fermi level or the VBM (for further references see [109, 123]).

Table 1.5: Schottky barriers (in eV) at the GaN/Al, GaN/Ag and GaN/Au interfaces.

	GaN/Al	GaN/Au	GaN/Ag
Φ_B	1.51	1.08	0.87

Table 1.6: Interplanar distances (in Å) between the different atomic planes in the GaN/Al, GaN/Ag and GaN/Au interfaces (first three columns) and Schottky barrier heights (in eV – last column).

	d_{int}^{Ga-N}	d_{int}^{N-M}	d_{int}^{M-M}	Φ_B
GaN/Al	1.11	1.11	1.88	1.51
Step I	1.11	1.32	1.88	0.76
Step II	1.11	1.32	1.60	0.80
Step III	1.07	1.32	1.60	0.71
GaN/Ag	1.07	1.32	1.60	0.87

The p-type SBH values obtained, shown in Table 1.5, include a spin–orbit perturbation $\Delta_{SO}^{GaN} \approx 0.1$ eV, but do not include quasi–particle corrections. We note that the SBH values in the noble–metal case are lower than the SBH in the GaN/Al interface ($\Phi_{B_p}(GaN/Al)$ = 1.51 eV). To better understand this result, we should consider that the Al and noble metal interfaces differ in two main aspects: (*i*) different chemical species of the metal overlayer and (*ii*) different structural properties, $i.e.$ different bond lengths at the interface that include an interfacial strain contribution. In particular, Ag and Au structures show very similar d_{int}^{N-M} and d_{int}^{M-M} interplanar distances [120], which are at variance with those with Al. In order to separate the chemical from the strain contribution, we evaluate the SBH for three different structures that can be regarded as intermediate steps necessary to bring the GaN/Al structure to match perfectly the GaN/Ag one. We show in Table 1.6 the interface interplanar distances and final SBH values for the equilibrium GaN/Al and GaN/Ag systems and for the three intermediate interfaces. In the first structure (Step I), the interplanar d_{int}^{N-M} distance of the GaN/Al SL is taken equal to that optimized for the GaN/Ag SL ($d_{int}^{N-M} = 1.32$ Å): the SBH is reduced from 1.5 eV to 0.76 eV (this surprising result will be discussed in detail later on). As a second step (Step II), we change d_{int}^{M-M} to recover that calculated for the GaN/Ag structure: $d_{int}^{M-M} = 1.60$ Å. As expected, the SBH is remarkably less sensitive to this parameter. In the third structure (Step III), the Ga-N interface distance is brought to its value in the GaN/Ag superlattice, $d_{int}^{Ga-N} = 1.07$ Å, and we have a system where Al atoms perfectly replace Ag in GaN/Ag. Although this last structural change is very small (about 4 $\%$), the potential lineup change is significant, due to incomplete screening in the semiconductor. This SBH is quite close (within 0.2 eV) to the value found for the real GaN/Ag interface, showing that interface strain plays a more important role than does the bare chemical contribution.

The most surprising result of our tests is the very strong dependence of the SBH on the interface N–Al distance, whose variation represents the larger contribution to the difference between the GaN/Al and GaN/Ag (Au) SBHs. Test calculations have shown an almost perfect linear behaviour of Φ_B against d_{int}^{N-Al}, leading to an Al effective charge $Z_L^* = 0.08$, ($Z_L^* = Z_T^*/\epsilon_\infty$, where Z_T^* is the Born dynamical charge and ϵ_∞ is the electronic static dielectric constant). This result is in sharp contrast with the case of GaAs/Al [124], where no significant changes were found for small elongations of the As-metal interface distance, therefore resulting in $Z_L^* \sim 0$ – an almost perfect metallic behavior.

Let us make a few rough assumptions, such as a simple Yukawa–like screened potential, and consider a "metallic" behavior inside the semiconductor up to distances of the order of

λ, the MIGS decay length; the potential difference across the metal/semiconductor junction induced by displacements of the Al interface atom scales with the factor $e^{-k_{TF}\ \lambda}$. If we now estimate values of the Thomas–Fermi screening lengths, k_{TF}, using the GaN/Al and GaAs/Al superlattice value of the density of states at the Fermi level ($N(E_F)$ [120]), and the extrapolated values of the MIGS decay length ($\lambda_{GaN} \approx 2$ Å [120] and $\lambda_{GaAs} \approx 3$ Å [125, 126]), we find that a unit displacement of the interface Al atoms produces a potential change across the interface which is roughly 7 times larger in GaN/Al than in GaAs/Al. Considering the crudeness of this model, such an estimate is in satisfactory agreement with the first–principles results, which indicate a factor of ≈ 10 for the same ratio. In other words, GaAs screens out almost perfectly all the structural changes in the interface region (namely, displacements of the interface Al atoms), while the same is not true for GaN.

The dispersion of the SBH values seems to exclude a *Fermi level pinning* in the GaN case, as experimentally confirmed by the large spread in values reported in the literature for the SBH between GaN and different metals. In particular, let us recall those obtained for n-GaN/Ag and n-GaN/Au: $\Phi_{B_p}^{expt}(n-GaN/Ag) = 2.7$ eV [127] and $\Phi_{B_p}^{expt}(n-GaN/Au) \approx 2.4$ eV [128] and 2.2 eV [129, 130]. On the other hand, recent photoemission measurements [130] performed for Au deposited on p-type GaN show that the Fermi level is stabilized around 1 eV above the p-GaN VBM, in apparent good agreement with our calculated value ($\Phi_B = 1.08$ eV). The disagreement between some of these values and our calculated ones are certainly related to the different conditions of the GaN surface (which is ideal in our calculations and subject to different preparations in the experimental case); moreover, we considered the GaN zincblende structure and [001] oriented interfaces, whereas all the experimental samples are grown on [0001] wurtzite GaN.

In conclusion, our calculations show that there is an appreciable density of MIGS in the noble metal interfaces considered (even higher than in the GaN/Al case); however, the presence of the gap states is relevant in the interface layer only, being strongly reduced already in the sub–interface layer. We demonstrate that the appreciable SBH reduction in going from the free–electron to the noble–metal case is mostly due to structural effects.We find that the largest structural differences between the various GaN/M interfaces considered are related to the N-M interface distance, mainly determined by the different bonding nature between N and free–electron–like or noble metals. Finally, we are able to show that the lack of Fermi level pinning in GaN can be understood in terms of electrostatic effects related to variations of the interface anion–metal dipole: these effects are not properly screened in GaN, so that they contribute considerably to the final potential lineup at the interface.

1.5 Applications of the first-principles FLAPW approach to studies of magnetism

1.5.1 Magnetism

State-of-the-art *ab initio* density functional electronic structure calculations have achieved great success in the exciting field of thin film magnetism, in both explaining existing phenomena and, more importantly, in predicting the properties of new systems. [131] The prediction of enhanced magnetic moments with lowered coordination number at clean metal surfaces

and interfaces has stimulated theoretical and experimental investigations for new magnetic systems and phenomena in man-made transition metal thin films, which has accompanied the renaissance of magnetism and led to a major impact on the magnetic recording industry [132].

Significant progress has been made for the treatment of the weak spin-orbit coupling (SOC) in magnetic transition metal systems, using modern first principles electronic structure methods, especially the highly precise full potential linearized augmented plane wave (FLAPW) approach [133]: Very reliable results for the magneto-crystalline anisotropy (MCA) energies, E_{MCA}, can now be obtained for most magnetic thin films (a few tenths meV/atom), and even for magnetic cubic bulk materials (a few μeV/atom). This enables us to solve a long-standing problem – the first principles determination of the magnetostrictive coefficients in bulk transition metals, and their alloys and compounds with rare-earth metals. Using linear response theory, magneto-optical properties such as the magneto-optical Kerr effect (MOKE) and soft X-ray magnetic circular dichroism (MCD) can now be determined. The results presented here for several selected systems indicate that high quality *ab initio* calculations of magnetic systems can achieve high accuracy and precision for a wide range of SOC induced magnetic properties of transition metal and rare-earth metal systems.

1.5.2 Magneto-crystalline anisotropy in thin films.

The lack of neighbors and the lowered symmetry at a surface or interface can give rise to a so called *magnetocrystalline surface anisotropy*. In addition to the uniaxial contribution due to the lattice strian, the MCA energy in magnatic thin films grown on different substrates may reach as much as 10^{-3} eV/atom, a value which is sufficient to overcome the shape anisotropy and turn the easy axis of magnetization to the perperdicular direction [134–139]. This is a very important phenomenon for high-density magnetic recoding [140] and challenges theoretical understanding for the key factors that control the orientation of magnetization.

Most previous first principles calculations of E_{MCA} employ the MCA force theorem (with a perturbative treatment for the SOC Hamiltonian, $H^{soc} = \xi\ \mathbf{s} \cdot \mathbf{L}$) [141, 142],

$$E_{MCA} = E(\rightarrow) - E(\uparrow) = \sum_{occ'} \varepsilon_i(\rightarrow) - \sum_{occ''} \varepsilon_i(\uparrow) + O(\delta\rho^n) \tag{1.66}$$

where ε_i stands for the band energy of the ith state and the arrows in the parentheses denote the directions of magnetization. Strong numerical uncertainties have been encounted because the sets of occupied states, i.e., $\{occ'\}$ and $\{occ''\}$, were determined through the usual Fermi filling scheme which relies on the very limited information from the eigenvalues, ε_i [143]. One had to use a huge number of k-points ($>$10,000 in the two dimensional Brillouin zone for thin films) to obtain reliable E_{MCA} and thus only few model systems (e.g., free monolayer or simple alloys) could be treated. A simple solution for this problem is the state tracking (ST) approach in which the $\{occ'\}$ and $\{occ''\}$ states are determined according to their projections back to the occupied set of unperturbed states [144]. Since this procedure ensures the minimum change in the charge and spin densities, as required by the force theorem, and excludes possible randomness in the Brillouin zone (tracking at a given k-point), very stable MCA results were obtained with a relatively small number of k-points for magnetic thin films such as Fe, Co and Ni monolayers in the free standing case as well as on various substrates [145].

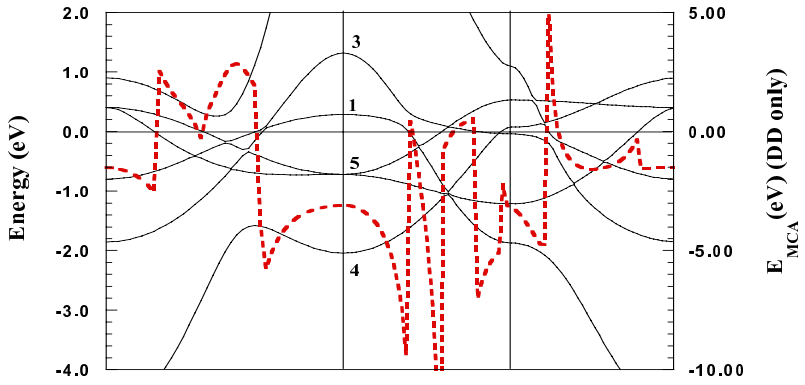

Figure 1.11: The calculated band structure (thin lines) and MCA energy of a free standing Co monolayer (a=4.83 a.u.) along the high symmetric lines in the two-dimensional Brillouin zone.

A torque (TQ) method can further depress the remaining uncertainties resulting from the SOC interaction between near-degenerate states around the Fermi level (so called surface pair coupling) [146]. We found for uniaxial systems, E_{MCA} can be directly evaluated through

$$E_{MCA} = \sum_{occ} < \Psi_i^{'}|dH/d\theta|\Psi_i^{'} > |_{\theta=45^\circ} = \sum_{occ} < \Psi_i^{'}|\partial H^{soc}/\partial\theta|\Psi_i^{'} > |_{\theta=45^\circ} \quad (1.67)$$

where $\Psi_i^{'}$ is the ith perturbed wave function. The advantage of the torque method is obvious since E_{MCA} is expressed as the expectation value of the angular derivative of H^{soc} and thus it is much more insensitive to distortions of the Fermi surface and only one Fermi surface needs to be determined.

To understand the behavior of MCA energies of magnetic films in different environments, it is instructive to analyze the electronic origin of the MCA energy for free standing magnetic monolayers. The k-distributions of the MCA energy, $E_{MCA}(\overrightarrow{k})$, and the band structures of a Co monolayer, for example, are plotted in Fig. 1.11 along the high-symmetry directions in the 2D BZ. The obvious correlation between major E_{MCA} changes and the locations of Fermi surfaces (where bands cross the Fermi level) indicates some simple physical insights for MCA, which once was thought to originate from very sophisticated interactions. Note that (i) only SOC interaction between the pairs of states across E_F contributes to E_{MCA}, and (ii) the pair with the same (different) magnetic quantum number(s), m, leads to a positive (negative) contribution to E_{MCA}.

From Fig. 1.11, the large negative MCA energy for the Co monolayer (-1.34 meV/atom) is mainly from the contributions around the $\overline{M}$ point. This is due to the SOC interaction between the occupied $d_{xz,yz}$ $(m = \pm 1)$ states and the unoccupied d_{z^2} state $(m = 0)$. Knowing the detailed information about the origin of MCA for model system, one can thus understand the MCA behaviors of more complicated systems and furthermore tailor the MCA energy. For Co thin films, for example, one can enlarge the energy separation between the Co $d_{xz,yz}$ and d_{z^2} through the proximity effect of different substrates. Owing to the Co-Cu d-band hybridization, for example, the $d_{xz,yz}$ states are splitted and diluted in a wide energy range for

these systems. As a result, the negative contribution to E_{MCA} around $\overline{M}$ is drastically reduced. The MCA energy for Cu/Co/Cu(001) becomes positive (0.54 meV/adatom, indicating a strong perpendicular anisotropy), as observed experimentally [135, 136]. Many calculations have been done in this direction to study the effects of metal substrates or capping layers on the MCA of ultra-thin magnetic thin films. It is well established now that high quality first principles theory can obtained quite satisfactory results of uniaxial E_{MCA} for magnetic thin films [131].

To optimize the atomic structures, however, the generalized gradient approximation (GGA) [147] improves the calculation since the description of local spin density approximation [148] for the exchange-correlation interaction is known to significantly underestimate the lattice constants of 3d transition metals. For example, with the in-plane lattice constant fixed (a=4.83 a.u.), the optimized Co-Cu interlayer distance in Co/Cu(001) and Cu/Co/Cu(001) is 3.44 a.u. from GGA calculations [149], but it is only 3.08–3.11 a.u. if the LDA is adopted [150, 151]. The large difference in atomic arrangement, as well as the gradient correction in exchange-correlation functionals, may strongly affect all the magnetic properties such as magnetic moments, magnetic ordering and MCA energies [152].

1.5.3 Higher-order magneto-crystalline anisotropy

The first principles determination of high-order E_{MCA} such as in cubic bulk magnetic Fe, Co and Ni or the in-plane anisotropy in square lattice is still one of the most challenging problems in condensed matter physics. The high-order E_{MCA} in these systems is extremely small – only about $1\mu eV$/atom. Quantitatively, such a scale of energy difference is very close to or beyond the limit of precision of total energy calculations for most approaches. Our FLAPW calculations found that the in-plane coefficients [153] of E_{MCA} is extremely sensitive to the change in environment and structural relaxation [149]. For cubic magnetic crystals, early calculations with the force theorem repeatedly gave the wrong sign for either Fe or Ni (or both). Using the LMTO-ASA approach, Daalderop *et al.* [154] obtained the right magnitude of E_{MCA}, but the wrong easy axis for hcp Co and fcc Ni. Guo *et al.* [155] and Strange *et al.* [156] also obtained the wrong easy axis or wrong magnitude for bulk Fe and Ni in their LMTO and KKR calculations. Based on the full potential LMTO method, Trygg *et al.* [157] treated the SOC Hamiltonian self-consistently but obtained (with $spd-$basis functions) almost the same results as Daaderop *et al.*. The accuracy of total energy calculations was re-examined by Halilov *et al.* [158], also using the LMTO-ASA method with combined corrections. They obtained the correct easy axis for all three metals through total energy calculations with a larger set of k-points. Beiden *et al.* [159] implemented a real-space locally self-consistent multiple scattering method. Again, they obtained the wrong easy axis for Ni and oscillatory results for hcp Co.

We extended the torque method [146] for the determination of E_{MCA} in cubic crystals, where the total energy can be well approximated in the form

$$E = E_0 + K_1 \left(\alpha_1^2\alpha_2^2 + \alpha_1^2\alpha_3^2 + \alpha_2^2\alpha_3^2\right) + K_2\alpha_1^2\alpha_2^2\alpha_3^2 \tag{1.68}$$

Here α_1, α_2 and α_3 are directional cosines referred to the cubic edges along the x, y and z

axes. Clearly, the E_{MCA} can be evaluated from the coefficients of K_1 and K_2 as

$$E_{111} - E_{001} = \frac{K_1}{3} + \frac{K_2}{27}; \qquad E_{110} - E_{001} = \frac{K_1}{4} \tag{1.69}$$

As in Eq. (3) for thin films, the torque here, T(θ), is defined as the derivative of the total energy with respect to the polar angle away from the z-axis (denoted as θ below). To determine the values of K_1 and K_2, we focus on two special cases: (1) for $\alpha_2 = 0$ ($\alpha_1^2 = 1 - \alpha_3^2$), we have

$$T_1(\theta) \equiv \left.\frac{dE(\theta)}{d\theta}\right|_{\phi=0^\circ} = \frac{K_1}{2}\sin(4\theta) \tag{1.70}$$

and (2) for $\alpha_1 = \alpha_2$ ($\alpha_1^2 = \alpha_2^2 = (1 - \alpha_3^2)/2$)

$$T_2(\theta) \equiv \left.\frac{dE(\theta)}{d\theta}\right|_{\phi=45^\circ} = T_1(\theta) + \frac{\sin(2\theta)\sin^2(\theta)}{4}\left[2K_1 + K_2(3\cos^2\theta - 1)\right] \tag{1.71}$$

where ϕ denotes the azimuzal angle in the xy plane. We have

$$T_1(\theta = 22.5^\circ) = K_1/2 \qquad T_2(\theta = 45^\circ) = (2K_1 + K_2/2)/8 \tag{1.72}$$

and finally the MAE coefficients K_1 and K_2 can be evaluated very efficiently through

$$K_1 = 2T_1(\theta = 22.5^\circ) \qquad K_2 = 16T_2(\theta = 45^\circ) - 4K_1 \tag{1.73}$$

The calculated K_1 and K_2 for bcc Fe with the FLAPW-GGA approach are given in Fig. 1.12. While K_1 is found to still be oscillatory but stable in sign with 70×70×70 k-points in the full BZ for the cubic cell (with two atoms), K_2 changes its sign very rapidly. It appears that more k-points are needed to get a converged result for K_2. Fortunately, K_2 remains very small and does not affect the anisotropy energy too much (cf., the 1/27 scaling factor in Eq. 6 for $E_{111} - E_{001}$). The calculated E_{MCA} ($E_{111} - E_{001}$) for bcc bulk Fe is 0.9 (0.7) μeV/atom with GGA (LDA) formula (the (001) direction is the easy axis). The LDA value is very close to the results obtained by Daalderop *et al.* (0.5 μeV/atom, with the force theorem) [154], Trygg *et al.* (0.5 μeV/atom, with total energy) [157] and Beiden *et al.* (0.78 μeV/atom, with a real space approach). The discrepancy between theory (0.5–0.9 μeV/atom) and experiment (1.4 μeV/atom) appears not to be due to numerical problems, but to other physical reasons such as possible orbital polarization [157, 160].

For fcc Co and Ni, the calculated E_{MCA} results with the FLAPW approach are also very close to those obtained in previous density functional calculations. With 50×50×50 k-points in the full BZ for the cubic cell (with four atoms), the correct easy axis is obtained for Co, but not for Ni. In addition, the theoretical E_{MCA} results are much smaller in magnitude than the experimental data. The failure of the density functional description for E_{MCA} in bulk fcc Ni appears to be mainly due to $s - d$ charge transfer. Note that with a=6.66 a.u., the calculated spin magnetic moments of Ni are 0.62 μ_B and 0.67 μ_B with LDA and GGA, respectively. These values are markedly larger compared to the experimental result, 0.57 μ_B. Since the spin magnetic moment in Ni is almost equal to the number of holes in its minority spin d-band, this discrepancy indicates that the Ni-d band has about 0.05–0.10 fewer electrons than what it should have. Such an error in band filling is enough to change the sign of E_{MCA}. E_{MCA} ($E_{111} - E_{001}$) could change sign by moving only 0.03 electrons from the Ni s-band to its d-band.

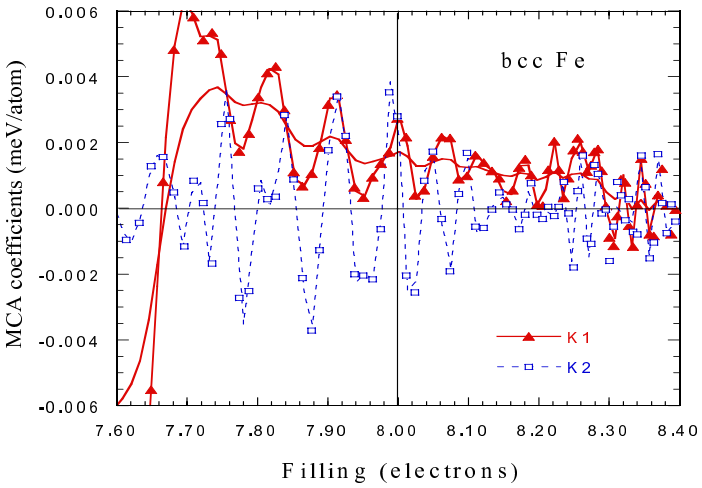

Figure 1.12: MCA coefficients of the bulk bcc Fe with GGA. The bold solid lines are for k_1 (with either 0 or 15 meV Gaussian broadening) while the thin dashed line is for k_2.

1.5.4 Magnetostriction

In general, the size of the magneto-elastic strain induced by rotation of the magnetization depends on the directions of the measured strain and of the spin moment with respect to the crystalline axes of the material. For a cubic material, the directional dependence of the fractional change in length can be expressed in terms of the direction cosines of the magnetization (α_i) and of the strain measurement direction (β_i) with respect to the crystalline axes [161]

$$\frac{\Delta l}{l_0} = \frac{3}{2}\lambda_{001}\left[\sum_{i=1}^{3}\alpha_i^2\beta_i^2 - \frac{1}{3}\right] + 3\lambda_{111}\sum_{i\neq j}^{3}\alpha_i\alpha_j\beta_i\beta_j \tag{1.74}$$

If the measurement is carried out along the (001) direction for example, $\beta_x = \beta_y = 0$ and $\beta_z = 1$, then Eq. (1.74) can be simplified as $\frac{\Delta l}{l_0} = \frac{3}{2}\lambda_{001}[\alpha_z^2 - \frac{1}{3}]$ or further, for systems with a single domain

$$\lambda_{001} = \frac{2}{3}\frac{l_0(\alpha_z = 1) - l_0(\alpha_z = 0)}{l_0(\alpha_z = 1)} \tag{1.75}$$

Clearly, λ_{001} represents the change in length along (001) when the magnetization turns from the x,y plane to the z direction.

The equilibrium length along the z direction, l_0, can be obtained by fitting the calculated total energy as a quadratic function of l

$$E(\alpha_z = 1) = al^2 + bl + c; \qquad E(\alpha_z = 0) = E(\alpha_z = 1) + E_{MCA}(l) \tag{1.76}$$

and so

$$\lambda_{001} = -2E'_{MCA}/3b \tag{1.77}$$

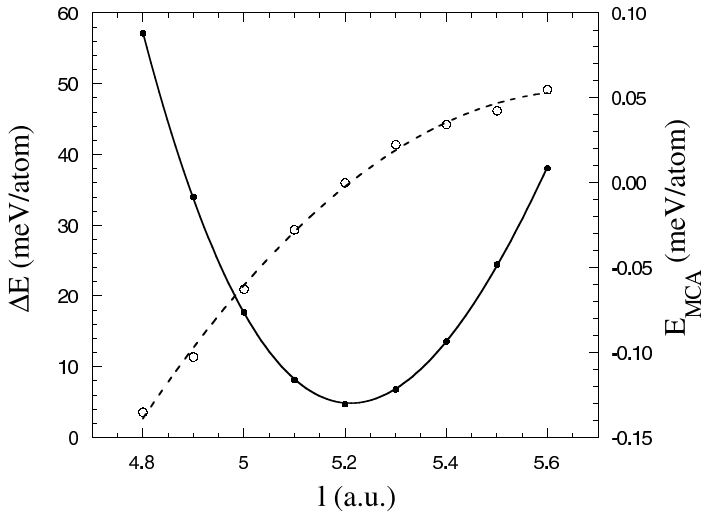

Figure 1.13: The calculated total and MCA energies of the bulk bcc Fe (with LDA) with respect to the length of c-axis. The constant volume distortion mode was adopted

Here $E'_{MCA} = dE_{MCA}/dl$, which is much smaller than the value of b. Note that b is always negative (since both a and l_0 are positive), and thus λ and E'_{MCA} have the same sign.

As an important benchmark test, the magnetostriction coefficients of cubic bulk magnetic transition metals are studied first. As shown in Fig. 1.13, the calculated MCA energy for the bulk bcc Fe is a smooth monotonic function of the vertical strain. The slope of E_{MCA} and thus the magnetostrictive coefficient (λ_{001}) are found to be positive for Fe and Co but negative for Ni [162]. This means that bulk Fe and Co (Ni) stretch (shrink) along the direction of magnetization, a conclusion that agrees well with experiment.

Quantitatively, the value of λ_{001} depends sensitively on the distortion mode (i.e., Poisson's ratio). As listed in Table 1.7, the value of Poisson's ratio for Fe, Co and Ni optimized through total energy minimization is about 0.40, which is very close to that obtained using the measured elastic stiffness constants ($\sigma = -c_{12}/(c_{11} + c_{12})$) for bulk Fe and Ni (0.37–0.38). As a result, satisfactory quantitative agreement is achieved for λ_{001} between our (zero temperature) theory and experiment. The theoretical result can be further improved by using the GGA [147]. As seen in Table 1.7, LDA leads to a 3% underestimation for the lattice constant and a more substantial difference for the spin magnetic moments at the equilibrium geometry. With GGA, most of the calculated values of the various magnetic properties are closer to experiment, especially for Fe in which the number of holes with majority spin is very sensitive to the change of environment.

The inverse effect of magnetostriction is strain-induced uniaxial E_{MCA} in thick epitaxial magnetic films. This effect is believed to play a key role for the spin-reorientation of Ni/Cu(001) when the Ni film becomes thicker than 7 layers [163] and magnetic anisotropy of other magnetic thin films [164]. For Ni/Cu(001), we calculated the volume contribution to the MCA energies of Ni films from fct bulk Ni with the fixed lateral lattice constant of the

Table 1.7: Calculated equilibrium lattice constants a (in a.u.), Poisson's ratio (σ), spin and orbital magnetic moments (M_S and M_L, in μ_B), $E_{111} - E_{001}$ (E_{MCA}, determined with the experimental lattice constants, in μeV) and magnetostriction coefficients (in 10^{-6}) obtained with LDA and GGA corrections.

	a	σ	M_S	M_L	E_{MCA}	λ_{001}
bcc Fe						
LDA	5.20	-0.409	2.05	0.048	0.7	52
GGA	5.37	-0.486	2.17	0.045	0.9	29
EXP	5.41	-0.368	2.22	0.08	1.4	21
fcc Co						
LDA	6.48	-0.374	1.59	0.076	$---$	92
GGA	6.67	-0.396	1.66	0.073	-0.6	56
EXP	6.70	$---$	1.72	$---$	-1.8	79
fcc Ni						
LDA	6.46	-0.332	0.62	0.049	0.7	-63
GGA	6.64	-0.376	0.66	0.050	0.8	-56
EXP	6.66	-0.376	0.57	0.05	-2.7	-49

Cu(001) substrate (a=6.831 a.u.) [165]. The E_{MCA} is found to be a linear function of the lattice distortion along the c-axis. When the measured length of the c-axis (l = 6.43 a.u.) is adopted, the calculated MCA energy is +65μeV/atom. This result agrees vary well with experiment, which gave E_{MCA} =+70 μeV/atom extrapolated to zero temperature [166]. Using the FLMTO approach, Hjortstam *et al.* [167] obtained a value of 60 μeV/atom for the strain induced E_{MCA}.

If the orbital polarization is included, Hjortstam *et al.* [167] obtained E_{MCA} =140 μeV/atom for fct Ni. They also gave a very large magnetostrictive coefficients for fct Ni, $\lambda_{001} = -270 \times 10^{-6}$ and $\lambda_{111} = -107 \times 10^{-6}$, which are almost three times larger in magnitude than experiment [168, 169], $\lambda_{001} = -71 \times 10^{-6}$ and $\lambda_{111} = -39 \times 10^{-6}$. Thus, it appears that the orbital polarization term, while improving the calculated orbital magnetic moments, overcorrects the SOC far too much for the determination of E_{MCA}. By contrast, our recent FLAPW-GGA-SOC calculations obtained $\lambda_{001} = -71 \times 10^{-6}$ and an equilibrium length of the c-axis of l_0 =6.43 a.u.; both results are in excellent agreement with experiment.

Now, Ni_xFe_{1-x} and Ni_xCo_{1-x} magnetic alloys are widely used in magnetic recording technology and invar materials. The calculated magnetostrictive coefficients are listed in Table 1.8. Reasonable agreement has been achieved for the alloys studied, providing that the experimental data taken quite a long time ago strongly depend on the temperature and composition [170]. Our recent studies for FeGa alloys indicate that the observed giant magnetostriction is not necessarily due to the ground state. While the B_2-like structure is unstable under tetragonal distortion and higher in energy that the $L1_2$ and DO_3 structure, it provides positive magnetostrictive coefficients (as observed in experiments) while the other two phases give negative magnetostriction. Owing to the reduced hybridization between Fe atoms, the magnetostrictive coefficient, λ_{001}, is enhanced by a factor of 10–20 compared to that for bulk bcc Fe.

Table 1.8: Calculated lattice constants a (in plane, in a.u.) and c (along z,in a.u.), magnetic moments (**M**, in μ_B), the Poisson ratio (σ), magneto-crystalline anisotropy energy (E_{MCA}, in μeV/cell) and magnetostriction coefficient (λ_{001}, in 10^{-6}). The corresponding experimental data are given in parentheses.

	FeCo	$FeCo_3$	FeNi	$FeNi_3$	CoNi	$CoNi_3$
a	5.38(5.39)	6.70	6.76(6.76)	6.70(6.71)	6.62(6.67)	6.66(6.65)
c	5.38(5.39)	6.70	6.76(6.76)	6.70(6.71)	6.78(6.67)	6.66(6.65)
E_{MCA}	0	0	63	0	143	0
σ	-0.35	-0.36	-0.33	-0.35	-0.34	-0.36
λ_{001}	83(126)	-68	$10(10-26)$	27(13)	$42\ (40-100)$	33

Table 1.9: Calculated and measured (in parentheses) lattice constant, a, total magnetic moment per perimitive unit cell, M, spin magnetic moment of itinerant electrons in rare-earth (M_{RE}) and transition metal M_{TM}, and magnetostrictive coefficient, λ_{001} for different compounds.

	a (a.u.)	M(μ_B)	$M_{RE}(\mu_B)$	$M_{TM}(\mu_B)$	$\lambda_{001}(10^{-6})$
$GdCo_2$	13.72(13.68)	4.99(4.9)	0.46	-1.24	$-407(-1200)$
$NdCo_2$	13.84(13.77)	5.28(3.8)	0.32	-1.14	-171
$SmCo_2$	13.74(13.71)	2.73(2.0)	0.52	-1.26	-290
$ErCo_2$	13.70(13.50)	7.06(7.0)	0.28	-1.10	$-516(-1000)$
$GaFe_2$	13.85(13.94)	3.85(2.8)	0.58	-1.96	44(39)

Rare-earth intermetallic compounds have attracted great attention since the late 1960's due to their extraordinary magnetic properties, especially their large magnetostrictive coefficients (10^{-3}) at room temperature [161,171,172]. While it was believed that the localized rare-earth $4f$ states play a dominant role in magnetization and magneto-elastic coupling, recent experiments found that the effects of itinerant states can be equally important [161, 173]. Although a phenomenological approach was developed long ago to describe the dependence of single crystal magnetostriction on magnetization and measurement directions, the magnetostrictive coefficient for a given material, especially the contribution of itinerant electrons, has never been accurately calculated [161].

Very recently, we investigated the magnetostrictive properties of several rare-earth compounds in the C15 cubic Laves phase structure, a close-packed arrangement of spheres with two different sizes. As listed in Table 1.9, the calculated magnetostrictive coefficient agree with the experimental data available. Furthermore, the large values of λ_{001}indicate that the contribution from itinerant electrons is comparable to that from the f-shell. Using a rigid band picture, we found that the difference in the magnetostrictive behaviors of $GdFe_2$ and $GdCo_2$ is mainly due to the change in band filling. A $GdFe_xCo_{2-x}$ compound ($x = 0.9 - 1.2$) is predicted to be a strong magnetostrictive material with a positive sign for λ_{001} ($+450 \times 10^{-6}$)

1.5.5 Magneto-optical effects

The magneto-optical Kerr effect (MOKE) is now a widely used *in situ* tool for studies of magnetic properties of thin films and surfaces [175]. It is known that the MOKE is induced by the SOC interaction among the d-states. In the polar geometry, the Kerr rotation angle, θ_K, and ellipticity, ε_K, can be expressed as

$$\theta_K + i\varepsilon_K = \frac{-\sigma_{xy}}{\sigma_{xx}\sqrt{1 + \frac{4\pi i}{\omega}\sigma_{xx}}} \tag{1.78}$$

where the diagonal (σ_{xx}) and off-diagonal (σ_{xy}) elements of the optical conductivity tensor can be evaluated by means of Kubo-Greenwood linear response theory [176] as

$$\sigma_{\alpha\beta} = \frac{-ie^2}{m^2\hbar\Omega}\sum_{\mathbf{k}}\sum_{mn}\frac{f_m - f_n}{\omega_{mn}}\frac{\mathbf{\Pi^{\alpha}_{nm}}(\mathbf{k})\mathbf{\Pi^{\beta}_{mn}}(\mathbf{k})}{\omega - \omega_{mn} + i\delta} \tag{1.79}$$

Here f_m is the Fermi function; ω_{mn} is the energy difference ($\hbar\omega_{mn} = \epsilon_m - \epsilon_n$) and $\Pi^{\alpha}_{nm}(\mathbf{k})$ is the momentum matrix element.

Following the pioneering work of Wang and Callaway [177], MOKE spectra can now be calculated with quite satisfactory results with several first principles approaches [178]. Prototype studies for bulk Fe, Co and Ni have been recently reported by many groups with basically similar results [179–183]. Theoretical calculations have been performed for many different kinds of materials, such as compounds, Heusler alloys, surfaces and multilayers [184–187]. To describe the strong correlation effects, the LDA+U scheme is usually employed when rare-earth and actinide elements are involved [188]. In general, Kerr rotation spectra vary with composition in a rather complex and unforeseeable way, even for simple systems like Co-Ni alloys. Therefore, the first principles calculations are essential to explain the measured MOKE spectra.

Stimulated by interesting experimental observations by Weller *et al.* [189], several groups have paid close attention to the anisotropy of MOKE in hcp bulk Co, CoPt and FePt alloys and compounds [190]. From our recent FLAPW calculations [191], we found that the anisotropy of the MOKE spectra for bulk Co is negligible for either the (001) or (111) magnetization direction.

1.5.6 Magnetic circular dichroism

The possibility to determine both the orbital and spin moments (denoted as $< S_z >$ and $< L_z >$, respectively) directly from X-ray magnetic circular dichroism (MCD) [192] spectra by applying recently proposed simple but powerful sum rules has attracted considerable excitement and attention [193]. As stated in the MCD sum rules, integrations of the MCD and total absorption spectra relate directly to $< L_z >$, $< S_z >$ and $< T_z >$ for the unoccupied states

$$\frac{I_m = \int_{L_3+L_2}\sigma_m dE}{I_t = \int_{L_3+L_2}\sigma_t dE} = \frac{< L_z > /2}{N_h = \int \rho(E)dE} \tag{1.80}$$

Table 1.10: Calculated values of $< L_z >$, $< S_z >$, $< T_z >$, $< S_e >$ and N_h and sum rule errors $R_1 = \frac{I_m}{I_t}/\frac{<L_z>}{2N_h} - 1$, $R_2 = \frac{I_s}{I_t}/\frac{<S_e>}{N_h} - 1$ and $R_3 = \frac{I_m}{I_s}/\frac{<L_z>}{2S_e} - 1$ for Ni(001), Co(0001) and Fe(001) surface (S) and bulk-like center (C) layers.

Atom	$< L_z >$	$< S_z >$	$7< T_z >$	$< S_e >$	N_h	R_1	R_2	R_3
Ni(S)	-0.069	-0.67	-0.082	-0.250	1.81	0.27	0.52	-0.10
Ni(C)	-0.051	-0.62	-0.027	-0.215	1.66	0.20	0.36	-0.11
Co(S)	-0.090	-1.61	0.240	-0.457	2.60	0.11	0.24	-0.09
Co(C)	-0.078	-1.52	0.014	-0.502	2.55	0.09	0.22	-0.10
Fe(S)	-0.111	-2.71	0.230	-0.828	3.70	0.10	0.16	-0.04
Fe(C)	-0.063	-2.10	0.028	-0.691	3.34	0.04	0.15	-0.09

and

$$\frac{I_s = \int[\sigma_s = \int(\sigma_{m,L_3} - 2\sigma_{m,L_2})]dE}{I_t = \int_{L_3+L_2} \sigma_t dE} = \frac{< S_e >= (< S_z > +7 < T_z >)/3}{N_h} \quad (1.81)$$

where $\sigma_m = \sigma_+ – \sigma_-$ and $\sigma_t = \sigma_+ + \sigma_- + \sigma_z$. **T** is the spin magnetic dipole operator, i.e., $\vec{T} = \frac{1}{2}[\vec{S} - 3\hat{r}(\hat{r} \cdot \vec{S})]$, ($T_z = S_z(1 - 3\cos^2\theta)/2$ for $\vec{S}$ aligned along the z direction). The number of valence holes, N_h, can be obtained from an integration over the unoccupied density of states ($\rho(E)$).

We carried out first principles calculations to check the validity and applicability of the sum rules for transition metal systems [194]. As listed in Table 1.10, the deviation of the spin and orbital sum rules is denoted by $R_1 = \frac{I_m}{I_t}/\frac{<L_z>}{N_h} - 1$, and $R_2 = \frac{I_s}{I_t}/\frac{<S_e>}{N_h} - 1$. Obviously, the orbital sum rule is seen to work very well (within 10%) for Fe and Co systems, and the error becomes larger for Ni since the number of s,p holes is almost equal to that of d holes (we used an energy cutoff of 6 eV above E_F). By contrast, the errors of the spin sum rule are much larger: it actually fails severely for the Ni surface since R_2 is as large as 52%. A better way is to combine the $< L_z >$ and $< S_z >$ sum rules, as was done recently in some experiments on bulk transition metals [195]. From our first principles calculations, we found that the error in the ratio $R_3 = \frac{I_m}{I_s}/\frac{<L_z>}{<S_e>} - 1$, is 10% or so for all systems studied.

In addition, the $< T_z >$ term in the spin sum rule is negligible only for atoms in cubic symmetry. For atoms in non-cubic environments such as surfaces and interfaces, as seen from Table 1.10, its importance is obvious, since its magnitude becomes 8.5%, 12% and 15% of $< S_z >$ for Fe(001), Ni(001) and Co(0001), respectively. The hybridization between different l shells is the main mechanism causing the failure of the MCD spin sum rule for transition metals [194]. Recently, these sum rules have been extensively applied for the determination of spin and orbital magnetic moments, magnetic ordering and element-specific hysteresis and MCA energies (a more comprehensive review is given by J. Stöhr [196]).

Based on a second order perturbation theory, Bruno [197] showed that E_{MCA} in magnetic thin films can be related to the anisotropy of the orbital magnetic moment ($< L_z > - < L_x >$). This model was corroborated by Weller *et al.* [198] and Dürr *et al.* [199], who measured the value of $< L_z > - < L_x >$ for Au/Co/Au, Ni and Co/Ni thin films with the MCD

sum rules. However, the relation is not universally valid. As pointed out by van der Laan [200] recently, the proportionality between E_{MCA} and $< L_z > - < L_x >$ relies on an assumption that all d-holes are in the minority spin band. This condition is usually satisfied for Co and Ni systems but not for Fe systems.

Acknowledgements

The work reported here was supported by the U.S. National Science Foundation through its MRSEC program at Northwestern University and by the U.S. Office of Naval Research. We are grateful to our various collaborators listed in the papers referenced and to Mary V. Lesniak and Dr. Julia E. Medvedeva for their invaluable assistance with this manuscript.

References

[1] P. Hohenberg and W. Kohn, Phys. Rev. **136,** B864 (1964).
[2] W. Kohn and L.J. Sham, Phys. Rev. **140,** A1133 (1965).
[3] L. Hedin, Phys. Rev. **139,** A796 (1965).
[4] J.P. Perdew and A. Zunger, Phys. Rev. B **23**, 5048 (1981).
[5] V.I. Anisimov, J. Zaanen, and O.K. Andersen, Phys. Rev. B **44**, 943 (1991).
[6] R.T. Sharp and G.K. Horton, Phys. Rev. **90**, 317 (1953).
[7] T. Kotani, Phys. Rev. Lett. **74**, 2989 (1995); T. Kotani, J. Phys. **10**, 9241 (1998).
[8] M. Städele, J.A. Majewski, P. Vogl, and A. Görling, Phys. Rev. Lett. **79**, 2089 (1997).
[9] L. Fritsche, Phys. Rev. B **33,** 3976 (1986).
[10] L. Fritsche, Physica B **172,** 7 (1991).
[11] L. Fritsche and Y.M. Gu, Phys. Rev. B **48,** 4250 (1993).
[12] B.M. Bylander and L. Kleinman, Phys. Rev. B **41,** 7868 (1990).
[13] A. Seidl, A. Görling, P. Vogl, J.A. Majewski, and M. Levy, Phys. Rev. B **53,** 3764 (1996).
[14] F. Gygi and A. Baldereschi, Phys. Rev. Lett. **62,** 2160 (1989).
[15] S. Massidda, A. Continenza, M. Posternak, and A. Baldereschi, Phys. Rev. Lett. **74,** 2323 (1995).
[16] A. Continenza, S. Massidda, and M. Posternak, Phys. Rev. B **60,** 15699 (1999).
[17] S. Massidda, M. Posternak, A. Baldereschi, and R. Resta, Phys. Rev. Lett. **82,** 430 (1999).
[18] S. Massidda, A. Continenza, M. Posternak, and A. Baldereschi, Phys. Rev. B **55,** 13494 (1997).
[19] M.M. Rieger and P. Vogl, Phys. Rev. B **52**, 16567 (1995).
[20] R.W. Godby, M. Schlüter, and L.J. Sham, Phys. Rev. B **37**, 10159 (1988).
[21] R. Asahi, W. Mannstadt, and A.J. Freeman, Phys. Rev. B **59,** 7486 (1999).
[22] W. Wolf, E. Wimmer, S. Massidda, M. Posternak, and C.B. Geller, Bull. Am. Phys. Soc. **43,** (1), 797 (1998).

[23] C.B. Geller, W. Wolf, S. Picozzi, A. Continenza, R. Asahi, W. Mannstadt, A.J. Freeman, and E. Wimmer, Appl. Phys. Lett. **79,** 368 (2001).

[24] R. Asahi, W. Mannstadt, and A.J. Freeman, Phys. Rev. B **62,** 2552 (2000).

[25] J. C. Slater, Phys. Rev. **51** (1937) 846.

[26] T.L. Loucks, The Augmented-Plane-Wave Method (Benjamin, New York) 1967.

[27] D. D. Koelling and G. O. Arbman, J. Phys. F **5**, (1975) 2041.

[28] O. K. Andersen, Phys. Rev. **12** (1975) 3060.

[29] H. J. F. Jansen and A. J. Freeman, Phys. Rev. **30** (1984) 561.

[30] E. Wimmer, H. Krakauer, M. Weinert, and A. J. Freeman, Phys. Rev. B **24** (1981) 864, and references therein.

[31] D. J. Singh, *Planewaves, pseudopotentials and the LAPW method* (Kluwer Academic, Boston, 1994).

[32] A. J. Freeman and E. Wimmer, Annu. Rev. Mater. Sci. **25**, 7 (1995).

[33] M. Weinert, E. Wimmer, and A.J. Freeman, Phys. Rev. B **26** (1982) 4571.

[34] R. Yu, D. Singh, and H. Krakauer, Phys. Rev. B **43**, (1991) 6411.

[35] R. Yu, H. Krakauer, and D. Singh, Phys. Rev. B **45** (1992) 8671.

[36] J. M. Soler and A. R. Williams, Phys. Rev. B **40** (1989) 1560; Phys. Rev. B **42** (1990) 9728.

[37] R. Wu and A.J. Freeman, Comput. Phys. Commun. **76**, 58 (1993).

[38] P. Hohenberg and W. Kohn, Phys. Rev. **136** (1964) B864.

[39] W. Kohn and L. J. Sham, Phys. Rev. **140** (1965) A1133.

[40] M. Born and R. Oppenheimer, Ann. Phys. Lpz. **84** (1927) 124.

[41] J. von Barth and L. Hedin, J. Phys. C **5**, 1629 (1972).

[42] O. Gunnarsson, B.I. Lundqvist, and S. Lundqvist, Solid State Commun. **11**, 149 (1972).

[43] L. Hedin and B.I. Lundqvist, J. Phys. C **4**, 2064 (1971).

[44] J.P. Perdew, J.A. Chevay, S.H. Vosko, K.A. Jackson, M. R. Pederson, D.J. Singh, and C. Fiolhais, Phys. Rev. B **46**, 6671 (1992).

[45] B.G. Johnson, P.M.W. Gill, and J.A. Pople, J. Chem. Phys. **98**, 5612 (1993).

[46] A.D. Becke, in *the challenge of d and f Electrons*, ACS Symposium series No. 394, eds. D.R. Salahub and M.C. Zerne (American chemical Society, Washington, DC, 1989), p. 165.

[47] A. Garcia, C. Elsaesser, J. Zhu, S. Louie, and M.L. Cohen, Phys. Rev. B **46**, 9829 (1992).

[48] Y.-M. Juan, E. Kaxiras, and R.G. Gordon, Phys. Rev. B **51**, 9521 (1995).

[49] A. Dal Corso, A. Pasquello, A. Baldereshi, and R. Car, Phys. Rev. B **53**, 1180 (1996).

[50] M. Körling and J. Häglund, Phys. Rev. B **45**, 13293 (1992).

[51] P.H.T.e, G. te Velde, and E.J. Baerends, Chem. Phys. Lett. **226**, 583 (1994).

[52] P. Hu, D.A. King, S. Crampin, M.-H. Lee, and M.C. Payne, Chem. Phys. Lett. **230**, 501 (1994).

[53] D. Porezag and M.R. Pederson, J. Chem. Phys. **102**, 9345 (1995).

[54] J. Baker, M. Muir, and J. Andzelm, J. Chem. Phys. **102**, 2063 (1995).

[55] B. Hammer, K.W. Jacobsen and J.K. Norskov, Phys. Rev. Lett. **70**, 3971 (1993).
[56] B. Hammer, M. Scheffler, K.W. Jarcobsen, and J.K. Norskov, Phys. Rev. Lett. **73**, 1400 (1994).
[57] T.C. Leung, C.T. Chan, and B.N. Harmon, Phys. Rev. B **44**, 2923 (1991).
[58] N. Moll, M. Bockstedte, M. Fuchs, E. Pehlke, and M. Scheffler, Phys. Rev. B **52**, 2550 (1995).
[59] D.R. Hamann, Phys. Rev. Lett. **76**, 660 (1996).
[60] A.D. Becke, Phys. Rev. A **38**, 3098 (1988); J.P. Perdew, Phys. Rev. B **33**, 8822 (1986); Phys. Rev. B **34**, 7406 (1986).
[61] J.P. Perdew, K. Burke, and M. Ernzerhof, Phys. Rev. Lett. **77**, 3865 (1996).
[62] M. Fuchs, M. Bockstedte, E. Pehlke, and M. Scheffler, Phys. Rev. B 57, 2134–2145 (1998).
[63] R.M. Dreizler and E.K.U. Gross, *Density Functional Theory, An Approach to the Quantum Many-Body Problem*, (Springer-Verlag, Berlin Heidelberg, 1990).
[64] J.P. Perdew and M. Levy, Phys. Rev. Lett. **51,** 1884 (1983).
[65] L.J. Sham and M. Schlüter, Phys. Rev. Lett. **51,** 1888 (1983); Phys. Rev. B **32,** 3883 (1985).
[66] O. Gunnarsson and K. Schönhammer, Phys. Rev. Lett. **56,** 1968 (1986).
[67] J.P. Perdew, R.G. Parr, M. Levy, and J.L. Balduz, Phys. Rev. Lett. **49,** 1691 (1982).
[68] C.S. Wang and W.E. Pickett, Phys. Rev. Lett. **51,** 597 (1983).
[69] A. Görling and M. Levy, Phys. Rev. A **52,** 4493 (1995).
[70] L. Hedin and S. Lundqvist, Solid State Physics **23**, eds. H. Ehrenreich, F. Seitz, and D. Turnbull (Academic, New York, 1969).
[71] M.S. Hybertsen and S.G. Louie, Phys. Rev. B **34**, 5390 (1986).
[72] F. Aryasetiawan and O. Gunnarsson, Rep. Prog. Phys. **61,** 237 (1998).
[73] W.G. Aulbur, L. JÖnsson, and J.W. Wilkins, *Solid State Physics,* edited by H. Ehnrenreich, F. Saepen (Academic, New York, 2000), Vol. 54, p. 1.
[74] J. Lindhard, Kgl. Danske Videnskap. Selskap, Mat.-fys. Medd. **28**, 8 (1954).
[75] G. Cappellini, R. Del Sole, L. Reining, and F. Bechstedt, Phys. Rev. B **47**, 9892 (1993).
[76] L. Liu and D. Brust, Phys. Rev. **173**, 777 (1968).
[77] F. Aryasetiawan, Phy. Rev. B **46**, (1992).
[78] R. Asahi, Ph.D. thesis, Northwestern University, 1999.
[79] J. van Elp *et al.*, Phys. Rev.B **44**, 1530 (1991).
[80] R.J. Lad and V.E. Henrich, Phys. Rev.B **38**, 10860 (1988).
[81] A.R.E. Mohammed and V. Sahni, Phys. Rev. B **29**, 3874 (1984).
[82] S. Chakravarty, J.H. Rose, D. Wood, and N.W. Ashcroft, Phys. Rev. B **24**, 1624 (1981).
[83] J.H. Rose and J.F. Dobson, Solid State Commun. **37**, 91 (1981).
[84] S. Massidda, M. Posternak, and A. Baldereschi, Phys. Rev. B **48,** 5058 (1993).
[85] A.-B. Chen and A. Sher, *Semiconductor Alloy, Physics and Materials engineering* (Plenum, New York, 1995), and references therein.
[86] *Handbook Series on Semiconductor Parameters*, edited by M. Levenshtein, S. Rumyantsev, and M. Shur (World Scientific, New York, 1996), vol.1

[87] V. Fiorentini Phy. Rev. B **46**, 2086 (1992), and references therein.

[88] H. Fu and A. Zunger, Phys. Rev. B **55**, 1642 (1997), and references therein.

[89] G.E. Engel, Phys. Rev. Lett. **78**, 3515 (1997).

[90] S. Moroni, D.M. Ceperley, and G. Senatore, Phys. Rev. Lett. **75**, 689 (1995).

[91] L.S.O. Johansson, R.I.G. Uhrberg, P. Mårtensson, and G.V. Hansson, Phys. Rev. B **42,** 1305 (1990).

[92] F.G. Allen and G.W. Gobeli, Phys. Rev. **127,** 150 (1962).

[93] M. Rohlfing, P. Krüger, and J. Pollmann, Phys. Rev. B **52,** 1905 (1995); **52,** 13753 (1995).

[94] M.S. Hybertsen and S.G. Louie, Phys. Rev. B **37,** 2733 (1988).

[95] J.E. Northrup, Phys. Rev. B **47,** 10032 (1993).

[96] A. Wang, J.R. Babcock, N.L. Edleman, A.W. Metz, M.A. Lane, R. Asahi, V.P. Dravid, C.R. Kannewurf, A.J. Freeman, and T.J. Marks, Proc. Natl. Acad. Sci. USA **98,** 7113 (2001).

[97] See, for example, "*Materials for Infrared Detectors and Sources*", R. Farrow, J.F. Schetzina and J.J. Cheung (Materials Research Society, Pittsburg. 1987), Vol.90.

[98] K. Shim and H. Rabitz, Phys. Rev. B **57**, 12874 (1998).

[99] See J.C. Woicik *et al.*, Phys. Rev. Lett. **79**, 5026 (1997) and F. Boscherini, C. Lamberti, S. Pascarelli, C. Rigo and S. Mobilio, Phys. Rev. B **58**, 10745 (1998) just to name a few recent experimental studies.

[100] See L. Bellaiche and A. Zunger, Phys. Rev. B **57**, 4425 (1998); L.-W. Wang and A. Zunger, Phys. Rev. B **56**, 12395 (1997), L.-W. Wang, L. Bellaiche, S.-H. Wei and A. Zunger, Phys. Rev. Lett. **80**, 4725 (1998) and A. Zunger, MRS Bull. **22**, 20 (1997) just to name some recent papers.

[101] P. Hohenberg and W. Kohn, Phys. Rev. **136**, B864 (1984); W. Kohn and L.J. Sham, *ibid.* **145**, 561 (1966).

[102] B.M. Bylander and L. Kleinman, Phys. Rev. B **41**, 7868 (1990).

[103] E. Wimmer, H. Krakauer, M. Weinert and A.J. Freeman, Phys. Rev. B **24**, 864 (1981); H.J.F. Jansen and A.J. Freeman, Phys. Rev. B **30**, 561 (1984).

[104] R. Asahi, W. Mannstadt and A.J. Freeman, Phys. Rev. B **59**, 7486 (1999).

[105] S. Picozzi, A. Continenza, R. Asahi, W. Mannstadt, A.J. Freeman, W. Wolf, E. Wimmer, and C.B. Geller, Phys. Rev. B **61**, 4677 (2000)

[106] Landolt-Bornstein, *Numerical Data and Functional Relationships in Science and Technology*, Vol. 17a (Springer-Verlag, Berline, 1982).

[107] S. Massidda, A. Continenza, A.J. Freeman, T.M. De Pascale, F. Meloni and M. Serra, Phys. Rev. B **41**, 12079 (1990).

[108] S. Picozzi, A. Continenza, and A.J. Freeman, Phys. Rev. B **B 52**, 5247 (1995)

[109] S. Massidda, B.I. Min and A.J. Freeman, Phys. Rev. B **35**, 9871 (1987).

[110] S. Baroni, M. Peressi, R. Resta, A. Baldereschi, *Theory of Band Offsets at Semiconductor Heterojunctions*, in *Proceedings of the 21th International Conference on the Physics of Semiconductors*, edited by Ping Jiang and Hou-Zhi Zheng (World Scientific, Singapore, 1993), p. 689.

[111] C.G. Van de Walle and R.M. Martin, Phys. Rev. B **35**, 8154 (1987).

[112] S.H. Wei and A. Zunger, Appl. Phys. Lett. **56**, 662 (1990).

[113] C.G. van de Walle, Phys. Rev. B **39**, 1871 (1989).

[114] M. Cardona and N. Christensen, Phys. Rev. B **35**, 6182 (1987).

[115] A. Franceschetti, S.H. Wei and A. Zunger, Phys. Rev. B **50**, 8094 (1994).

[116] A. Ichii, Y. Tsou E. Garmine, Journ. Appl. Phys. 74, 2112 (1993)

[117] S. Picozzi, A. Continenza, S. Massidda and A.J. Freeman, Phys. Rev. B **57**, 4849 (1998).

[118] S. Picozzi, A. Continenza, S. Massidda, A.J. Freeman and N. Newman, Phys. Rev. B **58**, 7906 (1998).

[119] S. Picozzi, A. Continenza, and A.J. Freeman, Phys. Rev. B **59**, 1609 (1999).

[120] S. Picozzi, A. Continenza, G. Satta, S. Massidda, A.J. Freeman Phys. Rev. B **61**, 16736 (2000).

[121] C.I Wu, and A. Kahn, J. Vac. Sci. Technol. **B 16**, 2218 (1998).

[122] M. von Schilfgaarde, and N. Newman, Phys. Rev. Lett. **65**, 2728 (1990).

[123] S.H. Wei and A. Zunger, Phys. Rev. Lett. **59**, 144 (1987).

[124] A. Ruini, R. Resta and S. Baroni, Phys. Rev. B **56**, 14921 (1997).

[125] S.G. Louie, J.R. Chelikowsky and M.L. Cohen, Phys. Rev. B **15**, 2154 (1977).

[126] C. Berthod, J. Bardi, N. Binggeli and A. Baldereschi, J. Vac. Sci. Technol. B **14 (4)**, 3000 (1996); M. Peressi, N. Binggeli and A. Baldereschi, J. Phys. D: Appl. Phys. **31**, 1273 (1998).

[127] T.U. Kampen and W. Monch, MRS Internet J. Nitride Semicond. Res. **1**, 41 (1996).

[128] M.R.H. Khan, T. Detchprom, P. Hacke, K. Hiramatsu and N. Sawaki, J. Phys. D **28**, 1169 (1995).

[129] S.C. Binari, H.B. Dietrich, G. Kelner, L.B. Rowland, K, Doverspike and D.K. Gaskill, Electron. Lett. **30**, 909 (1994).

[130] C.I. Wu and A. Kahn, J. Vac. Sci. Technol. B **16 (4)**, 2218 (1998).

[131] R.Q. Wu and A.J. Freeman, J. Magn. Magn. Mater. **200** (1999) 498; **100** (1991) 497.

[132] See review articles in the 200 volume of J. Magn. Magn. Mater.

[133] E. Wimmer, H. Krakauer, M. Weinert and A.J. Freeman, Phys. Rev. B **24**(1981) 864; M. Weinert, E. Wimmer and A.J. Freeman, Phys. Rev. B **26** (1982) 4571, and references therein.

[134] P.A. Gacia, A.D. Meinholdt and A. Suna, Appl. Phys. Lett., **47** (1985) 178.

[135] P. Krams, F. Lauks, R.L. Stamps, B. Hillebrands, and G. Güntherodt, Phys. Rev. Lett. **69** (1992) 3674.

[136] B.N. Engel, M.H. Wiedmann, and C.M. Falco, J. Appl. Phys. **75** (1994) 6401.

[137] F. Huang, G.J. Mankey, and R.J. Willis, J. Appl. Phys. **75** (1994) 6406.

[138] W. Weber *et al.*, Phys. Rev. B **54** (1996) 4075.

[139] S. Hope, E. Gu, B. Choi, and J.A. Bland, Phys. Rev. Lett. **80** (1998) 1750.

[140] J.E. Hurst Jr. and W.J. Kozlovsky, Jpn. J. Appl. Phys. **32** (1993) 5301.

[141] G.H.O. Daalderop, P.J. Kelly and M.F.H. Schuurmans, Phys. Rev. B **42** (1990) 1533; A.R. Mackintosh and O.K. Andersen, in *Electrons at the Fermi Surface*, edited by M. Springford (Cambridge University Press, Cambridge, 1980).

[142] X.D. Wang, D.S. Wang, R.Q. Wu and A.J. Freeman, J. Magn. Magn. Mater. **159** (1996) 337.

[143] J.G. Gay and R. Richter, Phys. Rev. Lett. **56** (1986) 2728; C. Li, A.J. Freeman, H.J.F. Jansen and C.L. Fu, Phys. Rev. B **42** (1990); 5433.G.Y. Guo, W.M. Temmerman and H. Ebert, J. Phys. C **3** (1991) 8205; J. Magn. Magn. Mater. **104–107** (1992) 1772.

[144] D.S. Wang, R.Q. Wu and A.J. Freeman, Phys. Rev. Lett. **70** (1993) 869; **71** (1993) 2166.

[145] D.S. Wang, R.Q. Wu and A.J. Freeman, Phys. Rev. B **47** (1993) 14932; J. Magn. Magn. Mater. **129** (1994) 327; Phys. Rev. B **48** (1993) 15883.

[146] X.D. Wang, R.Q. Wu, D.S. Wang, and A.J. Freeman, Phys. Rev. B **54** (1996) 61.

[147] J.P. Perdew *et al.*, Phys. Rev. B **33** (1986) 8800; Phys. Rev. B **46** (1992) 6671.

[148] U. von Barth and L. Hedin, J. Phys. C **5** (1972) 1629.

[149] V.G. Gavrilenko and R.Q. Wu, Phys. Rev. B **60** (1999) 9539.

[150] R.Q. Wu and A.J. Freman, J. Appl. Phys. **79** (1996) 6500; R.Q. Wu, L.J. Chen and A.J. Freeman, J. Magn. Magn. Mater. **170** (1997) 103.

[151] A.B. Shick, D.L. Novikov, and A.J. Freeman, Phys. Rev. B **56** (1997) R14259; J. Appl. Phys. **83** (1998) 7258.

[152] V.G. Gavrilenko and R.Q. Wu, J. Appl. Phys., **87** (2000) 6098.

[153] For systems with a fourfold symmetry with respect to the surface normal, their magnetic anisotropy energies, E_{MCA}, can be expressed in the lowest non-vanishing order of the polar and azimuth angles (θ and ϕ) as $E_{MCA} = K_1 sin^2\theta + K_2 sin^2(2\phi) sin^4\theta$, where K_1 and K_2 are coefficients of the leading uniaxial and in-plane contributions, respectively.

[154] G.H.O. Daalderop, P.J. Kelly and M.F.H. Schuurmans, Phys. Rev. B **41** (1990) 11919.

[155] G.Y. Guo, W.M. Temmerman and H. Ebert, Physica B **172** (1991) 61.

[156] P. Strange, J.B. Sraunton, B.L. Gyorffy and H. Ebert, **172** (1991) 51.

[157] J. Trygg, B. Johnansson, O. Eriksson and J.M. Wills, Phys. Rev. Lett. **75** (1995) 2871.

[158] S.V. Halilov, A. Ya. Perlov, P.M. Oppeneer, A.N. Yaresko and V.N. Antonov, Phys. Rev. B **57** (1998) 9557.

[159] S.V. Beiden *et al.*, Phys. Rev. B **57** (1998) 14247.

[160] O. Eriksson *et al.*, Phys. Rev. B **41** (1990) 7311; **42** (1990) 2707.

[161] J.R. Cullen, A.E. Clark and K.B. Hathaway, in *Materials Science and Technology*, Ed. R.W. Cahn, P. Hasen and E.J. Kramer, Vol. IIIB (1994) 529.

[162] R.Q. Wu, L.J. Chen, A. Shick and A.J. Freeman, J. Magn. Magn. Mater. **177–181** (1998) 1216.

[163] B. Schulz and K. Baberschke, Phys. Rev. B **50**, 13467 (1994).

[164] D. Sander and J. Kirschner *et al.*, J. Magn. Magn. Mater. 200 (1999) 439; 220 (1999) L1.

[165] L.J. Chen, R.Q. Wu and A.J. Freeman, J. Appl. Phys. **81**, 4417 (1997).

[166] M. Farle, W. Platow, A.N. Anisimov, P. Poulopoulos and K. Baberschke, Phys. Rev. B **55** (1997) 3708; **56** (1997) 5100.

[167] O. Hjorstam, K. Baberschke, J.M. Wills, B. Johansson and O. Eriksson, Phys. Rev. B **55**, 15026 (1997).

[168] D. Bonnenberg, K.A. Hempel and H.P.J. Wijn, in *Numerical Data and Functional Relationships in Science and Technology*, edited by H.P.J. Wijn, Landolt-Bornstein, New Series, Group 3 Vol. 19a (Springer-Verlag, Berlin, 1986).

[169] E.W. Lee and M.A. Asgar, Proc. R. Sco. London Ser. A **326**, 73 (1971); D.I. Bower, *ibid* **326**, 87 (1971).

[170] *Data in Science and Technology: Magnetic Properties of Metals*, edited by H.P.J. Wijn, (Springer-Verlag, Berlin, 1986).

[171] A.E. Clark, in *Ferromagnetic Materials*, Vol. 1, edited by E.P. Wohlfarth, (Amsterdam, North-Holland), page 531.

[172] K.N.R. Taylor, Advance in Physics, **2**, 551 (1971).

[173] K. Hathaway and J. Cullen, J. Phys. Condens. Matter **3** (1991) 8911.

[174] R.Q. Wu, J. Appl. Phys., in press.

[175] See S.D. Bader, J. Magn. Magn. Mater. **100** (1991) 440, and references therein.

[176] R. Kubo, J. Phys. Soc. Jap. **12** (1957) 570.

[177] C.S. Wang and J. Callaway, Phys. Rev. B **9** (1974) 4897.

[178] H. Ebert, Rep. Prog. Phys. **59** (1996) 1665.

[179] P.M. Oppeneer, T. Maurer, J. Sticht and J. Kübler, Phys. Rev. B **45** (1992) 10924.

[180] G.Y. Guo and H. Ebert, Phys. Rev. B **50** (1994) R10377; **51** (1995) 12633.

[181] N. Mainkar, D.A. Browne and J. Callaway, Phys. Rev. B **53** (1996) 3692.

[182] T. Casche, M.S.S. Brooks and B. Johansson, Phys. Rev. B **53** (1996) 296.

[183] A.J. Freeman, R.Q. Wu, L.J. Chen and L.P. Zhong, MRS Proc. (1998), to appear.

[184] Y.A. Uspenskii, E.T. Kulatov and S.V. Kaalilov, Phys. Rev. B **54** (1996) 474.

[185] S.P. Lim, D.L. Price and B.R. Cooper, IEEE Trans. Magn. **27** (1991) 3648.

[186] P.M. Oppeneer, M.S.S. Brooks, V.N. Antonov, T. Kraft and H. Eschrig, Phys. Rev. B **53** (1996) R10437.

[187] P.M. Oppeneer and V.N. Antonov, in *Spin-orbit Influenced Spectroscopies of Magnetic Solid*, edited by H. Ebert and G. Schütz, (Springer, Berlin, 1996) p.29.

[188] A.I. Lichtenstein, V.P. Antropov and B.N. Harmon, Phys. Rev. B **49** (1995) R10770; A.N. Yaresko *et al.*, Europhys. Lett. **36** (1996) 551.

[189] D. Weller *et al.*, Phys. Rev. Lett., **72** (1994) 2097; G.R. Harp *et al.*, Phys. Rev. B **48** (1993) 17538.

[190] G.Y. Guo and H. Ebert, Phys. Rev. B **50** (1994) 10377; P.M. Oppeneer, T. Kraft and H. Eschrig, Phys. Rev. B **52** (1995) 3577; J.M. MacLaren and W. Huang, J. Appl. Phys. **79** (1996) 6196.

[191] M.Y. Kim, R.Q. Wu and A.J. Freeman, Phys. Rev. B, in press.

[192] G. Schütz, W. Wagner, W. Wilhelm, P. Kienle, R. Zeller and G. Materlik, Phys. Rev. Lett. **58** (1987) 737; J. Stöhr, Science **259** (1993) 658.

[193] B.T Thole, P. Carra, F. Sette and G. van der Laan, Phys. Rev. Lett. **68** (1992) 1943; P. Carra, B.T. Thole, M. Altarelli and X-D, Wang, Phys. Rev. Lett. **70** (1993) 694.

[194] R.Q. Wu, D.S. Wang and A.J. Freeman, Phys. Rev. Lett. **71** (1993) 3581; **73** (1994) 1994; J. Magn. Magn. Mater., **132** (1994) 103.

[195] C.T. Chen *et al.*, Phys. Rev. Lett. **75** (1995) 152.

[196] J. Stohr, J. Magn. Magn. Mater. 200 (1999) 470.

[197] P. Bruno, Phys. Rev. B **39** (1989) 865.

[198] D. Weller *et al.*, Phys. Rev. Lett **75** (1995) 3752.

[199] H.A. Dürr *et al.*, Science **277** (1997) 213.

[200] G. van der Laan, Phys. Rev. Lett. **82** (1999) 640.

Solid-State Photoemission and Related Methods
Wolfgang Schattke, Michel A. Van Hove (Eds.)

2 Overview of core and valence photoemission

W. Schattke, M.A. Van Hove, F.J. García de Abajo, R. Díez Muiño, and N. Mannella

2.1 Introduction

This chapter attempts to give a general and systematic introduction to the theory and computation of photoelectron emission from both core and valence levels in surfaces and molecules. Given this subject's long history and ample literature, it is not possible, or indeed necessary, to cover all aspects and contributions here.

It is hoped that this chapter provides a basis for a better understanding of the other contributions in this volume, and that it offers an educational foundation for those wishing to enter or study the field: it is written in particular with the experimentalist and new reader in mind, stressing concepts and omitting detailed derivations.

Figure 2.1 describes the basic principles of photoelectron spectroscopy, illustrating various effects that can take place.

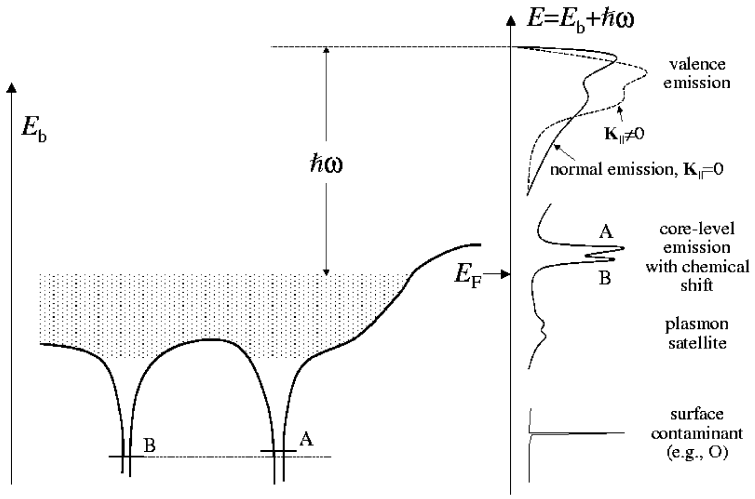

Figure 2.1: Photoemission spectroscopy from a surface, plotted as energy vs. position perpendicular to the surface, with the bulk at left. The curves at right represent measured photoemission yields. The photon energy is $\hbar\omega$. The potentials felt by a photoexcited electron may differ between atoms A and B, even if these are of the same type, as a result of a chemical shift due to the surface.

Solid-State Photoemission and Related Methods: Theory and Experiment. Edited by Wolfgang Schattke, Michel A. Van Hove

ISBN: 3-527-40334-5

The treatment of the photoemission process starts here with an introduction to Green function methods, which have found wide and profound applications to address one-particle as well as many-body problems, both analytically and numerically. The notion of Green functions is presented in a step-wise and didactic fashion in Section 2.2, to introduce the language and tools used by many theorists in tackling the relatively complicated many-body problem that underlies processes like photoemission. Simplified models are discussed in relationship to the more general and accurate description. In particular, the photocurrent expression is decomposed into its basic ingredients: initial state, final state, transition operator (matrix elements). And powerful concepts such as self-energy, quasiparticles and spectral representation are carefully introduced.

The famous Golden Rule is discussed in detail, connecting it with the one-step formulation of photoemission in Section 2.3: the distinction with the three-step formulation is shown to have mainly historical relevance, as it is no longer significant with current methods. The basic photoemission operator is introduced in its various representations and approximations, in particular the dipole approximation, in Section 2.4.

Of great importance for a numerically accurate treatment of photoemission is knowledge of the initial and final electronic states. For the initial state, in which the photoelectron resides before the photoemission process, a clear distinction is drawn between localized levels on the one hand (such as core levels in a solid surface, or any atomic levels in a free atom) and delocalized levels on the other hand (such as valence states in a solid surface or molecule). This is treated in Section 2.5.

The final state describing the photoelectron after excitation can be viewed either in a multiple-scattering representation, or in a band picture in terms of its full wavefunction. Computational methods to efficiently handle these often complicated states are also discussed in Section 2.6.

The photoemission matrix elements are treated in Section 2.7: these combine the initial and final states according to the photoexcitation operator. Again, a distinction is made between core and valence initial states: it is shown in particular how the case of extended states can be reduced to the case of localized states.

Optical effects due to the incoming photons are often neglected in modeling photoemission, in the hope that they are small. Here the focus is on the interaction of the photon with the material before a photoexcitation occurs. Examples include atomic resonances, treatable from a localized point of view (Section 2.8.1), and screening as well as plasmon resonances, which need a delocalized treatment (Section 2.8.2).

More generally, a variety of optical effects can be treated theoretically and computationally, and can be shown to be quite significant under suitable circumstances. These include short-wavelength local fields, non-local response, higher-order many-body Coulomb terms, and mean-field Fresnel considerations, even within a linear response assumption.

Very useful degrees of freedom in photoemission are the polarization of the incident photons, and the electron spin, usually measured as spin polarization of the outgoing electrons. In particular, these can be very fruitfully combined in studies of magnetism at surfaces and interfaces. They also provide high sensitivity to small effects such as relaxed atomic positions. Relativistic effects also contribute to spin polarization, and are covered as well in Section 2.9.

Finally, the success of the theoretical formalisms is borne out with the help of computational codes: these make it possible to actually compare theory to experiment, in a first

stage, and then to extract useful new information from experiment. A number of such codes have been produced, and several of them are advanced enough in their user-friendliness to be distributed for general use by surface and interface scientists, as discussed in Section 2.10.

The subjects covered in this chapter also highlight needs for the future. Topics such as dynamic screening of the electron hole, and inclusion of proper thermal vibrations have been much discussed but not implemented in a systematic way. Also lacking is a proper treatment of non-linear optical effects, observed with strong incident light; these will become even more important with free-electron lasers. Likewise, there is a need for inclusion of time-dependent effects in the theory, such as occur in pump-probe experiments. To some of these fields detailed reference is found in other chapters of this book.

2.2 Green function methods

2.2.1 Photoemission and the many-body problem

Fundamental to the behavior of a collective system are the interactions between the many participating bodies. The many-body problem can be defined as the study of how the interactions between bodies alters the behavior of the isolated, non-interacting bodies.

The photoemission process in its original concept is viewed as a single-particle probe – two-electron photoemission has been studied only recently (as described in two chapters [30, 36] of this volume). A single electron is removed from its binding environment and its spectral and angular distributions are recorded outside the material. Thus, two questions arise. First, how are the many-body effects on the one-particle spectra isolated so as to yield the simple and accustomed interpretation of one-electron photoexcitation? This asks for a quasi-particle picture, which is the subject of many treatments of many-body theory. Photoemission will directly reflect the distribution of those quasi-particles if the picture works at least in an approximate manner. This is by far the most widespread motivation and application of the technique. The second question is: what can be learned from photoemission about the many-body behavior of the system? The one-electron spectra describe excitations, but these do not necessarily have a quasi-particle-like character. Instead, several particles or even collective modes may mix into the excitations and thus affect the entire photoemission process. Then of course, the simple direct interpretation of spectra breaks down and one of the main advantages of this spectroscopy seems to be lost.

However, excitations of the many-body system clearly can be revealed by photoemission, as with any spectroscopy that couples to the excitation process. The angular-resolution capability of photoemission adds a valuable selection property typical for solid state systems. Thus, it is the many-body excitation spectrum which is hidden in the photoelectron spectral distribution. Investigations have made significant progress toward this goal, including analyses of the many-body spectral density, of the Fermi-liquid type or the shape of the Fermi surface [21, 94], of the intrinsic and extrinsic inelastic losses by plasmon shake-offs [49], and of magnetic excitations [55]. The momentum resolved gap in semiconductors hides many-body effects, and is an experimental quantity that can be extremely carefully determined by photoemission. Theoretical investigations have culminated in the quantitative evaluation of the GW-approximation now most common to bandstructure calculations. [37, 59] Strongly

correlated systems present another challenging problem of many-body physics [60] where spectroscopy has opened a new branch with two-electron photoemission, see [36].

Thus, the present development of photoemission increasingly requires the treatment of many-body effects. For that reason, we here introduce the main ideas of many-body theory at a relatively basic level, meant to offer non-specialists insight into the main concepts. A more extensive treatment is available in many books. [24, 61, 83] Several chapters of this handbook will address in much greater detail several aspects that are critical for photoemission and related techniques.

The importance of the many-body problem derives from the fact that almost any property of a real physical system of particles is to some degree governed by the quantum mechanical interactions between the particles themselves. Thus, the many-body problem is not necessarily a branch of solid-state, nuclear or atomic physics. It deals with general methods applicable to all many-body systems. The difficulty of solving the many-body problem is extreme, and because of this not much progress was made for a long time. The simplest way to deal with the many-body problem was simply to ignore it, i.e. to neglect the interactions between the particles of the system (One-Body Approximation). It is surprising and mysterious how this simple picture was able to produce good results nonetheless. An explanation such as 'many-body corrections often arise according to alternating semiconvergent series where subsequent terms tend to cancel, thus wisdom only keeps the lowest order' sounds mysterious as well and asks for examples and proof.

In a series of papers around 1956-57, it was shown that the methods of Quantum Field Theory, already famous for its success in elementary particle physics, were able to provide a powerful, systematic and unified way to attack the many-body problem. One of the most important results emerging from this approach is a new simple picture of matter according to which systems of interacting real particles are described in terms of approximately non-interacting fictitious bodies, called *quasi-particles*, and *collective excitations*. To a large extent, the properties of quasi-particles and the description of the collective excitations can be calculated by means of quantum-field-theoretical techniques pictorially assisted by the so-called Feynman diagrams. Actually, this represents the most general and systematic access to the many-body problem.

The discovery of the Hohenberg-Kohn theorem [56] has sparked a whole "industry" of bandstructure calculations for which photoemission has proved to be the most accurate tool of experimental investigation. The theorem describes the exact ground state energy as a functional of the electron density which is variationally exploited once this functional is known. Various approximations to the latter have been developed with increasing accuracy. Furthermore, in contrast to the fact that only the ground state is covered by the theorem, excitation energies are identified in an approximate way with the constraint parameters of the variational equations, the Kohn-Sham equations [69]. The agreement with experiment widely confirms this procedure in *density functional theory* (DFT). Because of their importance, many-body treatments can no longer be considered separately from DFT. It is well known [99] that the Kohn-Sham equations can be regarded as a procedure to solve the exact Dyson equation for Green functions with a suitable self-energy. Thus, the formulation of many-body theory with Green functions embeds DFT in its most frequently applied environment.

The general development of many-body theory for solids proceeds via Green functions and so does photoemission theory. Therefore, Green functions will be the basis of the fol-

lowing presentation. In Section 2.2.2, we will introduce Green functions in the context of the one-particle Schrödinger equation. In Section 2.2.3, we will discuss elementary excitations in systems of interacting particles. Section 2.2.4 will address the concept of the self-energy, while Section 2.2.5 will consider independent particle states and related methods. Perturbation expansions will be discussed in Section 2.2.6, and diagrams in many-body systems will be presented in Section 2.2.7. Section 2.2.8 introduces the spectral representation, while Section 2.2.9 deals with the photocurrent.

2.2.2 Green functions and one-particle Schrödinger equation

Let us consider a single quantum mechanical particle with Schrödinger's equation written in Dirac's notation as

$$(E\widehat{I} - \widehat{H}_0)|\psi\rangle = \widehat{V}|\psi\rangle \tag{2.1}$$

Here $\widehat{H}_0$ is a Hamiltonian for which the eigenfunctions ϕ_n and the eigenvalues E_n ($widehatI$, identity operator) are known, while $\widehat{V}$ is a

Such an equation can be solved provided that we know the inverse of the operator $(E\widehat{I} - \widehat{H}_0)$, namely the Green function $\widehat{G}_0 = (E\widehat{I} - \widehat{H}_0)^{-1}$ (we will often abbreviate "Green function" to GF). In light of this, we observe that the operators $(E\widehat{I} - \widehat{H}_0)$ and $\widehat{H}_0$ share the same eigenfunctions $\phi_n(\mathbf{r})$ since they commute, while the eigenvalues of the operator $(E\widehat{I} - \widehat{H}_0)$ are shifted, equal to $E - E_n$. The Green function of the operator $(E\widehat{I} - \widehat{H}_0)$ is therefore brought into the position representation, $G_0(\mathbf{r}, \mathbf{r}', E) =< \mathbf{r}|\widehat{G}_0|\mathbf{r}' >$, by expanding with respect to its eigenfunction system

$$G_0(\mathbf{r}, \mathbf{r}', E) = \sum_n \frac{\phi_n(\mathbf{r})\phi_n^*(\mathbf{r}')}{E - E_n} \tag{2.2}$$

Here we can appreciate a powerful feature of the Green function: by finding the values of the parameter E for which the denominator of the GF vanishes, we can obtain the eigenenergies of the operator $\widehat{H}_0$. This result motivates the use of the GF formalism later on when dealing with the much more complex problem of the interaction of a quantum mechanical particle within an interacting-particle system. In particular, we will see later that in that case the GF has poles at values of the parameter E equal to the excitation energies of the whole system.

By applying the GF operator we get from Eq. (2.1)

$$|\psi\rangle = |\psi_0\rangle + \widehat{G}_0\widehat{V}|\psi\rangle \tag{2.3}$$

where $|\psi_0\rangle$ is the solution of the associated homogeneous equation $(E\widehat{I} - \widehat{H}_0)|\psi_0\rangle = 0$. By successive approximations of the particular solution $\widehat{G}_0\widehat{V}|\psi\rangle$ through iteration of Eq. (2.3), it is possible to express the general solution as

$$|\psi\rangle = |\psi_0\rangle + \widehat{G}_0\widehat{V}|\psi_0\rangle + \widehat{G}_0\widehat{V}\widehat{G}_0\widehat{V}|\psi_0\rangle + \cdots \tag{2.4}$$

We can also consider the following problem: if we know the Green function $\widehat{G}_0$ for the operator $\widehat{H}_0$, what is the GF G for the operator $\widehat{H}_0 + \widehat{V}$? By definition,

$$\widehat{G}(E) = \left(E\widehat{I} - \widehat{H}_0 - \widehat{V}\right)^{-1}$$

Since $\left(E\widehat{I} - \widehat{H}_0 - \widehat{V}\right)\widehat{G}(E) = \widehat{I}$, we have

$$\left(E\widehat{I} - \widehat{H}_0\right)\widehat{G}(E) = \widehat{I} + \widehat{V}\widehat{G}(E) \tag{2.5}$$

and multiplying both sides by $\widehat{G}_0(E)$, we obtain

$$\widehat{G}(E) = \widehat{G}_0(E) + \widehat{G}_0(E)\widehat{V}\widehat{G}(E) \tag{2.6}$$

which is called *Lippman-Schwinger equation*. Projecting onto the position eigenstates $|\mathbf{r}\rangle$, Eq. (2.3) and the Lippman-Schwinger equation are respectively written as

$$\psi(\mathbf{r}) = \psi_0(\mathbf{r}) + \int G_0(\mathbf{r}, \mathbf{r}')V(\mathbf{r}')\psi(\mathbf{r}')\, d\mathbf{r}' \tag{2.7}$$

$$G(\mathbf{r}, \mathbf{r}', E) = G_0(\mathbf{r}, \mathbf{r}', E) + \int G_0(\mathbf{r}, \mathbf{r}'', E)V(\mathbf{r}'')G(\mathbf{r}'', \mathbf{r}', E)\, d\mathbf{r}'' \tag{2.8}$$

Both these equations are integral equations which can be solved up to the desired order by successive iterations. Both formulas find widespread application in multiple scattering theory.

Now we consider the time evolution of a single quantum mechanical particle with unperturbed Hamiltonian $\widehat{H}_0$. Schrödinger's equation in this case can be written as

$$\left[i\hbar\frac{\partial}{\partial t} - \widehat{H}_0\right]|\phi(t)\rangle = 0 \tag{2.9}$$

Projecting onto the position eigenstates, the Green function $G_0(\mathbf{r}, \mathbf{r}', t, t')$ of the operator $i\hbar\frac{\partial}{\partial t} - \widehat{H}_0$ satisfies the following differential equation

$$i\hbar\frac{\partial}{\partial t}G_0(\mathbf{r}, t, \mathbf{r}', t') - H_0\left(\mathbf{r}, \frac{\hbar}{i}\nabla\right)G_0(\mathbf{r}, t, \mathbf{r}', t') = \hbar\delta(t - t')\,\delta(\mathbf{r} - \mathbf{r}') \tag{2.10}$$

Equation (2.2) shows that the solution $G_0(\mathbf{r}, \mathbf{r}', t, t')$ of Eq. (2.10) is the Fourier transform of the Green function $G_0(\mathbf{r}, \mathbf{r}', E)$

$$G_0(\mathbf{r}, t, \mathbf{r}', t') = \frac{1}{2\pi}\int G_0(\mathbf{r}, \mathbf{r}', E)e^{-\frac{i}{\hbar}E(t-t')}dE \tag{2.11}$$

where the zeros of the denominator of the Green function $G_0(\mathbf{r}, \mathbf{r}', E)$ are appropriately avoided by suitable choice of an integration path in the complex plane. Equivalently, one integrates on the real axis and moves the zeros off that axis by defining

$$G_0^{r/a}(\mathbf{r}, \mathbf{r}', E) = \sum_n \frac{\phi_n(\mathbf{r})\phi_n^*(\mathbf{r}')}{E - E_n \pm i\delta} \tag{2.12}$$

with δ an infinitesimal positive quantity and the sign leading to a retarded (r) or advanced (a) choice(+ or - sign,respectively). It is possible to close the contour of integration in the lower half-plane if $t > t'$ and in the upper half-plane if $t < t'$, so that $G_0^r(\mathbf{r}, t, \mathbf{r}', t') = 0$ for $t < t'$ and $G_0^a(\mathbf{r}, t, \mathbf{r}', t') = 0$ for $t > t'$. The Green functions $G_0^{r/a}(\mathbf{r}, t, \mathbf{r}', t')$ are both solutions of equation (2.10), but with different prescriptions for the boundary condition on the time axis.

Through Eq. (2.10) an interesting property of the Green function shows that, given an arbitrary initial wave function $\phi(\mathbf{r}', t')$ at time t', it is possible to write the solution of the Schrödinger equation at a later time t as

$$\phi(\mathbf{r}, t) = i \int G_0^r(\mathbf{r}, t, \mathbf{r}', t')\phi(\mathbf{r}', t')d\mathbf{r}' \tag{2.13}$$

as proved with help of Eq. (2.10) and the equal-time property $iG_0^{r/a}(\mathbf{r}, t, \mathbf{r}', t) = \delta(\mathbf{r} - \mathbf{r}')$. For this reason G_0^r is called *retarded propagator*: G_0^r "propagates" the wave function through time. The condition $G_0^r = 0$ for $t < t'$ ensures that values $\phi(\mathbf{r}', t')$ for times later than t do not contribute to the determination of $\phi(\mathbf{r}, t)$. In this sense the Green function G_0^r and the corresponding *advanced* Green function G_0^a embody the principle of causality.

Now that we have the solutions of the unperturbed Green function Eq. (2.10), we can solve the problem of determining the time evolution for a quantum mechanical particle with Hamiltonian H_0 and with a perturbing potential $\widehat{V}(t)$ which can be time-dependent. In this case the Schrödinger equation can be written as

$$\left[i\hbar\frac{\partial}{\partial t} - \widehat{H}_0\right]|\Psi(t)\rangle = \widehat{V}(t)|\Psi(t)\rangle \tag{2.14}$$

The solution of this equation is obtained by applying the Green function operator on the RHS, so that

$$\Psi(r, t) = \phi(\mathbf{r}, t) + \frac{1}{\hbar}\int G_0^{r/a}(\mathbf{r}, t, \mathbf{r}', t')V(\mathbf{r}', t')\Psi(\mathbf{r}', t')d\mathbf{r}'dt' \tag{2.15}$$

where $\phi(\mathbf{r}, t)$ is the solution of the associated homogeneous Eq. (2.9) and $G_0^{r/a}(\mathbf{r}, t, \mathbf{r}', t')$ is the unperturbed Green function which corresponds to $\widehat{V} = 0$. The retarded version yields a *forward* solution, i.e. ϕ is the prescribed initial wave function before the potential $\widehat{V}$ is switched on, and the advanced version yields the *backward* solution, i.e. ϕ is the final wave function after $\widehat{V}$ has been switched off. Replacing in Eq. (2.10) $\widehat{H}_0$ by $\widehat{H} = \widehat{H}_0 + \widehat{V}$ and G_0 by the full Green function G constitutes the differential equation for G and is equivalent to an integral equation, namely

$$\begin{aligned} G^{r/a}(\mathbf{r}, t, \mathbf{r}', t') = {} & G_0^{r/a}(\mathbf{r}, t, \mathbf{r}', t') \\ & + \int G_0^{r/a}(\mathbf{r}, t, \mathbf{r}'', t'')V(\mathbf{r}'', t'')G^{r/a}(\mathbf{r}'', t'', \mathbf{r}', t')\, d\mathbf{r}''dt'' \end{aligned} \tag{2.16}$$

We notice that by Fourier transforming Eqs. (2.15) and (2.16) into the energy domain we get Eqs. (2.7) and (2.8) in the case that V does not depend on time.

When the particle propagator is expanded in a perturbation series by successive iteration of Eq. (2.6), the structure of the terms can be complicated. The use of GF as propagators is a powerful method to help visualizing the physical picture: we sketch this approach next.

The free propagation of the quantum mechanical particle (in the absence of interactions) can be drawn as a straight line. The effects of the interactions of the particle due to an external potential V are symbolized by open circles with attached broken line, as in Fig. 2.2a. We can now visualize the different orders of the interactions in the perturbation expansion of the propagator as a series of scattering events caused by the potential V. Each term in the perturbation expansion is represented by a diagram, so that each of the lines and circles in the diagrams has a definite factor associated with it. There is a one-to-one correspondence of each diagram with each term occurring in expression (2.6), or, in other words, with each term of the perturbation expansion of the propagator. The result of the infinite sum is the exact propagator depicted by a double line, as in Fig. 2.2b. The first aim of a perturbation theory is to regard the series as a power expansion with respect to a small parameter which leads to a cut-off at low order.

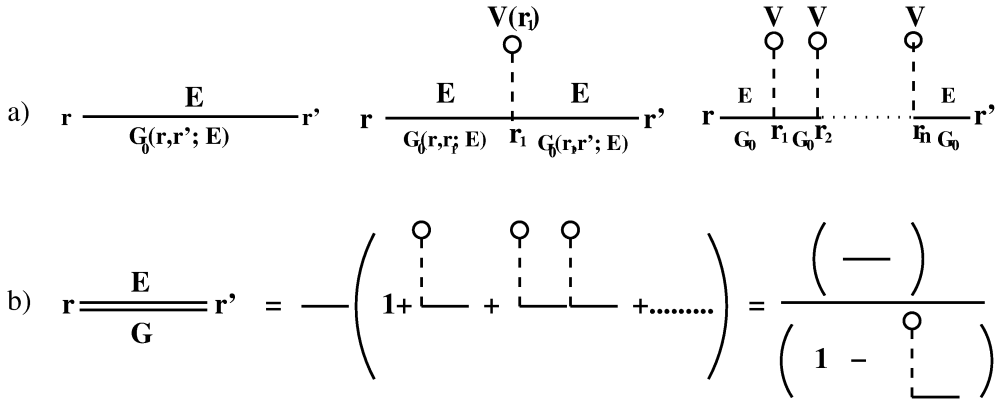

Figure 2.2: Graphical representation of Green function diagrams: a) Green function with zero, one, and n insertions of the perturbing potential; b) graphical summation of the geometrical series up to infinite order to get G

The perturbation series is sometimes evaluated by summing to infinite order over only a subset of diagrams, that is, summing only over some terms in the perturbation expansion corresponding to certain types of diagrams. This is the so-called *partial* or *selective summation*. The partial sum is usually evaluated by showing that it involves a convergent infinite series, or that it is equivalent to an integral equation which has already been solved.

As an example, consider a quantum mechanical particle which is moving under the influence of the sum of two external potentials V_A and V_B. If such an expansion were summed up to second order according to ordinary perturbation theory, one would retain only five terms: two linear terms (in V_A and V_B) and three quadratic terms (in V_A^2, V_B^2, and $V_A V_B$). If, on the contrary, one of the perturbations cannot be considered small, it is not possible to apply ordinary perturbation theory. For example, if $V_A \gg V_B$, it is possible to consider only the

diagrams involving V_A, neglecting V_B and resulting in the "partial" result

$$\begin{aligned}\widehat{G}(E) &= \widehat{G}_0(E) + \widehat{G}_0(E)(\widehat{V}_A + \widehat{V}_B)\widehat{G}(E) \\ &\approx \widehat{G}_0(E) + \widehat{G}_0(E)\widehat{V}_A\widehat{G}_0(E) + \widehat{G}_0(E)\widehat{V}_A\widehat{G}_0(E)\widehat{V}_A\widehat{G}_0(E) + \cdots \\ &= \widehat{G}_0(E) \cdot \sum_{n=0}^{\infty} \left(\widehat{V}_A\widehat{G}_0\right)^n = \frac{\widehat{G}_0(E)}{1 - \widehat{V}_A\widehat{G}_0} = \frac{1}{\widehat{G}_0^{-1}(E) - \widehat{V}_A}\end{aligned} \tag{2.17}$$

It is interesting to note how this approximation and the summation are visualized in terms of diagrams. In particular, the approximation consists in considering only the series pictured in Fig. 2.2a, while Fig. 2.2b shows how the diagrams can be effectively used as a symbolic guide to performing calculations, since they can be manipulated as if they were algebraic quantities.

2.2.3 Elementary excitations in systems of interacting particles

The elementary excitations play a dominant role in the low temperature behavior of a solid, up to room temperature for the electrons. Often, these excitations have quasi-particle properties in the sense that a group of several particles maintains its identity through the course of time and obeys a certain type of statistics, being e.g. of Fermi or Bose character. These quasi-particles have energy and momentum and can thus be treated much like normal particles in theory and experiment. Therefore, it is convenient to discriminate between an excitation which concerns a finite number of particles, such as an electron with its polarization cloud, and an excitation where all the particles are simultaneously involved, so-called *collective* excitations, such as phonons, spin waves, or current-carrying states of superconductivity. Many intermediate forms exist and can be imagined.

For a homogeneous non-interacting system, the energy E versus momentum dispersion relation of a single particle with momentum p and mass m is quadratic, i.e. $E(p) = p^2/2m$. When a real particle moves through a system of interacting particles, its motion is considerably modified. In fact, we can imagine that the real particle becomes surrounded by a cloud of other particles in the system. The system consisting of the real particle plus the cloud of other particles around it is called *quasi-particle*, or synonymously *dressed*, *clothed* or *renormalized particle*. The properties of the quasi-particles are different from those of the real particles: quasi-particles have an effective mass and a lifetime.

Since the real particle is screened by the other particles, quasi-particles interact only weakly with one another. This is why the formulation of the quasi-particle concept is so useful in studying many body systems: systems of strongly interacting real particles may be regarded as composed of independently and/or weakly interacting quasi-particles.

The quasi-particles are what we see when we probe such systems, and they can behave quite differently from the free particles. For example, the energy versus momentum dependence of a quasi-particle can be very different from that of a free particle. Such behavior is what angle resolved photoemission is in fact supposed to elucidate.

We can define quasi-particles as *effective single-particle states*, meaning that they act like free particles with a renormalized energy ϵ'_k replacing the energy ϵ_k of the bare particle, and a

lifetime τ_k. In an approximate manner, the finite lifetime of a single-particle state is described by regarding the energy as a complex quantity. By doing so, it is possible to account for the exponential decay in time of the amplitude of the wave function, thus describing the fact that the scattering due to a potential tends to knock a particle out of its single particle state. Thus, we consider the energy with real part equal to ϵ'_k and imaginary part equal to $-1/\tau_k$. In fact, the eigenfunction of a free particle with momentum $\hbar k$ can be written as $\phi_k(t) = \phi_k e^{-i\frac{\epsilon'_k}{\hbar}t}$. When interactions are turned on, the energy changes to ϵ'_k and the particle starts to decay out of the single particle state k, so that for a quasi-particle the wave function can be written as

$$\phi'_k(t) = \phi_k e^{-i\left(\frac{\epsilon'_k}{\hbar} - i\frac{1}{\tau_k}\right)t} = \phi_k e^{-i\frac{\epsilon'_k}{\hbar}t} e^{-t/\tau_k} \tag{2.18}$$

showing the exponential decay of the state with rate $\frac{1}{\tau_k}$.

The quasi-particles are more or less well defined, depending on the value of the decay time. Schemes like Hartree or Hartree-Fock, which rely on the solution of a one-particle-like Schrödinger equation, local or nonlocal, with hermitean Hamiltonian, conserve the particle number and thus also the identity of a single particle. The Kohn-Sham eigenvalues of density functional theory also exhibit definite single-particle properties, even though this approach is questionable because it describes only the ground state; however, it is empirically in wide use. An important criterion for the validity of the notion of a quasi-particle is that the lifetime of the quasi-particles has to be longer than the time required to detect the quasi-particle state. Since the many-body interactions scatter the particle out of its single-particle state, a measurement of the lifetime of the state is very useful because it gives insight into the interaction mechanisms.

At the other end of the scale of fictitious particles in a many-body system are the *collective modes* or *collective excitations*. These can be defined as the quanta associated with collective wave-like motion of the system as a whole. Examples of collective excitations include phonons, plasmons and magnons. Collective excitations have particle-like qualities, such as complex energies with finite lifetime. Unlike quasi-particles, however, they are not described in a localized picture.

An important aspect of many-body systems is that of the correlations in particle positions brought about by their mutual interaction, giving rise to coherence effects. Such correlations frequently take the form of screening, that is, the alteration in the effective interaction of a pair of particles brought about by the remaining particles in the system. In fact, the particle in a system cannot distinguish between an external perturbation and an internal potential produced by the response to that perturbation from the rest of the system. A particle reacts not to the external field but to the total field, including the response of all the other particles. The result of allowing the rest of the system to adapt itself is to reduce drastically the effective potential. For example, a given electron in a dense electron gas acts to polarize its immediate surroundings: it pushes other electrons away until its associated screening cloud possesses a charge nearly equal (and opposite) to its own. The quasi-particles (electrons plus screening clouds) interact via an effective short-range interaction of the order of the interparticle spacing, in contrast to the original Coulomb interaction which in principle has infinite range. One of the first big successes of many-body theory was the decomposition of the Coulomb excitations into extended plasma waves and short-ranged screening clouds, the former corresponding to collective excitations and the latter to quasi-particles. [12,77] Charges are locally balanced and the remaining long range interaction ($q = 2\pi/\lambda \to 0$) is connected with wave-like deviations

from this balanced charge equilibrium at significantly higher energies corresponding to the classical plasma frequency.

It should be noted that each bare particle is simultaneously the core of a quasi-particle and a transient member of the cloud of several other quasi-particles. Therefore, if one wants to describe a many-body system in terms of quasi-particles, caution is necessary because each particle will be counted more than once. For this reason, the quasi-particle concept is valid provided that one talks about a few quasi-particles at a time (few compared to the total number of particles in the system).

It is convenient to define quasi-particles in terms of an experiment in which one removes or adds a particle in a system, and observes the behavior of this extra particle (or hole) as it moves through the system. This picture is closely related to photoemission, direct and inverse, respectively. It is automatically accounted for in the formal definition of the Green function for a many-body system.

2.2.4 The self-energy

At this point it is natural to ask how we can describe the GF propagator when we consider the many-body interactions which are present in a system of particles. A useful aspect of the one-particle many-body Green function is that it allows retaining a one-particle picture while considering many-body systems. In fact, following Dyson, it is possible to describe the many-body interactions of a single particle by introducing an energy dependent effective potential called *self-energy* $\widehat{\Sigma}(E)$. As the name suggests, the self-energy includes all the particle interaction effects. In other words, the particles of the system are perturbed by the incoming particle in such a way that their motion follows (or "is correlated with") the motion of the incoming particle itself. The incoming particle affects the many-body system, which in turn acts back on the particle, altering its energy. The interactions between the incoming particle and the system take place in a dynamic rather than in a static way, so that the self-energy describes the dynamics of these interactions, i.e. the time dependence of the response of particle motion correlated with the incoming particle. For this reason the self-energy is an external effective potential which is time dependent, and hence energy dependent upon Fourier transforming.

In a crude way, the self-energy might be introduced by the following equation reminiscent of Eq. (2.1) with the potential V replaced by the self-energy $\widehat{\Sigma}$

$$\left(E\widehat{I} - \widehat{H}_0\right)|\Psi\rangle = \widehat{\Sigma}\,(E)\,|\Psi\rangle \tag{2.19}$$

where $\widehat{H}_0$ is a Hamiltonian whose eigenvalues and eigenfunctions are well known, typically taken to be of one-particle form. According to the derivation following Eq. (2.3), the formal solution of Eq. (2.19) is obtained through the corresponding GF which is determined by means of the Lippman-Schwinger equation, now called (when the self-energy is present) *Dyson equation*

$$\widehat{G}\,(E) = \widehat{G}_0\,(E) + \widehat{G}_0\,(E)\,\widehat{\Sigma}\,(E)\,\widehat{G}\,(E) \tag{2.20}$$

The Dyson equation can be solved formally

$$\widehat{G}(E) = \frac{1}{\widehat{G}_0^{-1}(E) - \widehat{\Sigma}(E)} \tag{2.21}$$

This shows how the poles of the GF are moved in energy by $\widehat{\Sigma}$ from those of the non interacting GF $\widehat{G}_0$, thus describing the motion of the particle through the system as a combination of its free motion and all of its interactions with the rest of the system, expressed by the self-energy. Equation (2.20) is depicted in Fig. 2.3, where the double lines are associated with the GF $\widehat{G}(E)$, while single lines denote the free propagator $\widehat{G}_0(E)$.

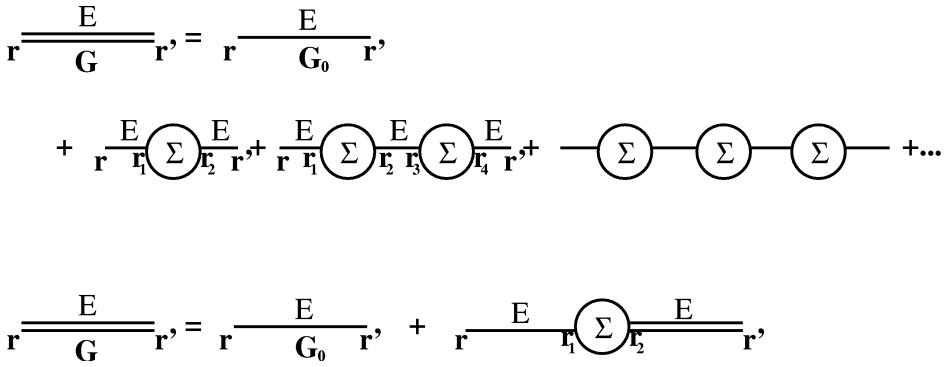

Figure 2.3: Self-energy: a) multiple insertions of self-energy to infinite order for G written in b) by summing them up in Dyson's equation.

The solution of Dyson's equation is symbolic, meaning that it is possible if we know how to calculate the self-energy $\widehat{\Sigma}$. This task, however, is impossible in full generality. It is possible to calculate it by means of approximations of the many-body interactions which are present in the system. A qualitative look at the methods which allow performing this many-body perturbation expansion will be the object of the next paragraphs. The method of *second quantization* or *occupation number formalism* historically facilitated the development significantly. The reason for this is twofold. First, this formalism allows handling systems with variable numbers of particles. This capability can be appreciated if we think about the fact that we will be able to describe test particles which are added to or removed from the system, as embodied in the definition of the GF. As another example, we can formally express the particle-hole approach, where the number of particles and holes is variable. Furthermore, the operators already describe (through the commutation relations that they satisfy) the symmetry properties of Fermi and Bose systems, so that we do not have to worry about keeping the wave functions properly symmetrized, the result being a simplification and a more compact form.

2.2.5 Independent particle states and related methods

It is necessary to use determinantal wavefunctions even for the simplest problems that satisfy the quantum statistics of fermions: such wavefunctions are unwieldy expressions, so it is desirable to find a formalism that is easier to manipulate. The required basic information is

how many particles are in the single-particle state α, how many in state β, and so on. In Dirac's notation:

$$|\Psi\rangle = |n_\alpha, n_\beta, \ldots, n_\nu, \ldots\rangle \tag{2.22}$$

In this *number representation* one defines the *construction* and *destruction* operators, $\widehat{c}^\dagger$ and $\widehat{c}$ respectively, to construct a state like Eq. (2.22). They increase and decrease, resp., by one the number of particles in a specified one-particle state $\rho, \sigma, \ldots$. The symmetry properties of the system are implicitly contained in the commutation relations obeyed by these operators, viz.

$$\widehat{c}^\dagger_\rho \widehat{c}^\dagger_\sigma = \pm \widehat{c}^\dagger_\sigma \widehat{c}^\dagger_\rho \qquad \text{or} \qquad \left[\widehat{c}^\dagger_\rho, \widehat{c}^\dagger_\sigma\right]_\mp = 0 \tag{2.23}$$

where we have the anticommutation relation (lower sign) for fermions and the commutation relation (upper sign) for bosons. An independent fermion state is written according to Eq. (2.22) as

$$|\Psi\rangle = (\widehat{c}^+_\alpha)^{n_\alpha} (\widehat{c}^+_\beta)^{n_\beta} \cdots (\widehat{c}^+_\nu)^{n_\nu} \cdots |0\rangle \tag{2.24}$$

by adding particles to the vacuum state $|0\rangle$.

The criterion according to which we write the operator in second quantization is that when operating between two states it gives the same matrix elements as given before in the more classical notation, between two many-particle wavefunctions. As an example, let us consider an operator like

$$\widehat{O} = \sum_{i=1}^{N} \widehat{O}_i \left(\mathbf{r}_i, \frac{\hbar}{i}\nabla_i\right) \tag{2.25}$$

along with its matrix element evaluated between two independent particle states differing by one single-particle wavefunction

$$\langle\rho|\widehat{O}|\sigma\rangle = \int d^3\mathbf{r}\, \phi^*_\rho(\mathbf{r}) O\left(\mathbf{r}, \frac{\hbar}{i}\nabla\right) \phi_\sigma(\mathbf{r}) \tag{2.26}$$

Such operators are called *one-body operators* since they are sums of operators each of which acts separately on one particle. An example of such an operator is the kinetic energy operator. In second quantization formalism, it can be shown that the expression for such operators is given by

$$\widehat{O} = \sum_{\rho\sigma} \langle\rho|\widehat{O}|\sigma\rangle \widehat{c}^\dagger_\rho \widehat{c}_\sigma \tag{2.27}$$

In an analogous way a two-body operator is represented by a product of two destruction and two creation operators and a corresponding matrix element.

Consider again a state in the form of Eq. (2.22) and disregard mathematical subtleties concerning the difference between discrete and continuous states. If we take as the single-particle states α, β, etc. the eigenstates of the position operator $\widehat{\mathbf{r}}_1, \widehat{\mathbf{r}}_2, \ldots, \widehat{\mathbf{r}}_i$, then $n_{\mathbf{r}_i}$ gives

the number of particles in the single-particle state $\delta(\mathbf{r}-\mathbf{r}_i)$, i.e., $n_{\mathbf{r}_i}$ particles at the point $\mathbf{r}_i$. Similarly, the creation and destruction operators become $\widehat{c}^{\dagger}_{\mathbf{r}_i}$ and $\widehat{c}_{\mathbf{r}_i}$, which respectively create and destroy a particle at $\mathbf{r}_i$. These two operators are usually called *field operators* and are denoted by $\widehat{\psi}^{\dagger}(\mathbf{r}_i)$ and $\widehat{\psi}(\mathbf{r}_i)$, respectively. The exact formal definition of the field operators is by means of linear combination of the creation and destruction operators, namely

$$\widehat{\psi}(\mathbf{r}_i) = \sum_k \widehat{c}_k \psi_k(\mathbf{r}_i)$$

with a suitable set of one-particle states $\psi_k(\mathbf{r})$. From the commutation relations satisfied by the operators $\widehat{c}^{\dagger}$ and $\widehat{c}$ it is easy to show the respective relations for the field operators. The expressions for the one-body and two-body operators in terms of the field operators become

$$\int d^3\mathbf{r}\, \widehat{\psi}^{\dagger}(\mathbf{r}) O(\mathbf{r},\mathbf{p}) \widehat{\psi}(\mathbf{r}) \tag{2.28}$$

$$\iint d^3\mathbf{r}_1 d^3\mathbf{r}_2\, \widehat{\psi}^{\dagger}(\mathbf{r}_1)\widehat{\psi}^{\dagger}(\mathbf{r}_2) O(\mathbf{r}_1,\mathbf{p}_1,\mathbf{r}_2,\mathbf{p}_2)\widehat{\psi}(\mathbf{r}_1)\widehat{\psi}(\mathbf{r}_2)$$

where the momentum $\mathbf{p}$ stands for the corresponding *nabla* (∇) expression and applies to its right.

A convenient starting point for a many-body calculation often can be taken from suitable one-body states. The Hartree-Fock (HF) method is a well known example. A determinantal ansatz of single-particle functions is used to minimize the variational energy and thereby fix these functions. The one-body potential might for instance be given by the nuclei's potential $U_{ion}(\mathbf{r}) = -\frac{Ze^2}{4\pi\epsilon_0}\sum_{\mathbf{R}} \frac{1}{|\mathbf{r}-\mathbf{R}|}$ and the two-body potential by the electron-electron Coulomb interaction. The ground state energy E_0 within the HF approximation, summed over electronic states, is given by

$$E_0 = \langle\Psi|\widehat{H}|\Psi\rangle = \sum_a^N \langle a|\widehat{h}|a\rangle + \frac{1}{2}\sum_{a,b}^N \langle ab||ab\rangle \tag{2.29}$$

where we denoted with $\widehat{h}$ the one-electron part of the Hamiltonian, that is, the kinetic energy and the one-body interaction operators. We also have defined

$$\langle ab||ab\rangle = \langle ab|\widehat{V}|ab\rangle - \langle ab|\widehat{V}|ba\rangle \tag{2.30}$$

The first term on the right hand side of Eq. (2.30) is the self-consistent field, while the second one is the exchange term. The HF equations are variationally obtained from Eq. (2.29) by varying the one-particle states involved in the matrix elements. The resulting one-particle states are then occupied according to their corresponding eigenvalues up to a maximum value, the Fermi energy, such that it exhausts the particle number. It is synonymous with the chemical potential in the case of a metal. The Hartree-Fock eigenvalues ϵ_k, referring to the chemical potential μ, are given by

$$\epsilon_k + \mu = \langle k|\widehat{h}|k\rangle + \sum_b^N \langle kb||kb\rangle \tag{2.31}$$

The split-off of the chemical potential from the one-particle energies is common practice in many-body statistical theory and is adopted here, too. Alternatively, in experimental practice, the chemical potential μ is often left out of this and the following two equations, providing a more direct connection between the eigenvalues of the Hartree-Fock hamiltonian, the binding energy and the electron affinity. At first, these eigenvalues arise as Lagrangian multipliers for norm conservation of the wave function, as in Ritz's variational principle. These eigenvalues get the meaning of one-particle excitation energies known as *Koopman's theorem*. To this end, one subtracts from Eq. (2.29) the corresponding expression with one particle missing and obtains the ionization potential IP, i.e. the energy required to remove from the N-particle ground state a particle occupying a single-particle state. In particular, we have

$$E_k^{N-1} - E_0^N - E_k^{N-1} = -\langle k|\widehat{h}|k\rangle - \sum_b^N \langle kb||kb\rangle = -(\epsilon_k + \mu) =: IP(k) \tag{2.32}$$

Therefore, we see that, given an N-particle Hartree-Fock ground state, the energy required to remove a particle in a single-particle state $|k\rangle$ is $-\epsilon_k$. In a similar way, we can consider the process of adding a particle in a single-particle state $|r\rangle$ to the ground state of the N-particle system. The assumption is that the remaining single particle states remain unchanged. The energy required for this process, the electron affinity EA, is then given by

$$E_0^N - E_r^{N+1} = \langle r|\widehat{h}|r\rangle + \sum_b^N \langle rb||rb\rangle = -(\epsilon_r + \mu) =: EA(r) \tag{2.33}$$

The sum of both expressions represents the excitation energy keeping the number of electrons constant. We note that the ionization potential and the affinity usually are positive quantities with suitable choice of the one-particle energy zero.

To solve the Hartree-Fock equations for a solid is quite cumbersome and the validity of the results is questionable. For example, the gap in insulators and semiconductors is sometimes overestimated by well over 100%. The reason is found in the exchange energy which is negative with an absolute value that is too high: this is due to neglect of the Coulomb hole, an electron's neighborhood of charge density reduced by screening. Thanks to the development of the Hohenberg-Kohn theorem, density functional theory (DFT) has become very successful and has almost entirely replaced all other single-particle-like methods. Various levels of accuracy and variants of the density functional are used. Details can be found elsewhere in this handbook [37, 70]. In the first version of the theory, gaps are underestimated by some 10%. This shortcoming is attributed to the failure of the ground state theory to describe excitations. Koopman's theorem does not hold, contrary to Hartree-Fock. Electron-electron interactions are partly present in the formalism, depending on the choice of the density functional, but its more or less local form does scarcely account for the neighboring electron configuration during excitation. Thus, transferring from a bonding to an antibonding state expands the charge which interacts with and changes the neighborhood via electrostatics and exchange, by Coulomb hole and screened exchange contributions. Improvements with respect to *correlation*, i.e. the difference between the true many-body state and the Hartree-Fock state, have been developed. Of course, they generally aim to take many-body corrections into account.

In DFT, the energy

$$E[n] = T[n] + \int d\mathbf{r} V(\mathbf{r}) n(\mathbf{r}) + \frac{e^2}{8\pi\epsilon_0} \int d\mathbf{r} d\mathbf{r}' \frac{n(\mathbf{r}) n(\mathbf{r}')}{|\mathbf{r} - \mathbf{r}'|} + E_{xc}[n] \tag{2.34}$$

has to be minimized under the constraint of particle number conservation with respect to the density n. Square brackets denote functional dependence. The exchange-correlation functional $E_{xc}[n]$ is adapted in an approximate way from its homogeneous electron gas form, thereby replacing the constant density n_0 by the true density n. The second term on the right of Eq. (2.34) includes the electron-nucleon potential and, if present, an external force. The third term is the classical electrostatic electron-electron interaction. The kinetic energy $T[n]$ can be chosen such that a set of Schrödinger-like equations arises as variational equations, the so-called *Kohn-Sham equations*

$$\left(-\frac{\hbar^2}{2m} \nabla^2 + v_{\text{eff}}(\mathbf{r}) \right) \phi_k(\mathbf{r}) = \epsilon_k \phi_k(\mathbf{r}) \tag{2.35}$$

with an effective one-body potential

$$v_{\text{eff}}(\mathbf{r}) = V(\mathbf{r}) + \frac{e^2}{4\pi\epsilon_0} \int d\mathbf{r}' \frac{n(\mathbf{r}')}{|\mathbf{r} - \mathbf{r}'|} + \frac{\delta E_{xc}[n]}{\delta n(\mathbf{r})} \tag{2.36}$$

The density is given by a sum over occupied states

$$n(\mathbf{r}) = \sum_k |\phi_k(\mathbf{r})|^2 \tag{2.37}$$

which can be solved iteratively to self-consistency together with Eq. (2.35).

2.2.6 Perturbation expansion

To develop a suitable perturbation approach, let us start with the formal definition of the *one-particle many-body time-ordered Green function* G for fermions:

$$\begin{aligned} G(k_1, t_1, k_2, t_2) = \quad & G^+(k_1, t_1, k_2, t_2) = -i \left\langle \Psi_0^N \middle| c_{k_1}(t_1) c_{k_2}^\dagger(t_2) \middle| \Psi_0^N \right\rangle, \; t_1 > t_2 \\ & G^-(k_1, t_1, k_2, t_2) = +i \left\langle \Psi_0^N \middle| c_{k_2}^\dagger(t_2) c_{k_1}(t_1) \middle| \Psi_0^N \right\rangle, \; t_1 < t_2 \end{aligned} \tag{2.38}$$

Here $c_k^\dagger(t)$ and $c_k(t) = e^{\frac{i}{\hbar}\widehat{H}t} c_k e^{-\frac{i}{\hbar}\widehat{H}t}$ are, respectively, the creation and destruction operators at time t in a single-particle state k. The time dependence used here is attributed to the so-called *Heisenberg representation*. By k we denote a set of quantum numbers like, for example, momentum $\mathbf{k}$ and spin α. An equation analogous to Eq. (2.10) can be derived for G by differentiating Eq. (2.38) with respect to time but with the essential difference that, besides the $H_0 \cdot G$ term in Eq. (2.10), expectation values over more than two particle operators arise, owing to the number of four c-operators in the interaction part of H. They cannot be

decomposed into a product of known quantities factoring out G in a closed form. Instead, by definition the self-energy Σ is formally introduced according to Eq. (2.20), while tools must still be developed to determine Σ explicitly. In the single-particle case, however, Eq. (2.38) defines G as obeying Eq. (2.10). The functions $G^{\pm}$ are also defined by Eq. (2.38), postulating them to be zero outside the ascribed time interval. They merely serve here for short hand notation. They are different from the retarded and advanced functions which are used in Eq. (2.12) for the one-particle case. The latter can be obtained by $G^r = G - G^<$ and $G^a = G - G^>$, respectively, through the quantities $G^>$ ($G^<$) which equal G^+ (G^-) but extend the specific definition (2.38) to the whole time domain. Let us now take a look at the physical interpretation of the above defined quantities.

An inspection of Eq. (2.38) suggests considering G^+ written as $G^+ = -i \langle B|A\rangle$, where $|A\rangle = c^\dagger_{k_2}(t_2)\left|\Psi^N_0\right\rangle$ and $\langle B| = |B\rangle^\dagger = \left(c^\dagger_{k_1}(t_1)\left|\Psi^N_0\right\rangle\right)^\dagger$. Then the many-body GF G^+ describes the following sequence of events. Initially, the system is in its ground state $\left|\Psi^N_0\right\rangle$. A particle is created at t_2 in a single-particle state (sps) k_2. Later on, at time t_1, the system has the added particle in the sps k_1. G^+ is proportional to the overlap of these two states, i.e. the probability amplitude that the system at time t_1, after a particle has been introduced at time t_2 in the sps k_2, has the added particle in a sps k_1, which corresponds to the physical interpretation given already. In an analogous way one obtains G^-, the propagator of a hole. When one wants to calculate the GF of Eq. (2.38), a big challenge lies in the fact that $\left|\Psi^N_0\right\rangle$ is the ground state of the interacting N-particle system, which is impossible to calculate in full generality. In fact, it would be more convenient to calculate the matrix elements appearing in Eq. (2.38) between the states corresponding to the ground state of the non-interacting N-particle system. In principle, the idea is to start off with a non-interacting system, "switch on" the interactions and wait until the new interacting stationary state has been achieved.

It is possible to arrive at a formula which allows calculating the propagator by successive approximations. To accomplish this, one moves to the interaction picture. So far we have worked within the Schrödinger picture, namely by using the Schrödinger equation as given by Eq. (2.9), with $\widehat{H}$ instead of $\widehat{H}_0$. To solve it approximately in terms of a perturbation expansion with respect to a small quantity one has to split off a relatively small part $\widehat{V}$ of the total Hamiltonian $\widehat{H} = \widehat{H}_0 + \widehat{V}$ and expand. The method is again not limited to simply cutting off the expansion at a certain order, but it allows partial summation over certain subsets which appear to yield dominant contributions to the exact result. This becomes especially clear if single terms diverge at any order for special values of the parameters involved. It indicates an instability which would also appear in the exact expression as some kind of singularity at the radius of convergence given by the special parameter values. The partial summation and also the exact result may even hide this singularity which artificially appears in the single expansion terms, because the derivatives may exist up to some order thereby smoothing the parameter dependence of the summed result. Think e.g. of a geometrical series of terms each diverging at the same special parameter value where, however, the series converges to zero and has by continuation a convergence radius which covers that parameter value.

Therefore, one has to design an expansion scheme such that a power series with respect to $\widehat{V}$ is generated, no matter whether it converges or not. This needs some formal manipulations of the Schrödinger equation where the known time evolution of the unperturbed Hamiltonian $\widehat{H}_0$ is taken into account from the beginning: the correction to this time dependence is

formulated as a new evolution equation in the so-called *interaction representation*. In this representation, the wavefunction of the system $|\psi(t)\rangle_I$ is transformed according to

$$|\psi(t)\rangle_I = e^{\frac{i}{\hbar}\widehat{H}_0 t}|\psi(t)\rangle \tag{2.39}$$

The time evolution of the states $|\psi(t)\rangle_I$ and operators in the interaction representation are given by

$$i\hbar\frac{\partial}{\partial t}|\psi(t)\rangle_I = \widehat{V}_I(t)|\psi(t)\rangle_I \tag{2.40}$$

$$\widehat{O}_I(t) = e^{\frac{i}{\hbar}\widehat{H}_0 t}\widehat{O}e^{-\frac{i}{\hbar}\widehat{H}_0 t} \tag{2.41}$$

Thus, in the interaction representation, the interaction wavefunction $|\psi(t)\rangle_I$ satisfies a Schrödinger equation with the Hamiltonian $\widehat{V}_I$, while all operators carry now an explicit time dependence defined by the non-interacting Hamiltonian $\widehat{H}_0$. We can now determine how the functions $|\psi(t)\rangle_I$ evolve with time in the interaction representation. Instead of the wave function we will use the Green function. We will omit the index I in the following, understanding all time dependence taken in the interaction representation.

The definition of the propagator Eq. (2.38) contains as unknown quantities the exact ground state and the time dependence of the Fermi operators through the full Hamiltonian. The transition to the interaction picture splits off the perturbation in a way similar to the procedure in the wave equation, see Eq. (2.40). The time dependence is then composed of the bare Hamiltonian via $\widehat{H}_0$ and a complicated correction which involves $\widehat{V}$. The latter is expanded in terms of $\widehat{V}$. The unknown ground state is dealt with in an analogous manner and reduced to the corresponding ground state of the unperturbed system by means of the adiabatic hypothesis. It consists in assuming that the interacting ground state is obtained from the bare ground state by switching on the interaction infinitely slowly, i.e. adiabatically or without change of energy. It turns out that a very convenient representation of the many terms of the different series occurs, through the time ordering which is denoted by $\widehat{T}$. All factors appearing after that operator have to be ordered in an ascending time sequence from right to left. Thus, one gets an expression for the GF in the form of a perturbation expansion, with the advantage that the matrix elements have to be evaluated between unperturbed ground state vectors of a many-body system. Such matrix elements consist of terms like $\langle\Phi_0|\,\widehat{T}\left\{\widehat{A}_1...\widehat{A}_n\right\}|\Phi_0\rangle$, where the operators $\widehat{A}_i$ are creation or destruction operators for particle and holes in the interaction representation. The propagator of Eq. (2.38) then reads

$$G(k_1,t_1,k_2,t_2) = -i\sum_{n=0}^{\infty}\frac{1}{n!}(-\frac{i}{\hbar})^n\int_{-\infty}^{\infty}dt_1'\int_{-\infty}^{\infty}dt_2'\ldots\int_{-\infty}^{\infty}dt_n' \tag{2.42}$$
$$\left\langle\Phi_0\left|\widehat{T}\left\{\widehat{V}(t_1')\widehat{V}(t_2')\ldots\widehat{V}(t_n')\widehat{c}_{k_1}(t_1)\,\widehat{c}^{\dagger}_{k_2}(t_2)\right\}\right|\Phi_0\right\rangle^C$$

The matrix elements are evaluated by using *Wick's theorem* which states that such an expectation value over a product of creation and destruction operators can be decomposed into a product of expectation values of pairs each containing one creation and one destruction operator,

i.e. the unperturbed propagators arise. Take Eq. (2.38), replace the true state Ψ_0 by the unperturbed state Φ_0, and use for the time dependence of the operators the unperturbed Hamiltonian $\widehat{H}_0$. A detailed explanation of the mathematics which allow calculating the matrix elements in a systematic way are beyond the scope of this introduction , see e.g. references [33, 80]. We want to stress, however, that to each term in the series expansion corresponds a proper diagram. In particular, some of the diagrams can be divided into different unconnected pieces, and for this reason they are called *disconnected diagrams*. It is possible to show that only connected or linked diagrams must be taken into account in the evaluation of the propagator, according to the so-called *linked cluster theorem*. That is indicated by the superscript C.

There is an alternative method to derive the perturbation expansion which is entirely equivalent to the above, and also frequently used. The association of Eq. (2.38) with the notion of a Green function as developed in the foregoing paragraphs is more suggestive in that procedure. Briefly, the method uses an equation of motion for the quantity (2.38) obtained from the time dependence of the creation and destruction operators in the Heisenberg representation. A four-operator product appears on the right hand side of this equation within the expectation value bracket. The time evolution of that higher order Green function yields in turn successively higher orders, leading to a hierarchy of equations with an increasing number of operators in the expectation value for the higher-order Green functions. The equation of motion has a structure formally equal to Eq. (2.10), thus suggesting the notion of a Green function. The diagrammatic expansion also follows the rules given below. However, the reasoning for approximations differs occasionally. What appears as a summing up of a subseries of the whole expansion in the language of diagrams is a decoupling or factorization of a higher-order Green function into lower-order ones.

2.2.7 Diagrams in many-body systems

We already introduced some diagrams in the case of a single quantum mechanical particle and introduced the concepts of selective summation. Here we extend the treatment to a system of N particles. The unperturbed Hamiltonian $\widehat{H}_0 = \sum_n < n|h|n > \widehat{c}_n^\dagger \widehat{c}_n$, is assumed diagonal in the single particle states, say of the one-particle potential of a solid. As $< \Psi_0^N|$ and $|\Psi_0^N >$ in Eq. (2.38) are the same states (fully occupied up to the Fermi surface), G_0 is diagonal in the configuration index n, as well. We now focus on a two-body particle-particle interaction. In second quantization the interaction terms have the form of the two-body operator $\widehat{V}_I = \frac{1}{2} \sum_{k,l,m,n} \langle kl|V|mn\rangle \widehat{c}_k^\dagger \widehat{c}_l^\dagger \widehat{c}_n \widehat{c}_m$, where the matrix element $\langle kl|V|mn\rangle$ involves four single-particle states. Such a matrix element describes the interaction between two particles or holes which, starting as single-particle states ϕ_m and ϕ_n, collide and scatter into the single-particle states ϕ_k and ϕ_l, respectively. This expression for $\widehat{V}_I$ has to be inserted in Eq. (2.42). Applying Wick's theorem as indicated will yield a sum of products of bare propagators $G_0\left(l_2, t_2, l_1, t_1\right)$ which are characterized by two time and two configurational indices.

The book-keeping of the whole series expansion is now illustrated by diagrams and rules governing their construction, their manifold, and the quantitative expression in Eq. (2.42) associated with them. Instead of Fourier transforming to energies, the original time variables

are used here. The propagator G_0 is drawn as a line with the endpoints 1 and 2 whose notation comprises occasionally both space and time variables, cf. Fig. (2.4). Each of these points is connected through the indices with an interaction matrix element, with the exception of the outer indices belonging to the left hand side of Eq. (2.42). The matrix element is plotted as a wavy line. It actually has four endpoints (connections) according to the indices of $\langle kl|V|mn\rangle$. They are grouped pairwise such that (k, m) and (l, n) are at opposite ends of the wavy line, with (m, n) on one side of the line and (k, l) on the other. One can think of the pair (k, m) as belonging to one particle and (l, n) to the other. For example, two matrix elements appear in Fig. (2.4c) associated with a wavy line, the left one with indices $\langle k_1 m|V|kl\rangle$ and the right one with $\langle kl|V|k_2 m\rangle$. The connecting points are called vertices and their indices are summed or integrated over, depending on whether the index labels discrete configurations or a continuous time, respectively. There is only one time associated with each wavy line. The perturbation series for the single particle propagators are built as the sum of all possible different connected diagrams which can be constructed with the basic two-body forces interaction diagram. Such diagrams illustrate how the many body interactions which take place in the system modify the single particle or hole propagators. There is a one to one correspondence between each of these diagrams and each of the terms in the perturbation series expansion. Besides the general case where one does not distinguish between different orders of time, diagrams can be ordered by time: this involves the explicit notation giving the time relation in the propagator, i.e., the notation with particle and hole propagators. Both pictures are valuable and used below.

We will limit our attention to some of the main diagrams which are obtained in the lowest order of approximation for the particular case of the single particle propagator. When ordered by time a particle diagram is drawn such that the particle enters at the start of a line, undergoes all the possible interactions with the background and then leaves at the end of a line. There are only two first order diagrams, corresponding to $n = 1$ in Eq. (2.42). The first diagram, shown in Fig. (2.4a), describes the direct interaction of the particle with any particle n of the background. One line leaves and enters at the same point, a so-called loop. It means equal times in that propagator.

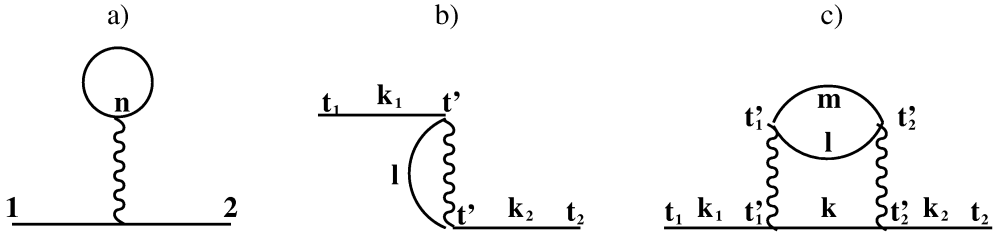

Figure 2.4: First order a) and b), second order c) Coulomb interaction graphs, instead of space momentum variables are denoted in b) and c); only GF indices are shown, matrix elements are e.g. $\langle 1n|V|2n\rangle$, $\langle k_1 l|V|lk_2\rangle$ in a), b), resp..

A propagator associated with a single loop represents the particle/hole occupation number. If the configuration index denotes the momentum of a homogeneous system and if the bare ground state is the free-electron Fermi sphere, then the vertex of the loop has two equal momentum indices, i.e. momentum does not change at one end of the interaction. If momen-

tum is conserved, as e.g. in the Coulomb interaction, then also at the other end no change of momentum can occur. The second process, shown in Fig. (2.4b), corresponds to a particle which undergoes *exchange scattering* against the background particles.

In second order, which means that there are two interactions, the particle propagator can be affected by several scattering processes. A well known and very important type of diagram is shown in Fig. (2.4c), and corresponds to the polarization of the background particles due to the perturbation induced by the incoming particle. Initially the particle (k_1) propagates freely, and then it interacts with the background particles by creating a particle-hole pair (lm). The original particle (now k) and the created particle-hole pair propagate free from interactions, until a new scattering interaction with the original particle annihilates the pair, so that the background returns to its original ground state. This diagram is a non-trivial example of self-energy diagrams. Such diagrams must be considered as an indirect interaction of the particle via the medium with itself. The particle creates a disturbance in the system (interaction) which is then reabsorbed by the particle as it propagates.

We have already pointed out how Dyson's Eq. (2.20) changes the problem of calculating the single particle GF into one of calculating the self-energy. Thus, rather than calculating the whole propagator series, the solution of the problem can be attempted by calculating the self-energy contribution starting directly from the diagrams, and then converting them into an analytical form.

We now illustrate qualitatively the use of Feynman's diagrams in expanding the self-energy. This process is the selective or partial summation, which is equivalent to performing an infinite summation on a series of terms which may even be divergent: in an extreme case, this can produce a new series in which all terms are finite. The original perturbation series usually are not convergent even if the single terms are finite, mostly they are only semiconvergent (asymptotically convergent). Thus they give only a formal representation of the exact expression. One tries to remedy both possible defects, lack of convergence and infinite values of individual terms of the series, by partial summation, which may involve reordering, cancellation of individual terms or cancellation of an infinite number of terms. Not only is the summation performed on self-energy diagrams, but also the interactions themselves are renormalized. This is equivalent to considering effective interactions rather than bare ones. The physical meaning of the effective interactions is that the bare interaction virtually polarizes the medium, and the polarization cloud in turn shields the bare interaction converting it to the much weaker effective interaction. The screened interaction between two points consists of a large number of excitations involving many electron-hole pairs, thus involving the system as a whole.

The diagrams describing the terms in the perturbation expansion can be divided into two classes: reducible (improper) and irreducible (proper). Reducible diagrams can be divided into two by cutting one internal fermion line as e.g. the last two diagrams in Fig. 2.3a, while irreducible ones cannot, as those in Fig. 2.4.

First we attempt to calculate the self-energy. We define as a self-energy part any diagram without external lines, which can be inserted into a particle or hole line. The solution of the Dyson equation is exact, in the sense that all the diagrams have been counted, proper ones and their repetitions. The repetitions appear through the iteration of the Dyson equation; the proper diagrams are to be contained already in the self-energy. Thus, the self-energy must not contain improper diagrams. In principal, it is possible to sum over all repetitions of all irreducible self-

energy parts. We have actually shown this process already in Fig. 2.3a. We have only summed over the repeated proper parts, but we still need to sum over the proper parts themselves. This is impossible in full generality, and is normally done with approximations. Understanding which diagrams have more weight in the self-energy expansion is actually challenging: such choice in fact reflects the approximations which are used to describe the system. In other words, choosing the right diagrams to sum over when expanding the self-energy is equivalent to outline the most important physical interactions which take place in a many-body system.

As we associate the full propagators to the straight lines instead of just G^+ or G^-, we have a particle line for the positive time difference, and a hole line otherwise. By suppressing the time order, the drawing of the diagrams can be greatly reduced to their topological equivalence and without any time arrows.

Now we look at the interactions. We define as proper or irreducible polarization part any diagram without external interaction lines which can be inserted into an interaction line and which cannot be split into two by cutting an internal interaction line. When we include all the possible polarization parts, we get the fully screened interactions, as diagrammatically sketched in Fig. 2.5. This procedure is called the dressing or renormalization of the interaction. As an effect of the renormalization, no interaction lines have inserted polarization parts and all interaction lines are dressed. Moreover, as shown in Fig. 2.5b, the interactions obey an equation with the same structure as Dyson's equation, obtained by summing the bare interaction lines with all the possible insertions of proper polarization parts.

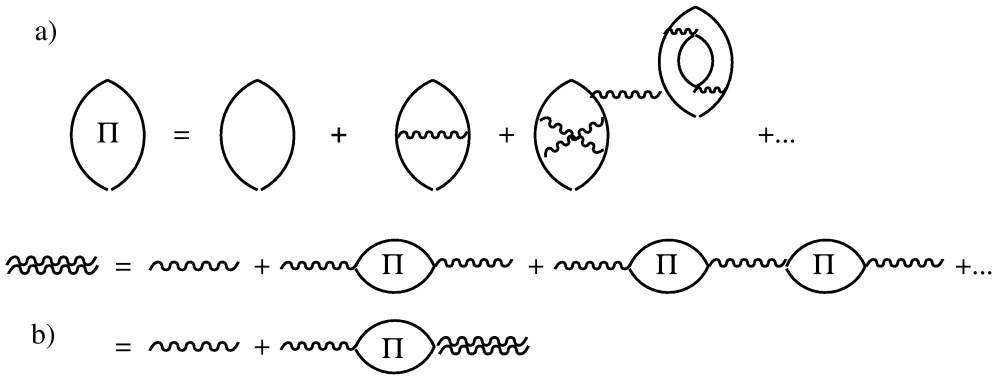

Figure 2.5: Renormalization of interaction by polarization diagrams: a) contributions to polarization, first two graphs are irreducible, third is reducible decomposing into two irreducible ones by cutting the interaction right of the left bubble and has to be removed from a) because it automatically appears in b); b) analog of Dyson equation for interaction.

So far we have seen that the series for the propagator can be expressed in terms of the proper self-energy Σ which can in turn be expressed in terms of the effective interactions. As in Fig. 2.3 we also dress propagator lines. In fact, the self-energy Σ is obtained by summing over all diagrams in which the propagator lines already contain the self-energy. This produces a series in which no propagator lines can be grouped into self-energy parts and all of them have been replaced by clothed propagators.

A vertex is defined as any point in a diagram determined by the intersection of two fermion lines and one interaction line. Then, the vertex part is any diagram without external lines which can be inserted in place of a vertex. The summation for the vertex part can be decomposed in a procedure analogous to renormalization into an irreducible part and its repetition. The lowest order vertex is just a point with three plug-ins, one for the interaction and two for fermions. Any approximation beyond the bare point is called vertex correction.

Altogether, it would be the aim to renormalize simultaneously the interactions, the propagators and the vertices. In the literature the double lines are often omitted, and it is stated that both the interactions and the propagator lines have been renormalized. The whole procedure sketched above produces a large simplification of the book-keeping, illustrating the series expansion of Eq. (2.42).

2.2.8 Spectral representation

We now show how the Green functions $G^{\pm}$ can be expressed in a form which is related to the excitation spectrum of the full Hamiltonian.

By inserting in the definition of the Green function, Eq. (2.38), the unity operator $I = \sum_{n,M} \left|\Psi_n^M\right\rangle \left\langle\Psi_n^M\right|$ (here, n denotes excited states of an M-particle system), we have with $t_1 = t$, $t_2 = 0$ and $k_1 = k_2 = k$

$$G^+(k,t) = -i\theta(t) \sum_n |\langle\Psi_n^{N+1}|\widehat{c}_k^\dagger|\Psi_0^N\rangle|^2 e^{-\frac{i}{\hbar}(E_n^{N+1} - E_0^N)t} \tag{2.43}$$

After Fourier transforming, we get an expression very similar to the one-particle case treated before, namely

$$G^+(k,E) = \sum_n \frac{|\langle\Psi_n^{N+1}|\widehat{c}_k^\dagger|\Psi_0^N\rangle|^2}{E - (E_n^{N+1} - E_0^N) + i\delta} \tag{2.44}$$

Similarly, we get G^- with $M = N - 1$ for hole creation, with negative imaginary part in the denominator, and with opposite sign of the energies within the parentheses of the denominator. As already pointed out earlier, the poles of the single particle propagator occur at the difference between the exact energy of the excited states of the $N \pm 1$-particle system and the exact ground state energy of the N-particle system. By introducing the $N \pm 1$ ground state energies $E_0^{N\pm1}$ and referring the total excitation energies to them, we obtain ε_n^{N+1} and ε_n^{N-1}. We define the *chemical potentials* $\mu^{N\pm1}$ of the N- and $N-1$-particle systems, respectively, by

$$E_0^{N+1} - E_0^N = \mu^{N+1}, \qquad E_0^N - E_0^{N-1} = \mu^{N-1} \tag{2.45}$$

These are assumed to be independent of the particle number for large N. Thus we have for G, see Eq. (2.38),

$$\begin{aligned} G(k,E) &= G^+(k,E) + G^-(k,E) \\ &= \sum_n \frac{|\langle\Psi_n^{N+1}|\widehat{c}_k^\dagger|\Psi_0^N\rangle|^2}{E - \varepsilon_n^{N+1} - \mu + i\delta} + \sum_n \frac{|\langle\Psi_n^{N-1}|\widehat{c}_k|\Psi_0^N\rangle|^2}{E + \varepsilon_n^{N-1} - \mu - i\delta} \end{aligned} \tag{2.46}$$

The structure of the denominators in $G^{\pm}$ accounts for the widespread application of the GF formalism in spectroscopy. In fact, we can see that the poles of the GF G^{+} and G^{-} give, respectively, the affinities and the ionization potentials of the N-particle system. Thus, a minimum $\varepsilon_n^{N\pm1} = 0$ refers to the lowest affinity and ionization potential in a conduction band of a metal. In particular, we may consider the conservation of energy for the photoemission process,

$$h\nu + E_0^N = \varepsilon_{\text{kin}} + E_n^{N-1} \tag{2.47}$$

where $h\nu$ is the photon energy and ε_{kin} the kinetic energy of the photoelectron outside the solid. We write W for $-\mu$, the work function, represented by the vacuum barrier. Eq. (2.47) is generally valid for atoms, molecules and solids. In the case of surfaces, it is common to explicitly take into account the effect of the solid-vacuum barrier, so that the work function W is added to $\varepsilon_{textkin}$ to get the binding energy ε_b from the difference to the photon energy. The binding energy of the photoelectron is then given by

$$\varepsilon_b = h\nu - \varepsilon_{\text{kin}} - W = E_n^{N-1} + \mu - E_0^N = \varepsilon_n^{N-1} \tag{2.48}$$

so that ε_b yields a measure of the excitation energies for the $N-1$-particle system. Note that it is defined as a positive quantity. In photoemission, binding energies are normally referred to the Fermi level, so that $\varepsilon_{textkin}$ is the kinetic energy measured by the spectrometer with the specific work function of the spectrometer. The latter is constant and can be subtracted from all measurements after standard calibration procedures. It is interesting to evaluate the many-body GF of Eq. (2.46) in the case of a system described in the Hartree-Fock approximation. Again we are assuming that the remaining single particle states remain unchanged in the process of adding to or subtracting a particle from the N-particle ground state, so that we can approximate the final states of the $N+1$- and $N-1$-particle systems as $|\Phi_n^{N+1}\rangle = \widehat{c}_n^{\dagger}|\Phi_0^N\rangle$ and $|\Phi_n^{N-1}\rangle = \widehat{c}_n|\Phi_0^N\rangle$, respectively. Thus the GF of Eq. (2.46) becomes

$$G(k,E) = \sum_n \frac{|\langle\Phi_0^N|\widehat{c}_n\widehat{c}_k^{\dagger}|\Phi_0^N\rangle|^2}{E - \varepsilon_n^{N+1} - \mu + i\delta} + \sum_n \frac{|\langle\Phi_0^N|\widehat{c}_n^{\dagger}\widehat{c}_k|\Phi_0^N\rangle|^2}{E + \varepsilon_n^{N-1} - \mu - i\delta} \tag{2.49}$$

Measuring the energy with respect to the chemical potential, $\epsilon := E - \mu$ and introducing $\varepsilon_n^{N+1} = \epsilon_k > 0$, $\varepsilon_n^{N-1} = -\epsilon_k > 0$ for the Hartree-Fock energies ϵ_k of particles and holes, respectively, we obtain

$$G(k,\epsilon) = \frac{\theta(k-k_F)}{\epsilon - \epsilon_k + i\delta} + \frac{\theta(k_F-k)}{\epsilon - \epsilon_k - i\delta} \tag{2.50}$$

We thus retrieve Koopman's theorem, according to which the value of $\epsilon_k + \mu$ are the affinity and the binding energy of the system for $k > k_F$ and $k < k_F$, respectively. If we leave out μ (as discussed earlier), the same equation (2.50) results. It is interesting to note that both residues around the poles are equal to one and the imaginary part goes to zero, reflecting the fact that these are exact single particle states with infinite lifetime.

As regards the photoemission process, it is of fundamental importance to observe that the derivation of Eq. (2.50) is based on the assumption that $|\Phi_n^{N-1}\rangle = \widehat{c}_k|\Phi_0^N\rangle$, that is, in the

process of subtracting from the N-particle ground state a particle in the sps k, the remaining single-particle states remain unchanged. This is the reason why Koopman's theorem provides the binding energies in the so called *frozen-orbital approximation*, meaning that only the sps state k is considered "active" in the photoemission process, while the other $N-1$ electrons are "passive" spectators, "frozen" in their original single-particle states.

The main ingredient which is neglected in the frozen-orbital approximation is the fact that when a photoelectron in a sps k is emitted from a N-particle system, the remaining $N-1$ electrons relax into a new energy state with energy lower than the Hartree-Fock energy E_n^{N-1} by an amount equal to δE_{relax}, called *relaxation energy*. As a result of neglecting the relaxations, such calculations tend to over-estimate the binding energy. Moreover, Koopman's theorem must be corrected with the electron-electron *correlation effects* which are obtained in going beyond the HF approximation and which reduce the total energy from its HF value.

The *correlation energy* is defined as the difference between the exact energy and the one calculated with Hartree-Fock, namely $E_{\text{corr}} = E_{exact} - E_{HF}$. The correlation energies must be considered for both the initial and the final states, and they are larger in absolute value for systems with higher particle number. Since the correlation energies are negative, the net contribution to the binding energies from correlation effects is positive, i.e. $\delta E_{\text{corr}} = E_{\text{corr}}^{N-1} - E_{\text{corr}}^{N} > 0$.

Therefore, taking into account relaxation and correlation effects, the correction to the expression of the binding energies obtained by Koopman's theorem is given by

$$\varepsilon_k = -\epsilon_k - \delta E_{\text{relax}} + \delta E_{\text{corr}} \tag{2.51}$$

We notice that the corrections due to relaxation effects and correlation effects tend to cancel each other out, so that Koopman's theorem provides a reasonable approximation for the binding energies in photoemission. Striking counterexamples are presented by insulators whose HF gaps are significantly overestimated.

We now define the *spectral density functions*:

$$A^{\pm}(k,\epsilon) = \sum_n \left|\left\langle \Psi_n^{N\pm1} \left|\widehat{a}\right| \Psi_0^N \right\rangle\right|^2 \delta\left(\epsilon - \varepsilon_n^{N\pm1}\right) \tag{2.52}$$

Here $\widehat{a}$ stands for $\widehat{c}_k^{\dagger}$ or $\widehat{c}_k$, respectively, for the upper or lower sign. The spectral density functions are obviously positive, vanish for $\epsilon < 0$, and are related to the momentum distribution function $\langle n_k \rangle = \left\langle \Psi_0^N \left| \widehat{c}_k^{\dagger}\widehat{c}_k \right| \Psi_0^N \right\rangle$ through

$$\int_0^{\infty} dx A^{+}(k,x) = 1 - \langle n_k \rangle\,, \qquad \int_0^{\infty} dx A^{-}(k,x) = \langle n_k \rangle\,, \tag{2.53}$$

From this the *sum rule* immediately follows:

$$\int_0^{\infty} dx \left[A^{+}(k,x) + A^{-}(k,x)\right] = 1 \tag{2.54}$$

We can represent the Green function of Eq. (2.46) with the help of the spectral functions,

namely

$$G\left(k,\epsilon\right)=\underbrace{\int_0^\infty dx\frac{A^+\left(k,x\right)}{\epsilon-x+i\delta}}_{G^+}+\underbrace{\int_0^\infty dx\frac{A^-\left(k,x\right)}{\epsilon+x-i\delta}}_{G^-} \tag{2.55}$$

which in turn yields the spectral functions via

$$A^{\pm}(k,\epsilon)=\mp\frac{1}{\pi}\,\mathrm{Im}\,G(k,\pm\epsilon),\qquad \epsilon>0 \tag{2.56}$$

Thus, the Green function G contains the particle as well as the hole spectrum whereas each spectral function A^+ and A^- is associated with only one spectrum. For free particles the spectral density is a δ-function

$$A^{\pm}\left(k,\epsilon\right)=\theta\left(\pm k\mp k_F\right)\delta\left(\epsilon-\varepsilon_n^{N\pm1}\right)=\theta\left(\pm k\mp k_F\right)\delta\left(\epsilon\mp\epsilon_k\right) \tag{2.57}$$

that is, the spectral functions are δ-functions at the energies of the single-particle states. In other words, if we are able to detect single-particle states in the system, these must have a spectral function which is a δ-function. Therefore, quasi-particles, which are effective single-particle states, must have a spectral function which resembles a δ-function, like a single peak. We can imagine any curve resembling a sharp peak as being composed of a quasi-particle peak plus a background. We can then make use of Eq. (2.55) with a spectral function which is not a δ-function any more but function with a certain width centered around the peak position. The spectral function dominates in the integral, and it may be assumed that the peak can be represented as a Lorentzian line, i.e. two complex conjugate poles at a quasi-particle state $\epsilon'_k\pm i\Gamma$ with peaked contribution in A^+ and at a quasi-hole state $-\epsilon'_k\pm i\Gamma$ peaked in A^-. If we write the spectral functions as

$$A^{\pm}(k,\epsilon)=\theta(\epsilon)\frac{1}{\pi}\frac{\Gamma Z}{(\epsilon\mp\epsilon'_k)^2+\Gamma^2}+\text{background} \tag{2.58}$$

then Eq. (2.55)yields the following Green function through contour integration – both parts G^+ and G^- complete the full real axis and of the poles at $\pm i\Gamma$ only that one is picked up which belongs to the imaginary half-plane opposite to that of the pole characterized by the infinitesimal δ in Eq. (2.55):

$$G(k,\epsilon)=\frac{Z}{\epsilon-\epsilon'_k+i\Gamma\mathrm{sign}(\epsilon)}+\text{background} \tag{2.59}$$

Note again that $\epsilon'_k>0$ holds for the particle case with A^+ carrying the peak contribution, and $\epsilon'_k<0$ for the hole case with A^-. We can view Z as the residue of $G^{\pm}$, the so-called renormalization constant. It represents the spectral weight of the dominant structure, the remaining background being smooth. Since $A^{\pm}\left(k,\epsilon\right)$ obeys the sum rule of Eq. (2.54), $Z<1$ follows, because the first term in Eq. (2.58) integrates to Z and the positive background accounts for the difference from unity according to the sum rule. Equation (2.59) reflects the fact that the quasi-particle is a single-particle state with a probability less than unity. The quantities Γ and

Z may depend on k as well as on ϵ, because they derive from the self-energy, the more important dependence owing to $\Gamma(\epsilon)$. For example, if $\Gamma(\epsilon)/\epsilon \to 0$ for $\epsilon \to 0$ in approaching the Fermi energy, the right part Eqs. (2.53) and Eq. (2.58) reveal that $< n_k >$ vanishes from above ($\epsilon'_k = 0^+$) and coincides with Z from below ($\epsilon'_k = 0^-$). Thus the Z is equal to the discontinuity of the momentum distribution function at the Fermi level: as expected, the discontinuity is equal to 1 for a noninteracting system, where the Fermi function is a θ function at $T = 0$ which drops discontinuously to zero, and it is less than 1 (and the step function gets partly smeared) when the interactions are turned on. A particle peak of finite width above the Fermi sea is not entirely confined to above the tail leading to a finite hole occupation below. That is reflected according to Eqs. (2.53) and (2.58) by non-vanishing $A^-(k, \epsilon)$ for $\epsilon'_k > 0$ with $\epsilon > 0$. A finite value of Γ shows a finite lifetime of the quasi-particle state. Investigating many-body effects such as in strongly correlated systems photoemission spectra predominantly are interpreted in terms of quasi-particle energies and the spectral function, which seduces because of its simplicity bearing the danger of misinterpretation, however. [39] The actual photoemission analysis becomes a little delicate if the energy-dependent lifetime vanishes at the Fermi level depending on the kind of Fermi-liquid. The spectral density is then no longer Lorentzian and is sensitive to the asymptotic law , which can be experimentally investigated. [20, 48] For a peak ϵ'_k within the Fermi sea, Z may be identified with the integral of A^- – compare Eq. (2.55) with (2.59) – which thus corresponds via Eq. (2.53) to the quasi-particle weight of the $T = 0$ occupation number.

In spite of the advantage offered by the quasi-particle picture, there still remains the question whether it is applicable in specific cases. However, if the perturbation theory for the proper self-energy holds and if the self-energy can be analytically expanded in a power series with respect to the perturbation parameter, then quasi-particle states may adequately reflect the excitations provided the obtained lifetime is reasonably long. The latter decreases e.g. in metals with decreasing distance from the Fermi level, so the picture may break down far from it.

For the particular case of photoemission, neglecting the Z factor, the hole GF for a quasi-particle (we should say "quasi-hole") can be written as

$$G(k, \epsilon) = \frac{1}{\epsilon - \epsilon'_k - i\Gamma} \tag{2.60}$$

with $\frac{1}{\hbar}\Gamma = \tau^{-1}$ being the inverse lifetime τ of the single-particle state. This form is particularly useful because it allows us to see a direct connection among GF, spectral function and self-energy, see Eq. (2.21). In fact, if the self-energy can be estimated, all the many body effects can then be described by considering a quasi-particle with renormalized energy equal to $\epsilon'_k = \epsilon_k + \Sigma_r + i\Sigma_i$, where ϵ_k is the energy of the bare particle and the self-energy is expressed by its real and imaginary parts as $\Sigma = \Sigma_r + i\Sigma_i$. Therefore, we see that the real part of the self-energy describes the correction to the value of the energy of the bare particle, while the imaginary part describes the finite lifetime of the quasi-particle state. In other words, we consider in Eq. (2.60) $\epsilon'_k = \epsilon_k + \Sigma_r$ and $\Gamma = \Sigma_i$.

We thus obtain the following formulas often found in the literature

$$G(k,\epsilon) = \frac{1}{\epsilon - \epsilon_k - \Sigma} = \frac{1}{\epsilon - (\epsilon_k + \Sigma_r) - i\Sigma_i} \tag{2.61}$$

$$A^-(k,-\epsilon) = \frac{1}{\pi}\,\mathrm{Im}\,G(k,\epsilon) = \frac{1}{\pi}\,\frac{\Sigma_i}{[\epsilon - (\epsilon_k + \Sigma_r)]^2 + \Sigma_i^2} \tag{2.62}$$

2.2.9 Photocurrent

A general expression for the photocurrent in photoemission is given by the expectation value of the current operator, cf. [64], using SI units:

$$\mathbf{j}(\mathbf{r},t) = 2\left(\frac{e\hbar}{2m}(\nabla'_{\mathbf{r}} - \nabla_{\mathbf{r}}) + \frac{ie^2}{m}\mathbf{A}(\mathbf{r},t)\right) G^<(\mathbf{r}t,\mathbf{r}'t)\Big|_{\mathbf{r}'=\mathbf{r}} \tag{2.63}$$

with $G^<$ the *electron-occupation propagator* as denoted by Caroli et al. [17] and $\mathbf{A}$ is the vector potential of the photon field. Imagine replacing the particle operators in $G^<$ by one-particle wavefunctions, then this expression reduces to what one derives for the current in usual quantum mechanics. A gauge is used with vanishing scalar potential. The last term in Eq. (2.63) leads to a paramagnetic contribution proportional to the vector potential $\mathbf{A}$. It occurs as a product of the particle density and $\mathbf{A}$ both taken at the position of the detector which lies far outside the solid, and thus vanishes. One is left with the first part where time has to be made infinite or which has to be averaged over time (according to the Abelian limit) so as to obtain the whole photocurrent, thereby leaving the DC component. The time averaging allows the representation by an energy integral of the Green function by Fourier transformation. However, energy resolution as achieved by experimental analyzers can be theoretically simulated by adding a retarding grid-like artificial vacuum level $W = W_0 + \varepsilon_{\mathrm{kin}}$ at the desired energy far outside the solid. Thus, the energy resolved current at time T with detector at position $\mathbf{R}$ is obtained by differentiating with respect to the work function:

$$\begin{aligned} -\frac{d\mathbf{j}(\mathbf{R},T)}{d\varepsilon_{\mathrm{kin}}} &= -\frac{d}{dW}\mathbf{j}(\mathbf{R},T)\Big|_{W=W_0+\varepsilon_{\mathrm{kin}}} \\ &= -\frac{e\hbar}{m}\frac{d}{dW}(\nabla_{\mathbf{R}'} - \nabla_{\mathbf{R}})G^<(\mathbf{R},\mathbf{R}';T,T)\Big|^{\mathbf{R}'=\mathbf{R}}_{W=W_0+\varepsilon_{\mathrm{kin}}} \end{aligned} \tag{2.64}$$

Here, the Green function includes, besides the full interacting Hamiltonian, an external field which depends explicitly on time. A convenient treatment in the framework of Green-function-based nonlinear transport theory is offered by the *Keldysh technique* [68]. It is very similar to usual ground-state or equilibrium perturbation theory, so the details are not important in this context. Because the time dependence of the field extends over the total interval of the measuring process, the particle operators in $G^<$ do not only locally depend on the time entering the field. The destruction of a particle at time t_2 occurs when the field could already act upon the ground state for some time. It acts further at times before and after the associated creation

of a particle at t_1, resulting in a state whose probability as part of the ground state is probed in $G^<$. These features have to be treated within this kind of perturbation expansion.

The diamagnetic part is expanded in powers of $\mathbf{A}$ according to a perturbation series. The zeroth order of $G^<$ carries no current and the first order contributes to the linear conductivity at the detector, which may be discarded by reasoning similar to the neglect of the paramagnetic current. The first non-trivial part arises in second order, $G^{(2)<}$, showing photoemission as a quadratic response effect. Much higher fields would require orders that are higher than the second considered in the following.

The one-body Hamiltonian of the external field consists of a linear and a quadratic expression in $\mathbf{A}$,

$$h_p + h_d = \frac{ie\hbar}{2m}(\mathbf{A}\cdot\nabla + \nabla\cdot\mathbf{A}) + \frac{e^2}{2m}\mathbf{A}^2 \tag{2.65}$$

a paramagnetic and diamagnetic part, respectively. The latter has to be treated in first order, the former in second order. In the first-order term, the time averaging of the photocurrent appearing in Eq. (2.64) simply yields the time average of $\mathbf{A}^2$ because the field-free ground-state Green functions depend only on the time difference. In frequency space, this means a static field which does not contribute to excitations of non-vanishing energy and thus not to those above the vacuum level for the photocurrent. Only the second order term remains

$$\begin{aligned} &G^{(2)<}(\mathbf{R},\mathbf{R}';T,T) \\ &\quad = \frac{i}{\hbar^2}\int d1d2 < N|\psi^\dagger(1)h_p(1)\psi(1)\psi^\dagger(\mathbf{R}',T)\psi(\mathbf{R},T)\psi^\dagger(2)h_p(2)\psi(2)|N > \end{aligned} \tag{2.66}$$

where the notation of space and time variables has been condensed into numbers 1 and 2. The time ordering in this time dependent formalism has already been inserted, thus leading to the above sequence of operators. To lowest order, i.e. no electron-electron interaction contained in the formal time dependence of $\psi^{(\dagger)}(t)$, $G^{(2)<}$ can be decomposed through decoupling into $(\psi,\psi^\dagger)$ pairs (Wick theorem):

$$\begin{aligned} G^{(2)<}(\mathbf{R},\mathbf{R}';T,T) = \frac{1}{8\pi}\int dE \int d^3(r_1,r_2) \\ G^r(\mathbf{R},\mathbf{r}_1;E)h_p(\mathbf{r}_1)G^<(\mathbf{r}_1,\mathbf{r}_2;E-\hbar\omega)h_p(\mathbf{r}_2)G^a(\mathbf{r}_2,\mathbf{R}';E) \end{aligned} \tag{2.67}$$

Here we have abbreviated $h_p(\mathbf{r}) = \frac{ie\hbar}{2m}(\mathbf{A}(\mathbf{r})\cdot\nabla + \nabla\cdot\mathbf{A}(r))$, the retarded $G^r = G - G^<$ and advanced $G^a = G - G^>$ Green functions, and specified the vector potential as $\mathbf{A} = \mathbf{A}(\mathbf{r})\cos(\omega t)$. Expression (2.67) must be inserted into Eq. (2.64) for the photocurrent. Only the absorptive part of $\cos(\omega t)$ contributes, leading to $E - \hbar\omega$. We recall that the above Green functions may still include the whole many-body interaction processes. However, the expansion in the external field cannot be fully decoupled without taking the interaction into account, i.e. there might be, for instance, a Coulomb interaction taking place between any two electrons before and after the excitation at $\mathbf{r}_1$, which is ignored by decoupling as a product of three Green functions. Instead, one should go back to Eq. (2.66), which consists of a product of six fermion operators to be averaged over the ground state. The presented term

corresponds only to that which factorizes into three Green functions which can of course be taken as dressed by the interactions in the form of self-energies. Other terms involve a higher number of Green functions which cannot be accounted for by that dressing. These processes yield an example of vertex renormalization. Let us represent the basic expression of Eq. (2.67) with undressed Green functions by the triangle as in Fig. 2.6a: then possible contributions are represented in Fig. 2.6b, dressing according to Eq. (2.67) as well as renormalizations of the vertex. The Green function considered in the figure has been doubly time-Fourier-transformed into the energy regime.

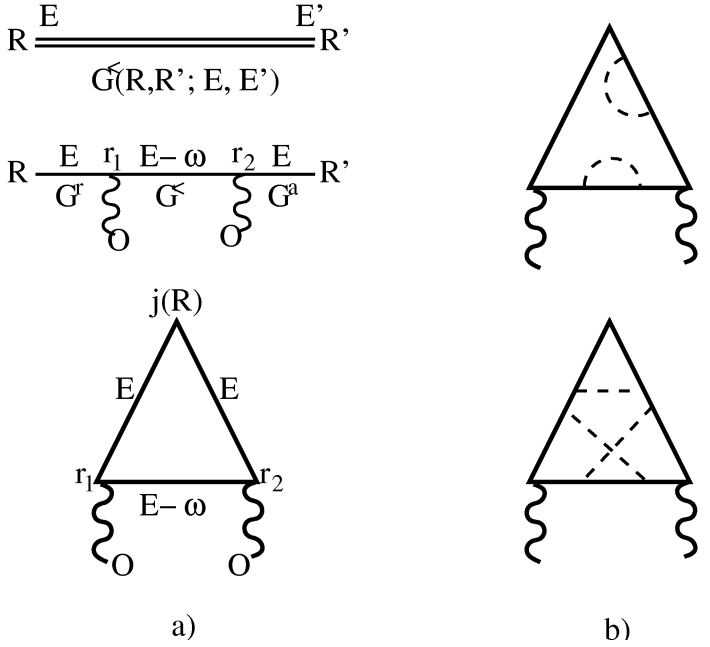

Figure 2.6: Schematic representation of contributions to photocurrent: a) General dressed Green function (top), second order with respect to external field O and interactions neglected (middle), and same as above closed to a vertex with upper corner decorated by external nablas of current (bottom); b) self-energy insertions contributing to the dressing of Green functions in equation (2.67) (top), vertex renormalizations beyond (2.67) (bottom), broken lines represent Coulomb interactions.

The equivalence of Eqs. (2.64) and (2.66) in the one-body limit with the *Golden Rule* formula and with other representations has been shown, see e.g. [31, 74, 75, 96]. With the asymptotics of *outgoing states*, see e.g. [41, 93] (we will come back to that point shortly), we expand with respect to a full set for energies $\varepsilon_k = W_0 + \varepsilon_{\rm kin}$ above the vacuum level W:

$$G^r(\mathbf{R}, \mathbf{r}_1; E) = \sum_k \frac{< \mathbf{R}|\Phi_k^- >< \Phi_k^-|\mathbf{r}_1 >}{E - \varepsilon_k - \mu + i\delta} \tag{2.68}$$

Similarly, G^a is obtained with a negative sign in front of the infinitesimal. Denoting the occupied one-particle bound states by $< \mathbf{r}|j >$ the electron-occupation propagator simplifies

to

$$G^{<}(\mathbf{r}_1,\mathbf{r}_2;E-\hbar\omega)=2\pi i\sum_j^{occ}<\mathbf{r}_1|j><j|\mathbf{r}_2>\delta(E-\hbar\omega+\varepsilon_j-\mu) \tag{2.69}$$

The $\mathbf{R}\to\infty$ behavior of Eq. (2.68) follows from Eq. (2.8) by using the asymptotics of the free-particle Green function which describes an outgoing spherical wave and by expanding in the exponent $|\mathbf{R}-\mathbf{r}|=R-\mathbf{r}\cdot R/R+...$

$$G^r(\mathbf{R},\mathbf{r};E)=-\frac{m\sqrt{\nu}}{2\pi\hbar^2R}e^{ik_0R}<\Phi^-_{k_0}|\mathbf{r}> \tag{2.70}$$

$$<\Phi^-_{k_0}|\mathbf{r}>=\frac{1}{\sqrt{\nu}}(e^{-i\mathbf{k}_0\cdot r}+\int d^3r_1e^{-i\mathbf{k}_0\cdot r_1}V(\mathbf{r}_1)G^r(\mathbf{r}_1,\mathbf{r};E)) \tag{2.71}$$

Periodic boundary conditions with cell volume ν have been applied. The function defined in Eq. (2.70) is the complex conjugate of an asymptotically plane wave with wave vector $\mathbf{k}_0=\sqrt{\frac{2mE}{\hbar^2}}\mathbf{R}/R$ leading to the detector, accompanied by scattering waves of the potential running into the solid. The function itself shows an "incident" plane wave from the detector to the sample and scattered waves leaving the sample, which characterizes the state in a low energy electron diffraction (LEED) experiment. However, the complex conjugate will appear in the subsequent matrix elements at those positions where the wave function should be present, similar to its appearance in Eq. (2.68). Consequently, it is the time-reversed LEED state which occurs as the final state in photoemission. This result is here inferred from the property of the retarded Green function. Note that $<\mathbf{R}|\Phi^-_{k_0}>$ vanishes below the vacuum barrier, thus a step function $\Theta(E-\mu-W)$ is implicit to the definition of Eq. (2.70).

Quantization of the light as one photon with energy $\hbar\omega$ and unit vector $\mathbf{e}$ of polarization yields:

$$h_p=\sqrt{\frac{e^2\hbar^3}{2\epsilon_0m^2\omega\nu}}\frac{1}{2}(\mathbf{e}\cdot\nabla+\nabla\cdot e) \tag{2.72}$$

Introducing the matrix elements

$$<\Phi^-_{k_0}|h_p|j>=:\sqrt{\frac{e^2\hbar^3}{2\epsilon_0m^2\omega\nu}}\Delta_{k_0j} \tag{2.73}$$

the expression (2.67) becomes:

$$G^{(2)<}(\mathbf{R},\mathbf{R}';T,T)$$
$$=\frac{im^2\nu}{16\pi^2\hbar^4RR'}e^{ik_0(R-R')}\int dE\sum_j^{occ}|<\Phi^-_{k_0}|h_p|j>|^2\delta(E-\hbar\omega+\varepsilon_j-\mu) \tag{2.74}$$

This is inserted into Eq. (2.64) and account is taken of the implicit step function $\Theta(E-W-\mu)$ in $|\Phi^-_k>$ with respect to the lower energy bound at $W+\mu$ when differentiating:

$$-\frac{d\mathbf{j}(\mathbf{R},T)}{d\varepsilon_{\text{kin}}}=\frac{1}{4\pi R^2}\frac{e\hbar\mathbf{k}_0}{m}\frac{e^2}{4\pi\epsilon_0}\frac{1}{\hbar\omega}\sum_j^{occ}|\Delta_{k_0j}|^2\delta(W_0+\varepsilon_{\text{kin}}+\varepsilon_j-\hbar\omega) \tag{2.75}$$

Equation (2.75) displays the differential photocurrent with respect to kinetic energy $d\varepsilon_{\rm kin}$ from the flux of one photon. The counts per solid angle $d\frac{d\mathbf{J}}{d\varepsilon_{\rm kin}}$ are obtained by multiplying with $R^2 d\Omega$. This is the *Golden Rule* formula, in valence band spectroscopy often denoted as the *one-step model* [91] because it implicitly includes the three steps of excitation, scattering by the lattice and penetration through the surface as a single step. The last two steps are completely contained in the LEED wavefunction whose time reverse obviously enters the matrix elements. The *Golden Rule* condenses these together with the excitation into one coherent process. It is clear that self-energy dressing of the Green functions does not violate the above derivation within the one-particle approximation. Thus, an optical potential in $G^r(G^a)$ describes a part of the extrinsic losses that the electron suffers after excitation. Instead of Eq. (2.69) the hole spectral density function A^-, see Eq. (2.52), may be introduced in the position representation, which takes account of intrinsic broadening, as for instance with the finite lifetime of a particle-hole excitation. However, photoelectron-photohole interaction is discarded in both.

The consideration of the general photocurrent is accomplished systematically via the Green function technique described below Eq. (2.67) with an expansion to arbitrary order.

Different physical insight is gained through exact decomposition of Eq. (2.66) with a complete set of states for $(N-1)$ particles, as given by Almbladh's derivation [3]. The time integration is carried out and only the light absorption part is retained, viz.

$$\begin{aligned} G^{(2)<}(\mathbf{R},\mathbf{R}';T,T) = \frac{i}{4}\int d^3(r_1,r_2)\sum_s \\ < N|\psi^\dagger(\mathbf{r}_1)h_p(\mathbf{r}_1)\psi(\mathbf{r}_1)\frac{1}{E_0^N+\hbar\omega-H-i\eta}\psi^\dagger(\mathbf{R}')|N-1,s> \\ < N-1,s|\psi(\mathbf{R})\frac{1}{E_0^N+\hbar\omega-H+i\eta}\psi^\dagger(\mathbf{r}_2)h_p(\mathbf{r}_2)\psi(\mathbf{r}_2)|N> \end{aligned} \tag{2.76}$$

where the index s enumerates the states of the set. The particle operators which appear with their arguments at an asymptotic distance are expanded with respect to a full set of one-particle states, $\psi^\dagger(\mathbf{R}') = \sum_{k'}\phi^\star_{k'}(\mathbf{R}')c^\dagger_{k'}$, chosen to asymptotically exhibit spherical-wave behavior, i.e. $\phi^\star_{k'} \propto \frac{1}{R'}e^{\pm ik'R'}$, both inbound and outbound. We denote as $\varepsilon_{k'}$ the corresponding energies of a free particle and consider the first matrix element in Eq. (2.76). An N-particle excited state with an electron at the detector position can be defined as

$$|N-1,s,\mathbf{R}'> \frac{m\sqrt{\nu}}{2\pi\hbar^2 R} := \frac{1}{E_0^N+\hbar\omega-H-i\eta}\psi^\dagger(\mathbf{R}')|N-1,s> \tag{2.77}$$

$$= \sum_{k'}\frac{\phi^\star_{k'}(\mathbf{R}')}{E_0^N+\hbar\omega-E_s^{N-1}-\varepsilon_{k'}-i\eta}(1+\frac{H-E_s^{N-1}-\varepsilon_{k'}}{E_0^N+\hbar\omega-H-i\eta})c^\dagger_{k'}|N-1,s> \tag{2.78}$$

Led by the one-particle derivation above, we consider here the first term in the parentheses which is the only one that remains when $c^\dagger_{k'}|N-1,s>$ is an eigenstate of H with energy $E_s^{N-1}+\varepsilon_{k'}$. Contour integration with respect to $\varepsilon_{k'}$ has to proceed along the lower half-plane

to yield a non-vanishing result, because it then encloses a pole, located at $\varepsilon_{k'} = E_0^N + \hbar\omega - E_s^{N-1}$. Only the negative sign in the exponent of $e^{\pm ik'R'}$ allows closing along the lower half-plane such that only a spherical wave which is incident onto the solid survives. Extracting this asymptotic factor similar to Eq. (2.70), the sum over the directions $\hat{\mathbf{k}}'$ leaves a state which has to overlap with the emitter volume for non-zero result. This fixes $\hat{\mathbf{k}}' = \mathbf{R}'/R'$ which yields a plane wave incident into the detector with wave vector $\mathbf{k}_0$ because $c_{k'}^\dagger|N-1,s>$ is asymptotically an *outgoing state*, in view of the sign of $-i\eta$. This is characteristic of a time-reversed LEED state, i.e. spherical wave *in* and plane wave *out* as seen from the emitter volume.

The second term in the parentheses corrects for the many-body coupling of this state to the emitter volume. Expanding $\psi(\mathbf{r}) = \sum_j \phi_j(\mathbf{r})c_j$ with respect to a set of states bounded within the emitter volume, inserting in Eq. (2.64), and using $\mu = -W_0$ we arrive at

$$-\frac{d\mathbf{j}(\mathbf{R},T)}{d\varepsilon_{\text{kin}}} = \mathcal{N}\sum_s \Big|\sum_{ij}\Delta_{ij} < N|c_i^\dagger c_j|N-1,s,\mathbf{R}>\Big|^2 \cdot \delta(E_0^N + \hbar\omega - E_s^{N-1} - \varepsilon_{\text{kin}}) \quad (2.79)$$

where $\mathcal{N}$ denotes the normalizing factor in front of the sum in Eq. (2.75). The δ-function of energy conservation arises again via an implicit step function within the state $|N-1,s,\mathbf{R}>$ which must vanish for energies below the detector's vacuum level.

We can see a relation to the sudden approximation by replacing in the notation of $|N-1,s,\mathbf{R}>$ the position $\mathbf{R}$ by the momentum $\mathbf{k}$ of the emitted electron, which is a convenient characterization of the exact outgoing state of Eq. (2.77).

In the *sudden approximation* [50, 51] the photoelectron is approximately decoupled from the solid by defining a particle operator with respect to that state

$$|N-1,s,\mathbf{k}> = c_{\mathbf{k}}^\dagger|N-1,s>$$

with the assumption that $c_k^\dagger$ does not depend on s and vice versa $|N-1,s>$ not on k. It leaves a matrix element $< N|c_i^\dagger c_j c_k^\dagger|N-1,s>$ which couples the isolated photoelectron $c_k^\dagger$ only to the density fluctuation $c_i^\dagger c_j$, but does not influence the choice of the excited $N-1$-particle states $|N-1,s>$. All of the latter are now summed independently disregarding the state of the photoelectron. It is similar to *suddenly* creating the photoelectron in the detector at a probability with which it is contained in the density fluctuations of arbitrary (non-adiabatic) excitations, see also the chapters by Hedin and by Rehr, Albers, and Ankudinov. The property of being sudden becomes still more apparent by approximately equating $c_j c_k^\dagger = \delta_{jk}$, i.e. neglecting its coupling to the fluctuations. The current can then be expressed as

$$-\frac{d\mathbf{j}}{d\varepsilon_{\text{kin}}} = \mathcal{N}\sum_s \Big|\sum_i \Delta_{ik} < N|c_i^\dagger|N-1,s>\Big|^2 \cdot \delta(E_0^N + \hbar\omega - E_s^{N-1} - \varepsilon_{\text{kin}}) \quad (2.80)$$

or with help of the spectral density matrix, see Eq. (2.52),

$$-\frac{d\mathbf{j}}{d\varepsilon_{\text{kin}}} = \mathcal{N}\sum_{ij}\Delta_{ik}A_{ij}^-(\hbar\omega - W_0 - \varepsilon_{\text{kin}})\Delta_{kj} \quad (2.81)$$

Unlike Eq. (2.52), a matrix generalization of the spectral density is implied with analogous definition, namely instead of the same index for both operators c and $c^\dagger$ squared, two indices have been applied. However, in its simplest version this sudden approximation assumes that the hermitean matrix A is already diagonal. With equation (2.81) we are back to the one-particle photoemission formula of Eq. (2.67) inserted in (2.64), with the Green functions appropriately dressed.

At the heart of the sudden approximation lies the assumption that in the photoemission process the photoelectron can be treated as if it were independent from the other particles of the system. Then, the photoemission process can be described as consisting of two decoupled and non interfering processes, the transition from an initial to a final one-particle state of the photoelectron and the many-body response of the $(N-1)$-particle system to the creation of the hole left behind.

The series of approximations within the sudden approximation usually goes further in simplifying the matrix elements Δ_{ik}, in the limit assuming them to be constant. The one-step model whose main achievement was the introduction of the time-reversed LEED state is then entirely lost.

According to their definitions, the spectral functions A^+ and A^- describe the spectrum of the excitation energies when a particle is added or removed from the system and are said to describe the situation of an idealized inverse or direct photoemission experiment. What these approximations omit from a realistic description of photoemission is that the particle will be measured with a detector that is still part of the system, even if separated from the solid by a surface. Also missing is that the process is a result of interaction with light which is associated with a cross section. Last but not least it lacks the treatment of the photoexcited particle with its screened hole when leaving the solid. Thus, in the many cases where the spectral density is taken as the theoretical counterpart of the photocurrent, also called sudden approximation, only a rather poor description is achieved. [39] Nonetheless, since effects of matrix elements and final states on the photoelectron energy distribution are governed by the energy scale of bandstructures, i.e. eV, it may sometimes be possible to single out and identify tiny structures due to many-body interactions on an meV scale, such as those seen in superconducting systems. [19] However, it remains true that the photoelectron is artificially and suddenly decoupled from the many-body system and no interaction is taken into account. Recently, it has been recognized theoretically [6, 78] as well as experimentally [13, 38] that matrix elements and their dependence on the final state are important in high temperature superconductivity and that their neglect could lead to misinterpretations of the spectra.

2.3 Three-step model versus one-step model

By way of introduction to this section, we shall focus on one aspect that has become a long-standing but also increasingly confusing concept, namely the issue of the three-step versus the one-step model of photoemission.

The three-step model dates back to Berglund and Spicer [9] on angle resolved photoemission from solids, which presents a first approach to its theoretical interpretation. The photocurrent is decomposed into three separate factors: the probability of excitation in the bulk solid, the probability of scattering of the excited electron on its path to the surface by

the atoms constituting the solid, and the probability of transmission through the surface for its final acceptance in the detector. The essential point is to calculate separate entities which are easily accessible if they do not interfere with each other. If valence level spectroscopy is the goal, then the focus of attention is on the excitation process from an occupied band state and the photocurrent shows the energy levels at specific directions which are identified with the $\mathbf{k}$ value (i.e. the electron momentum in the bulk). The two remaining factors, scattering and transmission, are considered to be less important: they may even be set to unity by neglecting those effects. By contrast, photoelectron diffraction might lie at the center of interest, as for instance in core level spectroscopy or in imaging methods like holography: in that case, the $\mathbf{k}$ dependence of the occupied states is trivial but the scattering by bulk and surface determines the angle variation of the photocurrent. Then, the first factor, excitation, becomes rather unimportant whereas the other two dominate the interpretation.

In contrast to the three-step model the coherent evaluation of all three steps which *a priori* do interfere is usually denoted as the one-step model. It was originally developed to obtain reliable intensities of valence band spectroscopy for investigating bulk as well as surface characteristics [34], so bringing the accuracy on an equal footing with LEED calculations where refined computer codes existed. [57, 58, 90] Thus, the scattering in the bulk and at the surface is condensed into a coherent final state which must be introduced into the matrix element of photoexcitation, the so-called time-reversed LEED state. [31] As photoelectron-diffraction schemes are closely related to LEED those calculations already obeyed the conditions of the one-step model in principle, though with an important practical simplification by considering only localized, i.e. atomic-like, transitions as they occur in core excitations.

Nowadays, state-of-the-art calculations of photocurrents use the one-step model, even though some valuable short cuts exist. The incorporation of "true" final states which correctly describe the scattering and propagation near and outside a surface is required by the physical situation of accepting the excited electron in the detector at infinite times away from the sample: this is the essential ingredient of the one-step model. The model exists at several levels of sophistication, depending on the extent to which many-body effects are taken into account. Originally, the one-step model was designed as a one-particle theory applying the Golden Rule for one-particle states. The many-body formulation according to the considerations in Sec. 2.2 in principle should use correct final states as well, and thus fits into the concept of the one-step model. Thus, it would be informative to characterize any given one-step model by describing its level of accuracy in addition to its "one-step" property.

Let us confine the remaining of this section to one single initial state as e.g. in core level spectroscopy. Incorporation of an arbitrary number of states as in the valence band regime will be described in subsequent sections. Current theories of photoemission in solids rely in general on one-electron effective potentials to describe the photoelectron. At low kinetic energies, these potentials must incorporate many-body effects in an effective way (e.g., exchange and correlation via the Hara or other approximation). Then, the photoelectron wave function can be expressed as

$$\psi(\mathbf{r}) = \int d\mathbf{r}' G^r(\mathbf{r}, \mathbf{r}') V_I(\mathbf{r}') \psi_i(\mathbf{r}')$$

where V_I describes the perturbation of the external light, ψ_i is the initial state one-electron

wave function of energy E_i, and

$$G^r(\mathbf{r},\mathbf{r}') = \sum_f \frac{\psi_f^*(\mathbf{r}')\psi_f(\mathbf{r})}{E_i + \hbar\omega - E_f + i\delta}$$

is the Green function of the solid at the photoelectron energy $E_i+\hbar\omega$, cf. Eqs. (2.7) and (2.12). The latter must incorporate all multiple elastic scattering effects of the photoelectron, as well as inelastic processes in which the photoelectron loses energy to create photons, plasmons, or other excitations in the solid.

2.4 Golden Rule

2.4.1 Linear response in the external field

Let us here start with the Hamiltonian of one electron in a system described by a potential $V(\mathbf{r})$, to which an external electromagnetic field is applied:

$$\begin{aligned} H &= \frac{1}{2m}\left(\mathbf{p} - \frac{e}{c}\mathbf{A}(\mathbf{r})\right)^2 + V(\mathbf{r}) \\ &= \frac{p^2}{2m} + V(\mathbf{r}) - \frac{e}{2mc}\left[\mathbf{A}(\mathbf{r})\cdot\mathbf{p} + \mathbf{p}\cdot\mathbf{A}(\mathbf{r})\right] + \frac{e^2}{2mc^2}|\mathbf{A}(\mathbf{r})|^2 , \end{aligned} \tag{2.82}$$

where $\mathbf{A}(\mathbf{r})$ is the vector potential associated with the field. Let us split the Hamiltonian H into two terms ($H = H_0 + V_I$), such that V_I describes the excitation:

$$\begin{aligned} H_0 &= \frac{p^2}{2m} + V(\mathbf{r}) \\ V_I &= \frac{-e}{2mc}\left[\mathbf{A}(\mathbf{r})\cdot\mathbf{p} + \mathbf{p}\cdot\mathbf{A}(\mathbf{r})\right] + \frac{e^2}{2mc^2}|\mathbf{A}(\mathbf{r})|^2 . \end{aligned} \tag{2.83}$$

For low intensities of the external field, first order perturbation theory can be used to study the interaction between the electromagnetic radiation and the system. Thus, applying the Golden Rule to calculate the photocurrent, we obtain:

$$I(f) = |M_{if}|^2 = |<\psi_f|V_I|\psi_i>|^2 , \tag{2.84}$$

where the one-electron wavefunctions ψ_i and ψ_f are eigenfunctions of the Hamiltonian H_0, and the final wavefunction ψ_f behaves as an outgoing wave at infinity (i.e., ψ_f is an inverse LEED state).

The flexibility introduced by the gauge choice in the theory of electrodynamics facilitates the calculation of the matrix element. A common choice is to work in the Coulomb gauge, in which:

$$\nabla\cdot\mathbf{A}(\mathbf{r}) = 0 , \tag{2.85}$$

and consequently

$$(\mathbf{A}(\mathbf{r})\cdot\mathbf{p} - \mathbf{p}\cdot\mathbf{A}(\mathbf{r})) = i\hbar\nabla\cdot\mathbf{A}(\mathbf{r}) = 0 . \tag{2.86}$$

The interaction potential V_I can thus be expressed as:

$$V_I(\mathbf{r}) \;=\; -\;\frac{e}{mc}\,[\mathbf{A}(\mathbf{r})\cdot\mathbf{p}] \;+\; \frac{e^2}{2mc^2}|\mathbf{A}(\mathbf{r})|^2\;. \tag{2.87}$$

So far, the most important approximations introduced in the theoretical formalism are the restriction to a one-electron picture, and the use of only first-order perturbation theory to calculate the interaction between the incident radiation and the system (Eq. (2.84)). The latter approximation is equivalent to neglecting terms of order $\sim |A|^2$ in the calculation of the photocurrent. In order to be consistent with this approximation, the term of order $\sim |A|^2$ in the interaction potential V_I (Eq. (2.87)) is omitted as well. This approximation remains valid provided that the flux of incident photons is relatively low. For higher intensities of the external field these terms cannot be neglected and the theoretical formalism becomes more intricate.

The matrix element M_{if} after keeping only the lowest-order terms can be written as:

$$\begin{aligned} M_{if} \;=\; <\psi_f|V_I|\psi_i> \;&=\; \frac{-e}{mc}\;<\psi_f|\mathbf{A}(\mathbf{r})\cdot\mathbf{p}|\psi_i> \\ &=\; \frac{ie\hbar}{mc}\;<\psi_f|\mathbf{A}(\mathbf{r})\cdot\nabla|\psi_i>\;, \end{aligned} \tag{2.88}$$

where we have used the identity $\hat{p} = -i\hbar\hat{\nabla}$. This way of writing the matrix element has been usually called in the literature the *velocity form* of the matrix element.

2.4.2 Dipole approximation

The theoretical description of the interaction between the electromagnetic field and the system is usually simplified by means of the so-called *dipole approximation*. The dipole approximation assumes that the variation of the external field $\mathbf{A}(\mathbf{r})$ is small in the spatial region in which the matrix element M_{if} is not negligible. The latter seems a reasonable assumption for the low energy range of the photon spectrum and/or for the photoexcitation of localized electrons, although it is more difficult to justify in some other cases (such as excitation from valence levels). In general terms, it works better in the evaluation of total cross sections than in the calculation of photoelectron angular distributions. Recent measurements in small systems show that significant deviations from the dipole approximation can be found even in systems for which it has been traditionally applied [22]. Nevertheless, let us restrict ourselves to the calculation of the photocurrent in the dipole approximation.

When the external electromagnetic field is periodic in space, it can be expressed as:

$$\mathbf{A}(\mathbf{r}) \;=\; A_0\;\mathbf{e}\;e^{i\mathbf{k}r} \;=\; A_0\;\mathbf{e}\;\left(1 + i\mathbf{k}r + \cdots\right)\;, \tag{2.89}$$

where A_0 is the complex amplitude of the field (a scalar number), $\mathbf{e}$ is a unitary vector in the direction of the light polarization, and $\mathbf{k}$ is a vector pointing in the propagation direction of the field. The dipole approximation consists in keeping only the first term of this expansion in the calculation of the photocurrent via Eq. (2.84) (i.e., it is assumed that $|\mathbf{k}r| \ll 1$). Notice that the range of $\mathbf{r}$ for which the approximation remains valid is delimited by the spatial extent of

the wavefunctions $\psi_i(\mathbf{r})$ and $\psi_f(\mathbf{r})$. The matrix element in the dipole approximation can thus be expressed as follows:

$$M_{if} \;=\; \frac{ie\hbar}{mc}\, A_0 \;<\psi_f|\mathbf{e}\cdot\nabla|\psi_i> \;. \tag{2.90}$$

Let us remember at this point that the momentum operator $\hat{\mathbf{p}}$ can be written as the commutator of two other operators:

$$\hat{\mathbf{p}} \;=\; -\,i\hbar\hat{\nabla} \;=\; -\,\frac{im}{\hbar}\left[\,\hat{\mathbf{r}}\,,\,\hat{H}_0\,\right]\,. \tag{2.91}$$

Hence, if ψ_i and ψ_f are eigenstates of the Hamiltonian H_0, the matrix element M_{if} can be calculated as:

$$M_{if} \;=\; -\frac{ie}{\hbar c}\, A_0\,(E_f - E_i) \;<\psi_f|\mathbf{e}\cdot\mathbf{r}|\psi_i> \;, \tag{2.92}$$

and this is known as the *length form* of the matrix element. A third form, known as the *acceleration form* of the matrix element, is sometimes used in the literature as well:

$$M_{if} \;=\; \frac{-ie\hbar}{mc}\,\frac{A_0}{(E_f - E_i)} \;<\psi_f|\mathbf{e}\cdot(\nabla V)|\psi_i> \;, \tag{2.93}$$

in which the identity

$$\begin{aligned} <\psi_f|\nabla|\psi_i> &= \frac{1}{(E_f - E_i)} \;<\psi_f|\,[H,\nabla]\,|\psi_i> \\ &= -\frac{1}{(E_f - E_i)} \;<\psi_f|\nabla V|\psi_i> \end{aligned} \tag{2.94}$$

has been used.

The three forms of the matrix element are in principle equivalent, provided that ψ_i and ψ_f are eigenstates of the Hamiltonian H_0. This is not always the case in real calculations of the matrix element, and some differences may be found in the final result depending on the form used. See for instance Ref. [81] for a discussion on the most accurate form of the matrix element depending on the problem under study.

For a single atom, the dipole approximation leads to certain selection rules in the symmetry of the photoemitted electron wavefunction. These selection rules can be easily derived by expanding the wavefunctions in the basis set of spherical harmonics $Y_{lm}(\Omega_{\mathbf{r}})$. For the sake of simplicity, let us assume that the initial wavefunction $\psi_i(\mathbf{r})$ of the electron is a core level whose quantum numbers l_i and m_i are well defined. $\psi_i(\mathbf{r})$ thus can be written as:

$$\psi_i(\mathbf{r}) \;=\; R^i_{l_i m_i}(r) Y_{l_i m_i}(\Omega_{\mathbf{r}})\;, \tag{2.95}$$

where $R^i_{l_i m_i}(r)$ is the radial part of the wavefunction.

The final wavefunction after photoemission has a similar form and can be written in general as:

$$\psi_f(\mathbf{r}) \;=\; \sum_{l_f, m_f} R^f_{l_f m_f}(r) Y_{l_f m_f}(\Omega_{\mathbf{r}})\;. \tag{2.96}$$

Let us first take linear polarization of the light, and assume that the polarization $\mathbf{e}$ is parallel to the OZ axis. The incoming light dipole operator (cf. Eq. (2.92)) can thus be expanded as:

$$\mathbf{e}\cdot\mathbf{r} \;=\; \left(\frac{4\pi}{3}\right)^{1/2} r\, Y_{10}(\Omega_{\mathbf{r}})\;. \tag{2.97}$$

The expansions of the wavefunctions and the dipole operator can be introduced into Eq. (2.92) to obtain the matrix element as:

$$\begin{aligned} M_{if} \;=\; & -\frac{ie}{\hbar c}\, A_0\, (E_f - E_i) \left(\frac{4\pi}{3}\right)^{1/2} \sum_{l_f,m_f} \left\{ \int \mathrm{d}r\, r^3 \left[R^f_{l_f m_f}(r)\right]^* R^i_{l_i m_i}(r) \right\} \\ & \times \left\{ \int d\Omega_{\mathbf{r}} Y^*_{l_f m_f}(\Omega_{\mathbf{r}}) Y_{10}(\Omega_{\mathbf{r}}) Y_{l_i m_i}(\Omega_{\mathbf{r}}) \right\}\;. \end{aligned} \tag{2.98}$$

The integral over angles $\Omega_{\mathbf{r}}$ determines the allowed symmetries for the final states. According to general properties of the spherical harmonics, this integral is different from zero only if $l_f = l_i \pm 1$ and $m_f = m_i$.

If the incoming light is circularly polarized, the mathematical description can be also simplified by modifying the geometry. In this case, let us take the OZ axis as parallel to the direction of propagation of the light. Hence the plane of polarization of the light is perpendicular to the OZ axis, and the incoming light dipole operator can be written as:

$$\mathbf{e}\cdot\mathbf{r} \;=\; \left(\frac{8\pi}{3}\right)^{1/2} r\, Y_{1m}(\Omega_{\mathbf{r}})\;, \tag{2.99}$$

where $m = 1$ corresponds to *right* circularly polarized light and $m = -1$ corresponds to *left* circularly polarized light (although the opposite convention is sometimes found in the literature as well). The matrix element for circularly polarized light can be calculated in a similar way as the matrix element for linear polarization (Eq. (2.98)). We only need to replace the spherical harmonic $Y_{10}(\Omega_{\mathbf{r}})$ by $Y_{1m}(\Omega_{\mathbf{r}})$. As a consequence, the integral over angles $\Omega_{\mathbf{r}}$ now generates new selection rules: $l_f = l_i \pm 1$ (as before), but $m_f = m_i + m = m_i \pm 1$.

The selection rules in the dipole approximation are strictly valid only for atomic systems. Nevertheless, in the case of molecules, clusters or solids, the scattering theory provides a simplified picture in which the selection rules fit as well. The photoemission process from a core level can be described as the photoexcitation from a single atom, followed by the transport of the photoelectron on its way to the detector. In this picture, the selection rules remain valid for the first step of the process (the photoexcitation from the single atom). The subsequent scattering of the outgoing electron by the surrounding atoms will add other partial-wave contributions to the final photoelectron pattern.

2.5 Initial state

2.5.1 Core levels

In core level spectroscopy photoelectrons emerge from single atomic levels which simplify the initial state as far as the single particle picture is concerned. Chemical shifts may change

the levels due to local effects near a surface, but the levels may still be considered to be independent (not counting systematic atomic-like degeneracies). Therefore, we will discuss this topic within the description of the final states, see Sec. 2.6, where the core level emission constitutes the simplest case to be treated. A rather more complicated situation arises if many-body effects are considered, see e.g. [87]. Then, the relaxation of the core hole multiplet together with its interaction with the photoelectron represents a challenging problem. Progress in this field is described in chapter [49] of this handbook. Aside from spectroscopy, in an extremely important development core level emission has served as source for photoelectron diffraction and holography [27] (see chapter [47] and chapter [28]), owing to the localized nature of the source of emission.

2.5.2 Valence bands

Angle resolved photoelectron spectroscopy represents the most general tool for full valence band investigation at highest accuracy. The aim is to extract from the photocurrent the band-structure over the whole Brillouin zone. Though *ab initio* bandstructure calculations have reached a high level of reliability, their accuracy is limited by computational restrictions and the physical border line of many-body effects. Thus, the experiment is needed as confirmation on one hand and as access to uncover new properties not considered in the bandstructure calculation on the other.

The interpretation of valence band spectra uses intuitive methods relying more or less on energy and momentum conservation or is assisted by full calculations of the intensities, at best. To discuss both, we write the Golden Rule formulation taking into account the continuum of valence band states ψ indexed by the band ν and the three-dimensional momentum $\mathbf{k}$

$$I \propto \sum_{\nu\mathbf{k}} \; | < \Phi^{\star}_{LEED}(E, \mathbf{k}^{\mathbf{0}}_{\parallel}) \mid \mathbf{O} \mid \psi_{\nu}(\mathbf{k}) > |^2 \delta(E - E_{\nu}(\mathbf{k}) - \hbar\omega). \qquad (2.100)$$

The final state Φ depends on the surface parallel momentum $\mathbf{k}^{\mathbf{0}}_{\parallel}$ and on the final state energy E which corresponds to the perpendicular momentum component in vacuum. The index LEED relates to a LEED state and the star refers to its time inverse. Energy conservation is guaranteed by the δ-function. Momentum conservation is reduced to the parallel momentum. It arises from the evaluation of the matrix element with operator $\mathbf{O} = \mathbf{A} \cdot \mathbf{p} + \mathbf{p} \cdot \mathbf{A}$. Translational invariance is only maintained parallel to the surface, the vector potential being assumed constant in the case of long wavelengths, including the vacuum ultraviolet regime. Discrete translations according to the lattice periodicity are meant here when speaking about invariance and the Bloch vector is thus associated with momentum. The surface breaks invariance in the perpendicular direction. The parallel momentum which is calculated in vacuum through kinetic energy and direction of the detector has to be folded back into the first surface Brillouin zone to be identified with $\mathbf{k}^{\mathbf{0}}_{\parallel}$ of Eq. (2.100).

From Eq. (2.100) it is obvious that three-dimensional momentum will be conserved if one replaces the final state by any eigenstate of a system with three-dimensional translational invariance. This is done within the *band-mapping* scheme where in the simplest case the final states are taken to be three-dimensional plane waves. In a more sophisticated treatment, the set of eigenstates of the bulk may be used as final states. Furthermore, solving the bulk hamiltonian with complex Bloch vectors generalizes this set and admits exponentially decreasing and increasing solutions; of the latter only those which increase in the direction towards the

surface are physically reasonable. All these sets are eigenstates of the Bloch momentum and thus conserve the total momentum in the matrix element. The interpretation of the photocurrent within these schemes identifies the possibilities of transitions between all valence states and all final states belonging to the chosen set and allowed by energy and three-dimensional momentum conservation, the so-called *direct transitions*. Primarily, this takes advantage only of the spectral peak positions. Their height will correspond in some way to the weight of the matrix element and their width may be associated with the lifetime of the valence states. In any case, this description yields a mapping between momentum and energy for all momentum space points which can be associated with peaks in the spectra, i.e. it yields parts of the band structure. [32, 65] It is more or less accurate depending on the ability to define a clear peak.

The accuracy of the band-mapping can be estimated by comparing it with a full calculation of Eq. (2.100). In Fig. 2.7 a spectrum computed accordingly is presented and interpreted by direct transitions which is represented by bars on top of the peaks obtained by a deconvolution procedure. Any of the known deconvolution techniques leads to similar positions. Above the spectrum the valence bandstructure together with the complex bandstructure is shown shifted by the amount of the photon energy such that the intersections give the allowed direct transitions. These intersections are also marked by bars in the spectrum. If both kinds of bars agree in position the momentum associated with the intersection has to be attributed to the peak and its binding energy. Of course, only distinct peaks may be considered. However, the result of Fig. 2.7 shows clear misfits which reach up to 200 meV. If we had taken the peaks of the spectra to be granted and with a knowledge of the final states bandstructure, had extrapolated through their energy to the associated momenta, then the momentum would be wrong and the maximum error in energy could reach values up to 200 meV. This error is large compared to the actual energetic resolution of photoelectron spectroscopy which can be below 10 meV. Nevertheless, it is the most advanced procedure within the framework of band-mapping, using the complex bandstructure, i.e. eigenstates of a hamiltonian which simulates the solid-vacuum system by bulk.

A different but less instructive view on the observed spectra entirely neglects the final states' bandstructure: it assumes that, because of the dense distribution of excited states at high energies, the δ-function can always be fulfilled and the matrix elements are constant throughout. Then the sum over initial states in Eq. (2.100) condenses into the density of initial states. As the parallel momentum is prescribed by the detector, this is a one-dimensional density of states which counts the states per energy only along the perpendicular direction. The selection rule for the perpendicular momentum is replaced now by the dominance of band edges and critical points, the only structures in the spectra surviving in this model. A single direct transition would have no weight, e.g. see insert of Fig. 2.7.

In physical reality both pictures, band-mapping and density of states, will contribute. However, the amount of nonconservation of perpendicular momentum and the necessity to refer to density-of-states effects can be estimated with a knowledge of the final states' bands. The final state in Eq. (2.100) can be decomposed in the interior of the solid with respect to the complex Bloch vector states and a weight is associated with each. The imaginary part of the Bloch vector partly results from the imaginary part of the self-energy and partly from the damped penetration from surface into bulk if the electron's energy coincides with a forbidden gap region. It determines the momentum broadening of the surface perpendicular component and thus limits the admissible uncertainty for a deviation. The equation sums up all these

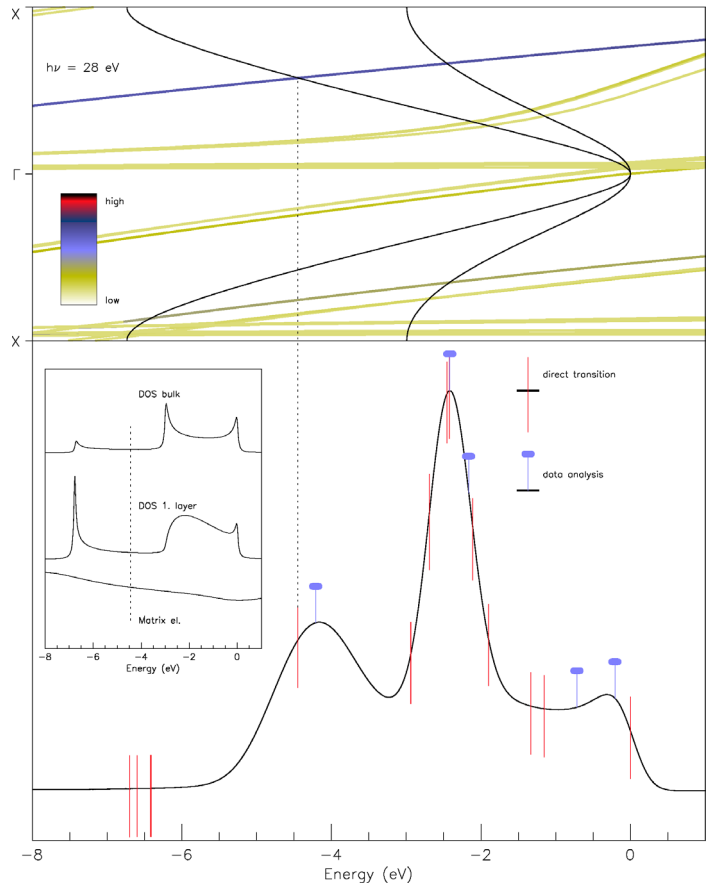

Figure 2.7: Ab initio computed spectrum of GaAs(001) for photon energy 28 eV (lower part) deconvoluted to yield peaks at energies marked by bars with full dots, compared with bare bars mapped from intersections of initial bands (black lines) with final bands (flat curves) shifted by photon energy down to binding energy scale (upper part), one example shown by dotted line; insert shows density of states and a matrix element, position of direct transition near -4.5 eV indicated. See also color figure on page 461.

contributions. Other transitions cannot occur and thus the density-of-states effect has to be embedded in direct transitions.

In contrast with its general deficiencies, the density of states interpretation has experienced a development towards many-body effects. The energy conservation δ-function can be seen as the imaginary part of the Green function if the imaginary part of the self-energy tends to zero. For finite lifetime this becomes the spectral density in the framework of many-body theory. The δ-function including valence wavefunction and the sum over band index ν has to be replaced by the spectral density matrix $A^{-}_{ij}(\mathbf{k}, E)$ in the representation by any basis set

$\mid i >$ with fixed Bloch vector $\mathbf{k}$ via

$$\sum_{\nu} \delta(E - E_{\nu}(\mathbf{k})) < i \mid \psi_{\nu}(\mathbf{k}) >< \psi_{\nu}(\mathbf{k}) \mid j > \rightarrow A^{-}_{ij}(\mathbf{k}, E), \tag{2.101}$$

see Eq. (2.52) where index k now denotes $(\nu, \mathbf{k})$. Thus, it takes into account the correct many-body distribution of valence levels if the terms with the Dirac brackets are generalized to the many-body transition amplitudes $< \Psi_n^{N-1} | \widehat{c}_i(\mathbf{k}) | \Psi_0^N >$ of Green functions in Eq. (2.101):

$$I \propto \sum_{ij\mathbf{k}} < \Phi^{\star}_{LEED}(E, \mathbf{k}^{\mathbf{0}}_{\parallel}) \mid \mathbf{O} \mid i >< j \mid \mathbf{O}^{+} \mid \Phi^{\star}_{LEED}(E, \mathbf{k}^{\mathbf{0}}_{\parallel}) > A^{-}_{ij}(\mathbf{k}, E) \tag{2.102}$$

compare with Eq. (2.81) and the discussion following it. In practice, one neglects the whole non-valence part of the Golden Rule, i.e. final states as well as matrix elements, and takes merely the diagonal A to represent the photocurrent. This procedure may be justified for instance in cases where the interesting structures of the photoemission spectra vary rapidly as compared to the variation induced by matrix elements. The latter is characterized by band energies of the order of magnitude of eV. As a consequence, the analysis of spectral features from HTC superconductivity with a meV scale of variation may be justified. [82]

Between the direct transition and density of states interpretations a series of intermediate schemes have been proposed in the literature, some of them occurring also in the context of other chapters in this book, where they are further described.

In the following, we present specific examples of full one-particle calculations in the framework of the Golden Rule formula.

The first main development in this respect concerned photoemission from metals for which the use of muffin-tin potentials in the framework of a multiple scattering method is suitable. [57, 91] The layer-KKR code had the time inverse LEED state implemented according to the calculational schemes for LEED intensities and used KKR for the valence state as well. It was thus designed for surfaces. Eq. (2.100) written in position space with help of the hole Green function G^{hole} reads

$$I \propto \mathrm{Im} \int d^3r \int d^3r' < \Phi^{\star}_{LD}(E, \mathbf{k}^{\mathbf{0}}_{\parallel}) \mid \mathbf{O} \mid \mathbf{r} > G^{hole}(\mathbf{r}, \mathbf{r}', E - \hbar\omega, \mathbf{k}^{\mathbf{0}}_{\parallel}) \cdot < \mathbf{r}' \mid \mathbf{O}^{+} \mid \Phi^{\star}_{LD}(E, \mathbf{k}^{\mathbf{0}}_{\parallel}) > \tag{2.103}$$

Both the Green function and the LEED state are expanded in terms of spherical harmonics in order to use the KKR scheme. An important simplification arose from the use of the matrix element in the acceleration form because between the muffin-tin spheres the potential V is constant. The integration in the matrix element is thus confined within the muffin-tin spheres: the wavefunctions need to be constructed here. An obstacle in this muffin-tin scheme was found in the treatment of the potential barrier at the surface.

This method has been further completed by generalizing to the relativistic case [1,2,14,15, 40,46,105] The 2x2 spin density matrix $\rho_{\tau,\tau'}$ is evaluated via a formula similar to Eq. (2.103) where the four component Dirac spinors $< \Phi \mid$ and $\mid \Phi >$ carry the index τ and τ', resp., $G^{<}(\mathbf{r}, \mathbf{r}')$ is a 4x4 component Dirac matrix, and the transition operator $\mathbf{O}$ contains the vector potential as $\alpha \cdot \mathbf{A}$ using 4x4 matrices $\alpha_{ik} = \sigma(1 - \delta_{ik}), i, k = 1, 2$ with Pauli spin matrices σ. Spin-averaged photocurrent, spin polarization, and individual spin-resolved photocurrent are obtained via spin averaging of the respective observables with the spin density matrix. A

transformation analogous to Eq. (2.93) confining integration to the muffin-tin spheres can be used in this case, too.

The above scheme was further developed to include non-spherical parts of the potential. [44] The multiple scattering scheme remained essentially the same. However, instead of a muffin-tin model the Wigner-Seitz cell with the so-called "true potential" inside and zero outside the cell was taken to solve the Schrödinger equation within the circumscribing sphere and matching to free solutions outside. The result served as the basis for the multiple scattering expansion.

The LEED scheme and similarly the above approaches according to their initial design showed slow convergence for low kinetic energies with low damping. Additionally, the full potential yields non-diagonal t-matrices which slows down the code again. A limitation to spherical potentials was out of the question when considering semiconductors. Especially, surface reconstructions specific to semiconductors made the scheme rather cumbersome. The surface bandstructure could not be obtained within the Bloch scheme used leading to the complex bandstructure only. The photoemission part of the code met similar difficulties in treating emission from surface states which near the valence band maximum are scarcely damped.

Thus, a separate approach was developed for such materials. It benefits from the existence of self-consistent ab-initio calculations for the bandstructure. A suitable basis $\mid \psi_i >$ adapted to or directly taking those solutions forms the representation for the initial states. It is condensed in a Green matrix G_{ij} for the halfspace system which includes an arbitrary surface potential and is used in Eq. (2.100) to yield

$$I \propto \mathrm{Im} \sum_{i,j} < \Phi^{\star}_{LD}(E, \mathbf{k}^{\mathbf{0}}_{\parallel}) \mid \mathbf{O} \mid \psi_i > G^{<}_{ij}(E - \hbar\omega, \mathbf{k}^{\mathbf{0}}_{\parallel}) \cdot < \psi_j \mid \mathbf{O} \mid \Phi^{\star}_{LD}(E, \mathbf{k}^{\mathbf{0}}_{\parallel}) > \tag{2.104}$$

The basis normally chosen used a layer resolved LCAO set with Bloch sums along surface parallel layers and respective Bloch vectors $\mathbf{k}^{\mathbf{0}}_{\parallel}$. Ab initio pseudopotentials are used for the evaluation of final states.

As an example, the result of a calculation via 2.104 for $TiTe_2$ is presented in Fig. 2.8. Slight deviations in binding energy shown by the different energy surfaces in that figure can be discriminated by a comparison of experimental with theoretical photoemission patterns which confirms the matching of both energy scales in this case. The demand of computer resources for such a calculation consists of the whole of separate runs for each angle and sums up to a still considerable amount even within this code which is fast compared to the original KKR schemes.

2.6 Final state

We now turn our attention to the final state. This higher-energy state describes how the photoelectrons scatter and propagate as they leave the emitter site and travel to the detector in the vacuum outside the solid.

One point to keep in mind is that an electron in the final state senses a different potential than an electron in the initial state: the difference in kinetic energy causes differences in the effective potential felt by an electron.

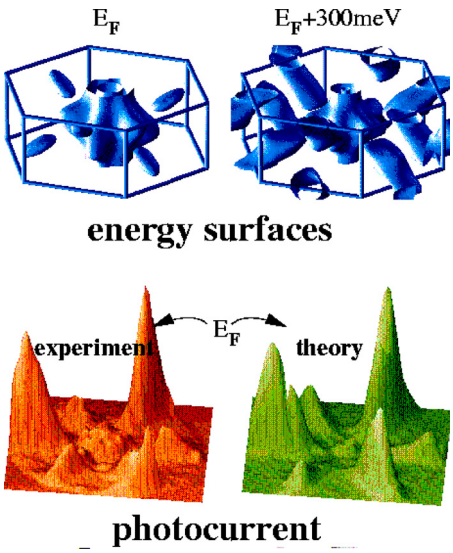

Figure 2.8: Theoretical and experimental pattern of photocurrent into emission hemisphere with $h\nu = 26$ eV from Fermi energy for $TiTe_2(0001)$ (bottom); Fermi surface plot (top left) compared with energy surface slightly above E_F (top right) . See also color figure on page 462.

2.6.1 Direct solution of Schrödinger equation

In contrast to the multiple scattering procedure which actually uses Green functions as to be subsequently discussed, the final states of photoemission may be directly incorporated via their wavefunctions. This is especially useful in the low kinetic energy range where the anisotropic potential in the interstitial region and at the surface becomes important. Plane-wave based descriptions are convenient in a pseudopotential version though augmented plane waves have started to be applied, too. [70] Thus, the path to an all-electron computation is paved. The pseudopotential formalism is comparably fast and has been applied in most cases.

The evaluation of wavefunctions proceeds via a direct solution of the Schrödinger equation. The formulation of the boundary condition is a little tricky because physical intuition would view it as an initial value problem solved backwards in time. The photoemission final state in principle must be described as an outgoing state with plane wave asymptotics characterized by the observed momentum in the detector at infinite time. Time is replaced by the coordinate perpendicular to the surface such that plane wave asymptotics are required at infinite distance from the surface in vacuum. An elliptic equation encounters numerical instabilities which become apparent when using a step procedure as solver. One has to transform the asymptotic condition into a boundary condition for a closed domain. This can be done at a sufficiently remote interface within vacuum which leads to mixed boundary values, i.e. a relation between the function and its derivative at that interface. [79] In formulating these conditions use has been made of smooth continuity and vanishing potential at that fictitious interface. It might be interesting to note that on the vacuum side of that interface a single plane wave travels to the detector whereas a set of plane waves propagates towards the interface in

order to satisfy a correct matching. From the solid side a similar set is impinging onto the surface such that the time reverse of all the terms constitutes a so-called scattering solution, i.e. one plane wave incident and scattered waves into all directions. This degenerates here, because of the unboundedness of the laterally infinite scatterer, into two sets of scattered waves traveling away from the interface into both half-spaces.

An intermediate step deserves separate consideration because it is appropriate for a shortcut interpretation of photoemission data. One obtains the complex bandstructure as the solution of the inverse bandstructure problem, i.e. prescribing the energy and solving for the eigenvalues of the perpendicular momentum. The Bloch condition yields real and complex values for that momentum, which is obvious especially for energies within the gap. One set, that with exponentially increasing wavefunctions towards the semi-infinite bulk, is discarded, but the remaining set constitutes a full set of states which are bounded in the bulk and are bounded up to the surface in the opposite direction. The energy vs. Real($k_\perp$) relation yields the complex bands with their imaginary part describing the exponential drop-off of such a band state in the interior. Considering the correct solution as a superposition of such states, those with large imaginary part will contribute less in view of a matching at the surface to the outside solution. The spatial variation proceeds on a scale given by the kinetic energy and this yields an order of magnitude beyond which a significantly shorter scale of decay will not contribute. Plotting the complex bandstructure for only reasonably low imaginary part together with the real bandstructure of the initial states of photoemission gives a first impression of the photocurrent to be expected in the direct transition model. Figure 2.9 shows electron distribution curves (EDC) for normal emission for GaN in comparing theory with experiment. [23] Agreement is obtained that is typical for this spectroscopy. The origin of the theoretical peaks is traced back in that figure to the intersection of the initial bands, shifted by the photon energy, with the final bands thereby assuming direct transitions, i.e. strict momentum conservation. The dispersion of the peaks with photon energy is indicated by dotted lines as a guide to the eye. Following the binding energies of the intersections when the bandstructures' shift by the photon energy is varied scans the observed dispersion in the theoretical and experimental spectra. In many cases it is appropriate to relax the accuracy slightly and to simplify the system so that it consists of the bulk pseudopotential including an optical potential and the sharp edge of a step-potential. In examples which need a more accurate modelling, e.g. of a surface layer, two potential steps are convenient as well. Then, a simple matching of the wavefunctions, i.e. plane waves in the region of constant potential and Bloch states of complex bandstructure in the bulk, gives reasonable results if used for the final states of a one-potential-step calculation. Matching instabilities at single energies occur which are manually removed by considering energies close by. This difficulty and the lack of some accuracy is balanced by an appreciable gain in computational time. The spectra in Fig. 2.9 are calculated by this scheme with one potential step.

Among several methods for the practical solution of the above mentioned boundary value problem, using the Laue representation together with layer doubling proved to be the fastest. The basis of that representation consists of plane waves in the surface parallel directions, their coefficients depending on the perpendicular coordinate z. The latter solve a system of ordinary differential equations (indexed by the reciprocal lattice vectors of the plane waves) with suitable boundary conditions with respect to the perpendicular coordinate. Discretizing z leads to an algebraic system with a matrix that is band diagonal with respect to z in its ki-

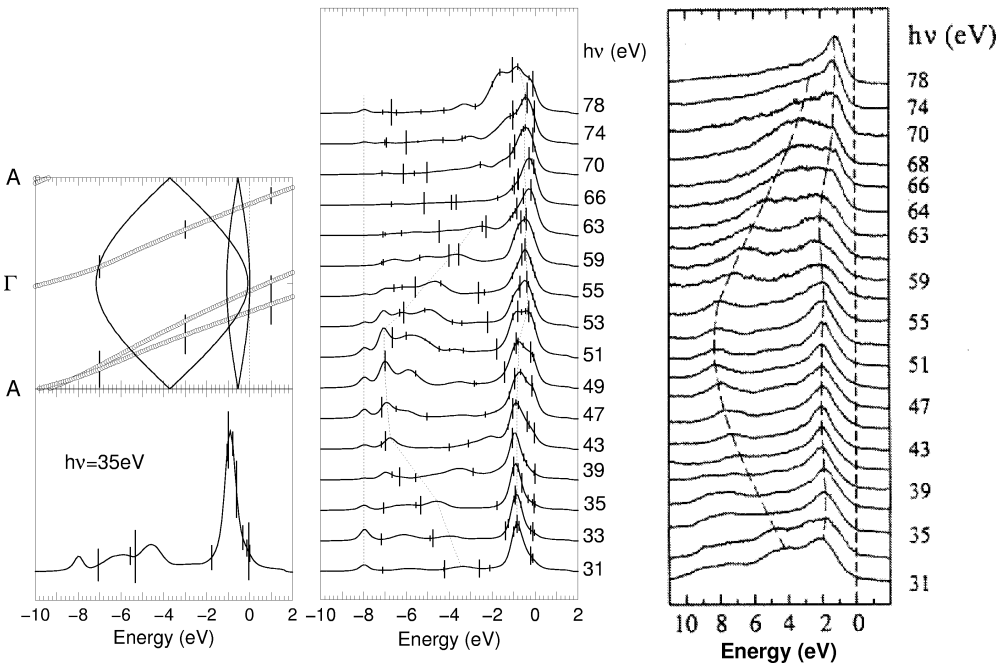

Figure 2.9: Theoretical (middle) and experimental [23] (right) normal emission spectra from Ga terminated GaN(0001)1x1, intensity vs. binding energy for various photon energies as marked, with single spectrum (bottom left) and both initial and complex final bandstructures (top left) for photon energy 35 eV; vertical bars at theoretical spectra indicate main direct transitions; final state decomposes into complex bands with weights denoted by bars at curves; both band systems are brought to coincidence through shifting by photon energy.

netic energy part but also in its potential part, provided the latter has a suitably limited range. With respect to the discretized z a layer doubling renormalization converges rapidly to the entire halfspace. The method uses pseudopotentials. Ab-initio pseudopotentials have to be transformed to a quasi-local form. [5, 11, 98] An example for such a final state wave function is shown in Fig. 2.10. Phase coherence is quickly lost in penetrating into the solid via more inclined directions. The potential may contain complex parts to account for the optical potential or more general many-body corrections, see below. In an example for $TiTe_2$ a series of final state wave functions between 5-100 eV has been computed and subsequently Fourier transformed with respect to its surface perpendicular position dependence to yield Fig. 2.11. Only slight differences occur by either fixing somehow or averaging the surface parallel position component. It is an obvious message that only one band, which, of course, is backfolded and actually is close to a parabola, dominantly contributes, i.e. plane waves distributed in a rather narrow range around the the parabolic dispersion constitute mainly the final state. This is often anticipated in experimental analyses. It was found for the layered transition metal dichalcogenides and for III-V semiconductors. However, the distribution becomes broader for higher energies and furthermore, the behaviour is best established for normal emission and

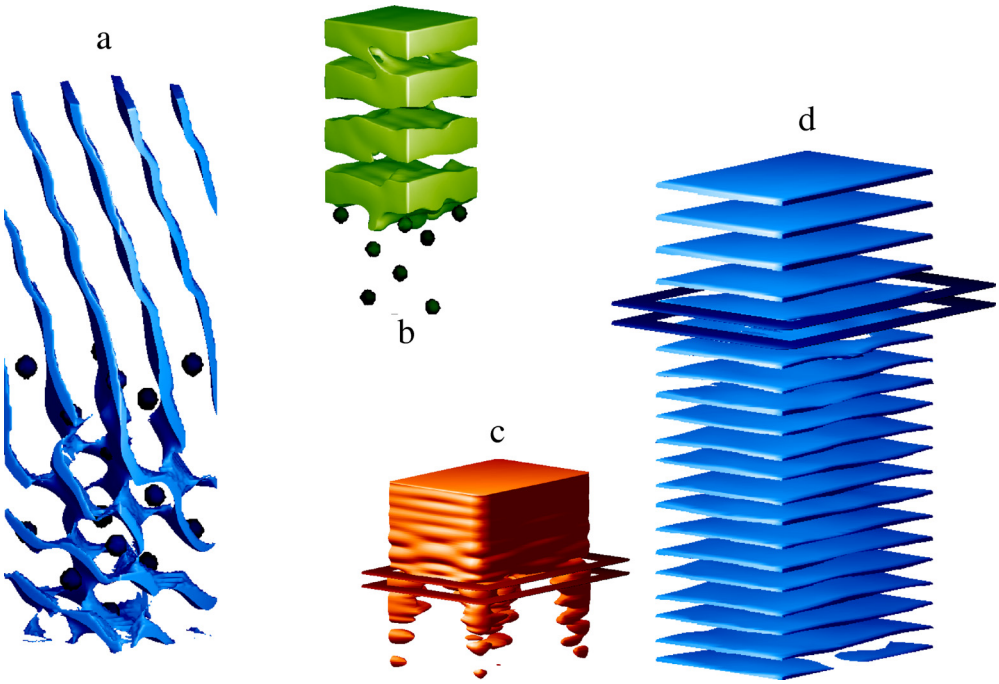

Figure 2.10: Plot of phase, a and d, and modulus, b and c, of wavefunction for Si(001) entering surface from vacuum (top) to solid (bottom), inclied electron escape (a,b), normal escape (c,d); dots show nuclei positions, frame indicates interface. See also color figure on page 462.

deteriorates for inclined directions. The experimental confirmation of the correctness of the final states' calculation arises from ARUPS rather indirectly because the latter is primarily determined by the initial states in valence band spectroscopy. Core-level initial states might give a more direct access because of their lack of dispersion, but that is not yet in actual favor. A direct method is available via very low energy electron diffraction (VLEED) with intensity spectra, $I(U)$, which yield the angle dependent electron reflection and absorption in the elastic channel. This is intimately described by the wavefunctions used for the final states which can thus be tested. [104]. Total current spectroscopy represents the complementary case of this method. [89, 98] A simple illustration follows from the fact that the incident electron is strongly reflected by the surface in those energy regions where a gap appears in the band structure of the solid.

Finally, the obtained wavefunction is inserted into the Golden Rule, Eq. (2.100), for $|\Phi^{\star}_{LD}(E, \mathbf{k}^{\mathbf{0}}_{\|}) >$ which is integrated in direct space to calculate the photocurrent.

At this point, a remark must be made about the optical potential physically motivated by the losses of the propagating electron and a necessary ingredient for convergence in the bulk. Seen from many-body theory, such losses are represented by the lifetime of a quasi-particle state, which corresponds to the imaginary part of the self-energy Σ. Apart from heuristic approaches to this quantity, especially to its energy dependence, it can be calculated nowadays

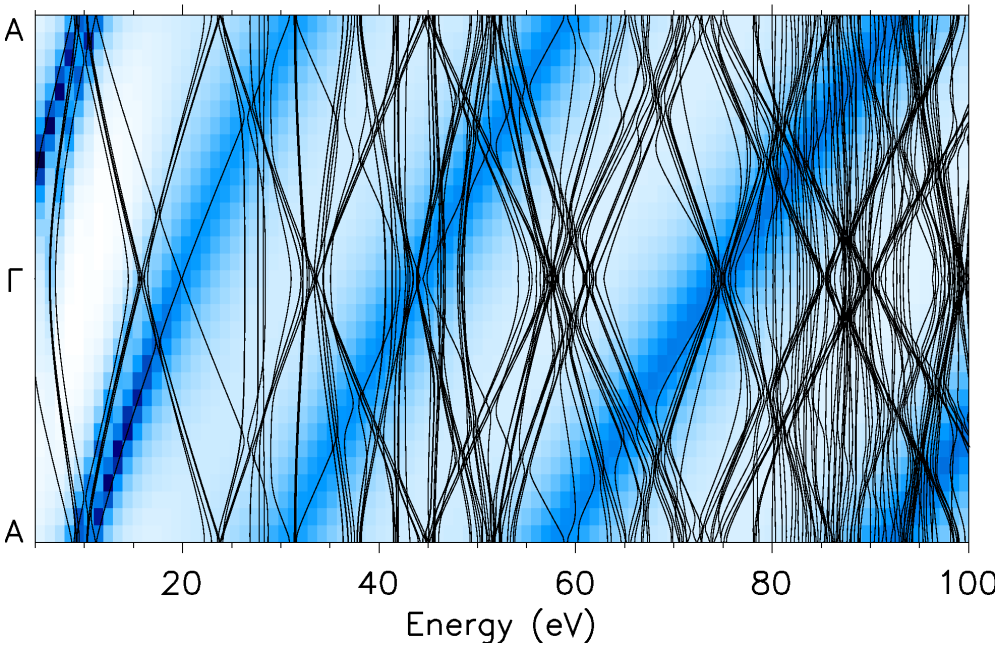

Figure 2.11: Wave functions Fourier transformed along (0001) direction ($A\Gamma A$) of $TiTe_2$(0001), for each energy intensity of shading represents modulus of Fourier coefficient vs. wave vector; real band-structure (black lines)is underlaid. See also color figure on page 463.

in a more systematic way, e.g. via the "GW" approximation, i.e. writing the self-energy as a product of the Green function G and the screened Coulomb interaction W according to the first term of an expansion with respect to W. Then the real part of Σ is accessible, too, and the entire quantity may be used as the quasi-particle correction to the final state. The solution for these states as described above can include the self-energy in a very general form, i.e. more general than in a merely energy dependent form.

The presence of the self-energy is required within the quasi-particle Green function which in turn is obtained by Dyson's equation, on one hand. On the other hand, the self-energy is represented by a set of quasi-particle states which are obtained from a solution of the homogeneous variant of the Dyson equation which corresponds to the usual Schrödinger equation plus a complex Σ. Thus, in the excited energy regime these states may be considered as final states of photoemission taking suitable boundary conditions. [98] In the occupied energy regime they represent the initial states. It follows that, because Σ is energy dependent, both sets of states belong to different one-particle hamiltonians even for the hermitean no-loss case. Therefore, it is not required that the states emerge from one single hamiltonian. This gives freedom to treat the states by different methods adapted more specifically to each energy range.

The form of $\mathrm{Im}\,\Sigma$ in the final states' regime follows a general shape, specifically, it increases from a low value, below a tenth of an eV at the bottom of the conduction states, with a significant jump at the plasma frequency up to several eV in the VUV range of photoelec-

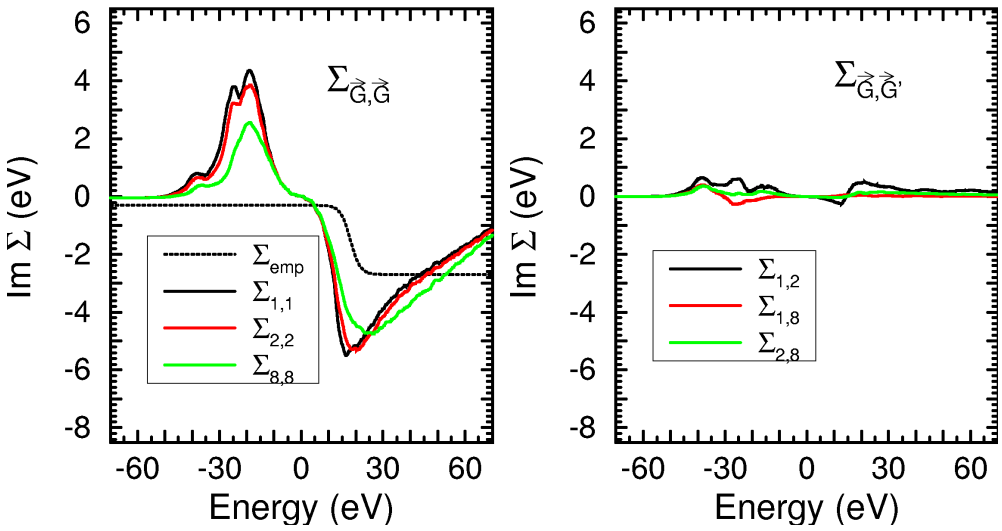

Figure 2.12: $\mathrm{Im}\,\Sigma$ as matrix in reciprocal lattice vectors calculated with GW for diagonal elements (left), (1,1) element to be compared with empirical optical potential, and for non-diagonal elements (right).

tron spectroscopy. The increase through plasmon losses is sometimes modelled by a Fermi function-like shape. [43] The consequence of that increase is generally an increase of the imaginary part of the Bloch vector and consequently of the perpendicular momentum non-conservation or spread of indirect transitions. It does not increase the width of the photoemission peaks. That is determined by the lifetime of the occupied states. Actual state-of-the-art calculations use the GW approximation. [35, 37, 97] A comparison for $TiTe_2$ between the heuristic shape and that calculated by GW for the unoccupied states reveals a rough agreement in the overall dependence whereas the details differ, see Fig. 2.12. Slope and edge position can thus be calculated. The asymptotic decrease in the magnitude of the GW result is attributed to the energy cut-off.

Some additional structure is present in the GW plot and is reminiscent of the electronic transitions which appear in the dielectric function involved in the screened interaction W. However, the details are smoothed by the integrations involved in the calculation. A scheme for an independent determination of $(\mathrm{Im}\,\Sigma)$ via VLEED has been recently described. [72]

2.6.2 Multiple scattering method

An alternative approach for dealing with the final state wave function is to actually consider the individual scattering events suffered by the photoelectron in its elastic interaction with the solid atoms along its way to the detector. This is the so called multiple scattering (MS) method, which consists in calculating the one-electron wave function of the photoelectron as the sum of the direct unscattered photoemission wave and the result of MS due to the surface atoms.

In this context, the surface atoms are usually described by spherically-symmetric muffin-tin potentials, and this is a good approximation for electrons with relatively high kinetic energy ($E > 50$ eV); these are insensitive to the details of the atomic potential tails and see the atoms basically as spherical entities [90]. The generalization to space-filling arbitrary potentials can be made with some care [42].

Two basic approaches are in use to represent a surface: the semi-infinite model which preserves periodicity in two dimensions, and often truncates the surface to a finite depth as a slab; and the cluster model, which retains only a finite-size piece of the surface, thus more easily allowing non-periodic structures to be represented. The semi-infinite model is used in particular in the work of Pendry, Tong and others [91, 107] In the following, we will describe the cluster model, which is simpler but also functions as an ingredient in many semi-infinite models.

Thus, we shall approximate the solid by a cluster of non-overlapping spherical muffin-tin potentials. The size of the cluster is dictated by the finite electron mean free path. Each muffin-tin potential represents a solid atom centered at a position $\mathbf{R}_\alpha$. The potential outside the muffin-tin spheres and within the solid is set to a constant value, the muffin-tin zero, to which the photoelectron energy E is referred. The effect of inelastic attenuation is incorporated by adding a small imaginary part to E [90] (which is equivalent to adding it to the photoelectron self-energy).

For simplicity, we shall consider core-level photoemission, so that the initial-state wave function is fully contained within the muffin-tin sphere of the emitter atom, which we will denote α_0. This will be generalized to extended initial states (e.g., in valence photoemission) in Sec. 2.7.

To represent scattering by the atoms, the electron wave function is then expressed in spherical harmonics and spherical Bessel functions centered on each atom of the cluster. In particular, the direct photoelectron wave function ϕ^0 (that is, the wave which originates at the emitter in the absence of MS) can be projected on a complete basis set of outgoing and incoming spherical waves centered on the emitter, and the physical requirement that there should be no net incoming flux for any partial wave component leads to the fact that only outgoing waves contribute in this case. More precisely,

$$\phi^0(\mathbf{r}) = \sum_{L'} h_{L'}^{(+)}[k(\mathbf{r} - \mathbf{R}_{\alpha_0})]\, \varphi_{L'}^0 \tag{2.105}$$

for $\mathbf{r}$ outside the muffin-tin sphere of the emitter α_0, where $h_L^{(+)}(k\mathbf{r}) = \mathrm{i}^l h_l^{(+)}(kr) Y_L(\Omega_\mathbf{r})$ represents an outgoing spherical wave, $h_l^{(+)}$ is a spherical Hankel function [85], $L = (l, m)$ labels spherical harmonics Y_L, and $k = \sqrt{2E}$ is the electron momentum relative to the muffin-tin zero.

In order to study MS effects, we need to consider $\phi^0(\mathbf{r})$ near the other cluster atoms $\alpha \neq \alpha_0$. This can be conveniently done by expressing each of the partial waves L' of ϕ^0 in terms of spherical waves centered on another atom $\alpha \neq \alpha_0$, which can be done by using the translation formula of spherical harmonics [88]

$$h_{L'}^{(+)}[k(\mathbf{r} - \mathbf{R}_{\alpha_0})] = \sum_L j_L[k(\mathbf{r} - \mathbf{R}_\alpha)] G_{\alpha\alpha_0, LL'}, \tag{2.106}$$

where

$$G_{\alpha\alpha_0,LL'} = 4\pi \sum_{L''} h^{(+)}_{L''}[k(\mathbf{R}_\alpha - \mathbf{R}_{\alpha_0})] \times \int d\Omega\, Y_L(\Omega) Y_{L''}(\Omega) Y^*_{L'}(\Omega) \tag{2.107}$$

and $j_L = \mathrm{i}^l j_l Y_L$ is a spherical wave centered at α that can be regarded as the spherical component of a plane wave passing by atom α.

The above translation allows one to express Eq. (2.105) as a sum of j_L waves in the vicinity of a given atom α. The contribution of the scattering of these waves from α is obtained if we make the substitution

$$j_L \rightarrow j_L + \sum_{L'} t_{\alpha,L'L} h^{(+)}_{L'}, \tag{2.108}$$

where $t_{\alpha,LL'}$ is the so-called scattering matrix, which for spherical atoms, becomes diagonal and is given in terms of the scattering phase shifts δ^α_l as [85]

$$t_{\alpha,LL'} = t_{\alpha,l}\delta_{LL'} = \sin\delta^\alpha_l \mathrm{e}^{\mathrm{i}\delta^\alpha_l}\delta_{LL'}. \tag{2.109}$$

The second term in Eq. (2.108) is the scattered part of a plane wave component, as obtained by standard partial wave analysis [90]. Then, summing over all possible first-order scattering events (i.e., over all atoms α), the photoelectron wave function calculated within first order reduces to

$$\phi^1(\mathbf{r}) = \sum_\alpha \sum_{L'} h^{(+)}_{L'}[k(\mathbf{r} - \mathbf{R}_\alpha)]\, \phi^1_{\alpha,L'}, \tag{2.110}$$

where

$$\phi^1_{\alpha,L'} = \phi^0_{\alpha,L'} + \sum_{LL''} t_{\alpha,L'L''} \sum_\beta G_{\alpha\beta,L''L}\phi^0_{\beta,L} \tag{2.111}$$

and $\phi^0_{\beta,L'} = \delta_{\beta\alpha_0}\varphi_{L'}$ are the direct wave coefficients, which are zero for atoms other than the emitter α_0.

This procedure can be repeated with each of the h_L components of Eq. (2.110) to lead to second-order scattering and so on. A recurrence relation can be obtained in this way, so that the coefficients of the expansion at order n can be obtained from those at order $n-1$ as

$$\phi^n_{\alpha,L} = \phi^0_{\alpha,L'} + \sum_{L'L''} t_{\alpha,LL''} \sum_{\beta\neq\alpha} G_{\alpha\beta,L''L'}\phi^{n-1}_{\beta,L'}, \tag{2.112}$$

where the restriction that $\beta \neq \alpha$ reflects the fact that the unscattered propagation from any atom to itself must be excluded.

In the $n \rightarrow \infty$ limit, Eq. (2.112) becomes a self-consistent secular equation,

$$\phi_{\alpha,L} = \phi^0_{\alpha,L'} + \sum_{L'L''} t_{\alpha,LL''} \sum_{\beta\neq\alpha} G_{\alpha\beta,L''L'}\phi_{\beta,L'}, \tag{2.113}$$

which has to be satisfied by the wave function components $\phi_{\alpha,L}$ of the photoelectron wave function

$$\phi(\mathbf{r}) = \sum_{\alpha} \sum_{L'} h_{L'}^{(+)}[k(\mathbf{r} - \mathbf{R}_\alpha)]\, \phi_{\alpha,L'} \tag{2.114}$$

outside the muffin-tin spheres.

From a numerical point of view, Eq. (2.113) can be approximated by a finite system of $N(l_{\max}+1)^2$ equations if one considers a cluster of N atoms and a maximum angular momentum number $l_{\max}$, which scales roughly as $l_{\max} \sim kr_{\mathrm{mt}}$ with the electron momentum k and the atomic muffin-tin radius r_{mt}. Unfortunately, the direct inversion of Eq. (2.113) is computationally very demanding and can be performed only for very limited cluster sizes and small values of $l_{\max}$ (low energies) [45]. Therefore, approximations have been introduced [90], some of them inspired by the high-energy limit, where the electron propagation reduces to plane-wave factors (plane-wave approximation) and each term in the MS series becomes a product of scattering amplitudes [7, 8, 62]. Beyond this, full curved-wave formulations of the problem have been also implemented [18, 26, 92].

Codes based upon the Rehr-Albers formalism make use of a convenient factorization of the path Green function into matrices that represent individual scattering events and that contain curved wave effects up to any required accuracy (e.g., MSCD [18]); this results in a computation time that scales with the cube of the number of atoms in the cluster, but a path-cut can be introduced to reduce the computational demand drastically at the expense of small errors arising in the truncation of the multiple scattering series.

It is also possible to solve the multiple scattering equations without any approximation in the Green function by using iterative techniques based upon the recursion method. This is the procedure employed in EDAC [26], which presents the advantage of preventing any eventual lack of convergence in the multiple scattering. The computation time in this code scales with the square of the number of atoms, which allows calculations for clusters of up to several thousand atoms.

2.7 Matrix elements: core versus valence levels

The theoretical model introduced in Sec. 2.6.2 for calculating the photoelectron intensity from a core level can also be applied to study the photoemission from extended states, such as valence levels of molecules, clusters or solids. When the initial state of the electron is extended over several atoms, the initial wavefunction can be expanded as:

$$\Psi_i(\mathbf{r}) \;=\; \sum_{a}^{\text{emitters}} \sum_{L} \kappa_L^a \psi_L^a(|\mathbf{r} - \mathbf{r}_a|) Y_L(\Omega_{\mathbf{r}-\mathbf{r}_a})\,. \tag{2.115}$$

In the latter equation, $\psi_L^a(\mathbf{r} - \mathbf{r}_a)$ are atomic orbitals centered about site a. The initial state is thus a combination of several atomic orbitals (hence the sum over L) at several sites (hence the sum over a). The factors κ_L^a are the coefficients of this linear combination.

Following a formalism similar to that of core-level photoemission, the wavefunction at the detector position $\phi(R_d)$ can be obtained as:

$$\phi(R_d) \;=\; \sum_{a}^{\text{emitters}} e^{-i\mathbf{k}\mathbf{r}_a} \sum_{L} \kappa_L^a \sum_{\alpha}^{\text{atoms}} \sum_{L'} \phi_{\alpha,L'}^{aL} \frac{e^{ik\mathrm{R}_d}}{k\mathrm{R}_d} Y_{L'}(\Omega_{R_d}) \,, \tag{2.116}$$

where the coefficients $\phi_{\alpha,L'}^{aL}$ now depend on L and a as well (the initial atomic orbital of quantum numbers L at emitter a), and the Hankel functions of Eq. (2.114) have been replaced by their asymptotic expansions. The final wavefunction (and consequently the photoelectron intensity at the detector position) is thus obtained as a coherent sum over emitters a with coefficients κ_L^a. An additional phase factor $e^{-i\mathbf{k}\mathbf{r}_a}$ accounts for the electron path difference between emitters. This assumes in-phase arrival of the incident photon wave at all emitter sites, namely an infinite photon wavelength; an additional phase factor can be inserted to account for a finite photon wavelength.

In the case of a perfect three-dimensional periodic lattice (for instance, an ideal infinite crystal without any surface), the initial state in the photoemission process can always be described as a Bloch state. In this case, the coefficients multiplying the atomic orbitals in Eq. (2.115) can be written in a different way, so that the Bloch condition is apparent:

$$\Psi_i(\mathbf{r}) \;=\; \sum_{a}^{\text{emitters}} e^{i\mathbf{k}\mathbf{r}_a} \sum_{L} K_L \psi_L^a(|\mathbf{r}-\mathbf{r}_a|) Y_L(\Omega_{\mathbf{r}-\mathbf{r}_a}) \,. \tag{2.117}$$

The new coefficients K_L do not depend on the site a because all sites are equivalent. They only depend on the quantum numbers L. The vector $\mathbf{k}$, which satisfies the Bloch condition, has the same dimensions of the periodic lattice. It does not change during the photoexcitation process (the electron momentum is conserved in the limit of an infinite photon wavelength). The final wavefunction at the detector position is then:

$$\begin{aligned}
\Psi_f(R_d) \;&=\; \sum_{a}^{\text{emitters}} e^{i\mathbf{k}\mathbf{r}_a} \sum_{L} K_L \sum_{\alpha}^{\text{atoms}} \sum_{L'} \phi_{\alpha,L'}^{aL} \frac{e^{ik\mathrm{R}_d}}{k\mathrm{R}_d} e^{-i\mathbf{k}(\mathbf{r}_\alpha+\mathbf{r}_a)} Y_{L'}(\Omega_{R_d}) \\
&=\; \sum_{a}^{\text{emitters}} \sum_{L} K_L \sum_{\alpha}^{\text{atoms}} \sum_{L'} \phi_{\alpha,L'}^{aL} \frac{e^{ik\mathrm{R}_d}}{k\mathrm{R}_d} e^{-i\mathbf{k}\mathbf{r}_\alpha} Y_{L'}(\Omega_{R_d}) \\
&=\; \mathcal{N} \sum_{L} K_L \sum_{\alpha}^{\text{atoms}} \sum_{L'} \phi_{\alpha,L'}^{aL} \frac{e^{ik\mathrm{R}_d}}{k\mathrm{R}_d} e^{-i\mathbf{k}\mathbf{r}_\alpha} Y_{L'}(\Omega_{R_d}) \,.
\end{aligned} \tag{2.118}$$

In the latter equation $\mathcal{N}$ is a normalization constant arising from the sum over equivalent lattice sites, with no important role in the calculation of the intensity. Eq. (2.118) shows that, for a 3D periodic system, the final wavefunction (and consequently the photoelectron intensity at the detector position) can be evaluated by calculating the photoelectron intensity *from one single site* a; more generally, from all those sites that are translationally inequivalent within a unit cell. Every single equivalent site of the lattice emits coherently but there is no phase shift among the photoemission processes from different equivalent sites for an infinite photon wavelength. A similar formalism can be developed for a system in which there is periodicity

in only two dimensions. Then emitters at different depths are no longer equivalent and their emission must be considered separately, but still coherently.

For a finite photon wavelength, the photon path differences among different emitters must be included in the previous equations. Especially for very large systems, such as with infinitely extended initial states, an additional phase factor, depending on the emitter position and on the light wavevector, will thus appear in Eq. (2.118).

2.8 Optical effects

Generally, the photons can be dressed by any type of excitation that they are able to produce in a solid (e.g., plasmons, phonons, and all kind of quasiparticles).

Screening of the external light is important for photoemission from solids, specially at low photon energies, and in particular near the plasmon energy, in which case the medium induces an electric field that can be comparable in magnitude to the external field provided by the light near the surface. It then can be also comparable in wavelength with the atomic spacing.

Strong variations of the electric field near the surface can play a substantial role in the so-called surface emission, which has been clearly observed in angle resolved photoemission [86], and that is relatively well described by the Fresnel equations [63], which requires knowledge of the dielectric function of the solid material. The latter can be obtained from experiment. In particular, for low photon energies (e.g., < 50 eV) complex collective excitations (e.g., plasmons) dominate the response. At these low energies, the photon wavelength (> 24 nm) is much larger than the typical surface lattice constant, and therefore, principally the medium should be well described by its macroscopic, frequency-dependent dielectric function, which neglects all kind of details on the atomic scale. But as it will be outlined in subsection 2.8.2, induced local fields yield important perturbations on a lattice scale near the plasmon frequency.

2.8.1 Resonant photoemission

Resonant photoemission is an interesting phenomenon which takes place when the photon energy is tuned to a resonance of the emitting atoms. Then, the photoelectron has two different emission channels: (i) direct excitation by absorbing an external photon and (ii) excitation of the resonance followed by its decay while the excess of energy is carried away by the photoelectron. These two different quantum channels leave the sample in exactly the same final state, and thus, they have to be added coherently, leading to interference effects that in general follow Fano profiles [29].

This phenomenon can be considered to be a screening effect: the external photon is dressed by interaction with a many-body system that is able to hold localized excitations (the atomic resonance), similar to excitons in solids. This is particularly important at low incidence angles, which can limit the penetration depth of the light dramatically, especially in metals, where the so-called skin depth of visible and near UV light is only a few nanometers. Also, dramatic effects have been observed under total reflection conditions [52, 84].

At higher photon energies (e.g., > 100 eV), the response is governed by the X-ray scattering factors of the solid atoms, so that the screening at those energies comes primarily from

dynamical X-ray scattering. Besides, the *effective* dielectric function at those energies is very close to 1, since the response is small. However, some effects can be observed at the energies of the absorption edges. More precisely, when the external light is tuned at the energy of an absorption resonance of one of the atoms in the solid, strong induced fields comparable in magnitude with the external field are produced, especially at low incidence angles. This has been recently observed in photoemission from O 1s in MnO illuminated with light near the Mn2p absorption edge (640 eV) [25, 66, 67]. The O 1s photoelectron signal showed a strong modulation near that photon energy, and this has been explained in terms of the Mn resonating atoms, which suffer virtual excitations by the incoming light to decay later while transferring the excitation energy to O 1s electrons.

This is the so-called multi-atom resonant photoemission (MARPE), which provides a way to identify the chemical nature of neighboring atoms in a solid, since the resonance energy is a characteristic of one kind of atoms while the observed photoelectrons are emitted from a different kind of atoms. An example of this if offered in Fig. 2.13 for emission from oxygen near the Mn2p absorption edge in MnO [25, 66, 67]. The theory in this figure is based upon first principles calculation of the atomic polarizability of Mn in MnO and multiple scattering of photons in between different Mn scatterers. The result of this multiple scattering produces an effect that can be also explained in terms of a dielectric model (using Clausius-Mossotti to convert the Mn polarizability into dielectric function), where the emission intensity maps the square of the external electric field at the surface region.

A very good agreement has been obtained between theory and experiment in this latter case, and also between a microscopic theory of the solid response based upon first principles calculations of the atomic scattering factors as compared with a macroscopic description using Fresnel's equations and the dielectric function derived from the Clausius-Mossotti relation.

Beyond this simple model, *ab initio* theories have been developed to compute the response function of the solid, although severe approximations have to be made in order to cope with the complexity of the surface. These models take into consideration the detailed band structure of the solid in order to construct the response function. In the simplest scheme, one simply uses one-electron wave functions to obtain the RPA susceptibility [59]. While this approach generally gives good results for metals, several problems emerge when it is applied to insulators: excitons are not described at all and one needs to go beyond the RPA and use the Bethe-Salpeter equation for a correct description of electron-hole pairs [33].

2.8.2 Photoemission by surface optical response fields

The assumptions in Eq. (2.89), with respect to periodicity as well as to long wavelength, must be questioned if the response of the emitting material to the incident light adds induced fields capable of appreciable separate excitations. Such fields change on a length scale of the lattice constant because they originate from the ionic polarizability, and they are non-periodic because of the surface. These effects become important for a small real part of the dielectric function $\epsilon(\mathbf{r}, \mathbf{r}', \omega)$ implying large fields for even small amplitude external light which might occur especially for ω near the plasmon frequency.

Because of their short wavelength these fields are denoted as "local fields" well known from optics: they drastically change the homogeneous dielectric constant $\epsilon_0(\omega)$ from its microscopic to the macroscopic observable value. The surface adds nonlocality to ϵ as stressed

by noting the dependence on two local variables $\mathbf{r}, \mathbf{r}'$. It arises e.g. from surface scattering of the electromagnetic wave and from further enhancement by plasmon generation. Though both effects are well known in the literature, (the latter especially has been first observed in connection with photoemission [73]), the full incorporation into one-step photoemission calculations is still lacking. A few calculations include the dielectric function in the determination of the photocurrent, but use more or less heuristic models. Two examples applying to solids will be described in the following (further details may be found in Ref. [97]): In particular, optical investigations carry more information about local fields [71] and surface response [76].

Local fields are conveniently illustrated in layered crystals, e.g. in $TiSe_2$ where they appear as polarization fields perpendicular to the layers, i.e. parallel to the axis of the valence Se-p_z orbitals across the layers. Thus, the induced field will couple to that orbital leading to additional photoemission from it. Quantitatively, the vector potential $\mathbf{A}$ in Eq. (2.87) must be

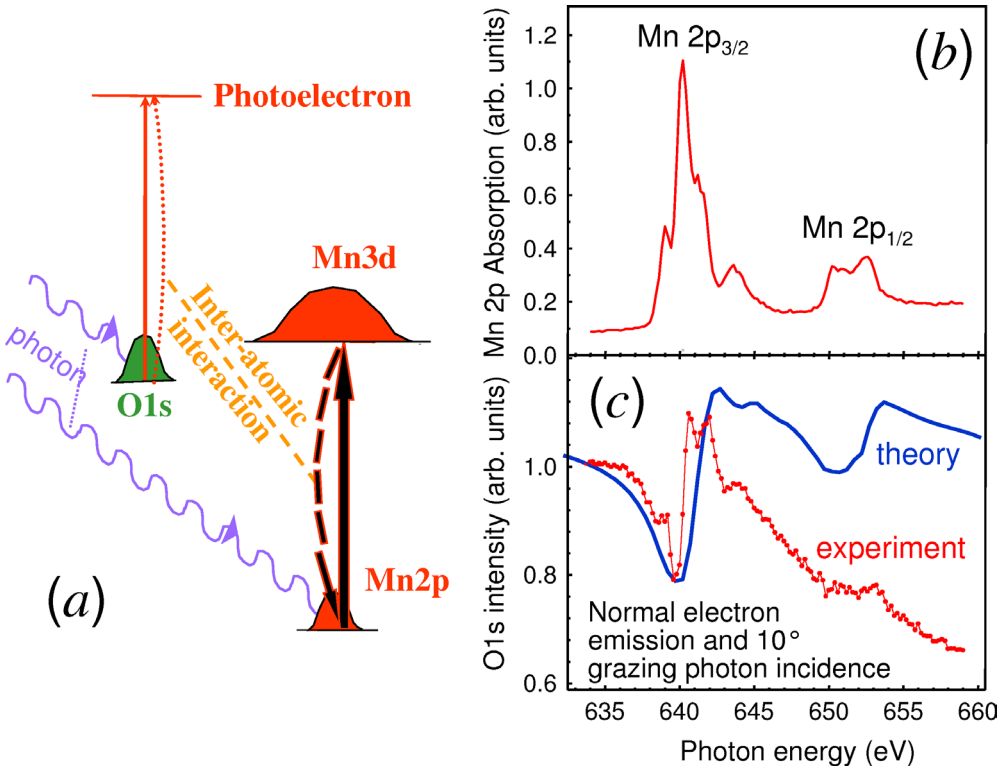

Figure 2.13: Multi-atom resonant photoemission in MnO(100) surfaces. **(a)** A photon can produce photoemission from an O atom, but in a different channel the same photon can excite a Mn atom of the sample, which decays transferring its energy to the first O atom. The final state in both channels is the same, so that they have to be added coherently. **(b)** Measured absorption spectrum near the Mn2p edge, showing the energies where Mn can actually be efficiently excited. **(c)** O1s photoelectron intensity within the Mn2p resonance energy range.

replaced by

$$\mathbf{A}_{\mathbf{G}}(\omega) = (\epsilon^{-1})_{\mathbf{G}0}\mathbf{A}_{\mathbf{0}}^{\text{ext}}(\omega) \tag{2.119}$$

where $\mathbf{A}^{\text{ext}}$ refers to the incident external light, $\mathbf{G}$ denotes a reciprocal lattice vector, and (ϵ^{-1}) refers to the matrix element with respect to the two vector indices $\mathbf{G}$ and $\mathbf{0}$. Here, the incident wavelength is assumed long compared to the lattice spacing, which is valid up to the vacuum ultraviolet regime. Values for ϵ must be taken from separate optical calculations. They show a strong enhancement near the plasma frequency, i.e. around 20 eV for $TiSe_2$, which can cause 100% changes in the photocurrent, leading to a dominating peak for the Se-p_z emissions. The reciprocal lattice vector $\mathbf{G}$ of the prominent induced-light component is $2\pi/c$ [0001], the first non-zero vector perpendicular to the layers corresponding to a wavelength equal to the perpendicular lattice spacing c. [10]

Nonlocal response also has been investigated for layered materials. Owing to the lack of any general ab-initio determination of the surface response, the hydrodynamic model of the bulk electron gas may give a first impression of the induced longitudinal plasmon waves and the correspondingly longitudinal response fields for photons above the plasmon frequency. Because of the boundary conditions, the induced field points perpendicularly to the surface and propagates into the interior of the solid. It varies locally on a scale involving the valence electron density and the difference between light and plasma frequency: the induced field increases when the plasma frequency increases and the light frequency decreases. Again, the corrected field is introduced into the photoemission calculation via Eq. (2.119). [95] Similar to the above case, the additional field can excite Se-p_z emissions, also yielding a 100% enhancement of the photocurrent close to the plasma frequency above it. [95]

This topic is now still developing from its rather model-like state, depending on the growth in computer power. The effect on the electron distribution curves of photoemission can be extremely large, such that its neglect produces doubtful peak heights and peak positions under the above circumstances of observation. In Fig. 2.14 the high significance of these effects becomes apparent. A structure dispersing between 0 and -2 eV which consists mainly of p_z orbitals is enhanced by including the local fields induced by the incident photon in contrast to the non-dispersive peak at -3 eV. The experiment reveals that the theory overestimates this effect which, of course, is related to the crude approach of using the bulk dielectric matrix for the local fields.

An ab-initio calculation of the full dielectric matrix function for semi-infinite systems has been completed recently. [16] Its application to photoemission with the aim considered here is in progress.

2.9 Spin effects

The spin of the electron plays an important role in photoemission from magnetic atoms or when states that suffer strong spin-orbit coupling are involved. Normal detectors do not discriminate between spin polarization of the photoelectrons, unless strongly spin-polarized initial states are considered [101,106]. However, the increasing enhancement in photon flux from new generations of synchrotrons and free-electron lasers are making it possible to collect reasonable signals using spin-selective Mott detectors, where the electron detection efficiency is

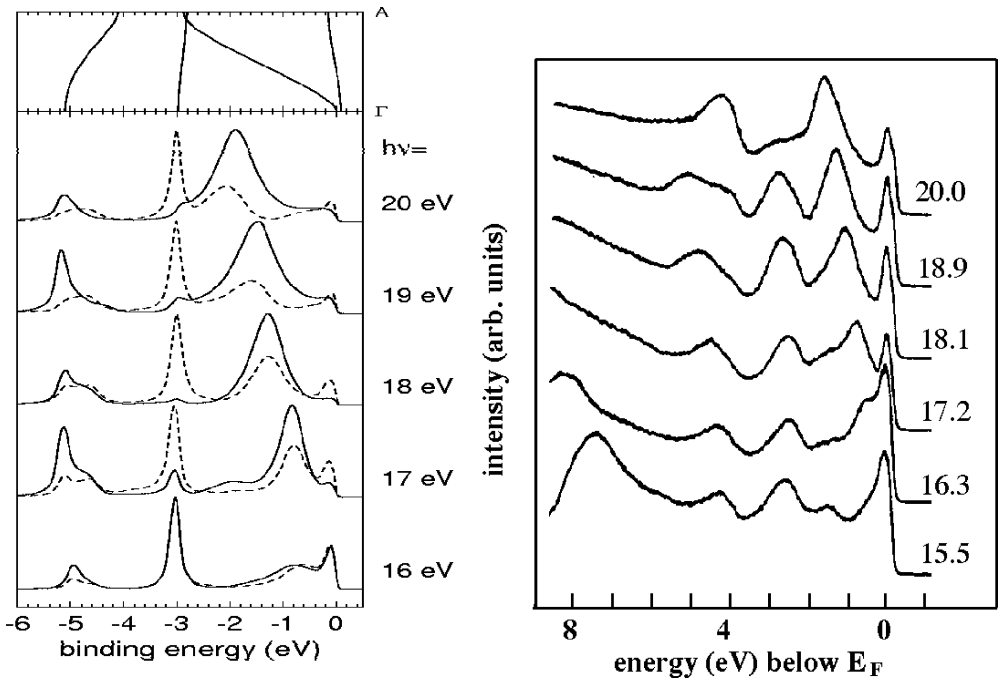

Figure 2.14: Theoretical photoelectron spectra at left, including (solid) and neglecting (broken) local fields, for normal emission from $TiSe_2$(0001) with bandstructure plotted on top, compared with experimental spectra [4] at right; photon energy as parameter at the curves

low since spin separation is performed by tiny differences in the angular distribution of Mott scattering of photoelectrons at the detector.

Magnetic samples define a category of experiments where spin is important. Common techniques in this context involve measuring magnetic dichroism, that is, the fractional change in photoelectron intensity either when the magnetization of the sample is reversed [54] or when the light polarization is changed (e.g., from left to right circularly polarized light [101]).

From an atomic point of view, the magnetic dichroism signal in core-level photoemission permits establishing the magnitude of spin-orbit coupling in the final state of the ionized emitting atom [100]. It also provides quantitative information on the magnetic moment of oriented magnetic atoms, and can be used to determine Curie and Néel temperatures near the surface of the material from which the photoelectron originates (these temperatures may differ from the bulk values [106]).

Spin effects are to some extent a reflection of the initial and final states of the emitting atom, which can be generally described by one-electron states in the case of closed shells (e.g., in emission from Fe2p or Gd4d [100]). General open shell configurations however involve complex many-electron states, which result in photoemission spectra composed of many multiplet lines.

Multiple scattering of the photoelectron introduces additional spin dependence originating in the different scattering properties of electrons polarized either parallel or antiparallel with respect to the magnetic moment of the atoms [53, 106]. Besides, spin-orbit coupling effects in photoelectron scattering from solid atoms (Mott scattering) can play an important role even in the VUV region. This is particularly true along scattering directions of strong spin anisotropy when they coincide with atomic bonds that produce forward focusing effects. These effects introduce spin dependence in multiple scattering for non-magnetic atoms as well [102].

Spin effects can be easily implemented in the multiple scattering scheme discussed in Sec. 2.6.2. In particular, the atomic scattering matrix needs to be supplemented by the electron spin quantum number. In magnetic atoms with negligible spin-orbit coupling, the scattering matrix can be split into disconnected spin-up and spin-down pieces, each of which is described by the corresponding atomic potential that takes into account exchange and correlation effects [108]. When spin-orbit coupling is included, a complex interplay with magnetic exchange leads to dense scattering matrices [102, 103]. Finally, the propagation of the electron in the muffin-tin interstitial potential can be performed in the same way as in Sec. 2.6.2, independently for each spin component. These possibilities are contemplated in the EDAC code [25] (see Sec. 2.10).

2.10 Computer codes for photoelectron diffraction and spectroscopy

A variety of computer codes have been written to simulate photoelectron diffraction. A majority of these codes were designed for surface structure determination, similar to LEED codes. This often includes some form of automatic fitting of structural parameters such as atomic coordinates that affect interlayer spacings or bond lengths near the surface. Other codes aim to study different aspects of surfaces, including magnetic or relativistic effects, electronic band structure and/or the spatial distribution of electrons.

We here discuss and compare several codes for which we have detailed information (a number of other codes exist):

- MSPHD by R. Gunnella, C.R. Natoli, F. Solal and D. Sébilleau (superfici.unicam.it/photoelectron_diffraction.htm)
- SPEC by D. Sébilleau;
- PRAPD by M.D. Pauli, H.C. Poon, D.K. Saldin and A. Wander (giotto.phys.uwm.edu) – this code also models Auger electron diffraction;
- 'Fritzsche' (as we will call this code, since it does not appear to have an established name) by V. Fritzsche;
- MSCD by Y. Chen, M.A. Van Hove, C.S. Fadley, F. Bondino and R. Díez Muiño (http://electron.lbl.gov/mscdpack/mscdpack.html);
- EDAC by F.J. García de Abajo, M.A. Van Hove and C.S. Fadley (http://electron.lbl.gov/edac, http://csic.sw.ehu.es/edac);

- ZBE110 by J.-V. Peetz and W. Schattke
  (http://www.theo-physik.uni- kiel.de/theo-physik/schattke/);
- KSAP by T. Strasser, C.-H. Solterbeck, J. Henk, A. Bödicker and W. Schattke
  (http://www.theo-physik.uni-kiel.de/theo-physik/schattke/);
- ISOLDA by E.E. Krasovskii, F. Starrost, O. Tiedje and W. Schattke
  (http://www.theo-physik.uni-kiel.de/theo-physik/schattke/).

The codes can be distinguished according to their basic geometric approach: atomic clusters of various shapes and sizes vs. two-dimensionally periodic surfaces of variable depth. As with electronic structure calculations at surfaces, the relative advantages and disadvantages of these two fundamental choices have been hotly debated. For core-level emission, in which a single atom emits waves of spherical character (since other atoms emit incoherently), the cluster approach is intuitive: it is used by MSPHD, SPEC, Fritzsche, MSCD and EDAC. For core- level emission, the periodic-surface model requires thinking in terms of 'inverse LEED states', so that plane waves become prominent and LEED-like layer-by-layer methods become applicable, as used in PRAPD, ZBE110 and KSAP.

Very few photoelectron diffraction codes can now handle valence-level emission; exceptions are KSAP and ISOLDA. With valence levels, the initial state is a molecular or band state that extends over several atoms or an infinite number of atoms. Photoemission from such a state can be viewed as the coherent superposition of atomic-like emissions, and this can be done within either a cluster model or a periodic-surface model; the latter has clear advantages for dealing with infinitely extended valence bands and resembles the current highly-developed bandstructure codes. As the photoemission final states are not accessible by these bandstructure codes, an independent confirmation through VLEED or TCS in this energy domain deserves interest. Such information is supported by calculations via codes such as ZBE110 because of their full-potential capability.

The different codes generally can model the various standard modes of data collection: polar and azimuthal scans, hemispherical scans, energy-dependent scans, and combinations of these. Most codes also accept both linear-polarized and unpolarized light, while a few allow circular and elliptical polarization of the incident light (MSCD, EDAC).

However, very few codes consider the effect that the surface has on the incident radiation itself: its refraction, change of polarization, attenuation, etc. KSAP is an exception, since it includes these effects via the input.

The photoexcitation is normally treated in the Golden Rule approximation, assuming the dipole and sudden approximations (MSPHD uses the $Z + 1$ approximation). With EDAC and KSAP, non-dipole effects can be included through an input file.

Relativistic and magnetic effects are usually only allowed to the extent that the electron scattering phase shifts that are input from an external source include relativistic effects. EDAC explicitly includes both relativistic and magnetic effects through spin-dependent phase shifts and scattering amplitudes, yielding for instance spin polarization. Furthermore, this code is fully automated, and in particular, scattering phase shifts and excitation matrix elements are calculated internally without the need for further input.

Many schemes for treating photoemission either by multiple scattering or by direct solution of the Schrödinger equation have been programmed: each code seems to use a different

formulation. However, it is accepted that all these schemes can converge to the same correct result if brought to full convergence, even though there are cases of divergence. Since in practice each scheme is truncated due to limits on computer size and especially computing time, some small differences in results are inevitable.

Inelastic effects (energy losses of the emitted electrons) are accounted for by one of two schemes: complex phase shifts that include the loss process in the atomic scattering (MSPHD, SPEC); or attenuation of the waves propagating from atom to atom with elastic atomic scattering (all other codes). Attenuation can be described either as a mean free path or as an imaginary component of the constant potential outside the atoms. In the direct solution of the Schrödinger equation a complex optical potential is applied throughout space.

The effect of vibrations is mostly modeled through an uncorrelated Debye-Waller factor acting at each scattering in a multiple-scattering path. Some codes neglect the effect altogether (MSPHD, KSAP); others include a correlated Debye-Waller factor (MSCD) which takes into account that the vibrations of nearby atoms are partly correlated, so that the apparent vibrations are less strong as seen by an electron scattering in succession from nearby atoms.

The emitted electron has to pass the potential barrier step between solid and vacuum. This is usually treated only as a refractive effect (with no reflection), but it is neglected in MSPHD: refraction makes an electron change its propagation direction due to its change of momentum perpendicular to the surface. In KSAP and ISOLDA, this effect is included to any desired accuracy, including reflection.

The computational time requirements of the different codes have various scaling laws as a function of the problem size: these scaling laws depend strongly on the particular algorithm used to perform the multiple scattering. The time requirements normally grow significantly with increasing electron energy, and with the number of inequivalent atoms. For instance, PRAPD scales roughly as g^{2N}, where g is the number of plane waves used and N is the number of atomic planes present in the surface slab of finite thickness. MSCD and EDAC scale as N^3 and N^2, respectively, if N is the number of atoms present in the cluster. KSAP and ISOLDA scale as N^3 with N being the number of atoms per surface unit cell of the semi-infinite system.

Most codes are written in Fortran, and are generally run under Unix or Linux. MSCD and EDAC are written in C++, having versions for PC, Mac, Unix and parallel machines (this one only for MSCD).

The degree of availability, documentation and support of the different codes varies widely: one should consult with the respective authors for details. MSPHD is available through Computer Physics Communications. SPEC has short documentation and in-house training. PRAPD is well documented and training is available. One may download MSCD with its extensive documentation. A demo version of EDAC may be interactively run on the web, while its full version is to appear in Computer Physics Communications. KSAP, ISOLDA and ZBE110, with brief comments, are available on the web.

Acknowledgements

Parts of this chapter strongly benefit from cooperation with C.-H. Solterbeck. This work was supported by the Director, Office of Science, Office of Basic Energy Sciences, Division of Materials Sciences and Engineering, of the U.S. Department of Energy under Contract No.

DE-AC03-76SF00098, by the Bundesministerium für Bildung, Wissenschaft, Forschung und Technologie (BBWFT) under contract Nos. 05 5FKTAB 1 and 05 605FKA 1, by the Basque Departamento de Educación, Universidades e Investigación, the University of the Basque Country UPV/EHU (9/UPV 00206.215-13639/2001), and the Spanish Ministerio de Ciencia y Tecnología (MAT2001-0946). RDM acknowledges financial support by the Gipuzkoako Foru Aldundia (Gipuzkoa Fellows Program).

References

[1] B. Ackermann and R. Feder. *Solid State Communications*, 54:1077, 1985.

[2] B. Ackermann and R. Feder. *Journal of Physics C*, 18:1093, 1985.

[3] C.-O. Almbladh. *Physica Scripta*, 32:341, 1985.

[4] O. Anderson. PhD thesis, Christian-Albrechts-Universität zu Kiel, 1986.

[5] G.B. Bachelet, D.M. Ceperley, and M.G.B. Chiocchetti. *Phys. Rev. Lett.*, 62:2088, 1989.

[6] A. Bansil and M. Lindroos. *Phys. Rev. Lett.*, 83:5154, 1999.

[7] J.J. Barton and D.A. Shirley. *Phys. Rev. A*, 32:1019, 1985.

[8] J.J. Barton and D.A. Shirley. *Phys. Rev. B*, 32:1906, 1985.

[9] C.N. Berglund and W.E. Spicer. *Phys. Rev.*, 136:A1030, 1964.

[10] A. Bödicker, A. Leventi-Peetz, and W. Schattke. *J. El. Spectrosc. and Relat. Phenomena*, 78:481, 1996.

[11] A. Bödicker and W. Schattke. *Phys. Rev. B*, 55:5045, 1997.

[12] D. Bohm and D. Pines. *Phys. Rev.*, 92:609, 1953.

[13] S.V. Borisenko, M.S. Golden, S. Legner, T. Pichler, C. Dürr, M. Knupfer, J. Fink, G. Yang, S. Abell, and H. Berger. *Phys. Rev. Lett.*, 84:4453, 2000.

[14] J. Braun, G. Thörner, and G. Borstel. *physica status solidi (b)*, 130:643, 1985.

[15] J. Braun, G. Thörner, and G. Borstel. *physica status solidi (b)*, 144:609, 1987.

[16] S. Brodersen and W. Schattke. *Phys. Rev. B*, 66:153303, 2002.

[17] C. Caroli, D. Lederer-Rozenblatt, B. Roulet, and D. Saint-James. *Phys. Rev. B*, 8:4552, 1973.

[18] Y. Chen, F.J. García de Abajo, A. Chassé, R.X. Ynzunza, A.P. Kaduwela, M.A. Van Hove, and C.S. Fadley. *Phys. Rev. B*, 58:13121, 1998.

[19] Y.-D. Chuang, A.D. Gromko, D.S. Dessau, Y. Aiura, Y. Yamaguchi, K. Oka, A.J. Arko, J. Joyce, H. Eisaki, S.I. Uchida, and Yoichi Ando K. Nakamura. *Phys. Rev. Lett.*, 83:3717, 1999.

[20] R. Claessen, R.O. Anderson, J.W. Allen, C.G. Olson, C. Janowitz, W.P. Ellis, S. Harm, M. Kalning, R. Manzke, and M. Skibowski. *Phys. Rev. Lett.*, 69:808, 1992.

[21] H. Daimon, F. Matsui, and K. Sakamoto. *this volume*.

[22] A. Derevianko, O. Hemmers, S. Oblad, P. Glans, H. Wang, S.B. Whitfield, R. Wehlitz, I.A. Sellin, W.R. Johnson, and D.W. Lindle. *Physical Review Letters*, 84:2116, 2000.

[23] S.S. Dhesi, C.B. Stagarescu, K.E. Smith, D. Doppalapudi, R. Singh, and T.D. Moustakas. *Phys. Rev. B*, 56:10271, 1997.

[24] O. Heinonen E.K.U. Gross, and E. Runge. *Many-Particle Theory*. Adam Hilger, 1991.

[25] F.J. García de Abajo, C.S. Fadley, and M.A. Van Hove. *Phys. Rev. Lett.*, 82:4126, 1999.

[26] F.J. García de Abajo, M.A. Van Hove, and C.S. Fadley. *Phys. Rev. B*, 63:075404, 2001.

[27] C.S. Fadley, Y. Chen, R.E. Couch, H. Daimon, R. Denecke, J.D. Denlinger, H. Galloway, Z. Hussain, A.P. Kaduwela, Y.J. Kim, P.M. Len, J. Liesegang, J. Menchero, J. Morais, J. Palomares, S.D. Ruebush, E. Rotenberg, M.B. Salmeron, R. Scalettar, W. Schattke, R. Singh, S. Thevuthasan, E.D. Tober, M.A. Van Hove, Z. Wang, and R.X. Ynzunza. *Progr. Surf. Sci.*, 54:341, 1997.

[28] C.S. Fadley, See-Hun Yang, Bongjin Simon Mun,and F.J. García de Abajo. *this volume*.

[29] U. Fano. *Phys. Rev.*, 124:1866, 1961.

[30] R. Feder and H. Gollisch. *this volume*.

[31] P.J. Feibelman and D.E. Eastman. *Phys. Rev. B*, 10:4932, 1974.

[32] P.J. Feibelman and D.E. Eastman. *Physical Review B*, 10:4932, 1974.

[33] A.L. Fetter and J.D. Walecka. *Quantum Theory of Many-Particle systems*. McGraw Hill, New York, 1971.

[34] B. Feuerbacher, B. Fitton, and R.F. Willis. *Photoemission and Electronic States Properties of Surfaces*. Wiley, Chichester, 1978.

[35] A. Fleszar and W. Hanke. *Phys. Rev. B*, 62:2466, 2000.

[36] N. Fominykh, J. Berakdar, J. Henk, S. Samarin, A. Morozov, F.U. Hillebrecht, J. Kirschner, and P. Bruno. *this volume*.

[37] A.J. Freeman, R. Asahi, A. Continenza, and R. Wu. *this volume*.

[38] H.M. Fretwell, A. Kaminski, J.C. Campuzano J. Mesot, M.R. Norman, M. Randeria, T. Sato, R. Gatt, T. Takahashi, and K. Kadowaki. *Phys. Rev. Lett.*, 84:4449, 2000.

[39] G.D. Mahan and E.W. Plummer. *Handbook of Surfaces, II: Electronic Structure of Surfaces*. ed. K. Horn and M. Scheffler, Elsevier-North Holland, 1995.

[40] B. Ginatempo, P.J. Durham, and B.I. Gyorffy. *Journal of Physics C*, 17:6483, 1989.

[41] M.L. Goldberger and K.M. Watson. *Collision Theory*. Wiley, New York, 1964.

[42] A. Gonis and W.H. Butler. *Multiple Scattering in Solids*. Springer, New York, 2000.

[43] T. Grandke, L. Ley, and M. Cardona. *Phys. Rev. B*, 18:3847, 1978.

[44] M. Graß, J. Braun, and G. Borstel. *Physical Review B*, 47:15487, 1993.

[45] R. Gunnella, F. Solal, D. Sebilleau, and C.R. Natoli. *Computer Phys. Comm.*, 132:251, 2000.

[46] S.V. Halilov, E. Tamura, H. Gollisch, D. Meinert, and R. Feder:. *Journal of Physics Condensed Matter*, 5:3859, 1993.

[47] R.J. Harder and D.K. Saldin. *this volume*.

[48] S. Harm, R.Dürig, R. Manzke, M. Skibowski, R. Claessen, and J.W. Allen. *J. Electron. Spectrosc. & Relat. Phenom.*, 68:111, 1994.

[49] L. Hedin. *this volume*.

[50] L. Hedin. *J. Phys.: Condens. Matter*, 11:R489, 1999.

[51] L. Hedin. *arXiv:cond-math, 27Sep2001*, page 0109517, 2001.

[52] B.L. Henke. *Phys. Rev. A*, 6:1972, 1972.

[53] B. Hermsmeier, J. Osterwalder, D.J. Friedman, B. Sinkovic, T. Tran, and C.S. Fadley. *Phys. Rev. B*, 42:11895, 1990.

[54] F.U. Hillebrecht, H.B. Rose, T. Kinoshita, Y.U. Idzerda, G. van der Laan, R. Denecke, and L. Levy. *Phys. Rev. Lett.*, 75:2883, 1995.

[55] F.J. Himpsel and K.N. Altmann. *this volume*.

[56] P. Hohenberg and W. Kohn. *Phys. Rev. B*, 136:864, 1964.

[57] J.F.L. Hopkinson, J.B. Pendry, and D.J. Titterington. *Computer Physics Communications*, 19:69, 1980.

[58] M.A. Van Hove and S.Y. Tong. *Surface Crystallography by LEED*. Springer, Heidelberg, 1979.

[59] M.S. Hybertsen and S.G. Louie. *Phys. Rev. B*, 34:5390, 1986.

[60] P. Fulde. *Electron Correlation in Molecules and Solids*. Springer Series in Solid-State Sciences, Vol. 100, 1991.

[61] J.K. Inkson. *The Many-Body Theory of Solids*. Plenum Press, New York, 1984.

[62] J. Mustre de Leon, J.J. Rehr, C.R. Natoli, C.S. Fadley, and J. Osterwalder. *Phys. Rev. B*, 39:5632, 1989.

[63] J.D. Jackson. *Classical Electrodynamics*. Wiley, New York, 1999.

[64] L.P. Kadanoff and G. Baym. *Quantum Statistical Mechanics*. Benjamin, New York, 1962.

[65] E.O. Kane. *Physical Review Letters*, 12:97, 1964.

[66] A. Kay, E. Arenholz, S. Mun, F.J. García de Abajo, C.S. Fadley, R. Denecke, Z. Hussain, and M.A. Van Hove. *Science*, 281:679, 1998.

[67] A. Kay, F.J. García de Abajo, S.-H. Yang, E. Arenholz, S. Mun, N. Mannella, Z. Hussain, M.A. Van Hove, and C.S. Fadley. *Phys. Rev. B*, 63:115119, 2001.

[68] L.V. Keldysh. *J. Exptl. Theoret. Phys.*, 47:1515, 1964.

[69] W. Kohn and L.J. Sham. *Phys. Rev. A*, 140:1133, 1965.

[70] E.E. Krasovskii. *this volume*.

[71] E.E. Krasovskii and W. Schattke. *Phys. Rev. B*, 63:235112, 2001.

[72] E.E. Krasovskii, W. Schattke, V.N. Strocov, and R. Claessen. *Phys. Rev. B*, 66:235403, 2002.

[73] H.J. Levinson and E.W. Plummer. *Phys. Rev. B*, 24:628, 1981.

[74] A. Liebsch. *Phys. Rev. B*, 13:544, 1976.

[75] A. Liebsch. *Theoretical aspects of photoemission in Festkörperprobleme ed. J. Treusch*, volume XIX. Vieweg, Braunschweig, 1979.

[76] A. Liebsch. *Electronic excitations at metal surfaces*. Plenum, New York, 1997.

[77] J. Lindhard. *Dan. Vidensk. Selsk. Mat. Fys. Medd.*, 28:8, 1954.

[78] M. Lindroos, S. Sahrakorpi, and A. Bansil. *Phys. Rev. B*, 65:054514(1), 2002.

[79] S. Lorenz, C.-H. Solterbeck, W. Schattke, J. Burmeister, and W. Hackbusch. *Phys. Rev. B*, 55:R13432, 1997.

[80] G.D. Mahan. *Many Particle Physics*. Plenum, New York, 1981.

[81] S.T. Manson and D. Dill. *Electron Spectroscopy: Theory, Techniques and Applications*. Ed. by C.R. Brundle and A.D. Baker, Academic Press, London, New York, San Francisco, 1978.

[82] G. Margaritondo, D.L. Huber, and C.G. Olson. *Science*, 246:770, 1989.

[83] R.D. Mattuck. *A Guide to Feynman Diagrams in the Many Body Problem*. Dover, 1992.

[84] M. Mehta and C.S. Fadley. *Phys. Lett. A*, 55:59, 1975.

[85] A. Messiah. *Quantum Mechanics*. North-Holland, New York, 1966.

[86] T. Michalke, A. Gerlach, K. Berge, R. Matzdorf, and A. Goldmann. *Phys. Rev. B*, 62:10544, 2000.

[87] C.R. Natoli, M. Benfatto, C. Brouder, M.F. Ruiz López, and D.L. Foulis. *Phys. Rev. B*, 42:1944, 1990.

[88] R. Nozawa. *J. Math. Phys.*, 7:1841, 1966.

[89] J.-V. Peetz, W. Schattke, H. Carstensen, R. Manzke, and M. Skibowski. *Physical Review B*, 46:10127, 1992.

[90] J.B. Pendry. *Low Energy Electron Diffraction*. Academic Press, London, 1974.

[91] J.B. Pendry. *Surf. Sci.*, 57:679, 1976.

[92] J.J. Rehr and R.C. Albers. *Phys. Rev. B*, 41:8139, 1990.

[93] P. Roman. *Advanced Quantum Theory*. Addison-Wesley, Reading, 1965.

[94] K. Roßnagel and L. Kipp. *this volume*.

[95] D. Samuelsen, E. Pehlke, W. Schattke, O. Anderson, R. Manzke, and M. Skibowski. *Phys. Rev. Lett.*, 68:522, 1992.

[96] W.L. Schaich. *Photoemission in Solids I, 105*. ed. M. Cardona, 1978.

[97] W. Schattke. *Progr. Surface Sci.*, 54:211, 1997.

[98] W. Schattke. *Progr. Surface Sci.*, 64:89, 2000.

[99] L.J. Sham and M. Schlüter. *Phys. Rev. Lett.*, 51:1888, 1983.

[100] K. Starke. *Magnetic Dichroism in Core-Level Photoemission*, volume 159. Springer Tracts in Modern Physics, Berlin, 2000.

[101] K. Starke, A.P. Kaduwela, Y. Liu, P.D. Johnson, M.A. Van Hove, C.S. Fadley, V. Chakarian, E.E. Chaban, G. Meigs, and C.T. Chen. *Phys. Rev. B*, 53:R10544, 1996.

[102] P. Strange. *Relativistic Quantum Mechanics*. Cambridge University Press, Cambridge, 1998.

[103] P. Strange, J. Staunton, and B.L. Gyorffy. *J. Phys. C*, 17:3355, 1984.

[104] V.N. Strocov, H. Starnberg, P.O. Nilson, H.E. Brauer, and L.J. Holleboom. *Phys. Rev. Lett.*, 79:467, 1997.

[105] G. Thörner and G. Borstel. *physica status solidi (b)*, 126:617, 1984.

[106] E.D. Tober, F.J. Palomares, R.X. Ynzunza, R. Denecke, J. Morais, Z. Wang, G. Bino, J. Liesegang, Z. Hussain, and C.S. Fadley. *Phys. Rev. Lett.*, 81:2360, 1998.

[107] S.Y. Tong and M.A. Van Hove. *Sol. St. Comm.*, 19:543, 1976.

[108] U. von Barth and L. Hedin. *J. Phys. C*, 5:1629, 1972.

Solid-State Photoemission and Related Methods
Wolfgang Schattke, Michel A. Van Hove (Eds.)

3 General theory of core electron photoemission

Lars Hedin

3.1 Introduction

Core electron photoemission spectroscopy (PES) is a mature and sophisticated subject with important applications in materials research and other areas of science. In a mature subject there are naturally many treatments on different levels. A recent comprehensive treatment of photoelectron spectroscopy in general is given by *Hüfner*. [1] *Inglesfield and Plummer* in a review article concentrated on the basic physics of photoemission. [2] Still relevant is an article by *Almbladh and Hedin*. [3] And there are many other reviews on specialized topics. So why one more review on this large classic subject? Hüfner's book looks at the subject from the viewpoint of an an experimentalist, while in this short chapter we will concentrate on basic theoretical concepts. Our presentation is more in line with the article by Inglesfield and Plummer, but they put the emphasis on valence electron PES, while we here discuss the core electron case. The Almbladh and Hedin work is twenty years old and much has happened since then.

The large literature we have on PES is very fragmented and there is no unified description which accounts for the basic many body physics. In principle the diagram expansion of the three-current correlation function should give us all the answers, but in practice this approach has mainly remained a rather sterile formal framework which has generated little of the simplified approximations which are the essence of physics. It has e.g. given no understanding of incomplete relaxation [4] or the closely related PES resonance phenomena [5, 6], where instead a discussion in terms of states classified by core hole configurations and use of quasi-boson models has given a detailed and practical description. [3] In this review we have avoided the diagram approach. Instead we have tried to derive *general* properties as far as possible, and we have then introduced a model Hamiltonian which maps many of the important general properties and allows us to obtain a number of explicit results. Such an approach presents a possibility to quantify the theory for comparison with experiment. This does not mean that once the physics is understood by a model approach, it could not also be illustrated, reproduced and perhaps extended by using diagrams. We will discuss general concepts like initial and final state properties, adiabatic and sudden, intrinsic and extrinsic, time-scales, shake-up and shake-down, satellites, one-step, three-step, and semi-classical approximations. We will also discuss fundamental physical effects as resonant PES (RESPES), the Mahan-Nozieres-de Dominicis effect (MND effect), multi-atom resonant PES (MARPE), photoelectron-Auger coincidence spectroscopy, and charge transfer processes. We will not take up *mixed valent systems*. This is a very specialized and sophisticated topic, and we instead refer to recent reviews. [7, 8]

Solid-State Photoemission and Related Methods: Theory and Experiment. Edited by Wolfgang Schattke, Michel A. Van Hove

ISBN: 3-527-40334-5

Core electron PES is basically a very simple experiment. A photon of energy ω (we use atomic units where $m = |e| = \hbar = 1$) is absorbed and an electron is ejected from a localized core level. The electron leaves the solid with the momentum $\mathbf{k}$ and energy $\varepsilon_{\mathbf{k}} = \mathbf{k}^2/2$. The direction and energy of the photoelectron is measured, which means that we know $\mathbf{k}$. Also the photoelectron spin as well as the direction and polarization vectors of the absorbed photon can be monitored. If we neglect the effects of the core electron life-time, the maximum kinetic energy the photoelectron can have is obtained when the system is left in its completely relaxed state in the presence of the core hole. The total energy E is conserved

$$E = \omega + E\left(N, 0\right) = \varepsilon_{\mathbf{k}} + E\left(N-1, 0\right). \tag{3.1}$$

The energy $E_c = E\left(N, 0\right) - E\left(N-1, 0\right)$ is called the core electron quasi-particle energy. The photoelectron energy $\varepsilon_{\mathbf{k}}$ is the photon energy ω minus the core electron binding energy $|E_c| = -E_c$, $\varepsilon_{\mathbf{k}} = \omega - |E_c|$. The ejection of the core electron may create excitations in the remaining system, and the photoelectron then, by energy conservation, has correspondingly less energy. Measuring the EDC (electron distribution curve) when the photon energy is fixed and the distribution of photoelectron energies is measured, shows a peak at the core quasi-particle energy and a more or less structured "*satellite*" at lower kinetic energies (higher "binding" energies). The satellite structure typically carries some 20-30 % of the total strength. There are also important cases (*charge-transfer systems*) when the leading peak has smaller strength than the following peak at lower kinetic energy. The leading peak is then sometimes called a *shake-down satellite*.

The loss of energy from the photoelectron to the remaining system may occur in the excitation process (*intrinsic loss*) or when the photoelectron travels through the solid on its way out through the surface to the detector (*extrinsic loss*). The extrinsic losses were first discussed by Berglund and Spicer in their three step model, excitation, transport (with losses) to the surface, and passage (with losses) through the surface. [9] These two loss mechanisms are not possible to separate sharply. This is clear for a small system like an atom or molecule, and also for a solid when the mean free path is short. The two loss *amplitudes*, as best we can define them, have to be added, and we can have interference effects. In a metal the losses can come from low energy electron-hole excitations. Such losses show up as a low energy asymmetry of the quasi-particle line, the perfectly sharp edge position given by E_c. The removal of the core electron also can cause excitations of the phonons. At zero temperature these excitations show up as structure below E_c, but at finite temperatures the phonons can also deliver energy to the photoelectron, giving structure *above* E_c. Due to the core hole lifetime this structure should be convoluted with a Lorentzian. We have here described the physics in terms of energy states, which is always possible and correct.

The final states in PES are identical with the states we have in electron scattering, and like in scattering, it is often useful to think about PES as a process in time. Quantitative results can be obtained by calculating electron scattering states, or by solving the time-dependent Schrödinger equation for the PES process. A time-dependent *semi-classical description* has been useful to calculate losses. The photoelectron is then taken as a classical particle moving on a straight line with constant velocity and the losses are calculated quantum mechanically from the time dependent perturbation of the moving photoelectron and the suddenly created core hole. This semi-classical description is however very dubious at low photoelectron velocities (*adiabatic limit*) since one has to neglect the difference in momentum of the electron

before and after the inelastic event. For photon energies which barely are large enough to take the electron above the Fermi level there is clearly no energy available to make satellites (or line shape asymmetry).

The first and most obvious property to study is the core electron energy E_c. The value of E_c varies depending on the chemical surrounding of the atom that is excited. The development of the instrumentation to measure these chemical shifts accurately enough and its application to "Electron Spectroscopy for Chemical Analysis" (ESCA) was rewarded a Nobel prize 1981 to *K. Siegbahn*. Today the resolution is in the meV range, and e.g. *surface core shifts* as well as the relation between (temperature dependent) *lineshapes* and phonon properties are studied in detail. [10, 11] For such studies often synchrotron radiation is used due to the high resolution, the tunability (e.g. to monitor the escape depth) and the low noise to signal ratio. [12]

To make the discussion more firm we start with some simple basic definitions and elementary derivations. We will mainly consider the zero temperature case, but some results will be extended to finite temperatures. For zero temperature the initial state is the ground state of the system, $|N\rangle$. We take $|N\rangle$ as the fully correlated state of N electrons with the nuclei stationary. The final state has a photoelectron "$\mathbf{k}$", and the state of the remaining $N-1$ electrons is defined as "s". When the photoelectron is about to be picked up by the detector the final state is a product $\phi_{\mathbf{k}}(\mathbf{r}_1)\,\Psi_{N-1,s}(\mathbf{r}_2, \mathbf{r}_3, \ldots, \mathbf{r}_N)$. We however need to know the final state also when the photoelectron is inside the solid, and we use the notation $|N-1, s; \mathbf{k}\rangle$ for a wavefunction where the photoelectron motion is correlated with that of the other electrons. A simple approximation is

$$|N-1, s; \mathbf{k}\rangle = c^\dagger_{\mathbf{k}} |N-1, s\rangle\,, \tag{3.2}$$

where $c^\dagger_{\mathbf{k}}$ is related to a wavefunction with (one-electron) scattering state boundary conditions (time-inverted LEED state, LEED stands for low energy electron diffraction). This approximation means that we neglect the interactions between the photoelectron and the solid left behind, i.e. the inelastic losses. The inelastic losses can never be neglected in a solid, and we will discuss them later in detail. They however mainly show up in the satellite region (more on satellites later) of the spectrum, and much information of interest can be extracted neglecting these losses.

The photo-electron current can be obtained from (many-body) scattering theory. [13] The current is proportional to a Golden Rule type expression, which we call $D(\mathbf{k}, \omega)$, [3]

$$D(\mathbf{k}, \omega) = \sum_s |\langle N-1, s; \mathbf{k}\,|\Delta|\,N\rangle|^2\, \delta(\omega - \varepsilon_{\mathbf{k}} + \varepsilon_s)\,. \tag{3.3}$$

As mentioned earlier $\varepsilon_{\mathbf{k}}$ is the energy of the photo-electron, $\varepsilon_{\mathbf{k}} = \mathbf{k}^2/2$, ε_s gives the energy of the final state of the solid as

$$\varepsilon_s = E(N, 0) - E(N-1, s)\,, \tag{3.4}$$

ω is the photon energy, and Δ the optical transition operator,

$$\Delta = Ap + pA = \sum_{ij} \langle i\,|\Delta|\,j\rangle\, c^\dagger_i c_j. \tag{3.5}$$

Calculation of Δ is a delicate problem since the electromagnetic field varies strongly at the surface, and also with frequency. [14] So far only limited progress has been made. [15] We should note that $\varepsilon_{\mathbf{k}}$ is the energy of a free electron and *not* the quasi-particle energy $E_{\mathbf{k}}$. In valence PES however $E_{\mathbf{k}}$ enters the theory through the conservation rules of the optical dipole matrix element Δ_{ij}. [16]

For non-interacting electrons $|N-1,s;\mathbf{k}\rangle$ and $|N\rangle$ are Slater determinants, and $|N-1,s;\mathbf{k}\rangle = c_{\mathbf{k}}^{\dagger}c_s\,|N\rangle$. Here the index "$s$" stands for an occupied one-electron state (e.g. a core electron state or a state in the valence band). Equation (3.3) reduces to the well-known form

$$D\left(\mathbf{k},\omega\right) = \sum_{s}^{occ} \left|\langle \mathbf{k}\left|\Delta\right|s\rangle\right|^2 \delta\left(\omega - \varepsilon_{\mathbf{k}} + \varepsilon_s\right), \tag{3.6}$$

where ε_s is a one-electron energy. We see that the photocurrent depends on the electron energies in the initial state ε_s as well as on the initial state wavefunctions "s", which appear in the dipole matrixelements $\Delta_{\mathbf{k}s}$. On this level of approximation PES thus maps initial state properties.

To do better than one-electron theory we use the product approximation in Eq. (3.2). If we insert the dipole operator, Eq. (3.5) in Eq. (3.3), and use Eq. (3.2), the matrixelement $\langle N-1,s;\mathbf{k}\left|\Delta\right|N\rangle$ becomes

$$\left\langle N-1,s;\mathbf{k}\middle|\Delta\middle|N\right\rangle \simeq \left\langle N-1,s\middle|c_{\mathbf{k}}\sum_{ij}\langle i\left|\Delta\right|j\rangle\, c_i^{\dagger}c_j\middle|N\right\rangle.$$

If the photo-electron "$\mathbf{k}$" is fast enough, there are no virtual states "$\mathbf{k}$" in $|N\rangle$ to annihilate, and then $c_{\mathbf{k}}$ must match $c_i^{\dagger}$

$$\langle N-1,s;\mathbf{k}\left|\Delta\right|N\rangle \simeq \left\langle N-1,s\middle|\sum_{j}\langle \mathbf{k}\left|\Delta\right|j\rangle\, c_j\middle|N\right\rangle. \tag{3.7}$$

This commonly made approximation, [17], becomes more accurate the higher the photoelectron energy is. For non-interacting systems this matching of course is exact. We now have

$$D\left(\mathbf{k},\omega\right) = \sum_{s}\left|\sum_{j}\langle \mathbf{k}\left|\Delta\right|j\rangle\,\langle N-1,s\left|c_j\right|N\rangle\right|^2 \delta\left(\omega-\varepsilon_{\mathbf{k}}+\varepsilon_s\right). \tag{3.8}$$

This is a very common level of approximation where $D\left(\mathbf{k},\omega\right)$ is given by the so called *one-electron spectral function* $A(\omega)$

$$A_{ij}\left(\omega\right) = \sum_{s}\langle N-1,s\left|c_i\right|N\rangle\left\langle N\left|c_j^{\dagger}\right|N-1,s\right\rangle\delta(\omega-\varepsilon_s),$$

$$D\left(\mathbf{k},\omega\right) = \sum_{ij}\langle \mathbf{k}\left|\Delta\right|j\rangle\, A_{ij}\left(\varepsilon_{\mathbf{k}}-\omega\right)\langle j\left|\Delta\right|\mathbf{k}\rangle.$$

For a core electron spectrum c_j refers to a one-electron core state "b", and

$$\sum_{j}\langle \mathbf{k}\left|\Delta\right|j\rangle\,\langle N-1,s\left|c_j\right|N\rangle = \langle \mathbf{k}\left|\Delta\right|b\rangle\,\langle N-1,s\left|b\right|N\rangle.$$

It is usually quite accurate to approximate $|N\rangle$ by a direct product of valence and core electron parts, $|N\rangle = |N_v, 0\rangle\,|N_c, 0\rangle$. We write $b\,|N\rangle = |N_v, 0\rangle\,|N_c - 1\rangle$, where $|N_c - 1\rangle = b\,|N_c, 0\rangle$. Similarly for $|N-1, s\rangle$ we write $|N-1, s\rangle = \left|\widetilde{N}_v, s\right\rangle |N_c - 1\rangle$. The tilde indicates that the valence electrons are influenced by the core hole potential. Collecting the pieces gives

$$D\left(\mathbf{k}, \omega\right) = \left|\langle \mathbf{k}\,|\Delta|\,b\rangle\right|^2 \sum_s \left|\left\langle \widetilde{N}_v, s|N_v, 0\right\rangle\right|^2 \delta\left(\omega - \varepsilon_{\mathbf{k}} + E_c - \omega_s\right), \tag{3.9}$$

where we have replaced ε_s by $E_c - \omega_s$

$$\varepsilon_s = E\left(N, 0\right) - E\left(N-1, s\right) = E_c - \omega_s.$$

Here $E_c = E\left(N, 0\right) - E\left(N-1, 0\right)$ gives the energy to remove a core electron and leave the system in its lowest possible state, the "completely relaxed state" (the removal energy is actually $-E_c$ since $E_c < 0$). The state $E\left(N-1, 0\right)$ of course is not stationary, it can decay by an Auger or a radiative transition. For many cases of interest this decay is slow, and it is then a good approximation to take $E\left(N-1, 0\right)$ as stationary. We have written E_c rather than ε_c to mark that we have the quasi-particle core electron energy, not the bare one-electron energy ε_c. The quantity ω_s is the excitation energy of the valence electrons moving in presence of the core hole

$$\omega_s = E\left(N-1, s\right) - E\left(N-1, 0\right) = E\left(\widetilde{N}_v, s\right) - E\left(\widetilde{N}_v, 0\right).$$

Equation (3.9) is very basic for core electron PES, and apart from the extrinsic losses and neglect of core-valence exchange, it gives an accurate representation, provided the photoelectron energy is not too small. We have neglected core electron shake-up excitations. They do not have a negligible amplitude, but they occur at energies outside the primary region of interest.

A common mode of PES measurement is to take the electron distribution curve (EDC), which corresponds to take $D\left(\mathbf{k}, \omega\right)$ as function of $\varepsilon_{\mathbf{k}}$ for fixed ω and fixed direction of $\mathbf{k}$. The maximum possible value of $\varepsilon_{\mathbf{k}}$ is $\omega + E_c = \omega - |E_c|$ since $\omega_s \geq 0$. The satellite curve is sharply cut at $\varepsilon_{\mathbf{k}} = 0$ since the photoelectron must have a positive energy, which means at an energy $\omega - |E_c|$ below the quasi-particle peak. Equation (3.9) gives the same EDC's for all ω values apart from the modulation by the matrix element $\left|\langle \mathbf{k}\,|\Delta|\,b\rangle\right|^2$ and apart from being cut at $\varepsilon_{\mathbf{k}} = 0$. This peculiar behavior signals that we cannot trust Eq. (3.9) for small $\varepsilon_{\mathbf{k}}$.

There are some consequences of Eq. (3.9) which can be discussed without any deeper analysis. First without core-hole potential we would have $\left\langle \widetilde{N}_v, s|N_v, 0\right\rangle = \langle N_v, s|N_v, 0\rangle = \delta_{s,0}$. Since ω_0 by definition is zero we see from the deltafunction in Eq. (3.9) that this means we have one sharp deltafunction peak at $\omega = \varepsilon_{\mathbf{k}} - E_c$. In reality we have an overlap matrix between states belonging to different Hamiltonians (with and without core hole potential) and we get a function $D\left(\mathbf{k}, \omega\right)$ which gives an EDC satellite down to $\varepsilon_{\mathbf{k}} = 0$ since the system has arbitrary large excitation energies ω_s. The function $D\left(\mathbf{k}, \omega\right)$ starts with, we expect, some *quasi-particle peak* as a relict of the deltafunction. In metals this peak has the famous power law behavior, $(\varepsilon_{\mathbf{k}}^{\max} - \varepsilon_{\mathbf{k}})^{-\alpha}$, where α is the MND (Mahan, Nozieres, de Dominicis, see Ref. [18])singularity index. We should remember that there is no guarantee that the spectrum

actually starts at the maximum possible value $\varepsilon_{\mathbf{k}} = \omega - |E_c|$ since the wavefunction overlap or the dipole matrix element can suppress or even in principle take away the intensity.

The peak is followed by what is called a *satellite structure* or *intrinsic loss structure*. The electron energy loss spectrum (EELS) gives a qualitative idea on the important excitation energies, in metals we e. g. expect a strong plasmon peak. Later we will actually find a close relation between the satellite structure and EELS. A recent review on EELS can be found in Ref. [19]. The *extrinsic losses*, which we so far have neglected, are also closely related to EELS, and experimentally we cannot separate these two contributions to the satellite structure.

We note that the spectrum rather measures final than initial state properties since the main information is the energy -E_c of the core hole state, which comes from the completely relaxed final state. Also the line shape and the satellite give information on final state properties, the distribution of excited states $\left|\widetilde{N}_v, s\right\rangle$ created by the sudden removal of the core electron. For metals the excited states with small energy, those that give the MND line, come from electron-hole and phonon excitations, while the strong plasmon peak comes from the creation of a plasmon.

The *shift in the core electron energy* in a solid as compared to that in a free ion has a simple physical background. The shift has two components. One is the Coulomb potential from the valence electrons in the ground state and the other is half the induced Coulomb potential from the distortion of the valence charge caused by the presence of the core hole. The factor one half is a simple classical effect connected with the adiabatic switch-on of the core hole potential. [20] The core electron energies may differ by say 0.1 eV between bulk and surface. Changes of adsorbate levels between different surface positions can be much larger, say 1 eV. There are many specialized effects which can be studied with core electron PES, but we will make no attempt to list them here.

3.2 Theory

3.2.1 General considerations

The general expression which gives the PES current was stated in Eq. (3.3). Thus besides the (ground) state wavefunction $|N\rangle$ we need the final state function $|N-1, s; \mathbf{k}\rangle$. The final state function is an eigenfunction of the fully interacting Hamiltonian H with the boundary condition that when one of the coordinates, say $\mathbf{r}_1$, becomes large the wavefunction has the form $\phi_{\mathbf{k}}(\mathbf{r}_1)\,\Psi_{N-1,s}(\mathbf{r}_2, \mathbf{r}_3, \ldots, \mathbf{r}_N)$ where $\Psi_{N-1,s}$ is the wavefunction for the residual system and $\phi_{\mathbf{k}}$ a plane wave. Also $\Psi_{N-1,s}$ is an eigenfunction of H. We have suppressed the spin variables. The one-electron wave function $\phi_{\mathbf{k}}(\mathbf{r}_1)$ is a scattering wavefunction with incoming waves boundary condition. For a small system, say an atom or molecule, the incoming waves are spherical waves, for a solid they are plane waves, and for solids one often speaks of "time-reversed LEED states".

For a small system we can make the usual configuration interaction (CI) expansion here called the *close coupling* approach (A is the anti-symmetry operator)

$$|N-1, s; \mathbf{k}\rangle = A \sum_n F_n(\mathbf{r}_1)\,\Psi_{N-1,n}(\mathbf{r}_2, \mathbf{r}_{3,}, \ldots, \mathbf{r}_N),$$

where all quantities on the right hand side depend on s, the F_n are scattering wavefunctions, and where the $\Psi_{N-1,n}$ are eigenfunctions of H, which in turn have CI expansions. If there is only one term in the sum, we have the sudden approximation; with many terms we have *interchannel interactions*. For small systems the Hulthén-Kohn or the Schwinger variational principles are very useful. [21]

For solids, where we have a continuum of states, CI is usually not practical. We then instead follow Chew and Low [22] and write

$$|N-1,s;\mathbf{k}\rangle = \left[1+\frac{1}{E-H-i\eta}\left(H-E\right)\right] c^\dagger_{\mathbf{k}}\left|N-1,s\right\rangle. \tag{3.10}$$

Here η is a positive infinitesimal, and E as usual the total energy, $E = E\left(N,0\right)+\omega = E\left(N-1,s\right)+\varepsilon_{\mathbf{k}}$. It is easy to check that this expression satisfies the Schrödinger equation, and if the states "$\mathbf{k}$" have the correct boundary conditions, so does $|N-1,s;\mathbf{k}\rangle$. It is interesting that the details of how the states "$\mathbf{k}$" behave inside the solid are arbitrary. If it were possible to write $H = H_0+V$ where $c^\dagger_{\mathbf{k}}\left|N-1,s\right\rangle$ is an eigenfunction of H_0 with eigenvalue E, and where V gave the interaction between the photoelectron and the residual solid, we would have a Lippman-Schwinger expression

$$|N-1,s;\mathbf{k}\rangle = \left[1+\frac{1}{E-H-i\eta}V\right] c^\dagger_{\mathbf{k}}\left|N-1,s\right\rangle. \tag{3.11}$$

Unfortunately this is not possible in general since the photoelectron and the electrons in the residual system are identical particles. In the high energy limit we can however identify a coupling potential V. To do this we follow Chew and Low and write Eq. (3.10) as

$$|N-1,s;\mathbf{k}\rangle = c^\dagger_{\mathbf{k}}\left|N-1,s\right\rangle + \frac{1}{E-H-i\eta}V_{CL}\left|N-1,s\right\rangle,$$

where

$$V_{CL} = \left[H,c^\dagger_{\mathbf{k}}\right] - \varepsilon_{\mathbf{k}}c^\dagger_{\mathbf{k}}.$$

We now use the freedom in the choice of the states "$\mathbf{k}$" to take them to diagonalize the Hartree-Fock like Hamiltonian

$$\left\langle \mathbf{k}_1\left|-\nabla^2/2+V_{nucl}\right|\mathbf{k}\right\rangle + \sum_{\mathbf{k}_2\mathbf{k}_3}\left\langle \mathbf{k}_1\mathbf{k}_2\left|\left|v\right|\right|\mathbf{k}\mathbf{k}_3\right\rangle \left\langle N-1,s\left|c^\dagger_{\mathbf{k}_2}c_{\mathbf{k}_3}\right|N-1,s\right\rangle,$$

which gives

$$V_{CL} = \sum_{\mathbf{k}_1\mathbf{k}_2\mathbf{k}_3} c^\dagger_{\mathbf{k}_1}\left\langle \mathbf{k}_1\mathbf{k}_2\left|\left|v\right|\right|\mathbf{k}\mathbf{k}_3\right\rangle \left(\frac{1}{2}\,c^\dagger_{\mathbf{k}_2}c_{\mathbf{k}_3} - \left\langle N-1,s\left|c^\dagger_{\mathbf{k}_2}c_{\mathbf{k}_3}\right|N-1,s\right\rangle\right),$$

where $\left\langle \mathbf{k}_1\mathbf{k}_2\left|\left|v\right|\right|\mathbf{k}\mathbf{k}_3\right\rangle$ is an anti-symmetrized Coulomb matrix element. "Hartree-Fock like" means that the Coulomb potential is precisely the correct Coulomb potential from the true charge density. Also the "exchange" term differs slightly from HF, however this change tends

to zero at high energy. So far the results are still general. We now take the high energy limit and can then obtain the V in Eq. (3.11) [23] as

$$V = \sum_{\mathbf{k}_1\mathbf{k}_2}^{\text{fast}} \sum_{\mathbf{l}_1\mathbf{l}_2}^{\text{slow}} c^\dagger_{\mathbf{k}_1} c_{\mathbf{k}_2} \left\langle \mathbf{k}_1\mathbf{l}_1 \left| v \right| \mathbf{k}_2\mathbf{l}_2 \right\rangle \left[c^\dagger_{\mathbf{l}_1} c_{\mathbf{l}_2} - \left\langle N-1, s \left| c^\dagger_{\mathbf{l}_1} c_{\mathbf{l}_2} \right| N-1, s \right\rangle \right]. \quad (3.12)$$

Here "fast" means fast electrons with energies of the same order as that of the photoelectron, and "slow" means electrons with velocities comparable to those of the valence electrons. At high energies we thus, as expected, can *treat the photoelectron as a distinguishable particle interacting with the density fluctuations of the residual system.* This result is true for all systems, also strongly interacting ones. The expression we need for PES now is

$$D\left(\mathbf{k},\omega\right) = \sum_s \left|\tau_s\left(\mathbf{k},\omega\right)\right|^2 \delta\left(\omega - \varepsilon_{\mathbf{k}} + \varepsilon_s\right),$$

$$\tau_s\left(\mathbf{k},\omega\right) = \left\langle N-1, s \left| c_k \left(1 + V \frac{1}{E - H + i\eta}\right) \Delta \right| N \right\rangle. \quad (3.13)$$

3.2.2 A model Hamiltonian with a priori determined parameters

A practical way to handle the PES problem [24] is to work with a model Hamiltonian $H = H_0 + V$, where

$$H_0 = \sum_{\mathbf{k}} \varepsilon_{\mathbf{k}} c^\dagger_{\mathbf{k}} c_{\mathbf{k}} + \sum_s \omega_s a^\dagger_s a_s, \qquad V = \sum_{s\,\mathbf{k}\mathbf{k}'} V^s_{\mathbf{k}\mathbf{k}'} \left(a_s + a^\dagger_s\right) c^\dagger_{\mathbf{k}} c_{\mathbf{k}'}. \quad (3.14)$$

This model Hamiltonian sums up a large amount of detailed properties. For energies $\varepsilon_{\mathbf{k}}$ below the vacuum level the index $\mathbf{k}$ stands for electrons in a crystal with a surface, while above the vacuum level it stands for time inversed LEED states. The index $\mathbf{k}$ stands for both crystal momentum and bandindex (below the vacuum level), as well as spin index. When $\mathbf{k}$ stands for a core level it is more appropriate to give it another name since the core level band width is usually negligible. The crystal potential is the Hartree-Fock (HF) one. The energies $\varepsilon_{\mathbf{k}}$ are free electron energies above the vacuum level, and HF energies below. The label "s" stands for excited states of the residual system with excitation energies ω_s like electron-hole pairs and plasmons, and the coupling coefficients $V^s_{\mathbf{k}\mathbf{k}'}$ are closely connected with the spectral resolution of the dielectric response function, in fact they are precisely charge fluctuation potentials. [25] To lowest non-trivial order the coefficients $V^s_{\mathbf{k}\mathbf{k}'}$ appear in a quadratic expression and can then be replaced by the imaginary part of the dynamic screened potential for a system with a surface, $\operatorname{Im} W\left(\mathbf{r},\mathbf{r}';\omega\right)$. When V is taken into account to second order the energies $\varepsilon_{\mathbf{k}}$ are renormalized to quasi-particle energies $E_{\mathbf{k}}$ to the level of the GW approximation. [25] Above the vacuumlevel V gives the photoelectron-residual system coupling in Eq. (3.12), (3.14) which is understandable if we recall that the $V^s_{\mathbf{k}\mathbf{k}'}$ are matrixelements of the density fluctuation operators. (compare a detailed discussion in Ref. [24]). A somewhat related approach, but based on the Bohm-Pines theory, was used by Penn to discuss losses in PES. [26, 27] $\operatorname{Im} W\left(\mathbf{r},\mathbf{r}';\omega\right)$ is directly connected with the electron energy loss function EELS. [19] Examples of fluctuation potentials $V^s\left(\mathbf{r}\right)$ for a jellium model are given in Fig. 3.1.

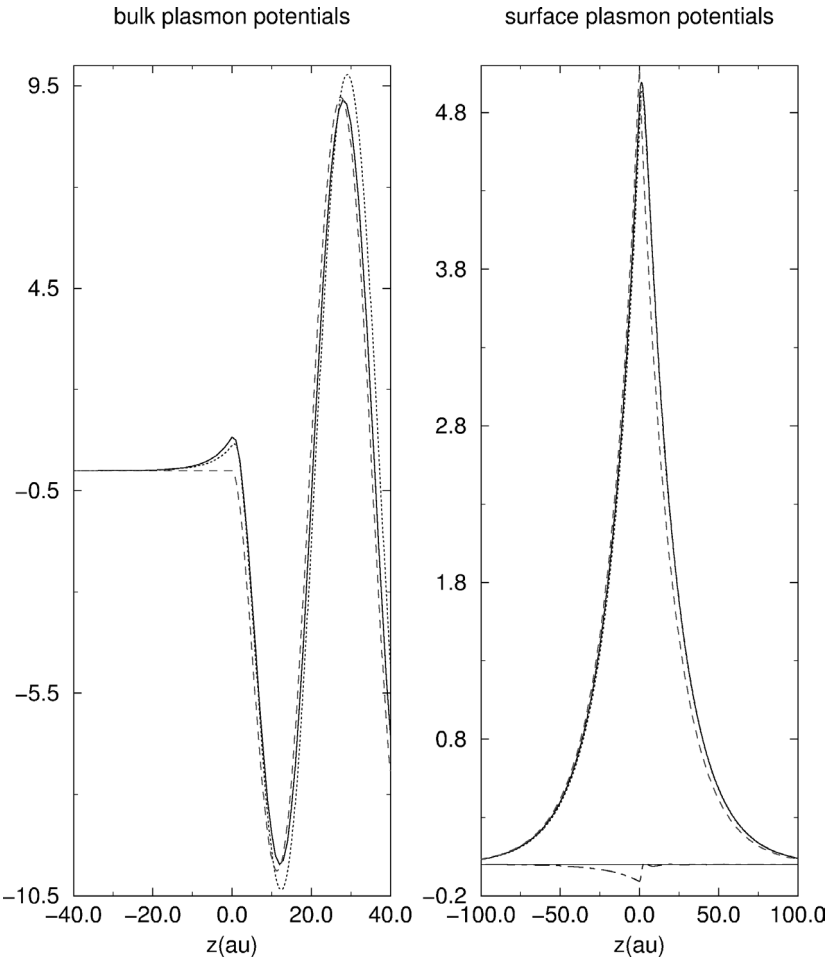

Figure 3.1: Bulk and surface plasmon potentials in a jellium model for parallel momentum Q=0.2 au (bulk) and Q=0.05 au (surface) according to Bechstedt (solid line), Inglesfield (dashed line), and RPA (dotted line) dielectric functions. The dot-dashed curve gives the imaginary part of the potential in the RPA case. [23]

How good is such a model Hamiltonian? The GW approximation has been very useful in improving LDA calculations for not too strongly correlated systems. It however only takes into account the coupling to charge density fluctuations. Also coupling to spin fluctuations are often important, maybe even for s and p electron systems. Further the short range strong correlations in d and f electron systems described by Anderson and Hubbard model Hamiltonians are missing. Here dynamic mean field theory (DMFT) [28] may be an important step forward beyond the simplified model Hamiltonians to include local strong correlations. There are also interesting attempts to combine GW with DMFT which would allow the basic band structure background and thus the chemistry to enter.

And how low in energy can the photoelectron-residual system coupling of Eq. (3.12) be trusted? There are unfortunately no estimates on this. Explicit calculations with quite crude approximations on sp-systems [23, 29, 30] give plausible results. The quantum mechanical results agree well with the semiclassical ones at higher energies, say above 100 eV, which is an indication that both may be correct. A stronger argument for the photoelectron-residual system coupling to be useful is the fact that it is of precisely the same form as the coupling successfully used in the GW approximation for bandstructure calculations, and there is nothing that precludes that it may work right down to the Fermi level.

We now can simplify Eq. (3.13). We expand $V\left(E-H+i\eta\right)^{-1}$ in Eq. (3.13) in powers of V

$$V\left(E-H_0+i\eta\right)^{-1}+V\left(E-H_0+i\eta\right)^{-1}V\left(E-H_0+i\eta\right)^{-1}+\cdots$$

Since V is bilinear in the operators $c_{\mathbf{k}}$ and $|N\rangle$ is a state which only has excitations "s" we can use basisfunctions of the form $|N-1,s\rangle\,|\mathbf{k}\rangle$ with only one photoelectron. The expression for $\tau_s\left(\mathbf{k},\omega\right)$ becomes

$$\tau_s\left(\mathbf{k},\omega\right)=\sum_{\mathbf{l}}\left\langle\mathbf{k}\right|\left\langle N-1,s\right|\left(1+V\frac{1}{E-H+i\eta}\right)c_{\mathbf{l}}\left|N\right\rangle\Delta\left|\mathbf{l}\right\rangle. \tag{3.15}$$

The transition amplitude $\tau_s\left(\mathbf{k},\omega\right)$ now has the form of a one-electron expression

$$\tau_s\left(\mathbf{k},\omega\right)=\sum_{\mathbf{l}}\left\langle\mathbf{k}\right|T_{\mathbf{l}}^s\left(\omega\right)\Delta\left|\mathbf{l}\right\rangle,$$

where

$$T_{\mathbf{l}}^s\left(\omega\right)=\left\langle N-1,s\right|\left(1+V\frac{1}{E-H+i\eta}\right)c_{\mathbf{l}}\left|N\right\rangle=\sum_{\mathbf{k}_1\mathbf{k}_2}T_{\mathbf{l}}^s\left(\mathbf{k}_1\mathbf{k}_2;\omega\right)c_{\mathbf{k}_1}^{\dagger}c_{\mathbf{k}_2}.$$

We can make a partial summation in V keeping only terms where two scatterings bring us back to $|N-1,s\rangle$. These "on-shell" terms renormalize $|\mathbf{k}\rangle$ to a "damped" state $\left|\widetilde{\mathbf{k}}\right\rangle$,

$$\left\langle\widetilde{\mathbf{k}}\right|=\left\langle\mathbf{k}\right|\left(\frac{i\eta}{\varepsilon_{\mathbf{k}}-h^{HF}-\Sigma^p+i\eta}\right),$$

which is an eigenfunction of the GW Hamiltonian $\varepsilon_k-h^{HF}-\Sigma^p$, where Σ^p is the dynamic (polarization) part in Σ_{GW}. [23, 30]. The renormalized functions have decaying tails inside the solid since $\mathrm{Im}\,\Sigma^p$ is non-zero. This is a crucial feature for having a realistic theory where the photocurrent is proportional to the surface area and not to the volume. The terms in $V\left(E-H+i\eta\right)^{-1}$ which have disappeared by the renormalization process, result in replacing V by a projection QVQ, where $Q=1-|N-1,s\rangle\,\langle N-1,s|$. As already discussed by van Hove [31], a finite number of extended excitations "s" does not have any effect on expectation values like the Hartree potential or the self-energy (see also Refs. [25, 32]). We hence can omit the Q projections in the expression for T^s and have

$$\tau_s\left(\mathbf{k},\omega\right)=\sum_{\mathbf{l}}\left\langle\widetilde{\mathbf{k}}\right|T_{\mathbf{l}}^s\left(\omega\right)\Delta\left|\mathbf{l}\right\rangle. \tag{3.16}$$

That we should have a renormalized state $\left|\widetilde{\mathbf{k}}\right\rangle$ is intuitively very clear. For one-electron PES for solids it was demonstrated by Adawi [33] that the final state is a time-inversed scattering state, and from Bell and Squires [34] we know that the potential entering elastic electron scattering from a many-body system is exactly the one-electron self-energy. How $\left|\widetilde{\mathbf{k}}\right\rangle$ enters an expression including inelastic scattering as in Eq. (3.16) is however not trivial to demonstrate. Equation (3.16) is easy to understand. The optical operator takes an electron from the occupied one-electron state $\mathbf{l}$ and then $T_{\mathbf{l}}^{s}(\omega)$ propagates it to its final photo electron state $\widetilde{\mathbf{k}}$. As usual in many-body theory the difficult correlation problems are transferred to an effective one-body operator, here $T_{\mathbf{l}}^{s}(\omega)$. The full expression for $D(\mathbf{k},\omega)$ becomes

$$D(\mathbf{k},\omega)=\sum_{s\mathbf{l}}\left|\tau_{s\mathbf{l}}(\mathbf{k},\omega)\right|^{2}\delta\left(\omega-\varepsilon_{\mathbf{k}}+E_{\mathbf{l}}-\omega_{s}\right).$$

Here we have specified the excited final states by the index $\mathbf{l}$ for the (non-decaying) quasi-particle state (the hole created by the photon), and s for the excitation state of the quasi-boson system,

$$\begin{aligned}
\varepsilon_{s\mathbf{l}} &= E(N,0)-E(N-1,s,\mathbf{l})=E_{\mathbf{l}}-\omega_{s},\\
E_{\mathbf{l}} &= E(N,0)-E(N-1,0,\mathbf{l}),\\
\omega_{s} &= E(N-1,s,\mathbf{l})-E(N-1,0,\mathbf{l})=\sum_{q}n_{q}^{s}\omega_{q}.
\end{aligned}$$

Here the n_q^s are the occupation numbers for the different quasi-boson states q.

We have here chosen to discuss PES from a basically very simple approach without involving any advanced techniques. The early pioneering papers by Caroli *et al.* [35] and by Feibelman and Eastman [36] used three-current correlation function which can be systematically expanded in Keldysh path ordered diagrams. The qualitative physical insight that can be obtained from the three current approach however also comes from the present elementary description, which in addition gives a practical way to obtain quantitative results. The diagram technique is as usual plagued with the difficulty what diagrams to sum and the inflexibility in the choice of basis functions. Thus e.g. the problem of bringing in $\left|\widetilde{\mathbf{k}}\right\rangle$ was not solved until the thorough and careful analysis by Almbladh 1985. [37] The Keldysh technique has recently been applied to the photoelectron diffraction problem by Fujikawa and Arai. [38]

3.2.3 Extrinsic and intrinsic losses in core electron photoemission

In core electron PES the electron is ejected from a specific core level, let's call it "b". The amplitude in Eq. (3.16) becomes

$$\tau_{s}(\mathbf{k},\omega)=\left\langle\widetilde{\mathbf{k}}\right|\left\langle N-1,s\right|\left(1+V\frac{1}{E-H+i\eta}\right)b\left|N\right\rangle\Delta\left|b\right\rangle. \tag{3.17}$$

We neglect the complications of spin and orbital degeneracy of the core level. We also take $|N\rangle$ and $|N-1,s\rangle$ as products of core and valence electron parts,

$$|N\rangle=|N_{c}\rangle\,|N_{v}^{\circ}\rangle\,,\ |N-1,s\rangle=b\,|N_{c}\rangle\,\left|\widetilde{N}_{v}^{s}\right\rangle.$$

We have put a tilde on the final state wavefunction $\left|\widetilde{N}_v^s\right\rangle$ to remember that the valence electrons move in the presence of the potential from the core hole. The core part $b\left|N_c\right\rangle$ can be taken out, and the amplitude becomes

$$\tau_s\left(\mathbf{k},\omega\right)=\left\langle\widetilde{\mathbf{k}}\right|\left\langle\widetilde{N}_v^s\right|\left(1+V\frac{1}{E-h-H_v-V-V_c+i\eta}\right)\left|N_v^0\right\rangle\Delta\left|b\right\rangle,$$

where we have used the Hamiltonian,

$$H=h+H_v+V+V_cbb^\dagger+\varepsilon_c^0b^\dagger b,$$

which is the same as in the well-known "Langreth" model [3], except that we have split off the photoelectron part h and the interaction V between the photoelectron and the valence electrons. We now can write the full amplitude as a sum of intrinsic and extrinsic amplitudes

$$\tau_s\left(\mathbf{k},\omega\right)=\tau_s^{\text{intr}}\left(\mathbf{k},\omega\right)+\tau_s^{\text{extr}}\left(\mathbf{k},\omega\right), \tag{3.18}$$

where,

$$\tau_s^{\text{intr}}\left(\mathbf{k},\omega\right)=\left\langle\widetilde{N}_v^s\;\middle|\;N_v^0\right\rangle\left\langle\widetilde{\mathbf{k}}\right|\Delta\left|b\right\rangle$$

$$\tau_s^{\text{extr}}\left(\mathbf{k},\omega\right)=\left\langle\widetilde{\mathbf{k}}\right|\left\langle\widetilde{N}_v^s\right|V\frac{1}{E-h-H_v-V-V_c+i\eta}\left|N_v^0\right\rangle\Delta\left|b\right\rangle,$$

and the photocurrent expression becomes

$$D\left(\mathbf{k},\omega\right)=\sum_s\left|\tau_s\left(\mathbf{k},\omega\right)\right|^2\delta\left(\omega-\varepsilon_{\mathbf{k}}+\varepsilon_s\right),$$

$$\varepsilon_s=E\left(N,0\right)-E\left(N-1,s\right)=E_c-\sum_q n_q^s\omega_q.$$

We remind that $E_c=E\left(N,0\right)-E\left(N-1,0\right)$ is the core electron quasi-particle energy. The excited states "s" are specified by the occupation numbers n_q^s of the different quasi-bosons labeled q,

$$E\left(N-1,s\right)-E\left(N-1,0\right)=\sum_q n_q^s\omega_q,$$

since only the valence electrons and not the ion core are allowed to be excited (c.f. Eq. (3.14)). The intrinsic amplitude has a no-loss part ($s=0\rightarrow n_q^0=0$). If we separate off the no-loss part we have[1]

$$D\left(\mathbf{k},\omega+\varepsilon_{\mathbf{k}}-E_c\right)$$
$$=\left|\left\langle\widetilde{N}_v^0\;\middle|\;N_v^0\right\rangle\right|^2\left|\left\langle\widetilde{\mathbf{k}}\right|\Delta\left|b\right\rangle\right|^2\delta\left(\omega\right)+\sum_{s\neq0}\left|\tau_s\left(\mathbf{k},\omega\right)\right|^2\delta\left(\omega-\sum_q n_q^s\omega_q\right).$$

[1] Up to the end of this subsection energy ω in $\tau_s(\mathbf{k},\omega)$ refers to $\omega+\varepsilon_{\mathbf{k}}-E_c$ with ω fixed by the δ-function. (eds.)

The ground state-ground state overlap $\left|\langle \widetilde{N}_v^0 | N_v^0 \rangle\right|^2$ in an insulator is typically 0.7–0.8. In an insulator the smallest ω_q is finite while it is zero in a metal (the small ω_q then correspond to electron-hole excitations). Thus in a metal we have no split-off deltafunction, and the delta function is replaced by the MND singular line. [18] We note that the dipole matrix elements involve damped photoelectron functions, $\langle \widetilde{\mathbf{k}} | \Delta | b \rangle$, and thus the photocurrent becomes proportional to the surface area and not to the volume of the crystal as in Eq. (3.6).

Comparing with Eq. (3.14) we have,

$$H_v = \sum_q \omega_q a_q^\dagger a_q, \quad V = \sum_q V^q \left(a_q + a_q^\dagger\right), \quad V^q = \sum_{\mathbf{k}\mathbf{k}'} V_{\mathbf{k}\mathbf{k}'}^q c_{\mathbf{k}}^\dagger c_{\mathbf{k}'}$$

$$h = \sum_{\mathbf{k}} \varepsilon_{\mathbf{k}} c_{\mathbf{k}}^\dagger c_{\mathbf{k}}, \quad V_c = -\sum_q V_{\mathbf{cc}}^q \left(a_q + a_q^\dagger\right).$$

To evaluate Eq. (3.18) we note that $\left|N_v^0\right\rangle$ is an eigenfunction of H_v, while $\left|\widetilde{N}_v^s\right\rangle$ is an eigenfunction of $\widetilde{H}_v \equiv H_v + V_c$. Since we have two harmonic oscillator Hamiltonians there is a simple relation between their eigenfunctions. The relation between the two ground states is

$$\left|N_v^0\right\rangle = e^{-a/2} \exp\left(-\sum_q \frac{V_{\mathbf{cc}}^q}{\omega_q} a_q^\dagger\right) \left|\widetilde{N}_v^0\right\rangle, \qquad a = \sum_q \left(\frac{V_{\mathbf{cc}}^q}{\omega_q}\right)^2.$$

To lowest order in the coupling coefficients V^q we only have excited states "s" with one quasiboson "q", $n_{q'}^s = \delta_{q,q'}$. [23] For simplicity we call these states "q". The transition amplitude becomes,

$$\tau_q(\mathbf{k}, \omega) = e^{-a/2} \left\langle \widetilde{\mathbf{k}} \right| \left(V^q G(\varepsilon_k + \omega_q) - \frac{V_{cc}^q}{\omega_q}\right) \Delta |b\rangle, \tag{3.19}$$

where

$$G(\omega) = \frac{1}{\omega - h - \Sigma^p(\omega)}.$$

Here $G(\omega)$ is the one-electron Green's function, and $\Sigma^p(\omega)$ the polarization part of its self-energy. The real part of Σ^p can be combined with h to an effective one-electron operator h_{eff}, and for the imaginary part of Σ it is reasonable to use (an energy-dependent) constant $-i\Gamma(\omega)$ $(\Gamma > 0)$,

$$G(\omega) = \frac{1}{\omega - h_{eff} + i\Gamma(\omega)}.$$

Equation (3.19) is straight-forward but complicated to calculate. We need the time-inverted LEED state $\left|\widetilde{\mathbf{k}}\right\rangle$ and the Green's function propagator G perhaps best expressed as a multiple scattering expansion as in photoelectron diffraction [39] and EXAFS [40]. We also need the fluctuation potentials V^q. When we take the square of $\tau_q(\mathbf{k}, \omega)$ we have a quadratic expression in the V^q which can be related to the imaginary part of the dynamically screened potential $\operatorname{Im} W(\mathbf{r}, \mathbf{r}'; \omega)$. Futher $\operatorname{Im} W(\mathbf{r}, \mathbf{r}'; \omega)$ has to be calculated in the presence of the

surface since the PES process takes place in a thin region close to the surface. The estimates which have been made so far have used fairly rough approximations. [16, 23, 29, 30, 41].

Equation (3.19) diverges for metals at small ω_q. It is however possible to sum the most divergent terms in the power series expansion for $D(\mathbf{k},\omega)$ and get an exponential expression [23] provided we introduce some approximations. We neglect reflection of the LEED function at the surface which makes the damped wave inside the solid match the outside wave with equal amplitude. The integral $\left\langle \widetilde{\mathbf{k}}\right| \Delta \left|b\right\rangle$ comes from a small region around $\mathbf{r}_c$, the position of the core hole, and we write

$$\left\langle \widetilde{\mathbf{k}}\right| \Delta \left|b\right\rangle = e^{i\widetilde{\mathbf{k}}\mathbf{r}_c} \left\langle \widetilde{\mathbf{k}}\right| \Delta \left|b\right\rangle^0,$$

where the index 0 indicates that the wavefunction $\left|\widetilde{\mathbf{k}}\right\rangle$ is centered at $\mathbf{r}_c$ and normalized in the cell around $\mathbf{r}_c$. The imaginary part in $\widetilde{\mathbf{k}}$ gives the reduction in amplitude of $\left|\widetilde{\mathbf{k}}\right\rangle$ at $\mathbf{r}_c$. We expand the Green's function around $\mathbf{r}_c$, and pick up the factor $\langle \mathbf{k}'| \Delta |b\rangle^0$ where $\mathbf{k}'$ is the wavevector that corresponds to the energy $\varepsilon_k + \omega_q$ in the Green's function. We neglect the difference between $\widetilde{\mathbf{k}}$ and $\mathbf{k}'$ in the two dipole matrix elements. This gives the amplitude

$$\tau_q(\mathbf{k},\omega) = e^{-a/2} e^{i\widetilde{\mathbf{k}}\mathbf{r}_c} \left\langle \widetilde{\mathbf{k}}\right| \Delta \left|b\right\rangle^0 \left[\int \phi^0_{\widetilde{\mathbf{k}}}(\mathbf{r})^* V^q(\mathbf{r}) G(\mathbf{r},\mathbf{r}_c;\mathbf{k}')\, d\mathbf{r} - \frac{V^q_{cc}}{\omega_q} \right],$$

where $\phi^0_{\mathbf{k}}$ is normalized in the cell with $\mathbf{r}_c$. Thus $\phi^0_{\mathbf{k}}$ grows exponentially going from $\mathbf{r}_c$ to the surface, while $G(\mathbf{r},\mathbf{r}_c;\mathbf{k}')$ decays exponentially. The two effects closely cancel when $\widetilde{\mathbf{k}}$ and $\mathbf{k}'$ are close.

In solids with pronounced plasmon structure the cancellation!between intrinsic and extrinsic amplitudes is very large up to energies in the keV region. In Fig. 3.2 we show results for bulk plasmon satellites for $\omega - \omega_{th}$ ranging from 2 to 90 au. "BS" stands for the "Berglund-Spicer" approach [9] where the intrinsic spectrum is convoluted with a loss function, "QM" for "Quantum Mechanical" (the present approach), and "SC" for "Semi-Classical", the approximation where the losses are calculated quantum-mechanically from the perturbation of a classical charge moving on a straight line and a suddenly switched-on core hole potential. Figure 3.3 shows the total intensity of surface and bulk plasmons relative to the elastic peak. The strong peak in the bulk plasmon intensity can be explained from the $\Gamma(\omega)$ curve. $\Gamma(\omega)$ starts to rise strongly, due to plasmon damping, at about $1.1\ au$, and has a maximum at about $2\ au$. When ω is below $2\ au$ the elastic photo-electron thus has a stronger damping than the electrons in the satellite, and the relative satellite intensity is increased. This effect does not come in the SC approximation, where the damping is put in by hand, and is the same for the elastic peak and the satellites.

Summation over the most divergent terms gives

$$D(\mathbf{k},\omega+\varepsilon_{\mathbf{k}}-E_c) \simeq \frac{\left|\left\langle \widetilde{\mathbf{k}}\right| \Delta \left|b\right\rangle^0\right|^2}{2\pi} \int_{-\infty}^{\infty} e^{i\omega t} \exp\left[\sum_q |g_q|^2 \left(e^{-i\omega_q t} - 1\right) \right] dt, \quad (3.20)$$

where

$$g_q = \int \phi^0_{\widetilde{\mathbf{k}}}(\mathbf{r}) V^q(\mathbf{r}) G(\mathbf{r},\mathbf{r}_c;\mathbf{k}')\, d\mathbf{r} - \frac{V^q_{cc}}{\omega_q}.$$

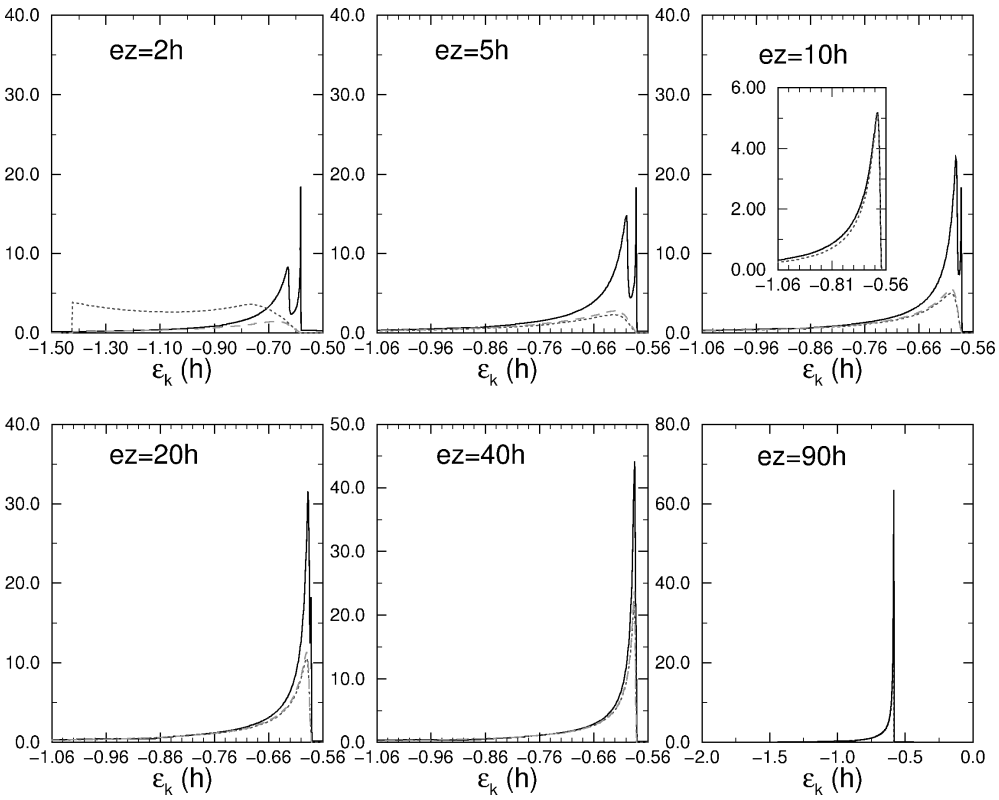

Figure 3.2: Bulk plasmon satellite spectra for various photon energies, and for three different approaches: BS (solid curves), QM (dotted curves), and SC (dashed curves). At 90 au no semi-classical results are shown. For the QM and SC results the Inglesfield's fluctuation potential has been used. The inset shows bulk QM results, with Bechstedt's potential (dotted curve) and with Inglesfield's potential (solid curve). The photo-electron energies are with respect to the elastic peak position. [23]

If we only keep the intrinsic losses Eq. (3.20) precisely reproduces the intrinsic terms. It also gives results which agree with the semiclassical ones for energies above about 100 eV. Detailed discussions are given in [23]. It should be noted that the calculations made so far are only exploratory and based on using plane waves. Also the more general expressions given here should be regarded as sketches on how to proceed. Any future detailed calculations must start from Eq. (3.19) and a more careful analysis of the damped waves and the Green's functions. In Fig. 3.4 we show the near edge structure of the spectrum calculated from Eq. (3.20). It is clear that the intrinsic amplitude completely dominates for small energies close to the edge. This is in contrast to the satellite region, where the intrinsic and extrinsic amplitudes are comparable, and strong interference takes place.

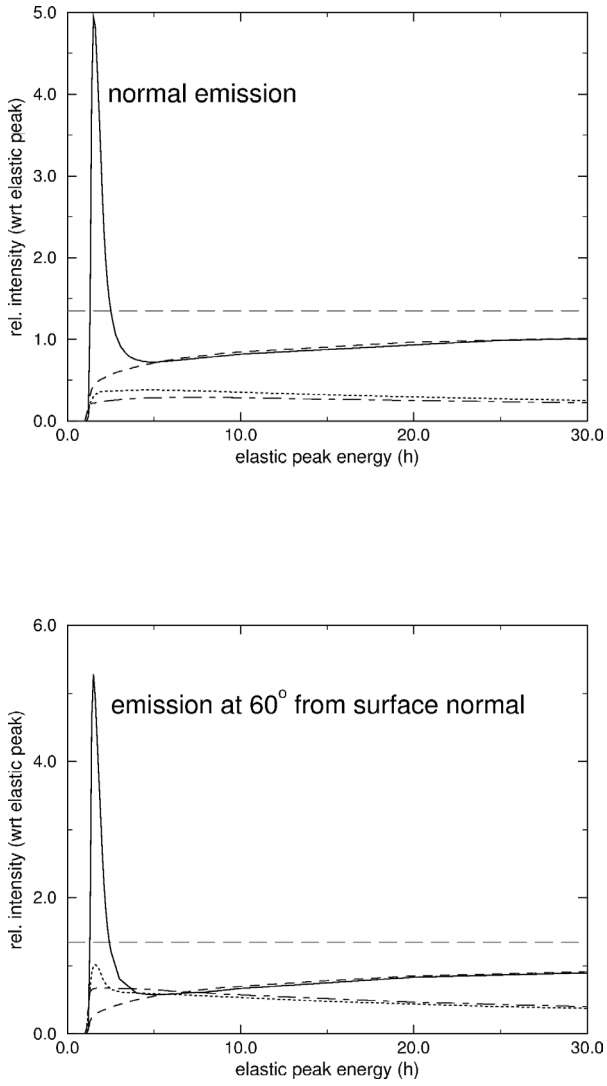

Figure 3.3: Total intensity of bulk and surface plasmon satellites relative to the elastic peak weight, as a function of photon energy. In the top panel the two upper curves give bulk, and the two lower surface plasmons. The QM bulk curve shows a strong peak, while the SC curve is smooth. In the lower panel (emission at 60°), the bulk curves change very little, while the QM surface plasmon curve has a small peak. Bulk modes from Inglesfield's potential, and surface modes from Bechstedt's. [23]

It is convenient to define an "asymmetry function"

$$\frac{\alpha(\omega)}{\omega} = \sum_q |g_q|^2 \, \delta(\omega - \omega_q) \,,$$

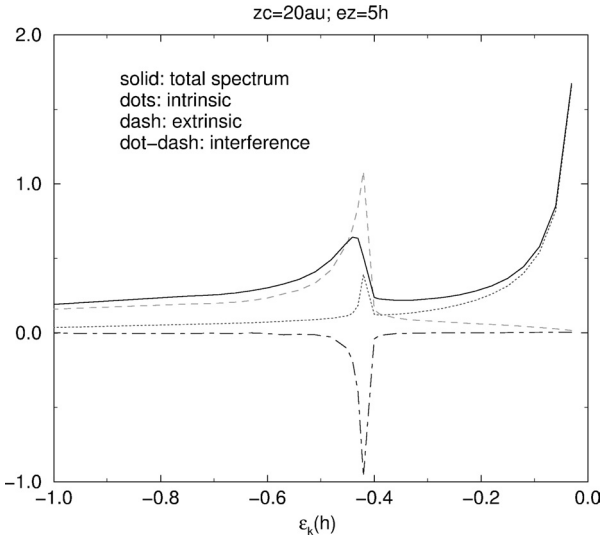

Figure 3.4: RPA result from particle-hole pairs plus surface plasmons for the energy 5au, and a core distance 20 au. Total spectrum – solid line, intrinsic spectrum – dots, extrinsic spectrum – dashed line, and interference contribution – dot-dashed line. [23]

giving

$$D\left(\mathbf{k},\omega+\varepsilon_{\mathbf{k}}-E_c\right) \simeq \frac{\left|\left\langle\widetilde{\mathbf{k}}\right|\Delta\left|b\right\rangle^{0}\right|^2}{2\pi}\int_{-\infty}^{\infty}e^{i\omega t}\exp\left[\int\frac{\alpha\left(\omega'\right)}{\omega'}\left(e^{-i\omega' t}-1\right)d\omega'\right]dt. \quad (3.21)$$

Then $\alpha_0=\alpha\left(0\right)$ gives the asymmetry index for the MND lineshape

$$D\left(\mathbf{k},\omega\right)\backsim\frac{1}{\left(\omega-\omega_{th}\right)^{1-\alpha_0}},\qquad\left(\omega-\omega_{th}\right)\rightarrow 0,$$

where $\omega_{th}=\varepsilon_k-E_c$ is the threshold value for exciting the core electron. There is a close relation between $\alpha\left(\omega\right)$ and the sum over momenta of the EELS function. [41] We now give a qualitative discussion of $D\left(\mathbf{k},\omega\right)$. The index function $\alpha\left(\omega\right)$ for a metal starts at a finite value α_0 and then slowly changes until stronger absorption processes enter. It is often reasonable to split $\alpha\left(\omega\right)$ in a "low energy" flat part and a "high energy" stronger part.

$$\begin{aligned}\alpha\left(\omega\right)&=\alpha_{LE}\left(\omega\right)+\alpha_{HE}\left(\omega\right),\\ \alpha_{LE}\left(\omega\right)&=\alpha_0\theta\left(\omega_0-\omega\right),\\ \alpha_{HE}\left(\omega\right)&=\left[\alpha\left(\omega\right)-\alpha_{LE}\left(\omega\right)\right]\theta\left(\omega-\omega_0\right).\end{aligned}$$

The omitted tail $\alpha(\omega) - \alpha_0$ out to ω_0 has a fairly small influence. [41] Since the two contributions add in an exponent we can write $D(\mathbf{k}, \omega)$ as a convolution,

$$D(\mathbf{k}, \omega) = \left| \left\langle \widetilde{\mathbf{k}} \right| \Delta \left| b \right\rangle^0 \right|^2 \int D_{LE}(\mathbf{k}, \omega - \omega') D_{HE}(\mathbf{k}, \omega') \, d\omega',$$

where both D_{LE} and D_{HE} are defined to be normalized to unity and we have put the origin for ω at $E_c - \varepsilon_{\mathbf{k}}$. For $D_{HE}(\mathbf{k}, \omega')$ we can make a Taylor expansion and keep only the first term,

$$D_{HE}(\mathbf{k}, \omega) = \left| \left\langle \widetilde{\mathbf{k}} \right| \Delta \left| b \right\rangle^0 \right|^2 \exp\left[- \int \frac{\alpha(\omega') \, d\omega'}{\omega'} \right] \left[\delta(\omega) + \frac{\alpha_{HE}(\omega)}{\omega} \right]. \tag{3.22}$$

We have then omitted the multiple quasi-boson excitations starting at $\omega = 2\omega_0$. D_{LE} can be obtained analytically for $\omega < \omega_0$. Broadened with a Lorentzian of width Γ ($FWHM = 2\Gamma$) we have for $\omega < \omega_0$

$$\begin{aligned} D_{LE}(\mathbf{k}, \omega) &= C(\alpha_0) \frac{\cos\left[\pi\alpha_0/2 - (1-\alpha_0)\arctan(\omega/\Gamma)\right]}{\left(1 + (\omega/\Gamma)^2\right)^{(1-\alpha_0)/2}}, \\ C(\alpha_0) &= \frac{e^{-\gamma\alpha_0}}{(\alpha_0 - 1)!\omega_0^{\alpha_0}\Gamma^{1-\alpha_0}\sin[\pi\alpha_0]}. \end{aligned} \tag{3.23}$$

where $\gamma = 0.577$ is the Euler constant. The coefficient $C(\alpha_0)$ in Eq. (3.23) was derived in Ref. [3] (see Eq. (162)). For $\omega > \omega_0$, $D_{LE}(\omega)$ has only a fairly weak tail with less than 10% of the norm (for $\alpha_0 < 0.4$). In the convolution with α_{HE} we take $D_{LE}(\omega)$ as a deltafunction and have

$$D(\mathbf{k}, \omega) \simeq \exp\left[- \int \frac{\alpha(\omega') \, d\omega'}{\omega'} \right] \left[D_{LE}(\mathbf{k}, \omega) + \frac{\alpha_{HE}(\mathbf{k}, z_0; \omega)}{\omega} \right].$$

In the high energy limit

$$\int \frac{\alpha(\omega') \, d\omega'}{\omega'} = \frac{z_0}{\lambda} + a_{HE}, \; a_{HE} = \int \frac{\alpha_{\text{intr}}(\omega') \, d\omega'}{\omega'}$$

where λ essentially is the mean free path. [23]

Al metal is rather special in having a very sharp plasmon peak carrying most of the loss spectral strength (see e.g. Fig. 4.14 in Ref. [1]). To study the effect of the shape of $\alpha(\omega)$, which reflects that of the loss function, we did some comparisons between Al and Cu. In Fig. 3.5 we show $\alpha(\omega)$ for Al at two different photoelectron energies, and compare results from taking only the intrinsic contribution (intr) with the BS and QM cases. Clearly both extrinsic and interference effects are strong also at the higher energy. In Fig. 3.5 we also show the photocurrent as function of the photon energy obtained with the exponential expression, Eq. (3.21) at the two photoelectron energies. The same results for Cu are shown in Fig. 3.6. It is clear that extrinsic and interference effects are just as strong in Cu as in Al. The difference in the loss spectra of the two metals however shows in the shape of the satellites, the Cu satellite

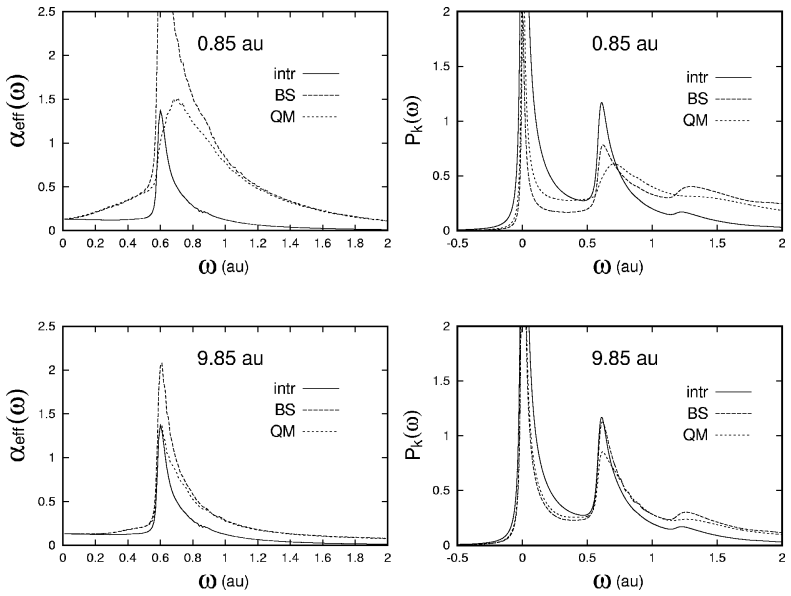

Figure 3.5: Curves of $\alpha(\omega)$ and $D(\mathbf{k},\omega)$ for Al metal with a photoelectron energy of $0.85\ au$ (upper panel) and $9.85\ au$ (lower panel). The $D(\mathbf{k},\omega)$ curves are for given $\mathbf{k}$ values as functions of ω, i. e. they are "constant final state spectra" (CFS).

is featureless as could be expected. The curves mirror well the prediction by Eq. (3.22). In Fig. 3.7 we show both the intrinsic (intr) and the quantum mechanical (QM) results for the quasi-particle peaks for Al and Cu, broadened by a Lorentzian of FWHM $= 600$ meV, and for two photoelectron energies. It is clear that both FWHM and asymmetry in practice are unaffected both by photoelectron energy and by extrinsic losses.

Losses in core electron PES have been discussed in a series of papers by Tougaard and collaborators from somewhat different types of approximations. [42, 43] Core level shifts and the lineshape problems, neglecting extrinsic losses, were recently treated in a review by Andersen and Almbladh. [11]

3.2.4 Charge transfer and shake-down satellites

The effect of the core hole potential on the outer levels can be large and even lead to a change in the level order. A well-known and important case is that of copper dihalides. In the initial state a ligand orbital ϕ_L is occupied while there is an unoccupied copper d-level ϕ_d. The core hole potential has a larger effect on the more localized d-level, and shifts it below the ligand level. The strengths of the main line and the satellite are given by the overlaps $I_M = \left\langle \widetilde{\phi}_d | \phi_L \right\rangle^2$ and $I_S = \left| \left\langle \widetilde{\phi}_L | \phi_L \right\rangle \right|^2$. If there were no change in the orbitals then $I_M = 0$ and $I_S = 1$, i.e. there would be no main line, only a satellite. Due to hybridization the levels mix, and the mixing is different in the initial and final states. The mixing depends on the hybridization coupling and on the position of the energy levels before and after the photoelectron ejection. Often the

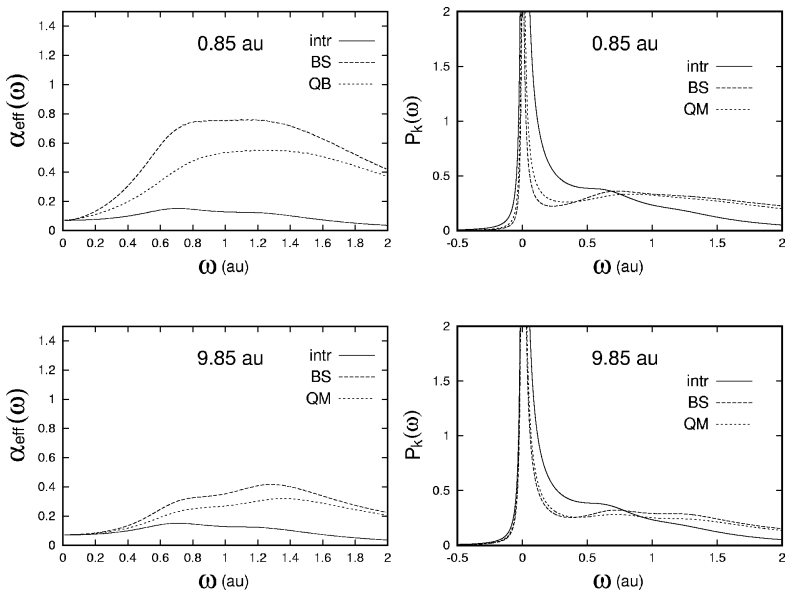

Figure 3.6: The same results as in Fig. 3.5 for Cu metal.

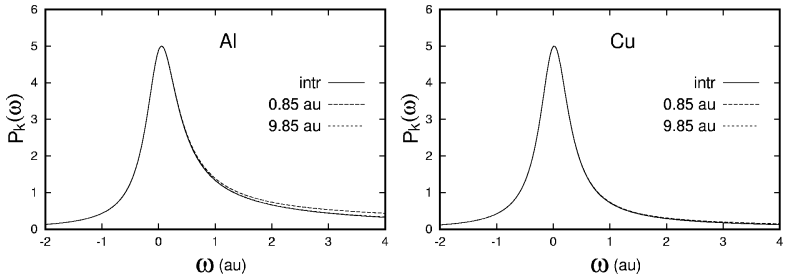

Figure 3.7: Curves of the asymmetric quasi-particle peak for Al metal (left) and Cu metal (right). The curves have a 300 meV Lorentzian broadening, and give results for emission from an atom 10 au from the surface. Results for a photoelectron kinetic energy of 0.85 and 9.85 au, and also when only the intrinsic contribution (independent of photoelectron energy) is included.

satellite is stronger than the main line. Since the satellite is stronger we could call it the main line, and call the line with a d-electron a satellite. This is then a *shake-down satellite* since the electron is shaken down from its ligand orbital into the lower lying d-orbital. This kind of situation is quite common, and it has been studied for rare earth compounds, chemisorption systems, transition metal compounds, and high-T_c compounds.(For references see [44]).

In a localized system this problem can be studied with a very simple model Hamiltonian which allows a numerically exact solution of the photoemission problem for all photon energies. [44] It was found that the effect of the photoelectron-residual system interaction becomes

small already at 5–10 eV above threshold. Perhaps surprisingly the variation of the dipole matrix element with energy was as large or larger than the variation due to the coupling to the photoelectron.

3.2.5 Resonant photoemission

Resonant photoemission spectroscopy (RESPES) has played an important role to map properties of strongly correlated systems. Typically we have a resonant effect when the core state (of say d symmetry) has a large dipole matrix element to a quasi-localized outer state (of say f symmetry) with a fairly sharply defined energy (we typically have a Coster-Kronig situation). With the photon energy tuned in the vicinity of this energy we will have two competing processes leading to the same final state. In one process the photon directly ejects an electron from the f-type state. The other process goes in two steps, first a (say) d-f transition and then an Auger decay which fills the d-hole and ejects an f-type electron. Since the final state is the same (one hole in the f-state) we have to add the amplitudes for the two processes and experimentally a Fano type line shape is seen. The resonance effects can be huge when the photon energy sweeps the resonance line, and one talks of giant resonances. RESPES is a large and complex topic, and we cannot here cover it in any depth. A comprehensive analysis of the theory is given in Ref. [3], and of experiment in Ref. [45]. In addition to summarizing the material in the earlier works we also discuss the extrinsic and intrinsic losses.

To discuss this case we cannot regard the core-hole state as stationary but have to include the Auger coupling term which allows it to decay. We now have two perturbations, the coupling between the photoelectron and the valence electrons, V, and the Auger coupling, V_A. We first treat V_A. The final state then is

$$|N-1,s;\mathbf{k}\rangle = \left[1+\frac{1}{E-H_0-V-V_A-i\eta}V_A\right]|N-1,s;\mathbf{k}\rangle^0\,, \tag{3.24}$$

where $|N-1,s;\mathbf{k}\rangle^0$ now includes the effects of the interaction V but not V_A. Both $|N-1,s;\mathbf{k}\rangle$ and $|N-1,s;\mathbf{k}\rangle^0$ are eigenstates with the core hole filled and a photoelectron "$\mathbf{k}$", The difference between the two states is that $|N-1,s;\mathbf{k}\rangle$ contains virtual contributions with a core hole, i.e. $|N-1,s;\mathbf{k}\rangle$ is a mixture of states with no core hole $|N-1,s;\mathbf{k}\rangle^0$ and states generated by V_A. Thus V_A destroys the photoelectron and creates a core hole, putting the two electrons in the resonance level. The operator V_A in the denominator can, after some algebra, be replaced by the self-energy Σ_c (a scalar),

$$\begin{aligned}|N-1,s;\mathbf{k}\rangle = \Bigg[1+\frac{P_c}{E-H_0-V-\Sigma_c^+}V_A \\ +\frac{1}{E-H_0-V-i\eta}V_A\frac{P_c}{E-H_0-V-\Sigma_c^+}V_A\Bigg]|N-1,s;\mathbf{k}\rangle^0\,,\end{aligned}$$

which is the usual Fano expression. Here Σ_c^+ is the self-energy connected with the core hole, which for a narrow resonance can be treated as a complex constant giving the level shift and the lifetime, and P_c is a projection operator on the manifold of states with a core hole. The upper index on Σ_c^+ signals a positive imaginary part. We remind of the well-known fact that,

at resonance, the term explicitly of second order in V_A gives a contribution comparable to those of zero and first order. Second order terms of course also appear in Σ_c. The transition amplitude is

$$^0\left\langle N-1,s;\mathbf{k}\right|\left[1+V_A\frac{P_c}{E-H_0-V-\Sigma_c^-}+V_A\frac{P_c}{E-H_0-V-\Sigma_c^-}V_A\frac{1}{E-H_0-V+i\eta}\right]\Delta\left|N\right\rangle. \quad (3.25)$$

The three terms describe the Fano resonance; the first term directly gives the photoelectron (PE), the second gives a resonance state followed by decay to give the PE, and the third gives a virtual PE, followed by an "inverse" Auger transition creating a core hole, and finally an Auger decay which fills the core hole and gives the PE. As mentioned all three terms are comparable in importance to produce the Fano line.

We now have to take account of the photoelectron-residual system interaction V, and evaluate $|N-1,s;\mathbf{k}\rangle^0$,

$$|N-1,s;\mathbf{k}\rangle^0=\left[1+\frac{1}{E-H_0-i\eta}V\right]c_{\mathbf{k}}^{\dagger}\,|N-1,s\rangle^0\,,$$

where $|N-1,s\rangle^0$ is a state for the residual system calculated without virtual core hole contributions. In Eq. (3.25) the right part is a sum of states of the form $c_{\mathbf{k}'}^{\dagger}\,|N-1,s'\rangle^0$

$$\left[1+V_A\frac{P_c}{E-H_0-V-\Sigma_c^-}+V_A\frac{P_c}{E-H_0-V-\Sigma_c^-}V_A\frac{1}{E-H_0-V+i\eta}\right]\Delta\,|N\rangle=\sum_{s'\mathbf{k}'}\alpha_{s'\mathbf{k}'}c_{\mathbf{k}'}^{\dagger}\,|N-1,s'\rangle^0\,. \quad (3.26)$$

In calculating the coefficients $\alpha_{s'\mathbf{k}'}$ the effect of V on the second term should be small since Δ has created a quasi-localized state, which then Auger decays. In the third term, where Δ generates a virtual photoelectron, V will cause both a damped propagation and inelastic scatterings. Explicit results can be worked out using the method presented in Ref. [25],

$$\frac{1}{E-H_0-V+i\eta}\,|N-1,s\rangle\,|\mathbf{k}'\rangle=\left[G^d+G^dVG^d\cdots\right]|N-1,s\rangle\,|\mathbf{k}'\rangle\,,$$

where

$$G^d=\sum_s P_sG_s^d,\qquad G_s^d=\frac{1}{E-\varepsilon_s-h-\Sigma^p\left(E-\varepsilon_s\right)},\qquad P_s=|s\rangle\,\langle s|\,.$$

H_0 is given in Eq. (3.14), and $\Sigma^p\left(E\right)$ is the self-energy from the photoelectron scattering with GW as the lowest approximation. The states $|s\rangle$ are eigenstates of (H_0-h). We note that the

expression in Eq. (3.26) converges also without using a damped propagator, and that the effect of the damped propagator should be to reduce this term (the asymmetry term) in magnitude.

We can do the same analysis as before to get a damped photoelectron state

$$
\begin{aligned}
&{}^0\Big\langle N-1,s;\mathbf{k}\Big|c^\dagger_{\mathbf{k}'}\Big|N-1,s'\Big\rangle^0 \\
&\qquad=\Big\langle\widetilde{\mathbf{k}}\Big|^0\Big\langle N-1,s\Big|1+V\frac{1}{E-H_0-V+i\eta}\Big|N-1,s'\Big\rangle^0\Big|\mathbf{k}'\Big\rangle. \qquad (3.27)
\end{aligned}
$$

This is a similar expression as we have for loss processes in valence electron PES, Eq. (3.15), and the damping here is, as before, necessary to get a photocurrent proportional to surface area and not to volume. We can expect the same type of loss effects in RESPES as in valence electron PES. Surprisingly both intrinsic and extrinsic losses can be large also in valence electron PES. [1] However structured loss peaks are mainly expected in solids with pronounced plasmon excitations and Coster-Kronig transitions are occurring in d and f electron systems where structured plasmon effects normally are absent.

Finally we note that the method to separate states with specific core configurations and coupling them with Auger terms does not work for *mixed valent situations*. The reason is that the "quasi-core" states in mixed valence have energies overlapping the valence band, and then the mixing terms in the Anderson Hamiltonian are important, terms which are small when the core configuration is well separated from the valence band, and which we have neglected here. [3]

Multiatom resonant PES (MARPE) is a related effect. Here the two interfering processes involve two different atoms A and B not too far from each other. In one process there is ordinary PES from a core level of atom A. In the other process the photon spends its energy by exciting an electron from a core level on atom B to a quasi-localized level on the same atom. In the next step the electron drops down leaving atom B unchanged and through an Auger matrix element excites the core electron on atom A to the same final state as in the first process. [46]

3.2.6 Phonons and temperature effects

These effects are pronounced only for quasi particle lines, where the intrinsic approximation works well. The theory was carefully mapped out in [3], and more recently in [11]. We find no reason to here summarize this classic and well-known subject.

3.3 Concluding remarks

Core electron photoemission is still under rapid development due to the continuing improvements in synchrotron radiation sources. The fundamental theory is well understood, but there is still a large gap to good quantitative methods to evaluate its consequences. The goal should be that theory can say something not only about characteristic structure in the spectra but on the full spectral form. Only then can the accurate experimental data have full impact on the theoretical understanding. To achieve this the electron loss problem must be handled in a much better way.

It seems true that quasi-particle line shapes are dominantly determined by the intrinsic spectra, i.e. the extrinsic losses are very small in that region. On the other hand many theoretical calculations on strongly correlated systems are made for two-dimensional systems, and then the shake-up effects on the embedding three dimensional system are lost. So when the 3D system has low energy excitations like electron-hole pairs and acoustic plasmons, the effects of these on the quasi-particle line shape are lost. [41]

Auger photoelectron coincidence (APECS) measurements were first made long ago by Haak, Sawatzky and Thomas. [47] It is a very difficult experiment, particularly for solids, but recently this field has become active due to improved instrumentation. [48] This interesting field relies on a description of the Auger decay as a one-step process, rather then the usual two-step process. Such theories are available. [3, 5]

There is a long-standing problem on how to treat pronounced atomic multiplet effects in a solid state environment. Although cluster calculations can go a long way to explain solid state systems as shown by the Sawatzky and Kotani groups, the full embedding problem remains to be solved. In recent work [41] a crude embedding model was proposed to treat a two-dimensional system in a three-dimensional surrounding. For theoreticians this remains an important area for future progress.

References

[1] S. Hüfner, *Photoelectron spectroscopy* in Springer Series in Solid State Sciences, Vol. 82 (Springer, Berlin 1995).

[2] J.E. Inglesfield and E.W. Plummer, *The physics of photoemission* in S.D. Kevan (ed.) *Angle-resolved photoemission*, (Elsevier 1992).

[3] C.-O. Almbladh and L. Hedin, *Beyond the one-electron model, many-body effects in atoms, molecules and solids* in *Handbook on Synchrotron Radiation* vol 1B, ed. by E.-E. Koch (North Holland, Amsterdam, 1983).

[4] C.-O. Almbladh, Phys. Rev. B **16**, 4343 (1977).

[5] O. Gunnarsson and K. Schönhammer, Phys. Rev. B **22**, 3710 (1980).

[6] L.A. Feldkamp and L.C. Davis, Phys. Rev. B 22, 3644 (1980); L.C. Davis and L.A. Feldkamp, Phys. Rev. B **23**, 6239 (1981).

[7] Akio Kotani, J. El. Spec. Rel. Phen. **100**, 75 (1999).

[8] O. Gunnarsson, K. Schönhammer, J.W. Allen, K. Karlsson, and O. Jepsen, J. El. Spec. Rel. Phen. 117-118, 1 (2001).

[9] C.N. Berglund and W.E. Spicer, Phys. Rev. **136**, A1030 (1964).

[10] A. Flodström, R. Nyholm, and B. Johansson, *Surface core level spectroscopy* in *Synchrotron Radiation Research*, ed. R.Z. Bachrach (Plenum Press, New York, 1992).

[11] J.N. Andersen and C.-O. Almbladh, *High resolution core level photoemission of clean and adsorbate covered metal surfaces*, J. Phys.: Condens. Matter **13**, 11267-291 (2001).

[12] G. Margaritondo, *Introduction to synchrotron radiation* (Oxford 1988).

[13] M.L. Goldberger, and K.M. Watson, *Collision Theory* (Wiley, New York, 1964).

[14] P.J. Feibelman, PRB **22**, 3654 (1980).

[15] W. Schattke, Progr. surface science **54**, 211 (1997).

[16] L. Hedin and J.D. Lee, J. El. Spec. Rel. Phen. **124**, 289 (2002).
[17] L. Hedin and S. Lundqvist 1969 in *Solid State Physics*, vol **23**, p. 1 (eds. Seitz, Turnbull, Ehrenreich), Academic Press.
[18] G.D. Mahan, Many-Particle Physics. Plenum Press (1981).
[19] J. Fink, M. Knupfer, S. Atzkern, and M.S. Golden, J. Elec. Spec. Rel. Phen **117-118**, 287 (2001).
[20] L. Hedin and A. Johansson, J. Phys. B **2**, 1336 (1969).
[21] C.J. Joachain, *Quantum collision theory*, North Holland 1975.
[22] G.F. Chew and F.E. Low, Phys. Rev. **101**, 1579 (1956).
[23] L. Hedin, J. Michiels, J. Inglesfield, Phys. Rev. B **58**, 15565 (1998).
[24] L. Hedin, J. Phys.: Condens. Matter **11**, R489 (1999).
[25] T. Fujikawa and L. Hedin, Phys. Rev. B **40**, 11 507 (1989).
[26] D.R. Penn, Phys. Rev. Lett. **38**, 1429 (1977).
[27] D.R. Penn, Phys. Rev. Lett. **40**, 568 (1978).
[28] A. Georges, G. Kotliar, W. Krauth, and M.J. Rozenberg, Rev Mod Phys **68**, 13 (1996).
[29] J.E. Inglesfield, Solid State Commun. **40**, 467 (1981); J. Phys. C **16**, 403 (1983).
[30] W. Bardyszewski and L. Hedin, Physica Scripta **32**, 439 (1985).
[31] L. van Hove, Physica **21**, 901 (1955).
[32] L. Hedin p. 307 in Recent progress in many-body theories vol **1**, eds. A.J. Kallio, E. Pajanne, R.F. Bishop, Plenum Press (1988).
[33] I. Adawi, Phys. Rev. **134**, A788 (1964).
[34] J.S. Bell and E.J. Squires, Phys. Rev. Lett. **3**, 96 (1959).
[35] C. Caroli, D. Lederer-Rosenblatt, B. Roulet and D. Saint-James, Phys. Rev **B 8**, 4552 (1973).
[36] P.J. Feibelman and D.E. Eastman, Phys. Rev. B **10**, 4932 (1974).
[37] C-O. Almbladh, Physica Scripta **32**, 341 (1985).
[38] T. Fujikawa and H. Arai, J. El. Spec. Rel. Phen. **123**, 19 (2002).
[39] C.S. Fadley, *The study of surface structures by photoelectron diffraction and Auger electron diffraction* in R.Z. Bachrach (ed.), *Synchrotron radiation research* (Plenum Press 1992).
[40] J.J. Rehr and R.C. Albers, Rev. Mod. Phys. **72**, 621 (2000) and the chapter by Rehr and Ankudinov in this book.
[41] L. Hedin and J.D. Lee, Phys. Rev. B **64**, 115109 (2001).
[42] S. Tougaard and P. Sigmund, Phys. Rev. **B 25**, 4452 (1982).
[43] A.C. Simonsen, F. Yubero and S. Tougaard, Phys. Rev. **B 56**, 1612 (1997).
[44] J.D. Lee, O. Gunnarsson and L. Hedin, Phys. Rev. B **60**, 8034 (1999).
[45] J. Allen, *Resonant photoemission of solids with strongly correlated electrons* in R.Z. Bachrach (ed), *Synchrotron radiation research* (Plenum Press 1992).
[46] A.W. Kay, F.J. Garcia de Abajo, S-H. Yang, E. Arenholz, B.S. Mun, N. Mannella, Z. Hussain, M.A. van Hove, and C.S. Fadley, Phys. Rev. B **63**, 115119 (2001).
[47] H.W. Haak, G.A. Sawatzky, and T.D. Thomas, Phys. Rev. Lett. 41, 1825 (1978).
[48] R.A. Bartynski, Q. Qian, and S.L. Hulbert, J. Phys. IV France **9**, Pr6-157 (1999).

Solid-State Photoemission and Related Methods
Wolfgang Schattke, Michel A. Van Hove (Eds.)

4 Valence band VUV spectra

I. Bartoš and W. Schattke

4.1 Introduction

Photoelectron spectroscopy provides the most direct information about the valence bands of crystals and of their surfaces. Some basic properties, like dispersion relation E(k), can be approximatively learned in a straightforward manner from angular resolved spectral peaks using only conservation laws for energy and momentum. Photoemission process, however, is not only affected by the occupied electron initial states but also by unoccupied excited states above the vacuum level. The spectra, due to the surface sensitivity of photoemission, do not reflect only the bulk valence bands but also characteristic surface properties. The traditional three-step model of photoemission had to be generalized to describe correctly the interference between bulk and surface contributions and so the one-step model has been developed. Into these frameworks it was also possible to incorporate, at least phenomenologically, some aspects of interelectron interactions like finite lifetimes of excited electrons and holes which determine the surface sensitivity of electron spectroscopies.

In order to exploit the rich information contained in the angular resolved spectra not only the peak positions and widths are to be used. In recent years progress of photoemission spectroscopy continued on the experimental side (synchrotron radiation sources, enhancement of energy and angular resolution etc.) and on the theoretical side (realistic structures, refinements in interaction description). This makes it possible to compare the full shapes of the measured and calculated intensities of photoemitted electrons. The comparison then enables to extract detailed information about the origin of various features in the experimental spectra following from layer- and orbital-compositions of theoretical spectra.

4.2 Electrons at crystal surfaces

Surfaces of solids represent a special interface: the interface between a solid and vacuum. Full specification of a surface requires that geometrical arrangement of atoms and their chemical nature are known. Surfaces, even in the most ideal cases of low-index clean surfaces, represent a region of finite thickness where physical properties differ from those in the underlying bulk: e.g. a geometrical atomic arrangement exhibits often complicated relaxations and reconstructions depending on surface preparation and growth temperatures. Only in exceptional cases the surface arrangement is close to an ideal termination of the bulk structure.

We will not discuss core electron states and concentrate on the occupied valence electron states and on unoccupied states above the vacuum level. In a description of the system of

Solid-State Photoemission and Related Methods: Theory and Experiment. Edited by Wolfgang Schattke, Michel A. Van Hove

ISBN: 3-527-40334-5

electrons, complicated theoretical analysis of the interacting system of ions and electrons has to be simplified. As in the bulk, two general approaches can be used, each stressing one of the two important classes of interactions: electron-electron or electron-ion. Only more recently, both interactions have been taken into account simultaneously to provide a realistic description of crystal surfaces.

Here, we will sketch the basic principles of the theoretical description of the electron structure of crystal surfaces referring to the literature for more details.

4.2.1 One-electron approach

When electron-ion interaction is stressed, the effective interaction in a crystal can be represented by some periodic potential. The solution of the Schrödinger equation gets substantially simplified by the Bloch theorem for the shape of the electron wave functions. In the semi infinite crystal, the translational symmetry is reduced to just two directions along the crystal surface. Therefore, only surface components of the wave vector remain good quantum numbers for electrons in crystals limited by a plane surface.

Simple one-dimensional models with a step-potential surface barrier are often used to give basic features of the surface electron structure. Qualitatively new types of states – surface states – can exist which, in contrast to the delocalized Bloch states from the bulk, display spatial localization in the direction perpendicular to the surface: the surface barrier restricts electron propagation into the vacuum and the band gap makes it impossible into the bulk of the crystal. Apart from surface states, electron states from the allowed energy bands are modified in the vicinity of the surface: the local density of states differs from that in the bulk due to the reflection of propagating electron states in the surface region. These changes may be very strong in the case of surface resonances which represent a continuation of surface state bands into (bulk) allowed bands. Similarly, above the vacuum level, band gaps are responsible for the enhanced reflectivity of the surface for electrons incident from the vacuum (LEED intensity). Historically, two one-electron approaches have been developed: crystal potential and crystal orbital methods [1].

In the first class of methods, formulated in the coordinate representation, the description is formulated as a standard problem of quantum mechanics: general solutions of the Schrödinger equation in the two half-spaces are found and then matched at the surface so that the electron wave function together with its derivative normal to the surface are continuous. To this end, the concept of the (real) band structure has been generalized [2] to include also solutions with the imaginary component of the wave vector perpendicular to the surface. In the complex band structure, e.g. individual branches of the real band structure are connected by the loops of solutions within the gaps.

In addition to the matched wave function also the general formula for the so called Surface Green function (SGF is defined only at the surface and is identical with the projection of the full Green function of a semi infinite crystal there) has been found [3] by matching of the Green functions of (infinite) crystal and of the vacuum; it enables to treat both the bound and scattering electron states on an equal footing. Full Green function can be obtained from the SGF in a straightforward manner [4].

In the crystal orbital methods, the electron wave function is expanded in terms of localized atomic orbitals as in the quantum chemistry (MO LCAO). The crystal surface is then

represented by broken bonds between neighbors at the surface. The advantages of this description are its simplicity together with intuitive understanding in terms of atomic orbitals and their hybridization. The simple boundary condition oversimplifies the problem so that gradual transition from bound to scattering electron states (LEED) is not possible.

Surface state energies and wave functions depend on the shape of the effective potential in the surface region. This potential is codetermined by the electron distribution here and the selfconsistent procedure is required for its determination. We have to start with some reasonable potential (e.g. model potential, strictly periodic till the surface), to solve the corresponding Schrödinger equation in order to obtain the charge distribution; from the Poisson equation then a new potential is determined. After several repetitions of this procedure a selfconsistent solution is obtained which provides a realistic description of the electron structure of a crystal.

First selfconsistent calculations have been performed [5] by matching the bulk general solution at a plane situated below the surface so that the surface deviations of the potential from the bulk behavior could be neglected there. Solutions have been found for Na(100) from the vacuum region by numerical integration through the modified surface region to the plane discussed above.

Another class of calculations [6] utilizes finite repeated slabs of the crystal to represent the crystal with a surface. In this representation with regularly alternating layers of crystal and vacuum the problem to be solved gets transformed into that of the infinite crystal. The dimension of the unit cell in the direction perpendicular to the surface (layer stacking direction) becomes substantially increased, of course.

General conclusions of model calculations that the surface region width (localization of surface states and of modifications of local densities of states) is limited to several atomic planes has been confirmed by selfconsistent calculations. Only the extent of bent bands in semiconductors is much wider and their bending can be described quasiclassically [7].

4.2.2 Many-electron approach

In the other extreme case, the role of electron-electron interaction is emphasized and electron-ion interaction is neglected. The jellium, where crystal periodic potential is replaced by uniform background charge, was treated in detail. For surface studies the semi infinite jellium with an abrupt termination of the background charge at a surface plane was investigated [8]. In this model, the electrons spill out into the empty half-space giving thus rise to the dipole part of the effective surface barrier and their density exhibits Friedel oscillations into the bulk. The electron work function, in addition to the dipole part, contains also a contribution from the exchange-correlation terms.

In the density functional theory (DFT) in the local density approximation (LDA) the effective surface barrier decays exponentially into the vacuum in contrast to the well known asymptotic 1/z behavior, required by the electrostatic laws (the image potential). The image potential, treated, first, in model calculations [9] and later for real metals [10], is responsible for the existence of the new type of electron surface states, so called image states. Because of the Coulomb asymptotics of the potential these states form Rydberg series below the vacuum level. This contrasts with surface states found in step barrier models. Also, the space localization of the image states is different: these are concentrated further into the vacuum and thus their interaction with the crystal bulk is reduced.

LDA DFT approximation, which is founded on exact theorems about the ground state of the many-electron system, is often used to provide also low-lying excited states of the system. The eigenvalues of the Kohn-Sham equations are then interpreted as energies of the excited states. There is no straightforward justification for this extension of the formalism. This procedure appeared to fail for example in getting correct magnitude of the gaps in semiconductors; in addition the lifetimes of these states are infinite.

Correct description of the excitations in the many-electron problem can be given by means of the Green functions. The self-energy $\Sigma(k, E)$ characterizes then the quasiparticle properties: its real part is responsible for the renormalization of the energy of excited electrons and holes and its imaginary part determines the (finite) lifetime. Evaluation of the screened interaction W is of central importance in the GW approximation [13]. This approximation provides results connected with the excited electron states (narrowing of bands, magnitude of gaps) in much better agreement with experimental data than the LDA. Detailed discussion and comparison of recent results, in particular for nearly free-electron metals, is given in [12].

The quasiparticle lifetime is determined by the imaginary component of the self-energy. The electron-electron interactions represent the dominating contribution (except at very low energy excitations where phonon contributions are important) to this quantity. Detailed investigations of the homogeneous system of interacting electrons – of jellium – show general energy dependence trends: in the ground state (electron at the Fermi level) the electron lifetime is infinite; inelastic collisions of an excited electron, accompanied by creations of the electron-hole pairs, give rise to the quadratic increase of the imaginary part of Σ above the E_f. Steep rise of $\mathrm{Im}\,\Sigma$ at higher energies is connected with overcoming the energy threshold for collective excitations – plasmons. Finally, with further increasing energy the $\mathrm{Im}\,\Sigma$ decreases. The electron lifetime, together with its group velocity, determines the electron inelastic mean-free path, which plays a central role in surface sensitivity of low energy electron spectroscopies. From the energy dependence of the electron lifetime then follows the well-known U-shaped "universal curve" of the inelastic mean-free path.
Crystals are inhomogeneous and therefore generally k-dependence or anisotropy of Σ is to be expected. In comparison with calculations of Re Σ for real crystals, only a smaller attention has been paid to $\mathrm{Im}\,\Sigma$ [15].

In crystals with surfaces, similarly the lifetimes of surface states can be studied. The image-type states can be expected to have long lifetimes due to their small interaction with bulk electrons. Detailed review of calculated and experimentally determined image-state lifetimes on various surfaces of metals have been given recently [11].

4.3 Photoelectron spectroscopy

In photoemission, the electromagnetic radiation incident on a solid excites the electrons from the ground state so that some electrons can be detected outside the irradiated sample in the surrounding vacuum. Photoelectron spectroscopy is usually performed with a monochromatic radiation (discharge lamps, synchrotron radiation in VUV range) and energy distribution curves (EDC) of photoemitted electrons are recorded: either the total electron flux or electron flux in specific direction only. For the study of the valence bands the VUV excitation sources are most suitable due to the large cross-section of the photoemission. In addition, the surface sen-

sitivity of the ultraviolet photoelectron spectroscopy (UPS) is predominantly determined by the short mean free path of emitted low energy electrons.The attenuation of the incident radiation in the surface region is mostly of minor importance and will not be discussed here. For radiation frequencies in the vicinity of the plasmon frequency this attenuation may become very important [16, 17].

The interpretation of the recorded spectra can be undertaken in various stages of sophistication: The scheme using only the energy conservation applies well to polycrystalline samples (no long-range order leading to the electron momentum conservation) and also to crystalline samples studied in the XPS regime: in the latter case the high energy of emitted electrons is responsible for effective averaging over the Brillouin zone even in the angularly resolved mode [20]. It can be expected that the EDC in the integral mode will reflect the energy dependence of the density of occupied electron states in the valence band. This simple picture is distorted by mixing of bulk and surface contributions and by the matrix elements giving different amplitudes of probabilities of various electron transitions from their occupied to unoccupied states.

4.3.1 Band mapping (peak positions)

More detailed information can be obtained from EDCs in the angular resolved photoemission using the energy and momentum conservation (in crystals). For crystals with ordered surfaces the three-dimensional bulk translational symmetry is preserved (or reduced) only in two directions along the surface. Therefore, only the surface component of the wave vector $k_{\|}$ remains a good electron quantum number. The small momentum of photons in VUV region can be neglected with respect to the dimensions of the (surface) Brillouin zone and the transitions of electrons will be direct, it is conserving the k vector (with the exception of Umklapp processes). The knowledge of the energy and of the wave vector of the detected electron permits determination of the initial state of this electron which is complete for two-dimensional systems (surface states and to a certain degree electrons in overlayers and layered materials) and only partial for three dimensional systems ($k_{\perp}$ component of the bulk electron remains undetermined). Band mapping, it is determining the electron dispersion E(k) is thus straightforward for 2D systems and less direct for 3D. The excitation process represents one of the three stages in the three-step model: bulk electron excitation, propagation to the surface and transmission through the surface barrier to vacuum. It has to be a vertical transition in the one-dimensional section of the band structure (for example, for normal photoemission the band structure along the line going through the Brillouin zone center in the direction perpendicular to the surface is to be considered). Then, ideally, the EDC should consist of a series of discrete δ-functions corresponding to vertical electron transitions from the occupied to the unoccupied branch of the band structure. In real spectra the isolated lines are replaced by peaks and their energy positions are used for the band structure determinations. In order to determine $k_{\perp}$ some assumption is needed about the form of the dispersion relation of the final electron states $E_f(k)$. Most often, the free-electron approximation is used (with a rigid shift determined by one parameter). Another possibility consists in utilizing the band structure calculations or more complicated schemes with triangulation techniques.

In Fig. 4.1 the final states' bands of bulk GaAs in a direction normal to the (110) surface are displayed together with the Fourier decomposition of the true inverse LEED states cal-

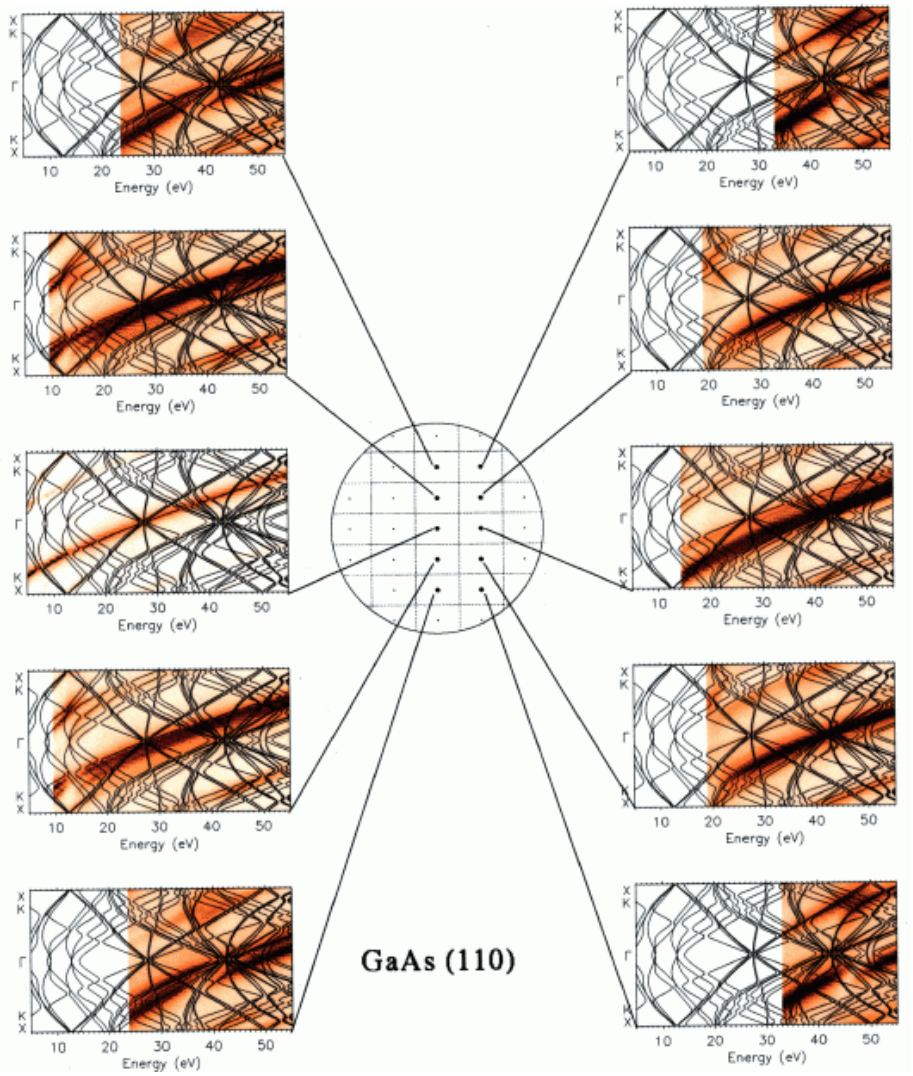

Figure 4.1: Wave vector Fourier decomposition of the inverse LEED state (brown shaded) for several $\bar{\Gamma}$ points with normal emission in center of circle and underlaid pseudopotential band structure (black lines). See also color figure on page 464.

culated for a pseudopotential half-space with step barrier to vacuum. A set of Γ points for several Brillouin zones with respect to $\mathbf{k}_{\|}$ is shown the underlaid band structure being identical, of course. The intensity of brown shading represents the amplitude of the wave function Fourier transformed with respect to the surface perpendicular wave vector for every energy above the escape threshold. The figure clearly suggests an overall roughly parabolic energy dispersion for the states coupling to vacuum with one branch in the case of the central Γ point

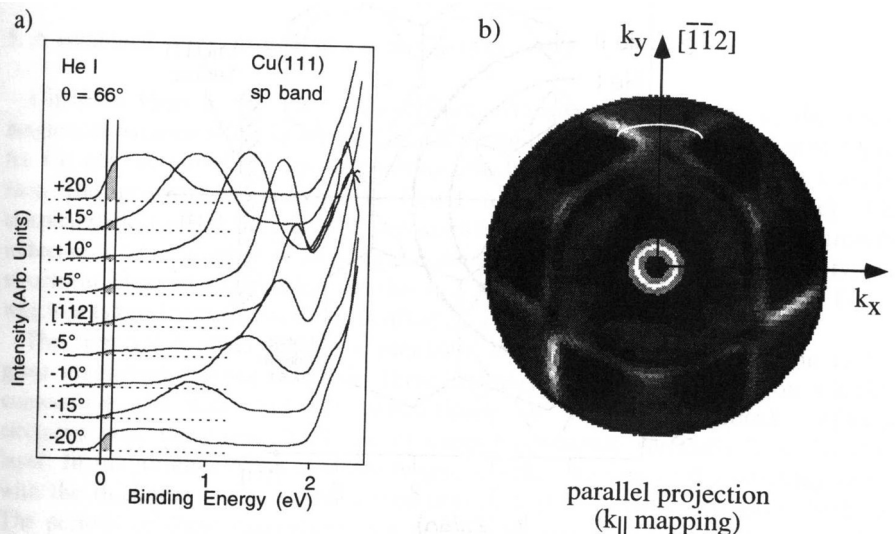

Figure 4.2: (a) He I excited energy spectra from Cu(111) at a polar angle of 66°, taken at various azimuthal angles around the $[\overline{1}12]$ direction. Vertical lines limit the energy window applied for obtaining the Fermi surface map shown in (b). The white arc indicates the azimuthal scan range for the spectra of (a) [37].

and several branches in the general case. It confirms the anticipated experimental data interpretation relying on a parabolic dispersion somehow, more for normal emission, less for inclined emission. Illustrations of the procedure and of the results of the band mapping for metal and semiconductor crystals as well as further references can be found in [18–20].

Another technique developed recently in this context consists in measurement of full hemispherical photoemission electrons in [37] (and references there), see Fig. 4.2.

By setting a narrow energy window at a selected energy in the valence band (instead of mapping E(k) along some direction) a section of the constant energy surface is imaged (e.g. at E_f for Fermi surface imaging) given by the frequency of the exciting radiation. The full picture of the constant energy surface in E(k) can be reached by continuous change of the frequency of this radiation (to enable transitions from the whole 2D surface of occupied states at a given energy into available unoccupied branches of the electron band structure), see Chapters 5 and 12. Despite its widespread application up to these days [21] the method has of course the limitations familiar to band mapping, as the neglect of the structure from final states and matrix elements which could be experimentally demonstrated. [22, 23]

For precision limits of the electron band structure mapping it should be kept in mind that the assumption of the three-step model consisting in conservation of the wave vector component perpendicular to the surface is not strictly valid. The errors introduced by this assumption have been demonstrated in the computer simulation of photoemission profiles evaluated in the one-step model [24]. The bands were known and the evaluated EDC were analyzed by standard experimental techniques; the deviations of "experimental" peak positions from energies of direct transitions were shown to be of the order of tenths of eV, see also Chapter 2.

The mapping of occupied electron states (from the valence band bulk states and from surface states) can be extended to unoccupied states also: to this end, either the inverse photoemission or the two-photon photoemission can be used. In the latter technique intensive laser irradiation is used for excitation of electrons: first photon excites electron from the occupied state to the intermediate (sufficiently long-lived) unoccupied state below the vacuum level and then the second photon excites the electron from the investigated state into the vacuum where it can be detected, Chapter 8 and [25](and references there).

So far, only the energies of peaks – peak positions – in the EDCs of photoemitted electrons have been needed. Next, the information contained in peak widths will be discussed.

4.3.2 Electron and hole lifetimes (peak widths)

Till now, electrons in their initial and final states were treated as noninteracting particles. In real systems interactions among electrons have to be taken into account and the electrons have to be treated as quasiparticles, it is as weakly interacting "dressed" particles. The quasiparticle in the state with wave vector k is described by the spectral function A(k,ω) which, for interacting particles, is no more δ-function in energy but has a finite spread in energy. The energy distributions of spectral functions for good quasiparticles are described by Lorentzians; their widths determine the quasiparticle lifetimes. In the three-step model of photoemission then the individual branches of the electron energy bands E(k) become correspondingly broadened and the energy conservation law can be easier fulfilled: instead of δ-function peaks in the EDCs in angular resolved spectra we can expect peaks with finite widths.

In contrast to broadening of the discrete eigenvalues the broadening in crystals, manifested in finite EDC peak widths, is affected not only by the electron and hole lifetimes but also by the slopes of the initial and final bands participating in the photoemission process. In a reasonable approximation it was shown that the intensity of photoemitted electron current as a function of a variable like energy or angle becomes also a Lorentzian and its half-width is given by a simple formula [26, 27], with γ_h, γ_e representing hole and electron inverse lifetimes and the derivatives of the initial and final bands normal to the surface , v_i, v_f.

Similar formulas applying also to other modes of photoemission than EDCs (taken at fixed excitation energies) like CIS (constant initial state) and CFS (constant final state) have been given in [28], see Fig. 4.3.

If the band structure is known for both the initial (occupied) and the final (unoccupied) bands the peak width is still determined by two inverse lifetimes γ_h, γ_e. In order to determine γ_e from the peak width Γ, transitions originating just below the E_f (where γ_h approaches zero) have to be investigated. The electron lifetimes have been studied by ARUPS either at fixed angle of exit, varying continuously the excitation energy (normal emission [26]) or at fixed excitation energy, varying the electron exit angle [27].

Determining the inverse lifetime of holes γ_h is straightforward for surface states with zero dispersion in a direction normal to the surface: then $\gamma_h = \Gamma$. Also bulk states at points of higher symmetry with zero slope of the initial band can be studied in this manner. Electron-electron correlation represents a dominant contribution to the electron/hole lifetime; this interaction is always present -even in perfect crystals. Any deviation from a perfect periodicity (disorder, impurities, vibrations) contributes to the broadening of photoemission peaks by relaxing the

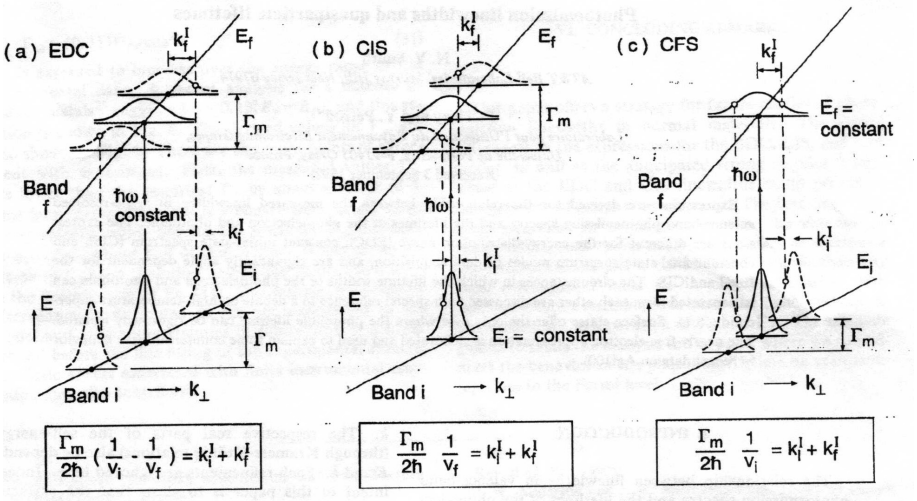

Figure 4.3: Geometrical representation of measured linewidths (Γ_m) for the three principal modes of photoemission data taking (a) EDC (energy-distribution curve), (b) CIS (constant initial-state spectrum), and (c) CFS (constant final-state spectrum), k_i^I, (k_f^I) refer to the inverse lifetimes $\gamma_h(\gamma_e)$ resp. via the dispersion [28].

momentum conservation conditions. Therefore, great care has to be given to analyzing the data so as to obtain the information about electron correlation in crystals [29].

Rather high experimental demands are imposed on energy and angular resolutions, in particular if excited electron states close to the Fermi level are investigated. The energy dependence of the electron lifetimes close to E_f is expected to bring important evidence about deviations from the Fermi liquid behavior expected e.g. in high temperature superconductors.

Collection of the hole and electron lifetimes obtained both from ARUPS peak widths and from the time-resolved two-photon spectroscopies was given in [30]. The two techniques have opposite limitations in their application range: whereas by means of linewidths very long-lived states cannot be studied, the time-resolved techniques fail with very short-lived states. The limitation is given by minimum energy resolution in the former case (5 meV) and by minimum time-resolution in the latter case (5 fs). In a case studied by both techniques (surface state on Cu(111)) good agreement of the determined lifetimes has been reported [30].

In the time-resolved techniques, the electron lifetimes measured at a given energy are influenced by two processes: drifting of electrons into the bulk shortens the measured lifetime, on the other hand, Auger (and subsequent cascade processes) processes increase the population of the investigated energy level and thus effectively increase the measured lifetime. These processes should be taken into account in detailed analyses of electron lifetimes due to electron-electron correlation [31, 32].

The energy region close to the Fermi level has been studied in detail: the energy dependence of electron lifetimes from experimental data was compared with theoretical predictions, in particular with quadratic energy dependence obtained for the interacting electron gas in the

Fermi liquid theory. Recent careful examination of d hole lifetimes at copper surfaces [33] showed deviations from a monotonous energy dependence due to the band structure (d-bands). This was also confirmed in the calculations of the electron self-energy in the GW approximation where in addition also substantial anisotropy of Σ has been reported. Although qualitative agreement of theory and experiment has been achieved, nonnegligible differences still do exist. Small scale energetic features as being especially investigated in research related to superconductivity are often discussed in terms of a proportionality between photocurrent and spectral density, see also Chapter 2. With highest experimental resolution and some assumptions on the principal shape of the spectral density detailed behavior of the hole self-energy can be deduced [34].

Electron lifetimes at low excitation energies can also be expected to be strongly affected by band structure effects in final unoccupied states: the electron lifetimes will not simply decrease with their energy and they will exhibit pronounced anisotropies [15]. New studies employing the STM techniques have been recently applied based on the investigation of the shape of the onset of electron tunneling into a surface state [35] and of the decay of the interface pattern in the local density of surface states in the step vicinity [36]. In these investigations structurally perfect parts of the surface can be analyzed and contributions of defects eliminated. Similarly, the role of finite temperature can be either taken into account or avoided when working at low temperatures.

4.3.3 Orbital orientation (peak intensities)

For the analysis of photoemission space distribution from surface atoms or bonds conservation laws are no more sufficient and some specific model of the photoemission process is necessary. For example, the simple geometrical idea about atomic shadowing in the electron path was adopted. In interpretations of pronounced azimuthal variations of electron photoemission from the d-part of the valence band in layered compound crystals [19] the shadowing concept provided incorrect conclusions. More successful was just the opposite idea of atoms acting like electron focussing lenses [38], in particular at higher electron energies. This model follows from the well-known fact that electron scattering probability from atoms has a strong forward contribution which clearly dominates at higher energies. The interpretations based on this simple idea (searchlight effect) succeeded in investigations of the surface crystallography of clean surfaces, of epitaxial layers and of molecular adsorbates [20]. More careful analysis revealed, however, that apart from focussing also defocussing effects [39] take place and that for more detailed investigations the photoemission process has to be treated more carefully.

Angular resolved photoemission, mostly with X-ray excitation of electrons from core levels to high energy states, is being used in the photoelectron diffraction for surface structure determinations [40]. For theoretical modelling cluster calculations either in single scattering approximation or with multiple electron scatterings are used.

Angular dependence of electron intensity emitted from oriented orbitals in atoms, which is expressed by the differential cross-section of photoemission, can be calculated in the one-step model by means of electron transitions from initial localized states into excited final delocalized states. The resulting electron space distribution gets extremely simply related to the initial state wave function if final state is approximated by a plane wave [41].Then the intensity of photoemitted electron distribution in space copies the initial orbital shape. This approxima-

tion is realistic at high electron energies (X-ray excitation), it describes well the main features of the azimuthal distributions for VUV excitations [19] and enables to chose the proper experimental geometry for the electron holography [42]. It fails to deliver more details at lower electron energies where the final electron state has to be described more realistically than by a simple plane wave. First, taking into account the atomic potential appears to be responsible for qualitative redistributions of photoemitted electrons which changes strongly with electron energy (interferences among different exit channels) as demonstrated in [43]. This modification of the final electron state may be dominant in emissions from isolated adsorbates when electron reflectivity from the underlying substrate is small. Second, multiple scatterings of an electron emitted from an atom with other atoms in the surface region introduces additional interfering paths into the final emitted electron distribution. When both of these effects have been taken into account [44] good agreement between experimental and theoretical azimuthal profiles has been achieved even in subtler details for excitations from d-levels in layered compounds [19]. In another example, excitation from a dangling bond surface state on GaAs(110), also very good agreement of experimental and theoretical azimuthal profiles of photoemission has been found [24]: the azimuthal distribution here is governed by the density of electrons in initial states but strongly superimposed by the space orientation of the dangling bonds. This result demonstrates the simultaneous impact of two aspects of studied orbitals: their spatial orientation and their translational periodicity along the surface.

From the theoretical analysis of the contributions from different regions in atoms [45] an important difference of the origin of ultraviolet and X-ray excited spectra appeared: whereas in XPS substantial contribution comes from the vicinity of atomic nucleus in UPS it is mostly the outer region of atoms which determines the photoemitted electron current, see Fig. 4.4.

Thus information about the bonds between surface atoms is reflected in the spectra obtained by means of ultraviolet radiation [45].

4.3.4 EDC spectra (profiles)

In addition to the analysis of individual EDC peaks and of their shifts and modifications with electron emission angle or excitation energy the overall picture of the valence band requires the whole shape of the EDC to be reasonably described in the one-step model. A proper description of initial and final electron states is needed to get photoemission intensities in ARUPS correctly, in particular at low energy excitations where band structure effects play an important role. In contrast to the three-step model in the one-step model electron states of a semi infinite crystal are to be used: bound states for initial occupied states and scattering (inverse LEED) states for unoccupied final states. These excited states are properly described by the self-energy Σ: its real part provides electron level shifts and its imaginary part determines electron and hole lifetimes due to electron-electron interactions. Comparison of various theoretical approaches to electron scattering states at crystal surfaces has been presented recently [54].

The self-energy is a rather complicated quantity (complex, energy dependent,nonlocal) and, therefore, various approximations have to be used. The simplest one describing homogeneous systems (jellium), is characterized by the energy dependent imaginary part (modelling thus the averaged electron mean-free path); a version of the local density approximation has been proposed recently to describe the inhomogeneity of the crystal and the results showed

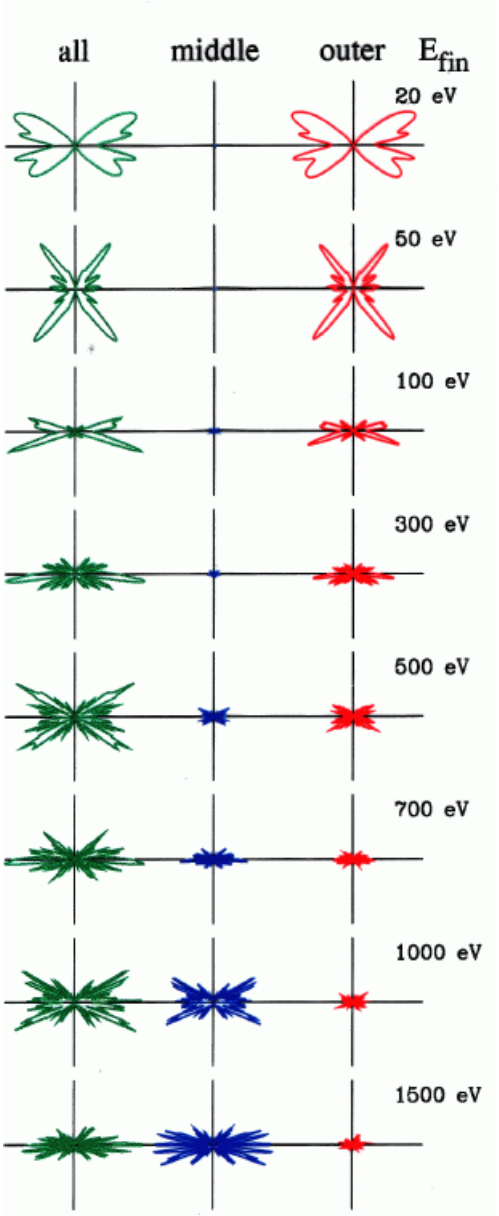

Figure 4.4: Spatial sensitivity of angular dependence on kinetic energy: photocurrent of excitation to several final energies E_{fin}, middle and outer region separated by sphere of radius of 0.3 Å from nucleus.

not only quite substantial deviations from the monotonous energy-dependence but also strong anisotropy of $\Sigma(k, E)$ in GaAs. [15]

Relatively straightforward tests of the quality of the final states above the vacuum level can be performed by means of elastic scattering of very low energy electrons (VLEED) from crystal surfaces and of closely related target current spectroscopy (TCS) where electric current through the sample is measured [46, 54].

Electron reflectivity in VLEED as a function of incident electron energy provides information about the electron band structure above the vacuum level E_v.For example, at normal incidence the absolute positions of band gaps in $E(k_\perp)$ and thus $Re\Sigma$ can be determined. From the peak widths also the information about the $Im\Sigma$ can be obtained: in this way evidence about its strong suppression at some energies in transition metals [48] has been found and about its anisotropy [49, 50] has been determined. Comparing TCS spectra with ab-initio calculations accurate information on $\Sigma(k, E)$ over an appreciable extent of the variables can be extracted [51]. Here, in contrast to photoemission where bound and scattering electron states are involved in determining the photoemission intensity, scattering states are isolated. These states may be slightly different due to the fact that a system with additional external electron is treated.

Depending on the value of the electron $\mathrm{Im}\,\Sigma$, i.e. the optical potential, the full range from direct transitions allowing a band mapping to dominance of the initial state's density (DOS) is covered with respect to the $k_\perp$-problem (correct choice of $k_\perp$) [52]. In the latter case e.g., a high density of states emerging in photoemission at a saddle point Van Hove singularity of low-dimensional systems may point at high critical temperatures of cuprate superconductors [53]. Limitations of a simple band mapping procedure occur in cases where translational symmetry is reduced (the translation period is increased) but the magnitude of the underlying atomic rearrangement or potential change is small. An example of such a change connected with translations along the surface represent surface reconstructions: translational period along the surface may be much bigger though the atomic displacements may be relatively small and limited to the topmost atomic layer. An example of a change in the direction perpendicular to the surface is given by superlattices where the thickness of individual components determines the enhanced translational period but the change of the effective potential may be rather small if a superlattice is composed from chemically similar components.

Intuitively it can be expected that the bulk electron structure cannot be changed strongly. Because of the backfolding of the bands into smaller Brillouin zone, on the other hand, new direct optical transitions should become possible. This contradiction is resolved if intensities of photoelectrons in the new channels are considered: they may be very small. This situation would be more reasonably described in terms of spectral representations $A(k, \omega)$ than just E(k).

The changes accompanying surface reconstructions may be illustrated on the c(4x4) reconstructed polar surface of GaAs(100). Here, the band mapping procedure applied to the surface state situated just below the valence band top requires shorter period in $E(k_\parallel)$ in both perpendicular higher symmetry directions along the surface: however, the experimental data show that only along $\overline{\Gamma}\ \overline{J'}$ the period is in agreement with the dimension of the Brillouin zone of the reconstructed surface; along $\overline{\Gamma}\ \overline{J}$ the period remains to correspond to the ideal surface [55]. The contradiction in the latter case was explained by a strong admixture of bulk states which contributes to the experimentally observed photoemission periodicity [56].

The translational period may be strongly increased in superlattices with regularly alternating crystalline epitaxial layers of different composition stacked during the growth process. Small dimension of the Brillouin zone in this direction is responsible for small E(k) dispersion in the direction perpendicular to the surface. Therefore, a simple feature distinguishing bulk states from surface states associated with dispersive or nondispersive character in this direction becomes inefficient. This behavior is developed already in superlattices with very thin components, e.g.in $(GaAs)_2(AlAs)_2$ [47, 57]. Because of the backfolding of the electron energy bands into smaller Brillouin zones the number of direct transitions allowed by energy and momentum conservation laws increases; these rules do not specify probabilities of allowed transitions and therefore the band mapping procedure becomes of limited value and the whole EDC profiles (experimental and theoretical) have to be compared. The intensities of photoemission in these materials with large unit cell in one direction may be, in addition, strongly influenced by electron confinement effects where electron localization in one part of the unit cell is encountered [58].

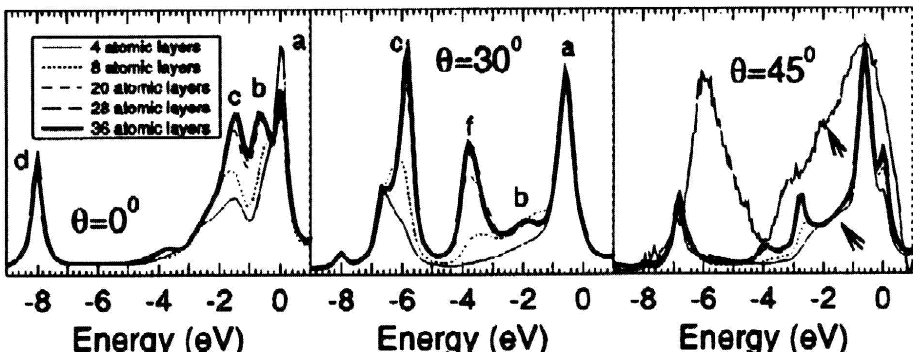

Figure 4.5: EDCs from GaAs(001)c4x4 in normal direction and along $\overline{\Gamma J}$ for HeI excitation; layer-resolved contributions, number counted from top, to photoemission intensity for electron emissions: (left) $\theta = 0^\circ$, (middle) $\theta = 30^\circ$, (right) $\theta = 45^\circ$; for 45° also experimental data are shown [56].

In particular, in the systems with larger unit cells the detailed interpretation requires to use complete information provided by the angular resolved photoemission: the full EDC profiles are to be compared with their theoretical counterparts. When good agreement is achieved, the detailed information extractable from theoretical modelling (contribution of individual layers, of individual atomic orbitals to the emitted intensity) can help in deep interpretation of the experimental spectra. For example, the important point in attributing the origin of individual features in the spectra to bulk or surface contributions can be solved investigating the byproducts of the theoretical calculation. Contributions of individual layers below the surface to the total photoemission intensity may converge gradually (bulk states) or the total outcome may be reached within the topmost layer (surface states) [56], see Fig. 4.5. Even a buried interface below 20 monolayers can still be detected in the EDC's, not through the photoexcitation of the atoms at the interface because of the prohibitively small escape depth but through the ground state wave function to be excited which experiences the interface as a kind of boundary condition [59].

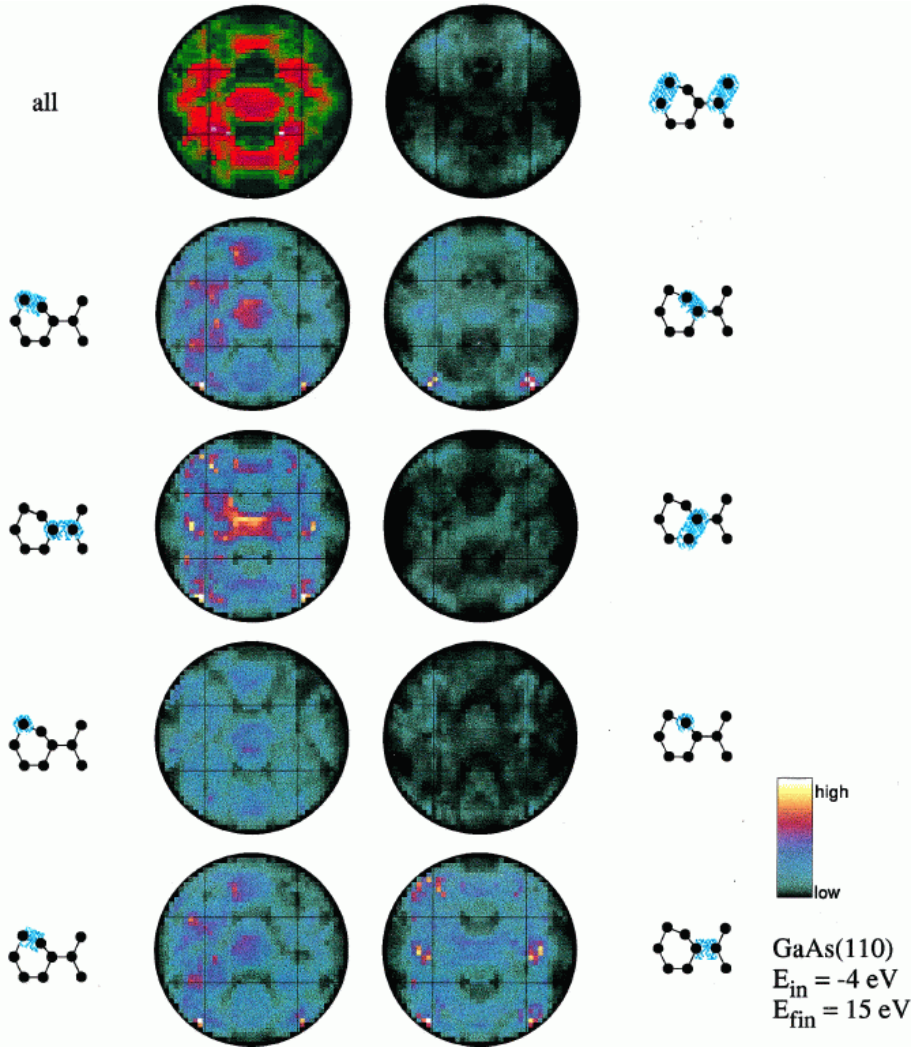

Figure 4.6: Local emissivity of extended initial states: hemispherical photocurrent plotted for selected spatial areas cutted out of the whole volume as depicted by the blue region in side view scheme of GaAs(110) surface aside each pattern; note that additionally interference between these areas exists and has to be taken into account. See also color figure on page 465.

In a similar way features in the hemispherical photoemission pattern can be traced back to special spatial emitting regions as shown in Fig. 4.6.

Also small changes in the angular distribution of the photoemission from adsorbates (or magnetic systems) when excited by left- or right- circularly polarized radiation can be adequately described by calculated angular plots [24, 40].

4.4 Summary

Angular resolved ultraviolet photoelectron spectroscopy provides rich information about the electron structure of crystals and of their surfaces. Basic characteristics like electron dispersion relation E(k) can be obtained relatively simply by band mapping procedures from the peak positions in the energy distribution curves. Quasiparticle features like lifetimes of excited states can be inferred in a straightforward manner from more detailed ARUPS peak widths studies and from two-photon time resolved spectroscopies. The experimental data represent important tests for theoretical descriptions of the electron structure in the ground state, about low-energy excitations and about the role of many-body effects there.

The full information from the angular resolved spectra (EDCs or angular plots) can be extracted when experimental data are reasonably described by corresponding calculations performed within the one-step model of photoemission. To this end, well resolved spectroscopic data from carefully prepared samples and calculations including all important interactions are required.

Acknowledgements

The work was supported by the DAAD and the BMBF, under contract nos. 05 SB8 FKA7, and TSR-075-97, as well as by the Grant Agency of the Academy of Sciences of the Czech Republic, grant no. A1010108.

References

[1] S.G. Davison, M. Steslicka: *Basic Theory of Surface States*, Clarendon Press, Oxford 1992.

[2] V. Heine, Proc. Phys. Soc. **81**, 1963.300.

[3] B Velický, I. Bartoš, J. Phys. **C4**, 1971, L104.

[4] F. García-Moliner, J. Rubio, Proc. Roy. Soc. **A324** (1971), 257.

[5] J.A. Appelbaum, D.R. Hamann, Phys. Rev. **B6** (1972), 2166.

[6] M. Schlüter, J.R. Chelikowski, S.G. Louie, M.L. Cohen Phys. Rev. **B12** (1975), 4200.

[7] A. Many, Y. Goldstein, N.B. Grover, *Semiconductor Surfaces*, North Holland 1965.

[8] N.D. Lang, Solid State Physics **28** (1973), 225.

[9] M. Kolář, I. Bartoš, Czech. J. Phys. **B23** (1973), 179.

[10] E.V. Chulkov, V.M. Silkin, P.M. Echenique, Surf. Sci. **437** (1999), 330.

[11] E.V. Chulkov, V.M. Silkin, P.M. Echenique, Surf. Sci. **391** (1997), L1217.

[12] G.D. Mahan, E.W. Plummer in *Electronic Structure*, (eds. K. Horn, M. Scheffler), North Holland 2000, p.954.

[13] A. Freeman, R. Asahi, A. Continenza, and R. Wu *this volume*

[14] R.W. Godby, in *Unoccupied Electronic States*, (eds. J.C. Fuggle, J.E. Inglesfield), Springer 1992.

[15] C.-H. Solterbeck, O. Tiedje, T. Strasser, S. Brodersen, A. Bodicker, W. Schattke, I. Bartoš, Journal Of Electron Spectroscopy and Rel. Phenomena **101-3** (1999), 473.

[16] E.W. Plummer, W. Eberhardt, in *Advances in Chemical Physics*, Wiley 1982,p.533.

[17] D. Samuelsen, E. Pehlke, W. Schattke, O. Anderson, R. Manzke, M. Skibowski, Phys. Rev. Letts. **68** (1992), 522.

[18] N.V. Smith, in *Photoemission in Solids I* (Eds. M. Cardona, L. Ley), Springer 1978.

[19] N.V. Smith, P.K. Larsen, in *Photoemission and the electronic properties of surfaces* (Eds. B. Feuerbacher, B. Fitton, R.f. Willis), Wiley 1978.

[20] S. Hüfner, *Photoelectron Spectroscopy*, Springer 1996.

[21] C.R. Ast, H. Höchst, Phys. Rev. Letts. **90** (2003) 016403.

[22] A. Bansil, M. Lindroos, Phys. Rev. Letts. **83** (1999) 5154.

[23] X. Gao, A.N. Koveshnikov, R.H. Madjoe, R.L. Stockbauer, R.L. Kurtz, Phys. Rev. Lett. **90** (2003) 037603.

[24] W. Schattke, Prog. Surf. Sci. **54** (1997), 211.

[25] T. Fauster, Prog. Surf. Sci. **46** (1994), 177.

[26] J.A. Knapp, F.J. Himpsel, D.E. Eastman, Phys. Rev. **B19** (1979), 4952.

[27] J.K. Grepstad, B.J. Slagsvold, I. Bartoš, J. Phys. **F12** (1982), 1679.

[28] N.V. Smith, P. Thiry, Y. Petroff, Phys. Rev. **B47** (1993), 15476.

[29] R. Matzdorf, Surf. Sci. Rep. **30** (1998), 153.

[30] A. Goldmann, R. Matzdorf, F. Theilmann, Surf. Sci. **414** (1998), L932.

[31] E. Knoesel, A. Hotzel, M. Wolf, Phys. Rev. **B57** (1998), 12812.

[32] H. Petek, H. Nagano, M.J. Weida, S. Ogawa, Chem. Phys. **251** (2000), 71.

[33] A. Gerlach, K. Berge, A. Goldmann, I. Campillo, A. Rubio, J.M. Pitarke, P.M. Echenique, Phys. Rev. **B64** (2001), 85423.

[34] T. Valla, A.V. Fedorov, P.D. Johnson, J. Xue, K.E. Smith, F.J. DiSalvo, Phys. Rev. Lett. **85** (2000) 4759.

[35] J. Li, W.D. Schneider, R. Berndt, O.R. Bryant, S. Crampin, Phys. Rev. Letts. **81** (1998), 4464.

[36] L. Bürgi, O. Jeandupeux, H. Brune, K. Kern, Phys. Rev. Letts. **82** (1999), 4516.

[37] J. Osterwalder, T. Greber, E. Wetli, J. Wider, H.J. Neff, Prog. Surf. Sci. **64** (2000), 65.

[38] W.F. Egelhoff, Jr., Phys. Rev. Letts. **59** (1987), 559.

[39] M.L. Xu, J.J. Barton, M.A. Van Hove, Phys. Rev. **B39** (1989), 8275.

[40] C.S. Fadley *et al.*, Prog. Surf. Sci. **54** (1997), 341.

[41] J.W. Gadzuk, Sol. St. Comm. **15** (1974), 1011, Phys. Rev. **B10** (1974), 5030.

[42] T. Greber, J. Wider, A. Verdini, A. Morgante, J. Osterwalder, europhysics news **32** (2001), 172.

[43] I. Bartoš, F. Máca, phys. stat. sol. **(b)99**,(1980), 755.

[44] A. Liebsch, Sol. St. Comm. **19** (1976), 1193.

[45] C. Solterbeck, W. Schattke, J.-W. Zahlmann-Nowitzki, K.-U. Gawlik, L. Kipp, M. Skibowski, C.S. Fadley, M.A. Van Hove, Phys. Rev. Letts. **79** (1997), 4681.

[46] I. Bartoš Prog. Surf. Sci. **59** (1998), 197.

[47] Y.Q. Cai, A.P.J. Stampfl, J.D. Riley, R.C.G. Leckey, B. Usher, L. Ley, Phys. Rev. **B46** (1992), 6891.

[48] R.C. Jaklevic, L.C. Davis Phys. Rev. **B26** (1982), 5391.

[49] I. Bartoš, M.A. Van Hove, M.S. Altman, Surf.Sci. **352-4** (1996), 660 .

[50] I. Bartoš M.A. Van Hove, M.S. Altman, Surf.Sci. **402-4** (1998), 697.

[51] E.E. Krasovskii, W. Schattke, V.N. Strocov, and R. Claessen, Phys. Rev. **B66** (2002), 235403.

[52] M. Lindroos, A. Bansil, Phys. Rev. Letts. **77** (1996), 2985.

[53] K. Gofron, J.C. Campuzano, A.A. Abrikosov, M. Lindroos, A. Bansil, H. Ding, D. Koelling, B. Dabrowski, Phys. Rev. Lett. **73** (1994), 3302.

[54] W. Schattke, Prog. Surf. Sci. **64** (2000), 89.

[55] J. Olde, G. Mante, H.P. Barnscheidt, L. Kipp, J.C. Kuhr, R. Manzke, M. Skibowski, J. Henk, W. Schattke, .Phys. Rev. **B41** (1990), 9958.

[56] T. Strasser, C. Solterbeck, W. Schattke, I. Bartoš, M. Cukr, P. Jiřiček, Phys. Rev. **B63** (2001), 85309.

[57] T. Strasser, C. Solterbeck, W. Schattke, I. Bartoš, M. Cukr, P. Jiřiček, C.S. Fadley, M.A. Van Hove, Phys. Rev. **B63** (2001), 195321.

[58] I. Bartoš, T. Strasser, W. Schattke, Surf.Sci. **507-10** (2002), 160.

[59] L. Aballe, C. Rogero, P. Kratzer, S. Gokhale, K. Horn, Phys. Rev. Letts. **87** (2001), 156801.

Solid-State Photoemission and Related Methods
Wolfgang Schattke, Michel A. Van Hove (Eds.)

5 Angle-resolved photoelectron spectroscopy: From photoemission imaging to spatial resolution

Kai Roßnagel, Lutz Kipp, and Michael Skibowski

5.1 Introduction

In the last two decades, angle-resolved photoemission spectroscopy (ARPES) has emerged as the most powerful probe of the momentum-resolved electronic structure of materials. This success story has largely been due to the construction of new sources for synchrotron radiation as well as due to the extreme progress in the field of spectrometer design. Today, modern photoelectron spectrometers not only provide very high energy and momentum resolution at a single electron emission angle, but automated angle scanning techniques also facilitate a full hemisphere mapping of the electron distribution in momentum space. As a consequence, ARPES has now become a powerful imaging technique providing very direct **k**-space images of band dispersions as well as of constant energy surfaces. Moreover, in combination with synchrotron radiation as a tuneable photon source the experimental restrictions of ARPES regarding full **k**-space accessibility are strongly relaxed and it is possible to study three-dimensional electronic structures in great detail.

In spite of the enormous potential of ARPES, however, there remains one disadvantage: the spatial resolution of the technique is generally limited to the spot size of modern light sources, i.e., generally to a few 100 μm. As one of the most important trends of photoemission spectroscopy, future efforts will tend to push down this limit by some orders of magnitude in order to be able to study the electronic properties of materials in the nanometer regime.

In this article the experimental technique of photoemission imaging will be introduced and its accuracy will be discussed on data of the layered transition metal dichalcogenide $TiTe_2$. This material serves as an excellent test case, since it provides a simple and intuitive connection between the measured photoemission images and the calculated three-dimensional band structure. We will then use the photoemission imaging technique to map the three-dimensional Fermi surface of layered $NbSe_2$ and investigate how Fermi surface geometry is related to the formation of charge-density waves in this compound. On surface states of GaAs(110), we will demonstrate how the spatial origin of photoelectrons can be deduced from photoemission intensity maps when they are compared to calculations within the one-step model of photoemission. And finally, we will introduce a more direct experimental approach to high spatial resolution in ARPES.

Solid-State Photoemission and Related Methods: Theory and Experiment. Edited by Wolfgang Schattke, Michel A. Van Hove

ISBN: 3-527-40334-5

5.2 Angle-resolved photoemission

The theory of angle-resolved photoemission has been excellently reviewed in this book by I. Bartos and W. Schattke. Therefore, we limit our discussion here to a few simple concepts that are necessary to understand intuitively the photoemission imaging technique.

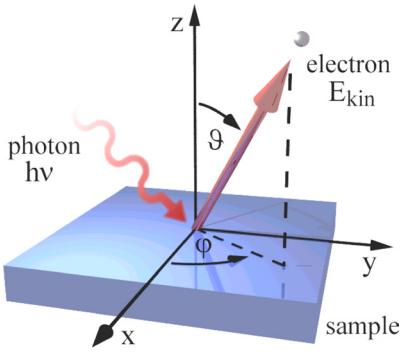

Figure 5.1: Basic principle of an angle-resolved photoemission experiment.

The general idea of an ARPES experiment is illustrated in Fig. 5.1. Monochromatic light of a given energy $h\nu$ is absorbed by a crystalline material and the intensity of the outgoing photoelectrons is measured as a function of their kinetic energy E_{kin} and emission angles ϑ and φ (other experimental parameters such as light polarization or electron spin will not be considered here). Via both energy and momentum conservation the measured quantities are directly related to the energy and momentum of the electrons inside the crystal, i.e., to the electronic band structure $E(\mathbf{k})$: the binding energy with respect to the Fermi level is simply given by

$$E = E_{kin} - h\nu + \Phi, \tag{5.1}$$

where Φ is the work function of the sample, and the surface-parallel wave vector $\mathbf{k}_\parallel$ can be calculated from the emission angles by

$$\mathbf{k}_\parallel = \sqrt{\frac{2m}{\hbar^2} E_{kin}}\, \sin\vartheta \begin{pmatrix} \cos\varphi \\ \sin\varphi \end{pmatrix}. \tag{5.2}$$

To arrive at Eq. (5.2), we had to make the assumption that the wave vector of the exciting photon is negligible compared to that of the electron, and we took advantage of the fact that the surface-parallel component of the wave vector $\mathbf{k}_\parallel$ is conserved while the electron is refracted at the boundary between the crystal and vacuum. In this process the surface-perpendicular component $k_\perp$ remains undetermined, so that additional information is needed to extract this value. Ideally, the problem is solved with previous knowledge from theory about the final states of photoemission for the investigated system. But often the straightforward approximation of a free-electron final state is already a very good starting point for describing the photoexcited electron within the solid.

In practice, for a fixed photon energy two experimental photoemission modes are most commonly applied to map the band structure of solids (see Fig. 5.2). Traditionally, complete

energy distribution curves (EDCs) were collected for rather few emission angles preferentially along high symmetry directions of the Brillouin zone. During the acquisition of an EDC, the variation of E_{kin} leads to simultaneous variation of the initial and final state energies, and if an allowed transition lies within the scanned energy window, a peak will appear in the photoemission signal. As illustrated in Fig. 5.2, an EDC closely corresponds to a (one-dimensional) vertical cut through $(E, \mathbf{k}_{\|})$ space.

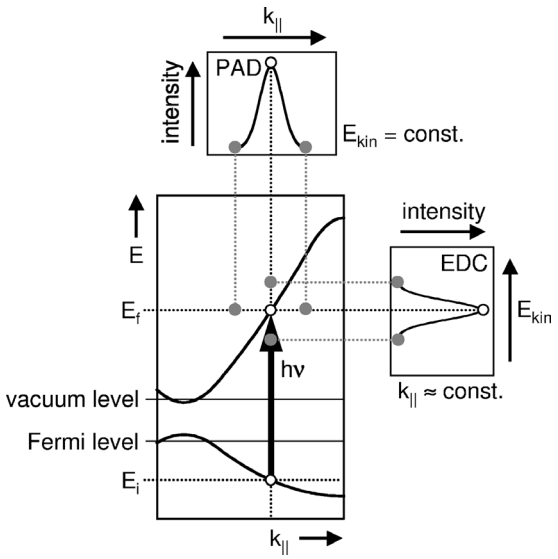

Figure 5.2: Electronic transitions for fixed photon energy in angle-resolved photoemission: mapping of the band structure $E(\mathbf{k}_{\|})$ in the EDC (energy distribution curve) and PAD (photoelectron angular distribution) mode. E_i and E_f denote the initial and final state energy.

In addition to the standard EDC, *photoelectron angular distributions* (PADs) have become very popular in recent years. In fact, this new way of data acquisition has turned ARPES into a powerful imaging technique, especially for Fermi surfaces [1,2]. In a PAD, we measure the intensity of photoelectrons with constant E_{kin} (i.e. constant initial and final state energy) as a function of the emission angles relative to the crystal and thus as a function of $\mathbf{k}_{\|}$. Hence, a PAD corresponds to a (two-dimensional) horizontal cut through $(E, \mathbf{k}_{\|})$ space, in which allowed transitions will again appear as a sharp rise in the photoemission signal (see Fig. 5.2).

Essentially, it is the combination of the two experimental procedures for locating energy bands that makes ARPES such a powerful technique. On the one hand, EDCs allow for a very accurate determination of band dispersions including band masses, band velocities and energy gaps, while on the other hand, PADs are used to image the topology of constant energy surfaces within **k**-space, particularly of Fermi surfaces.

5.3 Experimental considerations

As outlined above, measuring a PAD consists of sweeping the detected electron emission direction over the hemisphere above the sample surface and recording the photoemission intensity at the chosen kinetic energy. Two different experimental realizations have been followed for this procedure. First, display-type analyzers are used permitting very efficient parallel detection of a large piece of solid angle [3,4]. But in practice, these analyzers suffer from angular

distortions and limited energy resolution. Much more accurate measurements are carried out using sequential data acquisition of one angle or a small angle range at a time. In this second experimental approach either the sample is rotated and the analyzer is kept fixed in space or the sample is fixed and the analyzer is swept across the emission hemisphere. The principal difference between these two techniques is connected with the direction of light incidence: in the first case it is fixed relative to the electron emission direction, while in the second case it is fixed relative to the sample normal. Generally, both techniques provide equivalent information on the location of bands. However, the rotating analyzer technique is often preferred because the light polarization resides fixed inside the crystal and the resulting PADs thus contain additional information on the $\mathbf{k}_{\parallel}$ dependence of the photoexcitation matrix element which for example includes information on the orbital character of electronic states.

In the photoemission experiment of the University of Kiel at the Hamburger Synchrotronstrahlungslabor [5], from which all of the data presented here have been taken, an optimized hemispherical electron analyzer is rotated across the emission hemisphere by means of a two-axis goniometer (see Fig. 5.3). Angle-scanning is performed by computer-controlled stepper motors implementing a very high reproducibility and angular precision of 0.1°. Typically more than 3600 positions on the emission hemisphere are uniformly sampled in $\mathbf{k}_{\parallel}$ and at each angle several energy channels are detected. The acquisition time is in the range of 5 to 10 hours and energy and angular resolutions of better than 30 meV and 1° are routinely achieved.

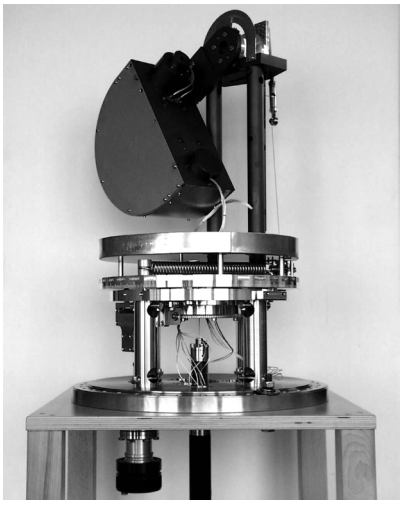

Figure 5.3: The ASPHERE spectrometer of the University of Kiel. The hemispherical analyzer is mounted on a two-axis goniometer.

5.4 Photoemission imaging: $TiTe_2$ as a test case

Alongside copper, the layered material $TiTe_2$ may be called the fruitfly of angle-resolved photoemission. $TiTe_2$ is characterized by conventional metallic transport properties, its electronic structure is simple and well known from both experiment and theory [6, 7], and it exhibits a

Ti $3d$-derived conduction band in close vicinity to the Fermi level whose photoemission spectra are remarkably free from any background or other emissions. Therefore, in many-body ARPES theory $TiTe_2$ has served as a prominent test case for Fermi liquid-type behavior [8, 9] as well as for the accuracy of Fermi surface determination [10, 11]. In addition, from the view of photoemission experiment, $TiTe_2$ has the advantage of producing a flat, clean and defect-free surface after simple cleavage in ultrahigh vacuum.

In order to illustrate the potential of the photoemission imaging technique, we present in Figs. 5.4(a) and 5.4(c) gray scale intensity maps that were taken from $TiTe_2$ at a photon energy of 24 eV using EDCs as well as PADs. In Fig. 5.4(a) a complete set of EDCs is shown taken as a function of angle along certain high symmetry azimuths and then mapped on to a regular $k_\parallel$ grid using Eq. (5.2). In this data representation the measured band dispersions can be compared directly to the corresponding calculated band structure [Fig. 5.4(b)] without employing any numerical fits. Although the experimental curves are smeared out due to the finite lifetimes of the initial and final states involved in the electronic transition, the correspondence between experimental and theoretical band dispersions is very good. In particular, we can identify all the predicted bands in the intensity map and confirm the semimetallic nature resulting from the small band overlap of the Ti $3d$-derived band at M and the two Te $5p$-dominated bands at Γ.

From the $E(\mathbf{k}_\parallel)$ representation of the band structure in Fig. 5.4(a) we can easily understand how the high emission intensities in the PADs in Fig. 5.4(c) are formed: direct transitions move through the constant energy chosen and lead to a relatively sharp intensity rise at the crossing $\mathbf{k}_\parallel$. These energy level crossings will naturally have some width in $\mathbf{k}$-space whereby the sharpness of the crossing mainly depends on the width of the energy peak and on the band velocity. For a flat dispersion, as e.g. for the Ti $3d$ band of $TiTe_2$ close to the Fermi level, the crossings will be rather broad and smeared out. Nevertheless, in the map taken at the Fermi energy we can clearly identify the well-known Fermi surface topology of $TiTe_2$ with the Ti $3d$-related ellipsoidal Fermi surface pockets centered on the M and M' points and the Te $5p$-derived pockets at the Brillouin zone center. In accordance with the calculated band structure, the Ti $3d$ emissions disappear at higher binding energies, while the Te $5p$ emissions become more intense and develop into a rather complex shape.

All PADs shown nicely reflect the topology of the constant energy cuts through the calculated band structure depicted in Fig. 5.4(d). However, there are some asymmetries in the measured contour intensities for $\mathbf{k}_\parallel$ points in the Brillouin zone that are otherwise related to each other by symmetry operations. In particular, two of the ellipsoidal Ti $3d$ Fermi surface pockets are almost completely suppressed. These strong photoemission intensity modulations are caused by the $\mathbf{k}_\parallel$ dependence of the excitation matrix element and are typical for experiments that have been carried out with polarized radiation in the rotating analyzer technique. In our case, linearly polarized synchrotron radiation enters from the right of the images at an angle of incidence of 45°. As can be seen, matrix element effects can obscure the band topology in some unfavorable cases, but quite generally we can say that any well-defined feature, regardless of its intensity, provides information on band locations in $\mathbf{k}$-space.

Now that we have seen the fascinating potential of photoemission imaging in revealing constant energy surfaces, we have to establish the accuracy of extracting band locations from

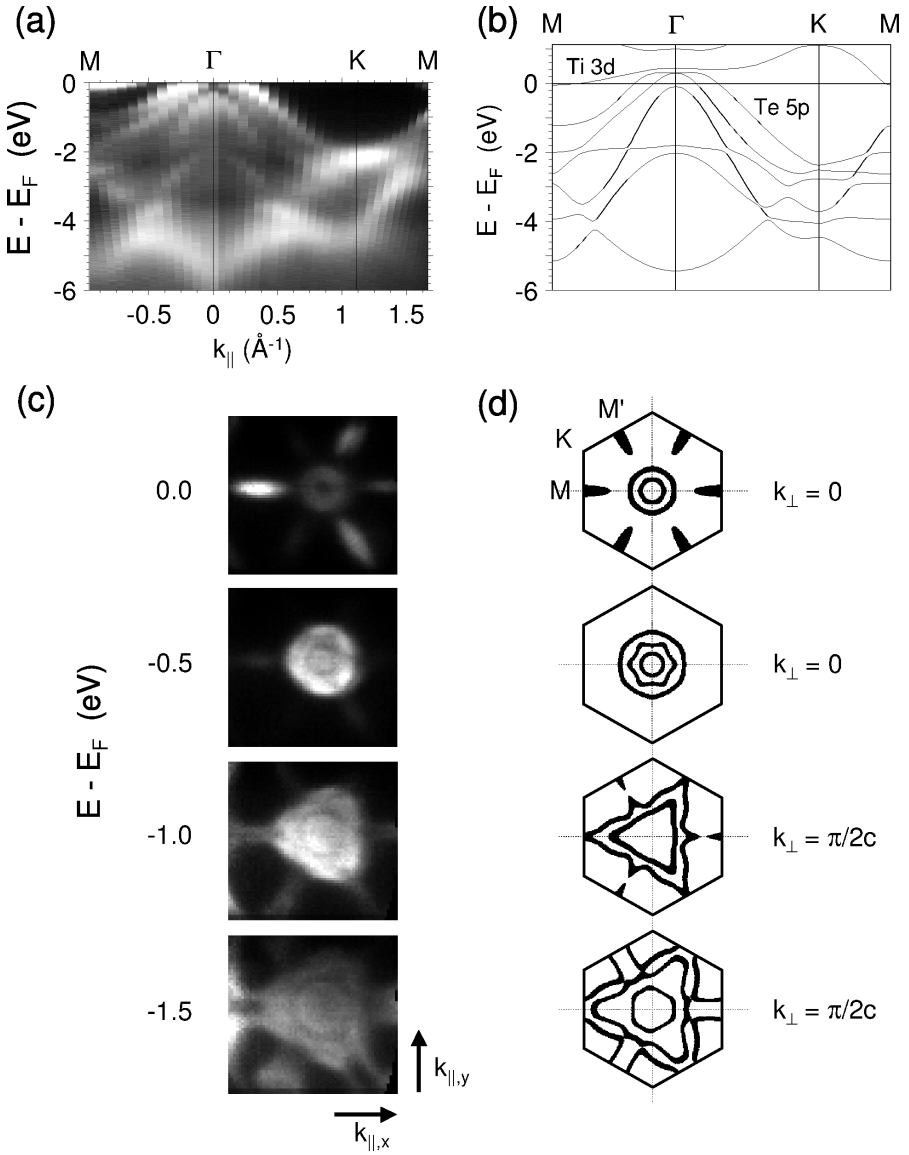

Figure 5.4: Photoemission images from $TiTe_2$. (a) Band mapping by ARPES: EDCs continuously taken as a function of polar angle along the ΓM direction and interpolated in $k_\parallel$ ($h\nu = 24\,\mathrm{eV}$). Photoemission intensity is represented in a linear gray scale with white corresponding to high intensity. (b) Corresponding theoretical band dispersions [7]. (c) Constant energy surface mapping by ARPES: PADs taken as a function of energy relative to the Fermi level ($h\nu = 24\,\mathrm{eV}$). (d) Corresponding horizontal cuts through the band structure $E(\mathbf{k}_\parallel)$ at certain values of $k_\perp$ [12].

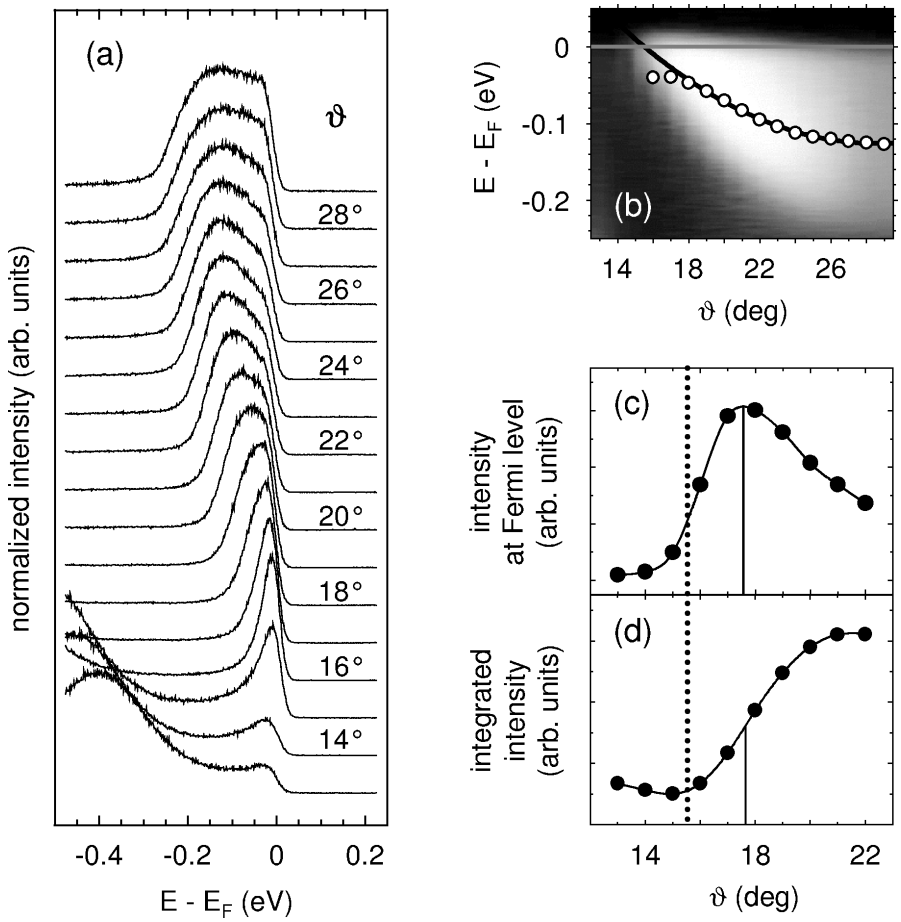

Figure 5.5: (a) Angle-resolved photoemission spectra of the Ti $3d$-related band along the ΓM direction of the Brillouin zone ($T = 30\,\mathrm{K}$, $h\nu = 19.5\,\mathrm{eV}$). (b) Gray scale representation of the photoemission spectra with white corresponding to high intensity. The energy versus emission angle dispersion of the center of gravity of the photoemission peak is indicated by open symbols. The thick solid line represents a polynomial fit to the data further away from the Fermi level. The extrapolated Fermi level crossing is at $15.5°$. (c) Photoemission intensity at the Fermi level. (d) Photoemission intensity integrated over the whole spectrum. Thin solid lines mark the positions of the maximum and the maximum gradient of the intensity, respectively. The dotted line indicates the Fermi level crossing obtained from (b).

these gray scale intensity maps. For this purpose we concentrate on the problem of Fermi surface determination. In Fig. 5.5(a) we display high-resolution EDCs measured on the Ti $3d$-derived band of $TiTe_2$ along the ΓM direction of the Brillouin zone at a temperature of 30 K. For high emission angles the ARPES peaks appear rather broad and asymmetric, while with decreasing ϑ they narrow considerably and shift closer to the Fermi level. Around $\vartheta = 16°$

the photoemission peak seems to have its smallest binding energy and width, and the strong intensity drop below indicates the Fermi level crossing. An extrapolation of the dispersion of the peak centroid quantitatively confirms the Fermi level crossing at $\vartheta_F = 15.5°$. We have to note, however, that near ϑ_F the center of gravity of the photoemission peak is not an adequate measure of the energy dispersion [see Fig. 5.5(b)].

Since PADs are taken at one single energy, we naturally do not gain information on band dispersions from these intensity maps. Hence, we need other methods to extract energy level crossings. In the case of Fermi surface maps, two criteria are most commonly applied to determine the Fermi vectors. The simplest method is to interpret a local maximum in the detected photoemission intensity at the Fermi energy as the Fermi level crossing of a conduction band. We will refer to this approach as the "maximum intensity method". Although this method has intuitive appeal and reproduces the band topology quite well [just compare the brightest contours in Fig. 5.4(c) with the theoretical ones in Fig. 5.4(d)], it is not at all clear how to justify the maximum intensity method from a physical point of view. In a simple approximation [13], the photocurrent in an ARPES experiment as a function of wave vector $\mathbf{k}$ and energy ω is given by the product of the transition matrix element $I_0(\mathbf{k})$ with the one-particle spectral function $A(\mathbf{k}, \omega)$, i.e.,

$$I(\mathbf{k}, \omega) = I_0(\mathbf{k}) A(\mathbf{k}, \omega) f(\omega) \tag{5.3}$$

where f is the Fermi-Dirac function. Though the spectral function exhibits in some cases a local maximum at the Fermi level crossing $(\mathbf{k}_F, E_F)$, the photocurrent will generally not.

Thus, to put the interpretation of Fermi surface maps on a more rigorous basis a second approach for extracting Fermi vectors has been proposed [10, 14]. This "maximum gradient method" is justified as follows: under the assumption of a weakly varying matrix element the *energy-integrated* ARPES spectrum is proportional to the momentum distribution function [15]

$$n(\mathbf{k}) = \int_{-\infty}^{\infty} d\omega \, f(\omega) \, A(\mathbf{k}, \omega) \tag{5.4}$$

and from Fermi-liquid theory it is well known that $n(\mathbf{k})$ drops discontinuously at the Fermi vector $\mathbf{k}_F$. Thus, the location of Fermi vectors can principally be determined from the extrema of the $\mathbf{k}$-space gradient of the energy-integrated ARPES intensity. In the experimental implementation of the maximum gradient method photoemission intensity has to be accumulated over a sufficiently wide energy range, ideally the entire conduction band width. In practice, the energy integration is often replaced by the finite energy resolution of the photoelectron spectrometer, but there is nonetheless a need to check on the adequate energy integration window, especially in the case of overlapping bands, which may lead to spurious peaks in the gradient map.

In Fig. 5.5(c) and 5.5(d) we present the photoemission intensity at the Fermi level and the intensity integrated over the whole spectrum as a function of the emission angle. The data were taken from the EDC series shown in Fig. 5.5(a) with the true, i.e., non-normalized intensity variations. As can readily be seen, both criteria—the maximum intensity as well as the maximum gradient method—locate the Fermi level crossing at $17.6°$ ($k_\parallel = 0.598\,\text{Å}^{-1}$). With respect to the value extrapolated from the dispersion of the peak centroid ($15.5°$ or

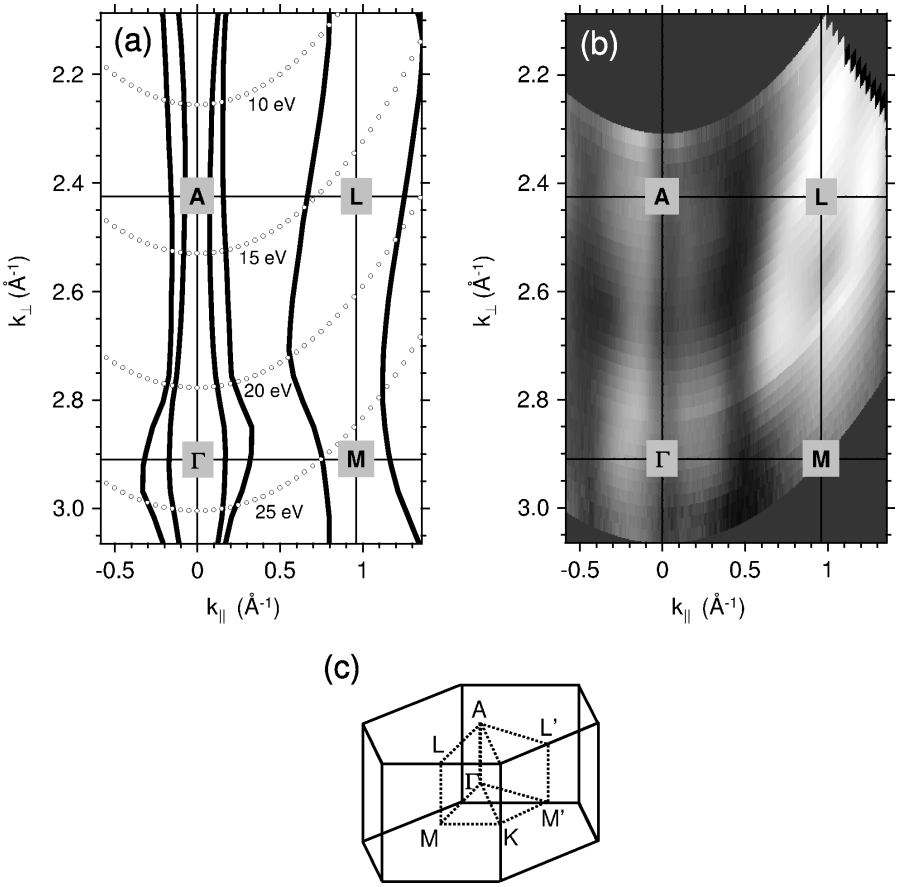

Figure 5.6: Fermi surface sections of $TiTe_2$ in a high symmetry plane perpendicular to the surface of the sample. (a) Theoretical Fermi surface (thick solid lines) obtained by bulk band structure calculation [7]. Open circles indicate free-electron final states for several photon energies. (b) Experimental Fermi surface map obtained by angle-resolved photoemission spectroscopy at photon energies from 11 to 26 eV. Photoemission intensity is represented in a logarithmic gray scale with white corresponding to high intensity. (c) Sketch of the Brillouin zone with all relevant high symmetry points.

$0.529\,\text{Å}^{-1}$, respectively) this corresponds to an experimental error in Fermi surface determination of $\Delta k_{\|} = 0.069\,\text{Å}^{-1}$ or about 7% of the relevant Brillouin zone dimension. Quite obviously, this error arises from a strong $\mathbf{k}_{\|}$ dependence of the transition matrix element. In other systems with stronger band dispersion and less varying matrix element the error in extracting energy level crossings might be smaller, but in general we have to keep in mind that PADs and particularly Fermi surface maps are not as reliable as the beauty of the electronic structures they reveal suggests.

As mentioned earlier, there is an implicit uncertainty of $k_\perp$ in the photoemission process. In fact, we do not know a priori at which value of $k_\perp$ the intensity maps in Figs. 5.4(a) and 5.4(c) are taken. The surface-perpendicular component of the wave vector is only implicitly given by the condition that the photon energy connects initial and final states in a direct transition. Thus, the determination of $k_\perp$ requires knowledge of the final state band dispersion which is generally not available. However, final states can often reasonably well be approximated by a simple free-electron-like dispersion, and we will now establish the precision with which a three-dimensional Fermi surface is represented by the mapping technique when using these free-electron final states for data interpretation.

In order to map the shape of a three-dimensional Fermi surface we have to measure the intensity of photoelectrons emitted from the Fermi level as a function of angle and photon energy, i.e., we make use of tuneable synchrotron radiation. In Fig. 5.6(b) we show such an intensity plot for the ΓMAL plane of $TiTe_2$ mapped on to a $k_\perp$ versus $k_\parallel$ grid. The surface-parallel component of the wave vector has been determined using Eq. (5.2) and $k_\perp$ has been calculated from the free-electron formula

$$E_{kin} + V_0 = \frac{\hbar^2}{2m}(k_\parallel^2 + k_\perp^2) \tag{5.5}$$

where V_0 denotes the so-called inner potential. In our case, a value of $V_0 = 14\,\mathrm{eV}$ gives the best fit between the experimental map and the theoretical Fermi surface cut shown in Fig. 5.6(a): the topology of the calculated Fermi surface with the Te $5p$ bands close to the ΓA line and the Ti $3d$ band near the ML line is clearly mimicked by the measured contours.

From Fig. 5.6 it is obvious that EDCs we refer to as measured e.g. "along the ΓM direction" are actually not scanned along this high symmetry line but rather along some parabolic path in the ΓMAL plane. Also, the PADs shown in Fig. 5.4(c) do not reflect horizontal but parabolic cuts through three-dimensional **k**-space. However, from the good agreement of the experimental maps and the constant energy cuts through the calculated band structure in Fig. 5.4 we can conclude that no pronounced $k_\perp$ effects occur within the individual PADs from $TiTe_2$. This observation is of course related to the relatively weak three-dimensional character of this layered material.

The agreement found in Fig. 5.6 for the experimental and theoretical Fermi surface contours puts in evidence that the free-electron final state approximation is a very good starting point for three-dimensional **k**-space mapping. Additionally, since the measured contours are quite sharp, it appears that $k_\perp$ is relatively well defined. We can estimate the uncertainty in determining $k_\perp$ to about $0.2\,\text{Å}^{-1}$, whereby this error is partly due to the uncertainty associated with the inner potential of the free-electron final states and partly due to the intrinsic uncertainty in $k_\perp$ which is a consequence of the principal relaxation of $k_\perp$ conservation caused by the damping of the initial and final states in the solid. So, we finally end up with the conclusion that photoemission images are very well suited for mapping band topologies within three-dimensional **k**-space, but that the accuracy of extracting exact band locations from these images is rather limited to about $5 - 20\%$ of a typical Brillouin zone dimension.

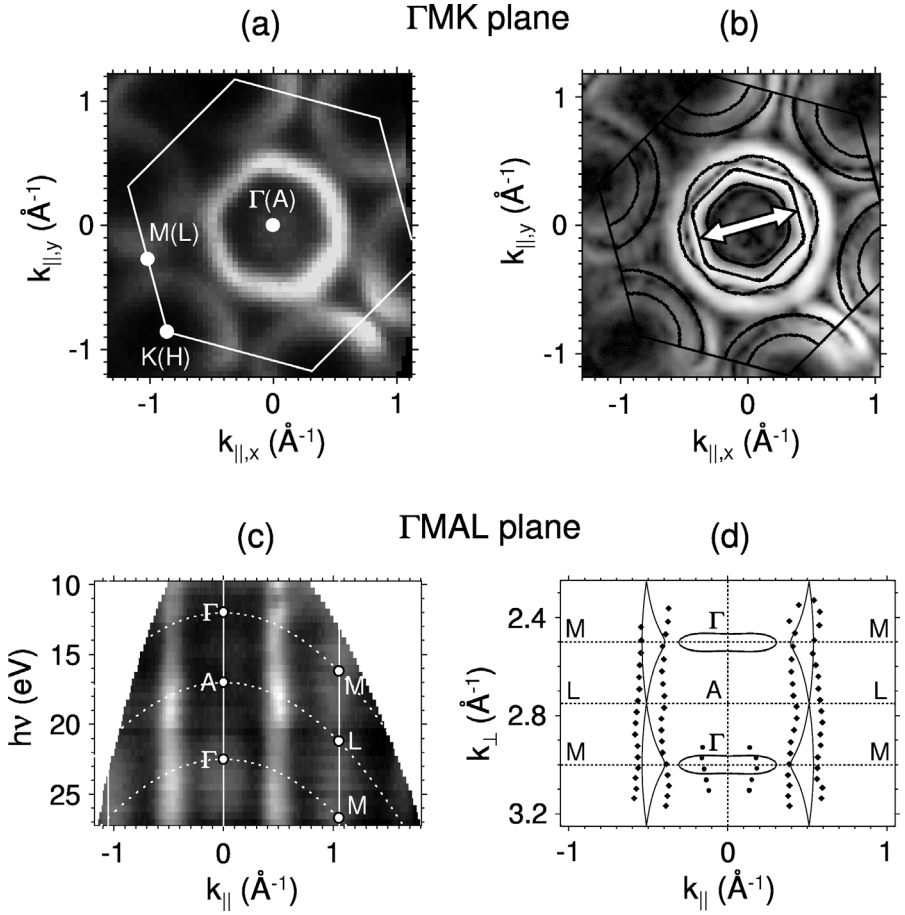

Figure 5.7: Fermi surface mapping of $NbSe_2$ by ARPES at $T = 50\,\mathrm{K}$ (left panel) and theoretical Fermi surface obtained by bulk band-structure calculations (right panel). Panel (a) shows the $\mathbf{k}_\parallel$ distribution of the photoemission intensity measured at $h\nu = 24.5\,\mathrm{eV}$ and panel (b) shows the modulus of the two-dimensional intensity gradient in comparison with the calculated Fermi surface cut at $k_\perp = 0$. A possible Fermi surface nesting vector is indicated. The $k_\perp$ dependent Fermi surface mapping obtained by polar angle scans along the ΓM direction of the Brillouin zone recorded at $h\nu = 10 - 27\,\mathrm{eV}$ is given in (c). The dashed lines illustrate the $h\nu$ dependence of $k_\perp$ along the zone boundaries. (d) The corresponding theoretical Fermi surface cut is compared to the locations of the maximum photoemission intensity gradient (indicated by filled symbols). The respective $k_\perp$ values are determined assuming free-electron final states. In (a), (b), and (c) the photoemission intensity is represented in a linear gray scale with white corresponding to high intensity. The Brillouin zone and the high-symmetry points are indicated.

5.5 Three-dimensional Fermi surface mapping: $NbSe_2$

As an example where the photoemission imaging technique can provide valuable information on the underlying physics of an interesting material, we present in Fig. 5.7 Fermi surface measurements on $NbSe_2$ [16]. This layered transition metal dichalcogenide undergoes a second-order phase transition into an incommensurate two-dimensional charge-density-wave (CDW) phase at 33.5 K, i.e., below this temperature the conduction electron density and the crystal lattice are periodically modulated. As confirmed by neutron scattering, the three equivalent CDW wave vectors of the hexagonal Brillouin zone are aligned parallel to the ΓM directions and have a magnitude of $0.688\,\text{Å}^{-1}$, this value being slightly temperature dependent [17].

In general, the occurrence of a CDW in low-dimensional materials is explained by an instability of the Fermi surface with the CDW wave vector given by the so-called nesting condition, which means that the CDW wave vector has to span large parallel portions of the Fermi surface. Evidently, three-dimensional Fermi surface mapping making use of synchrotron radiation is very well suited to verify this simple picture and probe the parallelism of certain Fermi surface sheets. And in fact, we find in Fig. 5.7(c) that the critical Fermi surface parts of $NbSe_2$, i.e., those parts of the central hexagon [see Fig. 5.7(a) and 5.7(b)] that are connected by the vector indicated in Fig. 5.7(b), are fairly parallel with respect to the $k_\perp$ axis. This high degree of two dimensionality—even higher than expected from the calculation shown in Fig. 5.7(d)—strongly suggests that the driving mechanism for the transition into the CDW state in $NbSe_2$ is indeed a simple Fermi surface nesting. However, this interpretation has to be contrasted with the fact that the distance between the critical Fermi surface features is larger than $0.8\,\text{Å}^{-1}$ as we can directly read off from Fig. 5.7(d). Since this value is quite far off the experimentally observed value of $0.688\,\text{Å}^{-1}$, it becomes obvious that simple Fermi surface nesting is not a sufficient explanation for the CDW phase transition in $NbSe_2$. Hence, we have to conclude our brief analysis of Fermi surface topology of $NbSe_2$ here with the statement that an appropriate model for the CDW phase transition in this compound must include a more sophisticated approach to electron-phonon interaction than the simple Fermi surface nesting model does.

5.6 Spatial origin of photoelectrons: GaAs(110) surface states

As we have seen above, angle-resolved photoemission is a very powerful technique for studying the electronic structure of solids. However, in the presented experimental results ARPES has only been used to investigate the energy positions of valence bands in three-dimensional **k**-space. That is, the intensities of the spectral peaks were not analyzed quantitatively and the information contained in the matrix element prefactor in Eq. (5.3) was omitted. One reason for this limitation in photoemission studies is the lack of any simple rules for explaining such spectra beyond those that have been found useful for band mapping. In angle-resolved photoemission the most often applied model is that of direct (wave-vector-conserving) transitions between bulk bands [20], with the final state often simplified to a plane wave [21]. Beyond this, free-electron final states with atomic like optical transitions [22, 23] and final state scattering of electrons emerging from a localized core orbital [24, 25] have been used to better

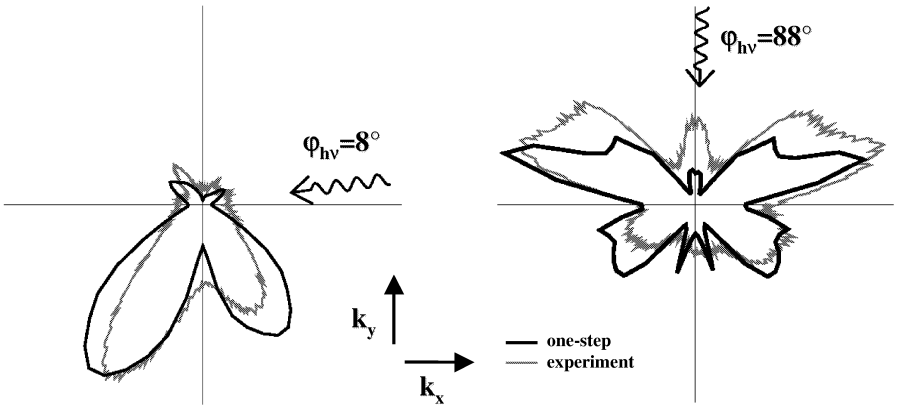

Figure 5.8: Measured (gray) and calculated (black) photocurrents at $k_{\parallel} = 0.6$ Å^{-1} for the dangling bond (left) and back bond (right) surface states of GaAs(110). Azimuthal angles of the incident light are indicated.

understand the resulting angular distributions in photoemission. Recently, the highly accurate one-step model of photoemission [26] has been applied to calculate photoemission intensities [27–29]. Measurements of photoelectron angular distributions (PADs) in combination with calculations then yield information about wave functions participating in the photoemission process [30].

Applying the PAD mode of ARPES on cleaved GaAs(110) surfaces we show two examples for the characteristic angular dependence of the photocurrent delivered by different surface states (Fig. 5.8). The polar plots show a comparison of experimental (light gray) and theoretical (dark gray) photocurrents at constant absolute wave vector of $k_{\parallel} = 0.6$ Å^{-1} for the dangling bond (left plot) and back bond surface state (right plot) of GaAs(110). Calculations of the photocurrent were performed in the highly accurate one-step model of photoemission [30]. Note the excellent agreement between the experimental and theoretical spectra. Calculated intensities very well reproduce the characteristic spectral features observed experimentally.

From photoemission experiment alone it is not possible to deduce the spatial origin of photoelectrons contributing to particular spectral features. In combination with theory accurately describing the experimental spectra, however, such information can be delineated. In Fig. 5.9 calculations of the back bond surface state photocurrent are shown when the integration runs over different areas in real space. Partial photocurrents emerging from the middle and outer areas around the Ga and As surface atoms are shown in comparison to the total current. The current from the middle region which is the spherical volume between radii of 0.08 and 0.29 Å around the As cores and 0.09 and 0.3 Å around the Ga is magnified by 100 relative to that from the outer region. The outer region is the space outside these spheres. It is evident that the main contribution to the photocurrent comes from the bonding region. From the localized middle area arises less than 1% of the total current. Contributions from the

innermost part are even smaller and completely negligible. This example demonstrates that measurements of photoelectron angular distributions in combination with theoretical calculations within the one-step model allow to delineate the spatial origin of VUV photoelectrons. It may be viewed as an extrapolation of X-ray photoelectron diffraction (XPD) towards low kinetic energies. Whereas with the effective localization at the core the XPD patterns reflect the geometry, angle-resolved photoemission in the VUV probes the bonding region with an intensity distribution showing information about the bonds.

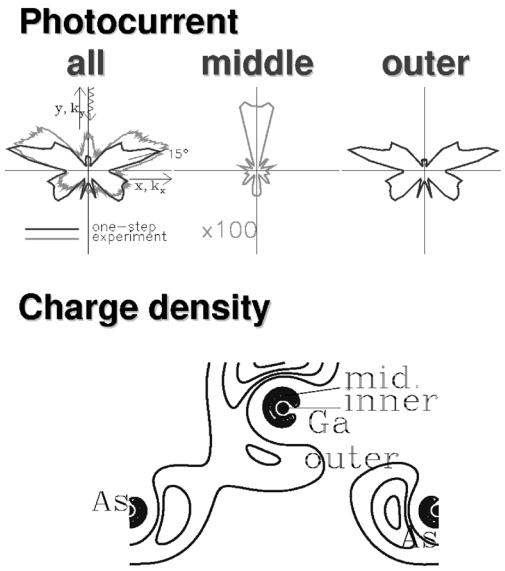

Figure 5.9: Spatial origin of VUV photoelectrons from GaAs(110). Summations of theoretical photocurrents over different spatial regimes.

5.7 Angle-resolved photoelectron nanospectroscopy

A more direct approach to spatial resolution in angle-resolved photoemission spectroscopy could be achieved by focusing the exciting radiation to very small spot sizes which then define the spatial resolution. Scanning the spot across the sample then provides a spatial resolved image of the electronic structure. However, spot sizes that can be achieved with 3rd generation synchrotron light sources are well above the micron scale. Using Fresnel zone plates to further focus the radiation down to about 30 nm can be achieved today. The intensity contained in the focus, however, is low such that angle-resolved measurements of photoemission are hardly possible on acceptable time scales.

Fourth-generation light sources based on free-electron lasers (FEL) will be capable of producing X-rays of such extreme brilliance that new ways of focusing the radiation will emerge. A device based on the simple concept of an array of pinholes, could be possible. The 'photon sieve' [31] exploits the monochromaticity and coherence of light from a free-electron laser to focus soft X-rays with unprecedented sharpness. The combination of an excellent focus with extreme flux will provide new opportunities for photoelectron spectroscopy with highest angle, energy *and* spatial resolution.

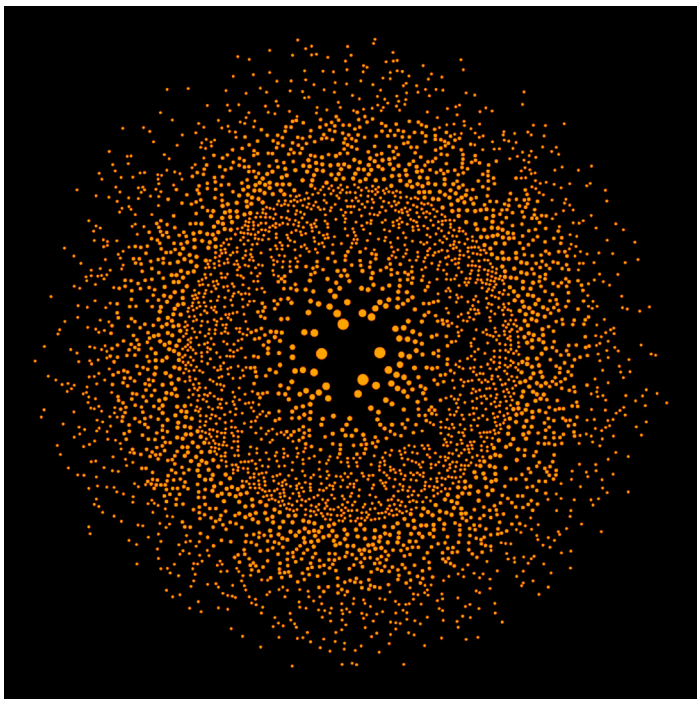

Figure 5.10: Photon sieve. Tens of thousands to millions of pinholes are arranged to diffract light or X-rays to a small focus.

Light passing a circular pinhole produces a diffraction pattern of concentric rings of decreasing width with increasing radius. If light is passed through a mask made up of the same pattern of rings a focus is formed. These Fresnel zone plates are used to focus soft X-rays where conventional optics fail because of strong absorption of all materials in this spectral region.

The ultimate resolution of a Fresnel zone plate is determined by the width of the outermost zone. The focal spot is surrounded by rings of intensity (secondary maxima) that blur the images obtained in X-ray microscopy and scanning spectroscopy.

These limitations can be overcome by using a large number of appropriately distributed pinholes instead of rings as the diffracting elements. To obtain a distinct first-order focus, the pinholes have to be positioned such that the optical path length from the source via the center of the pinholes to the focal point is an integral number of wavelengths.

The diameter of the pinholes is not limited by the width of the corresponding Fresnel zone. It can in fact be larger and yields a maximal contribution to the focus for a diameter of about 1.5 times the width of the zone. For larger pinholes up to about 2.4 times the ring width the contribution decreases but it still remains positive. This allows pinholes to be positioned on Fresnel zones that are narrower than the fabrication limit (20–40 nm) and the spatial resolution of the optical element could be better than 10 nm.

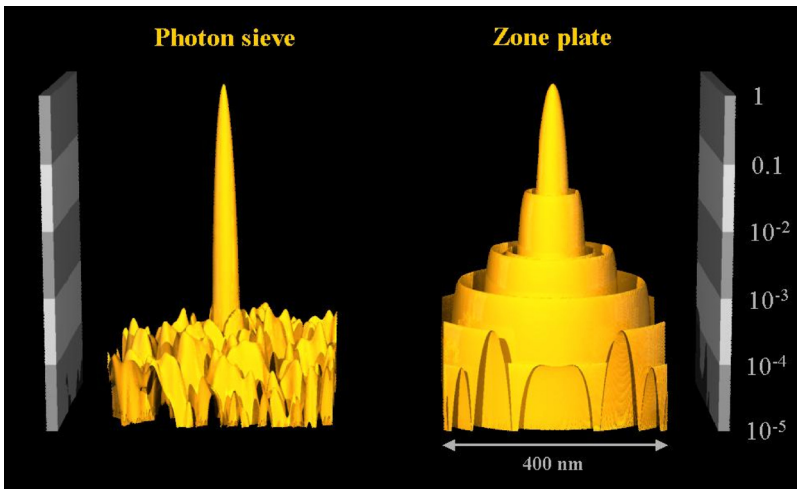

Figure 5.11: Intensity distribution on the focal plane of a photon sieve compared to a zone plate. Smallest structure size for both optical elements is 30 nm. For the photon sieve, the suppression of the secondary maxima is evident. This provides sharper images. See also color figure on page 466.

Furthermore, with photon sieves, the unwanted ring-like secondary maxima generated by zone plates can be suppressed. For a zone plate each ring contributes equally to the amplitude in the focus. This contribution drops abruptly to zero beyond the outermost ring which leads to strong intensity oscillations in the diffraction pattern. With a photon sieve the number of pinholes per ring can be readily adjusted to yield a smooth transition which minimizes the secondary maxima.

The development of fourth-generation synchrotron light sources that deliver coherent radiation in the soft X-ray regime in combination with photon sieves will provide a wealth of new opportunities in X-ray microscopy, spectroscopy and lithography. Photon sieves for use at the Hamburg Free-Electron Laser facility (HASYLAB at DESY) are currently being developed.

5.8 Conclusions

Photoelectron spectroscopy with high energy and angular resolutions applied to prototype examples ranging from two-dimensional layered transition metal dichalcogenides to covalent semiconductor surfaces has revealed a wealth of new information on the electronic structure of geometrically well defined samples going far beyond ”simple band mapping” which was the early domain of angle-resolved photoemission. However, on the way to extract more subtle information from spectroscopic results sophisticated theories become more and more important. Imaging wave functions and Fermi surfaces as well as probing spatial distributions of valence charges at VUV energies and their redistribution during phase transitions or reconstructions with highest spatial resolutions may be viewed as promising future directions interfacing experiment and theory.

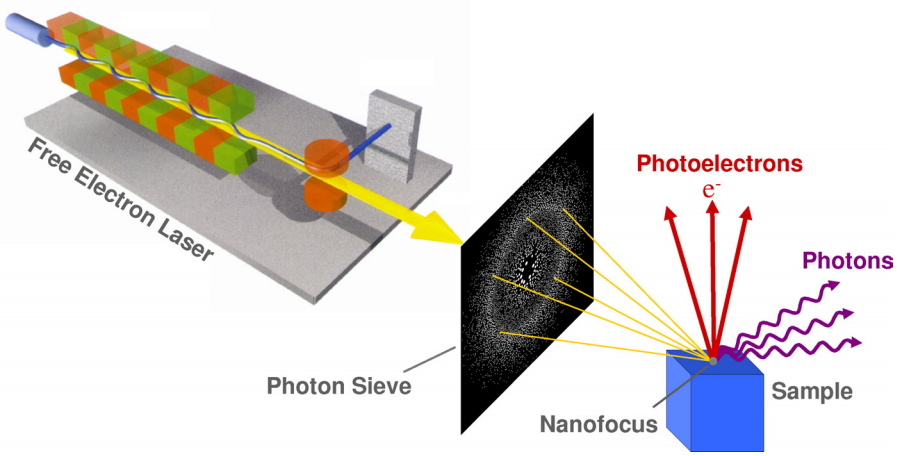

Figure 5.12: Schematic of a nanospectroscope capable of recording high-resolution images revealing chemical composition, morphology, and the electronic properties of materials in the nanometer regime. See also color figure on page 466.

Acknowledgements

The experimental work reviewed here is based on close collaboration with M. Skibowski, R. Adelung, K. Gawlik, S. Harm, O. Seifarth and J. Zahlmann-Nowitzki and with the theory groups of J. Pollmann and W. Schattke, in particular P. Krüger, A. Mazur, C. Solterbeck, T. Strasser and D. Voß. The authors are very grateful for their numerous individual contributions.

This research is supported by the BMBF, Germany (project Nos. 05 SE8 FKA and 05 SB8 FKB) and DFG Forschergruppe DE 412/21.

References

[1] A. Santoni, L.J. Terminello, F.J. Himpsel, and T. Takahashi, Appl. Phys. A **52**, 229 (1991).

[2] P. Aebi, J. Osterwalder, P. Schwaller, L. Schlapbach, M. Shimoda, T. Mochiku, and K. Kadowaki, Phys. Rev. Lett. **72**, 2757 (1994).

[3] D.E. Eastman, J.J. Donelon, N.C. Hien, and F.J. Himpsel, Nucl. Instrum. Meth. **172**, 327 (1980).

[4] H. Nishimoto, H. Daimon, S. Suga, Y. Tezuka, S. Ino, I. Kato, F. Zenitani, and H. Soezima, Rev. Sci. Instrum. **64**, 2857 (1993).

[5] K. Rossnagel, L. Kipp, M. Skibowski, and S. Harm, Nucl. Instrum. Methods Phys. Res. A **467-468**, 1485 (2001).

[6] R. Claessen, R.O. Anderson, G.-H. Gweon, J.W. Allen, W.P. Ellis, C. Janowitz, C.G. Olson, Z.X. Shen, V. Eyert, M. Skibowski, K. Friemelt, E. Bucher, and S. Hüfner, Phys. Rev. B **54**, 2453 (1996).
[7] K. Rossnagel, L. Kipp, M. Skibowski, C. Solterbeck, T. Strasser, W. Schattke, D. Voß, P. Krüger, A. Mazur, and J. Pollmann, Phys. Rev. B **63**, 125104 (2001).
[8] R. Claessen, R. Anderson, J. Allen, C. Olson, C. Janowitz, W. Ellis, S. Harm, M. Kalning, R. Manzke, and M. Skibowski, Phys. Rev. Lett. **69**, 808 (1992).
[9] S. Harm, R. Dürig, R. Manzke, M. Skibowski, R. Claessen, and J.W. Allen, J. Electron Spectrosc. Relat. Phenom. **68**, 111 (1994).
[10] Th. Straub, R. Claessen, P. Steiner, S. Hüfner, V. Eyert, K. Friemelt, and E. Bucher, Phys. Rev. B **55**, 13473 (1997).
[11] L. Kipp, K. Rossnagel, C. Solterbeck, T. Strasser, W. Schattke, and M. Skibowski, Phys. Rev. Lett. **83**, 5551 (1999).
[12] D. Voß, Ph.D. thesis, University of Münster, 2000.
[13] P.J. Feibelman and D.E. Eastman, Phys. Rev. B **10**, 4932 (1974).
[14] J.C. Campuzano, H. Ding, M.R. Norman, M. Randeria, A.F. Bellman, T. Yokoya, T. Takahashi, H. Katayama-Yoshida, T. Mochiku, and K. Kadowaki, Phys. Rev. B **53**, R14737 (1996).
[15] M. Randeria, H. Ding, J.-C. Campuzano, A. Bellmann, G. Jennings, T. Yokoya, T. Takahashi, H. Katayama-Yoshida, T. Mochiku, and K. Kadowaki, Phys. Rev. Lett. **74**, 4951 (1995).
[16] K. Rossnagel, O. Seifarth, L. Kipp, M. Skibowski, D. Voß, P. Krüger, A. Mazur, and J. Pollmann, Phys. Rev. B **64**, 235119 (2001).
[17] D.E. Moncton, J.D. Axe, and F.J. DiSalvo, Phys. Rev. Lett. **34**, 734 (1975).
[18] M. Skibowski and L. Kipp, J. Electron Spectr. Rel. Phen. **68**, 77 (1994).
[19] X. Zhu, S. Zhang, S. Louie, and M. Cohen, Phys. Rev. Lett. **63**, 2112 (1989).
[20] N.V. Smith, Phys. Rev. Lett. **23**, 1452 (1969).
[21] Z. Hussain, S. Kono, L. Petersson, C.S. Fadley, and L.F. Wagner, Phys. Rev. B **23**, 724 (1981).
[22] J.W. Gadzuk, Solid State Commun. **15**, 1011 (1974).
[23] J.W. Gadzuk, Phys. Rev. B **12**, 5608 (1975).
[24] A. Liebsch, Phys. Rev. Lett. **32**, 1203 (1974).
[25] A. Liebsch, Phys. Rev. B **13**, 544 (1976).
[26] J.B. Pendry, Surf. Sci. **57**, 679 (1976).
[27] J. Henk, W. Schattke, H. Barnscheidt, C. Janowitz, R. Manzke, and M. Skibowski, Phys. Rev. B **39**, 13286 (1989).
[28] J. Henk, W. Schattke, H. Carstensen, R. Manzke, and M. Skibowski, Phys. Rev. B **47**, 2251 (1993).
[29] C. Solterbeck, W. Schattke, and C.S. Fadley, Surf. Sci. **357–358**, 245 (1996).
[30] C. Solterbeck, W. Schattke, J. Zahlmann–Nowitzki, K. Gawlik, L. Kipp, M. Skibowski, C.S. Fadley, and M. Van Hove, Phys. Rev. Lett. **79**, 4681 (1997).
[31] L. Kipp, M. Skibowski, R.L. Johnson, R. Berndt, R. Adelung, S. Harm, and R. Seemann, Nature **414**, 184 (2001).

Solid-State Photoemission and Related Methods
Wolfgang Schattke, Michel A. Van Hove (Eds.)

6 Electronic states of magnetic materials

Franz J. Himpsel and K.N. Altmann

6.1 Introduction

Interest in the electronic structure of magnetic materials is growing with the advent of new magnetic materials that are tailored on the nanometer scale for applications in data storage, permanent magnets, and many other areas. The growing field of magnetoelectronics is based on the notion that the spin of an electron can play an equally important role as the charge in microelectronics. In fact, various "spintronic" devices have already been realized, such as reading heads for hard disks which use the effect of giant magnetoresistance (GMR) in magnetic multilayers. The latest improvements of these devices require engineering of magnetic interfaces down to the atomic scale for achieving maximum spin selectivity. Other magnetoelectronic devices have been prototyped, such as the magnetic random access memory (MRAM). Finally, there is a class that has been conceptually proven to be workable but is not practical yet, such as spin transistors.

In order to make systematic progress towards improved performance in these devices one needs a better understanding of the physics behind the phenomena [1]. Photoemission has proven to be a reliable method of probing the electronic structure of materials [2–4]. Combined with spin detection for the photoelectrons and circular polarization for the photons it is a powerful technique uniquely-suited for mapping all the quantum numbers of an electron in a solid. Advances in the energy resolution have made it possible to map out the states that are relevant to charge transport, magnetic coupling, and magnetic phase transitions. They lie within thermal energies around the Fermi level ($kT = 25$ meV at room temperature). Understanding the microscopic origin of these phenomena opens prospects for rational synthesis of nano-structured materials with tailored magnetic properties.

This review begins with a brief outline of the technique in Sec. 6.2. It will be shown how the observables in angle-resolved photoemission are mapped onto the quantum numbers of the electrons, resulting in a energy-versus-momentum band structure plot (6.2.1). The technique will be applied to the several classes of magnetic materials. We begin with delocalized ("itinerant") electrons, which exhibit significant $E(\mathbf{p})$ dependence (= band dispersion). Examples are ferromagnetic metals (6.2.2), antiferromagnetic metals (6.2.3), and magnetic alloys (6.2.4). Then we will discuss the other extreme, i.e., localized states with negligible band dispersion. These can be understood in terms of the energy levels of an atom surrounded by a small cluster of nearby ligands. The classic examples are magnetic insulators, such as transition metal oxides, but they also include the parent compounds of high temperature superconductors (6.3.1) and half-metals (6.3.2), which are insulating for one spin orientation and metallic for the other. Magnetic semiconductors in (6.3.3) and magnetic alloys in (6.6.2) will introduce the concept of magnetic doping.

Solid-State Photoemission and Related Methods: Theory and Experiment. Edited by Wolfgang Schattke, Michel A. Van Hove

ISBN: 3-527-40334-5

For each of these classes of materials we will attempt to boil down the complicated band structure to a few critical features that determine their magnetic properties. These are the group velocity, the magnetic splitting, and the gaps for charge and spin excitations. Often the magnetic properties are determined by just a few regions on the Fermi surface. The scope is expanded from the ground state to finite temperatures, and in particular to the magnetic phase transition in ferromagnets (6.4.1) and antiferromagnets (6.4.2). Section 6.5 progresses from bulk materials to multilayer structures, where the electronic and magnetic properties can be tailored by confining electrons at interfaces with spin-dependent reflection coefficients. Section 6.6 gives an outlook on the role that multilayer structures play in magnetoelectronic devices. A connection is made between the electronic properties determined by photoemission and the desired electronic properties, such as giant magnetoresistance (GMR) and spin-polarized tunneling.

6.2 Band structure of magnetic materials

6.2.1 Mapping of energy bands

To learn about the electronic states in a material, one has to identify the complete set of quantum numbers which characterizes an electron in a solid. In a bulk crystal these are energy $E = \hbar\omega$, momentum $\boldsymbol{p} = \hbar\boldsymbol{k}$, point group symmetry (the equivalent of angular symmetry in atoms), and spin [2]. All of these values can be summarized in a $E(\boldsymbol{k})$ plot with labels for point group symmetry and spin. Such a band structure plot, or band dispersion, in principle contains the complete information for characterizing electronic and magnetic properties (for an overview of band ferromagnetism, see [5]). For example, it is possible to calculate optical constants from a fit to an experimental band structure [6]. For disordered solids, such as random alloys, there is a finite momentum spread that leads to smeared-out $E(\boldsymbol{k})$ relations. The complete electronic picture will typically contain some localized electronic states with flat $E(\boldsymbol{k})$ band dispersions, e.g. the 4f levels in rare earths or the 3d states in ionic compounds, and delocalized s,p-states with steep $E(\boldsymbol{k})$ that correspond to a high group velocity $v_g = \partial E/\partial \boldsymbol{p} = \partial\omega/\partial\boldsymbol{k}$. The 3d-levels in the common transition metal ferromagnets Fe, Co, and Ni lie in between these extremes and have stimulated a long debate over which states are the most likely to make the biggest contribution to magnetism and transport properties. This issue becomes moot if one realizes that in a solid the distinction between s,p, and d angular momentum states becomes blurred because of the lower symmetry, which causes them to hybridize strongly.

Photoemission and inverse photoemission (Fig. 6.1) provide just the right number of independent variables for establishing a unique correspondence to the quantum numbers of an electron in a solid (for reviews on photoemission see [2–4, 7], for inverse photoemission [8–11]. Photoemission probes occupied states by removing an electron and creating a positive ion state, inverse photoemission maps out unoccupied states by adding an electron and creating a negative ion state. The energy of an electron in the neutral ground state is unobservable, because there is no way to measure it without taking the electron out. At best, one could preserve neutrality by promoting an electron to a higher-lying bound state. That corresponds to an electron-hole pair, which is more complicated than a single electron or hole. At kinetic

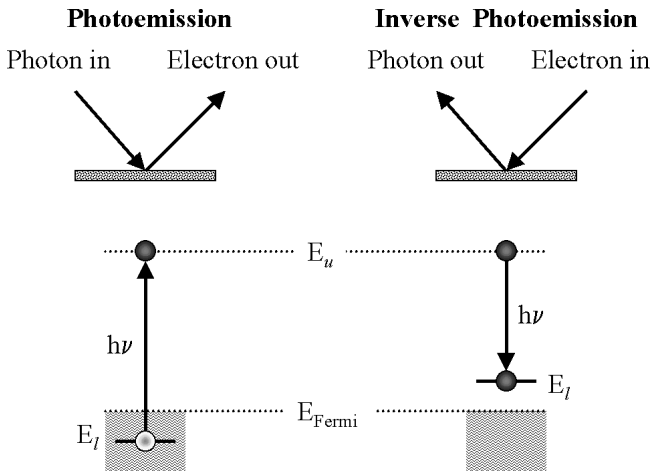

Figure 6.1: Photoemission and inverse photoemission as probes of occupied and unoccupied electronic states. Conservation laws make it possible to determine energy and momentum of the lower state (l) in the solid from the measured energy and momentum of the upper state (u) in vacuum by subtracting the photon energy hν. Occupied states correspond to holes and unoccupied states to extra electrons in the solid, a somewhat counter-intuitive notion. The electronic levels of the neutral ground state are unobservable.

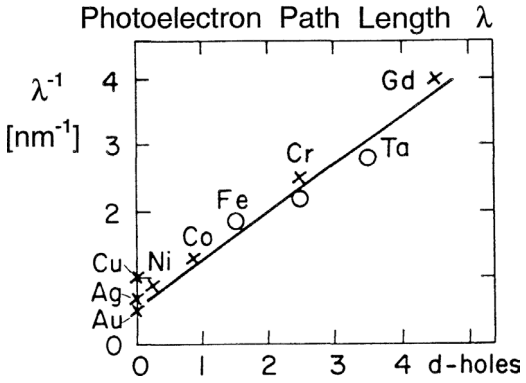

Figure 6.2: The probing depth in photoemission, determined by the mean free path λ of the photoelectrons. The phase space available for electron hole pair creation increases with the number of d-holes and shortens the mean free path (from [12]).

energies of 1–100 eV the mean free path of an electron is only a few atomic layers (Fig. 6.2, [12]). That makes it possible to detect bulk states as well as surface states.

The energy E is obtained from the kinetic energy of the electron. The two momentum components parallel to the surface, $\boldsymbol{k}^{||}$, are derived from the polar and azimuthal angles of the electron (ϑ and φ). The third momentum component, $k^{\perp}$, is varied by tuning the photon

energy $h\nu$. This is achieved by using tunable synchrotron radiation. The polarization of the photon provides the point group symmetry and the spin-polarization of the electron the spin quantum number.

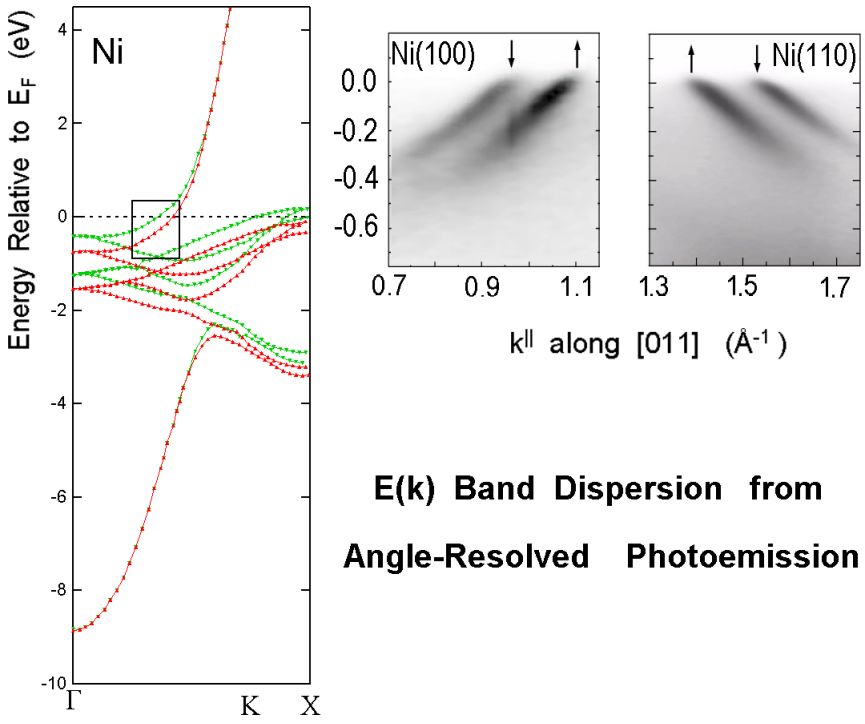

Figure 6.3: Energy-versus-momentum band dispersions of ferromagnetic Ni, showing the parabolic s,p-band crossing the flat 3d-bands [13]. There is an avoided band crossing near the Fermi level E_F, where s,p-states hybridize strongly with 3d-states. The 3d-bands are split by the ferromagnetic exchange splitting dE_{ex}. Modern electron spectrometers with energy and angle multidetection can map out the bands directly, as shown for the boxed-in area of the band structure. High photoemission intensity is shown dark.

A typical band dispersion of a ferromagnet is given in Fig. 6.3 for Ni. The calculated $E(\boldsymbol{k})$ dispersion contains two sets of bands, the lower-lying majority spin bands ("spin up") and the higher-lying minority spin bands ("spin down"). The experiment selects a small portion of the bands near the Fermi level E_F (indicated by a box in the calculated bands). These are states relevant to transport and magnetic coupling. A pair of spin up/down bands can clearly be identified close to E_F. The bands quickly broaden below E_F due to electron-electron scattering, and the spin splitting fades. Such many-electron effects have not been incorporated yet in most calculations.

For two-dimensional states, such as surface states and quantum well states, the determination of energy bands is almost trivial since only E and $\boldsymbol{k}^{||}$ have to be determined. The state we wish to learn about is the lower state l in Fig. 6.1 with energy E_l and parallel momentum $\boldsymbol{k}_l^{||}$.

The information we have is from the upper state u with the observed energy E_u (relative to the vacuum level) and parallel momentum $\boldsymbol{k}_u^{||}$. This state corresponds to the emitted photoelectron in photoemission or the incoming electron in inverse photoemission. The relations between them are straightforward due to simple conservation laws for energy, momentum, and spin. To begin:

$$|\mathbf{k}_u^{||}| = (2m\mathrm{E}_u)^{1/2}/\hbar \cdot \sin\vartheta = 0.51\ \text{Å}^{-1} \cdot (\mathrm{E}_u/\mathrm{eV})^{1/2} \cdot \sin\vartheta \tag{6.1}$$

Then E_l and E_u as well as $\boldsymbol{k}_l^{||}$ and $\boldsymbol{k}_u^{||}$ are related through conservation laws:

$$\mathrm{E}_l = \mathrm{E}_u - h\nu \tag{6.2}$$

$$\boldsymbol{k}_l^{||} = \boldsymbol{k}_u^{||} - \boldsymbol{g}^{||} \tag{6.3}$$

$h\nu$ is the photon energy and $\boldsymbol{g}^{||}$ a vector of the reciprocal surface lattice, which is negligible for most clean metal surfaces due to the absence of surface reconstruction.

For three-dimensional bulk states we need the perpendicular momentum $k^{\perp}$. It is not conserved when the electron crosses the surface barrier, requiring more elaborate methods [2]. At high enough electron energy (typically > 20 eV) the upper state can be approximated inside the solid by the parabolic band of a free electron, shifted by an inner potential V_0. That provides an additional equation for determining $k^{\perp}$:

$$\mathrm{E}_u \approx \hbar^2/2m \cdot \boldsymbol{k}_u^2 + V_0 = 3.81\ \text{eV} \cdot (\boldsymbol{k}_u^{||\,2} + k_u^{\perp\,2}) \cdot \text{Å}^2 + V_0 \tag{6.4}$$

A typical value of V_0 is -13 eV relative to the vacuum level E_{vac}, or -8 eV relative to the Fermi level E_F, using a typical work function $\Phi = \mathrm{E}_{vac} - \mathrm{E}_F \approx 5$ eV. For transitions between bulk states inside the solid one has full $\boldsymbol{k}$ conservation, therefore:

$$k_l^{\perp} = k_u^{\perp} \tag{6.5}$$

The accuracy of the nearly-free electron approximation for the upper band can be tested by symmetry checks and by taking data from surfaces with different crystallographic orientations, as shown in Fig. 6.3. Here the s,p-band is mapped along the [1 1 0] line in $\boldsymbol{k}$-space (= Σ) using two different crystal surfaces of Ni at different photon energies hν. Equation (6.4) is used to locate the spheres in $\boldsymbol{k}$-space where the transitions occur at a given hν (see Fig. 4 in [13]). For Ni(100) and h$\nu = 44$ eV one starts from Γ(2,0,0) at $\boldsymbol{k}^{||}$= 0 and moves towards X(2,1,1) at $\boldsymbol{k}^{||}$ = (0,1,1) (in units of 2π/a). For Ni(110) and h$\nu = 27$ eV one moves in the reverse direction from X(1,1,0) at $\boldsymbol{k}^{||}$= 0 to Γ(0,2,0) at $\boldsymbol{k}^{||} = (\overline{1}, 1, 0)$. The band dispersions in Fig. 6.3 are nearly mirror images of each other, as expected in the nearly-free electron approximation. The $\boldsymbol{k}$ scales coincide after subtracting the $\boldsymbol{k}^{||}$ values of the Ni(110) data from that of Γ(0,2,0), which is $\sqrt{2} \cdot 2\pi/a = 2.52\ \text{Å}^{-1}$.

The data in Fig. 6.3 were obtained with a state-of-the-art photoelectron spectrometer [14] which incorporates multidetection of energy E and polar angle ϑ. The E($\boldsymbol{k}^{||}$) band dispersion can be viewed directly on a television monitor. In fact, the results in Fig. 6.3 represent the time-average of such an image with the contrast inverted (high photoemission dark). Having angle multidetection is quite useful for mapping states at the Fermi level via a momentum

distribution curve (MDC) at constant energy, which corresponds to a horizontal cut in Fig. 6.3 (compare Sec. 6.2.4 and Fig. 6.8 below). Such a spectrum focuses on the sharp states at E_F that are relevant to magnetism and transport properties. Traditional spectrometers provide an energy distribution curve (EDC) at constant momentum, i.e., a vertical cut in Fig. 6.3. In that case the lifetime broadening varies across the spectrum, leading to distorted, asymmetric line shapes. In MDCs one finds simple Lorentzians with a single lifetime broadening.

The spin assignment of the data in Fig. 6.3 is obvious after comparing the two bands with the calculation, even though the experiment was done without explicit spin analysis. In more general cases, such as alloys or quantum wells, such an assignment cannot be taken for granted and an explicit spin analysis is needed. Spin polarized photoemission provides direct information about the spin of an electron band by measuring the spin of the photoelectrons and using the conservation of spin during the photoemission process (for reviews see [7, 15]. A typical system combines a hemispherical energy analyzer with a Mott detector. The photoelectrons are accelerated to 20–100 keV and scattered off a gold or thorium foil. Spin in the up/down direction give rise to a right/left asymmetry in the Coulomb scattering off the nuclei due to spin-orbit interaction [15]. A difficulty of spin-polarized photoemission experiments is the inefficiency of a Mott detector. A common figure of merit is $\eta = S^2 I/I_0$ measuring the ratio of the scattered and collected current I to the incident current I_0, and multiplying by the Sherman function which quantifies the discrimination between spin up and down. A typical value of the Sherman function is 10^{-4}, making spin-polarized photoemission a rather inefficient process compared to regular angle-resolved photoemission. Up to now, a choice has to be made between either resolving spin or resolving energy better than kT, but with the brightest synchrotron light sources it might become possible to achieve both. Spin-polarized inverse photoemission [16] uses a spin-polarized electron source, which typically consists of a cesiated GaAs surface illuminated with circularly-polarized light at the photoelectric threshold.

So far we have considered states consisting of a single electron or hole. In addition, there are two-electron excitations (such as electron-hole and hole-hole pairs) and many-electron excitations, such as spin waves. These can be described by an $E, \boldsymbol{k}$ diagram, too, where E and $\boldsymbol{k}$ are the collective energy and momentum (Fig. 6.4).

In a ferromagnet, a special type of electron-hole pair can be created by a spin-flip transition from an occupied spin-up band to the unoccupied portion of a spin-down band (Fig. 6.4a). At zero momentum transfer the energy of the spin-flip excitations corresponds to the magnetic exchange splitting $\delta \mathrm{E}_{ex}$ which separates spin up and spin down bands (Fig. 6.4b). Although forbidden for photons, such an electron-hole pair can be excited with electrons [17]. A minimum energy Δ_S is required in ferromagnets with a filled majority spin band, such as Co and Ni ("strong ferromagnets"). This Stoner gap Δ_S can be read off the band structures in Fig. 6.5, neglecting electron-hole interaction. In Co, it spans from $\mathrm{L}_3 = \Gamma_5^-$ to E_F and in Ni from X_5 to E_F. Fe lacks such a gap since the top of the majority spin band at H'_{25} lies above the Fermi level. The results are summarized in Table 6.1.

Hole-hole pair excitations are observed for 3d transition metals. The classic example is a satellite in the photoelectron spectrum of Ni at 6 eV below E_F which has been assigned to two d-holes on the same site [18, 19]. This peak takes away spectral weight from the single-particle bands all the way up to the Fermi level [20–24]. For example, the width of the d-bands is reduced by 40% in Ni and theFermi velocity diminishes accordingly. Furthermore, the two-

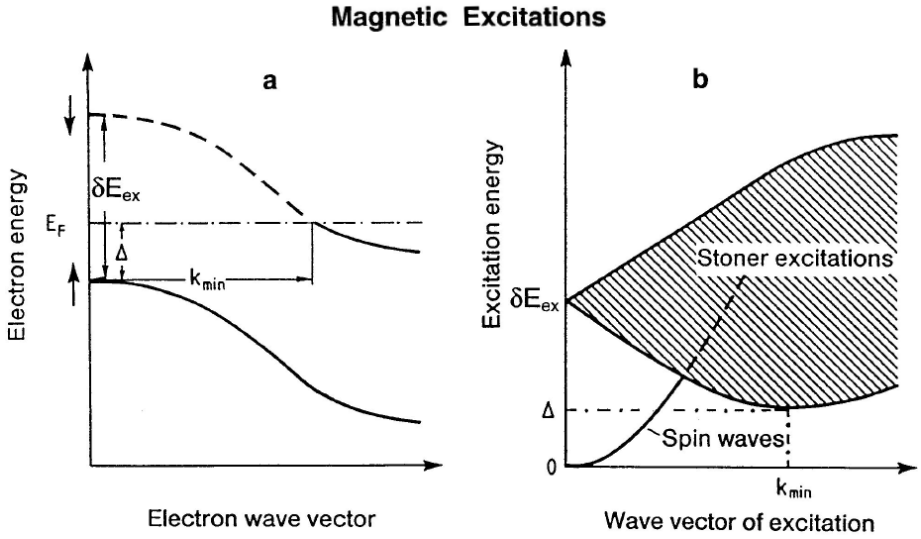

Figure 6.4: Magnetic excitations involving more than one electron or hole. They can be classified into electron-hole pairs (Stoner excitations) and spin waves (from [151]).

Table 6.1: Magnetic exchange splitting $\delta \mathrm{E}_{ex}$ and Stoner gap Δ_S of the elemental ferromagnets, compared to the magnetic moment μ.

	Fe	Co	Ni	Gd5d	Gd4f
$\mu\ [\mu_B]$	2.2	1.7	0.6	0.6	7
$\delta \mathrm{E}_{\mathrm{ex}}$ [eV]	1.8 – 2.4	0.93 – 1.05	0.17 – 0.33	0.8	12
	[37]	[37]	[37]	[34, 42, 162]	[195, 196]
Δ_S [eV]	–	0.35	0.11	–	–
		[197]	[22, 198]		

hole satellite is spin-polarized [25, 26] and thus affects the bands for spin-up and spin-down differently. As a consequence, the measured magnetic splitting in Ni is 2–3 times smaller than expected from local density calculations for the ground state.

The fundamental many-electron excitation is a spin wave or magnon, (see Fig. 6.4b). Spin waves are probed by neutron scattering. They start out with a well-defined, parabolic $E(\boldsymbol{k})$ dispersion at $\boldsymbol{k} = 0$ that broadens out when reaching the electron-hole pair excitations above the Stoner gap. Special spin wave modes develop at surfaces and in multilayers due to the altered boundary conditions [27, 28].

6.2.2 Ferromagnetic metals

The experimental bulk bands of the elemental ferromagnets Fe, Co, Ni, and Gd are shown in Fig. 6.5. These are empirical fits using a combined interpolation scheme [6, 29] which

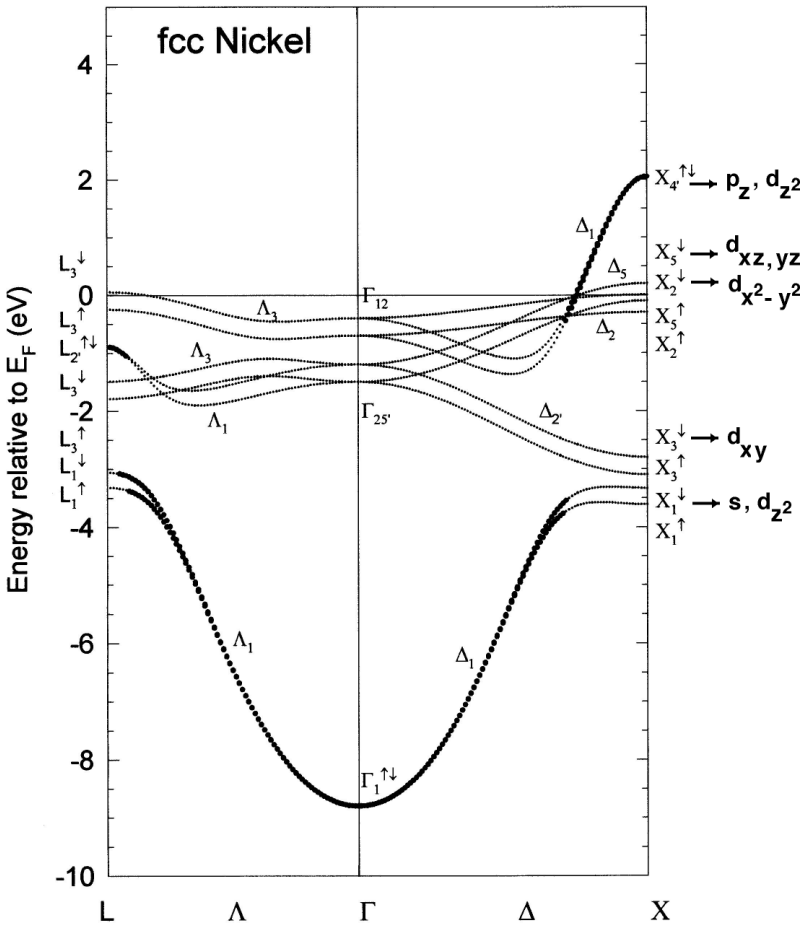

Figure 6.5: (a) Bulk band structure for ferromagnetic Fe, Co, Ni, and Gd [1].

condense a variety of angle-resolved photoemission data into a coherent set of bands. First principles, local density calculations work well for Fe [30–32]. However, they have difficulties explaining the magnetic splitting and d-band width in Ni due to the neglect of two-hole excitations in the spectral function (see above). There have been efforts to take two-hole effects into account, starting with tight binding models and evolving towards first principles methods [21–24].

The 3d transition metals are all characterized by a steep s,p-band dispersing across a region of flat d-bands, as exemplified most clearly for Ni in Fig. 6.3. The d-states disperse less than the s,p-states because they are more localized. That results in less overlap between adjacent atoms and a smaller energy spread between bonding and antibonding combinations of d-states. To a first approximation, the s,p-band can be approximated by a parabolic free-electron band whereas a d-band resembles a flat, atomic level. If s,p- and d-states have the same point group

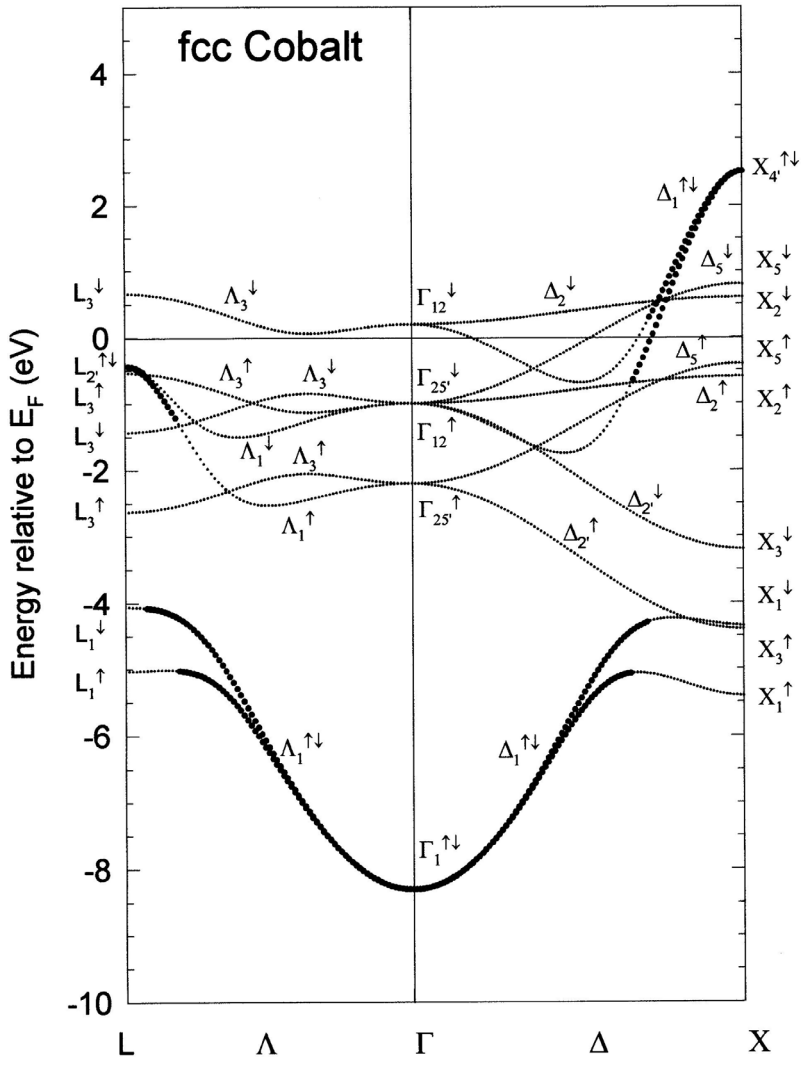

Figure 6.5: (b) Bulk band structure for ferromagnetic Fe, Co, Ni, and Gd [1].

symmetry an avoided level crossing occurs, where the band has both s,p- and d-character. That happens for Ni close to the Fermi level (Fig. 6.3, box) for the Σ_1 states with s,p_z,d_z^2- character along the [110] direction. As the atomic number increases from Fe to Co and Ni, the d-bands become increasingly-filled. The Fermi level moves past the top of the majority spin d-band in Co and Ni and creates a Stoner gap Δ.

In addition to the stable phases fcc Ni, hcp Co, and bcc Fe there exist additional phases that can be stabilized in thin films, such as fcc Co and Fe. Their band structures are also given in Fig. 6.5 in order to demonstrate the possibilities for altering the electronic structure

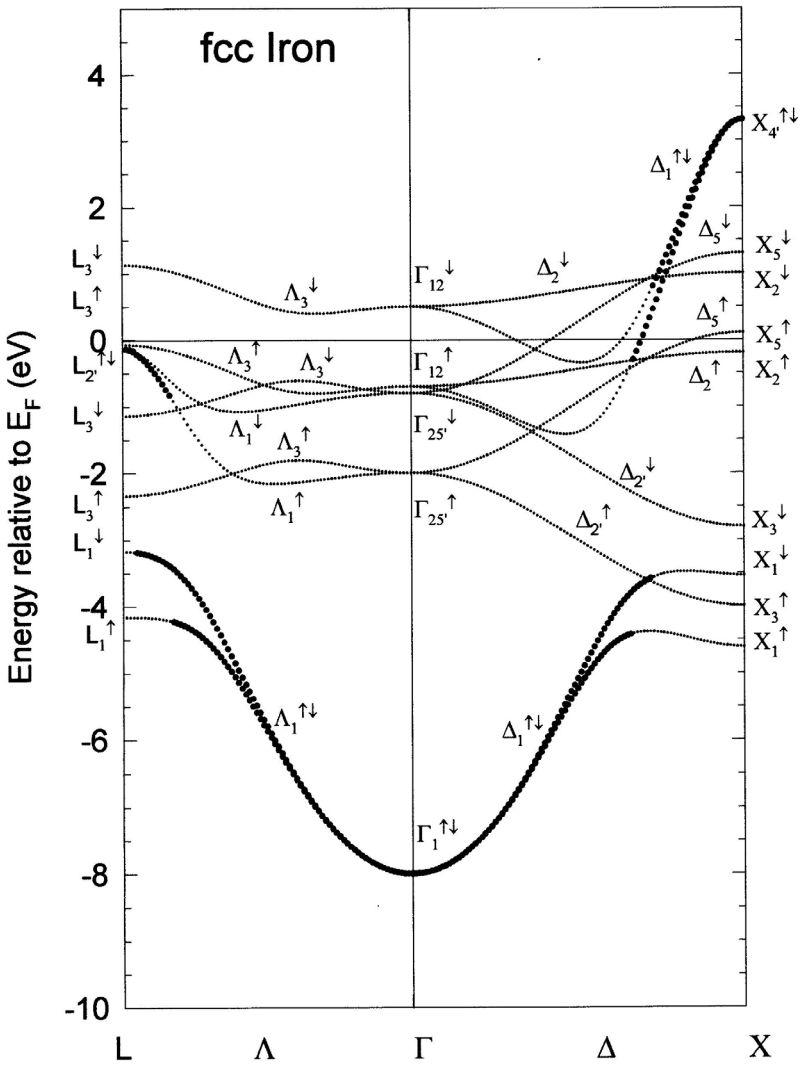

Figure 6.5: (c) Bulk band structure for ferromagnetic Fe, Co, Ni, and Gd [1].

of ferromagnets in thin films. The band topology and exchange change dramatically when going from bcc to fcc Fe. More details on these phases can be found in Sec. 6.4 of [1].

The rare earths exhibit additional f-states, which are so localized that they do not exhibit any measurable band dispersion. Gadolinium is the prototype rare earth ferromagnet. The others exhibit complicated, temperature-dependent magnetic order including antiferromagnetism and spiral spin waves. Since the f-shell is half-filled and fully-polarized in Gd according to Hund's first rule, one has an occupied f-level occupied by 7 spin-up electrons, combined with an unoccupied f-level containing 7 spin-down states (see Fig. 6.13 below).

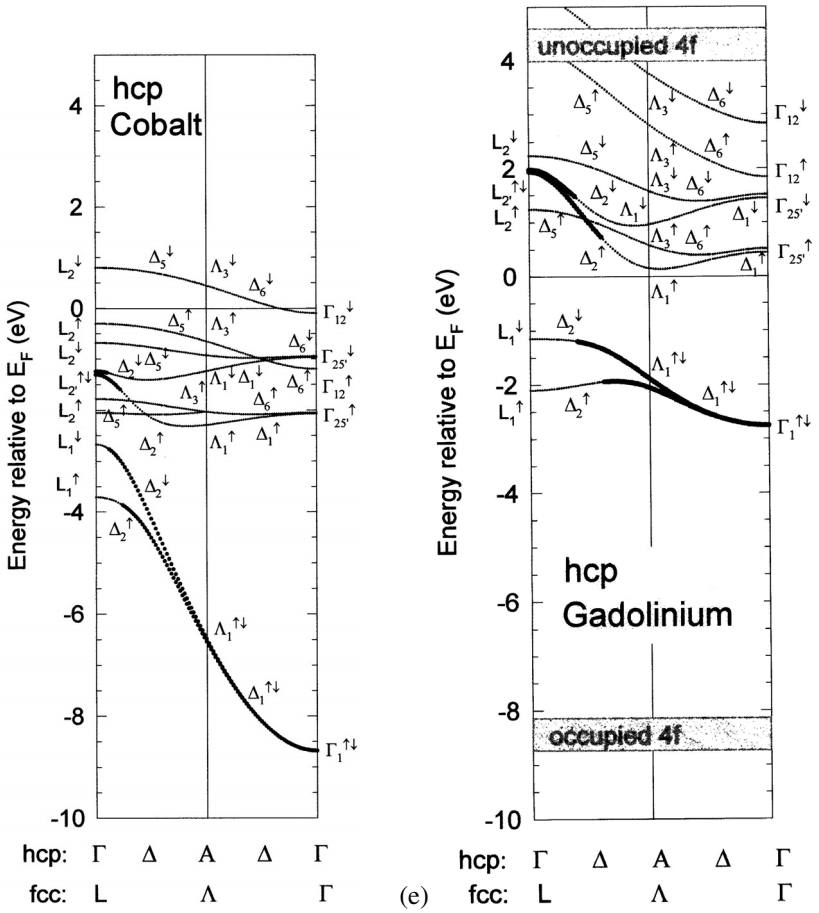

Figure 6.5: (d), (e) Bulk band structure for ferromagnetic Fe, Co, Ni, and Gd [1].

Apart from their dispersion, the s, p, d, and f states can be distinguished by the behavior of their cross sections with photon energy. For example, s,p-states dominate at low photon energies (below 10 eV), d-bands start at about 20 eV, and f states turn on above 30 eV. This behavior is determined by the overlap between the wave functions of the initial and final states in the matrix element for the optical transition from initial to final state. d- and f-states are more localized and require a shorter wavelength, thus higher energy of the final state for a match. An additional trick for selecting states with a particular angular momentum character is resonant photoemission [18, 19, 33–35]. This is an interference effect between a strong, $l \rightarrow l$+1 core-to-valence transition and the valence-to-continuum photoemission process. The 3p $\rightarrow$ 3d or 2p $\rightarrow$ 3d transitions enhance the 3d-states in transition metals (particularly excitations with two 3d holes), and the 4d $\rightarrow$ 4f or 3d $\rightarrow$ 4f transition bring out the 4f–states in rare earths. Taking the difference between a photoemission spectrum at resonance and a few eV below discriminates the d- or f-states from ligand states.

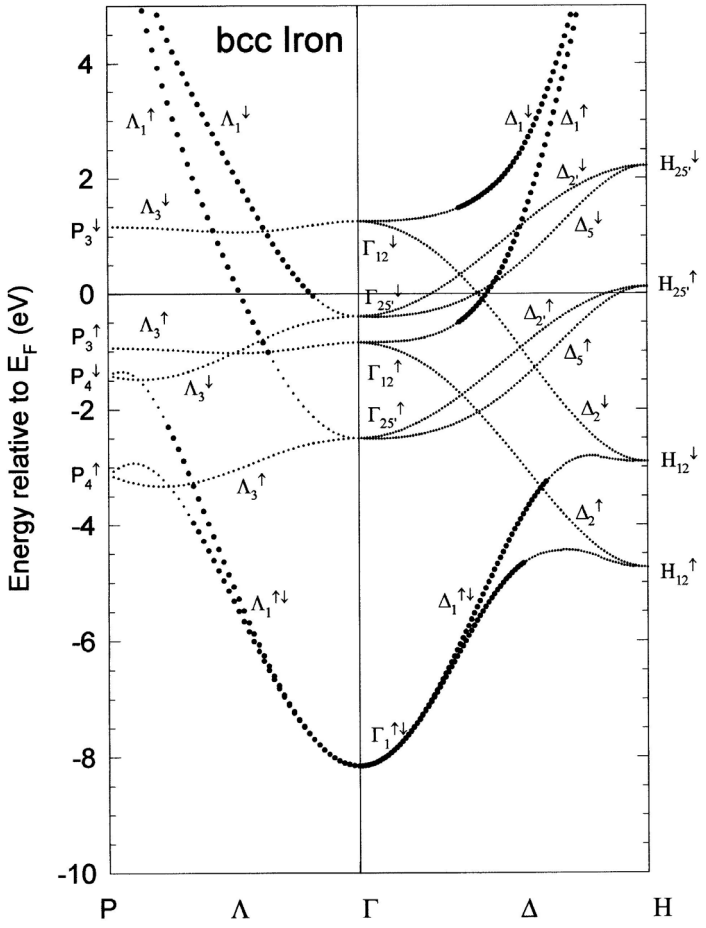

Figure 6.5: (f) Bulk band structure for ferromagnetic Fe, Co, Ni, and Gd [1].

The magnetic exchange splitting $\delta \mathrm{E}_{ex}$ between majority and minority spin bands is the key feature of a magnetic band structure. In a ferromagnet it is directly related to the imbalance in the occupation of majority and minority spin bands that creates the magnetic moment. As the magnetic moment increases, so does the magnetic splitting (see Table 1 and [36, 37]). Figure 6.6 shows results for $\delta \mathrm{E}_{ex}$ in Fe from spin-resolved photoemission [38] and inverse photoemission [39, 40]. In transition metals most of the moment is carried by the 3d electrons (about 110%), whereas the s,p-electrons are weakly-polarized in the opposite direction (about -10% of the total moment). For Gd one has a total moment of $7.6\mu_B$ carried mostly by the 4f electrons ($7\mu_B$), with the 5d electrons contributing $0.6\mu_B$.

There is some variation of $\delta \mathrm{E}_{ex}$ with momentum $\boldsymbol{k}$, which appears to be mainly tied to the symmetry of the bands. In Ni, bands with $\mathrm{t}_{2g}(\Gamma'_{25}\mathrm{X}_5)$ symmetry have a larger splitting than those with e_g (Γ_{12}, X_2) symmetry, e.g., 0.33 eV versus 0.17 eV [21, 22]. This varia-

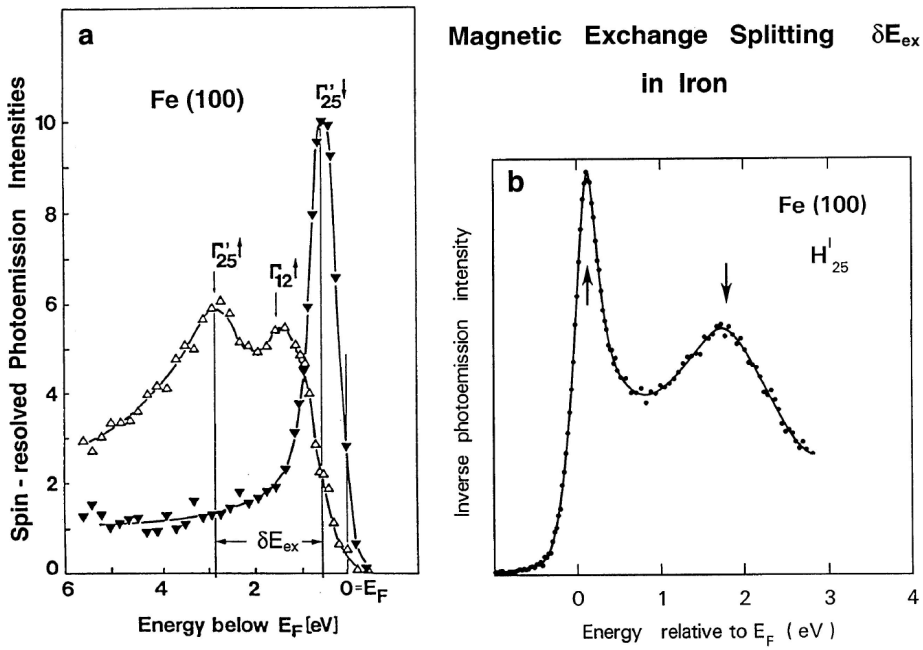

Figure 6.6: Observation of the ferromagnetic exchange splitting $\delta \mathrm{E}_{ex}$ in Fe by spin-polarized photoemission (left [38]) and by inverse photoemission (right [40]).

tion blurs the expected correlation between $\delta \mathrm{E}_{ex}$ and the magnetic moment. Nevertheless, the momentum- and symmetry-averaged value of $\delta \mathrm{E}_{ex}$ turns out to be an indicator of the local magnetic moment for 3d transition metals, not only for ferromagnets but also for antiferromagnets and, in the absence of long-range order, for spin glasses and free atoms. As a rule of thumb, the 3d moment is about 1 Bohr magneton per eV exchange splitting [37]. This trend provides a quick first look at the size of the local moments in thin films and monolayers. It is interesting to note that the $\delta \mathrm{E}_{ex}/\mu$ ratio is connected to the exchange integral I which appears in the Stoner criterion for ferromagnetism (see Sec. 6.4.1).

Surface states play an important role in transition metals and rare earths because the d orbitals are fairly directional and act similar to broken bond orbitals on semiconductors. As in the bulk, there exist d-like and s,p-like surface states, with d-states carrying most of the spin-polarization. Typically, their ferromagnetic exchange splitting is more than twice as large as that of s,p-states. A typical d-like surface state is seen on Fe(100) by photoemission [41], and s,p-like states have been found on Ni by inverse photoemission [5, 11]. The Gd(0001) surface exhibits an interesting d_z^2 surface state that straddles the Fermi level. The majority component is seen with photoemission [42], the minority component with inverse photoemission [43, 44], and both states are accessible to scanning tunneling spectroscopy [45]. Having two states with opposite spin close to the Fermi level in Gd has made it possible to perform spin-polarized scanning tunneling microscopy [45]. The spin distribution of this surface state is discussed in more detail in [11] and [199].

6.2.3 Antiferromagnetic metals

Antiferromagnets exhibit a band structure with a magnetic splitting, too, such as shown in Fig. 6.7 for Cr [46]. However, the splitting occurs only at special points in $\boldsymbol{k}$-space. These are related to of the extra reciprocal lattice vectors induced by the antiferromagnetic spin ordering. A doubling of the unit cell in real space by the anti-ferromagnetic order cuts the unit cell in reciprocal space in half. At the new zone boundary the extra potential induced by antiferromagnetic order creates small band gaps. These have magnetic character. The antibonding state at the upper end of the gap corresponds to a spin-down electron at a spin-up site and vice versa, the bonding state at the lower end of the gap is a spin-up electron at a spin-up site (or a spin-down electron at a spin-down site). This is rather similar to the situation in a ferromagnet. States that are locally in the minority lie at higher energy than local majority states.

In antiferromagnets with localized states there is little $E(\boldsymbol{k})$-dispersion, and one would expect the splitting to extend throughout most of the Brillouin zone, such as in oxides or in the parent compounds of high temperature superconductors. Such a situation can be described by a pair of Hubbard bands, each containing only one electron per unit cell (see Sec. 6.3).

6.2.4 Magnetic alloys

Determining the band structure of an alloy brings up conceptual questions. Is there a separate set of bands for each of the constituents, or is there a common band structure? Is there a difference between an ordered alloy and a random alloy? Band calculations have been performed for both cases [47–50]. An ordered alloy is equivalent to a superlattice, which gives rise to a dense set of backfolded bands that are difficult to disentangle. For a random alloy the bands remain simple, but they are expected to broaden according to band calculations using the coherent potential approximation.

With dilute magnetic alloys it is interesting to pursue the concept of magnetic doping (compare also Sec. 6.3.3 on magnetic semiconductors). There is a rapidly-developing field of magnetoelectronics with the goal of replacing charge currents by spin currents (see Sec. 6.5). By analogy with semiconductor electronics, one might be able to use spin-polarized impurities for shifting the balance between spin up and spin down carriers. In addition to manipulating the carrier density n there is the option of affecting the mean free path l using spin-selective scattering at magnetic impurities.

There is great interest in finding materials that approach 100% spin-polarization at the Fermi level and allow the injection of fully spin-polarized currents. Theoretically, this feat should be achievable with half-metallic ferromagnets which are metallic for the majority-spin electrons but semi-conducting for minority-spin. Among them are transition metal alloys, such as the Heusler alloys. Half-metals will be discussed in the context of oxides (Sec. 6.3.2).

Permalloy ($Ni_{0.8}Fe_{0.2}$) can be chosen as a prototype magnetic alloy. It is probably the most common material used in the magnetic data storage industry and plays a role equally as important as silicon in that sector of microelectronics. And yet, very little is known about the electronic structure of permalloy. There have been measurements of electronic states using photoemission [51–54], inverse photoemission [55], and appearance potential spectroscopy [56]. None of them provides a systematic mapping of the energy bands. This is in contrast

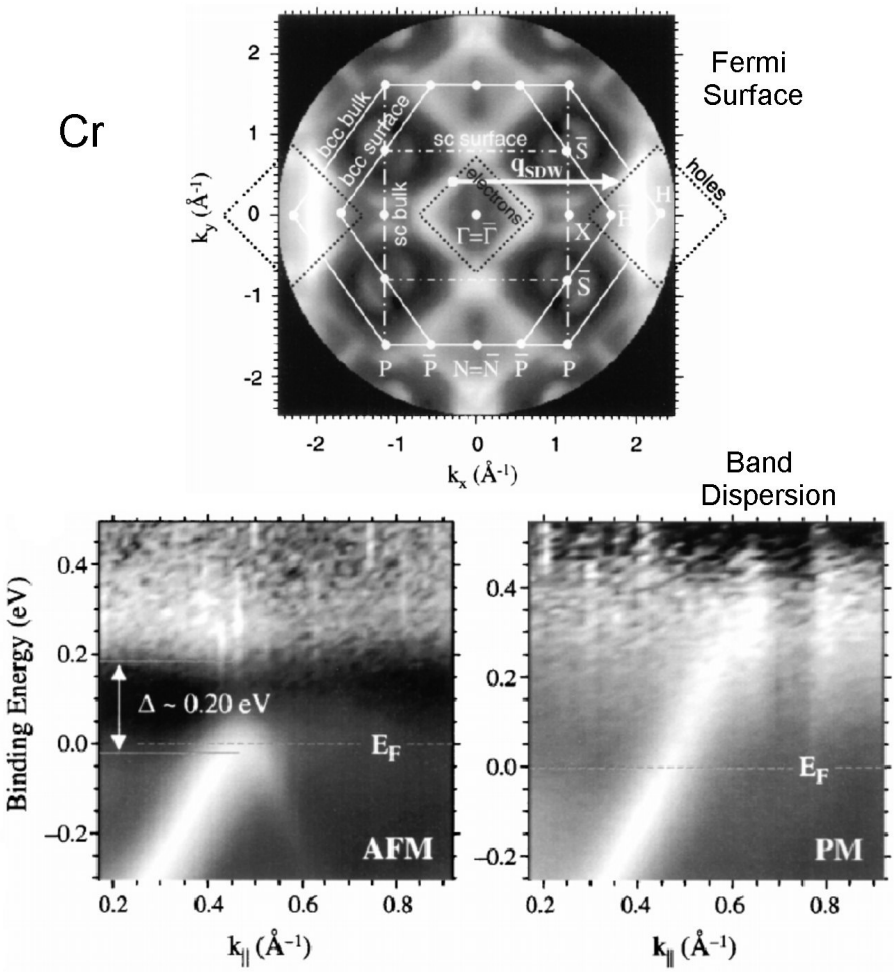

Figure 6.7: Fermi surface (top) and magnetic splitting (bottom left) of antiferromagnetic Cr (from [46]). The magnetic δE_{ex} splitting is labeled as Δ in the lower left. It vanishes above the Néel temperature (lower right). High photoemission intensity is shown bright.

to the extensive photoemission work on the energy bands of pure Ni [20, 22, 29, 57–62]. Calculations of the energy bands of permalloy and the related ordered alloy Ni_3Fe exist [48, 50, 63, 64]. However, one expects fairly large deviations from experiment for ground state calculations based on the difficulties explaining the band width and exchange splitting of Ni [20]. Fermi surface techniques, such as the de Haas van Alphen effect [65, 66], have difficulties handling alloys because of the reduced mean free path.

The band structure of permalloy has been mapped recently [67]. It closely resembles the bands of Ni along the $\Gamma\Sigma$KSX line, except when approaching the Fermi level. The most obvious difference is in the line width of the minority spin state (see Fig. 6.8). While the

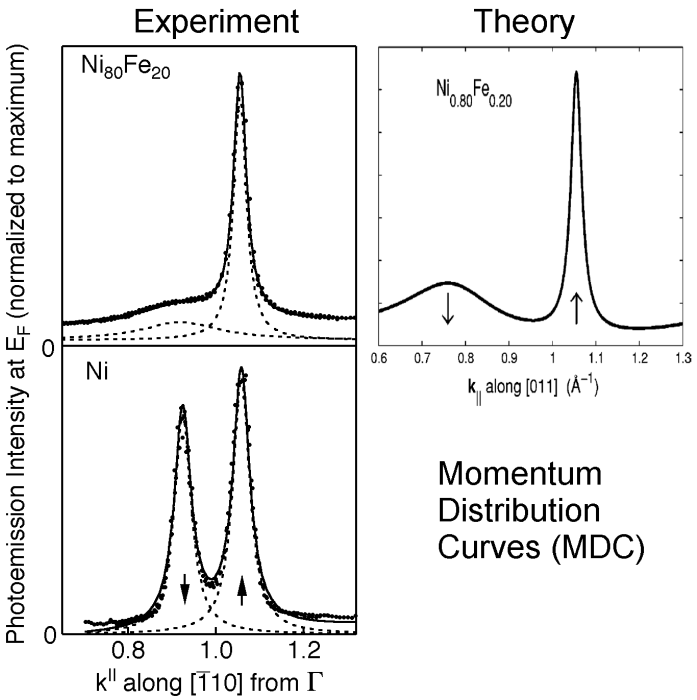

Figure 6.8: Momentum distribution curves (MDCs) of Ni and $Ni_{0.8}Fe_{0.2}$ (permalloy), taken at the Fermi level. Data on the left [67] are compared to a local density calculation on the right (from [64]). A small amount of Fe introduces a large momentum broadening of the minority spin states, i.e. it shortens the mean free path of minority spins and acts as spin filter. A mechanism based on scattering at spin-dependent potential barriers is shown in Fig. 6.9.

spin-up peak remains as narrow as in pure Ni (0.046 Å^{-1}), the spin-down peak broadens by a factor of five to 0.22 Å^{-1}. The inverse of the width corresponds to the mean free path [53, 67]. It is reduced from $>$ 22 Å in Ni to 5 Å for minority spins in permalloy (for a similar analysis on other alloys, see Sec. 6.6.2 and [67]. Secondly, the magnetic splitting is slightly larger in permalloy than in Ni ($\delta \mathrm{E}_{ex} = 0.27$ eV versus $\delta \mathrm{E}_{ex} = 0.23$ eV). The larger magnetic splitting of permalloy reflects its increased magnetic moment ($1.0\ \mu_B$ versus $0.6\ \mu_B$ in Ni [68, 69], following a general trend in 3d transition metals [37]. One of the other important parameters for magnetic transport that can be discerned from a band structure plot is the group velocity $v_F = \partial E/\partial \boldsymbol{p} = \hbar^{-1}\partial E/\partial \boldsymbol{k}$. In permalloy, the measured group velocity is $0.22 \pm 0.02 \cdot 10^6$ m/s. This compares quite closely to the value measured for Ni, $v_F = 0.28 \cdot 10^6$ m/s.

These band structure studies of permalloy allow extrapolation with regard to basic concepts about the band structure of alloys in general [70]. Overall, the results fit into a model that contains two competing energies, the band width W and the splitting δ between the bands of the two constituents. These numbers have to be considered for each band separately, in-

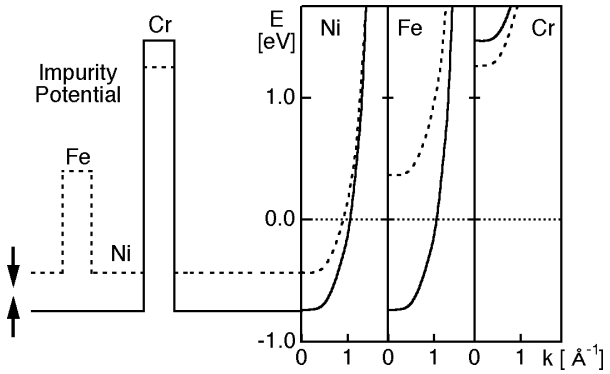

Figure 6.9: Model for spin-selective elastic scattering induced by impurities, with Fe and Cr in Ni as examples [67].

cluding spin. Estimates of W and δ can be obtained from the bands of pure Ni and fcc Fe in Fig. 6.5. For W>δ we can neglect the splitting between the bands to first order and arrive at a common band that is slightly broadened by an amount δ compare [71, 72]). For $W < \delta$ we arrive at two separate bands. In permalloy, the s,p-band has a large width $W \approx 10$ eV (Fig. 6.3) which explains why we do not observe a separate s,p-band for Fe upon alloying. The d-bands need to be considered individually for each spin. As shown schematically in Fig. 6.9, the d-bands line up for majority spin but are separated by $\delta_d \approx 0.8$ eV for minority spin. Therefore, one might expect a common majority d-band but separate minority d-bands. A second, Fe-like minority d-band would be consistent with the changes observed in the Fermi surface at higher Fe concentrations [73]. This extra d-band is expected to be mostly unoccupied due to the larger magnetic splitting of Fe, which matches its larger magnetic moment (2.7 μ_B for Fe vs. 1.0 μ_B for Ni in permalloy [74]). Near the Fermi level we have an avoided crossing of the s,p- and d-bands (compare Sec. 6.2.2 and Fig. 6.3). That makes W comparable to δ. Therefore, neither of the simple limits applies, and one has to rely on sophisticated first principles calculations. These have been performed recently for permalloy [64] and clearly show the strong broadening of the Ni minority band by alloying with Fe (Fig. 6.8 right).

6.3 Magnetic insulators

Magnetic insulators are typically ionic compounds, where the electrons relevant to magnetism become localized at a transition metal or rare earth ion. Examples are halides and oxides, the undoped parent compounds of high temperature superconductors, and the manganites, which exhibit colossal magnetoresistance (CMR). They can be ferromagnetic, antiferromagnetic, or ferrimagnetic. Their electronic structure is driven by strong correlations between localized electrons, which give rise to a wealth of interesting electronic phenomena including magnetic phases and metal-insulator transitions (for a review see [75]). Among the large variety of such compounds we focus on a few to demonstrate the principles of classifying electronic states that are localized. Some related materials are treated in other sections, such as the

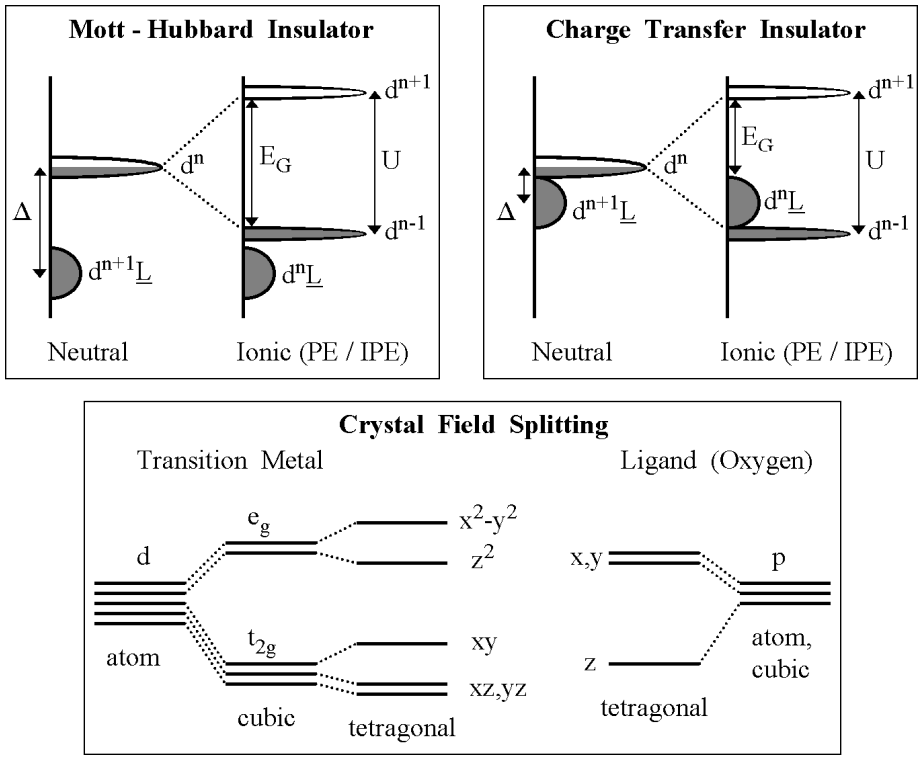

Figure 6.10: Level schemes explaining the energies relevant for localized electronic states and metal-insulator transitions (compare [75] and Eqs. (6.6), (6.7)). For a half-filled band, the (unobservable) ground state level (left) is split by the Coulomb interaction U into a positive and negative ion state (right), which represent photoemission and inverse photoemission. The charge energy Δ promotes an electron from a ligand L (for example oxygen) to a transition metal site. These levels are further split by the crystal field (below).

parent compounds of high temperature superconductors in Sec. 6.3.2 and half-metallic oxides in Sec. 6.3.1.

In many of these compounds the magnetic states are so localized that their band dispersion becomes small compared to the interactions that give rise to level splittings in atoms. Therefore, an atomic picture has been the preferred way of describing them (Fig. 6.10) and the band dispersion is added afterwards. d-electrons in transition metals and f-electrons in rare earths and actinides are assumed to be localized to specific atomic sites in the crystal lattice. An important interaction in a localized electron system is the on-site Coulomb energy U, which is the energy cost of creating a positive and a negative ion from two neutral sites i and j.

$$d_i^n + d_j^n + U \longrightarrow d_i^{n-1} + d_j^{n+1} \qquad d_i^n = \text{ground state} \tag{6.6}$$

Going from left to right we have removed a d-electron from site i and added it to site j. That is the basis of the classic Mott-Hubbard theory of metal-insulator transitions [76–78]. The

energy U splits an normal band into two Hubbard bands (Fig. 6.10 top). The lower Hubbard band corresponds to the photoemission state, where an electron has been removed from a site and has lost its Coulomb binding energy to the hole in the emission process. The upper Hubbard band is the inverse photoemission state, where an electron has been added to a site against the Coulomb repulsion by the electrons that are already there. Each of these contains one electron per unit cell, while a normal band holds two electrons, one spin-up and one spin-down. A normal band is metallic when half-filled, but becomes insulating if it splits into two Hubbard bands, as long as their separation U that is larger than their band width W. The magnetic exchange splitting $\delta \mathrm{E}_{ex}$ (see Sec. 6.2.2) adds to the Coulomb splitting U. These two quantities are frequently lumped together and their sum is labeled U or $\delta \mathrm{E}_{ex}$. For localized electrons the Coulomb part U dominates over the magnetic part $\delta \mathrm{E}_{ex}$, e.g. U $\approx$ 7 eV in NiO [79] compared to $\delta \mathrm{E}_{ex} \approx 1.3$ eV [80]. A second important energy in the system is the charge transfer energy Δ (Fig. 6.10 top). It is defined as the energy required to remove an electron from a ligand and add it to a localized d-site:

$$d_i^n + \Delta \longrightarrow d_i^{n+1}\underline{L} \qquad d_i^n = \text{ground state} \tag{6.7}$$

$\underline{L}$ stands for a ligand hole, e.g., O^{1-} instead of O^{2-}. This energy scale is included in the Anderson Hamiltonian [81]. The two most significant interactions U and Δ can be normalized to smaller, third energy scale T, which describes the hybridization between the localized d-states and the ligand, e.g., Ni3d and O2p in NiO. That leads to a general classification scheme for transition metal compounds [82]. Various regions in the U/T versus Δ/T "phase" diagram describe materials as diverse as Mott-Hubbard insulators, charge-transfer semiconductors, d-band metals, and "p"-type metals, where the holes reside in the ligand valence band (e.g., Mn in GaAs, see Sec. 6.3.3). The band gap E_g can be calculated if a fourth energy scale W is included, which represents the width of the ligand band.

All these interaction energies can be extracted from the photoemission and inverse photoemission spectra, such as those shown in Fig. 6.11 for NiO [75, 83–88]. The ground state configuration of NiO is predominantly d^8 (i.e., $Ni^{2+}O^{2-}$) with an admixture of $d^9\underline{L}$ ($Ni^{1+}O^{1-}$). Photoemission removes an electron and leads to states, such as d^7, $d^8\underline{L}$, $d^9\underline{L}^2$. Inverse photoemission (= bremsstrahlung isochromat spectroscopy BIS) adds an electron and creates the d^9, $d^{10}\underline{L}$ states. They can be assigned on the basis of cluster calculations that produce an atomic-like level spectrum [79, 82, 87, 89]. That provides values of the relevant energies in NiO: U $\approx$ 7 eV, $\Delta \approx 4$ eV, $\mathrm{E}_g \approx 4$ eV, T ≈ -1.4 eV [79]. Going across the series of transition metal oxides one finds that U increases when the 3d-shell becomes filled, due to the stronger localization of the 3d orbitals by the higher nuclear charge. Δ decreases across the transition metal series because the higher electronegativity makes it easier for the transition metal to pick up an electron from the ligand [75].

Note that the sign of the energy is reversed when comparing a photoemission spectrum [86] to a total energy diagram [82]. For example, if the total energy of d^7 is higher than $d^8\underline{L}$ in Eq. (6.7), then the d^7 peak comes out lower in the photoemission spectrum (Fig. 6.11), where the kinetic energy of a photoelectron is plotted. Promoting an electron to a higher energy state costs energy. Thus, the kinetic energy of the photoelectron is reduced. In all our figures we plot energies appropriate for photoemission spectra (see Figs. 6.10, 6.11, 6.13), but Eqs. (6.6), (6.7) are for total energies. This reversal does not happen for inverse photoemission because one

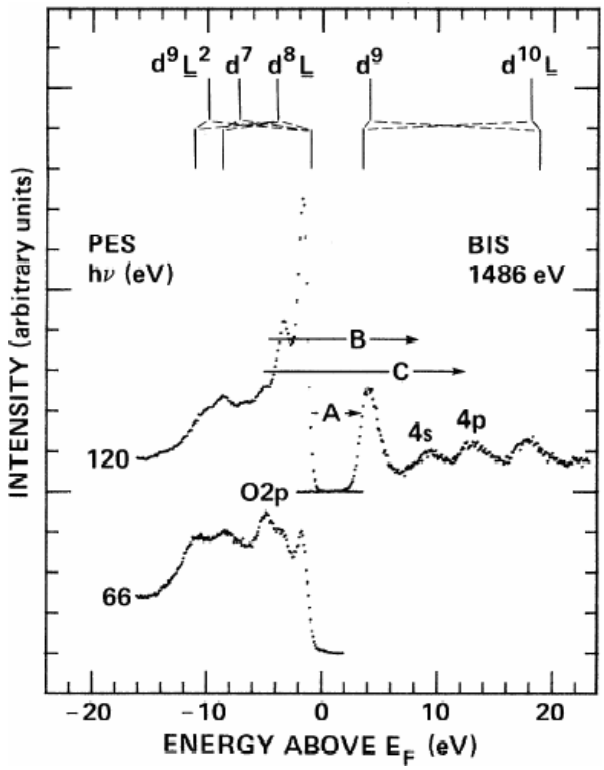

Figure 6.11: Interpretation of photoemission (PES) [83] and inverse photoemission (BIS) [86] of NiO in terms of localized states along the lines of Fig. 6.10 (from [86]; compare [75, 87]).

deals with electrons and not holes. After reversing the signs of photoemission (= positive ion) states in Eqs. (6.6), (6.7) one can use the assignment in Fig. 6.11 to find approximate values for U and Δ: U = $(d^9-d^8) + (d^8-d^7) = d^9-d^7 \approx 11$ eV and $\Delta = d^9\underline{L}-d^8 \approx d^9\underline{L}^2-d^8\underline{L} \approx 6$ eV. We have added a ligand hole $\underline{L}$ to the definition of Δ in Eq. (6.7) in order to get away from neutral states and move to the positive ion states seen in photoemission. Adding a ligand hole does not introduce a Coulomb energy in this simplest approximation, while adding a d-hole would. Other level assignments in Fig. 6.11 can be used as well [82]: U+Δ = $d^{10}\underline{L}$ - $d^9 \approx 14$ eV and U$-\Delta$ = $d^8\underline{L}-d^7 \approx 4$ eV. The sum and difference give U = $\frac{1}{2}$ [$(d^{10}\underline{L}-d^9)$ + $(d^8\underline{L}$ - $d^7)$] $\approx$ 9 eV and $\Delta = \frac{1}{2}$ [$(d^{10}\underline{L}-d^9) - (d^8\underline{L}$ - $d^7)$] $\approx$ 5 eV.

The band gap is given by the spacing between the photoemission and inverse photoemission spectra. One obtains $E_g \approx 4.3$ eV for NiO in this fashion by taking the half-height of the first peaks as band edges [86]. Care has to be taken with these insulating samples to make sure that there is no charging or resistive voltage drop, particularly for inverse photoemission where the current is higher. An extrapolation from elevated temperature (200°C) to room temperature and from typical currents of 100 μA to zero current was required in this case.

There are two general types of insulators (Fig. 6.10 top). For $\Delta > \mathrm{U}$ one has a Mott-Hubbard insulator, where the gap occurs between the d_i^{n-1} and d_j^{n+1} states. E_g scales linearly with U. For $\Delta < \mathrm{U}$ a charge transfer insulator is formed. The bottom of the gap corresponds to a ligand hole $\mathrm{d}_i^n\underline{\mathrm{L}}$ instead of a d-hole d_i^{n-1}. E_g scales linearly with Δ. The opposite trends of U and Δ with d-band filling produce Mott-Hubbard insulators for a nearly empty d-shell and charge transfer insulators for a nearly-filled d-shell.

In the assignment of the features in Fig. 6.11 to Ni3d versus O2p holes it is useful to vary the photon energy hν. The O 2p states are strong for hν $\leq$25 eV, the Ni3d states become strong at high hν and at the Ni3p resonance (hν = 66 eV, see Fig. 6.11 bottom curve [83, 90]).

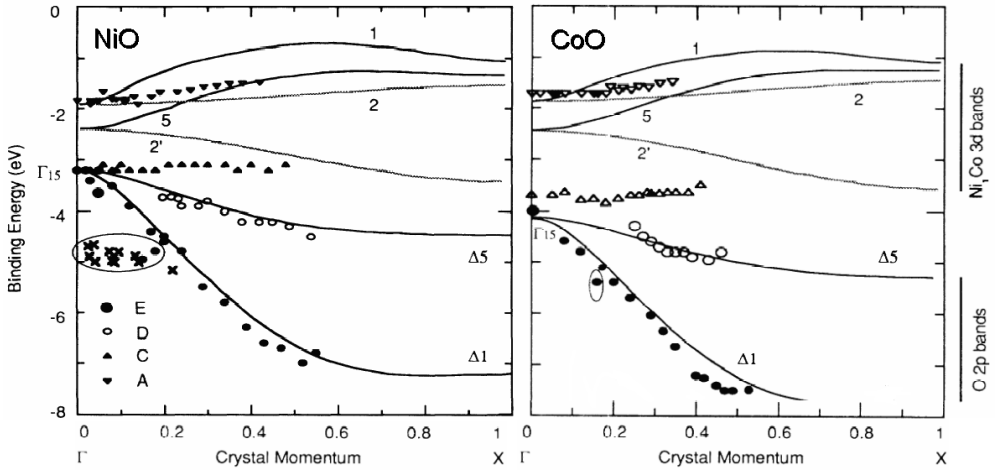

Figure 6.12: Angle-resolved photoemission from NiO and CoO showing both localized and delocalized states (flat versus dispersing bands) [91].

Band dispersions are resolvable for the more delocalized ligand bands by angle-resolved photoemission, as shown in Fig. 6.12 for the O2p bands in NiO and CoO [91–93]. They are well described by local density calculations. It is even possible to discern a back-folding of the bands due to the extra reciprocal lattice vectors in the antiferromagnetic phase. For the ligand band width in NiO and CoO one obtains W $\approx$ 4 eV. The dispersion of localized transition metal d-bands is barely detectable beyond the broadening of these bands. They are at least a factor of 4 narrower than calculated, showing that the localized 3d states are better treated as atomic levels. For describing both the localized transition metal states and the delocalized ligand states it is necessary to extend band calculations of the neutral ground state to the excited state in photoemission, where a hole is present. Such quasiparticle calculations have begun for NiO [94]. Qualitatively, one might think of the bands in Fig. 6.12 as hybrids between the Ni3d and O2p states in Fig. 6.10 bottom. Interaction between the two leads to bonding/antibonding combinations. The bonding part has mostly O2p character and is delocalized, as evidenced by the measured band dispersion in Fig. 6.12. The antibonding part has localized Ni3d character and corresponds to the nearly dispersionless upper band.

A full explanation of the NiO spectra in Fig. 6.11 needs to take the Ni4s,p states into account, not only the Ni3d and O2p states. Because of the charge transfer from Ni to O, the Ni4s,p states are unoccupied and show up in the inverse photoemission spectrum. They are best seen at low photon energies where the cross section for the Ni3d states has not yet turned on (see [95, 96]).

One more refinement of the level diagrams is the inclusion of multiplet splittings. They are a combination of two comparable interactions, i.e., the Coulomb-exchange interaction between all the electrons in the d-shell and the crystal field splitting. The many-electron multiplets essentially spread each d^n configuration into a whole spectrum of levels as indicated in Fig. 6.11 (for details we refer to [75]). The crystal field splitting is shown in Fig. 6.10 bottom for typical cases. A cubic crystal field splits the five atomic d-levels for each spin into two manifolds, a doubly-degenerate $e_g = \Gamma_{12}$ level containing the $d_{x^2-y^2}$ and d_z^2 states and a triply-degenerate $t_{2g} = \Gamma'_{25}$ level encompassing the d_{xy}, d_{yz}, d_{zx} states. The sign of the splitting provides additional information. It reverses itself between octahedral and tetrahedral environments, with the octahedral coordination typical for transition metals and their oxides. Examples are the Γ points in the band structures of the cubic transition metals Ni and Fe in Fig. 6.5 and the energy level schemes for CrO_2 and LaCaMnO in Fig. 6.13. Such level splittings are essential for understanding the 100% spin-polarization in half-metals (Section 6.3.2) and the effect of colossal magnetoresistance (CMR) in manganites. The alignment of the transition metal d-manifold with respect to the oxygen 2p levels changes as the d-shell fills up. If it is nearly empty, the d-levels are high and cause an interaction of the t_{2g} states with the $O2p_{x,y}$ states (see CrO_2 in Fig. 6.13). A nearly-filled d-shell lies lower and causes an interaction of the e_g states at the top with the $O2p_{x,y}$ states (see La_2CuO_4 in Fig. 6.13 and high temperature superconductors).

Figure 6.13 gives an overview of the level structures that are encountered with increasing number of d-electrons. They represent a best estimate based on available photoemission, inverse photoemission, and optical data combined with the results of first principles calculations, such as local spin density + U or Hartree-Fock-Slater (for Gd see [97, 98] for CrO_2 see [99–102], for LaCaMnO see [103–106], for NiO see [75, 86–89, 91, 92, 107], for CuO see [75, 108], for LaCuO see [35, 109]).

6.3.1 Magnetic superconductors

Despite the competition between magnetism and superconductivity there are examples of magnetic superconductors. Superconductivity coexists with antiferromagnetism in ternary rare earth (RE) compounds, such as (RE)Mo_6S_8, (RE)Mo_6Se_8, and (RE)Rh_4B_4 (for an overview, see [110, 111]). More complicated spiral spin structures occur in other superconducting rare earth compounds. Ferromagnetism is more difficult to reconcile with superconductivity, unless the pairing is p-wave. In that case the spins are parallel, whereas they are anti-parallel for conventional s-wave or d-wave pairing. Strontium ruthenate is a p-wave superconductor that is almost ferromagnetic (for photoemission results see [112, 113]). The possibility of a ferromagnetic surface phase is still being debated [114, 115]. $ZrZn_2$ is a superconducting ferromagnet with p-wave or inhomogneous s-wave [116].

A different class of ferromagnetic superconductors is based on the layered perovskite structure of the high temperature superconductors. $Ru_{1-x}Sr_2GdCu_{2+x}O_8$ is predominantly

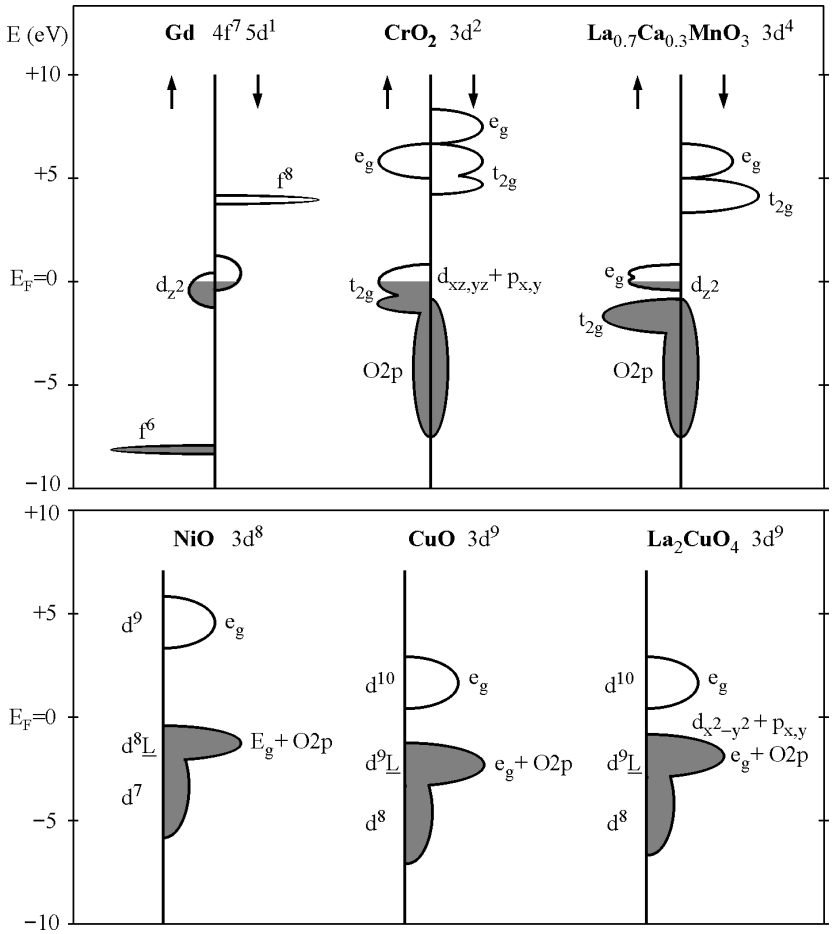

Figure 6.13: Semi-quantitative level diagrams for localized states with d- and f-electrons, based on photoemission, inverse photoemission, the optical band gap, and calculations (local spin density + U). The t_{2g} levels and then the e_g levels gradually become filled as the d-count increases from left to right and top to bottom. E_F corresponds to the neutral ground state, states below E_F are position ion states corresponding to photoemission (with an electron removed to infinity), and states above E_F are negative ion states corresponding to inverse photoemission (with an electron taken from infinity). (For sources see the text.)

antiferromagnetic with a magnetic moment $\mu_{Ru} \approx 1.2\mu_{\rm B}$, but it has a small ferromagnetic component with $\mu_{Ru} \approx 0.05\mu_B$. A possible explanation for the compatibility between ferromagnetism and superconductivity is a layered model, where superconductivity is localized in the CuO_2 planes and ferromagnetism in the RuO_2 planes (see [111] and references therein). That would be an extreme type II superconductor with the magnetic flux confined to individual atomic planes.

The undoped parent compounds of high temperature superconductors (for a review see [109]) are antiferromagnetic, e.g., La_2CuO_4. They resemble the transition metal oxides discussed in Sec. 6.3. In fact, the Cu^{2+} in the superconducting $[CuO_2]^{2-}$ planes is isoelectronic to CuO, which has been classified as charge-transfer semiconductor [82]. Typical band gaps are 2 eV. Antiferromagnetism gives way to superconductivity after doping with holes, e.g., by substituting Sr for La in $La_{2-x}Sr_xCuO_4$ with $x \approx 0.15$. A doped hole site in the $[CuO_2]^{2-}$ plane is isoelectronic to NiO, which falls into the intermediate region between Mott-Hubbard and charge-transfer insulators [82]. The NiO photoemission spectrum in Fig. 6.11 might provide a first insight into the rather complex spectra of high temperature superconductors. As in NiO, the superconducting holes have strong O2p ligand character, i.e., $d^9\underline{L}$ = $Ni^{1+}O^{1-}$ = $Cu^{2+}O^{1-}$ in the neutral ground state (which is not observable) and $d^8\underline{L}$ = $Ni^{2+}O^{1-}$ = $Cu^{3+}O^{1-}$ in the positive ion state of a photoemission experiment.

The oxygen character of the superconducting holes is evidenced by strong transitions from the O1s core level into the unoccupied hole states, which can be measured by electron energy loss spectroscopy [117] or by soft X-ray absorption [118–120]. Furthermore, from the polarization dependence of these transitions one can establish that the holes have in-plane $O2p_{x,y}$ orientation [120]. They hybridize with the $Cu3d_{x^2-y^2}$ states whose lobes point from the Cu towards the in-plane O atoms. The spin of the ligand hole $\underline{L}$ = O^{1-} = $O2p^5$ couples antiferromagnetically with the spin of the $Cu3d^9$ state of Cu^{2+}, thereby forming a singlet [121].

Angle-resolved photoemission has produced numerous contributions to the understanding of high temperature superconductors because of its ability to resolve the momentum of the electronic states. A review of this fast-moving field is beyond the scope of this chapter. Nevertheless, there are some intriguing connections to magnetism that are interesting to mention. The $d_{x^2-y^2}$ symmetry of the superconducting gap has been determined by angle-resolved photoemission. It contains nodes in $\boldsymbol{k}$-space as opposed to the isotropic, s-like symmetry of conventional superconductors. Such a symmetry suggests a magnetic pairing mechanism as opposed to the conventional phonon mechanism. In fact, the undoped parent compounds are antiferromagnets. Between the antiferromagnetic and superconducting regions lies an intermediate regime where the material is not yet superconducting, but already exhibits a pseudo-gap whose magnitude and angular dependence resemble that of the superconducting gap. Superconductivity and magnetism of the 3d orbitals seem to be related in these materials, although the exact connection is not clear yet. One of the possibilities is a phase separation into antiferromagnetic and superconducting stripes that fluctuate on the nanometer scale.

6.3.2 Half-metals

In a half-metal the bands are metallic for one of the two spin orientations and semiconducting/insulating for the other [122]. That gives rise to 100% spin-polarization at the Fermi level, a very attractive feature for magnetoelectronic devices. Several classes of materials are expected to be half-metallic from band calculations, such as the Heusler alloys (e.g., NiMnSb) and transition metal oxides (e.g., CrO_2). Experimentally it has been difficult to reach the expected 100% spin-polarization at E_F, due to spin-scattering at the surface (in photoemission) or at the interface (in transport measurements). The stoichiometry of these compounds is difficult to maintain all the way to the outermost atomic layer. Nevertheless, a record polarization of 98.4% has been reached in CrO_2 using Andreev reflection at point contacts [123]. Other

compounds exhibit appreciable spin polarization as well [124]. Spin-polarized photoemission is more surface sensitive than transport measurements and has generally given lower polarization [125–127]. For example, measurements on CrO_2 have been impaired by the stable Cr_2O_3 surface oxide that is formed by reduction of Cr^{4+} to Cr^{3+}[126, 127]. In the following we discuss the electronic structure of CrO_2 in more detail as a prototype of other half-metallic oxides.

Like many other transition metal oxides, CrO_2 has a fairly localized set of Cr3d levels that split into two main groups with approximate $e_g = \Gamma_{12}$ and $t_{2g} = \Gamma'_{25}$ symmetry (see Fig. 6.13). The t_{2g} states lie below the e_g states, as in the manganites and the ferromagnetic transition metals. A tetrahedral distortion of the splits the t_{2g} triplet into a singlet d_{xy} and a doublet $d_{xz,yz}$ and the e_g doublet into two singlets d_z^2 and $d_{x^2-y^2}$. Apart from the crystal field splitting one has to take the Coulomb energy U and the magnetic splitting δE_{ex} into account. A ferromagnetic exchange splitting $\delta E_{ex} \approx 1.6$ eV can be inferred from local density ground state calculations [99, 100, 128], which is in consistent with the magnetic moment of $2\mu_B$ according to the 1 eV/μ_B rule [37]. The observed magnetic splitting between the spin-up and spin-down states depends on whether both are in the same charge state or not. Using photoemission and inverse photoemission for the t_{2g} states one compares occupied spin-up states with unoccupied spin-down states, i.e., one has to add the on-site Coulomb energy U to the ground-state δE_{ex} for obtaining the observed magnetic splitting. (Note that the terms U and δE_{ex} are also used for the sum of the Coulomb and magnetic splitting). Subtracting the calculated $\delta E_{ex} \approx 1.6$ eV from the observed splitting of 5 eV one obtains U ≈ 3.4 eV [99]. The Coulomb energy U shifts the unoccupied part of the 3d t_{2g} orbital from its ground state position just above E_F to about 4 eV above E_F in the inverse photoemission spectrum. It should be possible to measure δE_{ex} directly by comparing the spin-up and spin-down e_g states, which are both unoccupied. However, it is difficult to resolve the e_g states from the dominating spin-up t_{2g} states in the inverse photoemission spectra.

For adding the O2p orbitals to this picture one could use the charge transfer energy Δ as an extra parameter. Since the calculations find an almost pure O2p band crossing E_F one would expect a negative Δ, i.e., the top of the O2p band lies above E_F [100]. Specific experimental information about the oxygen states comes from soft X-ray absorption, which probes transitions from the O1s core level into the empty O2p states. The metallic majority spin states just above E_F produce a strong peak, which indicates substantial hybridization of O2p states with the metallic Cr3d t_{2g} states [99, 102]. The magnetic character of these states is corroborated by the magnetic circular dichroism (MCD) observed for this peak [129]. The energy position at 0.7 eV above the O1s core level binding energy gives the center of the unoccupied part of the spin-up t_{2g} band [102]. It compares to a shoulder at 0.8 eV above E_F in inverse photoemission [99].

The orientation of the O2p orbitals can be obtained from the polarization dependence of the O1s-to-2p absorption spectrum [102]. The first absorption peak is excited with the electric field vector perpendicular to the tetragonal c-axis, i.e., in the a-a plane. Consequently, the 100% spin-polarized states at E_F are a mixture of $O2p_{x,y}$ and $Cr3d_{xz,yz}$. The situation is quite similar to the high temperature superconductors where the in-plane oxygen ligand holes are strongly hybridized with the transition metal 3d states at the Fermi level (see Sec. 6.3 and [120]. The only difference is the t_{2g} character of the 3d states in CrO_2 compared to e_g character in cuprate superconductors. This is due to the fact that the 3d shell is nearly empty

in CrO_2 and nearly full in the cuprates, which places E_F in the upper e_g manifold for the cuprates (see Fig. 6.13).

Having the relevant energies in hand one can construct a level diagram (Fig. 6.13) and populate the levels with the two 3d electrons of Cr^{4+} in the ground state configuration of CrO_2. These two electrons are accommodated by the spin-up t_{2g} orbital in agreement with Hund's first rule that maximizes spin. Since the upper $t_{2g}(d_{xz,yz})$ orbital is only half-filled we have a metallic configuration. Overall, the three energies U, δE_{ex}, and the $e_g - t_{2g}$ crystal field splitting are comparable for CrO_2 and make it difficult to come up with simple label in the classification scheme discussed in Sec. 6.3. A more realistic picture has to rely on detailed band structure calculations, such as local density theory with the Coulomb energy U added [100, 128, 130].

Photoemission from other half-metallic compounds has encountered problems with surface stoichiometry similar to those in CrO_2. The Heusler alloys, such as NiMnSb, have reached only 20–50% spin-polarization in photoemission [131, 132] and 28% in spin-polarized tunneling [133].

Manganites have a structure that is related to that of the high temperature superconductors. They are primarily studied for their colossal magnetoresistance effect (CMR), but they are also interesting as potential half-metals. $La_{0.7}Sr_{0.3}MnO_3$ has produced spin-polarized photoemission spectra with 100% spin-polarization near E_F at low temperature 40 K while unpolarized at 380 K [134]. Surprisingly, the spin-polarization measured in photoemission is higher than that in electrical measurements (54–81%) and theoretical predictions (36%). This could be due to an enhanced group velocity for majority spins giving a higher spin tunneling current [135], or caused by a different surface phase [136]. The level structure of manganites is similar to that of CrO_2, except for the higher occupancy of four electrons instead of two. They fill the majority spin t_{2g} level completely and bring the next higher level into play, an e_g state with d_z^2 character (Fig. 6.13, [105, 137]). Looking very closely at the energy region around the Fermi level with angle-resolved photoemission one finds a weak, dispersing band. The suppression of its intensity and an alteration of the band dispersion near E_F are taken as a sign of strongly electron-phonon interaction [138]. Indeed, polarons have been implicated in the mechanism for colossal magnetoresistance (CMR) in these materials.

6.3.3 Magnetic semiconductors

One of the latest developments in magnetoelectronics is the search for magnetic semiconductors that would allow a seamless coupling of magnetoelectronic and semiconductor devices. Injection of spin-polarized currents from conventional, metallic ferromagnets into semiconductors has not been successful due to depolarization at the interface, where disordered spins lead to spin-flip scattering. A better interface can be created between an intrinsic and magnetically-doped semiconductor, where the lattice is not disturbed. Doping of III-V and II-VI semiconductors with transition metals has been successful in producing ferromagnetic materials, but the Curie temperatures are still well below room temperature [139]. For example, Mn can be incorporated into GaAs up to a concentration of about 5%, reaching a Curie temperature of 110 K. At higher Mn concentration the cubic zincblende crystal structure starts breaking down, defects appear in high concentration, and eventually the structure transforms to hexagonal MnAs. Nanostructuring helps pushing T_C beyond room temperature.

Multilayers of MnAs/ZnSe achieve T_C= 325 K [140] and dot arrays of MnSb on GaAs exhibit large magnetoresistance at room temperature [141]; photoemission data exist, see [142]. Another possible pathway to room temperature ferromagnetism is Mn doping of large gap semiconductors, such as GaP and ZnO.

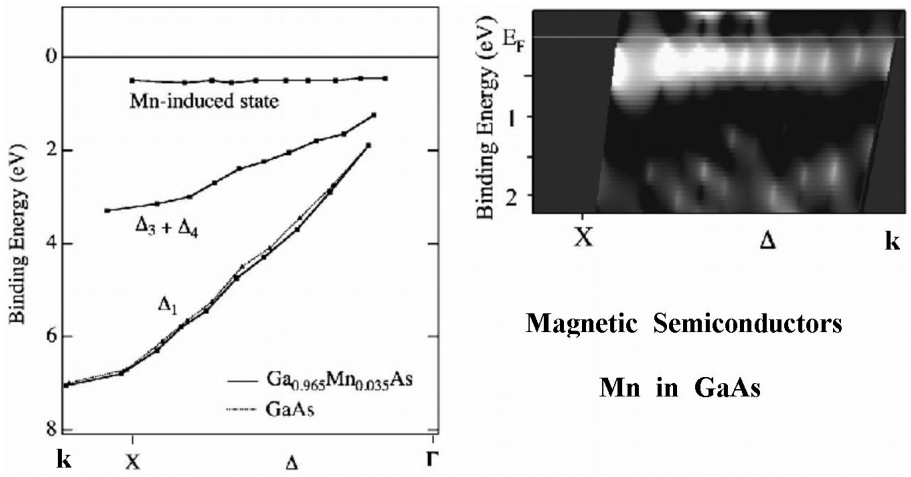

Figure 6.14: Magnetic semiconductor obtained by doping of GaAs with Mn. The Mn impurity creates magnetic states at the top of the valence band, which are seen in a difference spectrum between doped and pure GaAs (high photoemission intensity shown bright, from [143]).

Photoemission from Mn-doped semiconductors sheds light on the electronic states responsible for ferromagnetism, as shown in Fig. 6.14 for Mn in GaAs (from [143] Fig. 3c,d; For a review see [144]). Difference spectra between doped and undoped GaAs exhibit an extra, dispersionless feature near the Fermi level. It corresponds to holes induced by Mn in the As4p-like top of the valence band of GaAs. The Mn3d levels lie much lower at about 4.5 eV below E_F and have no direct influence on magnetic transport. Their role is to polarize the holes at the top of the valence band, and they are very efficient at that. One Mn dopant polarizes many holes, leading a very large g-factor for these carriers [145]. In the language used for magnetic oxides in Sec. 6.3 the holes near E_F correspond to the $\mathrm{d}^5\underline{\mathrm{L}}$ photoemission state, where on has a 4p hole at the As ligand. The state at 4.5 eV below E_F would be the d^4 state. A cluster model analysis finds that the As4p ligand holes at E_F are coupled antiferromagnetically to the Mn3d spins. That is a situation analogous to the high temperature superconductors, where where a O2p ligand hole couples antiferromagnetically to the Cu3d spin, forming a singlet [121, 146].

The small density of extra states induced by dilute Mn can be detected by resonant photoemission, utilizing the cross section enhancement at the Mn3p core level threshold near 50 eV photon energy [147]. Taking the difference between spectra at and below the resonance produces a density of states with Mn3d character. The state at 4.5 eV below E_F resonates like a 3d-like state, whereas the state near E_F does not, in agreement with the assignment above. Similar studies have been carried out for other magnetically-doped semiconductors, such as $\mathrm{Cd}_{1-x}\mathrm{Mn}_x\mathrm{S}$, Se, Te [148] and references therein) and $\mathrm{Zn}_{1-x}\mathrm{Mn}_x\mathrm{O}$ [149].

6.4 Phase transitions

After mapping out the electronic states of magnetic materials it is interesting to go one step further and explore whether it is possible to investigate to origin of magnetism. What are the energetic driving forces that stabilize magnetism? The magnetic splitting offers important clues. In antiferromagnets the splitting plays a role similar to that of the energy gap in superconductivity and charge density waves. It determines the critical temperature and the energy gain due to ordering. That brings up the question whether the magnetic splitting acts as order parameter and vanishes at the critical temperature. Ferromagnets do not exhibit such a simple behavior and lead beyond the mean field theory that describes superconductors.

6.4.1 Ferromagnets

Ferromagnetism occurs in rather few elements, i.e., Fe, Co, Ni, Gd, and a few rare earths with low Curie temperatures. (There are many more elemental superconductors than that!) The stability of ferromagnetism in just a few elements has been explained by the Stoner criterion (Eq. (6.8) and Fig. 6.15, from [150, 151]). The density of states at the Fermi level $\mathrm{D}(\mathrm{E}_F)$ and an atomic exchange integral I are taken as the only input. The prediction is that in ferromagnets the product of the two is larger than unity [36, 150, 152, 153]:

$$D(\mathrm{E}_F) \cdot I > 1 \tag{6.8}$$

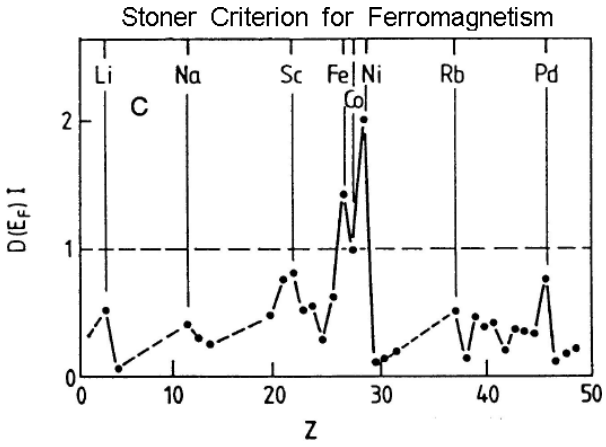

Figure 6.15: The Stoner criterion for the existence of ferromagnetism. The requirement that the product of the density of states at E_F and an atomic exchange integral I be larger than unity correctly selects Fe, Co, Ni as the only ferromagnetic elements with atomic number $Z < 50$ (from [150, 151]).

The Stoner criterion explains why Fe, Co, and Ni are singled out for ferromagnetism. Analogous to superconductivity, the density of states at the Fermi level $\mathrm{D}(\mathrm{E}_F)$ and a coupling parameter are the critical quantities (here the exchange integral I instead of the electron-phonon coupling λ). However, there is no energy prefactor that could lead to a simple formula

for T_C, such as the mean field equation in superconductivity and antiferromagnetism (Eq. (6.9) below). The simple Stoner model has failed miserably in predicting the Curie temperature of ferromagnets, typically coming out too high by a factor of two. The difficulty for a realistic calculation of the Curie temperature is the variety of single- and many-electron excitations that become thermally accessible near the Curie temperature [154]. Those excitations, combined with thermally-excited phonons broaden the photoemission spectra near T_C and make it difficult to tell whether or not there is a residual splitting. This may be an intrinsic problem that renders the question moot.

One of the key questions has been the possible persistence of local magnetic order at and above the Curie temperature T_C, despite the lack of long-range order [23, 152, 155, 156]. Experimentally, this question can be addressed by photoemission because the probing volume determined by the mean free path of the photoelectrons is very small, typically $(0.5\text{nm})^3$ (see Fig. 6.2). If there is still magnetic order within such a volume one expects the magnetic splitting to persist above T_C, even though the long range order disappears, and with it any spin-polarization signal. To illustrate this possibility consider an extreme case, the magnetic spitting of the 4f level in Gd. The spin alignment of the seven 4f electrons inside each Gd atom remains unaffected above T_C. Such an atomic alignment is not guaranteed for the 5d valence electrons in Gd.

Not every ferromagnet lends itself to studies of the magnetic splitting at the Curie temperature. High temperatures are involved in Fe and Co. However, the Ni3d and the Gd5d electrons have served as test cases for an extensive number of studies (for Ni3d see [57, 59, 61, 157–161], for Gd5d see [34, 42, 44, 45, 162]). There is still a great amount of debate about the spin-splitting near T_C, both experimentally and theoretically. Nevertheless, it is enticing to imply that the splitting of delocalized states vanishes at T_C as expected from mean field theory, whereas localized states preserve a residual splitting above T_C, such as in the extreme case of the Gd4f states. A measure of localization is the steepness of the bands, which determines the group velocity and the band width. The steepest band in Ni is the s,p-band, and its magnetic splitting vanishes at T_C [57, 61]. The more d-like the bands become, the more likely is the existence of a finite splitting and a finite local spin-polarization above T_C. In Fe the bands are rather flat near the Γ point and their behavior near T_C is more complicated than a simple collapse of the splitting with the magnetization [38].

Magnetic compounds offer an even larger variety of phenomena to be explored near T_C. For example, high-resolution spectroscopy of CoS_2 has found a sharp peak appearing at E_F when going below T_C, which has been assigned a partial population of a band that is unoccupied in the paramagnetic phase ([163]. Apparently, the magnetic exchange splitting in the ferromagnetic phase induces such an auto-doping.

Surface ferromagnetism is very sensitive to the local electronic structure at the surface. Figure 6.15 suggests that there are several elements very close to the ferromagnetic threshold, for example Pd. These might become magnetic at surfaces if the density of states is enhanced by the reduced band width that accompanies fewer neighbor atoms. On the other hand, reduced coordination will negatively affect a cooperative phenomenon, such as ferromagnetism. Indeed, the Curie temperatures in thin films decreases when the thickness is reduced and approaches zero for about a monolayer. These counteracting phenomena establish very rich magnetic phase diagrams of surfaces and thin films [164, 165]. The connection between magnetism and the electronic structure of thin films and surfaces is reviewed in [1], Chapters 4 and 5.

6.4.2 Antiferromagnets

Like ferromagnetism, antiferromagnetism is driven by a large density of states at the Fermi level. However, in this case only specific points in $\boldsymbol{k}$-space play a role, which are related to the antiferromagnetic reciprocal lattice vector [166]. The antiferromagnetic ordering opens a band gap E_g at these $\boldsymbol{k}$-points that lowers the energy of the occupied states at the bottom of the gap and removes the high density of states from the Fermi level. There is a close analogy with the opening of a gap in superconductivity. In fact, antiferromagnetic order in Cr behaves analogous to the superconducting order parameter in the mean field approximation. In both cases there is a relation between the critical temperature (here the Néel temperature T_N and the gap E_g:

$$\mathrm{E}_g \approx 3.5\mathrm{kT}_N \tag{6.9}$$

This relation is only a rough guide, as the case of Cr shows, where a Néel temperature of 311 K and an optical gap [167, 168] of 0.12 eV give $\mathrm{E}_g \approx 5\mathrm{kT}_N$. Surface-sensitive photoemission experiments [46] measure an enhanced gap of 0.2 eV combined with an enhanced Néel temperature of 440 K with a similar ratio (for enhanced surface magnetism, see [1] Chapter 5.1).

As with the ferromagnetic splitting one can pursue the development of the antiferromagnetic splitting when approaching the Néel temperature T_N. The data for Cr in Fig. 6.7 are consistent with a reduction of the splitting to zero at T_N [46]. As with ferromagnets, there are other, more localized electron systems, such as NiS, where there is no observable gap change near T_N [169].

6.5 Magnetic multilayers

The magnetism of bulk elements and alloys is a rich field by itself, but there is even more to be explored when thin magnetic films are considered. The electronic states of thin films are unique due to the reduction in dimensionality from the bulk. In addition, when magnetic layers get combined with other magnetic layers, with nonmagnetic metals, or with insulators, there are many new phenomena to consider, including quantum well states and oscillatory magnetic coupling. This leads to the possibility of tailoring the electronic and magnetic properties by the proper choice of magnets and spacers. In the following we select two highlights that are characteristic of this field and defer a more extensive discussion to [1], Chapter 5.

6.5.1 Quantum well states

The properties of magnetic layer structures are dependent on the reflection of electrons at interfaces. Electrons are confined to layers with lower inner potential and momentum and energy are quantized in the direction perpendicular to the layers. The resulting discrete states are quantum well states. The band dispersion in the plane of the film is not affected by the confinement and remains continuous. Particularly important for magnetism and transport are quantum well states at the Fermi level. Figure 6.16 shows the photoemission intensity at the Fermi level for of a Cu film on Fe as a function of Cu film thickness. The density of states

oscillates with a maximum appearing nearly every 6 layers. The maxima in the oscillations correspond to quantum well states number 2–5 crossing the Fermi level. The schematic on the right shows the square of the wave function for the $n = 3$ maximum. One might assume that there is a node in the wave function at the interfaces, but it turns out that there is a maximum, as evidenced by the peak in the density of states when approaching zero Cu thickness. A simple way of envisioning the formation of quantum well states is through an optical analog: the Fabry-Perot interferometer (Fig. 6.17, [170]). The Cu spacer has two interfaces which act as mirrors for electrons. By changing the spacing between the interfaces one produces interference fringes every half wavelength, as in the optical analog. A phase shift of zero at the interfaces produces the observed interference pattern. Thus, one has an interference device of atomic dimensions for electrons, which directly measures their wavelength.

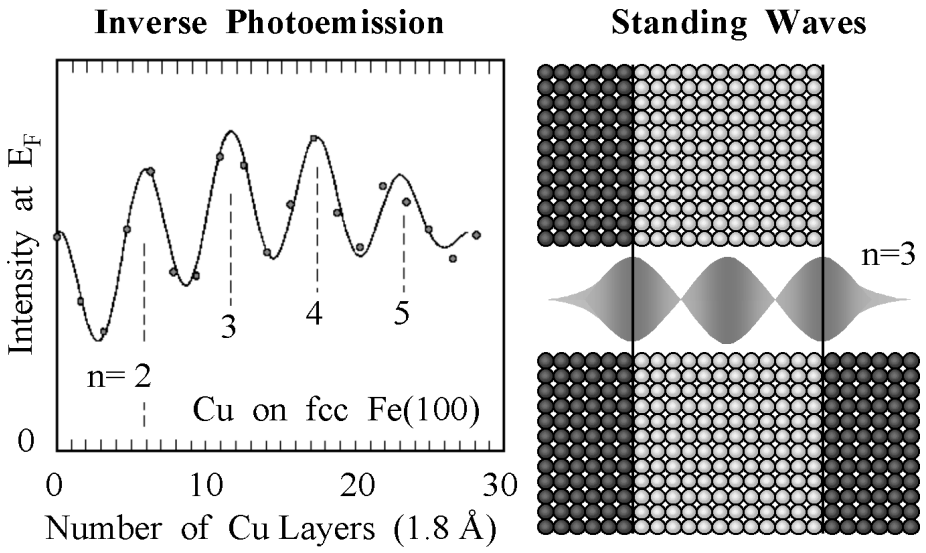

Figure 6.16: Quantum well states inducing oscillations in the density of states at the Fermi level for $\mathbf{k}^{||} = 0$ when the film thickness is varied [170, 172].

The density of states at the Fermi level is modulated by quantum well states quite significantly, as demonstrated in Fig. 6.16 for a specific $\boldsymbol{k}$ point. This modulation can be compared to the density-of-states variations in Fig. 6.15 that determine ferromagnetism, and it becomes obvious that there is a potential for tailoring magnetic properties via quantum well states. More generally, the density of states at E_F is able to trigger electronic phase transitions, such as superconductivity, charge density waves, ferromagnetism, and antiferromagnetism. Carriers for electrical and thermal transport are also located at the Fermi energy. The initial connection was made between quantum well states and oscillatory magnetic coupling [170–172]. Since then a variety of other connections have been established, for example with the magnetic anisotropy [173], with the magneto-optical response [174–176], with electrical measurements [177], and with "magic" thicknesses in the growth of thin films [178, 179].

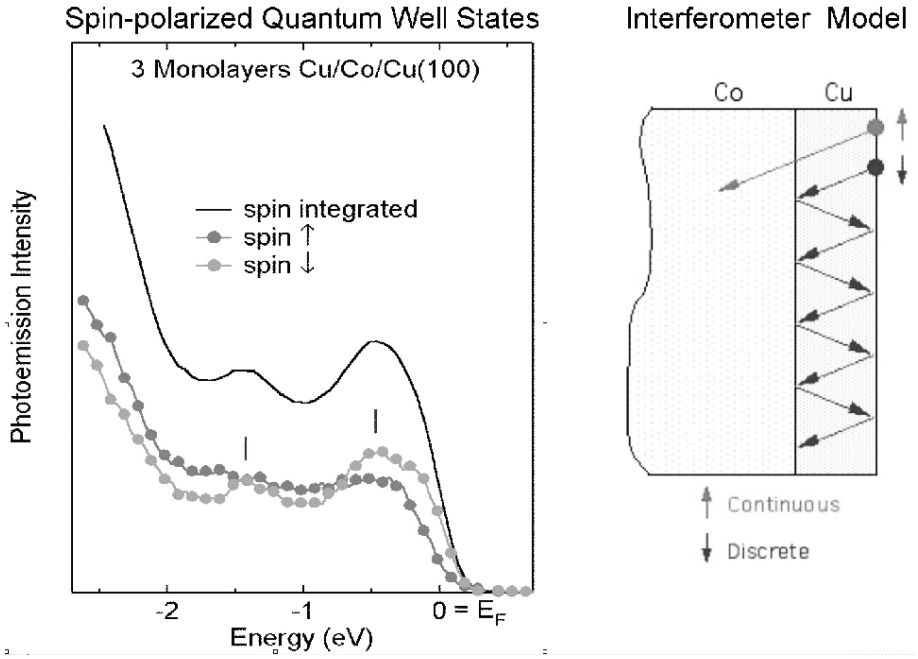

Figure 6.17: Spin polarized quantum well states [182] induced by a spin-dependent potential barrier at the Cu/Co interface (see Fig. 6.18).

Magnetic effects can only be transmitted if quantum well states are spin-polarized, even if they reside in a noble metal film. This rather counter-intuitive picture of a "magnetized" noble metal has been confirmed by spin-polarized photoemission [180–182]. Figure 6.17 shows spin-resolved spectra of a quantum well state in a Cu film on fcc Co(100) near the neck of the Cu Fermi surface [182]. The minority spin band splits into two peaks, while the majority spin band remains a continuum. There is a rather simple explanation for the spin-polarization of quantum well states in magnetic multilayers. The reflection coefficient for electrons at an interface depends on the inner potential in the materials. The inner potential for majority and minority spin electrons differs by the magnetic exchange splitting which causes a spin-dependent reflectivity. Only states with significant band offset to the non-magnetic spacer band are being confined. For metals to the right of the ferromagnets - particularly noble metals - the majority bands are nearly lined up (Fig. 6.18). Therefore, minority spins experience a band offset and are confined into quantum well states, but majority spins behave like a continuous bulk band that extends throughout noble metal and ferromagnet. For spacers to the left of the ferromagnets, e.g. Cr, the minority bands line up, and a majority spin polarization is expected for the quantum well states. This argument works independent of the specific band topology, but it does not guarantee full confinement, i.e. 100% reflectivity at the interface. Only in particular cases one encounters a situation where minority spins become totally Bragg-reflected since they run into a band gap in the ferromagnet. This is the case in the spectrum of Fig. 6.17.

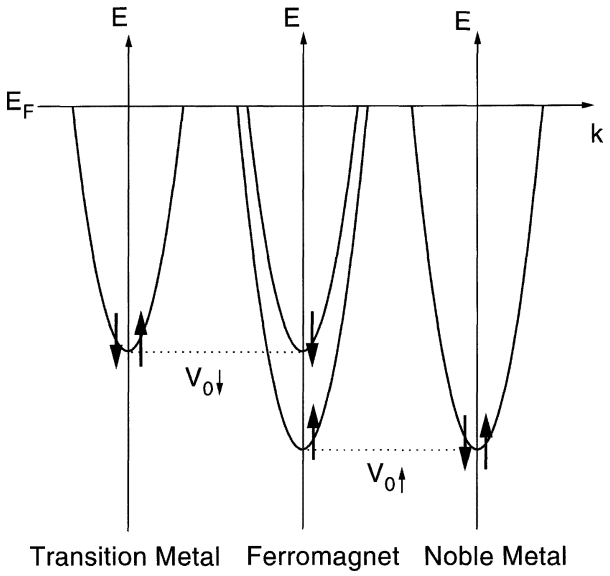

Figure 6.18: Spin-dependent step in the inner potential between ferromagnetic transition metals and noble metals (for example Co and Cu). The majority spin 3d-band of Ni and Co is filled and lines up with that of Cu, whereas the minority spin band of Co is shifted up by the magnetic splitting $\delta \mathrm{E}_{ex}$ [1].

6.5.2 Oscillatory coupling

Oscillatory coupling occurs in magnetic multilayers, where ferromagnetic layers are separated by nonmagnetic spacers. The prototype is a trilayer where two ferromagnetic layers are coupled by a noble metal, as shown in Fig. 6.16 (bottom right). The magnetization of the layers alternates between parallel and antiparallel when the thickness of the spacer is increased. Oscillatory magnetic coupling has been observed for many combinations of ferromagnets and spacer materials [183]. Typical oscillation periods are about 10 Å, but shorter and longer periods have been observed, too. A comparison with quantum well state oscillations, such as in Fig. 6.16, shows that the appearance of quantum well states at E_F roughly coincides with antiparallel coupling. The periods are identical wherever comparative data exist (see [1] Fig. 40). Figure 6.19b,c demonstrates that using a wedge-shaped Cu spacer to map the thickness dependence of the oscillations by photoemission [184]. Quantum well oscillations with two distinct periods are observed at two different $\boldsymbol{k}$ points. The periods are beat frequencies between the Fermi wavelength and the lattice spacing, i.e., 5.6 monolayers at the belly of the Cu Fermi surface in b, and 2.7 monolayers at the neck in c. The same frequencies determine the periodicity of the envelope wave function of the quantum well states, which is shown schematically in Fig. 6.16. In panel d, the interlayer coupling is shown, as determined by X-ray magnetic linear dichroism (XMLD). It clearly reflects the two periods of the quantum well states and matches the quantum well model in panel e.

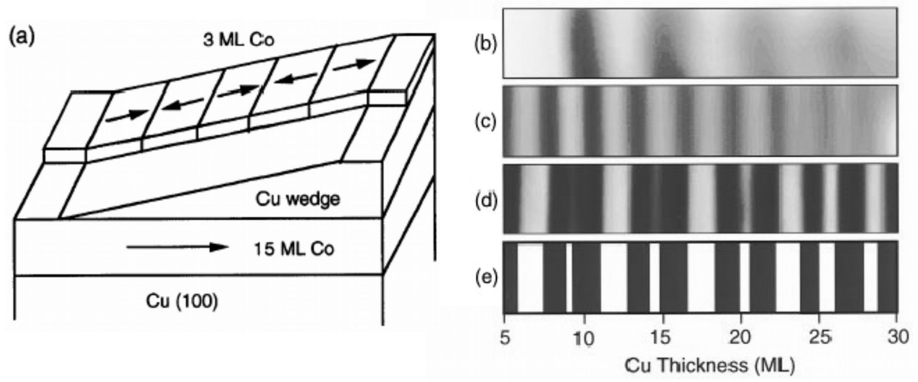

Figure 6.19: Quantum well states with two different periods (b) and (c) at different $\boldsymbol{k}^{||}$ are observed by a wedge technique (a). These give rise to oscillations in the magnetic coupling of Co/Cu/Co tri-layers with two periods (from [184]).

Another approach for explaining oscillatory coupling has been the RKKY (Ruderman-Kittel-Kasuya-Yosida) model [185]. It brings in the Fermi wavelength as well by coupling two spin impurities in an electron gas via spin density oscillations. The RKKY periods are usually identical to those obtained for quantum well states, and a close connection with the quantum well model can be established [186]. There is a simple way of viewing the similarity and potential differences between the two models. The RKKY oscillation is caused by a spin density wave in the electron gas, whereas a quantum well state represents a coupled spin and charge density wave. It is conceivable that the reflection coefficient of a spin wave at the boundary of the quantum well is different from that of a charge wave, particularly if the boundary is rough. For example, the magnetic roughness of an interface can be smaller than the roughness in the charge density, as demonstrated by resonant magnetic scattering of soft X-rays [187]. That might explain why oscillatory coupling can still be found in structures that are too rough to observe quantum well states.

6.6 Magnetoelectronics

The central goal of magnetoelectronics is the generation and switching of spin currents. The spin-dependent current density $\boldsymbol{j} = \sigma \boldsymbol{E}$ in an electric field $\boldsymbol{E}$ is controlled by the conductivity $\sigma = (\mathrm{e}^2/\mathrm{m})n\tau$ for the two spin directions. It is determined by the carrier density n and their lifetime τ, which is related to the mean free path l and the Fermi velocity v_F via $\tau = l/v_F$. Manipulating these quantities is the quest of the designer of new magnetic materials. Among the options are doping with magnetic impurities (Sections 6.6.2 and 6.3.3) and manipulating the spin-dependent reflectivity of interfaces (Secs. 6.5, 6.6). Multilayer structures with single digit nanometer dimensions confine electrons to quantum wells and allow for sophisticated combinations of spin reflectors and spin filters. Such structures are now widely used in reading heads for hard disks, and non-volatile magnetic random access memory (MRAM) is under development [188].

6.6.1 Giant magnetoresistance (GMR) and spin-polarized tunneling

Magnetoresistance is a key phenomenon in the development of magnetoelectronics. Reading heads in hard drives now make use of giant magnetoresistance (GMR), and the current development of magnetic memory (MRAM) depends on junction magnetoresistance (JMR) in spin-polarized tunneling. These two effects have much in common, due to their similar basic structural unit. Each phenomenon takes place in a trilayer where two ferromagnetic layers are separated by a nonmagnetic layer. The difference is that the separation layer is an insulator in magnetic tunneling and a metal in GMR. If the two ferromagnetic layers are oriented antiparallel, the resistance is high, if they are parallel the resistance decreases. Although the microscopic explanation is still rather sketchy, there is a simple optical analog that visualizes this effect (Fig. 6.20). Magnetic interfaces (or the magnetic layers themselves) act as spin filters. The parallel configuration transmits one of the two spin-polarizations, the antiparallel configuration blocks both, as with crossed optical polarizers. The goal of a device engineer is to maximize the magnetoresistance by optimizing the spin filtering effect. That can be achieved at the interfaces by adding monolayers of a ferromagnetic material as spin-reflective coating. Such interface engineering is already in use with GMR reading heads of hard disks. Alternatively, one might achieve spin filtering by spin-dependent scattering inside the magnetic layers. That brings in the concept of magnetic doping.

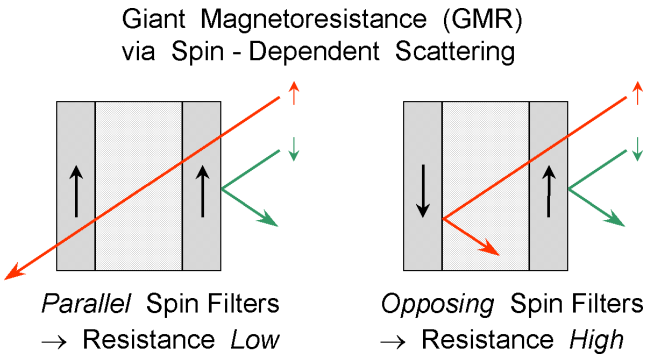

Figure 6.20: Explanation of giant magnetoresistance (GMR) as spin filter effect, using an analogy with parallel and crossed optical polarizers. Achieving spin-dependent reflectivity at interfaces is the key to obtaining large magnetoresistance.

Giant magnetoresistance occurs in two geometries, i.e., with the current in the plane of the layers (often labeled CIP) and perpendicular (CPP). The perpendicular geometry is much less practical than the in-plane, due to the extremely small resistance across the nanolayers, but it is conceptually simpler and exhibits larger magnetoresistance. The picture of GMR given in Fig. 6.20 for the perpendicular geometry allows majority and minority spins to be treated as separate current channels, as in a parallel resistor network.

There is still not complete agreement as to whether the spin-dependent scattering takes places at the interfaces or in the interior of the films. It might not even be specular, as in the simplified picture of Fig. 6.20, but rather diffuse, due to inelastic scattering by d-electrons. In either case, there is a resulting resistance change as long as there is spin-dependent scat-

tering. A natural explanation for interface scattering comes from the spin-dependent step in the inner potential (see the discussion of Fig. 6.18 in Sec. 6.5.1). In optimal cases one has a band gap that causes total reflection of minority spins and spin-polarized quantum well states. Spin-dependent bulk scattering is caused by electron-hole pair creation at the Fermi level. In ferromagnets with a filled majority spin d-band, such as Co and Ni, the majority spin bands are similar to that of a noble metal and the mean free path of spin-up electrons is long. Spin-down electrons, on the other hand, have many other spin-down states near E_F to interact with and do not travel far. Such an argument holds since spin is approximately conserved during scattering.

Spin-polarized tunneling can occur between various combinations of ferromagnets, normal metals, and superconductors [189]. In all cases the insulating spacer layer acts as barrier for planar tunneling. Due to the high barrier in the insulator, only electrons close to the Fermi level participate in the tunneling process, and of those the s,p-electrons with their more extended wave functions dominate. The density of majority states $\mathrm{n}_\uparrow$ is higher for s,p-states at the Fermi level than that of minority s,p-states $\mathrm{n}_\downarrow$. Consequently, a large number of majority spin electrons emitted into the junction meets a high density of empty states when the magnetic orientation is parallel. Therefore, the resistance is low, as in GMR. Defining the spin polarization as

$$P = \left[(n_\uparrow - n_\downarrow)/(n_\uparrow + n_\downarrow)\right] \tag{6.10}$$

and generalizing to two electrodes with different spin polarizations P_1 and P_2 one obtains a formula for δR/R.[190]

$$(\delta R/R) = 2P_1P_2/(1 + P_1P_2) \tag{6.11}$$

The formula shows that the tunneling magnetoresistance is sensitive to the spin polarization at the Fermi level of the electrodes. In this respect, the use of spin-polarized photoemission and the hunt for highly polarized or even half-metallic (Sec. 6.3.2) materials can have an impact on designing spin-polarized tunneling devices.

6.6.2 Spin scattering and magnetic doping

Transport measurements [191, 192] suggest that magnetic impurities can influence the mean free path of carriers and thereby create spin polarization. Importantly for magnetic transport, the mean free path in an alloy can be spin dependent. A change in the constituents or concentrations in an alloy will alter the mean free path of one or both of the spin channels. Careful selection, then, of an alloy's makeup will allow the possibility of magnetic doping, with impurities that shift the balance towards spin up or spin down carriers. Magnetoresistance measurements of multilayer structures and resistivity measurements on ternary alloys have provided estimates for the spin-dependent mean free path. However, relatively little is known about the microscopic mechanism that causes the spin dependence. In order to have the maximum impact on the theory of electronic states in these alloys, angle-resolved photoemission measurements of the relevant states near E_F are needed that resolve the momentum $\boldsymbol{k}$ of specific states on the Fermi surface. The energy resolution needs to be better than the thermal energy kT ($\approx$ 25 meV at room temperature), and the momentum resolution better

than an inverse mean free path (≈ 0.03 Å^{-1} at E_F; note that $\lambda^{-1} \approx 0.2$ Å^{-1} in Fig. 6.2 is for much higher energies of many eV above E_F).

The spin-dependent mean free path for an alloy can be determined from the momentum broadening by high-resolution photoemission [67]. Figure 6.8 shows a set of momentum distribution curves (MDCs) from permalloy ($Ni_{0.8}Fe_{0.2}$) and Ni collected with angle multidetection from data sets similar to those in Fig. 6.3. Similar data have been taken for NiCr alloys [67]. With MDCs, only the states at E_F are examined, which are the ones relevant to magnetism and transport properties. In this case, the Σ_1 band Fermi level crossing in Ni and NiFe alloys is shown. The widths $\delta k_\uparrow$, $\delta k_\downarrow$ of the two spin peaks provide the mean free paths $l_\uparrow$, $l_\downarrow$ through a straightforward application of the uncertainty relation. An exponentially-decaying wave function $\psi(x)$ whose probability density $\psi^*\psi$ decays with length l gives a Lorentzian for the probability density $\Psi^*\Psi$ of its Fourier transform $\Psi(k)$. The full width half maximum is $\delta k = 1/l$. In Fe-doped Ni only the minority peak is broadened. Its width $\delta k_\downarrow$ is roughly proportional to the Fe concentration x, i.e., the mean free path $l_\downarrow$ decreases like $1/x$. In Cr-doped Ni both peaks are broadened, with $\delta k_\uparrow$ slightly larger than $\delta k_\downarrow$ and both comparable to the $\delta k_\downarrow$ for Fe doping. In addition, the area ratio of minority/majority spins decreases by a factor of 2–3 with Fe impurities, thereby reinforcing the spin selectivity. While the magnetic splitting does not change significantly for the Fe concentrations considered here, it decreases with Cr doping, tracking the decreasing magnetic moment. δk_{ex} reaches zero at a Cr concentration close to 13% where NiCr alloys become paramagnetic.

Models for spin-selective scattering can be broadly divided into elastic and inelastic processes. The variation in the crystal potential at the impurity induces a random potential barrier (Fig. 6.9, compare also Fig. 6.18). That gives rise to elastic scattering of Bloch waves and broadens the energy bands [47]. The scattering is similar to the spin-dependent reflectivity that confines magnetic quantum well states (Fig. 6.17). In fcc Fe, the majority states are very close to their Ni counterparts, which has been tested by appearance potential spectroscopy, which maps the density of states of Fe and Ni separately [56]. The minority states, however, lie significantly higher due to the larger magnetic splitting (Fig. 6.5). Therefore, only the minority states see a scattering potential at a Fe impurity. For Cr, both spins have a significant band offset since the reduced filling raises the Cr bands (Fig. 6.9). The discontinuity is somewhat larger for spin up states. This model suggests a strategy for selecting hosts and dopants that favor minority spin carriers: Align the minority spin bands by choosing a host with a large ferromagnetic splitting, such as Fe and Co, and a dopant with lower band filling. Indeed, such systems exhibit inverse GMR [193, 194] and vastly different resistivity for the two spins [191, 192]. Sophisticated first principles calculation of the alloy band structure and the photoemission spectra have begun, which should make it possible to obtain a deeper understanding of the band structure of magnetic alloys [64]. The calculated momentum distributions in Fig. 6.8 agree well with the data. That suggests an elastic scattering process at the impurity potential, as depicted schematically in Fig. 6.9. The calculation will be able to give a much more realistic picture of the scattering potential.

Acknowledgement

This work was supported by NSF under Award Nos. DMR-9815416, DMR-9704196, DMR-0084402, DMR-0079983 and by DOE under Contract No. DE-FG02-01ER45917.

References

[1] F.J. Himpsel *et al.*, Adv. Phys. **47**, 511 (1998).

[2] F.J. Himpsel, Adv. Phys. **32**, 1 (1983).

[3] S.D. Kevan, editor, *Angle-resolved Photoemission*, (Elsevier, Amsterdam, 1992).

[4] E.W. Plummer and W. Eberhardt, Advances in Chemical Physics **49**, 533 (1982).

[5] K. Baberschke, M. Donath, and W. Nolting, eds. *Band-Ferromagnetism: Ground State and Finite Temperature Phenomena*. Springer Lecture Notes in Physics, (Springer, Berlin, 2001).

[6] N.V. Smith, R. Lässer, and S. Chiang, Phys. Rev. B **25**, 793 (1982).

[7] P.D. Johnson, Rep. Prog. Phys. **60**, 1217 (1997).

[8] V. Dose, Surf. Sci. Rep. **5**, 337 (1985).

[9] F.J. Himpsel, Comments Condens. Matter Phys. **12**, 199 (1986).

[10] N.V. Smith, Rep. Prog. Phys. **51**, 1227 (1988).

[11] M. Donath, Surf. Sci. Rep. **20**, 251 (1994).

[12] G. Schönhense and H.C. Siegmann, Annalen der Physik **2**, 465 (1993).

[13] F.J. Himpsel *et al.*, J. Magn. Magn. Mater. **200**, 456 (1999).

[14] N. Martensson *et al.*, J. Electron Spectrosc. Relat. Phenom. **70**, 117 (1994).

[15] F.B. Dunning, Nucl. Instrum. Methods Phys. Res. Sect. A-Accel. Spectrom. Dect. Assoc. Equip. **347**, 152 (1994).

[16] M. Donath, Appl. Phys. A-Mater. Sci. Process. **49**, 351 (1989).

[17] H. Hopster, Surf. Rev. Lett. **1**, 89 (1994).

[18] C. Guillot *et al.*, Phys. Rev. Lett. **39**, 1632 (1977).

[19] L.C. Davis, J. Appl. Phys. **59**, R25 (1986).

[20] F.J. Himpsel, J.A. Knapp, and D.E. Eastman, Phys. Rev. B **19**, 2919 (1979).

[21] A. Liebsch, Phys. Rev. Lett. **43**, 1431 (1979).

[22] P. Heimann, F.J. Himpsel, and D.E. Eastman, Solid State Commun. **39**, 219 (1981).

[23] W. Nolting *et al.*, Phys. Rev. B **40**, 5015 (1989).

[24] M.M. Steiner, R.C. Albers, and L.J. Sham, Phys. Rev. B **45**, 13272 (1992).

[25] A. Kakizaki *et al.*, Phys. Rev. B **55**, 6678 (1997).

[26] M. Sawada, A. Kimura, and A. Kakizaki, J. Phys. Soc. Japan **69**, 1891 (2000).

[27] R.E. Camley, T.S. Rahman, and D. Mills, Phys. Rev. B **27**, 261 (1983).

[28] A. Kueny *et al.*, Phys. Rev. B **29**, 2879 (1984).

[29] G.J. Mankey, R.F. Willis, and F.J. Himpsel, Phys. Rev. B **48**, 10284 (1993).

[30] V.L. Moruzzi, J.F. Janak, and A.R. Williams, *Calculated Electronic Properties of Metals*, (Pergammon, New York, 1978).

[31] D.A. Papaconstantopoulos, *Handbook of the Band Structure of Elemental Solids*, (Plenum Press, New York, 1986).

[32] C.S. Wang and J. Callaway, Phys. Rev. B **15**, 298 (1977).

[33] M. Weinelt *et al.*, Phys. Rev. Lett. **78**, 967 (1997).

[34] E. Weschke and G. Kaindl, J. Phys.-Condes. Matter **13**, 11133 (2001).

[35] L.H. Tjeng, N.B. Brookes, and B. Sinkovic, J. Electron Spectrosc. Relat. Phenom. **117**, 189 (2001).
[36] O. Gunnarson, J. Phys. F **6**, 587 (1976).
[37] F.J. Himpsel, Phys. Rev. Lett. **67**, 2363 (1991).
[38] E. Kisker *et al.*, Physicsl Review B **31**, 329 (1985).
[39] J. Kirschner *et al.*, Phys. Rev. Lett. **53**, 612 (1984).
[40] A. Santoni and F.J. Himpsel, Phys. Rev. B **43**, 1305 (1991).
[41] N.B. Brookes *et al.*, Phys. Rev. B **41**, 2643 (1990).
[42] D.Q. Li *et al.*, Phys. Rev. B **51**, 13895 (1995).
[43] D.L. Li *et al.*, Phys. Rev. B **49**, 7734 (1994).
[44] M. Donath, B. Gubanka, and F. Passek, Phys. Rev. Lett. **77**, 5138 (1996).
[45] M. Bode, M. Getzlaff, and R. Wiesendanger, Phys. Rev. Lett. **81**, 4256 (1998).
[46] J. Schäfer *et al.*, Phys. Rev. Lett. **83**, 2069 (1999).
[47] W.H. Butler *et al.*, J. Magn. Magn. Mater. **151**, 354 (1995).
[48] P. Lambin and F. Herman, Phys. Rev. B **30**, 6903 (1984).
[49] D.M.C. Nicholson *et al.*, J. Appl. Phys. **81**, 4023 (1997).
[50] A.E. Krasovskii, Phys. Rev. B **60**, 12788 (1999).
[51] R.G. Jordan, M.A. Hoyland, and E.A. Seddon, J. Phys.-Condes. Matter **2**, 779 (1990).
[52] M. Landolt, P. Niedermann, and D. Mauri, Phys. Rev. Lett. **48**, 1632 (1982).
[53] D.Y. Petrovykh *et al.*, Appl. Phys. Lett. **73**, 3459 (1998).
[54] V. Rogge, H. Neddermeyer, and T. Paul, J. Phys. F **17**, 1391 (1987).
[55] F. Schedin *et al.*, Phys. Rev. B **61**, 8932 (2000).
[56] J. Reinmuth *et al.*, Phys. Rev. B **56**, 12893 (1997).
[57] T.J. Kreutz *et al.*, Phys. Rev. B **58**, 1300 (1998).
[58] G.J. Mankey *et al.*, Phys. Rev. Lett. **78**, 1146 (1997).
[59] D.E. Eastman, F.J. Himpsel, and J.A. Knapp, Phys. Rev. Lett. **40**, 1514 (1978).
[60] W. Eberhardt and E.W. Plummer, Phys. Rev. B **21**, 3245 (1980).
[61] P. Aebi *et al.*, Phys. Rev. Lett. **76**, 1150 (1996).
[62] K.N. Altmann *et al.*, Phys. Rev. B **61**, 15661 (2000).
[63] M.C. Desjonqueres and M. Lavagna, J. Phys. F **9**, 1733 (1979).
[64] P.E. Mijnarends *et al.*, Phys. Rev. B **65**, 075106 (2002).
[65] D.C. Tsui, Phys. Rev. **164**, 669 (1967).
[66] A.V. Gold, J. Low Temp. Phys. **16**, 3 (1974).
[67] K.N. Altmann *et al.*, Phys. Rev. Lett. **87**, 137201 (2001).
[68] H. Hasegawa and J. Kanamori, J. Phys. Soc. Japan **33**, 1599 (1973).
[69] J.W. Cable and E.O. Wollan, Phys. Rev. B **7**, 2005 (1973).
[70] B.L. Gyorffy *et al.*, Solid State Commun. **23**, 637 (1977).
[71] H. Winter *et al.*, Phys. Rev. B **33**, 2370 (1986).
[72] T.-U. Nahm *et al.*, Phys. Rev. B **54**, 7807 (1996).
[73] M. Hochstrasser *et al.*, Phys. Rev. B **60**, 17030 (1999).
[74] S. Blügel *et al.*, Phys. Rev. B **35**, 3271 (1987).

[75] M. Imada, A. Fujimori, and Y. Tokura, Rev. Mod. Phys. **70**, 1039 (1998).
[76] N.F. Mott, Phil. Mag. **6**, 287 (1962).
[77] J. Hubbard, Proc. Roy. Soc. London, Ser. A **277**, 237 (1964).
[78] J. Hubbard, Proc. Roy. Soc. London, Ser. A **281**, 401 (1964).
[79] T. Mizokawa and A. Fujimori, Phys. Rev. B **53**, R4201 (1996).
[80] K. Terakura *et al.*, Phys. Rev. Lett. **52**, 1830 (1984).
[81] P.W. Anderson, Phys. Rev. **115**, 2 (1959).
[82] J. Zaanen, G.A. Sawatzky, and J.W. Allen, Phys. Rev. Lett. **55**, 418 (1985).
[83] S.-J. Oh *et al.*, Phys. Rev. B **26**, 4845 (1982).
[84] J.M. McKay and V.E. Henrich, Phys. Rev. Lett. **53**, 2343 (1984).
[85] S. Hüfner *et al.*, Solid State Communications **52**, 793 (1984).
[86] G.A. Sawatzky and J.W. Allen, Phys. Rev. Lett. **53**, 2339 (1984).
[87] A. Fujimori and F. Minami, Phys. Rev. B **30**, 957 (1984).
[88] G. Lee and S.J. Oh, Phys. Rev. B **43**, 14674 (1991).
[89] A. Fujimori, F. Minami, and S. Sugano, Phys. Rev. B **29**, 5225 (1984).
[90] L.C. Davis, Phys. Rev. B **25**, 2912 (1982).
[91] Z.X. Shen *et al.*, Phys. Rev. Lett. **64**, 2442 (1990).
[92] Z.X. Shen *et al.*, Phys. Rev. B **44**, 3604 (1991).
[93] Z.X. Shen *et al.*, Phys. Rev. B **42**, 1817 (1990).
[94] F. Manghi, C. Calandra, and S. Ossicini, Phys. Rev. Lett. **73**, 3129 (1994).
[95] H. Scheidt, M. Globl, and V. Dose, Surf. Sci. **112**, 97 (1981).
[96] F.J. Himpsel and T. Fauster, Phys. Rev. Lett. **49**, 1583 (1982).
[97] C. Schüssler-Langeheine *et al.*, Phys. Rev. Lett. **84**, 5624 (2000).
[98] F.J. Himpsel and B. Reihl, Phys. Rev. B **28**, 574 (1983).
[99] T. Tsujioka *et al.*, Phys. Rev. B **56**, R15509 (1997).
[100] M.A. Korotin *et al.*, Phys. Rev. Lett. **80**, 4305 (1998).
[101] Mazin, II, D.J. Singh, and C. Ambrosch-Draxl, Phys. Rev. B **59**, 411 (1999).
[102] C.B. Stagarescu *et al.*, Phys. Rev. B **61**, R9233 (2000).
[103] W.E. Pickett and D.J. Singh, Phys. Rev. B **53**, 1146 (1996).
[104] J.B. Goodenough, J. Appl. Phys. **81**, 5330 (1997).
[105] A. Berger *et al.*, J. Vac. Sci. Technol. A-Vac. Surf. Films **18**, 1239 (2000).
[106] D.S. Dessau *et al.*, J. Electron Spectrosc. Relat. Phenom. **117**, 265 (2001).
[107] S. Hüfner, Adv. Phys. **43**, 183 (1994).
[108] H. Eskes, L.H. Tjeng, and G.A. Sawatzky, Phys. Rev. B **41**, 288 (1990).
[109] W.E. Pickett, Rev. Mod. Phys. **61**, 433 (1989).
[110] M.B. Maple and O. Fischer, eds. *Superconductivity and Magnetism*.(Springer-Verlag, Berlin, 1982).
[111] M. Houzet, A. Buzdin, and M.L. Kulic, Phys. Rev. B **64**, 184501 (2001).
[112] A. Damascelli *et al.*, Phys. Rev. Lett. **85**, 5194 (2000).
[113] A.V. Puchkov *et al.*, Phys. Rev. B **58**, R13322 (1998).
[114] R. Matzdorf *et al.*, Science **289**, 746 (2000).

[115] X.J. Zhou *et al.*, Phys. Rev. Lett. **86**, 5578 (2001).
[116] C. Pfleiderer *et al.*, Nature **412**, 58 (2001).
[117] N. Nücker *et al.*, Phys. Rev. B **37**, 5158 (1988).
[118] J.A. Yarmoff *et al.*, Phys. Rev. B **36**, 3967 (1987).
[119] E. Pellegrin *et al.*, Phys. Rev. B **53**, 10667 (1996).
[120] F.J. Himpsel *et al.*, Phys. Rev. B **38**, 11946 (1988).
[121] F.C. Zhang and T.M. Rice, Phys. Rev. B **37**, 3759 (1988).
[122] R.A. De Groot *et al.*, Phys. Rev. Lett. **50**, 2024 (1983).
[123] A. Anguelouch *et al.*, Phys. Rev. B **64**, 180408 (2001).
[124] R.J. Soulen *et al.*, Science **282**, 85 (1998).
[125] K.P. Kämper *et al.*, Phys. Rev. Lett. **59**, 2788 (1987).
[126] R.H. Cheng *et al.*, Appl. Phys. Lett. **79**, 3122 (2001).
[127] R.H. Cheng *et al.*, Appl. Phys. Lett. **78**, 521 (2001).
[128] K. Schwarz, J. Phys. F **16**, L211 (1986).
[129] K. Attenkofer and G. Schütz, J. Phys. IV **7**, 459 (1997).
[130] S.P. Lewis, P.B. Allen, and T. Sasaki, Phys. Rev. B **55**, 10253 (1997).
[131] W. Zhu *et al.*, Phys. Rev. B **64**, 060403 (2001).
[132] G.L. Bona *et al.*, Solid State Communications **56**, 391 (1985).
[133] C.T. Tanaka, J. Nowak, and J.S. Moodera, J. Appl. Phys. **86**, 6239 (1999).
[134] J.H. Park *et al.*, Nature **392**, 794 (1998).
[135] B. Nadgorny *et al.*, Phys. Rev. B **63**, 184433 (2001).
[136] H. Dulli *et al.*, Appl. Phys. Lett. **77**, 570 (2000).
[137] M.B. Salamon and M. Jaime, Rev. Mod. Phys. **73**, 583 (2001).
[138] Y.D. Chuang *et al.*, Science **292**, 1509 (2001).
[139] H. Ohno, Science **281**, 951 (1998).
[140] J.J. Berry *et al.*, Appl. Phys. Lett. **77**, 3812 (2000).
[141] H. Akinaga *et al.*, Appl. Phys. Lett. **76**, 357 (2000).
[142] M. Oshima *et al.*, Int. J. Mod. Phys. B **16**, 1681 (2002).
[143] J. Okabayashi *et al.*, Phys. Rev. B **64**, 125304 (2001).
[144] A. Fujimori and T. Mizokawa, *Electronic Structure of 3d Transition-Metal Impurities in Semiconductors*, in *II-VI Semiconducting Componds*, M. Jain, Editor, (World Scientific, Singapore, 1993), p. 103.
[145] B. Beschoten *et al.*, Phys. Rev. Lett. **83**, 3073 (1999).
[146] T. Dietl *et al.*, Science **287**, 1019 (2000).
[147] J. Okabayashi *et al.*, Phys. Rev. B **59**, R2486 (1999).
[148] T. Mizokawa and A. Fujimori, Phys. Rev. B **48**, 14150 (1993).
[149] T. Mizokawa *et al.*, Phys. Rev. B **65**, 085209 (2002).
[150] J.F. Janak, Phys. Rev. B **16**, 255 (1977).
[151] H. Ibach and H. Lüth, *Solid State Physics*, (Springer-Verlag, Berlin, 1993).
[152] E.P. Wohlfarth, Rev. Mod. Phys. **25**, 211 (1953).
[153] D.G. Pettifor, J. Magn. Magn. Mater. **15–18**, 847 (1980).

[154] M. Uhl and J. Kübler, Phys. Rev. Lett. **77**, 334 (1996).
[155] V. Korenman and R.E. Prange, Phys. Rev. Lett. **53**, 186 (1984).
[156] P. Fulde, *Electron Correlations in Molecules and Solids*. Springer Series in Solid State Sciences 100, (Springer-Verlag, Berlin, 1991).
[157] C.J. Maetz *et al.*, Phys. Rev. Lett. **48**, 1686 (1982).
[158] H. Hopster *et al.*, Phys. Rev. Lett. **51**, 829 (1983).
[159] K.P. Kämper, W. Schmitt, and G. Güntherodt, Phys. Rev. B **42**, 10696 (1990).
[160] W. Von der Linden, M. Donath, and V. Dose, Phys. Rev. Lett. **71**, 899 (1993).
[161] L.H. Tjeng *et al.*, Phys. Rev. Lett. **81**, 734 (1998).
[162] B. Kim *et al.*, Phys. Rev. Lett. **68**, 1931 (1992).
[163] T. Takahashi *et al.*, Phys. Rev. B **63**, 094415 (2001).
[164] U. Gradmann, *Magnetic Surfaces*, in *Landolt-Börnstein New Series Group III*, H.P.J. Wijn, Editor, (Springer, Berlin, 1988), p. 1.
[165] U. Gradmann, *Magnetic Surfaces*, in *Landolt-Börnstein New Series Group III*, G. Chiarotti, Editor, (Springer, Berlin, 1994), p. 506.
[166] E. Fawcett, Rev. Mod. Phys. **60**, 209 (1988).
[167] L.W. Bos and D.W. Lynch, Phys. Rev. B **2**, 4567 (1970).
[168] K. Machida, M.A. Lind, and J.L. Stanford, J. Phys. Soc. Japan **53**, 4020 (1984).
[169] A. Fujimori *et al.*, Phys. Rev. B **37**, 3109 (1988).
[170] J.E. Ortega and F.J. Himpsel, Phys. Rev. Lett. **69**, 844 (1992).
[171] D.M. Edwards *et al.*, Phys. Rev. Lett. **67**, 493 (1991).
[172] J.E. Ortega and F.J. Himpsel, Phys. Rev. B **47**, 16441 (1993).
[173] W. Weber *et al.*, Phys. Rev. Lett. **76**, 1940 (1996).
[174] A. Carl and D. Weller, Phys. Rev. Lett. **74**, 190 (1995).
[175] T. Katayama *et al.*, J. Magn. Magn. Mater. **126**, 527 (1993).
[176] M.G. Koerkamp *et al.*, J. Appl. Phys. **79**, 5632 (1996).
[177] M. Jalochowski *et al.*, Phys. Rev. B **45**, 13607 (1992).
[178] A.R. Smith *et al.*, Science **273**, 226 (1996).
[179] D.A. Luh *et al.*, Science **292**, 1131 (2001).
[180] K. Garrison, Y. Chang, and P.D. Johnson, Phys. Rev. Lett. **71**, 2801 (1993).
[181] C. Carbone *et al.*, Phys. Rev. Lett. **71**, 2805 (1993).
[182] J.E. Ortega *et al.*, J. Magn. Magn. Mater. **203**, 126 (1999).
[183] S.S.P. Parkin, Phys. Rev. Lett. **67**, 3598 (1991).
[184] R.K. Kawakami *et al.*, Phys. Rev. Lett. **82**, 4098 (1999).
[185] P. Bruno and C. Chappert, Phys. Rev. Lett. **67**, 1602 (1991).
[186] M.D. Stiles, Phys. Rev. B **48**, 7238 (1993).
[187] J.F. MacKay *et al.*, Phys. Rev. Lett. **77**, 3925 (1996).
[188] G.A. Prinz, Science **282**, 1660 (1998).
[189] R. Meservey and P.M. Tedrow, Phys. Rep.-Rev. Sec. Phys. Lett. **238**, 173 (1994).
[190] M. Julliere, Phys. Lett. **54A**, 225 (1975).

[191] I.A. Campbell and A. Fert, *Transport Properties of Ferromagnets*, in *Ferromagnetic Materials*, E.P. Wohlfarth, Editor, (North Holland, 1982), p. 747.

[192] A. Fert and I.A. Campbell, J. Phys. F **6**, 849 (1976).

[193] S.Y. Hsu *et al.*, Phys. Rev. Lett. **78**, 2652 (1997).

[194] J.M. George *et al.*, Phys. Rev. Lett. **72**, 408 (1994).

[195] J.K. Lang, Y. Baer, and P.A. Cox, J. Phys. F **11**, 121 (1981).

[196] J.E. Ortega *et al.*, Solid State Communications **91**, 807 (1994).

[197] F.J. Himpsel and D.E. Eastman, Phys. Rev. B **21**, 3207 (1980).

[198] R. Raue, H. Hopster, and R. Clauberg, Phys. Rev. Lett. **50**, 1623 (1983).

[199] M. Donath, P.A. Dowben, and W. Nolting, Eds., *Magnetism and Electronic Correlations in Local-Moment Systems: Rare Earth Elements and Compounds*, (World Scientific, Singapore, 1998), p. 217.

Solid-State Photoemission and Related Methods
Wolfgang Schattke, Michel A. Van Hove (Eds.)

7 The band structure theory of LEED and photoemission

E.E. Krasovskii

7.1 Introduction

Photoemission measurements have been a source of most detailed information about the electronic structure of solids. Since the state-of-the-art *ab initio* calculations fail to pointwise reproduce the experimental spectra, the role of the theory remains to extract the information from the experiment. This concerns, in the first place, the understanding of the many-body interactions in solids, which are included in the theoretical calculations in very crude approximations. Simpler aspects of the band structure, such as the exact shape of the one-electron potential and wave functions, should be, however, taken into account as accurately as possible, so that unavoidable approximations are kept under control. This calls for the development of computational approaches that would draw on the progress in the bulk band structure methodology.

Within the independent-particle model photoemission is described by optical excitations of electrons into the time-reversed LEED states [1, 2]. LEED measurements have been traditionally used to study the crystal structure of surfaces. Since early 1980's the measurements at very low energies (VLEED) have become a tool to study also the unoccupied band structure of the substrate [3–5]. If the interaction of the photoelectron with the hole left behind in the photoexcitation process can be neglected the connection between the photoemission and the low energy electron diffraction experiment becomes very simple. In this chapter, we restrict ourselves to a simplest version of the one-particle picture: the wave functions are solutions of the Kohn-Sham equations and the interaction of the particles is taken into account by a self-consistent field. This approach has proven its wide applicability, and its adequacy and limitations have been extensively discussed in the literature (see Chapter 1).

The formulation of the scattering problem (LEED problem) in terms of Bloch waves is straightforward [6,7]. The space is divided into the vacuum half-space and the bulk half-space by a matching plane. In the crystal half-space the LEED function is a linear combination of bulk solutions. Far from the crystal surface, where the potential is periodic, they reduce to propagating and evanescent Bloch waves, and the coefficients are determined by matching the trial function in the bulk to the vacuum half-space at the plane. Until recently, the LEED or photoemission calculations within the Bloch waves theory have been performed only within the pseudo-potential approach using the plane-wave basis set (see review article [8]).

In this chapter, we consider an all-electron approach to the scattering states in the semi-infinite crystal, which makes use of the most robust and accurate band structure technique, the augmented plane waves method (APW). The APW method was proposed in 1937 by Slater. This computational algorithm attracted practical users by the possibility to achieve arbitrarily

Solid-State Photoemission and Related Methods: Theory and Experiment. Edited by Wolfgang Schattke, Michel A. Van Hove

ISBN: 3-527-40334-5

high accuracy of the variational band energies without having a complete basis set. The first APW calculation was performed in 1939 by Chodorow; since then the growth of computer technology has opened a way to intensively exploit the idea of augmentation. For decades the APW approach has been being developed in order to reconcile a linear-algebra formulation of the variational problem with the convergence properties of the original formulation and to extend the method to crystal potentials of general shape. Great progress of the APW methodology is due to the concept of linear methods introduced by Andersen in 1975. Augmented plane waves have become the basis for numerically most precise and reliable band structure techniques, such as, for example, the full-potential linear APW method, with which the majority of all-electron ground-state studies have been performed (see Chapter 1).

Originally designed for the boundary value problem, the APW approach has recently started to penetrate the field of electron scattering. The most direct access to the Bloch-wave treatment of low energy electron diffraction is given by the $\mathbf{k} \cdot \mathbf{p}$ formulation of the *inverse band structure problem*, i.e., the problem of constructing all Bloch states at a given energy with a given surface projection of the Bloch vector. The $\mathbf{k} \cdot \mathbf{p}$ method reduces the problem to a matrix eigenvalue equation, whose solutions form the complex band structure of the semi-infinite crystal.

In this chapter, after an introduction to the APW formalism and the computational properties of APW-like methods, we discuss the application of the band structure theory to electron scattering in semi-infinite crystals. Special attention will be paid to an optical-potential description of inelastic processes. The theory will be illustrated by a study of VLEED in $NbSe_2$ and surface state photoemission in Al.

7.2 Ultima ratio regnum: the APW method

The direct variational methods to calculate the one-electron Bloch states are divided with regard to the eigenvalue dependence of the basis set into nonlinear methods, e.g., the Korringa-Kohn-Rostocker method [9] and the APW method [10], and linear methods, of which the most widely used are the linear muffin-tin orbitals method (LMTO) [11] and the APW-like schemes [11–18]. The former approach requires that the trial function pointwise satisfy the Schrödinger equation inside the so-called muffin-tin spheres, whereas in the linear methods it is a linear combination of a number of spherical waves.

The nonlinear methods are precise in the sense that they allow the eigenenergies and wave functions to be determined with unlimited accuracy. However, they lead to a nonlinear eigenvalue problem and, in general, produce wave functions with a discontinuity in slope at the sphere boundary. In addition to this, in the case that the potential inside the muffin-tin spheres is not spherically symmetric, additional programming effort is required to construct the exact solution in the spheres. The above difficulties are avoided in the linear methods, which employ an eigenvalue-independent basis set. There the wave function is by construction continuous with continuous derivative everywhere in the unit cell. Another advantage of using the fixed basis set is that the formalism is easily extended to the case of a potential of general shape [22].

A common problem of direct variational methods is that a good convergence of eigenvalues does not ensure a high accuracy of eigenfunctions. The quality of the wave function in a

given region depends upon how sensitive to it is the eigenvalue. In calculations for the semi-infinite crystal, the requirements of the accuracy of wave functions are especially stringent because the observables depend on the behavior of the wave function at the matching surface (rather than on volume integrals, such as band energies or momentum matrix elements). In Sec. 7.2.1, we discuss various APW-like methods and their accuracy. In Sec. 7.2.3, we introduce the extended LAPW-$\mathbf{k}\cdot\mathbf{p}$ method – the basic computational tool of our studies. The $\mathbf{k}\cdot\mathbf{p}$ approach can be viewed as a compromise between pseudo-potential and all-electron[1] methods in the sense that the basis set is $\mathbf{k}$-point independent, but the potential remains all-electron and local.

7.2.1 The augmented plane waves formalism

In a variational method the wave function of Bloch vector $\mathbf{k}$ and band number λ is sought as a linear combination of basis functions satisfying the Bloch boundary conditions. The most straightforward way would be to expand the function in the Fourier series

$$\psi_{\mathbf{k}\lambda}(\mathbf{r}) = \sum F_{\mathbf{G}}^{\mathbf{k}\lambda}\, \exp[i(\mathbf{k}+\mathbf{G})\mathbf{r}]. \tag{7.1}$$

Here $\mathbf{G}$ are the reciprocal lattice vectors and $F_{\mathbf{G}}$ are variational coefficients. It has been realized by Slater that owing to the singularity of the crystal potential at the nucleus, the plane wave series would converge very slowly and the diagonalization of the Hamiltonian matrix in terms of plane waves is impracticable. Even with the modern computational hardware the plane waves are used only in the context of pseudo-potential calculations.

In the APW method the singularities are surrounded with so-called muffin-tin spheres, which do not overlap and usually are chosen such that they occupy maximum volume. By augmentation one understands the replacement of the Bessel functions $j_l(Kr)$ in the Rayleigh decomposition of the plane wave inside the sphere with radial functions $\Phi_l(K,r)$, which match the Bessel functions in value and in slope[2] at the sphere radius.

Inside the sphere located at $\mathbf{r}=0$ the APW reads

$$\xi(\mathbf{K},\mathbf{r}) = \sum_{lm} 4\pi i^l \Phi_l(K,r) Y_{lm}^*(\hat{\mathbf{K}}) Y_{lm}(\hat{\mathbf{r}}), \quad \mathbf{K}=\mathbf{k}+\mathbf{G}, \tag{7.2}$$

and the trial function is

$$\psi_{\mathbf{k}\lambda}(\mathbf{r}) = \sum_{i=1}^{N} C_i^{\mathbf{k}\lambda}\, \xi_i(\mathbf{K},\mathbf{r}). \tag{7.3}$$

The variational coefficients C_i uniquely determine the wave function in the interstitial. In *extended* linear methods additional variational coefficients are introduced, which are responsible

[1] By the word 'all-electron' one means a true crystal potential, which diverges as r^{-1} at the nucleus, as opposed to the pseudo-potential, in which the singularity is removed. That does not mean, however, that the LAPW calculation generates all states down to the 1s state. The core states do not appear among the LAPW eigenstates (unless it is desired for a specific purpose) because their overlap with the LAPW basis functions is negligible. The core states are treated separately by an atomic-like calculation.

[2] Among the linear methods the exception is the APW+lo method [17], in which the continuity of derivative is not required.

for the shape of the functions Φ_l and enter as coefficients of localized orbitals [16, 18, 25]. In contrast to linear methods, in Slater's formulation of the method the variation of functions Φ_l is achieved by their explicit dependence upon the energy to be found $E_{\mathbf{k}\lambda}$, which makes the procedure nonlinear.

Owing to the matching conditions at the boundaries of the muffin-tin spheres, the shape of the trial function inside the spheres is connected to its shape in the interstitial. Numerous versions of the linear APW can be divided into rigid schemes [11–14], in which the function is uniquely determined by its shape in the interstitial, and flexible schemes [15–18], which allow the functions Φ_l certain variational freedom after the matching conditions have been fulfilled.

The first linearization of the APW method was the modified APW method presented in 1970 by Bross [15]. However, this method has not been widely used and the majority of the APW calculations have been based on the LAPW formalism developed five years later by Andersen [11]. In the 1990s the growing requirements to the accuracy of band-structure calculations brought the flexible methods into wider use; extended versions of the LAPW [16–18] and LMTO [20] have been developed and applied to ground-state as well as to spectroscopic studies. There exists a variety of the APW schemes, which employ different prescriptions for the radial basis functions. However, the convergence properties of the APW methods are primarily determined by the degree of the flexibility of the radial basis set, while the shape of individual basis functions is of secondary importance. The simplest version of a rigid LAPW [11, 19] (see Sec. 7.2.2) has been adopted in the majority of studies, and more sophisticated rigid schemes [12–14] did not show any noticeable advantage over it.

In the majority of implementations the radial functions Φ_l are linear combinations of a number of solutions of the radial Schrödinger equation $\phi_{\nu l}(E_{\nu l}, r)$, and their energy derivatives $\dot{\phi}_{\nu l}(E_{\nu l}, r)$

$$(\hat{H}_r - E_{\nu l})\,\phi_{\nu l}(E_{\nu l}, r) = 0, \tag{7.4}$$

$$(\hat{H}_r - E_{\nu l})\,\dot{\phi}_{\nu l}(E_{\nu l}, r) = \phi_{\nu l}(E_{\nu l}, r), \qquad \left\langle\, \dot{\phi}_{\nu l} \mid \phi_{\nu l} \,\right\rangle = 0. \tag{7.5}$$

$E_{\nu l}$ are called energy parameters of the method. Of this set only two functions for each l are needed to match an APW in both value and slope at the sphere.

7.2.2 Andersen's LAPW

Let the augmentation function $\Phi_l(K, r)$ be a linear combination of two radial functions that matches the Bessel function $j_l(Kr)$ both in value and in slope at the sphere radius. To within a factor, the function $\Phi(K)$ is determined by its radial logarithmic derivative D. For the normalized radial function we shall use the notation $\Phi(D) = \Phi(K)/\sqrt{\langle\, \Phi(K) \mid \Phi(K) \,\rangle}$.

To represent $\Phi(D)$ by a linear combination of a solution ϕ_ν and its energy derivative $\dot{\phi}_\nu$ was suggested in 1967 by Marcus [24]. This way of augmentation results in a convenient and elegant formalism because the functions ϕ_ν and $\dot{\phi}_\nu$ are orthogonal and have the same energy expectation value E_ν. It leads to the classical LAPW method: one chooses a set of energy parameters $\{E_{\nu l}\}$ – one parameter per angular momentum channel – and solves the Eqs. (7.4) and (7.5) to obtain the potential parameters for constructing energy independent Hamiltonian and overlap matrices. The formalism of the method was described by Andersen in Ref. [11] and the properties of the method were analyzed by Koelling and Arbman in Ref. [19].

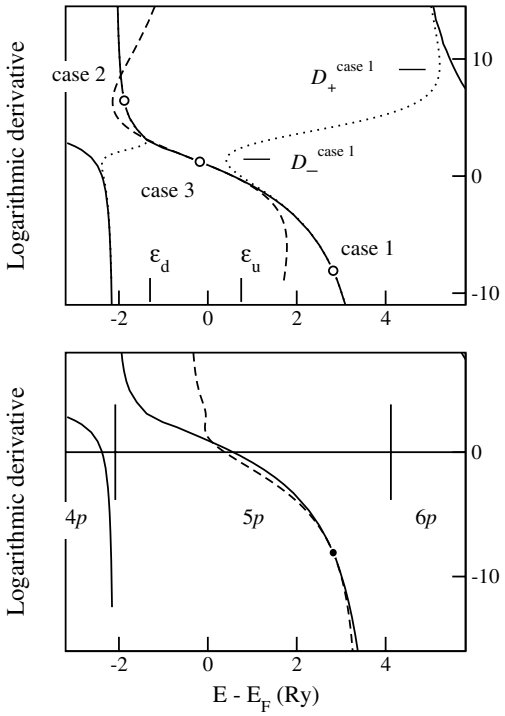

Figure 7.1: Behavior of the parametrization curve $E_{\rm par}(D)$ [see Eq. (7.7)] depending on the location of the energy parameter. The exact curve, $D^{\rm true}(E)$, is shown by full lines. The circles denote the location of the parameters for the three cases [see Eq. (7.10)]. Cases 1 and 2 are shown by dotted lines and case 3 by the dashed line. The dashed line in the lower panel shows the logarithmic derivative dependence of the energy expectation value of the radial function normalized so as to match the exact solution in both value and slope at the sphere. Note, that the choice of the energy parameter E_ν for p-orbitals in the valence band region (between -0.45 Ry and $E_F = 0$) leads to case 3.

To get the idea of how good the choice of the energy parameters is one compares the exact energy dependence of the radial logarithmic derivative,

$$D^{\rm true}(E) = S\,\frac{\phi_l'(E,r)}{\phi_l(E,r)}\bigg|_S, \tag{7.6}$$

to the energy parametrization curve

$$E_{\rm par}\,(D) = \langle\,\Phi_l(D)\mid \hat{H}_r \mid \Phi_l(D)\,\rangle. \tag{7.7}$$

The exact curve has a cotangent-like shape, the branches being referred to by the main quantum number. Figure 7.1 shows an example for the p-orbitals in the muffin-tin sphere of Nb metal. Using Eqs. (7.4) and (7.5) one can operate the Hamiltonian $\hat{H}_r$ on the function $\Phi_l(D)$ to obtain an analytical expression for the one-valued function $E_{\rm par}\,(D)$. By differentiating with respect to the argument D one can establish main characteristic features of the curve. Its slope changes sign twice at $D = D_+$ and $D = D_-$, see upper panel of Fig. 7.1,

$$D_\pm = D_{\dot\nu} + S^{-1}\left(\phi_\nu(S)\dot\phi_\nu(S) \pm \frac{\dot\phi_\nu^2(S)}{\sqrt{\langle\,\dot\phi_\nu \mid \dot\phi_\nu\,\rangle}}\right)^{-1}, \quad D_{\dot\nu} = S\,\frac{\dot\phi_\nu'(r)}{\dot\phi_\nu(r)}\bigg|_S. \tag{7.8}$$

The vertical asymptote of the curve $E_{\rm par}\,(D)$ is at

$$\epsilon_a = E_\nu - \frac{\phi_\nu(S)/\dot\phi_\nu(S)}{1 + \langle\,\dot\phi_{\nu l} \mid \dot\phi_{\nu l}\,\rangle\phi_\nu^2(S)/\dot\phi_\nu^2(S)}. \tag{7.9}$$

In the vicinity of $D_{\nu l} \equiv D^{\rm true}(E_\nu)$ the variational estimate (7.7) is correct to $o\,(E-E_\nu)^3$ [11, 19]. Depending on the position of E_ν relative to the asymptotes of the true curve, the parametrization curve adopts one of three possible shapes (see Fig. 7.1). For the n-th branch ($n > 1$) two energies, $\epsilon_d < \epsilon_u$, divide the branch into three intervals, the shape of the parametrization curve being determined by which interval E_ν belongs to:

$$\begin{aligned}
&\text{case 1,} && E_\nu \geq \epsilon_u: && D_{\dot\nu} \in [D_-, D_+], && D_{\dot\nu} \geq D_\nu,\\
&\text{case 2,} && E_\nu \leq \epsilon_d: && D_{\dot\nu} \in [D_-, D_+], && D_{\dot\nu} < D_\nu,\\
&\text{case 3,} && \epsilon_d < E_\nu < \epsilon_u: && D_{\dot\nu} \notin [D_-, D_+].
\end{aligned}$$

In the cases 1 and 2 the $E_{\rm par}\,(D)$ curve extends to the $(n+1)$-st and $(n-1)$-st branch respectively; in both cases the corresponding asymptotes are properly described, and the interval of the unphysical behavior of the parametrization, where $dD/dE > 0$, is finite. In the third case the parametrization curve has negative slope only within a finite interval, and its asymptote is far from those of the true curve. In band structure calculations the states in the vicinity of the asymptote are usually of physical interest, so case 3 is normally avoided.

Thus, if the energy parameters are close to the eigenvalue in question the accuracy can be systematically improved by including more APWs until the convergence in the interstitial is achieved. However, if the eigenvalue lies far from the energy E_ν the well-converged eigenvalue may happen to be much less accurate than the parametrization curve in the upper panel of Fig. 7.1. The reason is that two functions that have the same logarithmic derivative D and the same energy expectation value are not necessarily close to each other. Indeed, the functions $\phi_l(E)$ and $\Phi_l[D^{\rm true}(E)]$, whose energy expectation values are compared in the upper panel of Fig. 7.1, are equally normalized but have different values at the sphere radius, $\phi_l(E,S) \neq \Phi_l[D^{\rm true}(E), S]$. To assess the quality of the variationally obtained radial function one should compare the function to the exact solution having not only the same logarithmic derivative but also the same value at the sphere. If we lift the requirement of normalization and impose the constraint of matching to the interstitial then we arrive at the dashed line in the lower panel of Fig. 7.1, which shows the contribution to the energy of the function $\Phi_l[D(E), r]\cdot\phi_l(E,S)/\Phi_l[D(E),S]$. The energy range where the error of the radial function is small is seen to be considerably narrower than that suggested by the $E_{\rm par}\,(D)$ curve.

What we have analyzed so far is the accuracy of wave functions that have the correct logarithmic derivative $D^{\rm true}$ at the sphere. In practice, except for atomic-like states, the variational procedure almost never generates precise logarithmic derivatives (see Ref. [21]). As a result, in the rigid methods one can obtain perfectly parameterized radial functions, which are infinitely close to solutions of the radial Schrödinger equation, though for an energy which is far from the eigenvalue in question.

The only way to systematically improve the accuracy over a wide energy interval is to extend the basis set of the method by including further radial functions in addition to ϕ and $\dot\phi$. This approach gives rise to the extended LAPW method (ELAPW) [25] as well as to other flexible versions of the LAPW method, LAPW+LO (local orbitals) [16,26] and APW+lo [17]. The ELAPW method yields the wave functions of semi-core states, valence band, and free-electron-like states as orthogonal eigenvectors of a single matrix eigenvalue problem and without much computational effort provides reliable results over an energy interval of about 50 eV. The performance of the ELAPW method with regard to spectroscopic calculations

has been analyzed by the present author in Refs. [25] and [18]. The convergence properties of LAPW+LO and APW+lo methods in connection to the ground-state properties have been discussed by Singh in Refs. [16] and [26] and by Sjöstedt *et al.* in Ref. [17], respectively.

7.2.3 The extended LAPW - k·p method

The $\mathbf{k}\cdot\mathbf{p}$ formalism reduces the $\mathbf{k}$-point dependence of the basis set to a multiplication of the basis functions with a reference Bloch vector $\mathbf{k}_0$ by the function $\exp[i(\mathbf{k}-\mathbf{k}_0)\mathbf{r}]$. Then the Schrödinger equation

$$\hat{H}\psi_{\mathbf{k}\lambda} = E\psi_{\mathbf{k}\lambda} \tag{7.10}$$

leads to the matrix equation

$$\left[\hat{H}_{\mathbf{k}_0} + 2\Delta\mathbf{k}\cdot\hat{\mathbf{P}}_{\mathbf{k}_0} + (\Delta k^2 - E)\hat{O}_{\mathbf{k}_0}\right]\mathbf{C}^{\mathbf{k}\lambda} = 0, \tag{7.11}$$

$$\begin{aligned} H_{ij} &= \langle \xi_i^{\mathbf{k}_0} \mid -\frac{\hbar^2}{2m}\Delta + V(\mathbf{r}) \mid \xi_j^{\mathbf{k}_0}\rangle, \\ O_{ij} &= \langle \xi_i^{\mathbf{k}_0} \mid \xi_j^{\mathbf{k}_0}\rangle, \\ \mathbf{P}_{ij} &= \langle \xi_i^{\mathbf{k}_0} \mid -i\hbar\nabla \mid \xi_j^{\mathbf{k}_0}\rangle. \end{aligned}$$

The $\mathbf{k}\cdot\mathbf{p}$ formulation is convenient when the functions have sophisticated numerical representation, as, e.g., in the ELAPW method, because the time-consuming operations of setting up the Hamiltonian $\hat{H}$, overlap $\hat{O}$, and momentum $\hat{\mathbf{P}}$ matrices are performed only once for a given crystal potential.

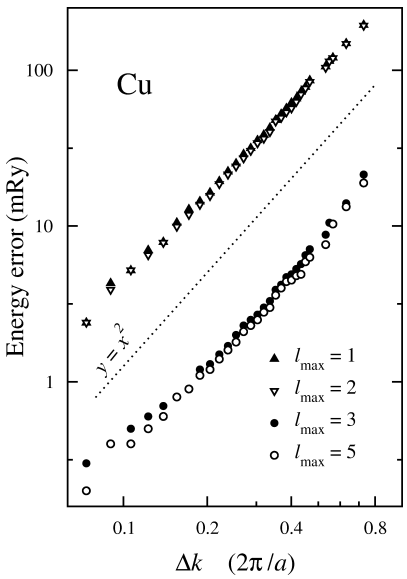

Figure 7.2: The energy error of the ELAPW-$\mathbf{k}\cdot\mathbf{p}$ method vs the distance from the reference point for several extensions [23]. The reference point is at the center of gravity of the irreducible part of the Brillouin zone. The energies $E_{\mathbf{k}\lambda}$ calculated on a uniform $\mathbf{k}$-point mesh by the ELAPW-$\mathbf{k}\cdot\mathbf{p}$ method and by the pure ELAPW are compared. Four basis sets have been considered with the radial extension for angular momenta up to $l_{\max} = 1$, 2, 3, and 5. The Δk-dependence of the error is averaged over the directions of $\Delta\mathbf{k}$ and over the energy interval from the bottom of the valence band to 0.5 Ry above the Fermi level.

That the basis set of a $\mathbf{k}\cdot\mathbf{p}$ method is not Bloch-vector-adjusted causes the accuracy of the method to deteriorate with the distance $\Delta k = |\mathbf{k}-\mathbf{k}_0|$ from the reference point. The problem is especially severe in the case of localized states, such as semicore states or d states of noble metals. For example, to reproduce an orbital $\Phi_{lm}(\mathbf{r}) = \Phi_l(r)Y_{lm}(\hat{\mathbf{r}})$ the trial function has to take the form $\Phi_{lm}(\mathbf{r})\exp[-i(\mathbf{k}-\mathbf{k}_0)\mathbf{r}]$, which is an infinite angular momentum series, with radial functions being not solutions of the radial Schrödinger equation any more. Owing to the extension of the radial basis set, the distorted functions can be reproduced with acceptable accuracy; an example for Cu is presented in Fig. 7.2. The energy error is seen to be a power function of the distance from the reference point, the exponent being close to 2. That means that the error in the wave function is approximately proportional to Δk. In the valence band of Cu localized d states dominate; it is seen that including the f-functions reduces the error by an order of magnitude, whereas functions of d, g, and h character are of virtually no importance. The great improvement is achieved by adding a new radial solution $\phi_f(E_2)$ and its energy derivative $\dot{\phi}_f(E_2)$ to the pair $\phi_f(E_1)$ and $\dot{\phi}_f(E_1)$ employed in the non-$\mathbf{k}\cdot\mathbf{p}$ calculation. To further improve the accuracy we have to add the functions arising from the product $\Phi_{lm}(\mathbf{r})\exp[-i(\mathbf{k}-\mathbf{k}_0)\mathbf{r}]$, namely, for the angular momentum l the orbitals of the first order in Δk, $\Phi_{l\pm1}(r)r$, and orbitals of the second order, $\Phi_l(r)r^2$ and $\Phi_{l\pm2}(r)r^2$ [31].

7.2.4 Back to plane waves

Owing to rapid oscillations of the all-electron wave function near the nucleus, its plane wave expansion (7.1) converges very slowly. The rapidly varying part can, however, be separated out, which offers a very convenient representation of the wave function. We introduce a sphere of radius $S_\gamma < S_{\mathrm{MT}}$ and strongly damp the function within the sphere by multiplying it by a smooth positive definite function $\gamma(r)$, which is equal to unity at $r = S_\gamma$ and vanishes at $r = 0$, see Fig. 7.3

$$\psi(\mathbf{r}) = \gamma(r)\psi(\mathbf{r}) + [1-\gamma(r)]\psi(\mathbf{r}). \tag{7.12}$$

The damped wave function $\gamma(r)\psi(\mathbf{r})$ coincide with the original one everywhere in the unit cell except for the small spheres surrounding the nuclei, and its plane wave expansion converges very fast. This is illustrated by Fig. 7.3, which shows the density distribution in the muffin-tin sphere of Li metal obtained from the plane wave expansion of the damped wave functions. The rapidly varying part of the density is 'gouged out', and the Fourier representation of the damped density is seen to become very accurate with the γ-spheres occupying less than 10% of the volume of the unit cell (dotted curve). On the other hand, even for this nearly-free-electron metal, the APWs strongly deviate from the plane waves, and the full density is poorly reproduced by the plane waves (dashed curve). By gouging less than 2% of the valence charge we transfer the error to the close vicinity of the nucleus. These 2% are, however, retained by the orbital representation.

It is desirable to be able to calculate the dipole matrix elements between the valence states and the outgoing photoelectron state in terms of plane waves. The Bloch vectors of the semi-infinite crystal eigenfunctions are complex, and the APW-based numerics becomes very sophisticated. Having obtained the all-electron eigenfunctions, one can change to a PW representation by performing the gouging. In the $\mathbf{k}\cdot\mathbf{p}$ method this is particularly simple because the transfer matrix between the APW and PW representation is $\mathbf{k}$-vector independent.

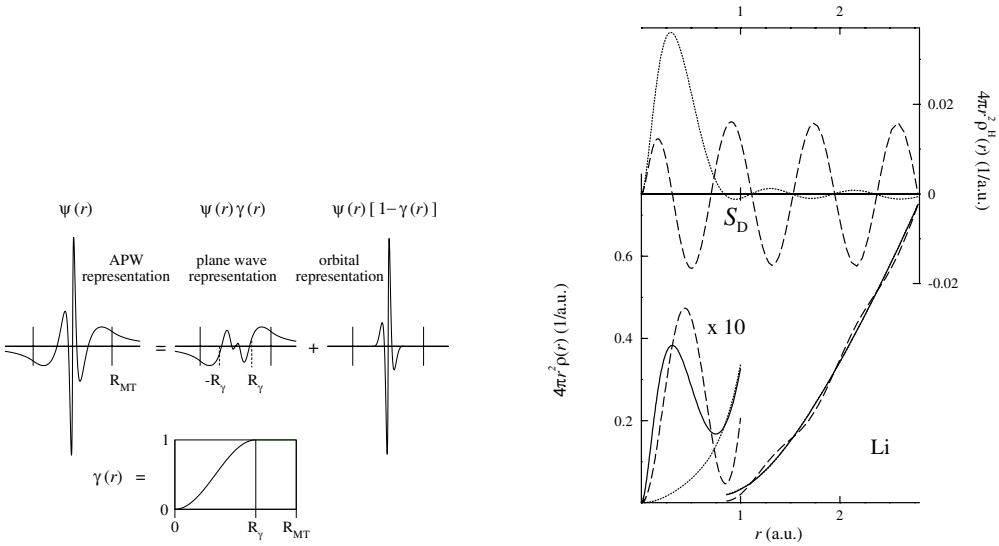

Figure 7.3: Left panel: Separation of an all-electron wave function into a damped and a localized part (see Eq. (7.12)). Right panel: The gouging transformation of the valence density of the bcc Li [29]. The true radial distribution is shown by the solid line in the lower panel. Even for this simple metal the Fourier decomposition of the damped density (dotted line) converges much faster than the Fourier decomposition of the true density (dashed line). The difference between the true density and the Fourier filtered density is shown in the upper panel. [In the lower panel for $r > S_{\mathrm{D}}$ the difference between the true density (full line) and damped density (dotted line) is not visible.]

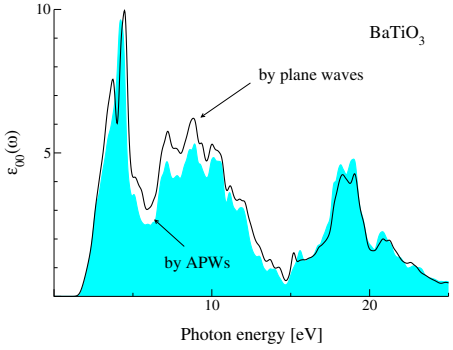

Figure 7.4: Imaginary part of the element ε_{00} of the dielectric matrix of $BaTiO_3$ [30]. The shaded area shows the spectrum obtained with momentum matrix elements (MME) calculated from original all-electron wave functions. The line corresponds to MME calculated from the plane-wave decomposition of gouged wave functions. The maximum at 18.5 eV results from the transitions from Ba $5p$ semi-core band located at -10 eV to Ba $5d$ resonance centered at 8.5 eV (energies are relative to the valence band maximum).

That this approximation works well is illustrated by Fig. 7.4, in which we compare the function $\varepsilon_{00}(\omega)$ of the $BaTiO_3$ perovskite as given by true wave functions and by damped ones. The radii R_γ are 1.4 a.u. for Ba and 0.4 a.u. for Ti and O. The PW set comprises 4945 PW's, approximately ten times more than the number of APWs. With these parameters the PW decomposition converges very fast, and only a small contribution to the matrix element from the close vicinity of the nuclei is sacrificed. The spectrum is seen to be reproduced with a reasonable quality, especially in the far UV region (Ba $5p \rightarrow 5d$ transitions).

7.3 Electron diffraction in semi-infinite crystals

A semi-infinite crystal is a 3D system with a 2D periodicity that is composed of bulk and vacuum half-spaces separated by a slab inside which the crystal potential changes from its bulk distribution to a constant value in the vacuum.

Within a simplified one-particle approach, the LEED problem reduces to solving the Schrödinger equation for a semi-infinite crystal given the energy E and the initial conditions of the incident electron, i.e., the asymptotics of the wave function in the vacuum. In the plane parallel to the crystal surface the LEED wave function obeys the Bloch theorem and is characterized by the 2D Bloch vector $\mathbf{k}^{||}$. In the vacuum, far from the crystal surface, it is a superposition of plane waves: the plane wave propagating towards the crystal defines incident current, and the total current carried by the LEED state is the transmitted current. The ratio of the two currents is the transmission coefficient $T(E)$.

Computational methods to treat the electron diffraction can be divided into two groups depending on whether the crystal is represented as a finite number of monolayers or is treated as a half-space. The former approach is adopted in the multiple-scattering layer KKR technique [32] and in purely direct-space methods [33], and the latter one gives rise to Bloch-waves based methods [6, 7].

In the Bloch-waves approach the LEED wave function in the bulk half-space is a linear combination of the Bloch functions Ψ_n for a given energy (propagating and evanescent), which form the complex band structure and thereby take into account all multiple scattering in the crystal [7]. In Sec. 7.3.1, we show how Ψ_n are obtained as solutions of a matrix eigenvalue problem. Their linear combination is then matched at a plane parallel to the surface to the solution in the surface region (a slab inside which the crystal potential changes from its bulk distribution to a constant value in the vacuum). The latter, in turn, must be matched to the wave function in the vacuum half-space, where it is a linear combination of the incident and the reflected plane waves. The matching problem is discussed in Sec. 7.3.2.

7.3.1 Inverse band structure problem

Similarly to the pseudopotential plane wave method [7], in the ELAPW-$\mathbf{k}\cdot\mathbf{p}$ method the complex band structure can be obtained by an analytical continuation of the $\mathbf{k}\cdot\mathbf{p}$ Eq. (7.11) to the complex $\mathbf{k}$ space. In the *direct* $\mathbf{k}\cdot\mathbf{p}$ method we fix the target point $\mathbf{k}$ and solve the eigenvalue problem

$$\left[\hat{H}_{\mathbf{k}_0} + 2\Delta\mathbf{k}\cdot\hat{\mathbf{P}}_{\mathbf{k}_0} + (\Delta k^2 - E)\hat{O}_{\mathbf{k}_0}\right]\mathbf{C}^{\mathbf{k}\lambda} = 0, \tag{7.13}$$

for the energies E [see also Eq. (7.11)]. Real $\mathbf{k}$ vectors yield the real band structure, and real eigenvalues corresponding to complex $\mathbf{k}$ vectors comprise the complex band structure.

In application to semi-infinite systems, we use the ELAPW-$\mathbf{k}\cdot\mathbf{p}$ method to solve the *inverse band structure problem*; i.e., given two real Cartesian components of the Bloch vector $\mathbf{k}^{\|} = (k_x, k_y)$ and the energy E, we find the values of $k^{\perp}$ that satisfy the Schrödinger equation

$$\hat{H}\Psi_n(E, \mathbf{k}^{\|} + \mathbf{n}k_n^{\perp}; \mathbf{r}) = E\Psi_n(E, \mathbf{k}^{\|} + \mathbf{n}k_n^{\perp}; \mathbf{r}) \tag{7.14}$$

for the Bloch vector with a complex z component $k_n^\perp$ ($\mathbf{n}$ is a unity vector normal to the surface). The choice of the reference point depends upon $\mathbf{k}^\parallel$: $\mathbf{k}_0 = \mathbf{k}^\parallel + \mathbf{n}k_0^\perp$. The normal projection $k_0^\perp$ is arbitrary, usually it is chosen at the center of the $k^\perp$-interval of interest. Now the $\mathbf{k}\cdot\mathbf{p}$ representation of the trial function

$$\Psi_{k^\perp}(E;\mathbf{r}) = \exp[\,i(k^\perp - k_0^\perp)z]\,\sum_i C_i^{k^\perp}(E,\mathbf{k}_0)\xi_i(\mathbf{k}_0,\mathbf{r}) \tag{7.15}$$

leads to the matrix equation

$$\begin{aligned}\left[\hat{H} + 2\delta_n^\perp\cdot\hat{P}^\perp + (\delta_n^{\perp 2} - E)\hat{O}\right]\mathbf{C}_n &= 0, \\ \hat{P}^\perp &= \hat{\mathbf{P}}\cdot\mathbf{n}, \\ k_n^\perp &= k_0^\perp + \delta_n^\perp.\end{aligned} \tag{7.16}$$

We define the vector $\mathbf{D}_n = -(2\hat{P}^\perp + \delta_n^\perp\hat{O})\,\mathbf{C}_n$ and reduce Eq. (7.16) to a matrix equation of twice the dimension:

$$\begin{pmatrix} 0 & \hat{H} - E\hat{O} \\ \hat{I} & 2\hat{P}^\perp \end{pmatrix}\begin{pmatrix} \mathbf{D}_n \\ \mathbf{C}_n \end{pmatrix} = \delta_n^\perp\begin{pmatrix} \hat{I} & 0 \\ 0 & -\hat{O} \end{pmatrix}\begin{pmatrix} \mathbf{D}_n \\ \mathbf{C}_n \end{pmatrix}. \tag{7.17}$$

Thus, the solutions of the inverse band structure problem $\delta_n^\perp$ are obtained as solutions of this generalized non-Hermitian eigenvalue problem. Solutions of Eq. (7.14) are orthogonal in the sense that at the plane $z = \mathrm{const}$ the non-diagonal elements of the current operator vanish:

$$\frac{\hbar}{2m}\int\limits_S\left[\left(-i\frac{d}{dz}\Psi_n\right)\Psi_{n'}^* - \left(-i\frac{d}{dz}\Psi_{n'}^*\right)\Psi_n\right]\,d^2r = J_{zn}\delta_{nn'}. \tag{7.18}$$

Here the integral is over the surface of the unit cell. In other words, the current carried by a sum of the Bloch states with the same E and $\mathbf{k}^\parallel$ is the sum of the individual currents [34].

An evanescent wave is a product of the 'Bloch part' and the decaying factor $\exp[-\kappa z]$. From Eq. (7.16) it follows that the expectation value of the momentum operator $\hat{P}^\perp$ for the Bloch part vanishes, and that its energy expectation value is $\kappa^2 + E$. It is well-known that the higher is the energy of the Bloch state the poorer is its convergence, i.e., the larger is the number of the plane waves (or, equivalently, the number of the spherical functions) that must be included in the basis set. This means that the accuracy of the evanescent waves deteriorates with increasing the imaginary part of the Bloch vector irrespective of the method of calculation.

Other formulations of the complex band structure problem in terms of APWs include the 'assembly of boundary controlled monolayers' method of Wachutka [35], a similar method of Stiles and Hamann [36], and a Green function approach of Wortmann *et al*. [45].

7.3.2 Matching the solutions at the crystal surface

Let Φ be a solution of the Schrödinger equation for a semi-infinite crystal. In the bulk, $z \le 0$, Φ is a linear combination of the eigenfunctions $\Psi_n(E,\mathbf{k}^\parallel)$. Far from the surface, where the

crystal potential is periodic, Ψ_n satisfy the Eq. (7.14) with $\mathrm{Im}\, k_n^\perp = 0$ for propagating Bloch states and $\mathrm{Im}\, k_n^\perp < 0$ for evanescent states. For a LEED state, the condition that the incident electron comes from the vacuum implies that Φ contains only the *partial waves* propagating (or decaying) into the interior of the crystal,

$$\Phi_{\mathrm{LEED}}(\mathbf{r}^\parallel, z) = \sum_n t_n \Psi_n(E, \mathbf{k}^\parallel; \mathbf{r}^\parallel, z). \tag{7.19}$$

Here $\mathbf{k}^\parallel$ is the surface projection of the wave vector of the incident electron. In the vacuum, the function is a linear combination of (propagating and evanescent) plane waves

$$\Phi_{\mathrm{LEED}}(\mathbf{r}^\parallel, z) = \exp[i\mathbf{k}^\parallel \mathbf{r}^\parallel - ik_0 z] + \sum_s a_s \exp[i(\mathbf{k}^\parallel + \mathbf{G}_s)\mathbf{r}^\parallel + ik_s z], \tag{7.20}$$

where the normal wave vector components k_s are connected to the surface reciprocal lattice vectors $\mathbf{G}_s$ and the kinetic energy E by the relation $\mid \mathbf{k}^\parallel + \mathbf{G}_s \mid^2 + k_s^2 = E$. The normal projections k_s are either purely real or purely imaginary with $\mathrm{Im}\, k_s > 0$.

In the case of a step-like surface barrier, with a periodic bulk potential $V(\mathbf{r})$ for $z < 0$ and a zero potential for $z \geq 0$, the two representations in both half-spaces hold right to the surface and the coefficients a_s and t_n are determined by matching the wave function and its derivative over the plane $z = 0$. The eigenfunctions $\Psi_n(\mathbf{r}^\parallel, z)$ are expanded into the 2D Fourier series[3]

$$\Psi_n(\mathbf{r}^\parallel, z) = \sum_{s=0}^{N_F - 1} f_{sn}(z) \exp[i\mathbf{K}_s \mathbf{r}^\parallel], \tag{7.21}$$

$$-i\frac{d}{dz}\Psi_n(\mathbf{r}^\parallel, z) = \sum_{s=0}^{N_F - 1} d_{sn}(z) \exp[i\mathbf{K}_s \mathbf{r}^\parallel], \qquad \mathbf{K}_s \equiv \mathbf{k}^\parallel + \mathbf{G}_s. \tag{7.22}$$

By simple algebra one can get rid of the mismatch in the values of $\Phi(\mathbf{r}^\parallel, 0)$ so that the function is continuous by construction; then the coefficients $\{a_s\}$ are expressed in terms of $\{t_n\}$, the latter being independent coefficients.

For a one-dimensional system the matching can be performed exactly, but for a 3D crystal, to match the functions pointwise over the surface would require an infinite number of constituents Ψ_n. Practical treatment of the semi-infinite crystal problem depends upon the answer to the question: **Given a finite set of bulk Bloch waves, what is the best approximation to the wave function?**

In the simple matching scheme [7], the coefficients t_n are determined by exactly matching N_F Fourier components (FCs). Then it is necessary to include $N_{\mathrm{sol}} = N_F$ solutions, and the rest of the Fourier components are left unmatched. However, it may happen that some of the

[3] To get a Laue representation of the wave functions becomes untrivial when the matching plane intersects the muffin-tin spheres. Here we again transfer to a plane wave decomposition, which is easy to obtain in a $\mathbf{k} \cdot \mathbf{p}$ method. The calculations are facilitated by the possibility to use the gouging technique described in Sec. 7.2.4. The technique is ideally suited for this problem: the gouging spheres are chosen so as to touch the matching plane, which provides a rapidly convergent plane wave expansion of the wave functions. An elegant method to avoid the intersection of the matching plane with the muffin-tin spheres has been developed by Ishida [37]. He introduced a buffer region and defined the boundary conditions on an artificial planar surface by integrating the Schrödinger equation in the buffer region.

N_F solutions contain more than N_F non-negligible FCs and the situation cannot be improved by increasing N_F.

A number of variational schemes have been proposed, in which $N_{\rm sol}$ is independent of N_F. Then the mismatch is allowed to distribute over all the N_F Fourier components, and the freedom can be used to reduce the integral mismatch as compared to the simple matching. The method of Bross [38] is aimed at minimizing the current mismatch at the interface. However, the current mismatch is not a positive definite quantity; consequently, the mismatches due to different $\mathbf{G}_s$ may compensate each other, thus providing a good current conservation, but producing a solution which is far from smooth. Appelbaum and Hamann [39] minimized the integral mismatch with a least squares method. A disadvantage of this procedure is that all the FCs are treated equally, and no preference is given to the $\mathbf{G}_s$ according to their individual contributions to the solution Φ. The mismatch is uniformly distributed over the vector set, and large $\mathbf{G}_s$, for which the amplitudes f_{sn} are very small and numerically unreliable, can contribute to the mismatch considerably. In order to cure this deficiency, Krasovskii and Schattke have suggested [27] to damp the unphysical contributions by introducing different weights for mismatches coming from different FCs. The weights are proportional to $\mid f_s \mid^2$ and are determined self-consistently in the course of matching. Thus, instead of neglecting the large $\mathbf{G}_s$ vectors, as one does in the simple matching, here one damps the components whose contribution to the current is unimportant. The details of the formalism and its performance in comparison to other methods are discussed in Ref. [27].

The above review reveals an ambiguity in assessing the 'smoothness' of the wave function. The question of whether the function is 'smooth enough' can, however, be avoided if we construct a smoothly continuous trial function Φ by continuing each solution Ψ_n of Eq. (7.14) with continuous derivative into the vacuum region [40]. For a given energy E and a given set of Bloch waves Ψ_n we require that their linear combination Φ minimize the energy deviation $\|(\hat{H} - E)\Phi\|$ under constraints dictated by the physical nature of the problem. Since Ψ_n are variational solutions, this criterion is quite natural: when the quality of the trial function becomes comparable to the quality of the individual partial solutions the inclusion of more evanescent states with larger $\mathrm{Im}\, k^\perp$ would not improve the results.[4]

The scheme is very easy to implement in the case when the potential in the vacuum half-space is constant. We smoothly continue the Laue decomposition (7.21) of each function Ψ_n to the half-space $z > 0$. The functions $f_{sn}(z)$ are extended by attaching a linear combination of two tails: a 'physical' tail, which has a correct asymptotics at $z \to +\infty$, and an auxiliary tail, which decays rapidly with the distance from the surface. The 'physical' tail

$$p_s(\mathbf{r}^\parallel, z) = \exp[i\mathbf{K}_s\mathbf{r}^\parallel + ik_s z], \quad K_s^2 + k_s^2 = E, \tag{7.23}$$

may be a propagating wave, $\mathrm{Im}\, k_s = 0$, or an evanescent wave, $\mathrm{Im}\, k_s > 0$, depending on E and K_s^2. For convenience, the auxiliary tail can be taken as a sum of evanescent plane waves

$$a_{sj}(\mathbf{r}^\parallel, z) = \exp[i\mathbf{K}_s\mathbf{r}^\parallel + iq_{sj} z], \quad K_s^2 + q_{sj}^2 = E_j, \tag{7.24}$$

[4] The accuracy of the partial Bloch waves according to the energy criterion inevitably deteriorates with increasing the imaginary part of the Bloch vector – see the discussion in the end of Sec. 7.3.1.

with $\mathrm{Im}\, q_{sj} > 0$. The auxiliary energies E_j are taken considerably lower than E, so that the auxiliary tails decay fast. For $G_s = 0$ the physical part $p_0(z)$ is always propagating: it is the outgoing (specular beam) plane wave. The functions Ψ_n are thereby defined in the whole space. However, none of them contain an incident wave. The incident wave enters in a linear combination with the outgoing and the auxiliary wave, which vanishes with vanishing derivative at the surface. The function constructed in this way is zero in the crystal half-space. It gives rise to the right hand side of a system of linear equations.

We have thereby arrived at a set of smoothly continuous functions, any linear combination of which by construction satisfies the Schrödinger equation in the bulk half-space and far from the surface in the vacuum.[5] The error is confined to the surface region (on the vacuum side). The minimization of $\|(\hat{H} - E)\Phi\|$ under the constraint that the incident current is equal to unity (LEED regime) leads to a system of linear equations. In the case of bounded states (no incident waves) it leads to an eigenvalue problem.

7.3.3 Embedding

The above formalism is easy to implement if we assume that the periodic bulk potential holds right to the surface, where it abruptly changes to the constant potential in the vacuum. This approximation works fairly well for the surfaces of elementary metals [40] and layered crystals [41]. However, for reconstructed surfaces or adsorbates the actual potential distribution in the surface region cannot be neglected. The ground state density distribution can be obtained within the DFT from a slab calculation (see Chapter 1), and the resulting potential can be then used as an approximation for the potential felt by the LEED wave. For a sufficiently thick slab, the potential in the depth of the slab matches the periodic bulk potential; the slab calculation provides us thereby with all necessary information to calculate the scattering states as well as bounded states. The latter are the initial states of the photoemission process, and for them the actual shape of the potential near the surface must be taken into account in the first place. The output of the slab calculation cannot, however, be immediately fed into the photoemission calculation because, for an isolated slab, the $\mathbf{k}^{\|}$ projected band structure represents a discrete set of energy levels, which does not contain any information about the $\mathbf{k}^{\|}$ projected density of states of the semi-infinite crystal. The photoemission experiment, on the contrary, reflects the one-dimensional density of states, which is a continuous function of energy and depends upon the band structure of the substrate.

Thus, we need to put several atomic layers on top of the substrate and develop a practicable computational formulation of the resulting aperiodic-potential problem. An embedding method has been proposed by Inglesfield [42], in which the substrate is represented by an energy dependent embedding potential defined on the matching surface and derived from the Green function for the perfect crystal. This potential enters the variational problem for the surface region, which is treated explicitly. The method has been implemented within the LAPW formalism and a number of self-consistent calculations for surfaces were performed [37, 43, 44]. Recently, the method has been extended to the calculation of electron transmission through the interface [45, 46].

[5] Owing to the variational character of the bulk partial solutions, the Schrödinger equation in the bulk region is satisfied only with a certain accuracy.

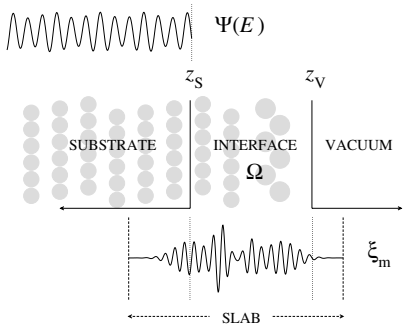

Figure 7.5: The embedding setup: The substrate is represented by the complex band structure of the ideal semi-infinite crystal and the interface region is a part of a slab.

We now present an alternative embedding method, in which the substrate is represented by its complex band structure. Consider an interface region composed of true surface layers attached to the substrate as shown in Fig. 7.5.

By embedding we mean the continuation of the substrate Bloch waves Ψ_n [that satisfy Eq. (7.14)] to the interface region Ω (see Fig. 7.5). Given the initial conditions at the plane $z = z_{\rm S}$ [f_s and d_s of Eqs. (7.21) and (7.22)] we must integrate the Schrödinger equation over the interface region. This region is a fraction of a slab, for which a boundary value problem has been solved, and a complete set of eigenfunctions $\{\xi_m\}$ has been obtained.

$$\hat{H}^{\rm slab}\xi_m = \epsilon_m \xi_m. \tag{7.25}$$

The continuation of the function Ψ_n can be expanded into a convergent series of the slab solutions

$$\Psi(\mathbf{r}) = \sum_m a_m \xi_m(\mathbf{r}). \tag{7.26}$$

(Here the subscript n of Ψ is dropped.) The set $\{\xi_m\}$ is complete in Ω because any function defined in Ω can be extended to the slab domain (i.e., to $z < z_{\rm S}$ and $z > z_{\rm V}$, see Fig. 7.5) so as to satisfy the slab boundary conditions. On the other hand, the set is overcomplete because such an extension is not unique. The coefficients a_m must satisfy the Schrödinger equation

$$(\hat{H}_\Omega - E)\sum_m a_m \xi_m = \sum_m a_m(\epsilon_m - E)\xi_m = 0 \tag{7.27}$$

and the initial conditions

$$\begin{aligned} \Psi(\mathbf{r}^\parallel, z_{\rm S}) &= \sum_m a_m \xi_m(\mathbf{r}^\parallel, z_{\rm S}), \quad \text{and} \\ \frac{d}{dz}\Psi(\mathbf{r}^\parallel, z_{\rm S}) &= \sum_m a_m \frac{d}{dz}\xi_m(\mathbf{r}^\parallel, z_{\rm S}). \end{aligned} \tag{7.28}$$

Similar to the procedure of Sec. 7.3.2 we find the coefficients a_m by minimizing the energy deviation

$$\|(\hat{H}_\Omega - E)\Psi\| = \sum_{m'm}(\epsilon_{m'} - E)(\epsilon_m - E)\,\langle\, \xi_{m'} \mid \xi_m \,\rangle_\Omega\, a^*_{m'} a_m \tag{7.29}$$

under the constraints (7.28). Computationally, the problem reduces to calculating the integrals

$$\langle\, \xi_{m'} \mid \xi_m \,\rangle_\Omega = \int_\Omega \xi^*_{m'}(\mathbf{r})\xi_m(\mathbf{r})\; d^3r. \tag{7.30}$$

An example of an embedding calculation for the surface state on the (100) surface of aluminum is shown in Fig. 7.6. In the region $z < z_{\rm S}$ the state is represented by a single evanescent eigenfunction of the bulk Hamiltonian (dashed line). With the initial conditions at $z_{\rm S}$ the Schrödinger equation for the aperiodic potential in the embedded region is integrated through the $z_{\rm V}$ plane, at which the function is matched to a sum of evanescent plane waves – the asymptotic vacuum solutions for each $\mathbf{G}_\parallel$. For a given shape of the potential in the interface region, the matching of the function and its derivative at both $z_{\rm S}$ and $z_{\rm V}$ is possible only at a certain energy, which the present calculation [47] has located at 2.62 eV below the Fermi energy. The resulting density distribution is shown by the full line. The dashed line for $z > z_{\rm S}$ is an attempt to replace the self-consistent potential distribution in the surface region by a step-like potential: the periodic potential of the bulk crystal is cut by a plane at $z = z_0$, at which the asymptotic vacuum solutions are attached (by matching in value and not in slope). The kink in the dashed curve at $z = z_0$ is not visible, which suggests that the change in energy due to the potential variation is not dramatic: indeed, for the step-like potential the surface-state occurs some 0.25 eV higher in energy. However, the wave function reacts much more strongly: the imaginary part of the evanescent tail Bloch vector changes by 20% from 0.036 to 0.045 Å^{-1}.

7.3.4 Current attenuation and current conservation

Gross features of the LEED spectrum depend upon the band structure of the bulk crystal: the energies at which the band ceases transmitting the current (e.g. when the group velocity vanishes) and other critical points are reflected in experimental spectra. For example, the transmission $T(E)$ drops abruptly to zero when an energy gap in the $\mathbf{k}^{||}$ projected band structure

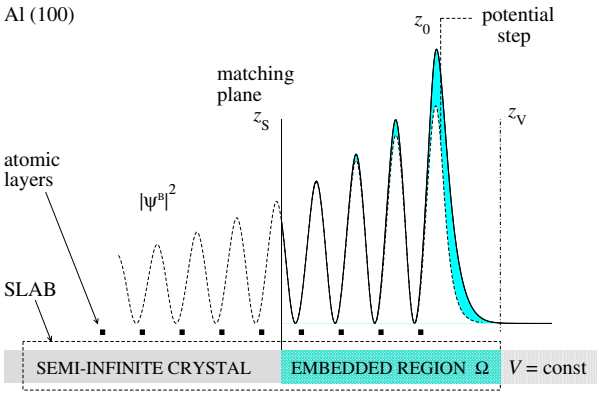

Figure 7.6: Density distribution in the surface state on the Al (100) surface. The surface state wave function is continued into the surface region with initial conditions defined at the plane $z_{\rm S}$. The full line is the plane-averaged density obtained with a realistic surface potential, which gradually grows in the embedded region. The shaded area shows the solution for a step-like potential; the location of the step is shown by the dashed line.

is encountered. However, owing to inelastic processes, one never observes zero transmission in the experiment, and instead of a sharp drop predicted by the simple theory one observes a rather smooth decrease of the transmission as a sign of the critical point.

In 1937 Slater [49] showed that the broadening of the spectral structures and the absence of energy gaps can be reproduced by adding an imaginary term, the optical potential $-iV_\mathrm{i}$, to the potential in the crystal half-space. Slater's idea is to associate the effect of the optical potential with a spatial damping of the wave functions rather than with a decay in time. Then the Bloch vector acquires an imaginary part (see Fig. 7.7). For sufficiently large group velocities $v^\perp$, $mv^{\perp 2} \gg V_\mathrm{i}$, the imaginary part $\mathrm{Im}\, k$ is of the order of $V_\mathrm{i}/\hbar v^\perp$, or, in terms of the mean free path $d = 1/\mathrm{Im}\, k$, it is $V_\mathrm{i} = \hbar v^\perp/d$. The optical potential is, thus, understood as the inverse lifetime of the quasi-particle.

In the case of a non-absorbing crystal potential ($V_\mathrm{i} = 0$) the LEED function obeys the current conservation rule: the flux through a cross-section S of the unit cell $z = \mathrm{const}$ is independent of z. In the vacuum the current is carried by the incident and reflected beams and in the bulk it is the sum of the currents carried by the Bloch constituents, see Eq. (7.18). An individual current is proportional to the group velocity of the Bloch wave, which is calculated as an integral over the unit cell of the bulk crystal,

$$\frac{1}{S}\int\limits_S \mathbf{j}(\mathbf{r})\; d\mathbf{S} = \Big\langle \psi \;\Big|\; -i\frac{\hbar}{m}\frac{d}{dz} \;\Big|\; \psi \Big\rangle. \tag{7.31}$$

Owing to the variational character of the wave functions and to the imperfectness of matching, calculated LEED functions conserve current only approximately. To assess the quality of the calculation one compares the flux at $+\infty$ (in the vacuum) and at $-\infty$ (in the bulk, by Eq. (7.31)). An example for a layered material VSe_2 is shown in Fig. 7.8. The current mismatch almost never exceeds some 5% of the incident current, which is physically quite acceptable.

In an absorbing medium the current is not conserved. The analogue of the current conservation law is given by the relationship between the current in the vacuum and the charge of the LEED electron in the crystal half-space

$$\int\limits_S \mathbf{j}(\mathbf{r})\; d\mathbf{S} = \frac{2V_\mathrm{i}}{\hbar}\int\limits_0^{-\infty}\int\limits_S |\Phi(\mathbf{r})|^2\; d^2r\; dz. \tag{7.32}$$

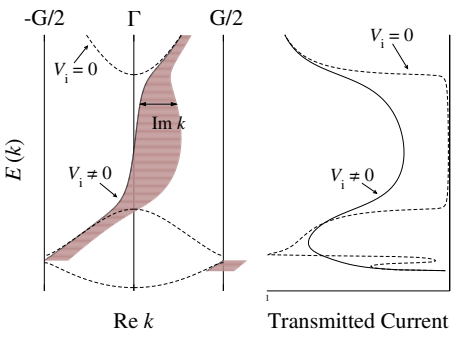

Figure 7.7: Effect of the optical potential on the band structure in a one-dimensional case. The 'elastic' band structure, $V_\mathrm{i} = 0$, is shown by dashed lines in the left panel, and the corresponding transmission spectrum in the right panel. Full lines correspond to a finite optical potential. The horizontal extent of the shaded band shows the imaginary part of the Bloch vector.

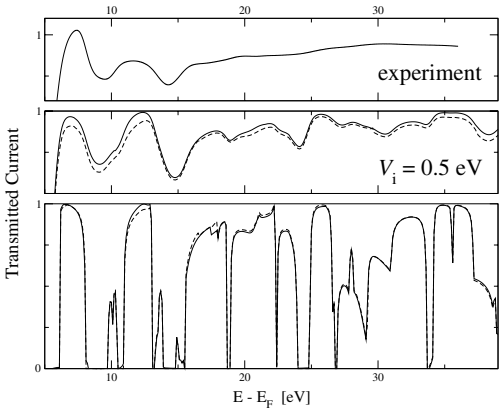

Figure 7.8: Target current spectrum of VSe_2. Lower panel: the no-absorption calculation; full line is the total current of the LEED state calculated in the vacuum half-space and dashed line is the current in the bulk. Middle panel: full line is the current in the vacuum for $V_i = 0.5$ eV and dashed line is the right-hand side of Eq. (7.32). Upper panel: experiment by Strocov *et al*. [4, 50].

The integration in the right-hand side is over the unit cell of the semi-infinite crystal, which has an infinite extent in the z direction. The central panel of Fig. 7.8 shows that Eq. (7.32) is well fulfilled in practical calculations. The density integration has been performed in the plane wave representation. Because of the gouging (see Sec. 7.2.4) the right-hand side is systematically smaller than the left-hand side. The idea to consider the penetrated charge was put forward by Strocov *et al.* [48, 51] as a way to compare the contributions to the transmitted/absorbed current from different Bloch constituents of the LEED state.

The inclusion of the optical potential is seen to bring the sharpness of the calculated structures into agreement with the experiment. Above 15 eV the experiment does not show any distinct structures, which exemplifies the general trend of the lifetime to diminish with energy. In the next section we show how a quantitative information on the energy dependence of V_i can be extracted from the measured $T(E)$ spectra by comparing the broadening of experimental and calculated spectral structures.

It should be noted that in the band structure theory of scattering the reflected beams in the vacuum feel the absorbing potential in the crystal via the matching conditions at the surface. Thus, one cannot expect that increasing V_i would always reduce reflectance. An example is presented by Fig. 7.7: even in a 1D case increasing the optical potential may lead to a decrease of transmission. However, the relationship (7.32) ensures that the LEED intensities behave physically: the reflected current cannot exceed unity and the evanescent states in the gaps always absorb current.

7.4 Is band structure a legitimate concept at high energies?

In analyzing the LEED or photoemission spectra we try to trace back the spectral structures to the features of the band structure of the solid. On the theoretical side the difficulties arise from the neglect of many-body effects in the band structure. A correct (quasi-particle) band structure would have resulted from a one-particle equation that includes the many-body effects through the exact self-energy operator $\hat{\Sigma}$ [52],

$$[\hat{H}_0 + \hat{\Sigma}(E)]|\psi\rangle = E|\psi\rangle, \tag{7.33}$$

where $\hat{H}_0$ describes the kinetic energy and Coulomb interaction, and the operator $\hat{\Sigma}$ is, in general, energy dependent, nonlocal, and not Hermitian. An *ab initio* determination of $\hat{\Sigma}$, even within the approximate theories (see Chapter 1), is very time consuming, and in the majority of the state-of-the-art calculations $\hat{\Sigma}$ is replaced with a local exchange-correlation potential $v_{xc}(\mathbf{r})$ obtained within the local density approximation. The potential $v_{xc}(\mathbf{r})$ is designed to describe the ground-state properties within the density functional theory, which does not ascribe any physical meaning to the unoccupied eigenfunctions. At the present-day level of the many-body theory it is not possible to *a priori* estimate the error of the simplified one-electron calculations, and the comparison with the experiment remains the main argument in judging on the adequacy of approximation.

Another source of uncertainty is the description of inelastic processes by a phenomenological parameter $V_{\rm i}$. The finite optical potential causes the wave functions to decay, which modifies the photoexcitation matrix elements. Its immediate consequence is that the band-gap emission becomes allowed, i.e., the photoemission due to genuine evanescent states in the gaps of the $\mathbf{k}^{\|}$ projected real band structure becomes comparable with the bulk photoemission. Optical potential is, thus, a necessary ingredient of the theory. It should be noted, that the particle in the Slater theory [49] (see Sec. 7.3.4), which is described by a damped wave, has an infinite lifetime, whereas the particle with a finite lifetime is not, strictly speaking, described by a wave function. Thus, the evaluation of the photoemission intensity from the matrix elements of a perturbation operator is a heuristic procedure. The same is true for the evaluation of the LEED intensity from the matching of the wave functions.

Nevertheless, as will be shown in the next two sections, the *ab initio* one-particle theory augmented by the optical potential provides a a fairly good description of the unoccupied electronic structure and offers a reasonable starting point for the understanding of experimental observations.

7.4.1 Target current spectroscopy of $NbSe_2$

The unoccupied band structures of layered quasi-2D materials, such as graphite [53] or transition metal dichalcogenides, [4, 54, 55] are particularly interesting: owing to the interlayer potential barrier, a nearly-free-electron model fails to provide even a qualitative picture of the unoccupied states. In particular, the experimental LEED spectra of 2H-$NbSe_2$ show very rich structure over the energy interval up to 50 eV above the Fermi level [41].

With the methodology of Sec. 7.3 we have performed a LEED calculation and analyzed the real band structure to determine the states responsible for transmitting the current into the crystal. The $\mathbf{k}^{||} = 0$ spectra of $NbSe_2$ along with the underlying real band structure are presented in Fig. 7.9. The $V_{\rm i} = 0$ calculation yields partial currents carried by the Bloch states (shown by whiskers). It reveals the 'current-carrying bands', thereby offering an interpretation of the VLEED spectrum in terms of conducting fragments of the band structure: the abrupt changes in $T(E)$ all reflect critical points in the conducting bands.

A special feature of the normal incidence spectrum is that the conducting bands do not overlap, i.e., there is only one dominant propagating constituent in the LEED function. In this respect the picture is similar to that of the Slater 1D model (Fig. 7.7). Already at a moderate value of $V_{\rm i} = 0.5$ eV (dashed curve in Fig. 7.9) the intensity variations level out and the narrow gaps in the $T(E)$ spectrum almost completely disappear, so one can hardly

expect them to be observed in the experiment. Wider gaps remain well visible, although the reflected intensities are strongly reduced and the structures broadened with respect to those obtained with a Hermitian Hamiltonian. If the theoretical and and the experimental peak positions agree well we can fit the shape of the calculated curve to the experiment by varying the function $V_{\rm i}(E)$. Thereby we extract the information about the damping of quasi-particles from the experiment.

In order to compare the calculated transmission coefficient $T(E)$ with the measured target current spectra $I(E)$ we, first of all, need to bring the $I(E)$ spectrum to the same absolute units as $T(E)$. This is not trivial because of the presence of the unknown background caused by the secondary electrons contributing to the reflectivity. In view of the close similarity of the fine structure of the measured $I(E)$ and theoretical $T^{\rm th}(E)$ spectra over a wide energy region, see Fig. 7.10, we can determine the *experimental* $T(E)$ curve by fitting $I(E)$ to $T^{\rm th}(E)$ with the linear transformation $T^{\rm exp}(E) = aI(E) + b + cE$. Here the function $b + cE$ represents a linearly varying background.

The energy dependence $V_{\rm i}(E)$ is calculated by comparing the sharpness of the dT/dE extrema (maxima and minima) in the experimental and theoretical spectra. Strong intensity variations in the $T(E)$ spectrum are much more important for the band structure information than the shape of the maxima [5], which are very broad even if the damping is neglected (see Fig. 7.9). The function $V_{\rm i}(E)$ derived from the experiment is presented in the right panel

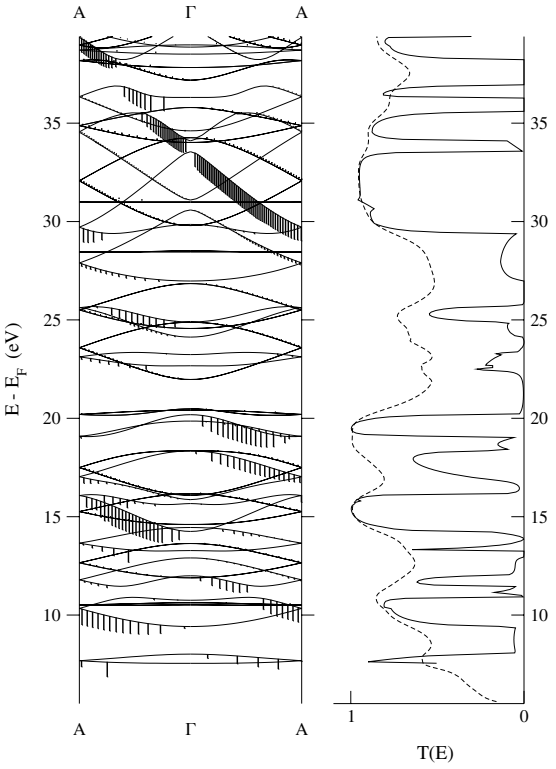

Figure 7.9: Calculated unoccupied band structure of $NbSe_2$ in the ΓA direction [41]. The lines in the left panel show the band structure $E(k^{\perp})$ for $V_{\rm i} = 0$ obtained with the direct ELAPW-$\mathbf{k}\cdot\mathbf{p}$ method. The conducting bands are marked by whiskers. The length of the whisker is proportional to the contribution of the Bloch wave to the target current. Transmission coefficient $T(E)$ is shown in the right panel by the solid line. The dashed line is the $T(E)$ spectrum with the optical potential $V_{\rm i} = 0.5$ eV added to the Hamiltonian $\hat{H}$ in Eq. (7.17).

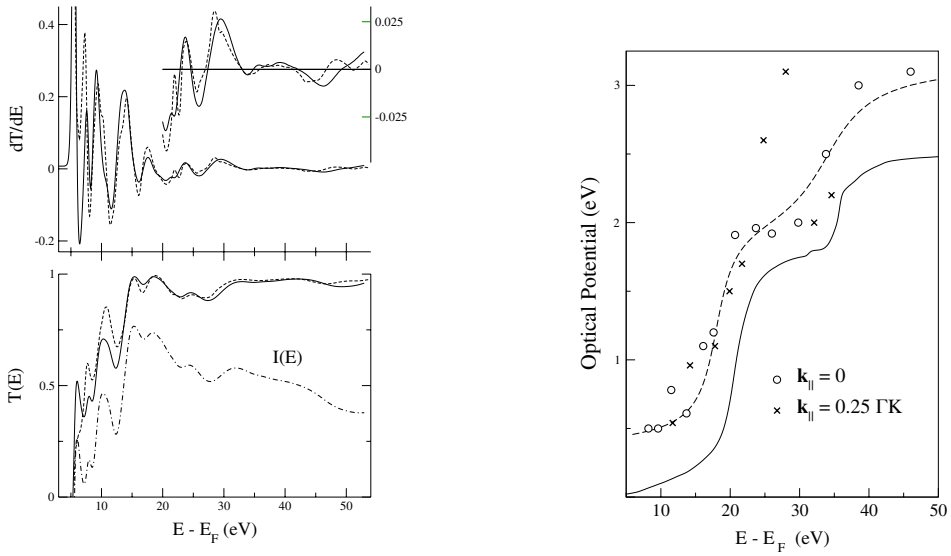

Figure 7.10: Left panel: Comparison of the normal incidence target current $I(E)$ and transmission coefficient $T(E)$ spectra of $NbSe_2$ [41]. The measured $I(E)$ curve is shown by the dot-dashed line. Theoretical $T(E)$ and dT/dE spectra are shown by dashed lines in the lower and upper panels respectively; they are calculated with an energy dependent optical potential (the $V_{\rm i}(E)$ function is shown in the right panel). To arrive at the experimental $T(E)$, the original $I(E)$ function is fitted to the theoretical $T(E)$ by a linear transformation that involves scaling and subtracting the background. The resulting experimental $T(E)$ and dT/dE curves are shown by solid lines.
Right panel: Dependence of the optical potential $V_{\rm i}$ on the incident electron energy extracted from the normal ($\circ$) and an off-normal ($\times$) incidence spectrum [41]. The function $V_{\rm i}(E)$ used in the calculations is shown by the dashed line. The solid line is the energy integral (7.34) of the loss function.

of Fig. 7.10. Two spectra are analyzed: the normal incidence data (circles) and the data for $\mathbf{k}^{||} = \frac{1}{4}\Gamma\mathrm{K}$ (crosses, $\frac{1}{4}|\Gamma\mathrm{K}| = 0.3$ Å). The absolute values of $V_{\rm i}$ agree very well, and both spectra suggest a sharp increase of $V_{\rm i}$ at around 20 eV.

An optical potential is associated with the imaginary part of the electron self-energy Σ, whose energy dependence is expected to reflect singularities of the energy loss function $-\mathrm{Im}[1/\varepsilon(\mathbf{q},\omega)]$. In particular, in the GW approximation [52], $\mathrm{Im}\,\Sigma$ is given by an integral, whose integrand contains the inverse dielectric function. A rough idea of the average effect of plasmon excitations on the energy dependence of the electron lifetime can be obtained from the DF for $\mathbf{q} = 0$ by plotting the integral

$$\int_0^E -\mathrm{Im}\left[\frac{1}{\varepsilon(\omega)}\right]\, d\omega. \tag{7.34}$$

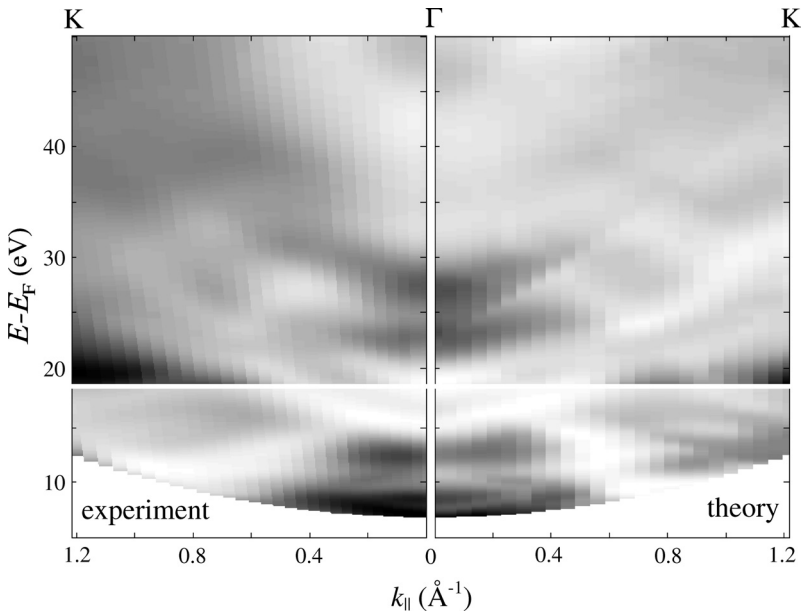

Figure 7.11: Experimental (left) and theoretical (right) $\mathbf{k}^{\|}$ distribution of the $T(E)$ spectral intensity shown in a linear gray scale [41]. White areas correspond to maximal $T(E)$. The energy region shown begins 0.5 eV above the transmission onset. Note the scale change at 18.5 eV (marked by a white line).

We have calculated the dielectric function *ab initio* in the random phase approximation. In Fig. 7.10 (right panel) the integral function 7.34 is compared to the experimental dependence $V_{\rm i}(E)$. The sharp increase of the optical potential agrees well with the location of the plasmon at 21 eV.

The values of $V_{\rm i}$ determined in this way are necessarily overestimated. First, in addition to the inelastic processes in the electronic system, there exist broadening mechanisms dependent upon experimental conditions, such as surface roughness and finite energy resolution. Also the angular spread of the incident beam contributes to the broadening owing to the $\mathbf{k}^{\|}$ dispersion of spectral structures. Second, our theoretical spectra do not take into account inelastic scattering in the surface barrier region, e.g., scattering on the surface defects. This effect results in an additional reduction of the spectral structures, but, unlike the inelastic scattering in the bulk, it hardly affects their energy broadening. These mechanisms should, however, be less significant for the layered materials because of rather small electron density at the surface and a small concentration of defects on the cleaved surface. On the other hand, our absolute values of $V_{\rm i}$ are in accord with the recent *ab initio* results on the quasi-particle lifetimes for noble and transition metals [56]: For energies around $E - E_F = 5$ eV the calculated lifetimes do not exceed a few femto seconds ($V_{\rm i} \sim 0.2$–0.7 eV).

Experimental and theoretical $T(E)$ spectra for $\mathbf{k}^{||}$ ranging from zero to ΓK are presented in Fig. 7.11 as a gray-scale $T(\mathbf{k}^{||}, E)$ plot. A very good agreement between the measured and calculated $\mathbf{k}^{||}$ dispersion of the $T(E)$ intensity proves that the theoretical approach de-

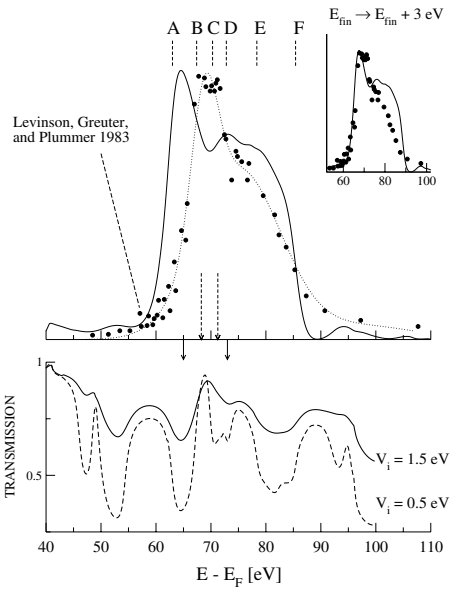

Figure 7.12: Comparison of the measured [57] energy dependence of the photoemission intensity of the surface state (full circles) with an *ab initio* ELAPW-$\mathbf{k}\cdot\mathbf{p}$ calculation (full line). The relevant transmission spectrum for two values of $V_{\rm i}$ is shown in the lower panel. The letters A to F label the dashed bars, which show the energies of the special points of the real band structure (see Fig. 7.13). The inset compares the theoretical spectrum shifted by 3 eV to higher energies with the experiment.

scribed in this chapter is adequate. The results have turned out rather sensitive to details of the potential distribution in the bulk half-space; it should be stressed that the advantage of the ELAPW-$\mathbf{k}\cdot\mathbf{p}$ method of accurately taking into account the strong non-muffin-tin effects makes the method an indispensable tool for studying the electron diffraction on layered materials.

7.4.2 Photoemission from the surface state on the Al (100) surface

The photoemission from an intrinsic surface state offers another possibility to efficiently probe the unoccupied band structure. In comparison to the valence band photoemission in the constant initial state mode, the deciphering of the experimental spectrum is simplified by the absence of the $k^{\perp}$ dispersion of the initial state. Unlike the continuous part of the energy spectrum, where the existing many-body effects or the uncertainties of the one-electron potential may lead to ambiguities in the choice of the initial state for the theoretical simulation, the intrinsic surface state, which is located in a gap of the $\mathbf{k}^{\parallel}$ projected real band structure, is easily identified. Thus, the energy dependence of the photoemission intensity provides an informative image of the unoccupied band structure.

The surface state on the Al (100) surface has been observed in a number of photoemission experiments, see Refs. [57] and [58] and references therein. According to the measurements of Ref. [57], the state at $\mathbf{k}^{\parallel} = 0$ is located at 2.75 eV below the Fermi level in a gap between the X_4' (experimentally at 2.83 eV) and X_1 (1.15 eV) states. The ELAPW LDA calculation [47] yields 2.78 and 1.78 eV for X_4' and X_1 respectively, and 2.62 eV for the surface state. In the crystal half-space the surface state is a single evanescent wave with the real part of the Bloch vector $k_{\rm ss}^{\perp}$ at point X and the imaginary part of 0.036 Å^{-1} (see Fig. 7.6 in Sec. 7.3.3). Close results have been obtained with a pseudo-potential method for a thick slab [59], in a scattering matrix approach (layer KKR) [60], and with the embedding method of Inglesfield [43].

The measured [57] energy dependence of the photoemission intensity of the surface state is compared in Fig. 7.12 with an *ab initio* ELAPW-$\mathbf{k}\cdot\mathbf{p}$ calculation. The LEED states $\mid \Phi_{\rm LEED} \rangle$ [see Eqs. (7.19) and (7.20)] are calculated as explained in Sec. 7.3, and the resulting electron transmission spectrum is shown in the lower panel of Fig. 7.12. In the upper panel the calculated photoemission intensities

$$J(E) \sim \sqrt{E - E_{\rm vac}} \mid \langle\, \Phi^*_{\rm LEED}(E) \mid -i\nabla \mid {\rm ss} \,\rangle \mid^2 \tag{7.35}$$

are depicted with the full line. To make the intensity variations over the spectrum comparable to those observed in the experiment, an optical potential of 2 eV was introduced. The damping of the final states has, however, small effect on the total width of the 'emission window': with $V_{\rm i} = 0$ it remains 23 eV wide (see the right panel of Fig. 7.13). The wide emission interval is a consequence of the localized nature of the surface state, which levels out the $k^\perp$ dependence of the transition probability and gives rise to an appreciable contribution from the evanescent part of the complex band structure. It is clear that since the real part of $k^\perp_{\rm ss}$ is at X and the imaginary part is rather small (0.023 $2\pi/a$), the resonance Bloch constituents $\Psi_n(E, k^\perp_n)$ [see Eqs. (7.19) and (7.14)] must be located in the vicinity of point X. (A periodic oscillatory behavior in surface-state emission intensity has been discussed in Ref. [61] within a spectral decomposition theory).

To understand the spectrum, one must take into account not only the details of the band structure, but also the coupling of the individual Bloch waves $\Psi_n(E, k^\perp_n)$ to the vacuum, i.e., the coefficients t_n of the Bloch waves [see Eq. (7.19)].[6] In Fig. 7.13 we show the relevant fragment of the real band structure superimposed on the $E(k^\perp_n)$ lines (thick lines) that mark the most important Bloch constituents of the photoemission final states. The letters A to F denote special points of the real band structure at which the real lines of the complex band structure originate. The individual contributions to the photocurrent are shown by the shaded area, whose horizontal extent is proportional to the matrix element $\mid t_n \langle\, \Psi_n \mid -i\nabla \mid {\rm ss} \,\rangle \mid$ (not squared). The $E(k^\perp_n)$ lines include the evanescent states, whose contribution to the spectrum is seen to be very important: the emission over wide intervals AB, CD, and EF is due to genuine evanescent states. Note that the two maxima in the theoretical curve, at 65 and at 73 eV, correspond to minima of transmission.

The calculated onset of the surface state emission is 3 eV lower than in the experiment (see the inset of Fig. 7.12), which may be a manifestation of self-energy effects. Apart from that, the expression (7.35) does not take into account the spatial variation of the vector potential in the surface region caused by the dielectric response of the solid (see Chapter 2). The local field effects may considerably modify the intensity distribution over the spectrum. Nevertheless, the simplified theory of Eq. (7.35) in connection with the realistic complex band structure explains the width of the emission band and locates it correctly in the 60-eV-wide interval of the final state energies.

---

[6] The evanescent solutions of the inverse band structure problem are not normalized, so the coefficients t_n have no physical meaning; still we write it as $t_n\Psi_n$ to emphasize that the coupling to the vacuum has been taken into account.

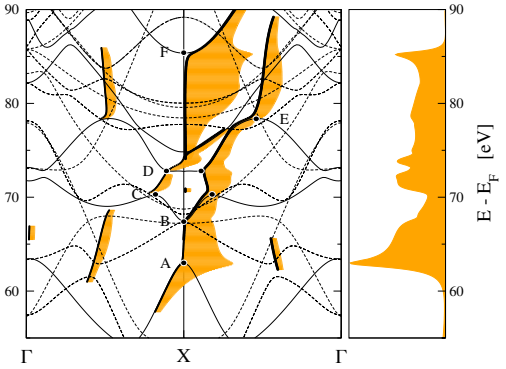

Figure 7.13: The band structure of aluminum along the ΓXΓ line $E(\mathrm{Re}k^{\perp})$. Thin lines show the real band structure ($\mathrm{Im}\ k^{\perp} = 0$). Thick lines show the constituents of the LEED states responsible for the photoemission. The letters denote special points of the real band structure. The horizontal extent of the shaded bands is proportional to the modulus of the dipole matrix element (not squared) of the transition from the surface state. The data are obtained with $V_{\mathrm{i}} = 0.25$ eV, the resulting photoemission spectrum is shown in the right panel.

References

[1] P.J. Feibelman, and D.E. Eastman, Phys. Rev. B **10**, 4932 (1974).

[2] *Angle-Resolved Photoemission*, edited by S.D. Kevan (Elsevier, Amsterdam, 1992).

[3] R.C. Jaklevic and L.C. Davis, Phys. Rev. B **26**, 5391 (1982).

[4] V.N. Strocov, H. Starnberg, P.O. Nilsson, H.E. Brauer, and L.J. Holleboom, Phys. Rev. Lett. **79**, 467 (1997); J. Phys. Condens. Matter **10**, 5749 (1998).

[5] V.N. Strocov, R. Claessen, G. Nicolay, S. Hüfner, A. Kimura, A. Harasawa, S. Shin, A. Kakizaki, H.I. Starnberg, P.O. Nilsson, and P. Blaha, Phys. Rev. Lett. **81**, 4943 (1998); Phys. Rev. B **63**, 205108 (2001).

[6] D.S. Boudreaux, V. Heine, Surf. Sci. **8**, 426 (1967).

[7] J.B. Pendry, J. Phys. C **2**, 2273 (1969).

[8] W. Schattke, Prog. Surf. Sci. **64**, 89 (2000).

[9] J. Korringa, Physica **13**, 392 (1947); W. Kohn and N. Rostoker, Phys. Rev. **94**, 1111 (1954).

[10] J.C. Slater, Phys. Rev. **51**, 846 (1937).

[11] O.K. Andersen, Phys. Rev. B **12**, 3060 (1975).

[12] T. Takeda and J. Kubler, J. Phys. F **9**, 661 (1979).

[13] D.J. Shaughnessy, G.R. Evans, and M.I. Darby, J. Phys. F **17**, 1671 (1987).

[14] D.D. Koelling, Phys. Rev. B **2**, 290 (1970).

[15] H. Bross, G. Bohn, G. Meister, W. Schubö, and H. Stöhr, Phys. Rev. B **2**, 3098 (1970).

[16] D. Singh, Phys. Rev. B **43**, 6388 (1991).

[17] E. Sjöstedt, L. Nordström, and D.J. Singh, Solid State Commun. **114**, 15 (2000).

[18] E.E. Krasovskii, A.N. Yaresko, and V.N. Antonov, J. Electron Spectrosc. Relat. Phenom. **68**, 157 (1994).

[19] D.D. Koelling and G.O. Arbman, J. Phys. F **5**, 2041 (1975).

[20] F. Aryasetiawan and O. Gunnarsson, Phys. Rev. B **49**, 7219 (1994).

[21] E.E. Krasovskii, V.V. Nemoshkalenko, and V.N. Antonov, Z. Phys. B **91**, 463 (1993).

[22] E. Wimmer, H. Krakauer, M. Weinert, and A.J. Freeman, Phys. Rev. B **24**, 864 (1981).

[23] E.E. Krasovskii and W. Schattke, Solid State Commun. **9**, 775, (1995).

[24] P.M. Marcus, Int. J. Quantum. Chem. Suppl. **1**, 567 (1967).
[25] E.E. Krasovskii, Phys. Rev. B **56**, 12866 (1997).
[26] D.J. Singh, *Planewaves, Pseudopotentials and the LAPW Method*, (Kluwer, Boston 1994).
[27] E.E. Krasovskii and W. Schattke, Phys. Rev. B **56**, 12874 (1997).
[28] D.D. Koelling and B.N. Harmon, J. Phys. C: Solid State Phys. **10**, 3107 (1977).
[29] E.E. Krasovskii, F. Starrost, and W. Schattke, Phys. Rev. B **59**, 10504 (1999).
[30] E.E. Krasovskii and W. Schattke, Phys. Rev. B **60**, 16251 (1999).
[31] E.E. Krasovskii and W. Schattke, Phys. Rev. B **63** 235112 (2001).
[32] J.B. Pendry, *Low Energy Electron Diffraction* (Academic Press, London, 1974).
[33] S. Lorenz, C. Solterbeck, W. Schattke, J. Burmeister, and W. Hackbusch, Phys. Rev. B **55**, 13432 (1997) and references therein.
[34] P.M. Marcus and D.W. Jepsen, Phys. Rev. Lett. **20**, 925 (1968).
[35] G. Wachutka, Phys. Rev. B **34**, 8512 (1986).
[36] M.D. Stiles and D.R. Hamann, Phys. Rev. B **38**, 2021 (1988).
[37] H. Ishida, Phys. Rev. B **63**, 165409 (2001).
[38] H. Bross, J. Phys. F **12**, 2883 (1982).
[39] J.A. Appelbaum and D.R. Hamann, Phys. Rev. B **6**, 2166 (1972).
[40] E.E. Krasovskii and W. Schattke, Phys. Rev. B **59** 15609 (1999).
[41] E.E. Krasovskii, W. Schattke, V.N. Strocov, and R. Claessen, Phys. Rev. B **66**, 235403 (2002).
[42] E. Inglesfield, J. Phys. C **14**, 3795 (1981).
[43] E. Inglesfield and G.A. Benesh, Phys. Rev. B **37**, 6682 (1988).
[44] S. Crampin, J.B.A.N. van Hoof, M. Nekovee, and J.E. Inglesfield, J. Phys.: Condens. Matter **4**, 1475 (1992).
[45] D. Wortmann, H. Ishida, and S. Blügel, Phys. Rev. B **65**, 165103 (2002).
[46] D. Wortmann, H. Ishida, and S. Blügel, Phys. Rev. B **66**, 075133 (2002).
[47] E.E. Krasovskii and W. Schattke, to be published
[48] V.N. Strocov, H. Starnberg, and P.O. Nilsson, J. Phys.: Cond. Matter **8**, 7539 (1996).
[49] J.C. Slater, Phys. Rev. **51**, 840 (1937).
[50] V.N. Strocov, private communication.
[51] V.N. Strocov, H.I. Starnberg, and P.O. Nilsson, Phys. Rev. B **56**, 1717 (1997).
[52] L. Hedin and S. Lundqvist, in *Solid State Physics*, edited by F. Seitz, D. Turnbull, and H. Ehrenreich, **23**, (Academic press, New York, 1969), p.1.
[53] V.N. Strocov, P. Blaha, H.I. Starnberg, M. Rohlfing, R. Claessen, J.-M. Debever, and J.-M. Themlin, Phys. Rev. B **61**, 4994 (2000); V.N. Strocov, A. Charrier, J.-M. Themlin, M. Rohlfing, R. Claessen, N. Barrett, J. Avila, J. Sanchez, and M.-C. Asensio, Phys. Rev. B **64**, 075105 (2001).
[54] E. Pehlke and W. Schattke, Solid State Commun. **69**, (1989) 419.
[55] V.N. Strocov, in *Electron spectroscopies applied to low-dimensional materials* (Kluwer, Netherlands, 2000)

[56] V.P. Zhukov, F. Aryasetiawan, E.V. Chulkov, I.G. de Gurtubay, and P.M. Echenique, Phys. Rev. B **64**, 195122 (2001); V.P. Zhukov, F. Aryasetiawan, E.V. Chulkov, and P.M. Echenique, *ibid*. **65**, 115116 (2002).

[57] H.J. Levinson, F. Greuter, and E.W. Plummer, Phys. Rev. B **27**, 727 (1983).

[58] S.D. Kevan, N.G. Stoffel, and N.V. Smith, Phys. Rev. B **31**, 1788 (1985).

[59] E. Caruthers, L. Kleinman, and G.P. Alldredge, Phys. Rev. B **8**, 4570 (1973).

[60] D. Spanjaard, D.W. Jepsen, and P.M. Marcus, Phys. Rev. B **19**, 642 (1979).

[61] S.G. Louie, P. Thiry, R. Pinchaux, Y. Petroff, D. Chandesris, and J. Lecante, Phys. Rev. Lett. **44**, 549 (1980).

Solid-State Photoemission and Related Methods
Wolfgang Schattke, Michel A. Van Hove (Eds.)

8 Time-resolved two-photon photoemission

Thomas Fauster

8.1 Basics of two-photon photoemission

In this chapter time resolution will be introduced to photoemission experiments. This means not just a series of regular photoemission measurements to monitor the changes of a sample with time. In two-photon photoemission the time delay between the two photons is an additional experimental parameter which can be controlled with femtosecond resolution, i.e., on a time scale relevant for electronic processes. At the same time, the introduction of the second photon leads to the participation of an additional electronic state in the energy diagram for photoemission.

8.1.1 Energy diagram

In Figure 8.1 the transition from initial state $|1\rangle$ to an intermediate state $|2\rangle$ after the absorption of the photon with energy $h\nu_a$ is shown. The second photon of energy $h\nu_b$ excites the electron out of the intermediate state into the final state $|3\rangle$. If the final state energy E_3 is above the vacuum energy E_{vac}, the electron might leave the surface and its kinetic energy E_{kin} is measured with an electron energy analyzer. Obviously, the initial state has to be occupied, i.e., its energy E_1 should be below the Fermi energy E_F. The intermediate state on the other hand has to be empty at first. In most cases it is desirable to keep the photon energy $h\nu_a$ below the work function $\Phi = E_{vac} - E_F$, because this constitutes the threshold for one-photon photoemission. This applies also to the other photon, because processes with the role of the two photons interchanged are possible as well.

8.1.2 Energy-resolved spectroscopy

The spectrum sketched at the right of Fig. 8.1 shows a peak at the final state energy E_3. The cutoff at kinetic energy zero corresponds to the vacuum level E_{vac} of the sample. Electrons with the highest energy after the absorption of the photons with energies $h\nu_a$ and $h\nu_b$ appear at kinetic energy $E_{max} - E_{vac} = h\nu_a + h\nu_b - \Phi$. These limits are familiar from regular photoemission spectroscopy and can be used to determine the work function from the width of the spectrum. Similarly, the momentum $k_\parallel$ of the electron parallel to the surface is conserved for single-crystal surfaces. For electrons emitted at an angle ϑ with respect to the surface normal one obtains $\hbar k_\parallel = \sqrt{2mE_{kin}}\,\sin\vartheta$. Umklapp processes would add reciprocal lattice vectors of the surface to the momentum conservation, but play usually no role in two-photon photoemission. One has to keep in mind that the kinetic energies are generally quite

Solid-State Photoemission and Related Methods: Theory and Experiment. Edited by Wolfgang Schattke, Michel A. Van Hove

ISBN: 3-527-40334-5

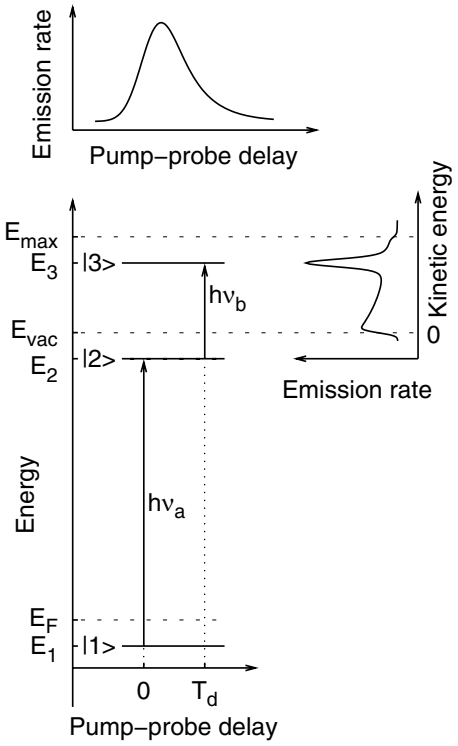

Figure 8.1: Energy diagram for a two-photon-photoemission process and results of time- (top) and energy-resolved (right) measurements.

low. The requirement that both photons should have energies below the work function leads to maximum kinetic energies less than the work function, i.e., usually below 5 eV. One consequence is a very limited accessible $k_{||}$ range. Most two-photon-photoemission experiments are performed at normal emission. This geometrical restriction permits the use of a negative bias voltage (typically a few Volts) at the sample in order to accelerate the electrons into the analyzer. At the low kinetic energies obtained without bias the transmission of most analyzers drops significantly and magnetic fields have to be shielded very carefully.

8.1.3 Time-resolved measurements

The two-photon photoelectron spectroscopy discussed in the previous section does not exploit the time delay between the two photons and it has been tacitly assumed, that the time delay is fixed. The time-resolved mode of two-photon photoemission is performed at fixed kinetic energy and the delay between the two photons is scanned. The first photon pumps the intermediate state and the second photon probes the population of this state. Such measurements are shown in Fig. 8.2 for the first two image-potential states (see Sec. 8.4.2) on Cu(001) and one recognizes a rapid increase of the emission rate followed by an exponential decay with pump-probe delay T_d. The time constant for the decay indicates the lifetime of the selected intermediate state. The increase of the signal and the delay zero are determined by the temporal shape of the photon pulses. Their cross correlation can be obtained from measurements

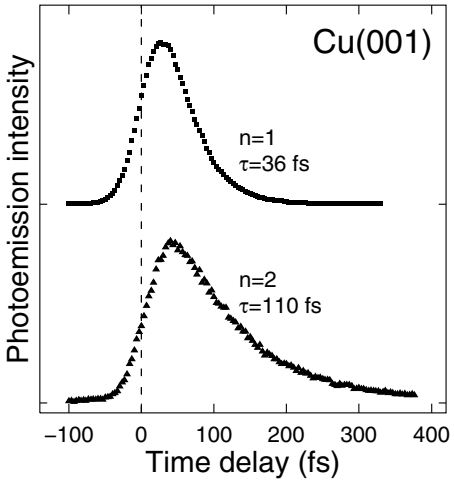

Figure 8.2: Two-photon photoemission signal for the lowest two image-potential states on Cu(001) as a function of pump-probe delay.

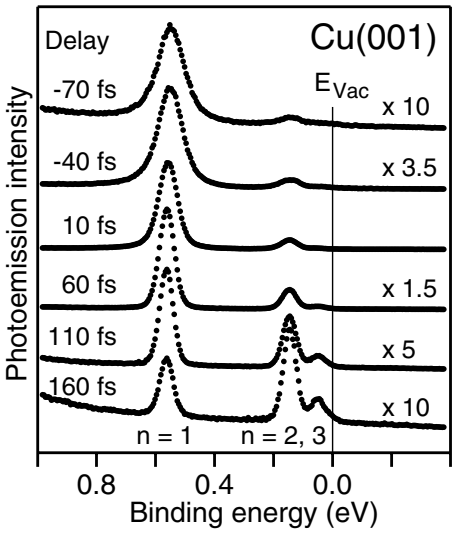

Figure 8.3: Two-photon photoemission spectra of image-potential states from Cu(001) for various pump probe delays.

at energies where the lifetime at the energy of the intermediate state is much shorter than the pulse durations. For the spectra in Fig. 8.2 the cross correlation has a full width at half maximum of 60 fs. For identical photon energies $h\nu_a = h\nu_b$ the cross correlation becomes symmetric (autocorrelation) and pump and probe pulses cannot be distinguished. For identical polarization of the two photon beams the autocorrelation is dominated by interference effects (see Fig. 8.7).

State-of-the-art lasers used for two-photon photoemission can produce pulses of some 10 fs. This time scale is comparable to the lifetime of electronic excitations at surfaces. The shift of the measured signal relative to the time zero obtained from the cross correlation is a good approximation for lifetimes shorter than the pulse widths [1, 2].

The time-resolved measurement mode presumes that the energy of the intermediate state is independent of the time delay. This is usually fulfilled, but should be checked by measuring energy-resolved spectra for a few selected time delays. An example for such a series of spectra is shown in Fig. 8.3 for image-potential states (see Sec. 8.4.2) on Cu(001). The spectra are normalized to same height and the intensity variation with time delay can be inferred from Fig. 8.2. The energy position of the peaks is indeed independent of the delay. The change of linewidth with delay will be discussed in Sec. 8.2.

8.1.4 Variation of photon energy

In regular photoelectron spectroscopy the variation of the photon energy leads to the constant initial or constant final state spectroscopy, depending on the particular state under investigation. In two-photon photoemission there are in addition intermediate states and two different photons. A constant intermediate state spectroscopy ($E_2 = \text{const.}$) could be done in different ways (cf. Fig. 8.1):

- Tune $h\nu_a$ at fixed $h\nu_b$ and E_{kin}.
- Tune $h\nu_b$ and E_{kin} at fixed $h\nu_a$.
- Tune $h\nu_a$, $h\nu_b$ and E_{kin}.

Similarly constant initial ($E_1 = \text{const.}$) and final ($E_3 = \text{const.}$) state spectroscopies could be done in a variety of modes. All these modes play no role in practice, because the photon energy of femtosecond lasers is rather difficult to tune. In addition, the delay between the two laser pulses has to be controlled very carefully. This makes a continuous variation of the photon energies for spectroscopic purposes infeasible.

Measurements at several discrete photon energies are, however, important in order to identify a particular peak in a spectrum as initial, intermediate, or final state:

- The energy of a final state should obviously not depend on either photon energy $h\nu_a$ or $h\nu_b$.
- The intermediate state is emitted after absorption of photon with energy $h\nu_b$. Its kinetic energy should therefore change proportional to the change $\Delta h\nu_b$. Because $h\nu_a$ and $h\nu_b$ might switch their role as pump and probe pulses, the change of kinetic energy could also be $\Delta h\nu_a$. This process would correspond of course to a different intermediate state energy [3]. It should be noted, that the sequence of the excitations may be determined also from time-resolved measurements [4]. If $h\nu_b$ is absorbed before $h\nu_a$, the exponential decay appears at negative delays (see Fig. 8.10).
- An initial state is excited directly by two photons. Consequently the change of the kinetic energies is given by the sum $\Delta h\nu_a + \Delta h\nu_b$.

An example for the photon energy dependence of initial and intermediate states is given in Fig. 8.4 for Cu(111) at 100 K [5, 6]. The $n = 0$-peak which shows the stronger variation with photon energy corresponds to the well-known occupied surface state (see also Sec. 8.4.1) on Cu(111) and is an initial state. The other peak shows less variation and is an $n = 1$

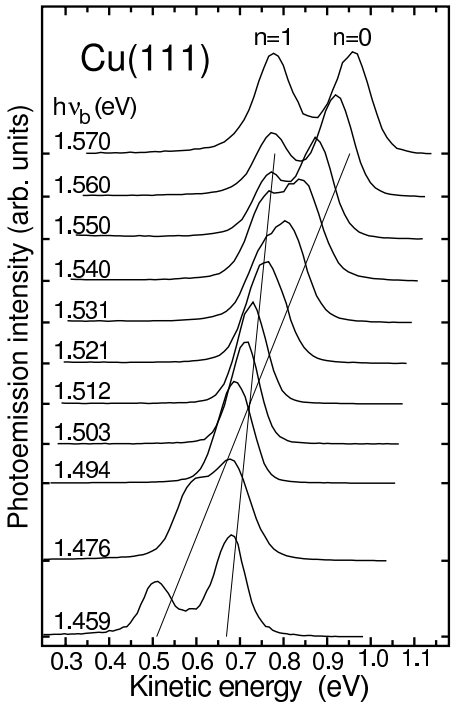

Figure 8.4: Series of two-photon-photoemission spectra from Cu(111) for various photon energies with $h\nu_a = 3h\nu_b$. The spectra are normalized to same height and plotted with an offset proportional to $h\nu_b$.

image-potential state (see Sec. 8.4.2) which is populated as intermediate state. At the photon energy $h\nu_a = 4.536$ eV a resonant excitation from the surface to the image-potential state occurs [7, 8]. This resonance enhancement cannot be seen in Fig. 8.4, because the spectra are normalized to same height.

The considerations of identifying initial, intermediate and final states by a variation of the photon energy apply strictly only to surface states which show no dispersion with momentum perpendicular to the surface. For transitions between bulk bands the energies of both involved bands change with photon energy in a way determined by the bulk band structure. This might lead to changes of the kinetic energy not covered by the cases listed in the previous paragraph. The observation of bulk bands by two-photon photoemission will be discussed in Sec. 8.3.1.

8.1.5 Experimental setup

The basic requirements for a two-photon-photoemission experiment are a light source and an electron energy analyzer. The main difference to a regular photoemission experiment rests in the light source which has to be intense enough to stimulate the second-order photoemission process. This involves pulsed lasers in all cases. A typical setup is shown in Fig. 8.5. A Ti:sapphire laser pumped by an all solid-state laser emitting green light produces pulses at 1.55 eV photon energy with pulse durations down to 12 fs at a repetition rate of 86 MHz. These pulses are frequency-doubled by second-harmonic generation and the third harmonic is generated by sum-frequency generation in non-linear optical crystals. The photon energies $h\nu_a$ and

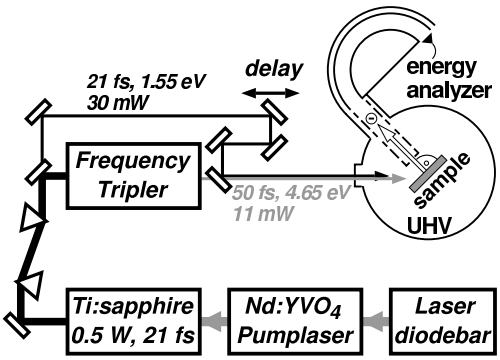

Figure 8.5: Experimental setup for two-photon photoemission.

$h\nu_b$ are usually based on a common fundamental laser frequency. Deriving the two laser pulses from the same laser source is essential for recombining the pulses with femtosecond precision on the sample for time-resolved experiments. The ultimate time-resolution is obtained by interferometric control of the delay stage to a fraction of the wavelength [9]. Interference occurs only for identical photon energies $h\nu_a = h\nu_b$ and polarization. For best performance of the experiment a good characterization of the laser pulses is necessary (see following Sec. 8.2 and Ref. [10]). This involves pulse compression by prism pairs such as shown in Fig. 8.5 and measurement of the autocorrelation and spectrum of the laser pulses (not shown). The proper characterization of the cross correlation or autocorrelation can, however, only be done by measuring the photoemission or second harmonic signal from the sample [1, 9, 11].

The main advantage of Ti:sapphire laser systems over excimer-laser-pumped dye lasers is the high repetition rate. Previous systems had comparable output power, but were limited by space-charge effects [12]. At high repetition rate a few electrons are emitted per laser pulse and no space charge can develop. Employing Ti:sapphire lasers the count rate could be increased by four orders of magnitude over previous systems [13] with the added bonus of time resolution in the femtosecond regime.

A reduction of the repetition rate below 1 MHz is necessary if the electron energy analysis is done by time-of-flight detection [14, 15]. The energy resolution for such a system can compete with hemispherical analyzers, because the kinetic energies of the electrons are rather low and consequently the flight times are quite long. The ultimate performance of any detection system is limited by the number of electrons which can be registered per laser pulse [16]. Hemispherical analyzers with several channeltrons as shown in Fig. 8.5 are best in combination with high-repetition-rate lasers. At low repetition rate, time-of-flight detection has the advantage of registering for each laser pulse all electrons with any kinetic energy.

Some two-photon-photoemission experiments combining lasers and synchrotron light sources have been reported [17]. The pulse length of the electron bunches in the synchrotron limits the time resolution and the synchronization between laser and synchrotron constitutes a difficult task [18]. However, such experiments might become more important in the future with the construction of new free-electron-laser sources. It is interesting to note that the laser sources for two-photon photoemission provide more photons per second than a state-of-the-art synchrotron beam line albeit typically at lower photon energies.

8.2 Theoretical description of two-photon photoemission

Two-photon photoemission involves the absorption of two photons and the two optical transitions are treated usually as independent consecutive processes. The matrix elements can be obtained according to the well developed theories for regular photoemission. The energy and momentum conservation have been exploited already in Sec. 8.1. An analysis of two-photon-photoelectron spectra using the obvious extension of the one-step model of photoemission [19] has not been done so far. There are a few aspects in the two-photon-photoemission process which are absent in regular photoemission and will be discussed in this section.

8.2.1 Coupling between electron and hole

In regular photoemission the optical transition couples to a free-electron wave function in vacuum. This holds also for the second transition in two-photon photoemission. The first optical transition in contrast occurs between two bound states, because the intermediate state has an energy below the vacuum level. This opens the possibility for a coupling between the initial-state hole $|1\rangle$ and the intermediate-state electron $|2\rangle$ and the formation of an exciton. Such effects have been predicted for the transition between the occupied surface state and the $n = 1$ image-potential state on Cu(111) shown in Fig. 8.4 [20]. An experimental verification is still lacking since the lifetime of this exciton is only a few femtoseconds and the energy shift is only a few meV. For semiconductors [21], molecular adsorbates [22, 23] or insulators [24] excitonic effects might be more important. One interesting aspect would be the lifting of momentum conservation by the spatial localization of the exciton [21, 22].

8.2.2 Phase coherence

In a time-resolved two-photon-photoemission experiment the pulse duration can be comparable to the time scale of the temporal quantum-mechanical evolution of the involved states. This can be stated in different ways depending on the particular circumstances:

- The lifetime is long compared to the pulse duration, or equivalently,
- the linewidth is narrow compared to the spectral bandwidth of the laser pulses.
- The energy differences of some states are comparable to the spectral bandwidth.

These statements apply also to the absorption of a single photon, but the time resolution in two-photon photoemission leads to particular effects which makes the phase coherence of the quantum-mechanical time evolution accessible. Note, that this refers not to the (spatial or temporal) coherence of the laser light which is described by the electric field. Coherence effects between the two laser pulses occur only for identical photon energies and polarization state. These lead to some special effects discussed in Ref. [9]. The formal description in this situation is identical to the one outlined here, if the interference of the photon fields is incorporated.

The interaction of the laser fields with the electronic states $|k\rangle$ leads to a superposition

$$|\Psi\rangle = \sum_k c_k(t)|k\rangle. \tag{8.1}$$

In the absence of the laser fields the time dependence $c_k(t)$ would be given by

$$c_k(t) = c_k^0\, e^{-t/2\tau_k} e^{i\phi_k(t)} e^{iE_k t/\hbar} \quad \text{with} \quad c_k^0 = c_k(0). \tag{8.2}$$

The exponential decay is described by the lifetime τ_k and the energy E_k determines the quantum-mechanical phase. The term containing $\phi_k(t)$ describes additional changes of the phase. Such phase-breaking events are (quasi-)elastic scattering of the electron with no or negligible change of energy or population $|c_k(t)|^2$. The experiment samples the population of the final state $|c_3(t)|^2$ and this quantity depends on both laser fields, and in particular on the time delay between pump and probe pulse, as can be inferred from Eq. (8.1). The sampling of a time-dependent population of the intermediate state $|2\rangle$ by the excitation with photon $h\nu_b$ into the final state $|3\rangle$ is the essential difference to regular photoemission which probes a constant population in the initial state $|1\rangle$.

For the calculation one has to introduce the Hamilton operator $\hat{H}_0$ of the unperturbed system which obeys $\hat{H}_0|k\rangle = E_k|k\rangle$. The photons are described in the dipole approximation by the time-dependent electric fields $\vec{\mathcal{E}}(t) = \vec{\mathcal{E}}_a(t) + \vec{\mathcal{E}}_b(t)$ leading to an interaction operator $\hat{V}$ with only off-diagonal matrix elements $V_{kl} \propto \langle l|\vec{\mathcal{E}} \cdot \vec{p}|k\rangle$ and the momentum operator $\vec{p}$. The solution of this problem may be done by perturbation theory up to fourth order in the electric fields [25]. The Liouville-von-Neumann equations [26] are basically equivalent and more convenient, because the density matrix $\hat{\rho}$ contains the population $\rho_{33} = |c_3(t)|^2$ directly:

$$\hbar \frac{d}{dt}\rho_{kl} = \frac{1}{i}\left[\hat{H}_0 + \hat{V}, \hat{\rho}\right]_{kl} - \Gamma_{kl}\rho_{kl} \tag{8.3}$$

The damping matrix $\hat{\Gamma}$ is introduced phenomenologically to describe the decay of population and phase included in Eq. (8.2). The matrix elements are real and can be written as [27]

$$\Gamma_{kl} = \frac{1}{2}(\Gamma_k + \Gamma_l) + \Gamma_{kl}^*, \quad \text{with} \quad \Gamma_{kl}^* = \Gamma_{lk}^* \quad \text{and} \quad \Gamma_{kk}^* = 0. \tag{8.4}$$

The decay rates Γ_k are directly related to the lifetimes $\tau_k = \hbar/\Gamma_k$, whereas the dephasing rates Γ_{kl}^* describe the breaking of the phase relation between states $|k\rangle$ and $|l\rangle$.

The system of differential equations (8.3) can be solved numerically. It may be simplified by retaining only terms with photon energies close to the energy differences between the states. For this case, only the envelopes of the electric fields have to be considered. The resulting optical Bloch equations [26] may be solved analytically in certain limiting cases [8, 10, 28] for a three level system. Instead of discussing solutions of the optical Bloch equations in detail, some of the more surprising features will be illustrated by selected results.

The description of regular photoemission spectra by two-level optical Bloch equations yields the familiar result of a Lorentzian convoluted with the spectrum of the laser pulse [10]. The Lorentzian width contains a sum of decay and dephasing rates, which cannot be separated. One- and two-photon photoemission start from a constant initial-state population, but the two-photon process samples a time-dependent intermediate-state population with the second photon. This time dependence changes upon tuning the photon energy on or off resonance for a transition between discrete initial and intermediate states. In Fig. 8.4 the linewidth at resonance ($h\nu_b = 1.512$ eV) is narrower than the linewidth observed for each state off resonance.

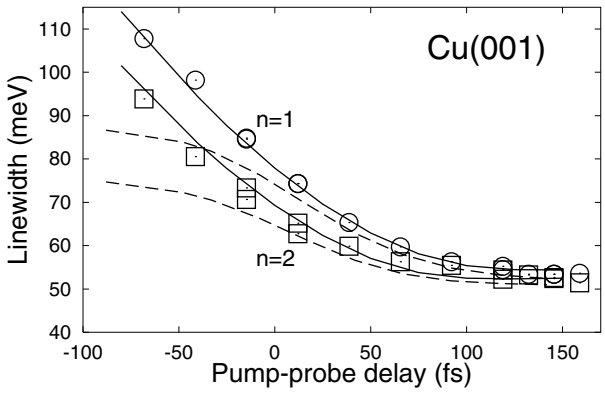

Figure 8.6: Linewidth for the $n = 1$ and $n = 2$ peaks (circles and squares) from Fig. 8.3 as function of pump-probe delay compared to the results of numerical calculations for Gaussian and hyperbolic-secant pulses (solid and dashed lines).

This has been observed also using 15 ns laser pulses [6]. A simple interpretation based on the multiplication of two Lorentzian lineshapes convoluted with a Gaussian apparatus function gave a satisfactory fit to the data [6, 27]. Using the optical Bloch equations for infinitely long pulses, the experimental lineshape can be described quite well and values for the decay and dephasing rates of the surface and image-potential state can be obtained [8].

The linewidths of the peaks observed in the energy-resolved spectra of Fig. 8.3 are plotted in Fig. 8.6 as a function of pump-probe delay. A constant value is reached for long delays, whereas a linear increase is obtained towards negative delays. This surprising behavior can be explained quantitatively by calculations with a three-level system of optical Bloch equations. The parameters decay and dephasing rates as well as pulse durations for the Gaussian-shaped pulse envelopes were fitted independently and results close to the values obtained from different, independent measurements were obtained [10]. The dashed lines show the results for hyperbolic-secant pulse envelopes which do not describe the experimental data for negative delays satisfactorily. Note that the pulse shape in the UV cannot be measured by autocorrelation and that even in the infrared it is difficult to measure the autocorrelation with sufficient accuracy to distinguish between Gaussian and hyperbolic-secant pulse shapes. It should be pointed out, that the spectral width of the femtosecond pulses can be larger than the analyzer resolution or linewidth of the electronic state.

Another example for the dependence of the lineshape on pump-probe delay is shown in Fig. 8.7. Using two identical photon beams the delay can be controlled interferometrically with subwavelength resolution. Two-photon photoemission spectra for the occupied surface state on Cu(111) (see Fig. 8.4 and Sec. 8.4.1) taken for in and out of phase conditions between the two electric fields show different lineshapes and energy positions [29]. In these experiments not only the phase of the wave function but also of the photon fields is important. This opens the possibility of a coherent control of the excitations.

In the last example the temporal phase of the wave function enters directly. If the energy separation of intermediate states is comparable to the bandwidth of the laser pulses, several states can be excited coherently. The optical Bloch equations have to be solved including several intermediate states [13, 30]. When the pump pulse is over, the intermediate state pop-

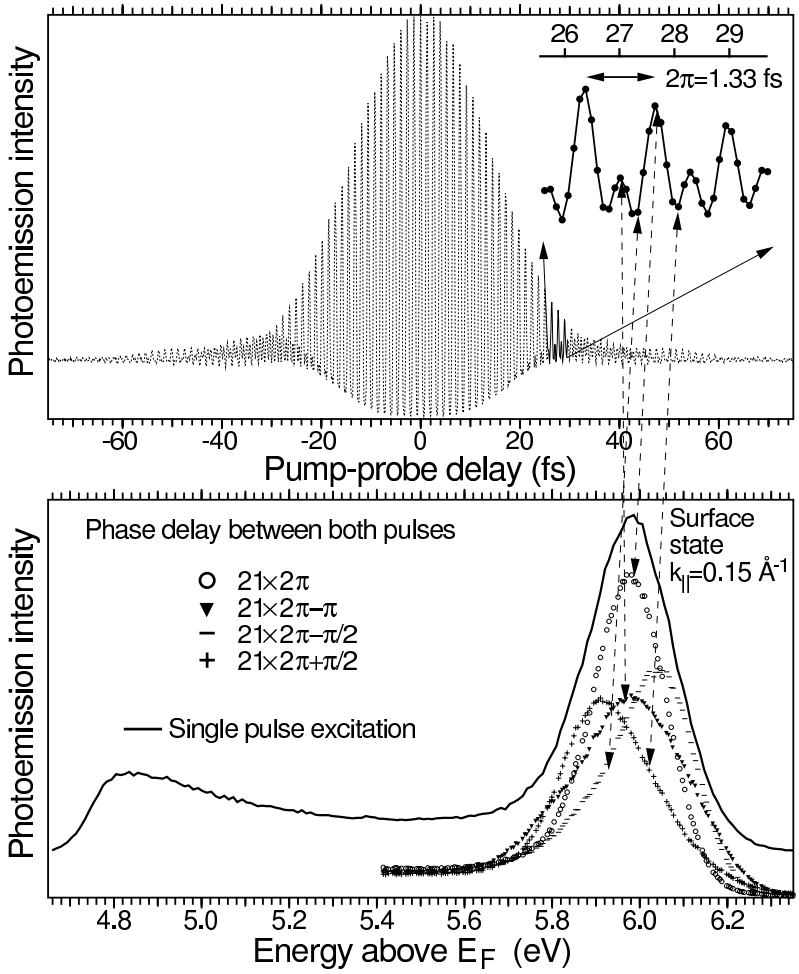

Figure 8.7: Top: Interferometric two-photon photoemission signal for the occupied surface state on Cu(111) as a function of pump-probe delay. Bottom: Spectra taken for in and out of phase conditions between pump and probe pulses (after Ref. [9]).

ulation is given by the square of the sum of all excited states $c_k(t)$ (see Eq. (8.2))):

$$\begin{aligned}\left|\sum_k c_k(t)\right|^2 = &\sum_k \left|c_k^0\right|^2 e^{-t/\tau_k} \\ &+ 2\sum_{k\neq l} \left|c_k^0\right|\left|c_l^0\right| \, e^{-t/2\tau_k - t/2\tau_l - \Gamma_{kl}^* t/\hbar} \cos((E_k - E_l)t/\hbar).\end{aligned} \tag{8.5}$$

The last term oscillates with a frequency which depends on the energy difference of the coherently excited states. These oscillations are damped by the lifetimes of the states and

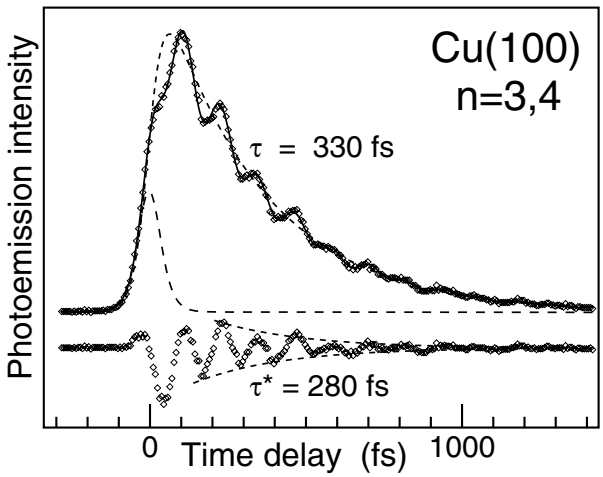

Figure 8.8: Coherent excitation of the $n = 3$ and $n = 4$ image-potential states leads to beating patterns as a function of pump-probe delay.

the loss of phase coherence described by the dephasing rates Γ^*_{kl}. The average population decays exponentially with time constants τ_k as indicated by the first term of Eq. (8.5). An experimental illustration is given in Fig. 8.8 for image-potential states (see Sec. 8.4.2) on Cu(100) [2, 13]. The oscillatory and exponential contributions can be separated and show different time constants for decay. Thus the decay and dephasing can be identified directly and assigned to different scattering processes.

A coherent control of the quantum beats could be achieved by adding a *chirp* to the laser pulses, i.e., manipulating the arrival time of the different spectral components while maintaining the spectrum of the pulse. One could then excite the $n = 4$ state before the $n = 3$ state and shift the phase of the quantum-beat pattern. Such effects have not yet been observed in two-photon photoemission, but have be used to control chemical reactions by feedback-optimized phase-shaped femtosecond laser pulses [31].

8.3 Bulk properties

This section deals with two-photon photoemission involving bulk states. Because electron spectroscopies are always surface sensitive, it is not easy to identify specific bulk features in two-photon photoemission spectra. In particular, the bulk-sensitive region at high kinetic energies known from regular photoemission is not accessible here. The discussion is divided between the observations of bulk states and the properties of hot electrons excited by femtosecond laser pulses in the sample.

8.3.1 Direct bulk transitions

The first report of transitions of bulk states by two-photon photoemission identified an unoccupied state at 1.48 eV above E_F on Cu(001) [32]. It was observed by a resonance from the occupied X_5 state (top of the d-bands) and assigned to the $X_{4'}$ point, the edge of the sp-band

gap at X. Later inverse photoemission measurements locate a surface resonance at 1.4 eV above E_F [33], which might reverse the assignment of the bulk transition to a surface state.

The second example also involves a reinterpretation of a previous result. In the pioneering work of Giesen *et al.* [34] an unoccupied state 1.92 eV above E_F was found for Ag(111) which could not be satisfactorily explained by any surface- or bulk-band-structure calculations. A later study showed, that there is no intermediate state involved, and assigned the transition to a two-photon excitation between two bulk sp-bands [35]. The dispersion of the bands in the relevant energy range leads to a photon-energy dependence mimicking an intermediate state. A similar direct transition between sp-bands has also been identified for Cu(111) [36].

These two examples show that the observation of a peak at a fixed intermediate state energy as a function of photon energy is not sufficient to assign the peak to a bulk or surface state. However, one can use the fact familiar from regular photoemission, that only bulk bands show a dispersion perpendicular to the surface and consequently with photon energy. Consequently, a transition which does not exhibit a constant initial, intermediate, or final state energy must involve bulk bands. Several examples for this behavior have been found on the Si(100) surface and assigned to various transitions between bulk bands [37]. The agreement between experiment and bulk band structure calculations is far from perfect. The strong intensity variations with photon energy [38, 39] leave the possibility of a reinterpretation.

The identification of transitions involving bulk bands can obviously be quite difficult in two-photon photoemission spectroscopy. This explains the lack of time-resolved measurements for bulk states. A notable exception might be the identification of a saddle point in the band structure of graphite through an anomaly in the lifetimes of hot electrons [40].

8.3.2 Lifetimes of hot electrons

A short high-intensity laser pulse creates a large number of electronic excitations in a sample. The electrons or holes are generated within the penetration depth of the light which is typically considerably larger than the escape depth of the electrons in a two-photon photoemission experiment. The excited (hot) electrons rapidly loose energy by scattering with the other electrons which are available at high density in a solid. The transfer of energy to the lattice via electron-phonon coupling occurs much slower on a time scale of ps.

The Fermi-Dirac distribution of the electron gas can be seen directly at the high-energy end of a regular photoemission spectrum. Using laser pulses with high intensity to heat the electron gas, the rise of the electron temperature and the cooling by the lattice was observed [41]. For photon energies within a few kT below the work function one-photon photoemission processes might still be observable at the low-energy end of the electron spectrum. Only the exponential tail of the Fermi-Dirac distribution is visible and the temperature of the electron gas can be measured [12]. If one- and two-photon processes are visible in a spectrum, the relative intensity of these processes can be estimated to $10^4 \ldots 10^5$ [12]. In order to distinguish between one- and two-photon processes, it can be helpful to measure the intensity dependence of the spectral features. For identical photons $h\nu_a = h\nu_b$ the electron signal depends linearly or quadratically on the laser intensity for one- and two-photon processes, respectively. When two different photons are used, one may use the disappearance of the two-photon features, if either of the two laser beams is blocked or a suitable time delay is introduced. Note that

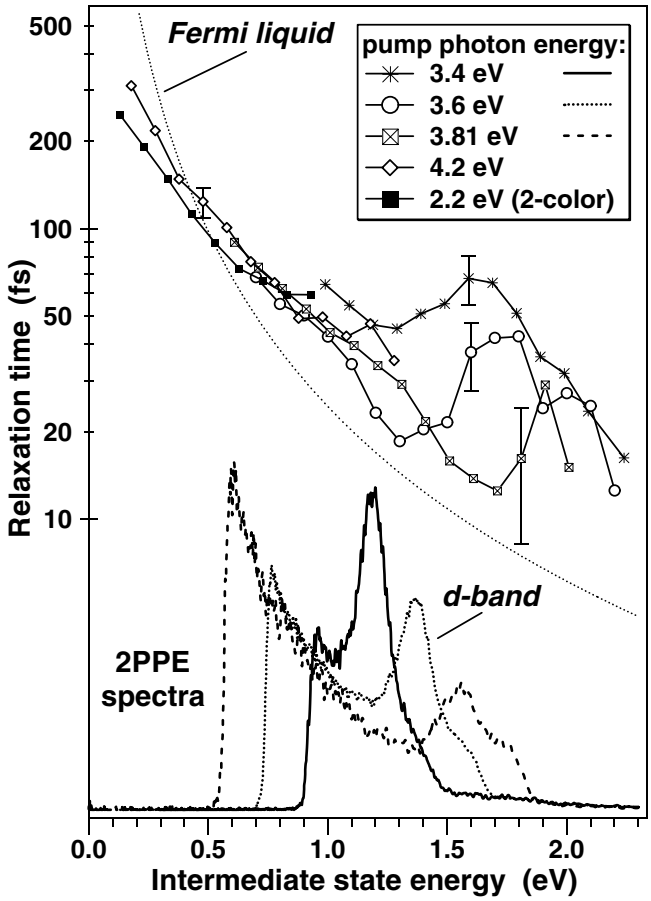

Figure 8.9: Two-photon photoemission spectra (linear scale at the bottom) and relaxation times of hot electrons (logarithmic scale at the top) from Cu(111) for various photon energies (after Ref. [42]).

processes involving two photons from a single laser pulse can be identified only by intensity variation, if they cannot be excluded by energy considerations (see Sec. 8.1.2)

Choosing the photon energies $h\nu \ll \Phi$ ensures that only two-photon photoemission processes are observed. Examples for spectra obtained at a Cu(111) sample are shown at the bottom of Fig. 8.9. The energy scale refers to an intermediate state which leads to opposing shifts of the vacuum edge (left) and the Fermi edge (right) with photon energy. The energy distribution of hot electron decreases monotonically with energy. The superimposed peak shifting parallel to the Fermi edge corresponds to emission from the top of the d-bands at constant initial-state energy. The relaxation time obtained at the respective intermediate-state energies is plotted at the top of Fig. 8.9 on a logarithmic scale. The dependence follows roughly the prediction $\propto (E - E_F)^{-2}$ from Fermi-liquid theory [43]. The deviations around 1.5 eV are

presumably due to secondary electrons arising from the Auger decay of d-holes [42, 44, 45]. The lifetime of d-holes is longer than the hot-electron lifetime at the respective energy [45] leading to an apparent increase of the observed relaxation time. The decay of the hot electrons themselves also leads to the generation of secondary electrons which appear at low kinetic energies. This intrinsic process makes the determination of lifetimes close to E_F difficult and can be reduced by using low photon energies [46]. In many studies this requires a lowering of the work function by suitable adsorbates [42, 44, 47]. There seems to be a negligible influence by the adsorbates on the measured lifetimes.

The last observation proves that mainly the properties of the hot electrons in the bulk are measured by these time-resolved two-photon photoemission experiments. The large penetration depth of the light compared to the escape depth of the electrons suggests that transport effects might influence the data. Some electrons from deeper layers can travel into the sampled volume near the surface while on the other hand some electrons leave the surface region. These effects can be modeled using ballistic transport [48] or bulk band structure calculations [42]. The latter method is able to explain the differences observed for various low-index copper surfaces [49]. A more direct proof of the transport effect is given by the dependence of hot-electron lifetimes on thickness of thin noble-metal films [50].

All these experiments show that in the absence of specific intermediate states time-resolved two-photon photoemission is able to obtain valuable information on the lifetime of hot electrons in the bulk, if secondary electrons and transport effects are taken into account. This applies also for (111) surfaces of noble metals where a band gap exists for emission in the measurement direction normal to the surface. Apparently, scattering associated with the emission process ensures that electrons from the whole Brillouin zone reach the detector. This ensures that the experiment samples the complete distribution of hot electrons in the bulk and explains the good agreement of the measured lifetimes with simple free-electron models based on Fermi-liquid theory.

8.4 Surface properties

The previous section showed that the lifetimes of electronic excitations in the bulk are usually quite short which makes time-resolved two-photon photoemission a surface-sensitive technique. Electrons coupled only weakly to the bulk can be found as surface states and in particular as image-potential states. Loosely bound adsorbates might also have long-lived states which are potentially important for photochemical reactions. One common feature of all these surface-related states is the absence of dispersion perpendicular to the surface which unambiguously makes them pure initial or intermediate states. The different types of states will be the topic of the final section of this chapter.

8.4.1 Surface states

On semiconductor surfaces the broken bonds lead to a rearrangement of the geometric and electronic structure which in most cases results in occupied and unoccupied dangling bond states separated by a band gap. Electrons in the lowest conduction band states (bulk or surface) can decay only by recombination with a hole. This process is quite unlikely and may

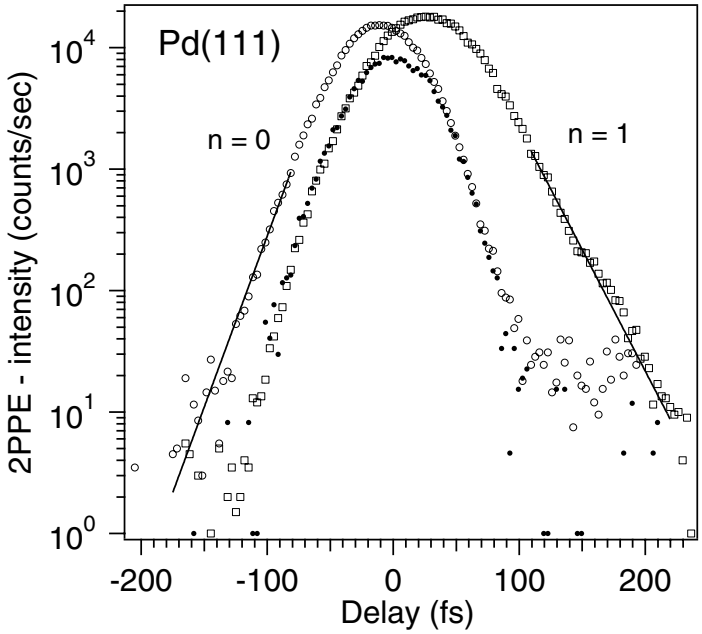

Figure 8.10: Time-resolved spectra for the surface (open circles, $n = 0$) and image-potential state (open squares, $n = 1$) on Pd(111). The solids dots show the cross correlation determined for the occupied surface state on Cu(111).

lead to rather long lifetimes of the respective states. The time scale of the relaxation of higher excited electrons might lead to a delayed filling of the conduction band minima. These processes are qualitatively similar to the generation of secondary electrons in metals as discussed in the previous section and can result in complex electron dynamics [39]. The work on semiconductor surfaces has been reviewed by Haight [51].

On metals a variety of surface states are well known from photoemission and inverse photoemission studies. Only states near the center of the surface Brillouin zone are accessible by two-photon photoemission, because of the low kinetic energies used. This restricts the studies mainly to close-packed surfaces. For Ag(111), Cu(111), and Au(111) the surface states have been observed by two-photon photoemission (see Figs. 8.4, 8.7 and Ref. [12]). Owing to the large work function three-photon photoemission has been employed on Pt(111) to excite the occupied surface state [52]. In time-resolved experiments occupied states show the cross correlation between pump and probe pulses and do not yield any interesting information on the electron dynamics. For Pd(111) the surface state is unoccupied and its lifetime has been determined [4]. The experimental data are shown in Fig. 8.10 on a semilogarithmic scale. The occupied surface state ($n = 0$) is pumped by the IR pulse and probed by the UV pulse. The population follows the cross correlation (solid dots) for positive delays and persists towards negative delays, when the UV pulse follows the IR pulse. The opposite behavior is displayed by the $n = 1$ image-potential state (see Sec. 8.4.2) which is pumped by the UV pulse. From

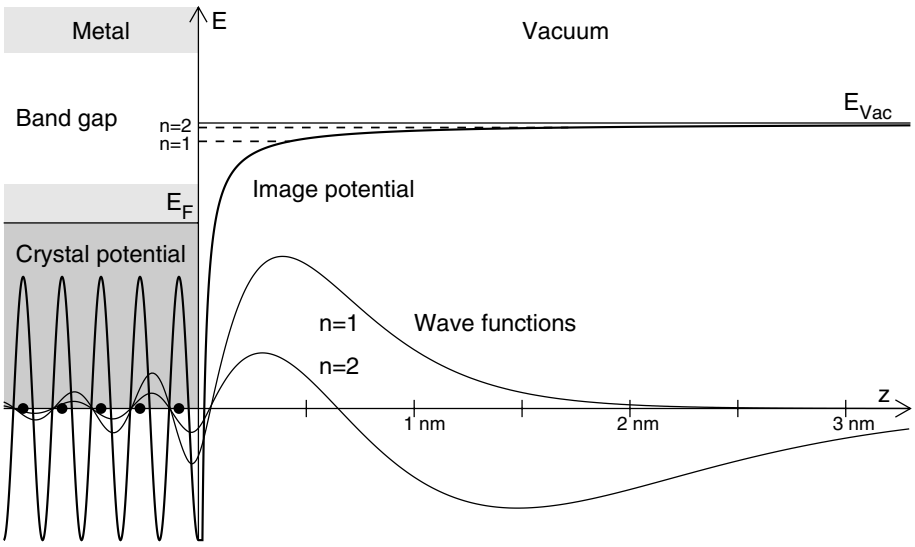

Figure 8.11: Potential and energy diagram for image-potential states at a Cu(001) surface. The wave functions for the $n = 1$ and 2 states are shown in the lower part.

data obtained over a dynamic range of several orders of magnitude one can extract the lifetime directly from the exponential decay of the intensity (straight lines in the semilogarithmic plot of Fig. 8.10) at delay times where the laser pulses show negligible intensity in the cross correlation (solid dots in Fig. 8.10). The results are confirmed by fits using the optical Bloch equations [4].

8.4.2 Image-potential states

Time-resolved two-photon photoemission was illustrated in the previous sections using examples involving image-potential states [12, 62–64]. The image force acting on an electron in front of a metal surface can be derived from a long-range Coulomb-like potential as illustrated in Fig. 8.11. A band gap in the band structure may impede the penetration of the electron into the metal along the direction of the motion. This results in a series of bound states with binding energies relative to the vacuum level of approximately 1/16 of the values in the hydrogen atom. Figure 8.11 shows the wave functions of the first two image-potential states on Cu(001) which hardly penetrate into the metal and have maxima several Ångstroms away from the surface. [62]. These states are only weakly coupled to the metal which leads to lifetimes matching the current experimental possibilities. The corresponding measured lifetimes are listed in Table 8.1 for normal emission ($k_{\|} = 0$). The data compilation shows the n^3 dependence of the lifetime for large quantum numbers n [62,65]. The importance of the band gap can be seen for Cu(111) where the first image-potential state has a longer lifetime than the second, which lies outside the band gap [15, 56]. The *ab initio* theoretical description of image-potential states is fairly complex due to the long-range potential arising from the screening in a many-body sys-

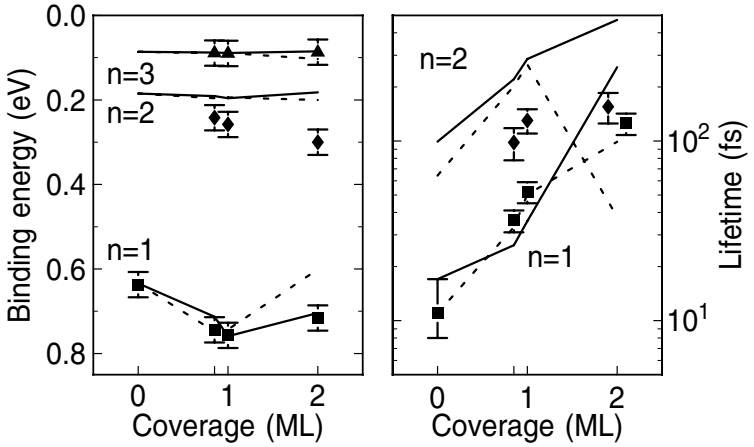

Figure 8.12: Binding energies (left) and lifetimes (right) for image-potential states as a function of Xe coverage on Ru(0001). The solid lines show the result of a tunneling model, the dashed lines correspond to a continuum model (after Ref. [60]).

tem. However the agreement between calculated and experimental values for binding energies and lifetimes is remarkably good [4, 43, 61].

Surface states are by their very nature always rather sensitive to adsorption. This holds also for image-potential states which are completely quenched by many adsorbates [14]. However, adsorbates without electronic states close to the vacuum level may be described as a dielectric spacer layer. The modification of the image potential can then be treated by classical continuum electrostatics [60, 66, 67]. For adlayers of noble gases the lifetime increases with layer thickness, because the coupling to metal is reduced. Figure 8.12 shows experimental data for

Table 8.1: Measured lifetimes in fs of image-potential states on clean metal surfaces.

	τ_1	τ_2	τ_3	τ_4	τ_5	Refs.
C(0001)	40 ± 6					[53]
Ni(111)	7 ± 3					[54]
Cu(001)	40 ± 6	120 ± 15	300 ± 20	630	1200	[11, 13]
Cu(119)	15 ± 5	39 ± 5	105 ± 15	200 ± 20	350 ± 40	[55]
Cu(117)	15 ± 5	39 ± 5	95 ± 15	190 ± 20	350 ± 40	[55]
Cu(111)	18 ± 5	14 ± 3	40 ± 6			[56, 57]
Cu(775)	18 ± 2					[58]
Ag(001)	55 ± 5	160 ± 10	360 ± 15			[11]
Ag(111)	32 ± 10	≤ 20				[59]
Ru(0001)	$11\ ^{+6}_{-3}$					[60]
Pd(111)	25 ± 4					[4]
Pt(111)	26 ± 7	62 ± 7				[61]

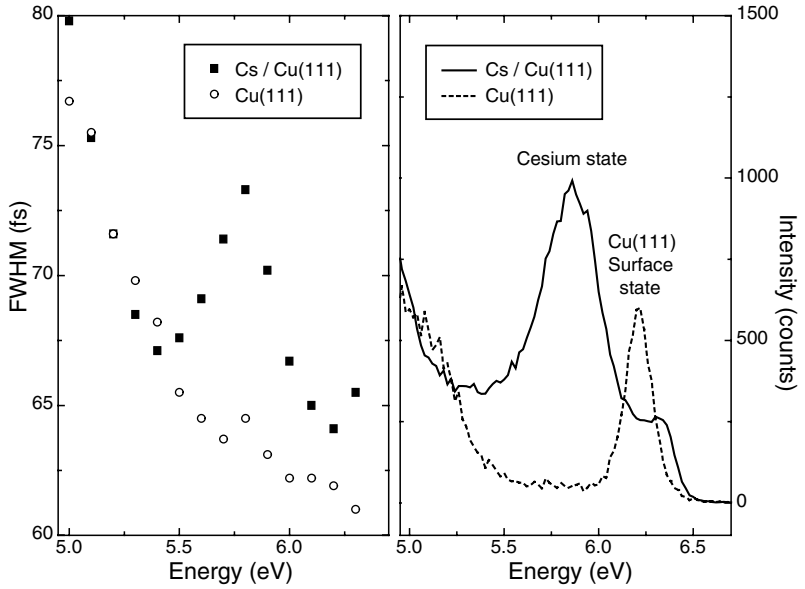

Figure 8.13: Full width at half maximum of the autocorrelation traces (left panel) and two-photon photoemission spectra (right panel) for a clean and Cs-covered Cu(111) surface. The photon energy is 3.3 eV and the electrons are accelerated by 4 eV to obtain the given kinetic energy in the analyzer (after Ref. [71]).

Xe on Ru(001), but illustrates also the problem of quantitative modelling the results [60]. For adlayers with electronic bands degenerate with the image-potential states a description by a quantum-well model is more appropriate [68–70].

8.4.3 Adsorbate states

The image-potential states provide a nice model system to study the electron dynamics at a surface with the experimental possibilities available today. With regard to the understanding and possible applications in photochemistry at surfaces it is important to gain access to the decay of electronic excitations at adsorbates or the charge transfer into the substrate. For many systems the relevant time scales are much shorter than the time resolution of two-photon photoemission experiments. Therefore only a few time-resolved studies of adsorbate states have been reported up to now. For C_6F_6 on Cu(111) an unoccupied molecular resonance could be identified and its lifetime was measured as a function of film thickness [70, 72, 73]. For Cs on Cu(111) an alkali-derived resonance is shown in the right panel of Fig. 8.13 at an energy 2.75 eV above E_F [71]. Its lifetime is significantly larger compared to the values obtained on the clean surface as shown by the increased width of the autocorrelation traces (left panel of Fig. 8.13). At low temperatures the electron resides even longer on the Cs atom [74]. This leads to desorption and the bond breaking can be monitored by changes in the electronic structure as a function of time and distance [75, 76].

8.5 Outlook

Time-resolution was introduced to two-photon photoemission about 15 years ago [77, 78]. With the advent of easy to use, high-repetition rate Ti:sapphire lasers the experimental possibilities expanded tremendously. Today it is possible to study more systems in ever more detail. Current work is directed to an understanding of electron scattering processes on a femtosecond time scale with high energy and momentum resolution [22, 66, 79–82]. Continuous progress is made in the development of solid-state and free-electron laser sources as well as improved detection systems. The list of interesting surfaces and adsorbates is far from being exhausted. We are therefore looking into a bright future for time-resolved photoemission with lots of new and surprising physics to come.

Acknowledgements

This work would not have been possible without the excellent contributions from Martin Weinelt and my graduate students. I thank Martin Aeschlimann, Michael Bauer, Pedro Echenique, Ulrich Höfer, Hrvoje Petek, Martin Wolf, and Xiaoyang Zhu for discussions, preprints, and figures. Continuous support from the Deutsche Forschungsgemeinschaft is acknowledged.

References

[1] T. Hertel, E. Knoesel, A. Hotzel, M. Wolf, and G. Ertl, J. Vac. Sci. Technol. A **15**, 1503 (1997).

[2] Ch. Reuß, I.L. Shumay, U. Thomann, M. Kutschera, M. Weinelt, Th. Fauster, and U. Höfer, Phys. Rev. Lett. **82**, 153 (1999).

[3] R. Fischer, S. Schuppler, N. Fischer, Th. Fauster, and W. Steinmann, Phys. Rev. Lett. **70**, 654 (1993).

[4] A. Schäfer, I.L. Shumay, M. Wiets, M. Weinelt, Th. Fauster, E.V. Chulkov, V.M. Silkin, and P.M. Echenique, Phys. Rev. B **61**, 13159 (2000).

[5] U. Thomann, Ph.D. thesis, Universität Erlangen-Nürnberg, Germany, 1999.

[6] W. Wallauer and Th. Fauster, Surf. Sci. **374**, 44 (1997).

[7] W. Steinmann and Th. Fauster, in *Laser Spectroscopy and Photochemistry on Metal Surfaces*, edited by H.L. Dai and W. Ho (World Scientific, Singapore, 1995), Chap. 5, p. 184.

[8] M. Wolf, A. Hotzel, E. Knoesel, and D. Velic, Phys. Rev. B **59**, 5926 (1999).

[9] H. Petek and S. Ogawa, Prog. Surf. Sci. **56**, 239 (1997).

[10] K. Boger, M. Roth, M. Weinelt, Th. Fauster, and P.-G. Reinhard, Phys. Rev. B **65**, 075104 (2002).

[11] I.L. Shumay, U. Höfer, Ch. Reuß, U. Thomann, W. Wallauer, and Th. Fauster, Phys. Rev. B **58**, 13974 (1998).

[12] Th. Fauster and W. Steinmann, in *Photonic Probes of Surfaces*, Vol. 2 of *Electromagnetic Waves: Recent Developments in Research*, edited by P. Halevi (North-Holland, Amsterdam, 1995), Chap. 8, p. 347.

[13] U. Höfer, I.L. Shumay, Ch. Reuß, U. Thomann, W. Wallauer, and Th. Fauster, Science **277**, 1480 (1997).
[14] D.F. Padowitz, W.R. Merry, R.E. Jordan, and C.B. Harris, Phys. Rev. Lett. **69**, 3583 (1992).
[15] E. Knoesel, A. Hotzel, and M. Wolf, J. Electron Spectrosc. Relat. Phenom. **88-91**, 577 (1998).
[16] R. Haight, Appl. Opt. **35**, 6445 (1996).
[17] J.P. Long, B.S. Itchkawitz, and M.N. Kabler, J. Opt. Soc. B **13**, 201 (1996).
[18] W.P. Leemans, R.W. Schoenlein, P. Volfbeyn, A.H. Chin, T.E. Glover, P. Balling, M. Zolotorev, K.J. Kim, S. Chattopadhyay, and C.V. Shank, Phys. Rev. Lett. **77**, 4182 (1996).
[19] J.B. Pendry, Surf. Sci. **57**, 679 (1976).
[20] B. Gumhalter and H. Petek, Surf. Sci. **445**, 195 (2000).
[21] M. Rohlfing and S.G. Louie, Phys. Rev. Lett. **83**, 856 (1999).
[22] N.-H. Ge, C.M. Wong, R.L. Lingle Jr., J.D. McNeill, K.J. Gaffney, and C.B. Harris, Science **279**, 202 (1998).
[23] K. Read, H.S. Karlsson, M.M. Murnane, H.C. Kapteyn, and R. Haight, J. Appl. Phys. **90**, 294 (2001).
[24] R. Lindner, R.T. Williams, and M. Reichling, Phys. Rev. B **63**, 075110 (2001).
[25] A.A. Villaeys, Y.J. Dappe, and F.P. Lohner, Phys. Rev. B **63**, 155113 (2001).
[26] R. Loudon, *The Quantum Theory of Light* (Oxford University Press, New York, 1983).
[27] H. Ueba and T. Mii, Appl. Phys. A **71**, 537 (2000).
[28] V.P. Chebotayev, in *High-Resolution Laser Spectroscopy*, Vol. 13 of *Topics in Applied Physics*, edited by K. Shimoda (Springer, Berlin, 1976), Chap. 6, p. 201.
[29] H. Petek, A.P. Heberle, W. Nessler, H. Nagano, S. Kubota, S. Matsunami, N. Moriya, and S. Ogawa, Phys. Rev. Lett. **79**, 4649 (1997).
[30] T. Klamroth, P. Saalfrank, and U. Höfer, Phys. Rev. B **64**, 035420 (2001).
[31] A. Assion, T. Baumert, M. Bergt, T. Brixner, B. Kiefer, V. Seyfried, M. Strehle, and G. Gerber, Science **282**, 919 (1998).
[32] T. Wegehaupt, D. Rieger, and W. Steinmann, Phys. Rev. B **37**, 10086 (1988).
[33] F.J. Himpsel and J.E. Ortega, Phys. Rev. B **46**, 9719 (1992).
[34] K. Giesen, F. Hage, F.J. Himpsel, H.J. Riess, and W. Steinmann, Phys. Rev. Lett. **55**, 300 (1985).
[35] S. Pawlik, R. Burgermeister, M. Bauer, and M. Aeschlimann, Surf. Sci. **402-404**, 556 (1998).
[36] D. Velic, E. Knoesel, and M. Wolf, Surf. Sci. **424**, 1 (1999).
[37] C. Kentsch, M. Kutschera, M. Weinelt, Th. Fauster, and M. Rohlfing, Phys. Rev. B **65**, 035323 (2002).
[38] K. Shudo and T. Munakata, Phys. Rev. B **63**, 125324 (2001).
[39] M. Kutschera, C. Kentsch, M. Weinelt, and Th. Fauster, to be published.
[40] G. Moos, C. Gahl, R. Fasel, M. Wolf, and T. Hertel, Phys. Rev. Lett. **87**, 267402 (2001).
[41] W.S. Fann, R. Storz, H.W.K. Tom, and J. Bokor, Phys. Rev. B **46**, 13592 (1992).

[42] E. Knoesel, A. Hotzel, and M. Wolf, Phys. Rev. B **57**, 12812 (1998).
[43] P.M. Echenique, J.M. Pitarke, E.V. Chulkov, and A. Rubio, Chem. Phys. **251**, 1 (2000).
[44] R. Knorren, K.H. Bennemann, R. Burgermeister, and M. Aeschlimann, Phys. Rev. B **61**, 9427 (2000).
[45] H. Petek, H. Nagano, M.J. Weida, and S. Ogawa, Chem. Phys **251**, 71 (2000).
[46] T. Hertel, E. Knoesel, M. Wolf, and G. Ertl, Phys. Rev. Lett. **76**, 535 (1996).
[47] H. Petek, H. Nagano, and S. Ogawa, Appl. Phys. B **68**, 369 (1999).
[48] C.A. Schmuttenmaer, M. Aeschlimann, H.E. Elsayed-Ali, R.J.D. Miller, D.A. Mantell, J. Cao, and Y. Gao, Phys. Rev. B **50**, 8957 (1994).
[49] S. Ogawa, H. Nagano, and H. Petek, Phys. Rev. B **55**, 10869 (1997).
[50] M. Aeschlimann, M. Bauer, S. Pawlik, R. Knorren, G. Bouzerar, and K.H. Bennemann, Appl. Phys. A **71**, 485 (2000).
[51] R. Haight, Surf. Sci. Rep. **21**, 277 (1995).
[52] I. Kinoshita, T. Anazawa, and Y. Matsumoto, Chem. Phys. Lett. **259**, 445 (1996).
[53] J. Lehmann, M. Merschdorf, A. Thon, S. Voll, and W. Pfeiffer, Phys. Rev. B **60**, 17037 (1999).
[54] S. Link, J. Sievers, H.A. Dürr, and W. Eberhardt, J. Electron Spectrosc. Relat. Phenom. **114-116**, 351 (2001).
[55] M. Roth, M. Pickel, J. Wang, M. Weinelt, and Th. Fauster, Appl. Phys. B **74**, 661 (2002).
[56] M. Weinelt, J. Phys.: Condens. Matter **14**, R1099 (2002).
[57] M. Weinelt, Appl. Phys. A **71**, 493 (2000).
[58] X.J. Shen, H. Kwak, D. Mocuta, A.M. Radojevic, S. Smadici, and R.M. Osgood, Chem. Phys. Lett. **351**, 1 (2002).
[59] R.L. Lingle, Jr., N.-H. Ge, R.E. Jordan, J.D. McNeill, and C.B. Harris, Chem. Phys. **205**, 191 (1996).
[60] W. Berthold, U. Höfer, P. Feulner, and D. Menzel, Chem. Phys. **251**, 123 (2000).
[61] S. Link, H.A. Dürr, G. Bihlmayer, S. Blügel, W. Eberhardt, E.V. Chulkov, V.M. Silkin, and P.M. Echenique, Phys. Rev. B **63**, 115420 (2001).
[62] P.M. Echenique and J.B. Pendry, J. Phys. C **11**, 2065 (1978).
[63] R.M. Osgood, Jr. and X.Y. Wang, in *Solid State Physics, Vol. 51*, edited by H. Ehrenreich and F. Spaepen (Academic Press, San Diego, 1997), Vol. 51, p. 1.
[64] C.B. Harris, N.-H. Ge, R.L. Lingle Jr., J.D. McNeill, and C.M. Wong, Ann. Rev. Phys. Chem. **48**, 711 (1997).
[65] Th. Fauster, Ch. Reuß, I.L. Shumay, and M. Weinelt, Chem. Phys. **251**, 111 (2000).
[66] C.M. Wong, J.D. McNeill, K.J. Gaffney, N.-H. Ge, A.D. Miller, S.H. Liu, and C.B. Harris, J. Phys. Chem. B **103**, 282 (1999).
[67] A. Hotzel, G. Moos, K. Ishioka, M. Wolf, and G. Ertl, Appl. Phys. B **68**, 615 (1999).
[68] R. Fischer and Th. Fauster, Phys. Rev. B **51**, 7112 (1995).
[69] J.D. McNeill, R.L. Lingle, Jr., N.-H. Ge, C.M. Wong, R.E. Jordan, and C.B. Harris, Phys. Rev. Lett. **79**, 4645 (1997).
[70] X.-Y. Zhu, Annu. Rev. Phys. Chem. **53**, 221 (2002).
[71] M. Bauer, S. Pawlik, and M. Aeschlimann, Phys. Rev. B **60**, 5016 (1999).

[72] K. Ishioka, C. Gahl, and M. Wolf, Surf. Sci. **454-456**, 73 (2000).
[73] C. Gahl, K. Ishioka, Q. Zhong, A. Hotzel, and M. Wolf, Faraday Disc. **117**, 191 (2000).
[74] H. Petek, M.J. Weida, H. Nagano, and S. Ogawa, Surf. Sci. **451**, 22 (2000).
[75] H. Petek, M.J. Weida, H. Nagano, and S. Ogawa, Science **288**, 1402 (2000).
[76] H. Petek, H. Nagano, M.J. Weida, and S. Ogawa, J. Phys. Chem. B **105**, 6767 (2001).
[77] R. Haight, J. Bokor, J. Stark, R.H. Storz, R.R. Freeman, and P.H. Bucksbaum, Phys. Rev. Lett. **54**, 1302 (1985).
[78] R.W. Schoenlein, J.G. Fujimoto, G.L. Eesley, and T.W. Capehart, Phys. Rev. Lett. **61**, 2596 (1988).
[79] A. Hotzel, M. Wolf, and J.P. Gauyacq, J. Phys. Chem. B **104**, 8438 (2000).
[80] W. Berthold, J. Güdde, P. Feulner, and U. Höfer, Appl. Phys. B **73**, 865 (2001).
[81] W. Berthold, U. Höfer, P. Feulner, E.V. Chulkov, V.M. Silkin, and P.M. Echenique, Phys. Rev. Lett. **88**, 056805 (2002).
[82] M. Roth, M. Pickel, J. Wang, M. Weinelt, and Th. Fauster, Phys. Rev. Lett. **88**, 096802 (2002).

Solid-State Photoemission and Related Methods
Wolfgang Schattke, Michel A. Van Hove (Eds.)

9 Low-energy (e,2e) spectroscopy

R. Feder and H. Gollisch

A review is given of the current status of low-energy (e,2e) spectroscopy from solid surfaces. An exposition of the basic concepts is followed by an outline of a general theoretical framework, of approximations made in view of computational viability, and of selection rules inherent in the Coulomb matrix elements. The analysis and interpretation of experimental and calculated (e,2e) spectra is demonstrated to provide information on (a) the near-surface electronic structure with an emphasis on surface state and (b) electron scattering dynamics regarding mainly elastic one-electron scattering and the Coulomb pair correlation. Using spin-polarized primary electrons reveals more details of spin-dependent collision dynamics and of magnetic surface properties.

9.1 Introduction

While angle-resolved ultraviolet photoemission spectroscopy (cf. e.g. [1–5], other Chapters in the present volume, in particular Chapters 1 and 6, and references therein) is the traditional and currently most widely used tool for studying the electronic and magnetic structure of solids and their surfaces, a particularly surface-sensitive new spectroscopy has evolved over the past decade, in which low-energy electrons rather than photons are used as projectiles.

For electrons impinging on atomic or solid targets an important reaction channel involves a single collision event with a valence electron resulting in two electrons leaving the solid. Energy- and angle-resolved (i.e. momentum-resolved) observation of these two electrons in coincidence is usually referred to as (e,2e)-spectroscopy. The history, the current status and recent highlights of this very wide field, which involves atomic and solid state physics, are covered in recent monographs ([6, 7], which also provide ample references to a vast body of original literature.

As for solids, (e,2e)-spectroscopy using high-energy primary electrons (10–50 keV) and operating in the transmission mode through a thin free-standing target membrane (i.e. detecting electron pairs emerging "on the other side") is a well-established technique with a rather long history of success (cf. e.g. [8–11] and references therein). Since at these high energies incoming and outgoing electrons can be described by independent plane waves, a golden-rule-type formula for the reaction cross section reduces to a product of an electron-electron collision factor and the valence or core electron spectral function in three-dimensional momentum space. Experimental data thus rather directly contain information on bulk-like electronic properties. A more recent experimental set-up operates in the reflection mode: primary electrons with medium-energy (about 300 eV) impinge on a surface and two electrons subsequently emerging from this surface are detected in coincidence (cf. [12–14] and references therein).

Solid-State Photoemission and Related Methods: Theory and Experiment. Edited by Wolfgang Schattke, Michel A. Van Hove

ISBN: 3-527-40334-5

Since a plane-wave approximation is no longer adequate, the theoretical treatment is more complicated. Application to highly oriented pyrolytic graphite yielded the bulk energy band structure and momentum density.

In view of accessing the surface electronic structure and of studying electron collision dynamics in the vicinity of the surface, a different reflection mode experiment was developed, which uses primary electrons at low energies (typically less than 50 eV) ([15, 16] and references therein). Two electrons arriving in coincidence at two position-sensitive detectors are individually energy-analyzed by means of a time-of-flight technique. Experimental achievements include in particular the observation of surface state on metal surfaces [17] and of the near-surface valence electron spin polarization of a ferromagnet [18, 19]. The understanding of the physical mechanisms, the quantitative interpretation of experimental data and the pointing out of future directions have been the aims of a number of theoretical investigations ([20–28] and references therein). At low electron energies, theory is much more demanding than at high energies, since firstly elastic multiple scattering of the incoming and of the outgoing electrons by the crystal lattice has to be fully taken into account, and secondly Coulomb correlation between the two outgoing electrons can be of importance.

In this article, we present a review of low-energy (e,2e) spectroscopy from surfaces, which is organized as follows. Section 9.2 is devoted to the basic concepts and some experimental key aspects. In Sec. 9.3, we outline a general theoretical framework, practicable approximations and selection rules. Section 9.4 illustrates experimental and theoretical results by some prototypical (e,2e) spectra. In Sec. 9.5 the analysis of (e,2e) spectra is shown to provide information on electron scattering dynamics with focuses on elastic scattering by the crystal lattice and on the Coulomb correlation between the two detected electrons. Section 9.6 addresses the information potential of (e,2e) spectroscopy on the valence electronic structure with an emphasis on surface sensitivity, surface state and symmetry resolution via selection rules. In Section 9.7 we demonstrate the use of spin-polarized primary electrons for studying spin-orbit coupling effects, spin-dependent scattering dynamics and ferromagnetic surface properties.

9.2 Setup and basic concepts

The geometry of (e,2e) spectroscopy in the reflection mode is sketched in Fig. 9.1. A primary electron, which at the source (electron gun) has kinetic energy E_1, momentum $\mathbf{k}_1$ and spin alignment $\sigma_1 = \pm$ with respect to some given axis $\mathbf{e}$, impinges on a solid surface system. As will be shown below, spin polarization has to be incorporated in theoretical treatments even if the corresponding experiment employs an unpolarized primary beam. The direction of incidence, which is given by the momentum direction, is conveniently characterized by the polar angle θ_1 relative to the surface normal (z-axis) and an azimuthal angle ϕ_1. Amongst the various possible reaction channels, the following one is selected by the experimental setup: the collision of the primary electron with a valence electron of energy $E_2 < E_F$, where E_F is the Fermi energy, produces two electrons, which leave the surface with kinetic energies E_3 and E_4, momenta $\mathbf{k}_3$ and $\mathbf{k}_4$ and spin alignments σ_3 and σ_4. Like σ_1, the latter two are essential in theory, although spin analysis of the two outgoing electrons is beyond present-day experimental capabilities.

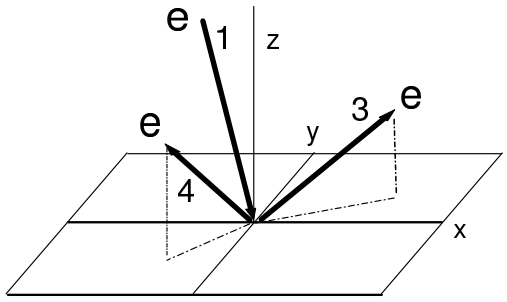

Figure 9.1: Geometry of (e,2e) spectroscopy. Upon impact of an electron (labeled as 1) on a surface and collision with a valence electron, two electrons (labeled as 3 and 4) exit into the vacuum region in the directions of two energy-analyzing detectors connected by coincidence circuitry.

The energy E_2 of the valence electron is determined from the known energies of the primary and the detected electrons by the conservation law $E_1 + E_2 = E_3 + E_4$. In the case of crystalline systems (including ultrathin metal films or other adsorbates on a crystalline substrate), which have lattice periodicity parallel to the surface, the valence electron is further characterized by the surface-parallel momentum $\mathbf{k}_2^{\parallel}$. Since the surface-parallel momenta $\mathbf{k}_1^{\parallel}$ of the incident electron and $\mathbf{k}_3^{\parallel}$ and $\mathbf{k}_4^{\parallel}$ of the outgoing electrons are given as the surface projections of the respective three-dimensional momenta, which are experimentally known, $\mathbf{k}_2^{\parallel}$ of the valence electron is determined by the conservation law $\mathbf{k}_1^{\parallel} + \mathbf{k}_2^{\parallel} = \mathbf{k}_3^{\parallel} + \mathbf{k}_4^{\parallel}$, modulo a surface reciprocal lattice vector.

From the above it is clear that (e,2e) spectroscopy can yield more specific information than the well-established related electron-energy-loss spectroscopy (EELS), in which only one outgoing electron with energy $E_1 - \Delta E$ is detected. Firstly, this electron may stem from a collective-excitation (e.g. plasmon) loss mechanism. Secondly, even if it originates from the collision with a valence electron, neither energy nor parallel-momentum of the latter are determined.

For details of experimental technique and apparatus in (e,2e) spectroscopy we refer to the original literature ([12, 13, 15, 16, 18, 22] and references therein) and to a review on two-electron photoemission spectroscopy [29], for which practically the same detection apparatus as in (e,2e) spectroscopy has been used. In the following we outline a few key features. (1) Two electrons are detected in coincidence, i.e. counted as an "event" if both of them arrive within a specified time window (typically 200 ns). Thus, in addition to pairs, which originate directly from a binary collision with a valence electron, one also counts collision events, in which the primary electron has suffered some energy loss (e.g. excitation of a plasmon or of an electron) before generating the outgoing pair, and (to an extent minimized by experimental skill) accidentally coincident electrons (e.g. if two primary electrons arrive within the specified time window and each of them produces only one outgoing electron). (2) Angular resolution can in principle be achieved by using multichannel plates as "position-sensitive" detectors, which may be viewed as an array of point-like detectors. Because of the concomitant loss of counting statistics, however, events have usually been summed over a finite detection cone (typically up to $\pm 10^\circ$ around the nominal detection direction). (3) The energy of each of the two detected electrons is determined separately by a time-of-flight technique: the times of flight from sample to detector (distance L), which we denote by T_3 and T_4, are measured and converted into the kinetic energies E_3 and E_4 according to $E_i =$

$(m/2)(L/T_i)^2$ with $i = 3, 4$. (4) While in the majority of experiments the primary electrons were unpolarized, very recently spin-polarized electrons (produced by a GaAs photocathode with circularly polarized light) were employed for the study of ferromagnets [18, 19].

9.3 Theory

9.3.1 Framework

Foregoing a full-fledged many-body theoretical formulation, which is rather abstract and presently by far defies numerical implementation, we adopt a theoretical framework, which retains a physically intuitive picture of the (e,2e) process (cf. Sec. 9.2) and which allows computations sufficiently realistic to quantitatively reproduce experimental data. The primary electron, the relevant valence electron and the two outgoing electrons are represented by quasi-particles, i.e. their interaction with the nuclei and the other electrons of the solid is subsumed in optical potentials. Taking the Coulomb interaction U between these "active" electrons, which is screened by the other electrons, as a perturbation, the reaction cross section is obtained by standard scattering theory.

The initial asymptotic state of the system is thus an antisymmetrized direct product of two single quasi-particle states, which represent the projectile electron and an individual valence electron, i. e. $|1, 2\rangle = |1\rangle \otimes |2\rangle$. The states $|1\rangle$ and $|2\rangle$ are solutions of a Dirac equation involving optical potentials V_1 and V_2, respectively, which include an effective magnetic field in the case of a ferromagnetic target. For a crystalline system with lattice periodicity parallel to the surface, one-electron states $|i\rangle$ are characterized by energies E_i, surface-parallel two-dimensional wave vectors $\mathbf{k}_i^{\parallel}$ and spin labels σ_i. The number i in $|i\rangle$ is thus an abbreviation for the set of quantum numbers $(E_i, \mathbf{k}_i^{\parallel}, \sigma_i)$. State $|1\rangle$, with the set $(E_1, \mathbf{k}_1^{\parallel}, \sigma_1)$ prescribed by the experimental conditions, comprises the elastic scattering by the crystal potential and is well known from Low-Energy Electron Diffraction (LEED) theory (cf. e.g. [30–32] and references therein). The Dirac equation is used, since spin-orbit coupling (SOC) and scalar relativistic effects are known to be important both for LEED (especially spin-polarized LEED, cf. [30, 33]) and for the valence electron structure (cf. e.g. [34, 35] and references therein). SOC in the valence bands manifests itself in particular in the spin polarization of photoelectrons produced from non-magnetic surface systems by circularly and by linearly polarized light, and in various forms of magnetic dichroism (i.e. intensity asymmetries upon magnetization reversal) in the case of ferromagnetic systems (cf. e.g. [36–39] and references therein).

The transition amplitude for the initial state $|1, 2\rangle$ to go over into the two-electron excited state $|3, 4\rangle$ is $\langle 3, 4|U|1, 2\rangle$. Strictly speaking, $|3, 4\rangle$ is a solution of a two-electron Dirac equation involving the total potential $V_{3,4} = V_3 + V_4 + U$, where V_3 and V_4 are one-particle optical potentials, and with asymptotic boundary conditions such that an electron with momentum $\mathbf{k}_3$ and spin alignment σ_3 arrives at one detector and an electron with momentum $\mathbf{k}_4$ and spin alignment σ_4 at the other detector. For a polarized primary beam, the spin-resolved (e,2e) scattering cross section ("intensity") is then given by the golden rule form

$$I^{\sigma_1}_{\sigma_3,\sigma_4} = \frac{k_3 k_4}{k_1} \sum_{E_2,\mathbf{k}_2^{\parallel},\sigma_2,n_2} |\langle 3, 4|U|1, 2\rangle|^2 \, \delta(E_1+E_2-E_3-E_4)\delta(\mathbf{k}_1^{\parallel}+\mathbf{k}_2^{\parallel}-\mathbf{k}_3^{\parallel}-\mathbf{k}_4^{\parallel}). \quad (9.1)$$

In the valence state summation, the index n_2 accounts for possible further degeneracies. All states in Eq. (9.1) are solutions of the respective quasiparticle equations, which involve complex self-energies. The quasiparticle Hamiltonians being thus non-Hermitian, one has to distinguish between "right-hand" and "left-hand" solutions (bi-orthogonal eigenfunctions) (cf. [40] and, specifically for the Dirac Hamiltonian, [41]). This distinction is implicit in the convention that all "bras" are left-hand solutions and all "kets" are right-hand solutions. The energies E_1, E_3 andE_4 are imposed as real by the stationary scattering states boundary conditions (at the electron gun and the detectors), but the energies E_2 of the bound valence states are complex if their finite life-time is taken into account (by means of an imaginary self-energy part). In this case, the energy δ function in Eq. (9.1) has to be understood as a Lorentzian with width $2\,\mathrm{Im}\,E_2$. We recall that the use of quasiparticle states ("Dyson orbitals") in a golden rule expression is well known in the context of photoemission (cf. [42,43] and references therein).

With the spin- and $\mathbf{k}^{\parallel}$-resolved valence electron spectral function

$$-\frac{1}{\pi}\,\mathrm{Im}\,G_2^r(E,\mathbf{k}_2^{\parallel},\sigma_2) = \sum_{E_2,n_2} |2\rangle\langle 2|\delta(E-E_2) \tag{9.2}$$

where G_2^r is the retarded single-particle Green function, the cross section Eq. (9.1) is easily rewritten as

$$I^{\sigma_1}_{\sigma_3,\sigma_4} = \frac{k_3 k_4}{k_1}\,\langle 3,4|U|1\rangle \left(-\frac{1}{\pi}\right)\mathrm{Im}\,G_2^r(E_3{+}E_4{-}E_1,\mathbf{k}_3^{\parallel}{+}\mathbf{k}_4^{\parallel}{-}\mathbf{k}_1^{\parallel},\sigma_2)\,\langle 1|U|3,4\rangle\,. \tag{9.3}$$

Representing the spectral function (Eq. (9.2)) in real space and taking its trace with the spatial integration restricted to the m-th atomic layer parallel to the surface, one obtains the $\mathbf{k}^{\parallel}$- and spin-resolved layer density of states $N_m(E,k_2^{\parallel},\sigma_2)$.

If the primary electrons are polarized relative to an axis **e** (i.e. spin polarization vector $\mathbf{P}_1 = \sigma_1\mathbf{e}$), one obtains spin-dependent intensities I^{σ_1} and an asymmetry A as

$$I^{\sigma_1} = \sum_{\sigma_3,\sigma_4} I^{\sigma_1}_{\sigma_3,\sigma_4} \qquad \text{and} \qquad A = (I^+ - I^-)/(I^+ + I^-) \tag{9.4}$$

9.3.2 Approximations and computational aspects

The expressions Eq. (9.1) and (3) contain the two-electron state $|3,4\rangle$. One thus faces the severe problem of solving a two-electron Dirac equation with the electron-electron interaction potential U. Since to date no computationally viable methods are available in the case of solids, one has to resort to approximations. The simplest and most frequently used one is to neglect U in the two-electron potential $V_{3,4} = V_3 + V_4 + U$. The state $|3,4\rangle$ then reduces to an antisymmetrized direct product of two independent one-electron states $|3\rangle$ and $|4\rangle$, each of which is a time-reversed relativistic LEED state. An approximate incorporation of U was put forward by [25] by transforming it into two one-electron potential parts v_3 and v_4 such that v_3 depends on the crystal momentum of electron 4 and vice versa. This amounts to a dynamical screening of the original one-electron optical potentials V_3 and V_4. Solution of the one-electron Dirac equations containing these screened potentials yields modified states $|3\rangle$ and $|4\rangle$, which are again combined into an antisymmetrized product. As has been found

in [25], the effect of U, i.e. Coulomb correlation, in $|3,4\rangle$ on (e,2e) spectra is rather strong for very low energies and for near-parallel exit directions. For a more detailed discussion of the Coulomb pair correlation problem we refer to [29] in the context of two-electron photoemission, for which pair correlation is of vital importance.

Taking $|3,4\rangle$ as an antisymmetrized product and writing the four one-electron states $|i\rangle$ as four-component Dirac spinors $\psi_i^{\sigma_i}(\mathbf{r})$, Eq. (9.1) becomes

$$I^{\sigma_1}_{\sigma_3,\sigma_4} = (k_3 k_4/k_1) \sum_{E_2,\mathbf{k}_2^{\parallel},n\sigma_2} \mid f_{\sigma_1,n\sigma_2,\sigma_3,\sigma_4} - g_{\sigma_1,n\sigma_2,\sigma_3,\sigma_4} \mid^2 \cdot \delta(E_1+E_2-E_3-E_4)\delta(\mathbf{k}_1^{\parallel}+\mathbf{k}_2^{\parallel}-\mathbf{k}_3^{\parallel}-\mathbf{k}_4^{\parallel}), \quad (9.5)$$

where f and g are direct and exchange scattering amplitudes:

$$f_{\sigma_1,n\sigma_2,\sigma_3,\sigma_4} = \int \psi_3^{\sigma_3 *}(\mathbf{r})\psi_4^{\sigma_4 *}(\mathbf{r}')U(\mathbf{r},\mathbf{r}')\psi_1^{\sigma_1}(\mathbf{r})\psi_2^{n\sigma_2}(\mathbf{r}')\, d\mathbf{r}d\mathbf{r}'; \quad (9.6)$$

the expression for g is the same except for $\mathbf{r}$ and $\mathbf{r}'$ interchanged in the first product term. The alternative formula Eq. (9.3), in which the valence electron is described by a Green function, can be evaluated along similar lines, yielding rather lengthy expressions (cf. [44]).

For numerical computations, the golden rule form Eq. (9.5) is much less demanding than the Green function form if the life-time of the valence-band hole is taken as infinite, i.e. E_2 is real. While finite hole life-time can in good approximation be incorporated ex post by convoluting the spectra with a Lorentzian, this approach has the drawback that surface state can practically not be included. In contrast, they are reliably and conveniently accessible by the Green function approach since they are a priori life-time-broadened and can therefore easily be found by scanning over a reasonably fine energy grid.

In the interaction U of the incident electron with a particular valence electron, magnetic and retardation effects (as are e.g. approximated by the Breit Hamiltonian) need not be taken into account in the present context, since they should be small in collisions at low energies. An order of magnitude estimate has, in the context of relativistic electron-atom scattering, been made in ref. [45]. We are thus left with a Coulomb interaction, which is screened by the ground state electrons of the target. Assuming this screening as static, we have

$$U(\mathbf{r},\mathbf{r}') = \int dr'' \epsilon^{-1}(\mathbf{r},\mathbf{r}'')/|\mathbf{r}''-\mathbf{r}'| \approx \frac{e^{-\frac{|\mathbf{r}-\mathbf{r}'|}{\lambda}}}{|\mathbf{r}-\mathbf{r}'|} \quad (9.7)$$

where $\epsilon(\mathbf{r},\mathbf{r}'')$ is the dielectric function of the crystalline surface system, and λ is a screening length, which for computational purposes has so far been taken as the Thomas-Fermi screening length for an electron gas with the valence electron density of the respective target system.

The incoming and the two outgoing one-electron states are LEED and time-reversed LEED states, respectively, and can therefore be readily calculated by the relativistic layer-KKR method routinely employed in LEED and photoemission calculations (cf. e.g. [30, 46]). All elastic multiple scattering events by the ion core lattice, i.e. loosely speaking "band structure effects", are thereby fully taken into account.

For the calculation of the valence electron spectral function a relativistic multiple scattering formalism of the layer-KKR type ([44, 46]), which has been successful in numerous photoemission studies (cf. [36, 39] and references therein), is most suitable. In order to compute the (e,2e) cross section in the simpler matrix element form of Eqs. (9.5), (9.6), one needs the valence electron wave function $\psi_2^{\sigma_2}(\mathbf{x})$ of the semi-infinite system. This wave function can be obtained by means of a Bloch wave matching method (cf. [22]). Briefly, one first calculates bulk Bloch waves by diagonalizing the layer transfer matrix and then matches at the surface those Bloch waves, which propagate from the interior outward towards, with linear combinations of inward-propagating and decaying Bloch waves and with linear combinations of decaying plane waves on the vacuum side. surface state may in principle be handled by this method (matching without an outward propagation Bloch wave), but are very hard to find in practice.

The construction of the effective one-electron potentials, which are required for numerical calculations, is a problem, which (e,2e) spectroscopy shares with LEED and with VUV valence band photoemission (cf. e.g. [3–5, 30, 31, 47], where many further references may be found). It must suffice here to briefly mention approximations, which are directly relevant for the numerical results presented in the following sections. The complex self-energy pertaining to the valence electron and to the scattering states is approximated by an empirical energy-dependent local potential. The imaginary part of the latter is uniform and increases from near-zero at E_F in forms taken from LEED and photoemission experience. For the real part we employ an $LDA + \beta$ potential, which is obtained from a self-consistent LDA-FLAPW [48] slab charge densitiy using a non-local exchange correlation approximation such that the calculated bulk bands agree with the quasi-particle bands determined by photoemission experiments (for details see [4]).

9.3.3 Selection rules

The Coulomb matrix elements give rise to selection rules (for details see [28]) if spin-orbit coupling is neglected. Replacing in Eq. (9.6) each spinor $\psi_i^{\sigma_i}$ by a product of a scalar wave function φ_i with a two-componont basis spinor, it is easily seen that nonvanishing amplitudes f and g exist only for a very reduced number of the sets $(\sigma_1, \sigma_2, \sigma_3, \sigma_4)$. If the valence electron spin is parallel to the primary electron spin, i.e. $\sigma_2 = \sigma_1 =: \sigma$, there is only the direct amplitude

$$f_{\sigma,n\sigma,\sigma,\sigma} = \int \varphi_3^*(\mathbf{r})\varphi_4^*(\mathbf{r}')U(\mathbf{r},\mathbf{r}')\varphi_1(\mathbf{r})\varphi_2^{(n)}(\mathbf{r}')\, d\mathbf{r}d\mathbf{r}' =: f_n \tag{9.8}$$

and the exchange amplitude g_n, which is obtained from f_n by interchanging $\mathbf{r}$ and $\mathbf{r}'$ in the first two terms. Eq. (9.6) (with the arguments of the two delta functions abbreviated by E and $\mathbf{k}^{\|}$) then yields the cross section for the production of a parallel-spin electron pair

$$I_{\text{par}} := I^{\sigma}_{\sigma,\sigma}(E_3, E_4) = (k_3k_4/k_1) \sum_{E_2,\mathbf{k}_2^{\|},n} \mid f_n - g_n \mid^2 \ \delta(E)\delta(\mathbf{k}^{\|}) \ . \tag{9.9}$$

For a valence electron with spin antiparallel to the primary electron spin, the outgoing electrons have antiparallel spins, with the reaction cross section

$$I_{\text{antipar}} := (k_3 k_4 / k_1) \sum_{E_2, \mathbf{k}_2^{\parallel}, n} (\mid f_n \mid^2 + \mid g_n \mid^2) \, \delta(E) \delta(\mathbf{k}^{\parallel}) \, . \tag{9.10}$$

The above is valid for arbitrary (e,2e) geometry (cf. Fig. 9.1). Consider now setups, in which the directions of the incident and of the two outgoing electrons are in the same plane (reaction plane), which is perpendicular to the surface. If this plane is a mirror plane of the semi-infinite crystalline system, the wave functions φ_1, φ_3 and φ_4 are symmetric under the mirror operation, while φ_2 is either symmetric or antisymmetric. In the latter case, the scattering amplitudes f_n and g_n are identically zero (cf. [28]). Consequently, the cross sections I_{par} (Eq. (9.9)) and I_{antipar} (Eq. (9.10)) and thence also the spin-unresolved (e,2e) cross section $I_{\text{par}} + I_{\text{antipar}}$ for an unpolarized primary beam are identically zero.

A second selection rule holds for coplanar symmetric geometry with normal incidence of the primary beam and equal energies $E_3 = E_4$ of the detected electrons if there is a mirror plane, which is perpendicular to the surface and to the reaction plane. If $\varphi_2^{(n)}$ is symmetric with respect to this mirror plane, the cross section I_{par} (Eq. (9.9)) for the production of parallel-spin pairs vanishes, whereas it is non-zero and determined by $4 \mid f_n \mid^2$, if $\varphi_2^{(n)}$ is antisymmetric. I_{par} thus selectively reflects collisions with valence electron states, which are antisymmetric with respect to a mirror plane perpendicular to the reaction plane.

For clarity, the selection rules have been formulated above for non-magnetic systems. They can however readily be extended to ferromagnets. Strictly speaking, they are valid only in the absence of spin-orbit coupling. If the latter is taken into account, they are relaxed due to hybridization of different spatial symmetry types, but still can be expected to be useful in a large number of situations, in which the valence electron spinor is dominated by a particular spatial symmetry type.

9.4 Prototypical spectra

In this section, we initiate the presentation of a topical selection of low-energy (e,2e) results by showing (in Fig. 9.2) typical experimental data obtained in the reflection mode from a W(001) surface by the time-of-flight coincidence technique, which has been developed by Kirschner and co-workers (cf. [15, 16, 22] and references therein). We recall (cf. also Sec. 9.2) that the primarily measured quantities are the times of flight of the two detected electrons, which we call T_3 and T_4. The time-of-flight scale is chosen such that its zero point corresponds to the arrival time of elastically reflected primary electrons.

In Fig. 9.2a we show, as an example, the two-dimensional time-of-flight distribution of time-correlated electron pairs obtained from W(001) in a coplanar symmetric geometry with normal incidence of primary electrons with energy $E_1 = 20$ eV. Coincidence events were integrated over the acceptance cones of the detectors ($\Omega = 0.21 sr$), without making corrections for the slightly different flight paths for the different angles. The coincidence events are displayed by a two-dimensional gray scale plot, in which black corresponds to the highest

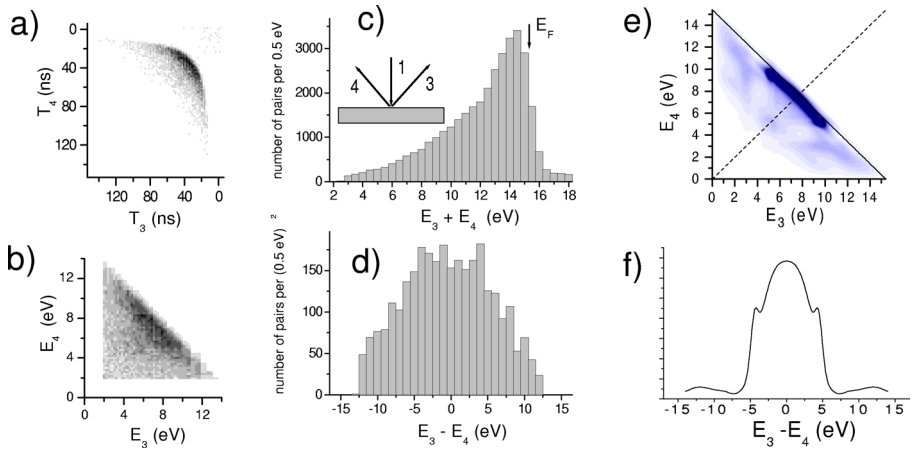

Figure 9.2: (e,2e) spectra from W(001) for normal incidence of primary electrons with energy $E_1 = 20$ eV and detection of two outgoing electrons in the (100) plane at polar angle 40° relative to the surface normal and azimuthal angles 0 and 180° with times of flight T_3 and T_4 and corresponding energies E_3 and E_4:
(a) Experimental two-dimensional time-of-flight distribution. The black point in the upper right corner corresponds to the accidental coincidence of two elastically reflected electrons and serves as a calibration point.
(b) Corresponding two-dimensional energy distribution.
(c) Histogram of the measured distribution as a function of the total energy $E_3 + E_4$ of a pair. The height of a column represents the number of events within the total energy band $E_3 + E_4 \pm 0.25$ eV.
(d) Energy sharing distribution of the detected pairs. The height of a column represents the number of pairs with the energy difference $E_3 - E_4$ within the total energy band $E_3 + E_4 = 15 \pm 0.25$ eV.
(e) Calculated two-dimensional energy distribution.
(f) Calculated energy sharing distribution within the total energy band $E_3 + E_4 = 15 \pm 0.25$ eV.
(Panels (a)-(d) from [22], panels (e) and (f) from present calculation).

number of events. A ridge-like maximum in this plot represents the most probable combinations of flight times. As one would expect from the symmetry of the set-up, the distribution looks quite symmetric with respect to the diagonal (dashed line) of the frame. Points on this line represent pairs with equal times of flight of both electrons.

Converting the times of flight T_3 and T_4 of the two detected electrons into their energies E_3 and E_4 (cf. Sec. 9.2), one obtains the energy distribution shown in Fig. 9.2b. The ridge-like maximum of the time-of-flight distribution is seen to be transformed into a diagonal "band" roughly located between the two lines defined by the "total energy" $E_3 + E_4$ values 14 eV and 15 eV. If the detected electron pair is produced in a single collision between the incident electron and a target electron, the corresponding energies E_2 of the target electrons (relative to the vacuum level) are obtained from energy conservation (cf. Sec. 9.2) as -6 and -5 eV,

i.e. — with the work function of W(001) 4.6 eV — 1.4 and 0.4 eV below the Fermi energy. The creation of electron pairs is thus seen to be most likely for target electrons with energies close to the Fermi level. Most of these electron pairs must have been created in a direct (e,2e) process, because any additional inelastic scattering would have decreased their total energy. Pairs with lower total energies may originate either from the excitation of bound electrons in deeper energy levels or from a multi-step electron-electron scattering process. From the above energy distribution, summation over the the number of events in total energy bands with $(E_3 + E_4) = \pm 0.25$ eV yields the "total energy distribution" histogram shown in Fig. 9.2c.

In order to display more details it is useful to plot, for a sequence of fixed values of $E_3 + E_4$, the number of pairs with energy difference $E_3 - E_4$ within an energy band centered at $E_3 + E_4$. As an example of such energy sharing distributions, we show in Fig. 9.2d the one obtained from the data in Fig. 9.2b for the total energy band $E_3 + E_4 = 15 \pm 0.25$ eV. It is seen to be symmetric with respect to the energy difference $E_3 - E_4 = 0$. This symmetry corresponds to the symmetry of the energy distribution in Fig. 9.2b with respect to the $E_3 = E_4$ line, which is dictated by the geometrical symmetry of the normal-incidence set-up.

Calculations of the reaction cross section on the basis of a relativistic layer-KKR formalism (cf. Sec. 9.3) yielded the spectra shown in Fig. 9.2e and Fig. 9.2f. Comparing the theoretical two-dimensional distribution (Fig. 9.2e) to its experimental counterpart (Fig. 9.2b), it first must be mentioned that the experimental setting of the time windows implied an energy cut-off at 1.8 eV. Consequently, pairs with very large energy differences could not be detected. Furthermore, the experimental data contain, in addition to the pure binary collision events treated in the calculations, accidental coincidences and events, in which the primary electron has suffered some energy loss before colliding with a valence electrons. This accounts for a substantial measured intensity for $E_3 + E_4$ below about 7 eV, where the calculated values are vanishingly small. Most importantly, the main experimental feature, the intense "band" for $E_3 + E_4$ above about 14 eV, is seen to be well reproduced by the calculations. This agreement corroborates that this "band" does originate from binary collisions of the incoming electrons with valence electrons in the vicinity of E_F.

The calculated energy sharing curve (Fig. 9.2f) (which involves a summation over sharing curves in the $E_3 + E_4$ interval of 0.5 eV) agrees with its experimental counterpart in the dominance of near equal energy sharing events. The larger width of the experimental energy sharing histogram is mainly due to the integration over a 22° angular acceptance cone rather than being restricted to the sharp angles used in the calculations. We emphasize that (calculated) energy sharing curves usually vary significantly over 0.5 eV total energy intervals. For the purpose of detailed interpretation and analysis, experiment should therefore, as has in fact been achieved more recently, narrow the energy interval.

9.5 Electron scattering dynamics

9.5.1 Elastic one-electron reflection

The primary electron as well as the two outgoing electrons experience elastic multiple scattering from the ion core lattice. In particular, they are back-diffracted (reflected) at lattice planes parallel to the surface. We denote the elements of the three relevant amplitude reflection matri-

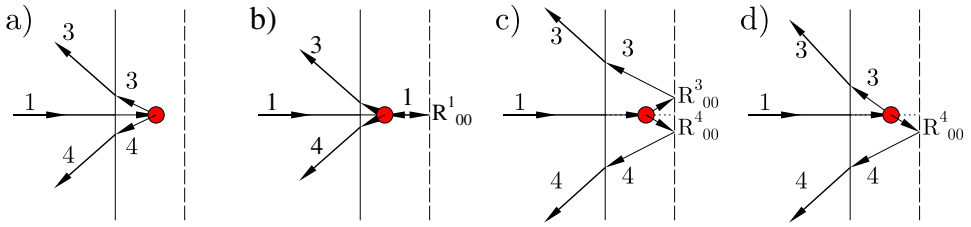

Figure 9.3: Symbolic diagrams of scattering paths in the (e,2e) process for normal incidence of the primary electron (labeled 1) and polar angles 40° of the detected electrons (3 and 4). The vertical thin solid line indicates the surface. The filled circle symbolizes the collision with the valence electron. The vertical thin dashed line stands for the atomic planes, and the $R^i_{gg'}$ at its right-hand side are the elastic reflection matrix elements, which are relevant in the individual diagrams. The refraction angle of electron 3 at the surface has been drawn equal to that of electron 4, which is actually the case only for $E_3 = E_4$. For $E_3 \neq E_4$, the diagrams are topologically equivalent to the ones shown, but – due to the energy dependence of refraction at the surface – the internal angles of electron 3 are different from those of electron 4.

ces by $R^{(i)}_{gg'}$, where the index $i = 1, 3, 4$ distinguishes between the primary electron state and the two ejected electron states, and g enumerates the surface reciprocal lattice vectors (with $g = 0$ corresponding to $\mathbf{g} = (0, 0)$). A selection of scattering paths, which consist of typical combinations of the collision with elastic reflections, is visualized by symbolic diagrams in Fig. 9.3. Diagrams like (b) are, in a terminology used in EELS, of the type "diffraction-loss" (DL), whereas diagrams like (c) and (d) are of the type "loss-diffraction" (LD). Formally, the diagrams correspond to additive terms in a scattering path expansion of the direct and exchange scattering amplitudes f and g (cf. Eq. (9.6)). Because of the absolute square in Eq. (9.5) it is clear that the magnitude of individual (e,2e) cross section features is in general not equal to the sum over partial intensities (obtained from the f and g parts symbolized by the diagrams). There may even be destructive interference. In numerical (e,2e) calculations, all elastic multiple scattering, and therefore especially the above reflections, is easily included, since such is standard in LEED theory (cf. e.g. [30–32]) and the primary electron and the two outgoing electrons are represented by LEED and time-reversed LEED states, respectively. The actual importance of elastic reflections for individual features in (e,2e) spectra can readily be determined by performing additional calculations, in which the reflection matrices are selectively taken as zero, i.e. switched off. We demonstrate this in Fig. 9.4 for two energy sharing curves from W(001). Without reflection of the primary electron ($R^{(1)} = 0$), the spectra are seen to have almost the same shapes as the actual spectra, but with an overall reduction of intensity. Without reflection of neither electron of the created pair, however, the line shapes change, most drastically so in the left-hand part of Fig. 9.4. If only electron 4 is reflected ($R^{(3)} = 0$), peak D is almost unchanged, but its partner D' is strongly reduced. This implies that the path, in which both electrons are reflected, is negligible compared to the two paths, in which one electron is reflected and the other one directly emitted (cf. Fig. 9.3d). Without any reflection, the shape is the same as without $R^{(3)}$ and $R^{(4)}$, but the intensity is reduced. Similar analyses for other primary energies and other geometries [22, 24]) also indicate an important role of the reflection of one or both of the outgoing electrons and a rather minor one of the

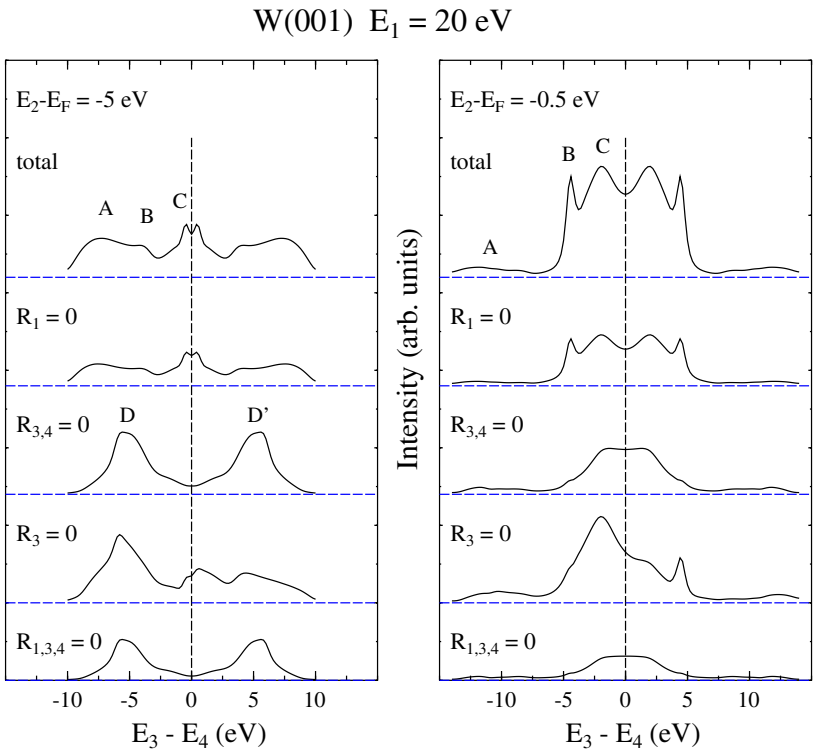

Figure 9.4: (e,2e) energy sharing curves from W(001) in symmetric coplanar geometry for primary electron energy 20 eV and pair total energy $E_3 + E_4 = 10.4$ eV (i.e. valence electron energy $E_2 = E_F - 6$ eV) (left-hand side) and 14.9 eV (i.e. $E_2 = E_F - 0.5$ eV) (right-hand side). Results of the "complete calculation" (uppermost panel on each side) are compared with results of calculations, in which elastic layer reflection matrices $R^{(i)}$ in the four one-electron states (1: primary electron, 2: valence electron, 3 and 4: outgoing electrons) were selectively switched off as indicated in the respective panels.

reflection of the primary electron. In a grazing incidence case, paths including $R^{(1)}$ were even found to reduce spectral features, i.e. to produce destructive interference.

9.5.2 Pair diffraction and coulomb correlation

The Coulomb correlation between the two outgoing electrons, which corresponds to the deviation of the actual two-electron state $|3,4\rangle$ from an antisymmetrized product of one-electron states, can be studied by viewing the pair as a single compound particle, which is characterized by the center-of-mass wave vector $\mathbf{K}^+ = \mathbf{k}_3 + \mathbf{k}_4$ and the interelectronic wave vector $\mathbf{K}^- = (\mathbf{k}_3 - \mathbf{k}_4)$, i.e. an internal degree of freedom (cf. [49, 50]). Diffraction of the pair by the lattice is governed by the Laue-like condition $\mathbf{K}^+_{\|} = \mathbf{k}^{\|}_3 + \mathbf{k}^{\|}_4 + \mathbf{g}_{\|}$, where $\mathbf{g}_{\|}$ is a surface

reciprocal lattice vector. Only the center-of -mass wave vector of the pair enters in this condition. The above is equivalent to the diffraction of a fictitious particle located at the pair's center of mass. While $\mathbf{K}^+$ thus determines the positions of the diffraction peaks, their height and shape is controlled by the interelectronic correlation. This is illustrated by the measured and calculated cross sections in Fig. 9.5. The asymmetry between K_x^+ and $-K_x^+$ is due to the off-normal incidence of the primary beam, i.e. a nonzero k_{1x} in the above diffraction condition.

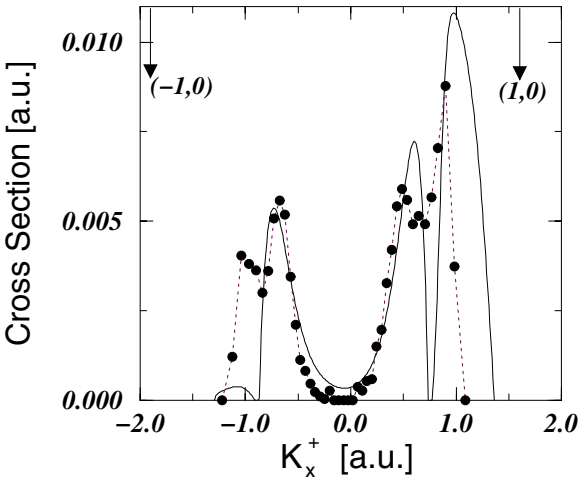

Figure 9.5: (e,2e) from Fe(110) with unpolarized primary electrons of energy 50 eV incident in the x-z plane at polar angle $\theta_1 = 5^\circ$. The two detectors are in the same plane at azimuthal angles 0 and 180° and polar angles 50° and 35°. The experimental (fat dots with a broken line to guide the eye) and theoretical (solid line) cross section is shown as a function of the surface-parallel component K_x^+ of the electron pair momentum at fixed pair energy $E_3 + E_4 = 44$ eV. (From [49]).

In a more quantitative investigation of Coulomb pair correlation effects, (e,2e) cross section distributions from the W(001) surface were calculated using a dynamical screening model and compared to their counterparts calculated without Coulomb correlation [25]. While the modifications of fixed-geometry (e,2e) intensity distributions were in general fairly modest, a drastic effect was found for a set-up, in which the detection direction of one electron is fixed and that of the other sweeps over the entire hemisphere. We show this in Fig. 9.6. Without correlation, the emission probability is seen (cf. upper half of Fig. 9.6) to be maximal when the two electrons escape into the same direction and with the same velocity. This unphysical result is remedied by the pair interaction (cf. lower half of Fig. 9.6) which carves a considerable "pair correlation hole" around the position where electrons are close to each other in velocity space. For regions where the two electrons emerge with diverging directions, the effect of the pair correlation becomes less and less visible.

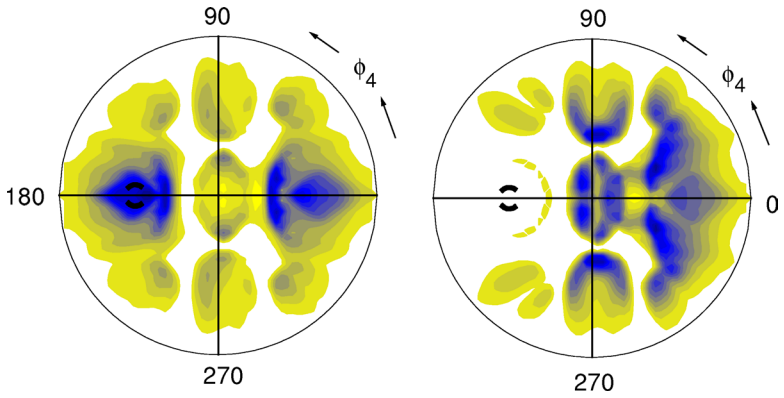

Figure 9.6: Calculated (e,2e) angular distribution from W(001) for primary electrons of energy 17.2 eV incident at polar angle $\theta_1 = 88^\circ$ (grazing incidence) and azimuthal angle $\varphi_1 = 0^\circ$. The outgoing electrons have energies $E_3 = E_4 = 6$ eV. One detector is in a fixed direction defined by $\theta_3 = 47^\circ$ and $\varphi_3 = 180^\circ$, and the other scans over the angles θ_4 and φ_4, which correspond to the radial and angular coordinates in the contour plots. The Coulomb pair correlation is switched off in the left-hand panel and taken into account in a dynamical screening approximation (cf. [25]) in the right-hand panel. The broken circle around $\theta_4 = 47^\circ$ and $\varphi_4 = 180^\circ$ marks the direction of parallel escape of the two electrons, i.e. the center of the 'pair correlation hole'. (From [25]).

9.6 Valence electronic structure

In the following, we address the information, which (e,2e) spectra may yield on the valence electronic structure. We demonstrate that there is a strong weighting on the surface region and that selection rules may be harnessed to resolve with respect to spatial symmetry types.

9.6.1 Surface sensitivity and surface states

Since the Coulomb matrix elements, which determine the scattering cross section (cf. Sec. 9.3), involve three one-electron states decaying into the crystal (the incident electron state and the two outgoing ones), it seems plausible that low-energy (e,2e) spectroscopy should in general be more surface sensitive than LEED or photoemission, in which there is only one decaying one-electron state. This expectation was confirmed theoretically by layer-resolved (e,2e) calculations for the cases of Fe(110) [23] and W(001) [27, 44]. Experimentally, spectra from W(001) were found to change distinctly upon contamination of the surface and to reveal surface state and resonances [17] in accordance with earlier photoemission results (cf. [51] and references therein). An adsorbate state was observed for p(2x1) O/W(001) [52].

A very instructive case, which has been studied theoretically [26], is the Cu(111) surface. It exhibits (cf. Fig. 9.7) the text-book paradigm of a Shockley surface state, which resides — near E_F and well above the d-band region — in an s-p like bulk energy gap and forms a two-dimensional nearly free electron gas. References to the large amount of literature, which

has been dealing with this surface state, may e.g. be found in the photoemission papers [4,53] and in the report on the observation by scanning tunnelling microscopy of two-dimensional standing electron wave patterns [54].

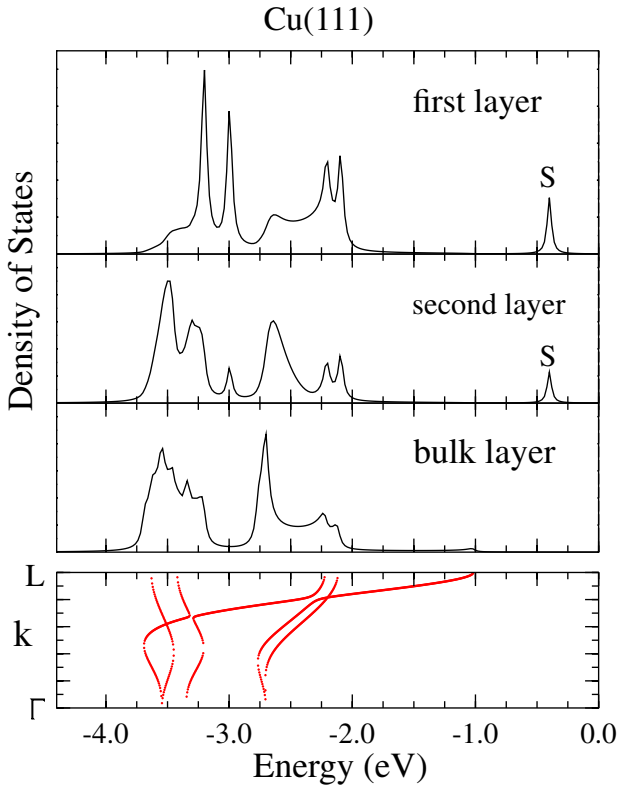

Figure 9.7: Layer-resolved density of states (LDOS) of Cu(111) for $\vec{k}^{\parallel} = 0$. S denotes the sp-derived Shockley surface state. The bottom panel shows the corresponding bulk band structure of Cu along Γ-L. On the energy axis, 0 corresponds to the Fermi energy.

Calculated (e,2e) spectra and underlying layer densities of states are shown in Fig. 9.8 for a symmetric coplanar setup with normal incidence. For fixed primary energy E_1, reaction plane and exit angles $\theta_3 = \theta_4$, the (e,2e) cross section is then a function $I(E_3, E_4)$ of the energies of the two outgoing electrons and can be represented by a contour plot in the (E_3, E_4) plane. Furthermore, for each pair (E_3, E_4), the pair $(E_2, \mathbf{k}_2^{\parallel})$ — with $E_2 = E_3 + E_4 - E_1$ and $\mathbf{k}_2^{\parallel} = \mathbf{k}_3^{\parallel} + \mathbf{k}_4^{\parallel} - \mathbf{k}_1^{\parallel}$ —, at which the valence electron spectral function in Eq. (9.3) is evaluated, is uniquely determined. Obviously, $\mathbf{k}_2^{\parallel}$ is in the reaction plane, with the component $k_2^{\parallel} = (\sqrt{2E_3} - \sqrt{2E_4})\sin(\theta_3)$ (in atomic units). The layer-restricted trace of the valence electron spectral function, i.e. the density of states $N_m(E_2, \mathbf{k}_2^{\parallel})$ for the m-th layer, can therefore also be represented by a contour plot in the (E_3, E_4) plane. In this plot, the diagonal $E_3 = E_4$, on which $k_2^{\parallel} = 0$, can be viewed as the E_2 axis, and the other diagonal, which marks the

Fermi energy, as the $k_2^{\|}$ axis (with a non-linear scale). In this manner, the first two columns of Fig. 9.2 represent the first and second layer densities of states N_1 and N_2 for $\theta_3 = \theta_4 = 30°$ and $60°$ With increasing $k_2^{\|}$ the d-band LDOS has almost no dispersion, whereas the surface state feature is seen to disperse upward towards E_F. The narrowing of the apparent dispersion relation with increasing $\theta_{3,4}$ is readily understood from the above expression for $k_2^{\|}$.

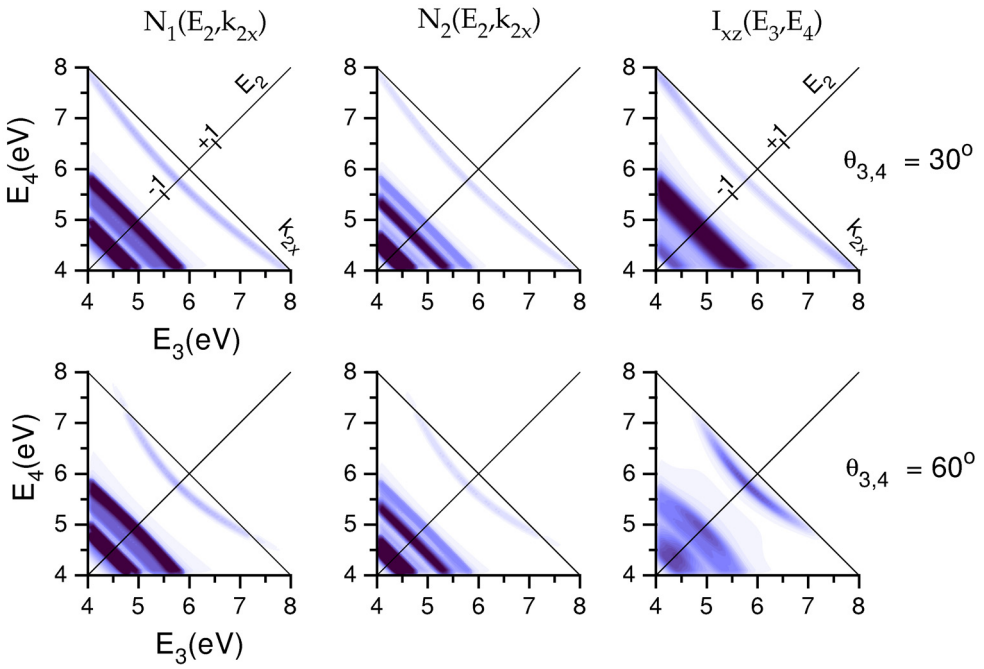

Figure 9.8: Calculated (e,2e) cross sections and corresponding valence electron surface DOS of Cu(111) in symmetric coplanar geometry with normally incident 17 eV primary electrons and detection of the emerging electrons at polar angles $\theta_3 = \theta_4$ and azimuthal angles $\varphi_3 = 0$ and $\varphi_4 = \pi$ The orientation of the surface (in the xy plane) is such that x is along the [1,−1,0] direction and y along [−1,−1,2], i.e. the yz plane is a mirror plane of the semi-infinite crystal, which is normal to the reaction plane (xz).
Top row : For $\theta_3 = \theta_4 = 30°$, the three panels show the surface layer DOS $N_1(E_2, k_{2x})$, the second layer DOS $N_2(E_2, k_{2x})$ and the (e,2e) intensity distribution $I_{xz}(E_3, E_4)$.
Bottom row : as top row, but for $\theta_3 = \theta_4 = 60°$.

Comparing the (e,2e) intensity distribution (see Fig. 9.8) with the LDOS plots, we notice a strong overall similarity. In the d-band region, $I_{xz}(E_3, E_4)$ is be roughly a superposition of N_1 on the one hand and of N_2 and deeper-layer N on the other hand, with some broadening and a modified weighting of individual features, which is due to matrix element effects. The surface state appears with a substantial weight and the shape of its dispersion is perfectly preserved. The mirror symmetry with respect to the diagonal, i.e. upon interchange of E_3 and E_4, is readily understood from the fact that the reaction plane is perpendicular to the (yz) mirror plane of the semi-infinite crystal.

Most recently, an experimental (e,2e) investigation of Cu(111) clearly produced the Shockley surface state and its dispersion [55].

Table 9.1: Selection rules in coplanar symmetric equal-energy (e,2e) spectroscopy from fcc(110) surfaces: cross sections I_{antipar} (Eq. (9.10)) and I_{par} (Eq. (9.9)) for the detection of antiparallel-spin and parallel-spin pairs from valence states with spatial symmetry types $\Sigma_1, \Sigma_2, \Sigma_3, \Sigma_4$. The topmost row indicates the scattering planes as (x,z) and (y,z), where x and y are in the surface plane along [1 −1 0] and [001], respectively, and z is normal to the surface.

	(x,z) plane		(y,z) plane	
	I_{antipar}	I_{par}	I_{antipar}	I_{par}
Σ_1	$2 \mid f_1 \mid^2$	0	$2 \mid f_1 \mid^2$	0
Σ_2	0	0	0	0
Σ_3	0	0	$2 \mid f_3 \mid^2$	$4 \mid f_3 \mid^2$
Σ_4	$2 \mid f_4 \mid^2$	$4 \mid f_4 \mid^2$	0	0

9.6.2 Symmetry resolution by selection rules

The (e,2e) selection rules presented in Sec. 9.3.3 provide access to the spatial symmetry types of the valence electrons. We demonstrate this for Cu(110) both analytically and numerically.

In the symmetric coplanar geometry with normal incidence of the primary beam and equal energies of the two detected electrons, parallel-momentum conservation dictates that the relevant valence electron states have $\mathbf{k}_2^{\parallel} = 0$. The wave functions $\varphi_2^{(n)}(\mathbf{r})$ of the semi-infinite system (crystal half-space plus vacuum-half-space) can therefore be classified according to the spatial symmetry types Σ_n with $n = 1, 2, 3, 4$. Choosing the coordinate system such that z is along the surface normal [110], and x and y are in the surface plane along [1 −1 0] and [001], respectively, the $\varphi_2^{(n)}$ thence show the following behavior under reflection at the surface-perpendicular mirror planes (x, z) and (y, z): $\varphi_2^{(1)}$ is symmetric with respect to both, $\varphi_2^{(2)}$ is antisymmetric with respect to both; $\varphi_2^{(3)}$ is antisymmetric with respect to (x, z) and symmetric with respect to (y, z), while for $\varphi_2^{(4)}$ it is the other way round. Choosing the reaction plane firstly as (x, z) and secondly as (y, z), application of our above two selection rules immediately yields the results summarized in Table 9.1. Valence states of Σ_2 symmetry can thus not be "seen" in the (e,2e) spectra, whereas Σ_3 and Σ_4 states individually manifest themselves in the spectra I_{par} (Eq. (9.9)) for emitted pairs with parallel spins because of $g_3 = -f_3$ and $g_4 = -f_4$, respectively. The spectra I_{antipar} for anti-parallel spins (Eq. (9.10)) are determined by the sums $2 \mid f_1 \mid^2 + 2 \mid f_3 \mid^2$ and $2 \mid f_1 \mid^2 + 2 \mid f_4 \mid^2$, respectively. The Σ_1 contribution $I(\Sigma_1)$ can therefore readily be retrieved from (measured or calculated) antiparallel- and parallel-spin spectra according to $I(\Sigma_1) = I_{\text{antipar}} - I_{\text{par}}/2$.

We note that the above results are the same for $\sigma = +$ and $\sigma = -$, i.e. they do not depend on the spin orientation of the primary beam. They therefore hold as well if one uses unpolarized primary electrons. If the relative spin orientation of the emitted electrons is not detected, as is the case in present-day experiments, one observes the sum of I_{par} and I_{antipar} and thus forfeits the second selection rule.

The first selection rule however holds even for completely spin-unresolved experiments: Σ_2 states do not contribute, and Σ_3 or Σ_4 states are excluded depending on the choice of the reaction plane.

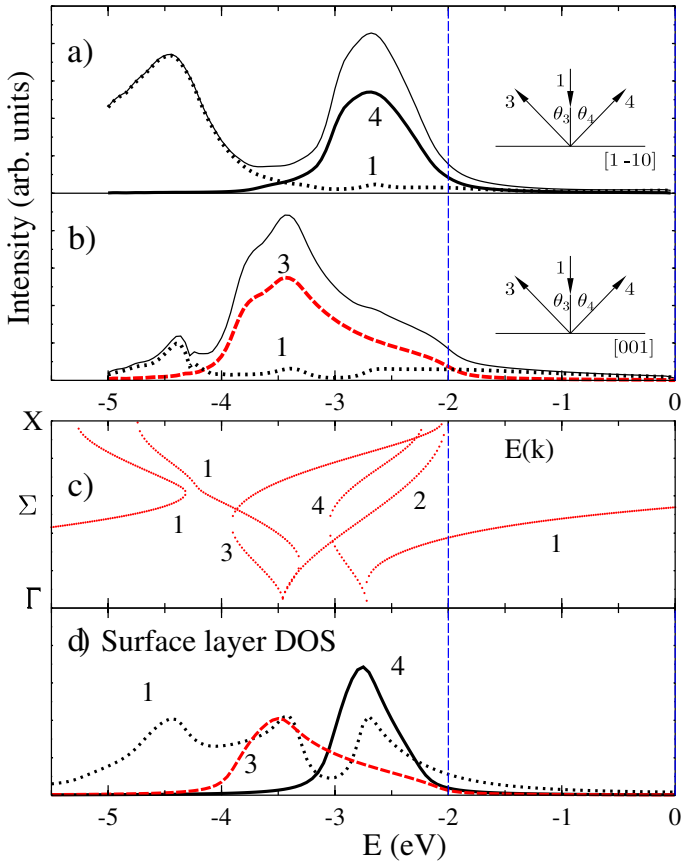

Figure 9.9: Valence state symmetry resolution by selection rules. *Panels (a) and (b)*: scalar-relativistically calculated (e,2e) intensity spectra from Cu(110) in symmetric coplanar geometry (cf. insets) with normally incident primary electrons with energy $E_1 = 17$ eV and detection of emitted electrons with energies $E_3 = E_4$ at polar angles $\theta_3 = \theta_4 = 45^\circ$ and azimuthal angles $\varphi_4 = \varphi_3 + \pi$. The intensities are thus functions of $E_3 = E_4$ and can, because of energy conservation $E_2 = 2E_3 - E_1$, also be regarded as functions of the valence electron energy E_2, which we take (relative to the Fermi energy) as the abscissa. The reaction plane intersects the surface along $[1\,{-1}\,0]$ (panel (a)) and along [001] (panel (b)). *Thin solid lines*: total intensities $I_{\text{par}} + I_{\text{antipar}}$ (cf. Eqs. (9.9) and (9.10)); *thick solid line and thick dashed line*: I_{par} originating from Σ_4 and Σ_3 states, respectively; *dotted lines*: $I(\Sigma_1) = I_{\text{antipar}} - I_{\text{par}}/2$. *Panel (c)*: Bulk band structure (without SOC) along $\Gamma - (\Sigma) - X$ with the numbers 1 to 4 indicating the spatial symmetry types Σ_i of the individual bands. *Panel (d)*: Valence electron surface DOS of Cu(110) resolved with respect to $\vec{k}^{\parallel} = 0$ and symmetries Σ_i. (The Σ_2-DOS is not shown since transitions from Σ_2 states are absent in accordance with our first selection rule).

Numerically calculated results are shown in Fig. 9.9. The I_{par} spectrum in panel (a) (labeled as 4) has a broad peak between -3.2 and -2 eV, i.e.the energy range of the Σ_4 bulk band and the Σ_4 surface layer DOS peak. This is obviously in accordance with our selection rules

(cf. Table 9.1). Likewise, the I_{par} spectrum in panel (b) (labeled as 3) extends between -4 and -2 eV, the energy range of the Σ_3 bulk band and surface DOS. The peak near -3.4 eV coincides with the surface DOS peak and the high bulk DOS near the Γ point, and the peak around -3.8 eV appears to reflect the bulk DOS at the bottom of the Σ_3 band. In accordance with our first selection rule, Σ_3 valence states do not manifest themselves in (e,2e) spectroscopy in the first reaction plane case (panel (a)) and Σ_4 valence states not in the second one (panel (b)). Σ_2 contributions are absent in both cases. The substantial difference of the Σ_1 feature between -5 and -4 eV in the two reaction plane cases is ascribed to the fact that the off-normal time-reversed LEED states ψ_3 and ψ_4 and consequently the matrix elements are quite different in the two cases. All the partial spectra in Fig. 9.9 mainly reflect the respective surface densities of states (for $\mathbf{k}^{\parallel} = 0$) but have some contributions from the electronic structure in sub-surface layers.

In the above two cases, the reaction plane is parallel to a mirror plane of the crystalline system. Excitation of Σ_2 valence states is therefore forbidden by the first selection rule, just as it is by non-relativistic dipole selection rules in normal photoemission. If however the reaction plane is rotated about the surface normal by some arbitrary angle, Σ_2 valence states will manifest themselves — together with states of the other three symmetry types — in the partial and total (e,2e) cross sections.

Experimentally, the first selection rule is inherent in all (e,2e) spectra obtained to date using an unpolarized or polarized primary beam. The second selection rule is not yet accessible, since it requires spin analysis of the outgoing electron pair.

9.7 Spin-polarized (e,2e) spectroscopy

In the cases presented above, the primary electron beam is unpolarized and the (e,2e) cross section is therefore the average over the spin-dependent cross sections I^+ and I^- (cf. Sec. 9.3). Since spin polarization effects due to spin-orbit interaction and magnetic exchange interaction are abundant in LEED and photoemission, they must occur also in (e,2e) which involves the same types of one-electron states.

9.7.1 Non-magnetic surfaces

Spin-orbit coupling effects in (e,2e) have been investigated by symmetry considerations and numerical calculations for coplanar geometries [24]. Consider electrons with spin polarization vector $-\mathbf{P}_1$ impinging on a cubic (001) surface ((x,y) plane). The reaction plane is chosen as the (x,z) plane, which is parallel to the (010) plane and hence is a mirror symmetry plane of the crystal. Furthermore, it is a mirror plane of the complete set-up if the primary beam is unpolarized or has its spin polarization vector $\mathbf{P}_1$ parallel to the y-axis. If $\mathbf{P}_1$ is parallel to the (x,z)-plane, the mirror operation M_{xz} transforms it into $-\mathbf{P}_1$ while leaving the remainder of the set-up unchanged. In particular, the intensity I^+, which is a scalar quantity, is invariant under M_{xz}. This implies $I^+ = I^-$, i.e. the asymmetry A (Eq. (9.4)) is identically zero in this case. In contrast, for $\mathbf{P}_1$ parallel to y, i.e. normal to the reaction plane, there is no general connection between I^+ and I^-. One can thus in general expect a non-vanishing asymmetry A. We recall that the above findings are analogous to what is well-known in spin-polarized

LEED (SPLEED) (cf. e.g. [30]). For our numerical investigations of spin-polarized (e,2e), we therefore choose the primary electron spin alignment along y.

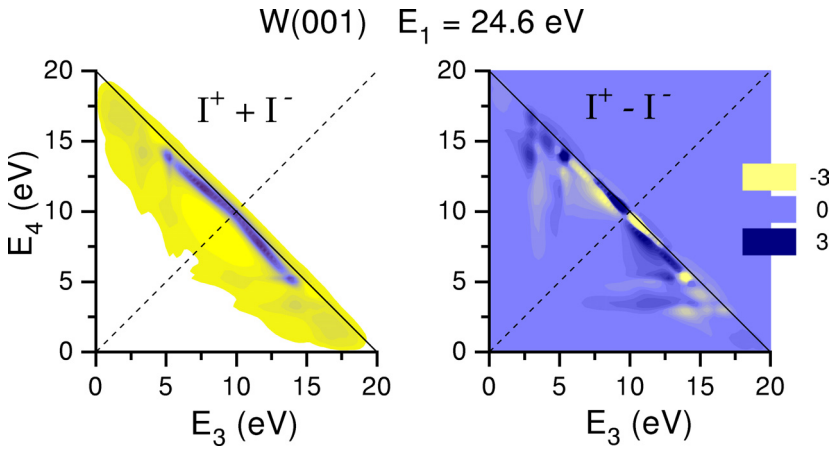

Figure 9.10: Spin polarized (e,2e) from W(001) in symmetric coplanar geometry with the emerging electrons at polar angles $\theta_3 = \theta_4 = 40^\circ$ and azimuthal angles $\varphi_3 = 0$ and $\varphi_4 = \pi$. The two panels show the sum and the difference of the cross sections I^+ and I^- calculated for normally incident primary electrons of energy 24.6 eV with spins aligned parallel and antiparallel to the y axis (normal to the reaction plane).

Numerical calculations were done for W(001), in which spin-orbit coupling is strong because of its large atomic number $Z = 74$. A typical spin-dependent spectral distribution result is shown in Fig. 9.10 for coplanar symmetric geometry and primary electron energy 24.6 eV. Since $I^+ + I^-$ is equivalent to I obtained for an unpolarized primary electron beam, the left-hand contour plot is roughly similar to the one (for $E_1 = 20$ eV) presented above (Fig. 9.2e). In particular, most of the emitted electron pairs are associated with valence electrons close to E_F. The distribution of the intensity difference (right-hand plot in Fig. 9.10) is firstly seen to be antisymmetric with respect to the $E_3 = E_4$ diagonal, i.e. changes sign upon interchanging the two detected electron energies. This is easily understood by applying the mirror operation with respect to the (y,z) plane. Secondly, $I^+ - I^-$ is more richly structured than $I^+ + I^-$. This suggests that it contains additional and more detailed physical information. A few typical energy sharing curves are shown in Fig. 9.11, which demonstrate that there are sizeable differences between I^+ and $-I^-$, which correspond to asymmetry values up to 30 %. With the aid of additional calculations, in which spin-orbit coupling was selectively switched off in the four one-electron states, spin-orbit coupling in the valence state was identified as the main source of the asymmetry. The intensity peak, which is seen in the upper panel at $E_3 - E_4 = 0$, originates from a surface resonance, which exists for $\mathbf{k}_2^{\parallel} = 0$ at $E_2 = E_F - 0.3$ eV and is well known from photoemission work (cf. [51] and references therein).

On the experimental side, a very recent spin-polarized (e,2e) study of W(001) [55] produced asymmetry spectra, which are in encouraging agreement with their theoretical counterparts.

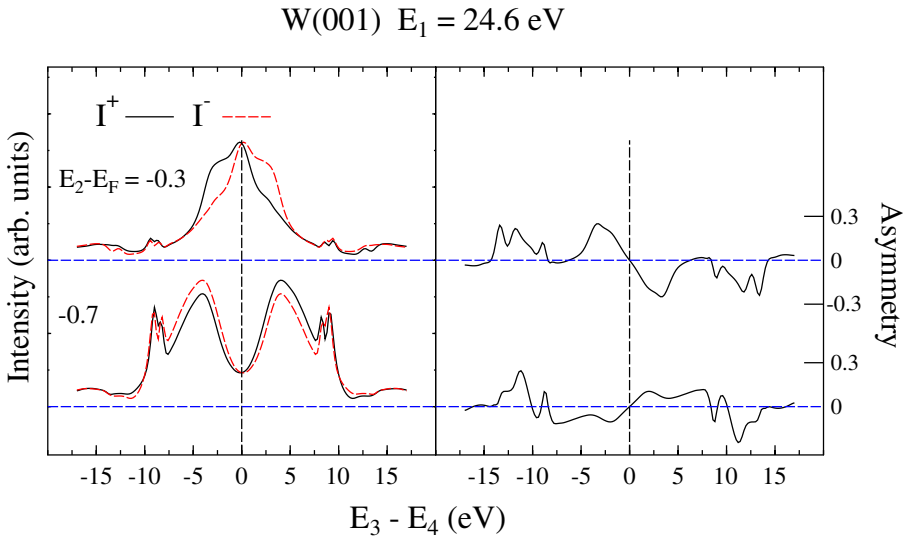

Figure 9.11: Spin polarized (e,2e) from W(001) for conditions as in Fig. 9.10: I^+, I^- and asymmetry $A = (I^+ + I^-)/(I^+ - I^-)$ energy sharing curves for pair energies 19.7 and 19.3 eV, i.e. valence electron energies 0.3 and 0.7 eV below the Fermi energy.

9.7.2 Ferromagnetic surfaces

The exchange-induced dependence of the (e,2e) reaction cross section on the spin polarization of the primary electron beam has recently been investigated experimentally and theoretically for the case of the ferromagnetic Fe(110) surface [18, 19, 23, 56]. It is maximal if the spin polarization vector P_1 of the primary electron is collinear with the magnetization direction, which for Fe(110) is in the surface plane and normal to the chosen reaction plane. In the following, the primary electron spin label $\sigma_1 = \pm$ refers to $\mathbf{P}_1$ parallel/antiparallel to the majority spin direction.

In Fig. 9.12 we show an example of experimental and theoretical I^+ and I^- spectra obtained for equal energies $E_3 = E_4$ of the outgoing pair as functions of the valence electron energy E_2 relative to E_F. The dominant feature, peak C, is obtained for $\sigma_1 = +$. This may seem surprising at first glance, since for E_2 near E_F and $\mathbf{k}_2^{\parallel} = 0$ the (layer-resolved) density of states (right-hand part of Fig. 9.12) is much larger for minority spin than for majority spin. It is however readily explained by the second selection rule presented in Sec. 9.3.3. The valence states near E_F being symmetric with respect to the plane, which is normal to the surface and to the reaction plane, $I^-_{\rm par}$ for the collision of a spin-down primary electron with a spin-down valence electron (resulting in a parallel-spin pair) vanishes, which leaves $I^+_{\rm antipar}$, i.e. collisions of spin-up primary electrons with spin-down valence electrons. Differently put, there is singlet scattering only. (The small peak C' is a "shadow" of C due to the degree of spin polarization of the primary beam being 65 % rather than 100 %). Likewise, the I^- peak A arises from collisions of spin-down electrons with majority spin valence electrons. The cross section asymmetry (cf. Eq. (9.4)) thus semi-quantitatively reflects the negative of the valence

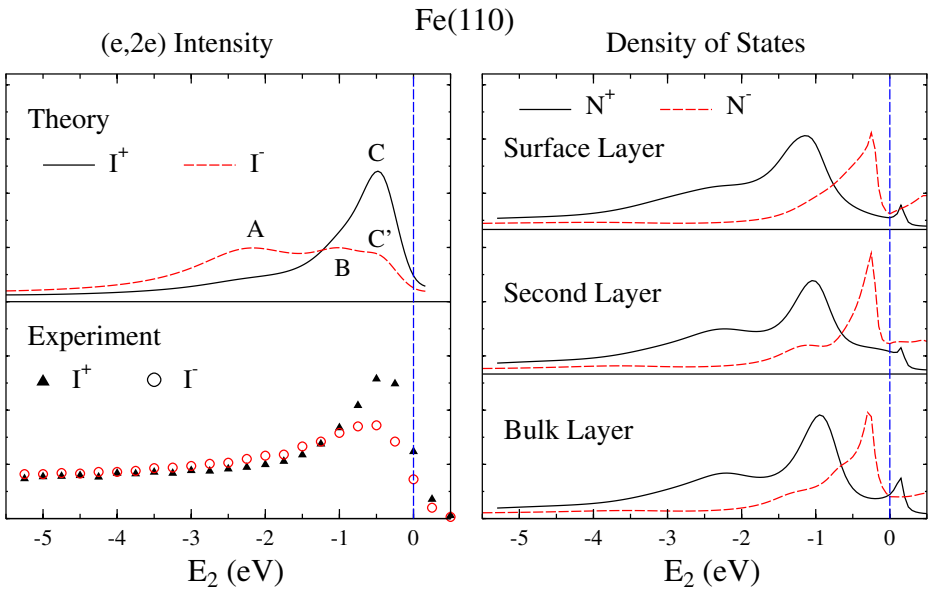

Figure 9.12: Spin polarized (e,2e) from ferromagnetic Fe(110) (with magnetization $\vec{M}$ parallel to the surface along [1,0,0] (y axis)) in coplanar symmetric geometry (reaction plane (x,z)) with the electron detectors at polar angles $\theta_3 = \theta_4 = 40^\circ$. The normally incident primary electrons of energy 22.6 eV are spin-polarized antiparallel/parallel to $\vec{M}$ (i.e. parallel/antiparallel to the majority spins of the target) with a polarization degree of 65 %. *Left:* Experimental [55] and theoretical [56] spin-dependent intensities I^+ and I^- for equal energy sharing ($E_3 - E_4 = 0$ in the calculations and between -0.1 and $+0.1$ ($E_3 + E_4$) in the experimental data) as functions of the valence electron energy E_2 (relative to E_F). *Right:* Layer-resolved density of states of majority- and minority-spin valence electrons for $\vec{k}_2^{\parallel} = 0$.

electron spin polarization $P_2(E_2) = (N^+(E_2) - N^-(E_2))/(N^+(E_2) + N^-(E_2))$. As the displacement of the I^- peak C relative to the minority DOS peak near E_F indicates, however, matrix element effects are of importance. This is supported by further calculations, according to which peak C moves when the primary energy E_1 is varied [56]. An identification of surface features in distinction from bulk-like features is rather complicated and still under investigation in the case of Fe(110), since there are numerous surface resonances, which have substantial weight over the first few layers, from which most of the detected electron pairs originate.

In Fig. 9.13 we show an experimental energy sharing curve of the asymmetry A together with its calculated counterpart. The energies have been chosen such that the relevant valence electron energy E_2 is within about 1 eV from E_F. The decline of the asymmetry, i.e. the increasing weight of I^- relative to I^+ as one moves away from equal energy sharing (i.e. away from $\mathbf{k}_2^{\parallel} = 0$) is qualitatively plausible: collisions between parallel-spin-down electrons become increasingly possible. This trend is however modified due to majority electron states occurring closer to E_F. To disentangle the various contributions, spin resolution of the outgoing electrons would be most useful. Experimentally, this might be achievable by placing a

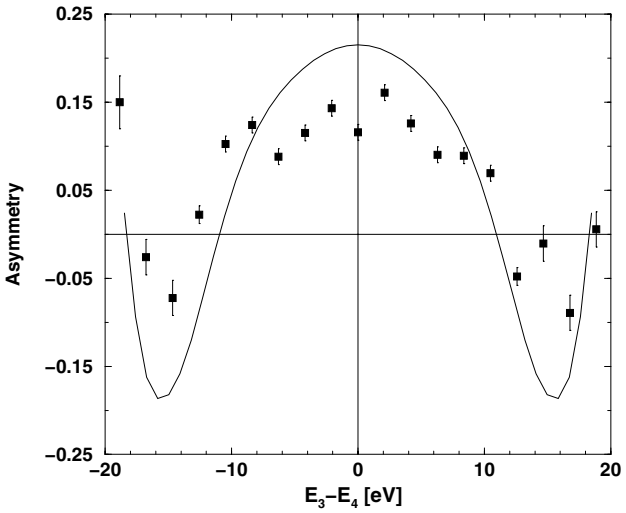

Figure 9.13: Spin polarized (e,2e) from ferromagnetic Fe(110) for set-up as in Fig. 9.12 and primary energy 26 eV: Measured and calculated energy sharing distributions of the asymmetry A for fixed pair energy $(E_3 + E_4) = 21$ eV. The theoretical results are averaged over the angular resolution of the detectors. (From [23]).

spin analyzer foil consisting e.g. of a free-standing Au/Co /Au film (cf. [57]) in the electron paths between the sample and the detectors.

While the theoretical curve in Fig. 9.13, which was calculated without spin-orbit coupling, is symmetrical with respect to $E_3 - E_4 = 0$, the experimental data are somewhat asymmetrical. Rather than ascribing this completely to experimental uncertainties, it is tempting to regard it partly as a manifestation of the interplay between spin-orbit coupling and exchange interaction. The investigation of magnetic dichroism phenomena is one of the future directions of (e,2e) spectroscopy.

Acknowledgements

We would like thank A. Morozov and J. Kirschner (Max-Planck-Institut für Mikrostrukturphysik, Halle) for discussions on experimental aspects and for making available most recent data.

References

[1] S.D. Kevan (Ed.), *Angle-resolved Photoemission: Theory and Current Applications*, Elsevier, Amsterdam (1992).

[2] S. Huefner, *Photoelectron Spectroscopy*, Springer, Berlin (1995).

[3] W. Schattke, Progr. Surf. Sci. 54, 211 (1997).

[4] R. Courths, M. Lau, T. Scheunemann, H. Gollisch, and R. Feder, Phys. Rev. B **63**, 195110 (2001).

[5] I. Bartos and W. Schattke, article in the present volume.

[6] C.T. Whelan and H.R.J. Walters (Eds.), *Electron Coincidence Studies of Electron and Photon Impact Ionization*, Plenum, New York 1997.

[7] J. Berakdar and J. Kirschner (Eds), *Many-Particle Spectroscopy of Atoms, Molecules and Surfaces*, Kluwer Academic / Plenum Publishers, New York - London (2001).

[8] S.A. Canney, M. Vos, A.S. Kheifets, N. Clisby, I.E. McCarthy, and E. Weigold, J. Phys. C.M. **9**, 1931 (1997).

[9] M. Vos, Z. Fang, S.A. Canney,, A.S. Kheifets, I.E. McCarthy, and E. Weigold, Phys. Rev. B **56**, 963 (1997).

[10] E. Weigold and I.E. McCarthy, *Electron Momentum Spectroscopy*, Kluwer Academic / Plenum Publishers, New York - London (1999).

[11] E. Weigold and M. Vos, in J. Berakdar and J. Kirschner (Eds), *Many-Particle Spectroscopy of Atoms, Molecules and Surfaces*, Kluwer Academic / Plenum Publishers, New York - London (2001).

[12] S. Iacobucci, L. Marassi, R. Camilloni, S. Nannarone, and G. Stefani, Phys. Rev. B **51**, 10525 (1995).

[13] S. Rioual, S. Iacobucci, D. Neri, A.S. Kheifets, and G. Stefani, Phys. Rev. B **57**, 2545 (1998).

[14] A.S. Kheifets, S. Iacobucci, A. Ruocco, R. Camilloni, and G. Stefani, Phys. Rev. B **57**, 7360 (1998).

[15] J. Kirschner, O.M. Artamonov, and S.N. Samarin, Phys. Rev. Lett **75**, 2424 (1995).

[16] O.M. Artamonov, S.N. Samarin, and J. Kirschner, Appl. Phys. A **65**, 535 (1997).

[17] S. Samarin, R. Herrmann, R. Schwabe, and O. Artamonov, J. Electron Spectroscopy **96**, 61 (1998).

[18] S. Samarin, J. Berakdar, O. Artamonov, and J. Kirschner, Phys. Rev. Lett. **85**, 1746 (2000).

[19] O. Artamonov, J. Berakdar, A. Morozov, and J. Kirschner, Surface Sci. **482**, 1015 (2001).

[20] H. Gollisch, D. Meinert, Xiao Yi, and R. Feder, Solid State Commun. **102**, 317 (1997).

[21] J. Berakdar and M.P. Das, Phys. Rev. A **56**, 1403 (1997).

[22] R. Feder, H. Gollisch, D. Meinert, T. Scheunemann, O.M. Artamonov, S. Samarin, and J. Kirschner, Phys. Rev. B **58**, 16418 (1998).

[23] J. Berakdar, Phys. Rev. Lett. **83**, 5150 (1999).

[24] H. Gollisch, T. Scheunemann, and R. Feder, J. Phys.: Condens. Matt. **11**, 9555 (1999).

[25] J. Berakdar, H. Gollisch, and R. Feder, Sol. State Commun. **112**, 587 (1999).

[26] H. Gollisch, T. Scheunemann, and R. Feder, Sol. State Commun. **117**, 691 (2001).

[27] R. Feder, H. Gollisch, T. Scheunemann, J. Berakdar, and J. Henk, in J. Berakdar and J. Kirschner (Eds), *Many-Particle Spectroscopy of Atoms, Molecules and Surfaces*. Kluwer Academic / Plenum Publishers, New York - London (2001).

[28] R. Feder and H. Gollisch, Sol. State Commun. **119**, 625 (2001).

[29] N. Fominykh, S.N. Samarin, A. Morozov, F.U. Hillebrecht, J. Henk, J. Berakdar, P. Bruno, and J. Kirschner, article in the present volume

[30] R. Feder (Ed.),*Polarized Electrons in Surface Physics*, World Scientific, Singapore (1985).

[31] M.A. Van Hove, W.H. Weinberg, and C.M. Chan, *Low-Energy Electron Diffraction*, Springer, Berlin (1986).

[32] W. Moritz, article in the present volume

[33] E. Tamura, R. Feder, G. Waller, and U. Gradmann, phys. stat. sol. (b) **157**, 627 (1990)

[34] A.J. Freeman, article in the present volume

[35] S.V. Halilov, H. Gollisch, E. Tamura, and R. Feder, J. Phys.: Condens. Matt. **5**, 4711 (1993).

[36] R. Feder and J. Henk, in H. Ebert and G. Schütz (Eds), *Spin-Orbit Influenced Spectroscopies of Magnetic Solids*, No. 466 in *Lecture Notes in Physics*, Springer, Berlin (1996).

[37] W. Kuch, A. Dittschar, K. Meinel, M. Zharnikov, C.M. Schneider, J. Kirschner, J. Henk, and R. Feder,

[38] A. Rampe, D. Hartmann, T. Klug, G. Guentherodt, T. Scheunemann, J. Henk, and R. Feder, Phys. Rev. B **57**, 14370 (1998)

[39] R. Feder, J. Henk, and B. Johannson, Sol. State Commun. **108**, 713 (1998).

[40] P.M. Morse and H. Feshbach, *Methods of Theoretical Physics* vol.1, McGraw Hill, New York (1953).

[41] E. Tamura, Phys. Rev. B **45**, 3271 (1992).

[42] C.O. Almbladh and L. Hedin, in E.E. Koch (Ed.), *Handbook on Synchrotron Radiation*, North-Holland (1983).

[43] J. Inglesfield and W. Plummer, in S.D. Kevan (Ed.), *Angle-resolved Photoemission: Theory and Current Applications*, Elsevier, Amsterdam (1992).

[44] D. Meinert, Ph.D. thesis, Universitaet Duisburg, 2000.

[45] G.D. Carse and D.W. Walker, J. Phys. B **6**, 2529 (1973).

[46] S.V. Halilov, E. Tamura, H. Gollisch, D. Meinert, and R. Feder, J. Phys. Condens. Matter **5**, 3859 (1993).

[47] C. Solterbeck, O. Tiedje, T. Strasser, S. Brodersen, A. Boedicker, W. Schattke, and I. Bartos, J. Electron Spectroscopy 101–103, 473 (1999).

[48] P. Blaha, K. Schwarz, and J. Luiz, computer code WIEN97, Vienna University of Technology, 1997. Improved and updated version of the original copyrighted WIEN-code, which was published by P. Blaha, K. Schwarz, P. Sorantin, and S.B. Trickey in Comput. Phys. Commun. **59**, 399 (1990).

[49] J. Berakdar, S. Samarin, R. Herrmann, and J. Kirschner, Phys. Rev. Lett **81**, 3535 (1998).

[50] S. Samarin, J. Berakdar, O. Artamonov, H. Schwabe, and J. Kirschner, Surface Sci. **470**, 141 (2000).

[51] G.S. Elliott, K.E. Smith, and S.D: Kevan, Phys. Rev. B **44**, 10826 (1991)

[52] S. Samarin, J. Berakdar, R. Herrmann, R. Schwabe, O. Artamonov, and J. Kirschner J. Phys. (Paris) IV **9**, 127 (1999).

[53] S.D. Kevan and R.H. Gaylord, Phys. Rev. B **36**, 5809 (1987).

[54] M.F. Crommie, C.P. Lutz, and D.M. Eigler, Nature **363**, 524 (1993).
[55] A. Morozov and J. Kirschner, private communication
[56] H. Gollisch, T. Scheunemann, and R. Feder, to be published.
[57] D. Oberli, D. Riesen, S. Weber, and H.C Siegmann J. Mag. Mag. Mat. **198–199**, 140 (1999).

Solid-State Photoemission and Related Methods
Wolfgang Schattke, Michel A. Van Hove (Eds.)

10 One-photon two-electron transitions at surfaces

N. Fominykh, J. Berakdar[1]*, J. Henk, S. Samarin, A. Morozov, F. U. Hillebrecht, J. Kirschner, and P. Bruno*

10.1 Introduction

The theoretical description of the behaviour of N interacting electrons moving in an external field implies the solution of a complicated many-body problem. An efficient, and in many cases adequate approach to this problem of interacting fermions has been provided by the effective field approach, i. e., by considering an individual particle to move independently in an effective field created by the average interaction with other particles. The Hartree-Fock scheme and the density functional theory within the local density approximation are prominent representatives for effective field procedures [1–3], which in general yield accurate predictions for a number of properties of materials. The limitations of these approaches become however evident when strongly correlated systems are considered, e. g., transition-metal oxides and heavy Fermion compounds [1].

In this work we focus on one of the tools to assess the effects of electronic correlations and the range of validity of effective field models. Generally speaking, one can expect the effective field approximation to break down whenever the strong short-range components of the electron-electron interaction are relevant. This is because in such an approach the electrons move independently from each other. This implies that the wavefunction contains a large portion of configurations, in which two electrons are so close to each other that they are exposed to the strong repulsive electron-electron interaction. In this situation, the concept of an effective, averaged field is clearly inadequate. In the realm of many-body theory a number of methods have been proposed to deal with this kind of correlation effects. Here we mention the Brueckner hole-line expansion [4–6], the 'exponential S' or coupled cluster method [7, 8], quantum Monte-Carlo techniques [9, 10], and the Green's function method which we shall employ in the following. All these methods provide correlated many-body wavefunctions that account for the details of the inter-particle interaction. At the same time, the question arises which kind of experimental techniques are suitable to expose the effect of the short-distance electron-electron interaction and to assess the range of validity of various theoretical models.

To show the effect of correlation in a heuristic way let us consider the case of an infinite, homogeneous electron gas: The mean-field wavefunction is then a Slater determinant built out of plane-wave states, labeled by wavevectors $\boldsymbol{k}_i$. All single-particle states with k_i smaller than the Fermi wavenumber k_F are occupied. Including correlations in this uncorrelated state leads to a partial depletion of some single-particle states with $k_i < k_\mathrm{F}$ and a nonvanishing occu-

[1] Corresponding author.

Solid-State Photoemission and Related Methods: Theory and Experiment. Edited by Wolfgang Schattke, Michel A. Van Hove

ISBN: 3-527-40334-5

pation of some states with higher wavenumbers. This simple example illustrates that a study of the high-momentum components in the single-particle wavefunctions has the potential to uncover the effects of short-range correlations. A way to investigate experimentally the high-momentum components is offered by measuring the coincident spectrum for the electron-pair emission upon electron impact, i. e., the (e,2e) experiment (one electron in, two electrons out). This kind of studies is reviewed by Feder and Gollisch in this book [11]. Another spectroscopic method for electronic correlation is the coincident, photon-induced electron-pair emission (γ,2e). This technique is even more sensitive to the effects of correlations than (e,2e) experiments. In fact, it can be shown that the cross section for (γ,2e) vanishes in absence of correlations [12]. Experimentally, the realization of the (γ,2e) process at surfaces has long been a challenge due to the low count rates (compared to single electron emission) which is inherent to coincidence studies. First experiments with a momentum resolution of the photoelectrons have been reported in Refs. [13, 14]. For atomic, molecular and nuclear matter the multi-particle coincidence technique is well established and has yielded a wealth of important information on the many-particle excitation dynamics. This information has been used to test various many-body theories (for recent reviews we refer to [15–20]). In this article we extend this multi-particle spectroscopy to solids and surfaces. A brief account is given on the theoretical and the experimental status of the photo-induced two-electron emission from surfaces. The formal theory and the current numerical implementations will be discussed and the results for the angular and the energy-correlation functions of the two photoelectrons will be presented and compared with presently available experimental data.

10.2 General considerations

This section provides the formal theoretical foundations and the calculational ingredients needed for a theoretical description of the (γ,2e) process. We also point out relation between the (γ,2e) and the (e,2e) reactions. There are a number of theoretical tools to deal properly with electronic correlations, however most of them, like the hole-line expansion and the coupled-cluster methods [3, 21], are restricted to deal with ground-state properties. An appropriate framework for the treatment of (γ,2e) and (e,2e), which involves correlated excited states, is provided by the Green's function approach. This method offers an access to dynamic properties like, e. g., the single- and the two-particle spectral functions which are closely related to the cross section of single and two-particle emission [as produced by (e,2e) and (γ,2e) processes]. A general description of the Green's function approach can be found in various textbooks [21–25]. Here we focus on the aspects which are of immediate relevance to (γ,2e) and (e,2e).

10.2.1 The single-particle Green's function

The single-particle Green's function $g(\alpha t, \beta t')$ can be considered as an expectation value for the time-ordered product of two operators evaluated with respect to the correlated, exact ground-state $|\Psi_0\rangle$ of the N electron system (we assume $|\Psi_0\rangle$ to be properly normalized):

$$\mathrm{i}\, g(\alpha t, \beta t') = \langle \Psi_0 | \mathcal{T}[a_{\mathrm{H}\alpha}(t)\, a^{\dagger}_{\mathrm{H}\beta}(t')] | \Psi_0 \rangle, \tag{10.1}$$

where $\mathcal{T}$ is the time ordering operator. $a^\dagger_{\mathrm{H}\beta}(t')$ and $a_{\mathrm{H}\alpha}(t)$ stand respectively for the fermionic creation and annihilation operators in the Heisenberg picture represented in an appropriate basis, the members of which characterized by quantum numbers α and β. For a translationally invariant system, the appropriate basis states are the momentum eigenstates. The effect of the chronological operator $\mathcal{T}$ can be described in terms of the step function $\Theta(t-t')$, in which case the Green's function is given by

$$\begin{aligned} \mathrm{i}g(k,t-t') &= \Theta(t-t')\langle\Psi_0|a_{\mathrm{H}k}(t)a^\dagger_{\mathrm{H}k}(t')|\Psi_0\rangle \\ &\quad - \Theta(t'-t)\langle\Psi_0|a^\dagger_{\mathrm{H}k}(t')a_{\mathrm{H}k}(t)|\Psi_0\rangle \\ &= \Theta(t-t')\sum_\gamma e^{-\mathrm{i}\left[E^{(N+1)}_\gamma - E^{(N)}_0\right](t-t')}\left|\langle\Psi^{(N+1)}_\gamma|a^\dagger_k|\Psi_0\rangle\right|^2 \\ &\quad - \Theta(t'-t)\sum_\delta e^{-\mathrm{i}\left[E^{(N)}_0 - E^{(N-1)}_\delta\right](t-t')}\left|\langle\Psi^{(N-1)}_\delta|a_k|\Psi_0\rangle\right|^2 . \end{aligned} \tag{10.2}$$

In this equation, $\Psi^{(N+1)}_\gamma$ and $\Psi^{(N-1)}_\delta$ denote a complete set of eigenstates of the $(N+1)$- and the $(N-1)$-particle system, respectively. The energies $E^{(N)}_0$, $E^{(N+1)}_\gamma$, and $E^{(N-1)}_\delta$ refer to the exact energies for the correlated ground state of respectively the N-, the $(N+1)$-, and the $(N-1)$-particle system. The exponential with the energies in Eq. (10.2) is due to the Hamiltonians in the exponential functions in the definition of the Heisenberg operators.

Noting that the step function has the integral representation

$$\Theta(t) = -\lim_{\eta\to 0}\frac{1}{2\pi\mathrm{i}}\int_{-\infty}^{\infty}\mathrm{d}\omega\frac{e^{-\mathrm{i}\omega t}}{\omega+\mathrm{i}\eta}, \tag{10.3}$$

the Green's function in energy space can be obtained via Fourier transforming the time difference $t-t'$ to the energy variable ω. This yields the spectral or Lehmann representation of the single-particle Green's function [26],

$$\begin{aligned} g(k,\omega) = \lim_{\eta\to 0}\Bigg[&\sum_\gamma\frac{\left|\langle\Psi^{(N+1)}_\gamma|a^\dagger_k|\Psi_0\rangle\right|^2}{\omega-[E^{(N+1)}_\gamma - E^{(N)}_0]+\mathrm{i}\eta} \\ &+\sum_\delta\frac{\left|\langle\Psi^{(N-1)}_\delta|a_k|\Psi_0\rangle\right|^2}{\omega-[E^{(N)}_0 - E^{(N-1)}_\delta]-\mathrm{i}\eta}\Bigg]. \end{aligned} \tag{10.4}$$

Relation (10.4) points out that the single-particle Green's function is representable in terms of measurable quantities: The poles of $g(k,\omega)$ correspond to the change in energy (with respect to $E^{(N)}_0$) if one particle is added ($E^{(N+1)}_\gamma - E^{(N)}_0$) or one particle is removed ($E^{(N)}_0 - E^{(N-1)}_\delta$) from the reference ground state with N interacting particle. The residua of these poles are given by the *spectroscopic factors*, i. e., the measurable probabilities of adding and removing one particle with wavevector $\boldsymbol{k}$ to produce the specific state γ (δ) of the residual system. Clearly, the latter probability is of a direct relevance to the (e,2e) process. The infinitesimal

quantity η in Eq. (10.4) shifts the poles below the Fermi energy [the states of the $(N-1)$ system] to slightly above the real axis and those above the Fermi energy [the states of the $(N+1)$ system] to slightly below the real axis.

It is customary to write the spectral representation of the single-particle Green's function in terms of the hole and particle spectral functions that are defined as

$$\begin{aligned} S_{\mathrm{h}}(k,\omega) &= \frac{1}{\pi}\operatorname{Im} g(k,\omega), \quad \text{for } \omega \le \epsilon_{\mathrm{F}} \qquad (10.5)\\ &= \sum_{\gamma} \left| \langle \Psi_{\gamma}^{(N-1)} | a_k | \Psi_0 \rangle \right|^2 \delta\big(\omega - (E_0^{(N)} - E_{\gamma}^{(N-1)})\big), \\ S_{\mathrm{p}}(k,\omega) &= \frac{1}{\pi}\operatorname{Im} g(k,\omega), \quad \text{for } \omega > \epsilon_{\mathrm{F}} \\ &= \sum_{\gamma} \left| \langle \Psi_{\gamma}^{(N+1)} | a_k^{\dagger} | \Psi_0 \rangle \right|^2 \delta\big(\omega - (E_{\gamma}^{(N+1)} - E_0^{(N)})\big). \qquad (10.6) \end{aligned}$$

The single-particle Green's function is then written as

$$g(k,\omega) = \lim_{\eta \to 0} \left(\int_{-\infty}^{\epsilon_{\mathrm{F}}} \mathrm{d}\omega' \frac{S_{\mathrm{h}}(k,\omega')}{\omega - \omega' - \mathrm{i}\eta} + \int_{\epsilon_{\mathrm{F}}}^{\infty} \mathrm{d}\omega' \frac{S_{\mathrm{p}}(k,\omega')}{\omega - \omega' + \mathrm{i}\eta} \right). \qquad (10.7)$$

The single-particle Green's function is particularly important since it establishes a direct link to experimental processes that study the effect of a removal or an addition of a particle to the correlated system. As mentioned above, the (e,2e) process is related to the hole spectral function. In addition, the Green's function allows the evaluation of the expectation value for *any* single-particle operator $\hat{O}$ (this is because $\langle \hat{O} \rangle = \sum_{\alpha\beta} \int_{-\infty}^{E_{\mathrm{F}}} \mathrm{d}\omega S_{\mathrm{h}}(\alpha\beta,\omega) \langle \alpha | O | \beta \rangle$ where $\langle \alpha | O | \beta \rangle$ is the matrix representation of $\hat{O}$ in the basis $|\alpha\rangle$). This in turn highlights the importance of single-particle removal or addition spectroscopies, such as single photoemission [27, 28] and (e,2e) processes, which allow insight into the respective part of the Green's function. A further advantage of the Green's function approach is that it offers a systematic way for approximations using the diagram technique [23]. In the diagrammatic expansion for g one introduces the concept of the self-energy Σ [29]. The knowledge of Σ allows the evaluation of g according to the Dyson equation

$$g(\alpha\beta;\omega) = g_0(\alpha\beta;\omega) + \sum_{\gamma\,\delta} g_0(\alpha\gamma;\omega)\, \Sigma(\gamma\delta;\omega)\, g(\delta\beta;\omega), \qquad (10.8)$$

where g_0 is the Green's function of a (noninteracting) reference system. The self-energy Σ accounts for all excitations due to the interaction of the particle with the surrounding medium and acts as a nonlocal, energy-dependent, and complex single-particle potential.

10.2.2 The two-particle Green's function

As discussed in detail in Ref. [23], the Dyson equation (10.8) can be derived algebraically and the single particle propagator $g(\alpha t, \alpha' t')$ can be related to the two particle Green's function $g^{\mathrm{II}}(\beta t_1, \beta' t_1', \gamma t_2, \gamma t_2')$. This is a first cycle in a hierarchy that links the N-particle propagator

to the $(N+1)$-particle propagator [30,31]. Of direct relevance to this work is the two-particle propagator $g^{\mathrm{II}}(\beta t_1, \beta' t_1', \gamma t_2, \gamma t_2')$.

Repeating the steps outlined above for the single particle case, one arrives at the Lehmann representation of the two-particle Green's function in terms of energies and states of the systems with N and $N \pm 2$ particles [the $(N-2)$-particle state of the system is achieved upon a (γ,2e) reaction]:

$$\begin{aligned} g^{\mathrm{II}}(\alpha\beta, \gamma\delta; \Omega) = & \sum_n \frac{\langle \Psi_0^{(N)} \mid a_\beta a_\alpha \mid \Psi_n^{(N+2)} \rangle \langle \Psi_n^{(N+2)} \mid a_\gamma^\dagger a_\delta^\dagger \mid \Psi_0^{(N)} \rangle}{\Omega - \left[E_n^{(N+2)} - E_0^{(N)}\right] + \mathrm{i}\eta} \\ & - \sum_m \frac{\langle \Psi_0^{(N)} \mid a_\gamma^\dagger a_\delta^\dagger \mid \Psi_m^{(N-2)} \rangle \langle \Psi_m^{(N-2)} \mid a_\beta a_\alpha \mid \Psi_0^{(N)} \rangle}{\Omega - \left[E_0^{(N)} - E_m^{(N-2)}\right] - \mathrm{i}\eta}. \end{aligned} \tag{10.9}$$

Upon analogous considerations made for the one particle case to arrive at the single particle spectral functions, Eqs. (10.5) and (10.6), one can obtain from g^{II} the hole-hole spectral function as $S_{\mathrm{hh}}(\boldsymbol{k}_1, \boldsymbol{k}_1, \Omega) = \mathrm{Im}\, g^{\mathrm{II}}(\boldsymbol{k}_1, \boldsymbol{k}_1, \Omega)$, $\Omega \leq 2\epsilon_{\mathrm{F}}/\pi$ which is intimately related to the (γ,2e) reaction.

The two-particle Green's function involves two kinds of diagrams: The first type includes two noninteracting single-particle propagators [cf. Eq. (10.8)] and is supplemented by similar diagrams that include all possible self-energy insertions [21]. The second defines the vertex function Γ. The latter involves all generalization of the lowest-order correction to the two-particle propagator in which two particles interact once. To visualize the role of Γ we write g^{II} in the form [21]

$$\begin{aligned} & g^{\mathrm{II}}(\alpha t_1, \alpha' t_1', \beta t_2, \beta' t_2') \\ & \quad = \mathrm{i}\big[g(\alpha\beta, t_1 - t_2)\, g(\alpha'\beta', t_1' - t_2') - g(\alpha\beta', t_1 - t_2')\, g(\alpha'\beta, t_1' - t_2)\big] \\ & \qquad \times \int \mathrm{d}t_a\, \mathrm{d}t_b\, \mathrm{d}t_c\, \mathrm{d}t_d \sum_{abcd} g(\alpha\, a, t_1 - t_a)\, g(\alpha'\, b, t_1' - t_b) \\ & \qquad \times \langle ab|\Gamma(t_a, t_b; t_c, t_d)|cd\rangle\, g(c\,\beta, t_c - t_2)\, g(d\,\beta', t_d - t_2'). \end{aligned} \tag{10.10}$$

From this equation it is clear that Γ can be considered as the effective interaction between dressed particles. In addition, Γ plays a decisive role in the determination of its single-particle counterpart, the self-energy Σ [21].

In energy-space, the result for the noninteracting (free) product of dressed propagators including the exchange contribution, i. e., the zero-order term of Eq. (10.10) with respect to Γ, reads

$$\begin{aligned} g_{\mathrm{f}}^{\mathrm{II}}(\alpha\beta, \gamma\delta; \Omega) = & \frac{\mathrm{i}}{2\pi} \int \mathrm{d}\omega \big[g(\alpha, \gamma; \omega)\, g(\beta\,\delta; \Omega - \omega) - g(\alpha, \delta; \omega)\, g(\beta\,\gamma; \Omega - \omega)\big] \\ = & \sum_{mm'} \frac{\langle \Psi_0^{(N)}|a_\alpha|\Psi_m^{(N+1)}\rangle \langle \Psi_m^{(N+1)}|a_\gamma^\dagger|\Psi_0^{(N)}\rangle \langle \Psi_0^{(N)}|a_\beta|\Psi_{m'}^{(N+1)}\rangle \langle \Psi_{m'}^{(N+1)}|a_\delta^\dagger|\Psi_0^{(N)}\rangle}{\Omega - \left\{[E_m^{(N+1)} - E_0^{(N)}] + [E_{m'}^{(N+1)} - E_0^{(N)}]\right\} + \mathrm{i}\eta} \\ - & \sum_{nn'} \frac{\langle \Psi_0^{(N)}|a_\gamma^\dagger|\Psi_n^{(N-1)}\rangle \langle \Psi_n^{(N-1)}|a_\alpha|\Psi_0^{(N)}\rangle \langle \Psi_0^{(N)}|a_\delta^\dagger|\Psi_{n'}^{(N-1)}\rangle \langle \Psi_{n'}^{(N-1)}|a_\beta|\Psi_0^{(N)}\rangle}{\Omega - \left\{[E_0^{(N)} - E_n^{(N-1)}] + [E_0^{(N)} - E_{n'}^{(N-1)}]\right\} + \mathrm{i}\eta} \\ - & \quad (\gamma \longleftrightarrow \delta). \end{aligned} \tag{10.11}$$

The integration over ω has been carried out by utilizing the Lehmann representation for the single-particle Green's functions. The ladder approximation to the two-particle propagator is then given by:

$$g_{\mathrm{L}}^{\mathrm{II}}(\alpha\beta,\gamma\delta;\Omega) = g_{\mathrm{f}}^{\mathrm{II}}(\alpha\beta,\gamma\delta;\Omega) + \frac{1}{4}\sum_{\epsilon\eta\theta\zeta} g_{\mathrm{f}}^{\mathrm{II}}(\alpha\beta,\epsilon\eta;\Omega)\langle\epsilon\eta|V|\theta\zeta\rangle g_{\mathrm{L}}^{\mathrm{II}}(\theta\zeta,\gamma\delta;\Omega), \tag{10.12}$$

where V stands for the naked two-body interaction. This integral relation can now be iterated to yield a set of a ladder diagrams. The corresponding ladder sum for the effective interaction Γ , as it appears in [cf. Eq. (10.10)] can be deduced from this result as

$$\langle\alpha_1,\beta_2|\Gamma_{\mathrm{L}}(\Omega)|\alpha_1',\beta_2'\rangle = \langle\alpha_1\,\beta_2|V|\alpha_1'\,\beta_2'\rangle + \frac{1}{4}\sum_{\epsilon\eta\theta\zeta}\langle\alpha_1\,\beta_2|V|\epsilon\,\eta\rangle g_{\mathrm{f}}^{\mathrm{II}}(\epsilon\,\eta,\theta\,\zeta;\Omega)\langle\theta,\zeta|\Gamma_{\mathrm{L}}(\Omega)|\alpha_1',\beta_2'\rangle. \tag{10.13}$$

The analogous operators to $g_{\mathrm{L}}^{\mathrm{II}}$ and $\Gamma_{\mathrm{L}}(\Omega)$ in absence of the surrounding medium (e. g., as is the case in a dilute gaseous system) are the Green function G and the transition operator T which have been utilized to study multiple ionization of gaseous atomic and molecular targets upon photon and particle impact [32, 33].

As noticed above, g^{II} is of a direct relevance to the (γ,2e) reaction. It should be noted however that the ladder approximation (10.12) for the two-particle Green's function can be employed to define the self-energy Σ [23, 31] which can then be used to obtain the single-particle Green's function via Eq. (10.8). On the other hand, this Green's function enters in the definition of the two-particle Green's function, as clear, e. g., from Eqs. (10.11), (10.12). Thus in principle, the Dyson Eqs. (10.8) and (10.12) for the one-body and two-body Green's functions have to be solved in a self-consistent manner.

As in the single particle case where we established the relevance of the spectral representation to the (e,2e) experiments, one can relate g^{II} to the (γ,2e) measurements by means of Eq. (10.9): g^{II} shows poles at energies (relative to the ground state) corresponding to adding $[E_n^{(N+2)} - E_0^{(N)}]$ or removing $[E_0^{(N)} - E_n^{(N-2)}]$ two particles from the unperturbed ground state. The residua of these poles are related to the measurable spectroscopic factors for the addition or removal of the two particles, e. g., as done in a (γ,2e) experiment. From the above discussion we conclude thus that (γ,2e) and (e,2e) provide quite different information. On the other hand they are related in as much as the single-particle and the two-particle spectral functions are related to each other.

10.3 Photo-induced double-electron emission

Before we implement the expressions in the preceding section into a calculational scheme for the evaluation of the coincident (γ,2e) signal, it is useful to discuss the experimental conditions and limitations.

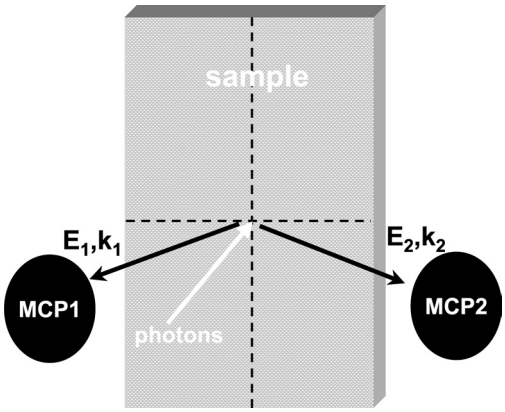

Figure 10.1: The schematic view of the experimental arrangement. The photon beam from the synchrotron source impinges under normal incidence onto the sample, and electron pairs ejected from the sample are detected by two channel-plate assemblies. The center axes of the two detectors are at 40° to the light incidence direction. The sample may be rotated about an axis within its surface, normal to the plane of light and detector axes.

10.3.1 Experimental details

Since double photoemission has a much smaller cross section than single photoemission, detectors with a large acceptance are needed. The method of choice is a time-of-flight technique which allows for a large acceptance both geometrically and in terms of electron energy [13]. By determining the electron energy from the time required by the electron to travel the distance from sample to detector, the large acceptance is achieved without compromising on the energy resolution. In our experiment, we use two time-of-flight spectrometers to detect pairs of electrons ejected from the sample by absorption of one photon (cf. Fig. 10.1). Each detector consists of a pair of 75 mm channel-plates with position sensitive detection via a resistive anode. The detectors are at a distance of 160 mm from the sample, the two detector axes are at $\pm 40^\circ$ with the light axis. Position sensitive detection is necessary to avoid energy broadening caused by different electron flight distances to the center or edge of the detectors.

Time-of-flight techniques require a pulsed photon source. Pulsed UV photon beams are provided by synchrotron radiation sources, therefore the experiments shown here were performed in the single bunch mode of the electron storage ring BESSY I in Berlin. The repetition frequency of the storage ring in the single bunch mode is 5 Mhz, i.e. the time between two light pulses is 200 ns, and their width is about 0.6 ns. To keep the accidental coincidence rate below or comparable to the real coincidence rate, the mean beam intensity was adjusted such that on average there was less than one photon per bunch.

To obtain the time-of-flight spectrum, the time difference between the photon bunch marker signal delivered by the synchrotron and a fast timing signal provided any of the channel-plate detectors was measured by time-to-amplitude conversion. The overall time resolution achieved in both channels was about 1.2 ns. This yielded an energy resolution of the detected electrons ranging from 0.1 eV for $E_{kin} = 5$ eV to 3.15 eV for $E_{kin} = 50$ eV. The fast timing signals from both detectors were passed to an electronic time-coincidence condition, ensuring that only those events were registered in which two electrons reached the detectors within a time window of 200 ns. As the number of photons per bunch is distributed according to Poisson statistics, a certain number of bunches contained more than one photon. Thus, in addition to correlated electron pairs, one normally detects a background of uncorrelated electrons, i.e., electron pairs generated by two different photons within one bunch. In our experiments this

background was about 15% of the true coincidence rate. For subtracting this contribution from the coincidence spectra, we measured separate background runs by increasing the coincidence window from 200 ns to 1 ms, such that essentially only uncorrelated electron pairs generated by different photon bunches were detected. Before subtraction, the coincidence and background runs were normalized on the integrated single photoemission yield of both runs.

Because of the small escape depth of low energy electrons, the probing depth in an experiment involving the detection of two electrons may be expected to be below 5 monolayers for the energies considered here. Samples are prepared in the usual way by sputtering and annealing of bulk single crystals, sample cleanliness is determined by Auger spectroscopy. The small probing depth allows to investigate materials in the form of thin films deposited on a substrate, which can be considered as representative for the surface of a bulk crystal.

10.3.2 Pathways for the electron-pair emission

For the kind of photons specified in the experimental section, we can treat the electromagnetic field classically and employ the dipole approximation, as shown in detail in Ref. [12]. The electric dipole operator is a sum over single-particle operators. Hence, the photon can be absorbed only by one electron. The other electrons which are emitted in the course of this process have to interact in some way with the photo-excited electron. This is the underlying reason why double photoelectron emission is so sensitive to electronic correlation. In Fig. 10.2 we show the leading Feynman diagrams for the DPE process: In Fig. 10.2(a-b) the two-electron scattering takes place in the initial state (i. e., prior to the photon absorption) via the effective particle-particle interaction. In addition, the photon can excite a collective mode of the system which then decays into two electrons, as schematically shown in Fig. 10.2 (c). Other types of correlations that induce a DPE signal are termed final-state interactions (FSI) [Fig. 10.2(d,e)]. As schematically shown in Fig. 10.2(d,e), one of the ground-state electrons absorbs the photon and then scatters from a second electron. The latter scattering is mediated also by the effective electron-electron interaction. A further important channel for DPE is depicted in Fig. 10.2(f) where one electron absorbs the photon just like in single photoemission (SPE) and undergoes a series of collisions with the crystal potential and with other electrons until it has lost coherence with its initial phase. This photoelectron then scatters from another electron into a two-electron vacuum state. Therefore, the process shown in Fig. 10.2(f) can be considered as product of independent events (cross sections): a single photoemission process followed by an (e,2e) scattering. There is a series of additional diagrams, in particular a combination of the processes represented by Fig. 10.2(a,b) and Fig. 10.2(d,e), i. e., process where the two electrons interact in the initial and the final states. In principle, a division between initial and final state correlation is only a matter of semantics as far as the (γ,2e) process is concerned, as demonstrated by the diagrams in Fig. 10.2(a,b) and Fig. 10.2(d,e): The difference between collisions taking place in the initial or final state is in the time ordering of the electron-electron interaction and the absorption process. This ordering is however of no relevance for the two-photoelectron current $\mathcal{J}$ whose derivation involves an integration over time. In fact, as derived in Ref. [34] $\mathcal{J}$ has the form

$$\mathcal{J} \propto \langle \boldsymbol{k}_1, \boldsymbol{k}_2 | g^{\mathrm{IIr}}\, \Delta\, S^{\mathrm{II}}_{\mathrm{hh}}(\boldsymbol{k}'_1, \boldsymbol{k}'_2, E)\, \Delta^{\dagger}\, g^{\mathrm{IIa}} | \boldsymbol{k}_1, \boldsymbol{k}_2 \rangle, \tag{10.14}$$

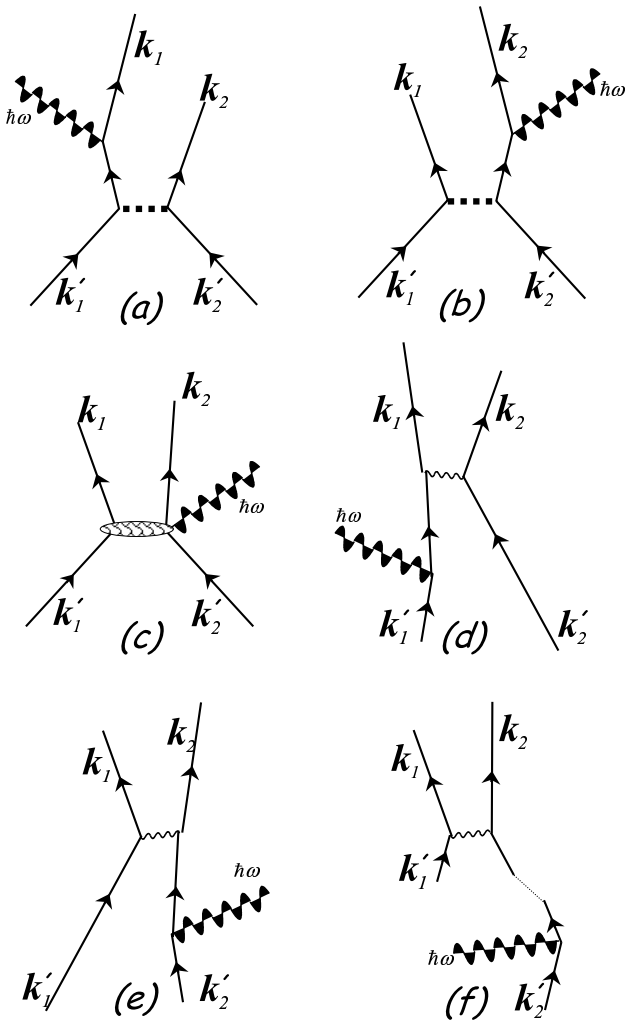

Figure 10.2: The lowest-order Feynman diagrams that contribute to the photo-induced generation of electron-pairs with asymptotic wave vectors $\boldsymbol{k}_1$ and $\boldsymbol{k}_2$. The crystal momenta of the two initially bound electrons are denoted by $\boldsymbol{k}_1'$ and $\boldsymbol{k}_2'$. The thick dotted line indicates an interaction between the electron mediated by the effective electron-electron interaction in the medium whereas the wiggly line symbolize the electron-electron final-state interaction. The photon is indicated by its energy $\hbar\omega$. In inset (c) the photon excites both the electron pair and collective modes of the system. The dotted line in (f) means that the single photoemission process and the subsequent electron-electron scattering take place in two steps and therefore these two processes are incoherent.

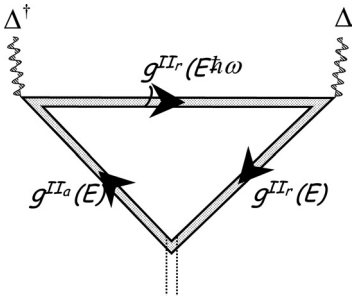

Figure 10.3: Diagrammatic representation of the photocurrent expression Eq. (10.14). Wavy lines represent the photon, double straight lines with arrows correspond to the retarded and advanced two-particle Green's functions as indicated on the plots. The double dashed line symbolizes the electrons emitted into the vacuum.

where Δ is the dipole operator, $S^{\mathrm{II}}_{\mathrm{hh}}$ is the hole-hole spectral function, and g^{IIa} (g^{IIr}) is the advanced (retarded) two-particle Green's function.

Similar to the case of single photoemission, the photocurrent can be represented by the two-particle Caroli diagram, as shown in Fig. 10.3, which explicitly shows no signature of time ordering. On the other hand, one can tune to initial or final state correlation by choice of the wave vectors that appear in the current expression Eq. (10.14): If $\boldsymbol{k}_1$ and $\boldsymbol{k}_2$ are very large (compared to the Fermi wave vector), one can expect the final-state interactions to be limited to a small region in phase space where the two electrons escape with almost the same velocities. Apart from this regime, FSI become less important which allows to highlight the effect of initial-state correlations. On the other hand, if the two electrons escape with very low (vacuum) velocities, FSI become the determining factor. These statements will be illustrated below with numerical examples.

10.4 Numerical realization and experimental results

As is clear from Eq. (10.14), the evaluation of g^{II} is the key ingredient for the numerical evaluation of the two-photoelectron current. On the other hand, we have seen in the preceding section that the single-particle Green's function g is needed to obtain g^{II}, and in turn g^{II} goes into the determination of g. Till now this self-consistent loop has been too complicated to be realized numerically within a realistic description of the surface, i. e., for an inhomogeneous electron gas. In fact, the exact evaluation of the generally valid Eq. (10.14) is still an open question even for a system of few interacting charged particles, such as a few-electron atom. This kind of systems is currently subject of active research, with DPE being the principle tool to uncover the effect of particle-particle correlations and to test the validity of various numerical suggestions for the evaluation of Eq. (10.14). For a recent reviews on this topic, we refer to Refs. [15–19]. In the present case, we need to account for the few-particle scattering in the presence of the surrounding inhomogeneous system of electrons.

10.4.1 Simple model calculations

The effect of the medium on the electron-electron interaction V can be estimated for the case of a semi-infinite homogeneous electron gas in the long-wavelength regime (Thomas-Fermi

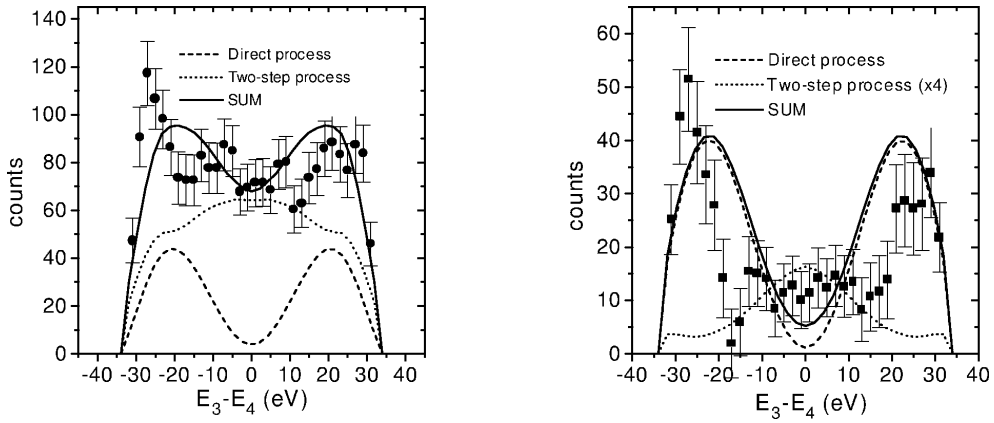

Figure 10.4: (γ,2e) energy-sharing distributions from Cu(001) (left-hand panel) and Ni(001) (right-hand panel) due a 45 eV photon incident normal to the surface. The experimental data ([13, 14]) are for electron pairs with sum energies $E_1 + E_2$ between 33 eV and 35 eV. The two photoelectrons are emitted at 40° symmetrically to the left and to the right of the surface normal. The theoretical curves show the coherent contributions from the diagrams depicted in Fig. 10.2(d,e) (dashed lines) whereas the dotted line indicate the results for the cross section obtained from the process shown in Fig. 10.2(f) (for the Cu case the dotted curve has been scaled up by a factor of 4 for visibility). The solid line is the summed cross section, i.e. the incoherent sum of the dotted and dashed lines.

limit). In this case, V is well described by the modified, local potential U where [35]

$$U = \frac{\mathrm{e}^{-(|\boldsymbol{r}_1 - \boldsymbol{r}_2|)/\lambda}}{|\boldsymbol{r}_1 - \boldsymbol{r}_2|}. \tag{10.15}$$

Here, $\boldsymbol{r}_1 - \boldsymbol{r}_2$ is the relative distance between the two electrons. The screening length λ is related to density of states at the Fermi level. With the electron-electron interaction potential, the first order term in the ladder approximation for g^{II} has been employed and the photocurrent has been evaluated taking into account the diagrams shown in Fig. 10.2 (d,e,f) [cf. Eqs. (10.12) and 10.14]. It should be stressed here that the diagrams Fig. (10.2) (d,e,f) should be calculated within the same model, in which case the relative contributions of each of these processes can be determined.

Figure 10.4 shows measured and calculated two-electron energy correlation functions. The two electrons have a fixed total energy of 35 eV this energy is chosen such that the two electrons are emitted from the vicinity of the (two-particle) Fermi level. Results are shown for the (001) surfaces of Cu and Ni. The material properties within the theory enters via the density of state which determines the screening length and via the characteristics of the surface potentials. As shown in Ref. [12], the present model predicts that the two-photoelectron current can be cast into the form $\hat{\boldsymbol{\epsilon}} \cdot (\boldsymbol{k}_1 + \boldsymbol{k}_2)\, L$, where L is a complicated function of the electrons' wave vectors and energies. $\hat{\boldsymbol{\epsilon}}$ is the polarization vector of the light. Hence, for $\boldsymbol{k}_1 = -\boldsymbol{k}_2$ or for $\hat{\boldsymbol{k}}_1 \perp \hat{\boldsymbol{\epsilon}} \perp \hat{\boldsymbol{k}}_2$ the cross section vanishes. This is the origin of the minima for equal

energy sharing, as observed in Fig. 10.4. This figure also indicates that the diagrams shown in Fig. 10.2(f) and Fig. 10.2(d,e) deliver comparable contributions to the total current, which is comprehensible, as all of these diagrams involve the same order of the electron-electron and electron-photon interactions.

10.4.2 Numerical scheme with a realistic single-particle band structure

To improve on the above two-particle interacting jellium model, while taking into account the electron-electron interaction explicity and treating the two photoelectrons on equal footing, we proceed as follows: If we assume the two photoelectrons to be independent, then, according to Eq. (10.12), the two-particle Green's function g^{II} reduces to $g^{\mathrm{II}} = g_{\mathrm{f}}^{\mathrm{II}}$. This means g^{II} simplifies to an anti-symmetrized product of single-particle Green's function $g_j(\boldsymbol{k}_i, E_i)$, $i = 1, 2$, which can be used to generate the single-photoelectron states. Employing the one-step model for photoemission we can then calculate the single-photoelectron current. Our approach towards this single-particle problem is based on the layer Korringa-Kohn-Rostoker (LKKR) method which utilizes a density-functional approach combined with an empirical function for the complex part of the self-energy. This single-particle part of the problem is essentially the same as in the case of as in single photoemission [36, 37] and (e,2e) which has been reviewed in details in the chapter by Feder and Gollisch of this volume. Therefore we focus here on how the two independent photoelectron currents can be coupled to evaluate a finite two-electron photocurrent $\mathcal{J}$ (we recall that $\mathcal{J}$ vanishes in absence of correlations].

For this purpose, we utilize the interaction potential U, defined by Eq. (10.15), as a starting point and rewrite it in the following form:

$$U = \frac{Z_1}{r_1} + \frac{Z_2}{r_2} \qquad \text{with} \qquad Z_j = a_j^{-1} \exp\left(-\frac{2a_j}{\lambda} r_j\right), \qquad j = 1, 2. \tag{10.16}$$

In these relations, we have introduced the functions $a_j = r_{12}/(2r_j)$. Equation (10.16) can be interpreted in the following way: The effect of the electron-electron interaction potential can be viewed as a modification Z_j/r_j to the single-particle potentials. This means that the inter-electronic correlation is subsumed into a dynamic nonlocal screening interaction w_j of the electron with the lattice. The behaviour of this screening is dictated by the functions Z_j, and has the following features: When the two electrons are on top of each other ($r_{12} \to 0$) the potential w_j turns repulsive as to simulate the strong, short-range electron-electron repulsion. If the two electrons are far away from each other ($r_i \gg r_j$, $i \neq j \in [1, 2]$), the screening strengths Z_1 and Z_2 become negligible and we end up with two independent particles. It should be stressed that, within our model, the dynamic screening as introduced in Eq. (10.16) is exact, since we merely performed rearrangements of the interactions involved in Eq. (10.15). Hence, the evaluation of the two-photoelectron current will face the same problems as when Eq. (10.15) is utilized. To circumvent the numerical difficulties we approximate the dynamical screening strengths Z_j by $\bar{Z}_j$ where $\bar{Z}_j = \bar{a}_j^{-1} \exp(-2\bar{a}_j r_j/\lambda)$ and $\bar{a}_j = k_{12}/(2k_j)$. Here $\boldsymbol{k}_{12} = \boldsymbol{k}_1 - \boldsymbol{k}_2$ is the inter-electronic relative wave number. This approximation is valid, if, e. g., $\boldsymbol{r}_j \propto \boldsymbol{k}_j$. In other words, the *potential* (10.15) is exactly diagonalized when the particles proceed along trajectories satisfying the relation $\mathbf{r}_j \propto \boldsymbol{k}_j$, e. g., uniform orbits. With this screening being included, the modification $\bar{Z}_j/r_j$ to the original single-particle potential w_j can be taken into account and the single-particle Green's function $\bar{g}_j$ is generated. However,

in contrast to g, each $\bar{g}_j$ is dependent on the wave vectors of *both* electrons as well as on the mutual, relative wave vector of the escaping electrons. The two-particle Green's function is approximated by $\bar{g}^{\mathrm{II}}$ which is the anti-symmetrized, direct product of the modified single-particle Green's functions $\bar{g}_j$ (the first term in the ladder approximation, Eq. (10.12)). With this model reasonable results have been obtained for the (e,2e) cross sections [11, 38, 39].

10.4.3 Numerical results for the angular pair correlation in Cu(001)

We discuss in this section pilot results for the correlated two-photoelectron current from a clean Cu(001) surface. Only the diagrams shown in Fig. 10.2(d,e) have been evaluated. The ground-state potentials have been calculated self-consistently with the scalar-relativistic LMTO method. Life-time broadening of the spectra was simulated by employing a complex optical potential. The photoelectrons' current due to emission from the first 20 outermost layers was calculated. Convergence of the results with respect the maximum angular momentum, number of reciprocal lattice vectors, and accuracy of the energy integration has been achieved.

To get an insight into the profound difference between single and double-photoelectron emission, we compare in Fig. 10.5 the angular distribution of the photoelectron currents for single photoemission (labeled SPE) and the double photoemission (indicated by DPE) for an incoming s-polarized photon. The intensity variation is shown as function of the angular position of one photoelectron with 9 eV kinetic energy. The photon energy is 15.5 eV in the single photoemission case and 31 eV for double photoemission. We note that in the latter case both photoelectrons escape with the same kinetic energy of 9 eV.

In single photoemission, the point group of the surface $4mm$ is reduced to $2mm$ in the angular distribution (as indicated by the horizontal and vertical lines in Fig. 10.5) because the electric-field vector of the incident photon (which lies in a mirror plane of the surface) is not invariant under the operations C_4 and C_4^{-1}. On the other hand in double photoelectron emission, the group $2mm$ is reduced further to m (horizontal line in Fig. 10.5). This is due to the presence of the second photoelectron whose emission direction is fixed in space and is indicated on the plot by the small circle.

The influence of the correlation between the two photoelectrons is readily visible Fig. 10.5: The repulsion between the two escaping photoelectrons leads to a vanishing photoelectron current when the two electrons are close to each other. This is the origin of the *correlation hole* surrounding the fixed detector position. On the other hand, if the two electrons are far from each other, the electron-electron interaction diminishes in strength. Consequently, the two-electron current drops dramatically, for this current must vanish in absence of correlation. The interplay between these two effects leads to a 'localization' of the angular intensity distribution of one of the photoelectrons around the position of the second one, as observed in Fig. 10.5. It should be stressed that the two detected photoelectrons are not only coupled to each other via the interaction (10.15) but also to the crystal potential. Therefore, the *correlation hole* is not isotropic in space and depends sensitively on the photoelectrons' energies.

To illustrate the dependence of the *correlation hole* on the short-range components of the electron-electron interaction, we recall that the strength of the electron-electron scattering potential (10.15) is primely determined by the screening length λ, which depends on the density of state. Therefore, for the sake of demonstration, we can regard λ as a parameter and study the correlation between the two-photoelectron current and the value of λ. This is depicted

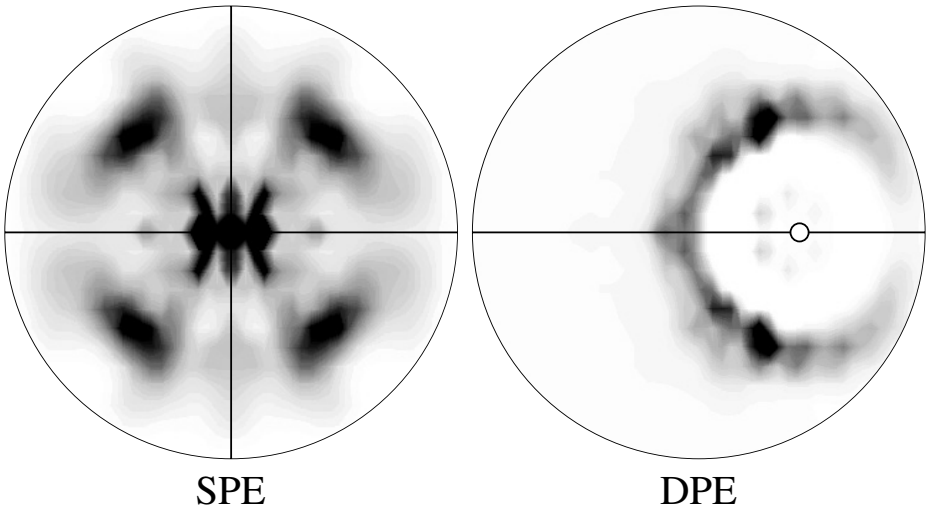

Figure 10.5: Angular distribution of the photoemission intensity from Cu(001) in single-electron (labeled SPE) and double-electron photoemission (labeled DPE). The kinetic energy of the photo-electrons is 9 eV, the photon energy of the s-polarized light 15.5 eV in the SPE case whereas in DPE the photon energy is increased to 31 eV as to compensate for the additional energy needed to emit two electrons instead of one. For the DPE case, the small circle indicates the emission direction of one of the detectors (polar angle with respect to the surface normal is $\vartheta = 40^\circ$). Low (high) intensities correspond to light (dark) gray scale in the stereographic projection. Horizontal and vertical lines emphasize the symmetries of the angular distributions.

in Fig. 10.6 which evidently shows that the correlation length λ is intimately related to the two-photoelectron current. In fact, an angular measurement of the kind shown in Fig. 10.6 can provide an estimate of the correlation length λ in the material under study.

The difference between Fig. 10.6 and Fig. 10.5 is that the photoelectrons' kinetic energies are increased from 9 eV for each electron in Fig. 10.5 to 15 eV for each electron in Fig. 10.6. As clear from the calculations shown in these figures the extent of the correlation hole shrinks considerable when the electrons' energies are increased. In fact, at extremely high energies, the two electrons interact only in a very limited region when they are emitted in the same directions and their velocities are comparable. This can be deduced directly from the interaction potential (10.16).

10.4.4 Energy-correlation functions

In the preceding section we discussed the mutual angular correlation between the two photoelectrons escaping with well-defined energies. Now, we study the energy electron-pair correlations at a fixed angular position of the emitted electrons. This is done in Fig. 10.7 where we present the two-photoelectron current from Cu(001) as a function of electrons' energies E_1, E_2 for a fixed photon energy (p-polarized light) and fixed angles of emission. Again, only

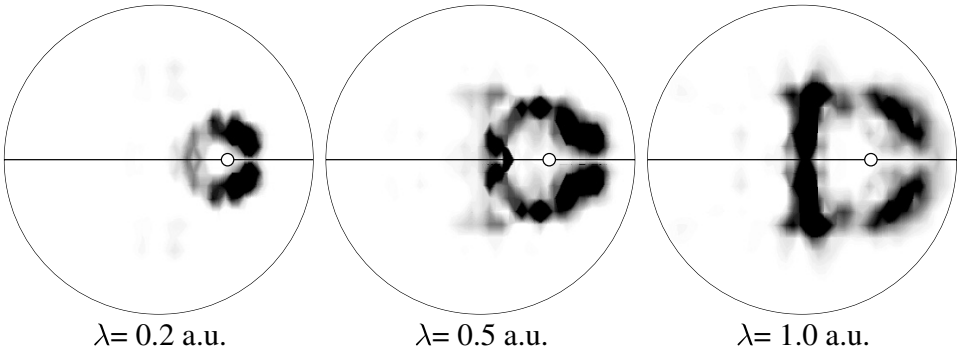

Figure 10.6: The effect of the correlation length λ on the angular distribution of the two-photoelectron current from Cu(001). The photon is s-polarized and has an energy of 45 eV. The photoelectrons have equal kinetic energies of 15 eV. The angular arrangement of the detection geometry is as in Fig. 10.5. The stereographic images show angular distributions for $\lambda = 0.2$ a. u. (left), 0.5 a. u. (middle), and 1.0 a. u. (right). The horizontal lines emphasize the mirror symmetry of the angular distributions.

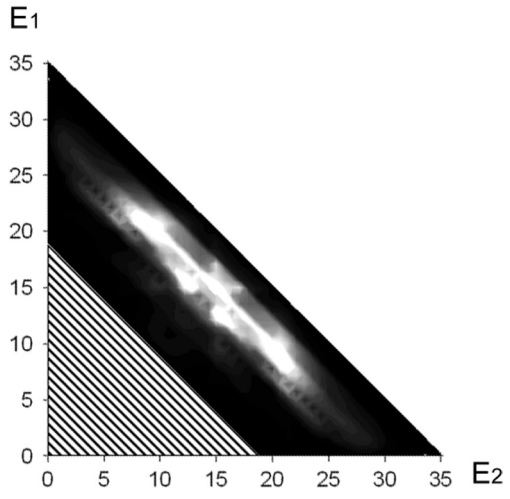

Figure 10.7: The two-photoelectron current as a function of energies E_1, E_2 of the two photoelectrons. Black and white contrasts correspond to low and high intensities, respectively. The emission angles of the electrons are fixed at $\theta = 30^\circ$ symmetrically to the left and right of the surface normal. The photon energy is $\omega = 45$ eV. The shaded triangle indicates the region below the bottom of the conduction band.

the diagrams depicted in Fig. 10.2 (d,e) have been taken into account. As in the case of the angular distribution, we notice that the photoelectron current is appreciable in the region where the two electrons can interact efficiently. According to our interaction potential (10.16), this is the case when the two electrons do not differ too much in their kinetic energies. This is reflected in the behaviour of the photoelectrons current as observed in Fig. 10.7.

From Fig. 10.7 we also notice that the photoelectron current (white region) originates basically from the energy region $E_1 + E_2 = E = 25 \cdots 35$ eV, where E is the total kinetic energy of the pair. From energy conservation it is readily concluded that this energy interval corresponds to the d-band of copper ($\approx$3 eV band below the Fermi level) from which the initial state electrons originate mostly; only a negligible fraction of electron pairs are emitted in the

region $E < 25$ eV and in the narrow black band just below the line marked by the $E = 35$ eV. This is due to the low density of the initial states in these configurations. It should be noted in this context that in Fig. 10.7 we basically scan the two-photoelectron current through the conduction band starting at the Fermi level (correspond to $E \approx 35$ eV) and ending at the bottom of the conduction band (which is at $E \approx 18$ eV). In this case it is very important to account (e.g. via a realistic self-energy function) for additional multiple elastic and inelastic scattering processes of the electrons pairs [29]. In the calculations shown in Fig. 10.7 it has not been yet possible to include this kind of additional processes. This limitation of theory is however not applicable to the angular distribution results shown in Fig. 10.5, since in this case the energy of the electrons can be chosen such that the photoelectrons are emitted from the Fermi level where inelastic energy-loss processes can be deemed small.

10.5 Conclusions

The aim of the present work is to provide a general overview of the foundations and of the numerical methods for describing the photo-induced two-electron emission from surfaces. A brief account of the experimental techniques have been given and the experimental data have been discussed in light of the numerical results. We have seen that the double photoelectron emission is well suited for the study of particle-particle correlation in a very direct way, i.e., in actually detecting the two particles at the same time. A general expression has been given to evaluate the $(\gamma, 2e)$ current and some approximate calculation schemes have been outlined. In particular, we employed a local but wave-vector dependent approximation of the electron-electron interaction between the photo-electrons and established a multiple-scattering scheme which is closely related to the well-studied one-step model of single photoemission. In particular, we can treat within the same numerical approach single and double-photoelectron emission which allows for a reasonable comparison between the two processes. First numerical results for the angular and the energy correlation functions of the photoelectrons emitted from Cu(001) revealed the characteristics of the electronic correlation, as can be observed in $(\gamma, 2e)$. Future improvements of the present approximate model include the implementation of a realistic single-particle self energy in the one-particle part of the problem as well as taking explicitly into account the non-local screened Coulomb interaction.

References

[1] P. Fulde, *Electron Correlation in Molecules and Solids*, Springer Series in Solid-State Sciences, Vol. 100, Springer Verlag, 1991.

[2] R.M. Dreizler and E.K.U. Gross, *Density Functional Theory*, Springer Verlag, 1990.

[3] I. Lindgren and J. Morrison, *Atomic Many-Body Theory*, Springer Verlag, 1982.

[4] K.A. Brueckner, Phys. Rev. **97** (1955) 1353.

[5] H.A. Bethe, Ann. Rev. Nucl. Sci. **21** (1971) 93.

[6] J.P. Jeukenne, A. Legeunne, and C. Mahaux, Physics Reports **25** (1976) 83.

[7] H. Kümmel, K.H. Lührmann, and J.G. Zabolitzky, Physics Reports **36** (1978) 1.

[8] R.F. Bishop, in *Microscopic Quantum Many-Body Theories and Their Applications*, eds. J. Navarro and A. Polls, Springer, 1998.

[9] K.E. Schmidt and D.M. Ceperley, in *Monte Carlo Methods III*, ed. K. Binder, Springer, 1991.

[10] D.M. Ceperley, Rev. Mod. Phys. **67** (1995) 279.

[11] R. Feder and H. Gollisch, this volume.

[12] J. Berakdar, Phys. Rev. B **85** (1998) 9808.

[13] R. Herrmann, S. Samarin, H. Schwabe, and J. Kirschner, Phys. Rev. Lett. **81** (1998) 2148.

[14] R. Herrmann, S. Samarin, H. Schwabe, and J. Kirschner, J. Phys. (Paris) IV, **9** (1999) 127.

[15] J. Berakdar, and J. Kirschner, eds. *Many-Particle Spectroscopy of Atoms, Molecules, Clusters and Surfaces*, Kluwer Acad/Plenum Pub., 2001.

[16] J.S. Briggs and V. Schmidt, J. Phys. B **33** (2000) R1.

[17] G.C. King and L. Avaldi, J. Phys. B **33** (2000) R215.

[18] V. Schmidt, *Electron Spectrometry of Atoms using Synchrotron Radiation*, Cambridge Monographs on Atomic, Molecular and Chemical Physics Cambridge, University Press, 1997.

[19] J. Berakdar and H. Klar, Phys. Rep. **340** (2001) 473.

[20] C.J.G. Onderwater *et al.*, Phys. Rev. Lett., **81** (1998) 2213.

[21] A.L. Fetter and J.D. Walecka, *Quantum Theory of Many Particle Systems*, McGraw-Hill, New York, 1971.

[22] G.D. Mahan, *Many-Particle Physics*, second ed., Plenum Press, London, 1993.

[23] A.A. Abrikosov, L.P. Gorkov and I.E. Dzyaloshinski, *Methods of Quantum Field Theory in Statistical Physics*, Dover, 1975.

[24] J. Negele and H. Orland, *Quantum Many-Particle Systems*, Addison-Wesley, 1988.

[25] R.D. Mattuck, *A Guide to Feynman Diagrams in the Many-Body Problem*, McGraw-Hill, 1976.

[26] H. Lehmann, Nuovo Cimento A **11** (1954) 342.

[27] S.D. Kevan (Ed.), *Angle-Resolved Photoemission: Theory and Current Application*, Elsevier, 1992.

[28] S. Hüfner, *Photoelectron Spectroscopy*, No. 82 in Springer Series in Solid-State Science, Spinger Verlag, 1995.

[29] L. Hedin, J. Phys. C **11** (1999) R489.

[30] P.C. Martin and J Schwinger, Phys. Rev. **115** (1959) 1342.

[31] A.B. Migdal, *Theory of finite Fermi Systems*, New York, 1967.

[32] J. Berakdar, Phys. Rev. Lett. **85** (2000) 4036.

[33] J. Berakdar, Phys. Rev. A **63** (2001) 012706.

[34] N. Fominykh, J. Henk, J. Berakdar, P. Bruno, H. Gollisch, R. Feder, Solid State Commun., **113** (2000) 665.

[35] D. Pines, *The Many-Body Problem*, Bejamin, 1962.

[36] R. Feder (Ed.), *Polarized electrons in surface physics*, Advanced Series in Surface Science, World Scientific, 1985.

[37] J. Henk, in *Handbook of Thin Film Materials* (ed.) H.S. Nalwa, Academic Press, 2001.

[38] J. Berakdar, H. Gollisch and R. Feder, Solid State Commun. , **112** (1999) 587.

[39] N. Fominykh *et al.*, in *Many-particle spectroscopy of Atoms, Molecules, Clusters and Surfaces*, Kluwer Acad/Plenum Pub., 2001.

Solid-State Photoemission and Related Methods
Wolfgang Schattke, Michel A. Van Hove (Eds.)

11 Overview of surface structures

M.A. Van Hove

The atomic-scale structure of a surface is fundamental to understanding its various properties, be they electronic, magnetic, optical, chemical, or tribological. This chapter surveys the current state of knowledge of surface structure, and includes a discussion of the main methods employed to determine surface structure.

11.1 Introduction

Surface science [1, 2] has enabled the detailed structural determination of a large number of well-prepared surfaces since about 1970 [3]. A wide variety of materials has been studied, with particular emphasis on metals and semiconductors of interest for understanding catalysis and electronic devices, respectively.

Ultra-high vacuum techniques have made it possible to control the composition and condition of interfaces at the atomic level, and to determine their structure by using electrons, photons, ions and other probes. Atomically clean crystalline surfaces can be prepared, and can serve as substrate for deposition of foreign matter in submonolayer to multilayer amounts, often called "adsorbate". The interface between a substrate and a multilayer film can also be studied structurally, although with greater difficulty.

Surfaces and interfaces are models for the understanding of many phenomena of technological importance, such as those occurring in semiconductor devices, in heterogeneous catalysis, oxidation and corrosion, electrochemistry, friction and wear.

The substrate can be a metal, an alloy, a semiconductor (whether elemental or compound), an insulator, or any other substance that crystallizes. The clean or adsorbate-covered substrate surface can "reconstruct" into a lattice that is quite different from the three-dimensional bulk lattice, a very characteristic phenomenon of surfaces.

Many types of adsorbate can be deposited on a substrate. Typically, one deposits molecules, resulting frequently in atomic adsorbates due to molecular decomposition, or resulting in adsorbed molecular species directly related to or different from the initial molecule. Atoms or clusters can also be deposited, sometimes in ionic form. Deposition of metals often forms metallic films. Chemisorption occurs when strong substrate-adsorbate bonds form. Otherwise physisorption can occur (at low enough temperatures).

Submonolayer adsorbates often do not order into a lattice, but remain disordered, or else they may create two-dimensionally ordered superlattices; they may also generate close-packed islands. Multilayers can grow into thin films that may be epitaxial, i.e. grow in some orientational coincidence with the substrate lattice, or that may be pseudomorphic, i.e. have periodic crystalline coincidence with the substrate.

Solid-State Photoemission and Related Methods: Theory and Experiment. Edited by Wolfgang Schattke, Michel A. Van Hove

ISBN: 3-527-40334-5

11.2 Techniques of surface structure determination

Since about 1970, many methods have been developed and applied to determine the atomic-scale structure of surfaces and interfaces [4]. We will here focus on those methods that are capable of finding atomic positions within about 0.1 Å (0.01 nm). The following list gives the acronyms and full names of many of these techniques:

AD	atomic diffraction
AED	Auger electron diffraction
ARPEFS	angle-resolved photoelectron emission fine structure
ARUPS	angle-resolved ultraviolet photoemission spectroscopy
ARXPD	angle-resolved X-Ray photoelectron diffraction
GIXS	grazing-incidence X-Ray scattering
HEIS	high-energy ion scattering
HREELS	high-resolution electron energy loss spectroscopy
ICISS	impact-collision ion scattering spectroscopy
IS	ion scattering
ISS	ion scattering spectroscopy
LEED	low-energy electron diffraction
LEIS	low-energy ion scattering
LEPD	low-energy positron diffraction
MEED	medium-energy electron diffraction
MEIS	medium-energy ion scattering
NEXAFS	near-edge X-Ray absorption fine structure
PD	photoelectron diffraction
PED	photoelectron diffraction
RBS	Rutherford backscattering
RHEED	reflection high-energy electron diffraction
SEELFS	surface extended-energy-loss fine structure
SEXAFS	surface extended X-Ray absorption fine structure
STM	scanning tunneling microscopy
TED	transmission electron diffraction
TOF-SARS	time-of-flight scattering and recoiling spectrometry
XAFS	X-Ray absorption fine structure
XANES	X-Ray absorption near-edge spectroscopy
XRD	X-Ray diffraction
XSW	X-Ray standing waves

In this list, the same technique may appear under different acronyms or names. An example is photoelectron diffraction, which appears as ARPEFS, ARUPS, ARXPD, PD and PED. Another example is ion scattering: HEIS, ICISS, IS, ISS, LEIS, MEIS and RBS. The different names often reflect different conditions or parameter ranges, such as ultraviolet light (ARUPS) vs. X-Rays (ARXPS), or low (LEED, LEIS), medium (MEED, MEIS) vs. high (RHEED, HEIS) energies.

Figure 11.1 graphs the number of structures determined by those techniques that have produced detailed and complete structures up through the year 2000 [3]. It illustrates the predominance of LEED in surface structure determination, followed by photoelectron diffraction (in its various forms) and ion scattering (in its various forms).

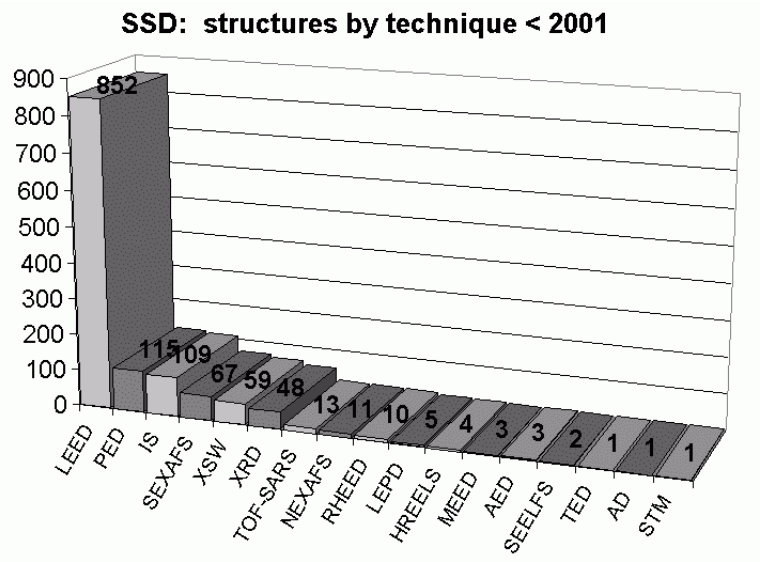

Figure 11.1: Graph of solved surface structures [from ref. 3], showing the number of structures solved by different techniques through the year 2000. To be included in this graph a technique must have solved structures accurately and completely. As an example, STM had solved only one structure in detail, by comparing STM images to STM theory.

Figure 11.2 breaks down the relative contribution from the different techniques on a yearly basis [from ref. 3]. This graph shows that LEED was the only technique in use until about 1978 and that it has continued to produce more than 50% of determinations since then. At that time, several techniques using synchrotron radiation became available, including prominently photoelectron diffraction, as well as ion scattering, which relies on ion accelerators.

In the next few sections, we will briefly describe groups of techniques, according to their basic mechanism: diffraction, (non-diffractive) scattering, etc.

Then, we will discuss ordering principles at surfaces, which are responsible for the periodic crystallinity of most of the solved structures. Next we will address the types of surface structure that have been solved, grouped according to types of surfaces, and discuss the kinds of structures that have been found to occur: reconstructions, adsorption of atoms and molecules as overlayers, penetration of adatoms into surfaces, etc.

11.2.1 Diffraction techniques

Diffraction has been a most successful approach to atomic-scale structure determination of bulk materials and surfaces. Diffraction can deliver atomic coordinates at surfaces with preci-

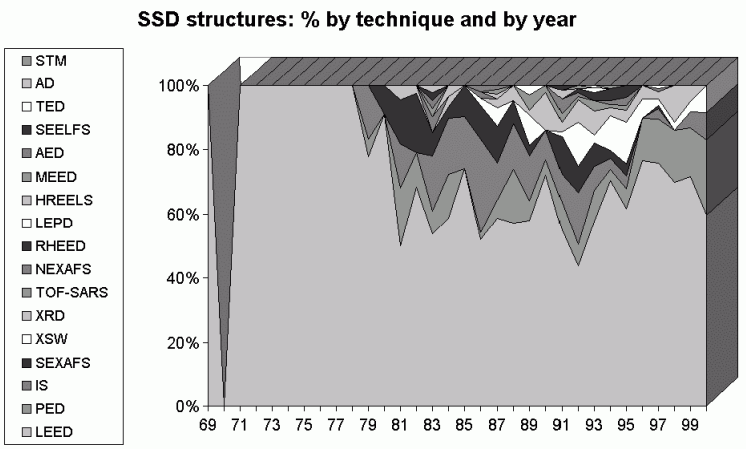

Figure 11.2: Graph of solved surface structures [from ref. 3], showing year by year the relative contributions from different techniques (no structure was determined in 1970). The techniques are labeled and drawn from bottom up in order of decreasing number of structures determined.

sions in the range of 0.01 to 0.1 Å. LEED, PED and XRD are the main diffraction techniques which have been applied to surface structure determination.

The majority of known surface structures has been studied with low-energy electron diffraction (LEED) [5, 6]. LEED uses as probes elastically diffracted electrons with energies in the 20–300 eV range, which corresponds to electron wavelengths in the 0.5–2 Å range. Monoenergetic electrons are beamed at a surface, from which they are diffracted (only elastically scattered electrons are normally recorded). Inelastic scattering processes severely limit the penetration depth of such electrons into a surface to about 5–10 Å, giving a surface sensitivity of only a few atomic layers.

Interferences between different scattering paths pick up the local surface structure information in the form of modulations of diffracted electron beam currents. Elastic interactions are strong enough that multiple scattering of electrons from one atom to another is important in this energy range. This complicates the analysis of experimental diffraction data, but the necessary theoretical methods have been very successful in obtaining bond lengths and angles at surfaces of almost any chemical composition (hydrogen atoms being the major exception).

The methods employed to analyze LEED measurements simulate the entire multiple scattering process in a way similar to the calculation of electronic band structures in the bulk and at the surface. An important part of the process is the fitting of atomic positions to reproduce experimental diffraction data.

X-Ray diffraction, with its inherent conceptual simplicity, has been an obvious choice for surface crystallography [7]. However, long mean free paths of X-Rays in solids permit the desired surface sensitivity only when grazing incidence and/or emergence are used: angles within a fraction of a degree from the surface plane are required. This demands extremely flat surfaces and strict control of diffraction angles, both challenging experimental tasks. Also a sufficient photon flux is required, which is often sought at synchrotron radiation facilities.

In fact, the relative impact of XRD has grown with the increased availability of synchrotron radiation.

A variant of X-Ray diffraction has been applied to obtain interlayer spacings between adsorbates and bulk atomic planes. These bulk atomic planes include not only the planes parallel to the surface, but also any crystallographic planes inclined to the surface. Then "triangulation" allows the adsorption site to be determined. This approach uses X-Ray standing waves due to reflection from atomic planes in the crystal bulk [8]. This method is used in conjunction with detection of the fluorescence that is unique to the adsorbate. The fluorescence is sensitive to interference between the directly reflected beams and beams reflected from the bulk planes; hence it can tell the interplanar separation.

A number of diffraction techniques use internal localized point sources of electrons, instead of external beams. In the case of photoelectron diffraction [9, 10, 11], electrons are photoemitted from particular electronic orbitals, such as core levels in individual surface atoms. Often synchrotron radiation is used as a source of photons. Those electrons scattered from nearby atoms toward the detector interfere with electrons traveling directly from the emitting atom to the detector, in a way that depends on the local geometry. The electrons are emitted with kinetic energies up to a few thousand eV, where single-scattering events dominate to give a qualitatively simple scattering picture (but multiple scattering must be taken into account for accuracy).

Another point-source diffraction technique is X-Ray absorption fine structure (XAFS) [12, 13, 14, 15]. Again, photoelectrons are excited and allowed to scatter from nearby surface atoms. However, in this case the electrons return to the emitting atom and modulate (by wave interference) the emission process itself. This modulation is again interpreted in terms of the local geometry. SEXAFS (surface extended XAFS) uses electron kinetic energies of the order of 1000 eV, and a single-scattering model is often adequate to interpret the experimental data. Any emitted particle can be chosen for detection, including photons, electrons and ions.

Closely related to SEXAFS is near-edge X-Ray absorption fine structure (NEXAFS, also called XANES) [14]. NEXAFS is SEXAFS conducted at much lower electron kinetic energies, where multiple scattering is strong. This technique is primarily used to monitor excitations among valence electrons, from which structural information like molecular orientation and bond lengths is accessible. And the polarization of the incident photons can be used to detect the orientation of bonds and thus the orientation of molecules relative to the surface plane, for example.

Another approach uses "electron holography" [16, 17, 10]. The angular distribution of an emitted electron (e.g. a photoelectron) can be viewed not only as a diffraction pattern to be fit, but also as a hologram to be inverted: such a pattern or hologram is due to interference between the directly emitted wave and the same wave scattered from nearby atoms, in analogy with optical holography. From this hologram, one can computationally reconstruct an image of the neighborhood of the emitting atom, by a Fourier-transform-like inversion. The result is a map that approximates the positions of atoms: each atom in principle is represented by a maximum in this three-dimensional map. The method suffers however from distortions due to electron scattering phase shifts and multiple scattering effects. But it has been found that including holograms taken at multiple energies, together with energy-dependent phases, can appreciably improve the quality of the resulting map. This approach is not guaranteed to work in all cases, but when it does work it saves much effort in solving a structure. Typically, after holographic inversion, a more standard fitting is performed to fine-tune atomic positions.

11.2.2 Scattering techniques

A number of techniques rely on scattering, as opposed to diffraction (interference), to obtain geometrical information from surfaces. Of particular value has been ion scattering both at low energies (around 1 keV) [18, 19] and at medium and high energies (100–1000 keV) [20].

Low-energy ions cast wide shadows behind surface atoms. These shadows obscure further atoms if they lie within the shadow cone. By varying the incidence direction, the shadow cone can be swept through the surface and expose or hide individual atoms. It is possible to monitor the disappearance and emergence of atoms in the shadow cone, thereby obtaining structural information. This information tends to be restricted to the top one or two atomic layers, since the shadows obscure all deeper layers. The technique is generally called LEIS (low-energy ion scattering) [18]. Alkali ions provide particularly good structural sensitivity when monitored near the 180° scattering direction: this feature is used in ALICISS (alkali-ion impact collision ion scattering spectroscopy) [21].

Medium- and high-energy ions (helium nuclei and protons are commonly used) are directed along bulk crystal axes of the surface material. The ions can channel relatively deeply into the crystal between rows of atoms, because the shadow cones are in this case very narrow. But if surface atoms deviate from the ideal bulk lattice positions and block the channels through which the ions move, the ions will scatter strongly back out of the surface. This conceptually simple approach has been used successfully to obtain detailed structural information for a number of clean and adatom-covered surfaces. It is uniquely suited to study buried solid-solid interfaces (i.e. interfaces that lie deep in the bulk below a surface), since the ions can be made to penetrate relatively deeply into a surface. The technique still requires ultra-high vacuum for its operation, because the ion beams can only be formed in such a vacuum [22]. Depending on the energy range used, and other experimental choices, the technique is known under the names of medium-energy ion scattering (MEIS) or high-energy ion scattering (HEIS).

11.2.3 Microscopic and topographic techniques

A number of powerful techniques have been developed that study surfaces in a microscopic sense: they image directly individual microscopic parts of a surface rather than structure as averaged over macroscopic distances. Some, like field-ion microscopy (FIM) [23, 24] and scanning tunneling microscopy (STM) [25, 26] can image individual atoms.

However, none of these microscopic techniques readily provides complete information about bond lengths or other bonding details (unless a close comparison with theory is made). In special conditions, distances parallel to the surface can be obtained with some accuracy, but mostly these techniques are used to map out surface topography or composition, down to atomic resolution in the case of STM and FIM.

11.3 Two-dimensional ordering

Deposition of adsorbates on a single-crystal substrate can produce quite different two-dimensional periodicities than the clean surface has. And the clean surface may have a differ-

ent two-dimensional periodicity than one would expect from simple truncation of the three-dimensional bulk lattice. We shall in this section first address the question of how ordering takes place at surfaces, with emphasis on the case of adsorbates. Then we shall introduce the main nomenclature that is used in surface science to describe ordered surface structures, whether due to adsorbates or due to reconstructions.

11.3.1 Ordering principles at surfaces

A large number of ordered surface structures can be produced experimentally on single-crystal surfaces, especially with adsorbates [27]. Ordering can manifest itself both as commensurate and as incommensurate structures. There are also many disordered surfaces.

We shall here adopt the following common definitions of the terms coverage and monolayer (however, one should be aware that other definitions are also often used). The surface coverage will be unity when each two-dimensional surface unit cell of the unreconstructed substrate is occupied by one adsorbate (the adsorbate may be an atom or a molecule). A coverage of 1/2 per cell thus corresponds to filling every other equivalent adsorption site. The term monolayer will here indicate a saturated single adsorbate layer with a thickness equal to the dimension of the adsorbate perpendicular to the surface. Thus, deposition after this coverage can only be achieved by starting a second monolayer growing on top of the first monolayer.

The driving force for surface ordering originates, analogous to three-dimensional crystal formation, in the interactions between atoms, ions, or molecules in the surface region. The physical origin of the forces is of various types (covalent, ionic, Van der Waals), and the spatial dependence of these interaction forces is often complex.

For adsorbates, an important distinction must be made between adsorbate-substrate and adsorbate-adsorbate interactions. The adsorbate-substrate interaction is due to strong covalent or ionic chemical forces in the case of chemisorption, or to weak Van der Waals forces in the case of physisorption. Adsorbate-adsorbate interactions may also be of different kinds: they may be strong covalent bonding interactions (as with dense metallic layers), weaker orbital-overlapping interactions or electrostatic interactions (e.g. dipole-dipole interactions), or weak Van der Waals interactions, etc. These are many-body interactions that may be attractive or repulsive depending on the system.

Frequently, an adsorbate lattice is formed that is simply related to the substrate lattice. In the ordered case this yields commensurate superlattices. The most common of these are simple superlattices with one adsorbate per superlattice unit cell. They occur for adsorbate coverages of 1/4, 1/3 or 1/2 per cell, for example. An incommensurate relationship exists when there is no common periodicity between an overlayer and the substrate. Such a structure is dominated by adsorbate-adsorbate interactions rather than by adsorbate-substrate interactions. The classic example is that of rare-gas monolayers physisorbed (weakly adsorbed) on almost any substrate.

11.3.2 Nomenclature

Single-crystal surfaces are characterized by a set of Miller indices that indicate the particular crystallographic orientation of the surface plane relative to the bulk lattice. Thus, surfaces are

labeled in the same way that atomic planes are labeled in X-Ray crystallography. For example, a Pt(111) surface exposes a hexagonally close-packed layer of atoms, given that platinum has a face-centered cubic bulk lattice. For reference, such a surface is often additionally labeled (1×1), thus Pt(111)-(1×1): this notation indicates that the surface is not reconstructed or otherwise modified into a periodicity different from that expected from simple truncation of the bulk lattice.

Most surfaces exhibit a different two-dimensional periodicity than expected from the bulk lattice, as is most readily seen in diffraction patterns: often additional diffraction features appear which are indicative of a "superlattice". This corresponds to the formation of a new two-dimensional lattice on the surface, usually with some simple relationship to the expected "ideal" (1×1) lattice. For instance a layer of adsorbate atoms may occupy only every other equivalent adsorption site on the surface, in both surface dimensions. Such a lattice can be labeled (2×2): in both surface dimensions the repeat distance is doubled relative to the ideal substrate.

In general, the (2×2) notation can take the form $(m \times n)\mathrm{R}\alpha^\circ$, called Wood notation (Wood, 1964). Here the numbers m and n are two independent stretch factors in different surface directions. These numbers need not be integers: irrational values yield incommensurate lattices, while rational values, expressible as an integer or as a ratio of integers, correspond to commensurate lattices. In addition, this stretched unit cell can be rotated by any angle α° about the surface normal. Thus, the Wood notation allows the (1×1) unit cell to be stretched and rotated; however, it conserves the angle between the two unit cell vectors in the plane of the surface, disallowing "sheared" unit cells.

A more general notation is available for all unit cells, including those that are sheared, so that the superlattice unit cell can take on any shape, size and orientation. It is the matrix notation, defined as follows (Van Hove et al, 1986a). We connect the unit cell vectors **a'** and **b'** of the superlattice to the unit cell vectors **a** and **b** of the substrate by the general relations:

$$\mathbf{a}' = m_{11}\mathbf{a} + m_{12}\mathbf{b},$$

$$\mathbf{b}' = m_{21}\mathbf{a} + m_{22}\mathbf{b},$$

The coefficients m_{ij} define the matrix

$$\mathbf{M} = \begin{pmatrix} m_{11} & m_{12} \\ m_{21} & m_{22} \end{pmatrix},$$

which serves to denote the superlattice. The (1×1) substrate lattice and the (2×2) superlattice are then denoted by the matrices

$$\mathbf{M} = \begin{pmatrix} 1 & 0 \\ 0 & 1 \end{pmatrix}$$

and

$$\mathbf{M} = \begin{pmatrix} 2 & 0 \\ 0 & 2 \end{pmatrix},$$

respectively.

11.4 Clean surfaces

Once a clean surface has been prepared, it is often found to have the two-dimensional periodicity which one would expect from simple ideal truncation of the bulk lattice parallel to the surface plane. However, there are many exceptions: they are often called reconstructions and we shall define them to be those clean structures that involve relatively large atomic displacements from an ideally-terminated bulk structure, including in particular the breaking of remaining bonds and/or the making of new bonds. In all cases, whether reconstructed or not, there is the possibility that bond lengths and interlayer spacings near the surface can differ from those in the bulk: this is usually called "surface relaxation".

Figure 11.3 gives an idea of the types of substrate for which the surface structure has been solved (combining clean and adsorbate-covered surfaces). Notable is the preponderance of non-reconstructed elemental metal surfaces. A good number of reconstructed semiconductor surfaces is also included. There are far fewer structures known for surfaces of alloys and other compounds, such as insulators.

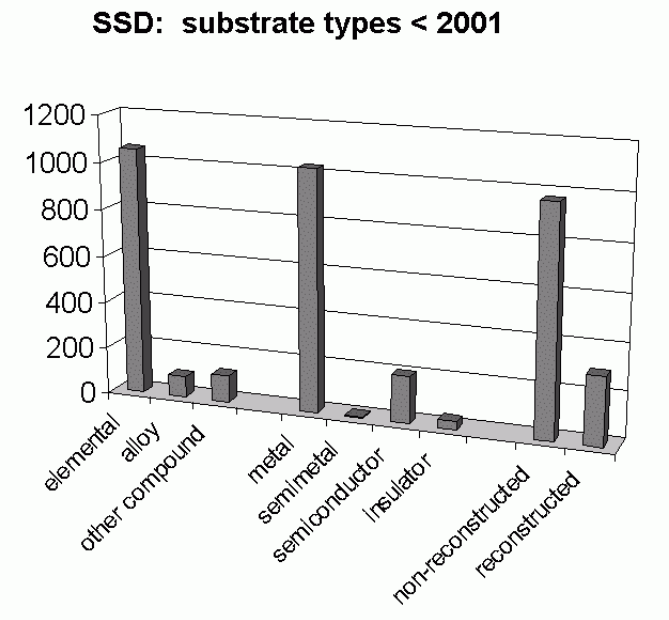

Figure 11.3: Numbers of solved surface structures classified by types of substrate, through the year 2000 [from ref. 3]. These numbers include both clean and adsorbate-covered surfaces.

Figure 11.4 breaks the surface structures down by substrate lattice. This makes clear that most structure determinations were performed for fcc, bcc and hcp metal surfaces, as well as diamond-lattice surfaces (mainly silicon).

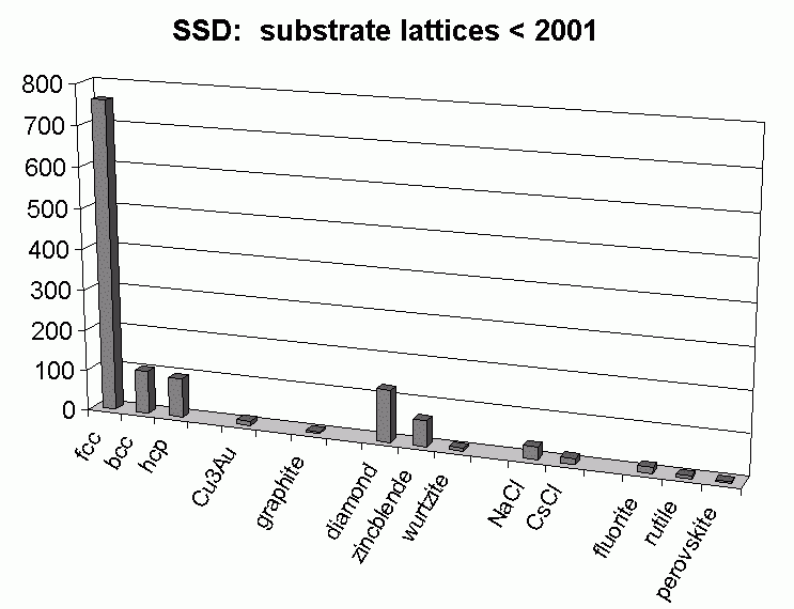

Figure 11.4: Numbers of solved surface structures classified by substrate lattice, through the year 2000 [from ref. 3]. These numbers include both clean and adsorbate-covered surfaces.

11.4.1 Bulk-like lattice termination

A number of clean surfaces exhibit a bulk termination (with perhaps some minor relaxations which we will discuss in Section 11.4.3). They are then denoted as having a (1×1) surface lattice.

This occurs most prominently with many pure metal surfaces that have low Miller indices, such as fcc(111), fcc(100), fcc(110), bcc(110), bcc(111), hcp(0001) and hcp(10–10). Among the few oxide surfaces which have been studied, the low-index surfaces derived from the bulk NaCl lattice also exhibit a (1×1) lattice, e.g. NiO(100). A number of alloy surfaces (again, few have been studied) also have a bulk-like termination. Some semiconductor compounds also have the (1×1) termination, such as the (110) surface of many III-V and II-VI compounds (GaAs, AlAs, AlP, GaP, GaSb, InAs, InP, InSb, CdTe, ZnS, ZnSe and ZnTe), although they may involve large atomic displacements (relaxations).

By contrast, the phenomenon of surface premelting has been well documented, at least for certain Pb surfaces, particularly the (110) surface of this fcc metal [28]. Premelting within a few outermost surface layers is observed already some 100 K below the bulk melting temperature of about 600 K.

11.4.2 Stepped surfaces

Well-annealed clean fcc and bcc metal surfaces often exhibit steps between adjacent flat terraces. So-called vicinal surfaces (which are cut somewhat off from a low-Miller-index plane), have regular arrays of such steps. Such steps are found to be mostly of mono-atomic height [2]. This is partly due to the fact that on ideal fcc and bcc surfaces, successive steps are structurally equivalent and multiheight steps are less favorable. On hcp metal surfaces, however, steps are often of double height. The difference is that on most hcp surfaces mono-atomic height steps alternate among two inequivalent structures and can compose a more favorable double-height step. Similarly, steps on many semiconductor surfaces have a two-atom height. Little is known about step structures at bimetallic and other surfaces.

11.4.3 Relaxations

Surface atoms have a highly asymmetrical environment: they have neighbors toward the bulk and in the surface plane, but none outside the surface. This anisotropic environment forces the atoms into new equilibrium positions, relative to the bulk. For clean unreconstructed surfaces, there is generally a contraction of bond lengths between atoms in the top layer and in the second layer under the surface, relative to the bond length in the bulk: the contraction is on the order of a few percent [3]. This relaxation in the topmost interlayer spacing is larger the more open (or rougher) is the surface, i.e. the fewer neighbors the surface atom has [29]. The closest packed surfaces, such as fcc(111) and fcc(100), show almost no relaxation; there may even be a very slight expansion for metals like Pd and Pt(111). Relatively large inward relaxations occur by contrast at surfaces like fcc(110), with interlayer spacings contracted by about 10%. The contractions are material dependent, Pb(110) showing a particularly large interlayer spacing contraction of 16%, corresponding to a bond length contraction of 3.7% [30].

Relaxations of interlayer spacings occur also deeper than the second layer [29, 31]. The amplitudes of these relaxations decay approximately exponentially with depth. At least in metals, it is common to observe alternating contractions and expansions in the interlayer spacings. Typically, one may find, in penetrating the surface, first a contraction, then an expansion, followed by another expansion, and then again a contraction.

Relaxations parallel to the surface are also expected and observed for atoms at step edges [29, 31]: they tend to relax sideways toward the upper terrace of which they are a part.

Semiconductor surfaces often present larger relaxation effects than metal surfaces, because there is more room for bond angle changes in the less close-packed semiconductors [32, 33]. The bond lengths also appear to change more than they do in metals. For example, in GaAs(110) and a number of similar unreconstructed surfaces of III-V and II-VI compounds, large rotational relaxations occur. Whereas the bulk has tetrahedral angles of 109.5°, some of the bond angles at surface atoms are reduced to $90 \pm 4°$ while others are increased to $120 \pm 4°$. These changes vary from layer to layer, and decay to the bulk value within a few atomic layers. In these examples, bond lengths change by up to 9%, but more typically by about 5%; both contractions and elongations occur in the same structure. Such effects are due to the rehybridization of atomic orbitals around the surface atoms. At (110) surfaces of III-V compounds, the group III element (anion) rehybridizes toward sp^2 and a planar neighborhood with

120° bond angles, whereas the group V element (cation) adopts a distorted p^3 hybridization that favors 90° bond angles.

11.4.4 Reconstruction

Among the clean metal surfaces, nearly a dozen are known to reconstruct. Over 40 clean semiconductor reconstructions have been reported. Numerous reconstructions have also been found for oxides and other compounds. Depending on preparation methods, some of these surfaces can present different superlattices, some of which are metastable. Thus, Si(111) reconstructs readily into a stable (7×7) structure, but can also be prepared as a (2×1) structure, a $(\sqrt{3} \times \sqrt{3})$R30° structure and even an unreconstructed (1×1) form, all of which are metastable. Similarly, Ir(100) normally reconstructs into a (1×5) lattice, but can be prepared in a metastable (1×1) structure.

Several types of clean-surface reconstruction can be distinguished [34]. First, one finds displacive reconstructions, in which atoms are displaced slightly from their ideal bulk-like positions in different directions which break the ideal periodicity and create a superlattice. Generally, no bonds are broken or created in this type of reconstruction, but bond lengths and angles are changed. Mo and W(100) are good examples.

Next are the missing-row reconstructions, exemplified by Ir, Pt and Au(110) [35]. In this case, rows of atoms are missing from the ideally-truncated substrate. This creates narrow facets which are more close-packed than the ideal surface. The most common missing-row reconstruction produces a (2×1) unit cell with facets 2 atoms wide.

Another type of reconstruction seen on metal surfaces is the formation of a closer-packed top layer. Such a reconstruction occurs for Ir, Pt and Au(100), as well as Au(111) [36]. In these cases, the interatomic distance within the topmost layer shrinks by a few percent parallel to the surface. It then becomes more favorable for this layer to collapse into a denser layer that is nearly hexagonally close packed rather than maintain the square lattice of the underlying layers.

Semiconductors often exhibit bond breaking and creation in one or more surface layers, relative to the ideal truncation [32, 33]. This effect is due to the directionality of the bonding in these materials. The "dangling" bonds broken by the creation of the surface are energetically unfavorable.

An important driving mechanism for semiconductor reconstruction is the minimization of the number of such dangling bonds. This is accompanied by more or less drastic rearrangements of the surface lattice. A relatively simple case occurs with Si(100), where atom pairing satisfies half of the dangling bonds, forming a (2×1) superlattice. A more extensive rearrangement is found in the (2×1) reconstruction of Si(111) and diamond C(111): here atoms bond in zigzag chains along the surface, while the 6-membered rings of the bulk are replaced by 5- and 7-membered rings next to the surface.

The Si(111)-(7×7) surface is the most complex reconstruction solved to date [37, 38]. It incorporates many of the abovementioned effects, and some additional ones. This reconstruction involves 12 "adatoms" per (7×7) unit cell. One half of the unit cell presents a stacking fault between the first and second bilayers, as if the top bilayer had been rotated by 180° about the surface normal. This stacking fault joins the non-faulted half of the unit cell at a seam that consists of paired atoms. Six such seams meet at large and deep holes (one hole per unit cell),

which expose the second bilayer. The combination of adatoms, dimers and stacking fault reduces the number of dangling bonds per (7×7) unit cell from 49 on the ideal unreconstructed surface to 19 on the reconstructed surface.

11.4.5 Surface segregation

A number of bulk compounds like oxides, carbides, sulfides and semiconductors maintain their bulk composition at the surface. There are, however, numerous exceptions that exhibit a deviating surface composition. An example is the case of the (111) faces of GaAs, GaP, and other such semiconductors, where a deficiency of Ga leads to a (2×2) reconstruction due to Ga vacancies [39].

The clean metallic alloys fall into two main categories: those for which the bulk alloy is ordered and those for which it is disordered. It appears that the surface structures of ordered bulk alloys are generally also ordered and maintain the bulk concentration. With disordered bulk alloys, the surface is most often also disordered, but surface segregation can be very marked and can be strongly layer-dependent, with the possibility of an oscillating layer-by-layer concentration. Other alloys, exemplified by Cu-rich CuAl [40], are disordered in the bulk, but order at some faces for certain bulk compositions.

11.4.6 Quasicrystals

Certain alloys form so-called quasicrystals: they are mostly ternary alloys with a majority component of Al. Quasicrystals have orientational order but no translational periodicity, and they can exhibit symmetries that are not allowed in periodic crystals, such as 5-, 8-, 10- and 12-fold rotational symmetry.

The surface structure of the 5-fold symmetrical surface of two quasicrystals has been studied: AlPdMn [41] and AlCuFe [42]. The main features are a bulk-like termination of the lattice, exposing an Al-rich layer, with interlayer relaxations similar to those seen of metal surfaces such as fcc(110).

11.5 Adsorbate-covered surfaces

A large number of atomic and molecular adsorbates have been studied on single-crystal surfaces over the last decades [27]. Very different structures are found when physisorption is compared with chemisorption, or when comparing atomic with molecular adsorption, or when mixing in a second type of adsorbate. Such differences will be addressed in this section. We shall also discuss multilayer growth, relaxations, reconstructions, compound formation and surface segregation of surfaces upon adsorption.

Figure 11.5 compares the numbers of surface structures solved for different adsorption modes. Simple atomic overlayers form the great majority. There are also a good number of molecular adsorbate structures, as well as a series of pseudomorphic ultrathin films (these have a 2-dimensional lattice that coincide with that of the substrate).

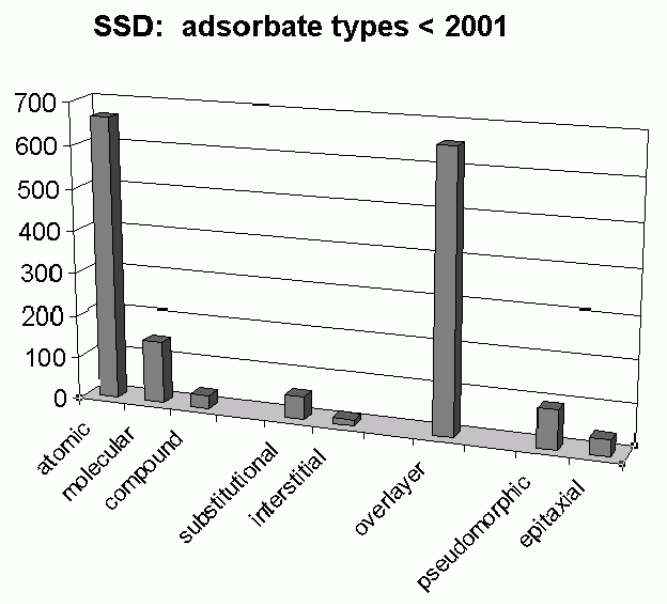

Figure 11.5: Numbers of solved surface structures classified by type of adsorption, through the year 2000 [from ref. 3].

11.5.1 Physisorption

At low enough temperatures most gas-phase species will physisorb on any surface. Particularly with inert gases and with saturated hydrocarbons, physisorption is commonplace and stable on many types of substrate.

The simpler among the observed LEED patterns for physisorbed species can often be easily interpreted in terms of structural models. The known Van der Waals sizes of the species lead to satisfactory structures which are more or less close-packed. This is especially straightforward with inert gases.

Physisorption allows the formation of multilayers, which normally grow with their own lattice constant on any substrate. For example, xenon films exposing a Xe(111) surface have been grown on an Ir(100) substrate and analyzed by LEED to show that the bulk fcc Xe structure is maintained [43].

11.5.2 Atomic chemisorption sites and bond lengths

Frequently, chemisorbed atoms order well on surfaces, particularly at specific coverages like 0.25, 0.5, 0.75, etc. per cell, where regular superlattices can develop. In many cases, order-disorder transitions are observed as the temperature is raised.

We first consider the adsorption site of chemisorbed atoms. The simple atomic adsorption structures on metal surfaces are generally characterized by the occupancy of high-coordination

sites. Thus, Na, S, and Cl overwhelmingly adsorb over "hollows" of the metal surface, bonding to as many metal atoms as possible [3].

The situation is slightly more complicated with the smaller adsorbates, such as H, C, N, and O, on metal surfaces. And all adsorbates appear to behave in a more complex manner on semiconductor surfaces. By contrast, little crystallography has been accomplished on atomic adsorption on other types of substrates, such as insulating compounds and alloys.

With the adsorption of smaller adsorbates, there still remains a preference for high-coordination sites. However, the atoms often penetrate deeper within or even below the first substrate layer. The penetration can be interstitial (as occurs with small atoms on metals) or substitutional (as is relatively more frequent on semiconductors and compounds). In either case the surface can reconstruct as a result, especially at higher coverages. For instance, a monolayer of N penetrates into interstitial octahedral sites between the first two layers of Ti(0001) with minimal distortion of the Ti lattice [44]. Both C and N burrow themselves within the hollow sites of the Ni(100) surfaces so as to be almost coplanar with the topmost Ni atoms [45, 46, 47]. The nearest Ni atoms are also pushed sideways by perhaps 0.4 Å, a good example of adsorbate-induced reconstruction.

One of the few known structures of an adatom at steps is that of O on Cu(410) [48]. The Cu(410) surface consists of (100) terraces, 3 atoms wide, on which the O adatoms can arrange themselves in a c(2×2) array at hollow sites. Oxygen atoms bond within the step edge between adjacent Cu step atoms: the bonding arrangement is just like the 4-fold hollow site, except that one of the four surrounding Cu atoms is missing.

Atomic adsorption on semiconductors shows three emerging major trends in the adsorption sites: low-coordination adatoms, high-coordination adatoms, and substitutional atoms.

Some atoms adsorbed on the (111) face of C (diamond), Si and Ge cap the dangling bonds of the ideally truncated surface. For instance, H, Cl, Br and I choose capping sites on Si(111), forming bonds through single coordination to Si atoms. These adatoms in effect continue the bulk Si lattice outward, removing any clean-surface reconstruction when the adatom coverage is large enough.

The second trend is illustrated by several adsorbed atoms on Si(111) and Ge(111) which at low coverage appear to prefer the so-called T_4 adatom site (the same site that Si and Ge adatoms occupy in the clean-surface reconstructions: this site lies above a triangle of substrate atoms, with one other substrate atom just below, resulting in 4 adsorbate-substrate bonds). The adatoms are thereby bonded to 4 substrate atoms of the top bilayer. Examples are Pb on Ge(111) [49], and both Al (50, 51) and Ga on Si(111) [52]. It appears from these results that the larger adatoms induce larger distortions in the substrate.

The third trend involves substitutional penetration of the adsorbate into the substrate. One example is boron on Si(111): instead of becoming a T_4 adatom, B interchanges its position with the Si atom immediately below the T_4 site (this substitutional site is called B_5 site) [53]. Another example is Al on GaAs(110), in which Al substitutionally replaces Ga atoms, largely retaining the relaxations of clean GaAs(110) [54].

Next we consider bond lengths between adsorbate and substrate atoms. The observed bond lengths generally fall well within 0.1 Å of corresponding bond lengths measured in bulk compounds and molecules. In a few cases the accuracy is sufficient to detect chemically significant variations in bond lengths. As a dramatic example, when the surface coverage of Cs atoms is varied from 1/3 to 2/3 per cell on Ag(111), the Ag-Cs bond length changes from

3.20 to 3.50 Å [55]. In this case the charging state of the adsorbate changes with coverage (as observed through work function changes), with a concomitant effect on bond lengths. This also illustrates an expected effect of mutual interactions between adsorbates: the denser the adsorbate layer, the weaker the individual adatom-substrate bonds.

11.5.3 Atomic multilayers

Atomic multilayer growth has been studied most frequently for metal deposition on metal surfaces, and for semiconductor or metal deposition on semiconductors [56, 57, 58]. Also, the growth of oxides and other compounds has been studied, but rarely in structural detail. Two aspects are of particular interest: 1) the growth mode, whether layer-by-layer and/or epitaxial or as three-dimensional crystallites; and 2) the interface structure between the substrate and the growing film. For metals, the growth mode tends to attract the most attention, while the interface structure is of particular interest for growth on semiconductors.

Metallic adsorption on metals

At low coverages, most of the metallic adsorbates form commensurate ordered overlayers: the overlayer unit cells are closely related to the substrate unit cells. Furthermore, in many cases a (1×1) LEED pattern is observed. This suggests that these adsorbed metal atoms attract each other to form two-dimensional close-packed islands. On the other hand, a disordered LEED pattern is observed when the adsorbed metal atoms repel each other. This is found for example in the case of alkali metal adsorption on a transition metal, since the charged adatoms undergo repulsive interactions.

Some metals undergo layer-by-layer growth, while others form three-dimensional crystallites ("balls"). Many cases fall between these two extremes. Comparison of the surface tension of the adsorbate metal and of the substrate metal gives a rough and not very reliable guide to these phenomena.

The limit of layer-by-layer growth has been studied in structural detail, thanks to the frequent formation of simple (1×1) overlayer unit cells. Striking is the growth of metastable films with lattices that are not favored in the bulk. Fe grown on Ni(100) [59] and Cu(100) [60] has received considerable attention: the Fe film can be made to grow with an fcc-like lattice (which continues the fcc lattice of Cu), rather than with its bcc bulk lattice. On Ni, the outermost Fe layer tends to relax into a wavy pattern of positions. The spacing between overlayers varies both from layer to layer and, for a given layer, as the film thickness grows, so that the Fe film does not adopt a perfectly cubic lattice; but the Fe is 12-fold coordinated, as in the fcc lattice. Such effects are particularly interesting in view of the magnetic properties of thin metallic films, which appear to depend strongly on the growth geometry.

Multilayer growth on semiconductors

Multilayer growth on semiconductor substrates is of great importance to the semiconductor industry: it is highly relevant to the formation and electrical properties of semiconductor-metal contacts, of semiconductor-semiconductor heterojunctions and of "superlattices" (here understood to mean the stacking of thin films of alternating composition). Nevertheless, relatively

little structural information on the Ångström level is available. On a more qualitative level, many of the features described above for metal-metal interfaces are thought to apply here as well [58].

One reason for the scarcity of structural information of such interfaces is the difficulty in studying deeply buried interfaces. Even with interfaces buried only a few atomic layers below a solid-vacuum surface, few experimental techniques are capable of sampling the buried structure. The technique which has been most successful in this respect has been high-energy ion scattering (HEIS), while LEED, SEXAFS and LEIS have also contributed by studying shallow buried interfaces.

A few interfaces between Si and a metal silicide have been investigated in detail. Examples are the Si(111)-$NiSi_2$(111) interface [61] and the similar interface produced with Co instead of Ni [62]. In both cases, the two materials match very closely in lattice constant parallel to the interface, forming a (1×1) surface lattice. Despite the identical lattices of $NiSi_2$ and $CoSi_2$, the bonding arrangement across the silicon-silicide interface is topologically slightly different between the two cases.

11.5.4 Molecular adsorption

Well over 400 ordered LEED patterns have been reported for the adsorption of molecules [27]. By far the most frequently studied substrates are metals. Platinum substrates have been most extensively used, due no doubt to their importance in heterogeneous catalysis. The most common adsorbates are CO (carbon monoxide), NO (nitric oxide), C_2H_2 (acetylene), C_2H_4 (ethylene), C_6H_6 (benzene), C_2H_6 (ethane), HCO_2 (acetate), HCOOH (formic acid), and CH_3OH (methanol).

Ordered LEED patterns for organic adsorption are frequent at lower temperatures. They can often be interpreted in terms of close-packed layers of molecules, consistent with known Van der Waals sizes and shapes. These ordered structures usually are commensurate with the substrate lattice, indicating strong chemisorption in preferred sites. It appears that many hydrocarbons lie flat on the surface, using unsaturated π-orbitals to bond to the surface. By contrast, non-hydrocarbon molecules form patterns that indicate a variety of bonding orientations. Thus CO and NO are found to strongly prefer an upright orientation. However, upon heating, unsaturated hydrocarbon adsorbates evolve hydrogen and new species may be formed which bond through the missing hydrogen positions, often in upright positions. An example is ethylidyne, CCH_3, which can be formed from ethylene, C_2H_4, upon heating. Ethylidyne has the ethane geometry (H_3CCH_3), but three hydrogens at one end are replaced by three substrate atoms: the resulting assembly could be denoted M_3CCH_3, where M is a metal atom.

Molecular adsorption sites and ordering

When the adsorbate-substrate bond is strong and localized, the molecule presents clear preferences for particular adsorption sites and it orders well. Thus, ethylidyne (CCH_3) bonds through one carbon atom to a three-fold coordinated hollow site on many fcc(111) surfaces, and typically orders as a (2×2) overlayer [63, 64].

When the molecular species is large and bonds to many metal atoms simultaneously, as is the case with benzene lying flat on a surface, there is less preference for particular sites, which

then depend on the metal and can easily be affected by coadsorbed species (e.g. acceptors like CO). For instance, benzene will shift its center from a bridge site to a hollow site when coadsorbed with CO on Rh(111). Ordering is relatively weak under such conditions. Thus, benzene does not order at room temperature on Pd and Pt(111) surfaces, and only weakly on Rh(111). (But coadsorption with CO produces stable ordering through strong interactions between the distinct molecules.)

In the case of weaker chemisorption, such as when CO or NO adsorb intact, there is also relatively little site preference and ordering is less pronounced as well: such molecules choose sites that depend on the metal and on the coverage, as well as on coadsorbates, while low order-disorder transition temperatures are found.

CO and NO adsorption

Detailed structural studies of adsorbed carbon monoxide and nitric oxide have been performed for about 20 surface structures, primarily on close-packed metal surfaces [3]. They have largely confirmed the site assignments based on vibrational frequencies, as originally derived for metal-carbonyl and similar complexes [65], with, however, some notable exceptions at higher coverages. On many metals, CO prefers low-coordination sites at low coverages, e.g. linear coordination at top sites for CO on Rh(111). However, the low-coverage site depends strongly on the metal and the crystallographic face: it is a bridge site on Pd(100) and a 3-fold hollow site on Pd(111).

At higher coverages the coordination generally increases, towards two-fold bridge sites and three-fold hollow sites (but apparently never four-fold hollow sites). The metal-C bond length has been found to increase strongly with coordination, and the C-O bond length increases slightly at the same time [66]. This is again in agreement with the case of metal-carbonyl complexes, and confirms the C-O bond weakening implied by the decreasing vibration frequency.

At high coverages, crowding occurs and part of the CO and NO molecules have to settle for less favorable sites. For instance, at a coverage of 3/4 per cell on Rh(111), one third of the adsorbed CO molecules occupy the favored top sites, while another third occupies 3-fold-coordinated “fcc-hollow” sites, while the remainder bond above “hcp-hollow” sites [67] (the fcc- and hcp-hollow sites differ in that the latter has a metal atom right below this site in the second metal layer, while the former does not). NO in the same circumstances behaves in exactly the same manner [68].

Coadsorption of CO or NO with other adsorbates affects the adsorption site markedly and can lead to dissociation. It is apparent that CO and NO are unusually sensitive monitors of the surface condition. They react strongly to changes in substrate identity, coverage, and coadsorbates. The changes are easily measured, especially through vibrational analysis (HREELS and IRAS).

Benzene adsorption

Benzene adsorbs parallel to fcc(100), fcc(111) and hcp(0001) surfaces, and probably also on other close-packed surfaces [3]. Benzene does not order easily on close-packed metal surfaces, compared to CO, NO and especially atomic adsorbates. At room temperature, benzene does

not order at all on Pt and Pd(111), while it weakly orders on Rh(111) (a short exposure to the LEED electron beam is sufficient to destroy the ordered structure).

The adsorption site of benzene is variable, depending on metal, crystallographic face and coadsorbates. It has so far only been determined on fcc(111) and hcp(0001) surfaces [3, 69]. On Pt(111), the molecule centers itself over a bridge site, whether benzene is mixed with CO or not [70, 71]. On Rh(111), the same site is found for a pure benzene layer, but a 3-fold hollow site emerges in the presence of coadsorbed CO [72]. On Pd(111), in the presence of CO, the 3-fold site is also found [73], while the site is not known for the pure benzene layer. Since the 3-fold hollow site does not exist on other crystal faces, this already implies a change of site in some of these cases.

11.5.5 Adsorbate-induced relaxations

Chemisorption on a surface modifies the chemical environment of the surface atoms and therefore affects the structure. In particular, upon adsorption, any clean-surface relaxation is generally reduced as the surface atoms of the substrate move back towards the ideal bulk-like position or even beyond. Relaxations of deeper interlayer spacings are also usually reduced upon adsorption. In addition, it is becoming increasingly clear that small local distortions on the scale of 0.1 Å are induced around each adsorption site in directions other than the surface normal.

Good examples of the outward relaxation of interlayer spacings are provided by atomic adsorption on the (110) surfaces of nickel and other fcc metals [74]. The clean (110) surfaces typically exhibit contractions by about 10% (0.1 to 0.15 Å) in the topmost interlayer spacing relative to the bulk value. Upon adsorption these contractions are reduced to less than 3 to 4% (0.03 to 0.05 Å).

11.5.6 Adsorbate-induced reconstructions

Adatoms can induce a restructuring of a surface in a variety of ways [74, 75]. A mild form of reconstruction occurs when substrate atoms are displaced by small amounts in different directions, thereby changing the unit cell of the substrate (displacive reconstruction). An opposite situation is the removal of a clean-surface reconstruction by an adatom. Also possible is the change from one reconstruction to another. Adatoms can furthermore give rise to new compound formation, or can change surface segregation in an existing compound. On a larger scale, adatoms have also been found to cause macroscopic reshaping of surfaces.

The energy needed for surface restructuring is paid for by the increased bond energies between the adsorbed atom and the substrate. Therefore, such surface restructuring is expected only upon chemisorption where the adsorbate-substrate bond energies are similar to or larger than the bond energies between the atoms in the substrate. This is clearly the case for the adsorption of carbon, oxygen, and sulfur on many transition metals.

Displacive local reconstruction induced by adsorption

The adsorption of atoms may displace substrate atoms to provide better adsorbate-substrate bonding, in such a way that a new unit cell results in the substrate [34]. This is a generalization

of the adsorbate-induced relaxations discussed above. The local displacements are of the same order of magnitude, at most a few tenths of Å.

The effect is well illustrated with the structure induced by carbon or nitrogen adsorbed on Ni(100) [45, 46, 47], also seen with O on Rh(100) [76]. The adatom occupies a four-fold site, which it expands by pushing the four neighboring metal atoms outward from the site, parallel to the surface. This allows the adatom to penetrate deeper into the metal surface and to bond not only to the four first-layer metal atoms but also to a metal atom in the next layer. The surrounding metal lattice cannot accept a corresponding compression at a coverage of 0.5 per cell and instead forces a rotation of the square of four metal atoms about the surface normal. Thereby, the average metal density in the top layer is kept constant, while accommodating the additional foreign stoms.

Removal of reconstruction by adsorption

The chemisorption of atoms frequently removes surface reconstruction and produces a more bulk-like surface structure.

Examples of this effect are offered by the removal with hydrogen of the reconstruction of clean Si(100), Si(111) and diamond C(111), and the removal with carbon, oxygen or CO of the reconstructions of the (100) and (110) faces of Ir and Pt. Electron acceptors, like O and S, are particularly effective at removing reconstructions. Sometimes small amounts of adsorbate suffice to remove a reconstruction, but more frequently amounts comparable to a monolayer are required. Hydrogen has to be adsorbed to a coverage of 2 per cell to remove the W(100)-c(2×2) reconstruction [77].

Creation of reconstruction by adsorption

Adsorbates have frequently been found to induce new reconstructions on surfaces that were not reconstructed in the clean state [74]. Often a small fraction of a monolayer suffices to make the entire surface reconstruct.

Electron donors, like alkali metals, are particularly well known to induce reconstructions on metal surfaces. For example, a small coverage (below 0.1 per cell) of disordered alkali adatoms is sufficient to cause reconstruction of the Ni [78], Cu [79], Pd [80], and Ag(110) [81] surfaces, which transform to the (1×2) missing-row structure. Cs adsorbed on the (1×2) reconstruction of Au(110) causes a (1×3) structure, with only about 5% coverage per cell [82]. This structure is also of the missing-row type, but with deeper troughs than the clean (1×2) structure. A likely reason for this is that large alkali atoms bond more strongly (thanks to more near neighbors) within the deep troughs of the missing rows than in the shallow troughs of the ideal (110) surface [83, 84].

Another good example is given by Li or Na adsorbed on Cu(100) or Ni(100) [85]. This forms a series of complex reconstructions that involve a mix of both substitutional adsorption within the top substrate layer and overlayer adsorption above that layer.

More generally, electron-donating adsorbates tend to stabilize metal reconstructions. Stabilization is exemplified by alkali adsorption on the hexagonal reconstruction of Ir(100) [86]. There the clean-surface reconstruction is maintained in the presence of alkali atoms.

Change of reconstruction by adsorption

It stands to reason that surfaces which are already reconstructed when clean are particularly prone to further reconstruction in the presence of adsorbates. This is especially apparent with semiconductor surfaces.

Numerous examples exist where adatoms change the reconstruction of semiconductor surfaces. However, the number of resulting structures which have been solved is relatively small. They concern mostly metal adatoms, such as Al, Ga, and Pb deposited on Si and Ge(111) [52, 49, 53]. The substrate lattice relaxes noticeably around the adsorption site, with displacements up to about 0.3 Å. Larger adatoms induce larger displacements. The relaxation is noticeable down to the second double layer, which is strongly buckled.

11.5.7 Compound formation and surface segregation

In compound formation from adsorption, a reconstruction occurs that resembles a bulk compound. Continued addition of adsorbate atoms may enable the formation of a thicker film with the three-dimensional lattice of a bulk compound. Such behavior is characteristic of oxidation, nitridation, carbide formation and alloying of metal surfaces. Questions of interest include whether the compound is ordered and, if so, which is the crystallographic orientation of the growing compound. Also the question of lattice matching is important: most growing compounds have a lattice which is mismatched to the substrate [74].

The initial oxidation step of a metal typically involves oxygen atoms nestling between metallic surface atoms. For example, on Ta(100) a submonolayer amount of oxygen takes interstitial positions between the first and second metal layers [87]. An intermediate nitridation step which has been observed consists of the penetration of one monolayer's worth of N atoms between the first and second metal layers of Ti(0001) [88]; the same happens for N adsorbed on Zr(0001) [89].

S on Ni(111) has been observed to form a compound monolayer of composition Ni_2S [90]. It is suggested to have a square lattice of Ni atoms, with every other hollow site occupied by S atoms in a c(2×2) array. This monolayer would lie on the Ni(111) substrate with a $(5\sqrt{3} \times 2)$rect coincidence superstructure [91].

Metal silicide compounds are commonly formed after adsorption of metal atoms onto silicon surfaces. Thus, upon Ni deposition on Si(111), $NiSi_2$ grows with its (111) surface interfaced to the substrate [61]. Cobalt [62] and other transition metals behave similarly. For example, Al forms a substitutional GaAsAl compound after deposition on GaAs(110) [54].

Adsorbates may induce large changes of surface composition in multicomponent systems. i.e. surface segregation [74]. Such changes involve atomic diffusion perpendicular to the surface, and thus bond breaking and rebonding. This occurs particularly when the chemisorption bond energies between the alloy components are very different.

One example is the behavior of the Ag-Pd alloy [92]. The clean surface of a Ag-Pd alloy is enriched in silver at any bulk composition because of the lower surface energy of Ag as compared to Pd. Upon adsorption of CO, the surface composition changes rapidly. Because of the greater strength of the Pd-CO bond as compared to the Ag-CO bond, the Pd atoms move to the surface and the alloy surface becomes enriched in Pd. Upon heating CO desorbs and the surface excess of Ag is reestablished.

Acknowledgement

This work was supported by the Director, Office of Science, Office of Basic Energy Sciences, Materials Sciences Division of the U.S. Department of Energy under Contract No. DE-AC03-76SF00098.

References

[1] A. Zangwill, *Physics at Surfaces*, Cambridge Univ. Press, Cambridge, 1988.

[2] G.A. Somorjai, *Chemistry in Two Dimensions*, Cornell University Press, Ithaca, 1981.

[3] P.R. Watson, M.A. Van Hove and K. Hermann, *NIST Surface Structure Database Ver. 4.0*, NIST Standard Reference Data Program, Gaithersburg, 2002.

[4] M.A. Van Hove, *Surf. Interface Anal.* 1999, 28, 36.

[5] J.B. Pendry, *Low-Energy Electron Diffraction: The Theory and its Application to Determination of Surface Structure*, Academic Press, London, 1974.

[6] M.A. Van Hove, W.H. Weinberg, C.-M. Chan, *Low-Energy Electron Diffraction: Experiment, Theory, and Structural Determination*, Springer-Verlag, Heidelberg,

[7] R. Feidenhans'l, *Surf. Sci. Rep.* 1989, 10, 105.

[8] P.L. Cowan, J.A. Golovchenko, M.F. Robbins, Phys. Rev. Lett. 1980, 44, 1680.

[9] C.S. Fadley, in *Synchrotron Research: Advances in Surface Science*, Ed. R.Z. Bachrach, Plenum, New York, 1993.

[10] C.S. Fadley, Y. Chen, R.E. Couch, H. Daimon, R. Denecke, H. Galloway, Z. Hussain, A.P. Kaduwela, Y.J. Kim, P.M. Len, J. Liesegang, J. Menchero, J. Morais, J. Palomares, S.D. Ruebush, S. Ryce, M.B. Salmeron, W. Schattke, S. Thevuthasan, E.D. Tober, M.A. Van Hove, Z. Wang, R.X. Ynzunza and J.J. Zaninovich, *J. Surf. Anal.* 1997, 3, 334.

[11] D.P. Woodruff and A.M. Bradshaw, *Rep. Prog. Phys.* 1994, 57, 1029.

[12] See various articles in: *X-ray Absorption: Principles, Applications, Techniques of EXAFS, SEXAFS, and XANES*, Eds. D.C. Koningsberger and R. Prins, Wiley, New York, 1988.

[13] J.E. Rowe, in *Synchrotron Research: Advances in Surface Science*, Ed. R.Z. Bachrach, Plenum, New York, 1993.

[14] J. Stöhr, *NEXAFS Spectroscopy*, Springer-Verlag, Berlin, Heidelberg, New York, 1992.

[15] B. Ravel and J.J. Rehr, *J. de Physique* 1997, *IV 7 (NC2)*, 229.

[16] J.J. Barton, *Phys. Rev. Lett.* 1988, 61, 1356.

[17] D.K. Saldin, P.L. de Andres, *Phys. Rev. Lett.* 1990, 64, 1270.

[18] M. Aono, Y. Hou, C. Oshima and Y. Ishizawa, *Phys. Rev. Lett.* 1982, 49, 567.

[19] H. Niehus and G. Comsa, *Surf. Sci.* 1984, 140, 18.

[20] J.F. van der Veen, *Surf. Sci. Rep.* 1985, 5, 199.

[21] H. Niehus, G. Comsa, *Surf. Sci.* 1984, 140, 18.

[22] J.F. van der Veen, *Surf. Sci. Rep.* 1985, 5, 199.

[23] E.W. Müller, T.T. Tsong, *Field Ion Microscopy*, American Elsevier, New York, 1969.

[24] G. Ehrlich, in *The Structure of Surfaces*, Eds. M.A. Van Hove, S.Y. Tong, Springer-Verlag, Heidelberg, 1985, p. 375.

[25] H. Kumar Wickramasinghe, *Scanned-Probe Microscopes*, Scientific American, Vol. 261, No. 4, October 1989, p. 98.

[26] R. Wiesendanger, *Scanning Probe Microscopy and Spectroscopy: Methods and Applications*, Cambridge Univ. Press, Cambridge, 1994.

[27] H. Ohtani, C.-T. Kao, M.A. Van Hove, G.A. Somorjai, *Progr. Surf. Sci.* 1987, 23, 155.

[28] J.F. Van der Veen, B. Pluis, A.W. Denier van der Gon, in *Chemistry and Physics of Solid Surfaces VII*, Eds. R. Vanselow, R. Howe, Springer-Verlag, Heidelberg, 1988.

[29] F. Jona, P.M. Marcus, in *The Structure of Surfaces II*, Eds. J.F. van der Veen, M.A. Van Hove, Springer-Verlag, Heidelberg, Berlin, 1988, p. 90.

[30] J.W.M. Frenken, F. Huussen, J.F. van der Veen, *Phys. Rev. Lett.* 1987, 58, 401.

[31] Y. Tian, K.W. Lin, F. Jona, *Phys. Rev.* 2000, $B62$, 12844.

[32] C.B. Duke, in *Surface Properties of Electronic Materials*, Eds. D.A. King, D.P. Woodruff, Elsevier, Amsterdam, 1988, p. 69.

[33] C.B. Duke, in *Reconstruction of Solid Surfaces*, Eds. K. Christman, K. Heinz, Springer-Verlag, Heidelberg, 1991.

[34] S. Titmuss, A. Wander and D.A. King, *Chem. Revs.* 1996, 96, 1291.

[35] E.C. Sowa, M.A. Van Hove, D.L. Adams, *Surf. Sci.* 1988, 199, 174.

[36] M.A. Van Hove, R.J. Koestner, P.C. Stair, J.P. Bibérian, L.L. Kesmodel, I. Bartoš, G.A. Somorjai, *Surf. Sci.* 1981, 103, 189 and 218.

[37] K. Takayanagi, Y. Tanishiro, M. Takahashi, S. Takahashi, *J. Vac. Sci. Technol.* 1985, $A3$, 1502.

[38] S.Y. Tong, H. Huang, C.M. Wei, W.E. Packard, F.K. Men, G. Glander and M.B. Webb, *J. Vac. Sci. Technol.* 1988, $A6$, 615.

[39] S.Y. Tong, W.N. Mei and G. Xu, *J. Vac. Sci. Technol.* 1984, $B2$, 393.

[40] R.J. Baird, D.F. Ogletree, M.A. Van Hove, G.A. Somorjai, *Surf. Sci.* 1986, 165, 345.

[41] M. Gierer, M.A. Van Hove, A.I. Goldman, Z. Shen, S.-L. Chang, P.J. Pinhero, C.J. Jenks, J.W. Anderegg, C.-M. Zhang, and P.A. Thiel, *Phys. Rev.* 1998, $B57$, 7628.

[42] T. Cai, F. Shi, Z. Shen, M. Gierer, A.I. Goldman, M.J. Kramer, C.J. Jenks, T.A. Lograsso, D.W. Delaney, P.A. Thiel and M.A. Van Hove, *Surf. Sci.* 2001, 495, 19.

[43] A. Ignatiev, J.B. Pendry, T.N. Rhodin, *Phys. Rev. Lett.* 1971, 26, 189.

[44] H.D. Shih, F. Jona, D.W. Jepsen, P.M. Marcus, *Surf. Sci.* 1976, 60, 445.

[45] J. Onuferko, D.P. Woodruff, B.W. Holland, *Surf. Sci.* 1979, 87, 357.

[46] Y. Gauthier, R. Baudoing-Savois, K. Heinz and H. Landskron, *Surf. Sci.* 1991, $251/252$, 493.

[47] R. Terborg, J.T. Hoeft, M. Polcik, R. Lindsay, O. Schaff, A.M. Bradshaw, R.L. Toomes, N.A. Booth, D.P. Woodruff, E. Rotenberg and J. Denlinger, *Surf. Sci.* 2000, 446, 301.

[48] K.A. Thompson and C.S. Fadley, *Surf. Sci.* 1984, 146, 281.

[49] H. Huang, C.M. Wei, H. Li, B.P. Tonner, S.Y. Tong, *Phys. Rev. Lett.* 1989, 62, 559.

[50] H. Huang, S.Y. Tong, W.S. Yang, H.D. Shih, F. Jona, *Phys. Rev.* 1990, $B42$, 7483.

[51] W. Chen, H. Wu, W.K. Ho, B.C. Deng, G. Xu and S.Y. Tong, *Surf. Rev. Lett.* 2000, 7, 267.
[52] A. Kawazu, H. Sakama, *Phys. Rev.* 1988, $B37$, 2704.
[53] H. Huang, S.Y. Tong, J. Quinn, F. Jona, *Phys. Rev.* 1990, $B41$, 3276.
[54] A. Kahn, J. Carelli, D. Kanani, C.B. Duke, A. Paton, L. Brillson, *J. Vac. Sci. Technol.* 1981, 19, 331.
[55] G.M. Lamble, R.S. Brooks, D.A. King, D. Norman, *Phys. Rev. Lett.* 1988, 61, 1112.
[56] J.H. Van der Merwe, in *Chemistry and Physics of Solid Surfaces V*, Eds. R. Vanselow, R. Howe, Springer-Verlag, Heidelberg, 1984.
[57] R.W. Vook, *Int. Metals Rev.* 1982, 27, 209.
[58] R. Ludeke, *J. Vac. Sci. Technol.* 1984, $B2$, 400.
[59] S.H. Lu, Z.Q. Wang, D. Tian, Y.S. Li, F. Jona and P.M. Marcus, *Surf. Sci.* 1989, 221, 35.
[60] K. Heinz, S. Mueller and P. Bayer, *Surf. Sci.* 1995, 337, 723.
[61] E. Vlieg, A.E.M.J. Fischer, J.F. Van der Veen, B.N. Dev, G. Materlik, *Surf. Sci.* 1986, 178, 36.
[62] A.E.M.J. Fischer, E. Vlieg, J.F. Van der Veen, M. Clausnitzer, G. Materlik, *Phys. Rev.* 1987, $B36$, 4769.
[63] R.J. Koestner, M.A. Van Hove, G.A. Somorjai, *Surf. Sci.* 1982, 121, 321.
[64] R.J. Koestner, M.A. Van Hove, G.A. Somorjai, *J. Phys. Chem.* 1983, 87, 203.
[65] M.R. Albert, J.T. Yates, Jr., *The Surface Scientist's Guide to Organometallic Chemistry*, American Chemical Society, Washington,
[66] H. Ohtani, M.A. Van Hove, G.A. Somorjai, in *The Structure of Surfaces II*, Eds. J.F. van der Veen, M.A. Van Hove, Springer-Verlag, Heidelberg, Berlin, 1988, p. 219.
[67] M. Gierer, A. Barbieri, M.A. Van Hove and G.A. Somorjai, *Surf. Sci.* 1997, 391, 176.
[68] I. Zasada, M.A. Van Hove and G.A. Somorjai, *Surf. Sci.* 1998, 418, L89.
[69] D. Menzel, *Surf. Rev. Lett.* 1999, 6, 835.
[70] D.F. Ogletree, M.A. Van Hove, G.A. Somorjai, *Surf. Sci.* 1987, 183, 1.
[71] A. Wander, G. Held, R.Q. Hwang, G.S. Blackman, M.L. Xu, P. de Andres, M.A. Van Hove and G.A. Somorjai, *Surf. Sci.* 1991, 249, 21.
[72] A. Barbieri, M.A. Van Hove and G.A. Somorjai, *Surf. Sci.* 1994, 306, 261.
[73] A. Barbieri, M.A. Van Hove and G.A. Somorjai, *Surf. Sci.* 1994, 306, 261.
[74] G.A. Somorjai, M.A. Van Hove, Progr. *Surf. Sci.* 1989, 30, 201.
[75] M.A. Van Hove, K. Hermann and P.R. Watson, Landolt-Börnstein, Ed. H. Bonzel, Vol. III/42, Part 1, Chapter 4.1, 2002, in print.
[76] J.B. Pendry and K. Heinz, *Surf. Sci.* 1990, 230, 137.
[77] M.A. Passler, B.W. Lee, A. Ignatiev, *Surf. Sci.* 1985, 150, 263.
[78] R.J. Behm, D.K. Flynn, K.D. Jamison, G. Ertl, P.A. Thiel, *Phys. Rev.* 1987, $B36$, 9267.
[79] M. Copel, W.R. Graham, T. Gustafsson, S. Yalisove, *Sol. St. Comm.* 1985, 54, 695.
[80] C.J. Barnes, M.Q. Ding, M. Lindroos, R.D. Diehl, D.A. King, *Surf. Sci.* 1985, 162, 59.
[81] B.E. Hayden, K.C. Prince, P.J. Davie, G. Paolucci, A.M. Bradshaw, *Sol. St. Comm.* 1983, 48, 325.

[82] P. Haeberle, T. Gustafsson, *Phys. Rev.* 1989, $B39$, 5810.
[83] R.J. Behm, D.K. Flynn, K.D. Jamison, G. Ertl, P.A. Thiel, *Phys. Rev.* 1987, $B36$, 9267.
[84] K.W. Jacobsen, J. Nørskov, *Phys. Rev. Lett.* 1988, 60, 2496.
[85] H. Tochihara and S. Mizuno, *Progr. Surf. Sci.* 1998, 58, 1.
[86] K. Heinz, H. Hertrich, L. Hammer, K. Müller, *Surface Sci.* 1985, 152/153, 303.
[87] A.V. Titov, H. Jagodzinski, *Surf. Sci.* 1985, 152/153, 409.
[88] H.D. Shih, F. Jona, D.W. Jepsen, P.M. Marcus, *Surf. Sci.* 1976, 60, 445.
[89] P.C. Wong and K.A.R. Mitchell, *Surf. Sci.* 1987, 187, L599
[90] Y. Kitajima, T. Yokoyama, T. Ohta, M. Funabashi, N. Kosugi and H. Kuroda, *Surf. Sci.* 1989, 214, L261.
[91] J. Luedecke, A.R.H.F. Ettema, S.M. Driver, G. Scragg, M. Kerkar, D.P. Woodruff, B.C.C. Cowie, R.G. Jones and S. Bastow, *Surf. Sci.* 1996, 366, 260.
[92] R. Bouwman, G.H.M. Lippits, W.M.H. Sachtler, *J. Catal.* 1972, 25, 350.

Solid-State Photoemission and Related Methods
Wolfgang Schattke, Michel A. Van Hove (Eds.)

12 Angle resolved photoelectron spectroscopy: From traditional to two-dimensional photoelectron spectroscopy

Hiroshi Daimon, Fumihiko Matsui, and Kazuyuki Sakamoto

Angle resolved photoelectron spectroscopy (ARPES) has provided decisive evidences in solving various issues in surface- and solid- physics and chemistry. Its angular dependence directly shows energy band structures. Traditional ARPES uses electron energy analyzers having small acceptance angles so that angular resolution is high enough. Two applications on the Si-adsorbate systems are described here as examples for concise pictures of photoelectron spectroscopy by a traditional method. One is on the order-disorder transition of metallic overlayers, and another is on the oxidation process at the initial stage.

Recently many full solid-angle ARPES measurement have been done especially for Fermi surface mapping and photoelectron diffraction studies. In these measurements much detailed information is obtained. However, different quality of information can be obtained when the full solid-angle ARPES is measured by using a display-type analyzer and polarized incident-light. In this case the non-uniformity of photoelectron peak intensity has fruitful information in the relation to the polarization. By probing photoelectrons from core levels using circularly polarized light, three-dimensional atomic geometries are derived. On the other hand, the comprehensive information on the motion and the character of valence electrons can be visualized by two-dimensional valence band photoelectron spectroscopy using linearly polarized light. Some examples are described here.

12.1 Experiment – semiconductors

12.1.1 Photoemission from semiconductor surfaces

12.1.1.1 Introduction

Motivated by the extremely wide use of semiconductor devices in electronic industry, studies of semiconductor surfaces have been an active field. For most common semiconductors, sp^3 hybrid bond orbitals are formed from the linear combinations of *s*- and *p* orbitals within an atomic picture. In bulk, the bonding and anti-bonding levels, which are produced by the overlapping of the sp^3 hybrid orbitals between neighboring atoms, are broadened into the valence and conduction bands, respectively. On the surface, the atoms of the topmost layer have no pairing atoms on the vacuum side, and each surface atom has one or two dangling bonds,

Solid-State Photoemission and Related Methods: Theory and Experiment. Edited by Wolfgang Schattke, Michel A. Van Hove

ISBN: 3-527-40334-5

whose number depends on the index of the surface. These dangling bonds are undesirable, and in general, structures of clean semiconductor surfaces reconstruct to minimize the surface energy by decreasing the number of dangling bonds. For example, one of the most frequently studied semiconductor surface, the Si(111) surface, shows a metastable (2×1) reconstructed structure for a cleaved surface, and a stable (7×7) structure after annealing the (2×1) surface to above 600 K. In the case of the Si(111)-(2×1) surface, the atoms of the topmost layer rehybridize from sp^3 into sp^2 orbitals and form π-bonded chains that reduce the number of dangling bonds [1]. Regarding the Si(111)-(7×7) surface, the number of dangling bonds is reduced by a factor of 19/49 from the number of a Si(111)-(1×1) ideal surface by the reconstruction into the dimer-adatom-stacking-fault (DAS) structure [2]. The electronic structures of the Si(111)-(2×1) [3,4] and (7×7) [5–7] surfaces were measured using angle-resolved photoelectron spectroscopy (ARPES) studies, and their electronic structures were reported to be semiconducting and metallic, respectively.

In connection with development of nano-electronic devices, technological and fundamental scientific interests in both metal/semiconductor interfaces and oxidation process of semiconductors increase. Adsorption of metal atoms modifies the electronic structures of clean semiconductor surfaces, and in many cases, changes their geometric structures. To obtain accurate information about these modified electronic and geometric structures, one needs to compare experimental and theoretical results. It is possible to perform such comparison by studying well-ordered systems. Regarding on the oxidation process of semiconductors, a great deal of effort has been devoted to the atomic level understanding of the oxidation of Si. One of the most important issues in the initial oxidation stage, is the presence of metastable oxygen adsorbed on the Si(111)-(7×7) surface. In this section, we first review recent results obtained by ARPES that show the surface electronic structures of ordered low-dimensional (one- and two-dimensional) overlayers on semiconductor surfaces (for former review see for example Ref. [8]), and ARPES and high-resolution core-level spectroscopy studies performed to determine the origin of phase transitions of low-dimensional structures formed on semiconductor surfaces. Then, we review recent photoemission studies on the initial stage of oxidation process of the Si(111)-(7×7) surface, which is not only important to understand the oxidation process but is also an example of studies of non-ordered systems.

12.1.1.2 Ordered overlayers on semiconductor surfaces

Due to its simple electronic structure, the adsorption of alkali metal (AM), which has only a single *s* electron interacting with the surface, is one of the prototype systems to study metal/semiconductor interfaces. Among the reconstructions of AM/Si(111) surfaces, the (3×1) structure, which is formed with a coverage of 1/3 ML, is the ordered structure observed for all AM's [9]. Figures 12.1(a) and (b) show the ARPES spectra of the Na/Si(111)-(3×1) surface measured along the $[11\bar{2}]$ and $[10\bar{1}]$ directions, respectively [10]. Surface states that have quite similar binding energies and show almost the same dispersions were also observed for the Li [11] and K [12] adsorbed Si(111)-(3×1) surfaces. The origins of surface states of AM/Si(111)-(3×1) surfaces are, however, not so easy to understand though a simple electronic structure is expected. That is, the electronic structure of AM/Si(111)-(3×1) surface cannot be explained by the adsorption of AM on a simple substrate structure, e.g., the saturation of every third dangling bond of a (1×1) ideal surface, and thus suggests that the Si substrate has a

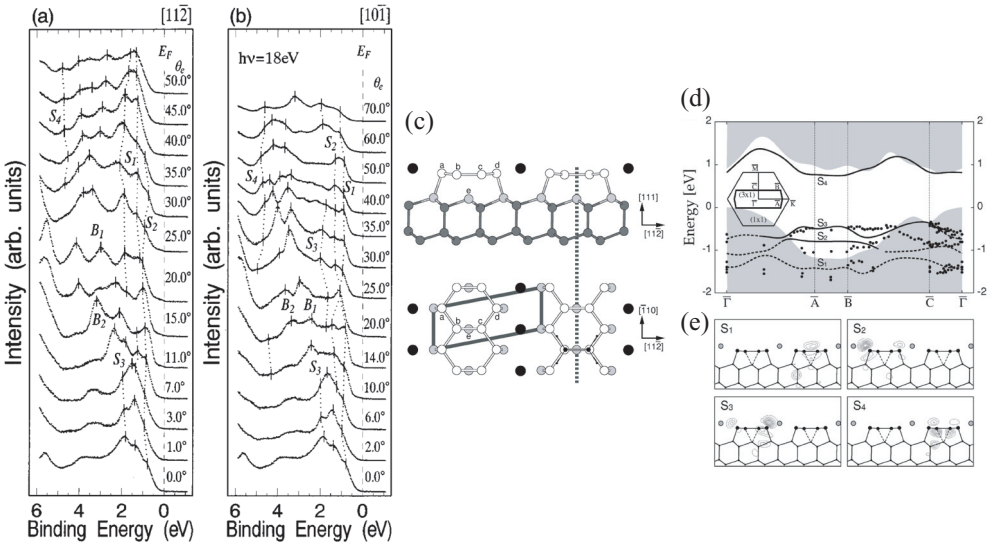

Figure 12.1: ARPES spectra of the Na/Si(111)-(3×1) surface measured along the (a) [11$\bar{2}$] and (b) [10$\bar{1}$] directions from Ref. [10]. The HCC model proposed for the metal adsorbed Si(111)-(3×1) surface is shown in (c) (from Ref. [17]). (d) Calculated surface band structure (solid and dashed lines) with the surface Brillouin zone of the Na/Si(111)-(3×1) surface from Ref. [19]. The filled circles in (d) represent the experimental data of Ref. [10]. (e) Charge character of the representative surface states at the $\bar{A}$ point (from Ref. [19]).

complicated geometric structure. The atomic geometry of the metal adsorbed Si(111)-(3×1) surface has been studied using a vast number of experimental and theoretical methods, and several structural models have been proposed [11–16]. Among them, the model shown in Fig. 12.1(c), which is energetically more stable than the former ones, was reported independently by several groups [17–19]. This model, called the honeycomb-chain-channel (HCC) model, consists of four inequivalent Si surface atoms (labeled a-d in Fig. 12.1(c)) that form a honeycomb-chain along the [$\bar{1}$10] direction, and AM atoms that sit in the channel formed by neighboring honeycomb chains. Further, the Si atoms labeled b and c rehybridize from sp^3 into sp^2 and p_z, and form π bonds in this model. Based on the HCC model, the electronic structure of the Na/Si(111)-(3×1) surface was calculated by density-functional theory [19]. As shown in Fig. 12.1(d), the calculated band structure (solid and dashed lines) agrees well with the experimental results shown in Figs. 12.1(a) and (b) (filled circles in (d)). The good agreement between the experimental and calculated results supports the HCC model for the AM/Si(111)-(3×1) surfaces, and gives the following pictures for the origins of the surface states. The surface states labeled S_1 and S_2 in Fig. 12.1(a) (S_3 and S_2 in Fig. 12.1(d)) originate from the bonding states between the AM and the Si atom labeled a and that between the AM and the Si atom labeled d, respectively, and the S_3 (S_1 in Fig. 12.1(d)) state results from the π bonding state (Fig. 12.1(e)).

The Si(111)-(3×1) surface is formed by not only AM but also by alkaline-earth metals, rare-earth metals (Sm and Yb), and Ag. Although some of the adsorbates actually show dif-

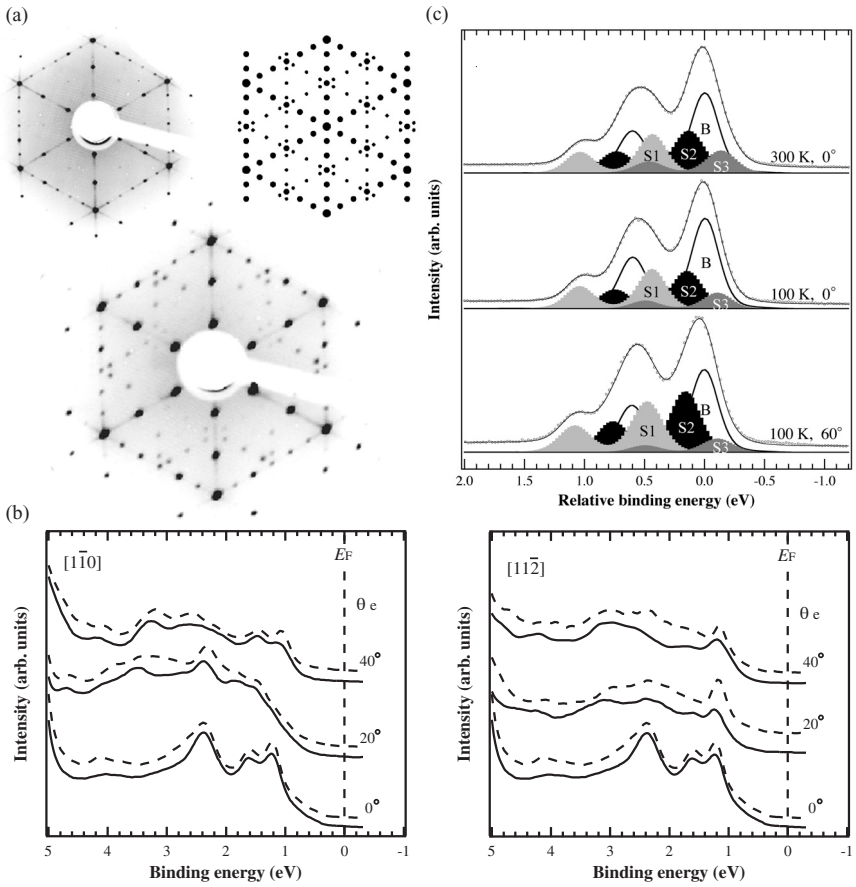

Figure 12.2: (a) LEED pattern of the three domain Ag/Si(111)-(6×1) surface at 300 K, at 100 K, and the schematic LEED pattern of a three domain Si(111)-*c*(12×2) surface. (b) Valence band photoelectron spectra of three-domain Ag/Si(111)-(6×1) and *c*(12×2) surfaces measured at emission angles of 0°, 20°, and 40° along the [1$\bar{1}$0] and the [11$\bar{2}$] directions. Solid and dashed lines correspond to the Ag/Si(111)-(6×1) and the Ag/Si(111)-*c*(12×2) surfaces, respectively. (c) Decomposition of the Si 2*p* core-level spectra of the Ag/Si(111)-(6×1) surface measured at 300 K with a photon energy ($h\nu$) of 130 eV and an emission angle (θ_e) of 0°, and the Ag/Si(111)-*c*(12×2) surface measured at 100 K were recorded with $h\nu$ =130 eV at $\theta_e = 0^\circ$ and 60°. From Ref. [28].

ferent diffraction patterns, e.g., Ag shows a (6×1) pattern [20, 21], all reconstructed surfaces are widely believed to have a quite similar structure based on the similarity of the low-energy electron diffraction (LEED) I-V curves [22, 23], scanning-tunneling-microscopy (STM) images [15, 24–26], and surface core-level shift (SCLS) measurements [11, 26, 27]. In the case of the Ag/Si(111)-(6×1) surface, the structure originates from a slight displacement of the surface atoms of the (3×1) structure [17, 21]. Further, the Ag/Si(111)-(6×1) surface transforms into a *c*(12×2) structure by cooling to 100 K [28]. Figure 12.2(a) shows the LEED

pattern of the three domain Ag/Si(111)-(6×1) surface at 300 K, the LEED pattern obtained after cooling the Ag/Si(111)-(6×1) surface to 100 K, and the schematic LEED pattern of a three domain Si(111)-c(12×2) surface. The valence band spectra of the Ag/Si(111)-(6×1) and c(12×2) surfaces are shown in Fig. 12.2(b). From Fig. 12.2(b), one notices that the spectra of the Ag/Si(111)-(6×1) and c(12×2) surfaces are very similar along both the $[1\bar{1}0]$ and $[11\bar{2}]$ directions. The analyzed Si 2*p* core-level spectra of the Ag/Si(111)-(6×1) and c(12×2) surfaces, which give quantitative information for the structures, show that both the Ag/Si(111)-(6×1) and c(12×2) surfaces have three surface components that agree well in the energy shifts (Fig. 12.2(c)). Such results for the valence band and the Si 2*p* core-level spectra from different surface structures, were also observed on the clean Si(001) surface [29]. That is, the room temperature Si(001)-(2×1) and low temperature c(4×2) phases show very similar valence band spectra, and almost the same Si 2*p* spectra that have surface components with the same energy shifts. In this case, the similarity of the Si 2*p* core-level spectra indicates that the local surface structure is the same for the two phases, and that the room temperature (2×1) phase results from the dynamical flipping of the asymmetric dimers [30] at a high frequency. Since the translational vectors of the c(12×2) unit cell are twice as long compared to the (6×1) reconstructed structure, there should be an alternate displacement of Ag atoms and/or the site of the top-layer Si atoms along both translational vectors. The observation of only the (6×1) pattern at a higher temperature indicates a disorder in the atomic displacements due to thermal vibrations in similarity with the clean Si(001) surface. These results reveal that the basic unit cell of the so-called Ag/Si(111)-(6×1) surface has a c(12×2) periodicity, and the (6×1) phase results from the thermally induced disorder of the atomic displacements of the c(12×2) structure. Further, the origins of the Si 2*p* surface components are well explained using the HCC model, and thus these photoemission results reveal that the structure of the Ag/Si(111)-c(12×2) surface is basically the same as that of the HCC model but with a slight displacement of Ag and/or top-layer Si atoms to introduce the necessary atomic displacements.

Besides the (6×1) structure, the Ag adsorbed Si(111) surface shows different phases at different coverages and temperatures. At a coverage of 1 ML, a $(\sqrt{3}\times\sqrt{3})$ phase is formed after annealing the sample to above 600 K. Below room temperature, $(\sqrt{21}\times\sqrt{21})$ and (6×6) phases are formed by adding extra Ag on the $(\sqrt{3}\times\sqrt{3})$ surface [31, 32]. One of the interests about these three phases is the change in the surface conductance, especially the high surface conductance value of the $(\sqrt{21}\times\sqrt{21})$ phase [32]. The high surface conductance of the Ag/Si(111)-$(\sqrt{21}\times\sqrt{21})$ surface and the low conductance of the (6×6) surface results from their metallic and semiconducting electronic structures observed using ARPES [33]. Regarding the Ag/Si(111)-$(\sqrt{3}\times\sqrt{3})$ surface, a partially occupied dispersing surface state band, which is labeled S_1 in Fig. 12.3(A) and labeled S in (B), is observed in a number of ARPES studies [34, 35]. Since the number of electron is even in the $(\sqrt{3}\times\sqrt{3})$ unit cell, and thus Ag/Si(111)-$(\sqrt{3}\times\sqrt{3})$ surface should have a semiconducting electronic structure according to the electron counting, a question arises on the metallic band observed in ARPES. That is, is the partially occupied surface state observed in ARPES intrinsic or extrinsic? In order to answer this question, a theoretical calculation [36] was performed on the two models proposed for the Ag/Si(111)-$(\sqrt{3}\times\sqrt{3})$ surface, i.e., the honeycomb-chained-triangle (HCT) [37, 38] and the inequivalent triangle (IET) [36] models (Figs. 12.3(C)). As shown in Fig. 12.3(D), one band crosses the bulk valence-band barely in the HCT model, while the crossing is clearer in the IET model in the calculated band structures. Taking into account that the IET model is

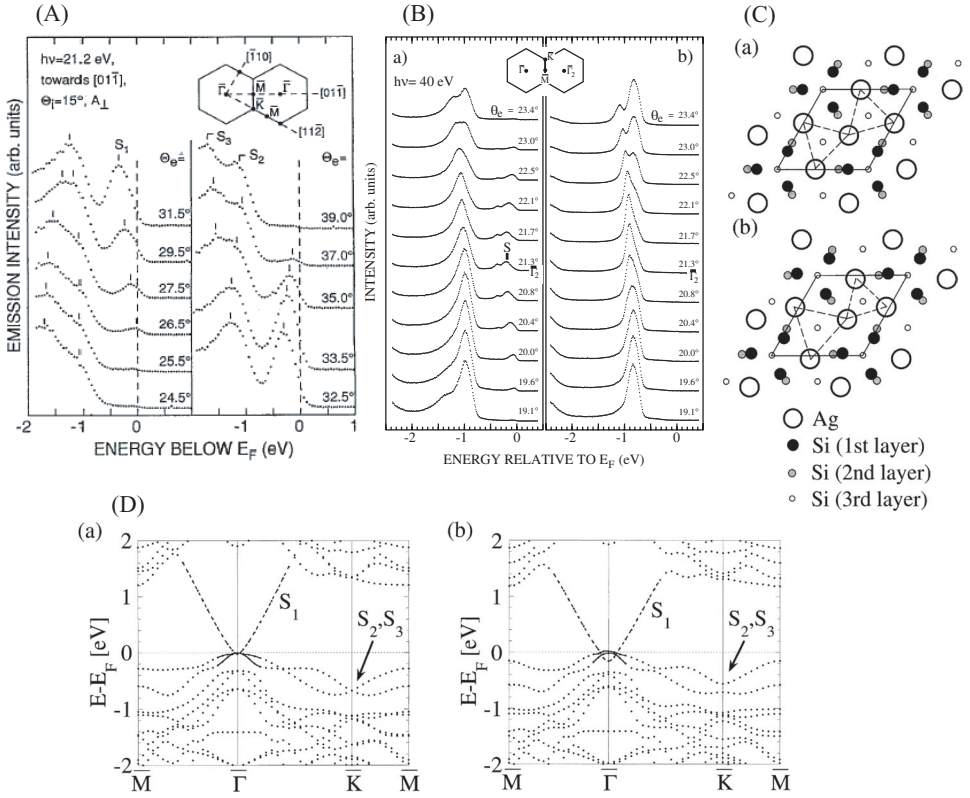

Figure 12.3: (A) ARPES spectra of the Ag/Si(111)-($\sqrt{3} \times \sqrt{3}$) surface surface recorded with a photon energy of 21.2 eV in the [01$\bar{1}$] direction from Ref. [34]. The emission angles correspond to emission around the $\bar{\Gamma}$ point of the second ($\sqrt{3} \times \sqrt{3}$) surface Brillouin zone. (B) ARPES spectra recorded with $h\nu$ =40 eV for the Ag/Si(111)-($\sqrt{3} \times \sqrt{3}$) surface prepared by annealing the 1.2 ML adsorbed sample at 813 K in (a) and at approximately 873 K in (b) (from Ref. [39]) (C) (a) Honeycomb-chained-triangle (HCT) and (b)inequivalent triangle (IET) models proposed for the Ag/Si(111)-($\sqrt{3} \times \sqrt{3}$) surface from Ref. [36] (D) Calculated band structures of the HCT and IET models are shown in (a) and (b), respectively (from Ref. [36]).

energetically more stable than the HCT model, this theoretical study suggested the IET model to be the structure of the Ag/Si(111)-($\sqrt{3} \times \sqrt{3}$) surface and the observed metallic band to be intrinsic. Another feature of the IET model is the split of the two bands labeled S_2 and S_3 at the $\bar{K}$ point, which are degenerate in the HCT model. However, in the ARPES measurement [33], no splitting was observed at the $\bar{K}$ point. This means that the IET model is not supported experimentally, and that the metallic band observed in Figs. 12.3(A) and (B) would be an extrinsic feature. Since the extra Ag atoms on the Ag/Si(111)-($\sqrt{3} \times \sqrt{3}$) surface at low temperature do not only play a role for the formation of the superstructures but also affect the electronic structure by donation of their outermost *s* electron to an unoccupied surface band [33], it is natural to consider that the presence of extra Ag at room temperature

can also affect the electronic structure of the $(\sqrt{3} \times \sqrt{3})$ surface that is intrinsically unoccupied. Figure 12.3(B) shows the ARPES spectra of the Ag/Si(111)-$(\sqrt{3} \times \sqrt{3})$ surface formed by annealing a 1.2 ML Ag adsorbed Si(111) surface at 813 K in (a), and by annealing at approximately 873 K in (b) [39]. Although both samples annealed at 813 K and 873 K showed excellent $\sqrt{3} \times \sqrt{3}$ LEED patterns, the spectra displayed in Figs. 12.3(B)(a) and (b) are quite different. A metallic surface band is observed in Fig. 12.3(B)(a), whereas no state crosses the Fermi level in Fig. 12.3(B)(b). Taking into account that Ag atoms desorb from the surface at a temperature around 873 K, the difference observed in the ARPES spectra results from the different amount of extra Ag on the surface. That is, a certain amount of extra (< 0.2 ML) Ag exists on the surface even after annealing at 813 K, whereas there is no extra Ag after annealing at 873 K. This ARPES result indicates that the Ag/Si(111)-$(\sqrt{3} \times \sqrt{3})$ surface is intrinsically semiconducting, and the presence of extra Ag produces a metallic band by a donation of electron to an intrinsically unoccupied surface band. Further, this result gives the following suggestions. LEED observations is not enough to characterize the surface, and a careful attention is necessary for the sample preparation to obtain intrinsic surface electronic structures.

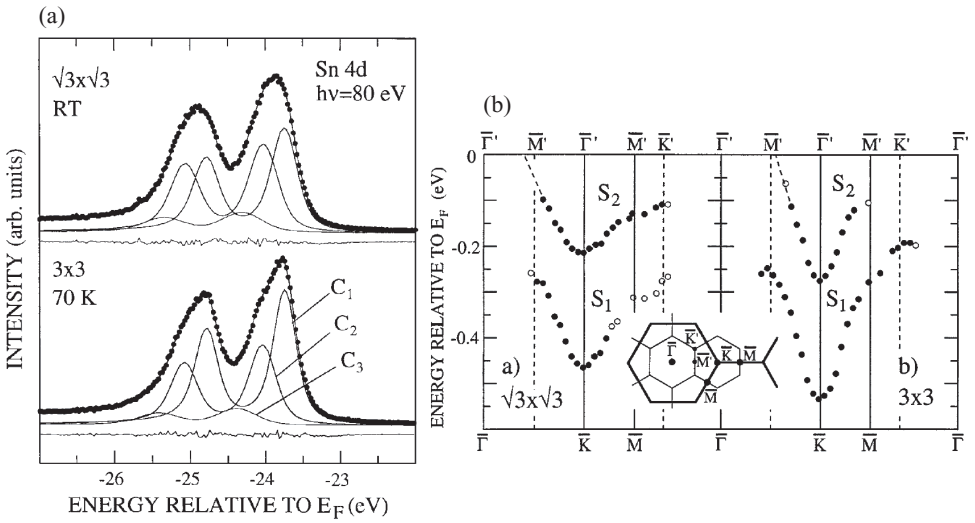

Figure 12.4: (a) Sn 4*d* core-level spectra from the Sn/Ge(111)-$(\sqrt{3} \times \sqrt{3})$ and (3×3) surfaces from Ref. [49]. (b) Surface state dispersion of the Sn/Ge(111)-$(\sqrt{3} \times \sqrt{3})$ and (3×3) surfaces along the major symmetry lines of the surface Brillouin zones. Symmetry points of the $(\sqrt{3} \times \sqrt{3})$ and (3×3) surface Brillouin zones are indicated below and above the panels, respectively. Inset shows the $(\sqrt{3}\times\sqrt{3})$ (thick lines) and (3×3) (thin lines) surface Brillouin zones (from Ref. [47]).

Compared to the complicated geometric structure of the Ag/Si(111)-$(\sqrt{3} \times \sqrt{3})$ surface, the $(\sqrt{3} \times \sqrt{3})$ surfaces induced by group III atoms (Al, Ga and In) on Si(111) or Ge(111) surfaces are quite simple. That is, these $(\sqrt{3} \times \sqrt{3})$ surfaces are formed by the adsorption of 1/3 ML of adatoms on the T_4 sites of the (1×1) ideal surface [40]. The Ge(111)-$(\sqrt{3} \times \sqrt{3})$ surfaces induced by Sn or Pb, whose structures have also been considered to be the T_4

model, were reported to show an interesting transition into a (3×3) periodicity below room temperature using STM [41,42]. This change in periodicity has been described to be a charge density wave (CDW) transition driven by either electron-phonon coupling [41] or electron-electron correlation [42,43]. Taking into account that all Sn atoms are adsorbed on equivalent sites in the T_4 model and that two different types of Sn are observed in STM for the (3×3) phase, one expects to observe only one type of Sn atoms for the ($\sqrt{3} \times \sqrt{3}$) phase and two for the (3×3) phase in the core-level study within the CDW transition picture. However, most of the Sn core-level studies [44–49] show the presence of two types of Sn atoms for the ($\sqrt{3} \times \sqrt{3}$) phase, and almost the same Sn core-level lineshape as that of the ($\sqrt{3} \times \sqrt{3}$) phase is observed for the (3×3) phase [46–49]. That is, as shown in Fig. 12.4(a), the two major components (C_1 and C_2), which originate from Sn atoms that form the superstructures, are observed in both phases (the C_3 component results from the Ge substitutional defects). In the valence band spectra, two surface bands are observed on both the ($\sqrt{3} \times \sqrt{3}$) and (3×3) phases (Fig. 12.4(b)) [47]. Further, the two surface bands observed on the (3×3) phase show the same dispersion as those on the ($\sqrt{3} \times \sqrt{3}$) surface. The similarities observed in the core-level studies and the valence-band study for the ($\sqrt{3} \times \sqrt{3}$) and (3×3) phases indicate that the atomic structure of the two phases should be very similar, and that there should be two types of Sn on both surfaces. The presence of two types of Sn reveals that the structure of the ($\sqrt{3} \times \sqrt{3}$) phase cannot be the simple T_4 model. These photoemission results imply that the origin of the ($\sqrt{3} \times \sqrt{3}$) $\leftrightarrow$ (3×3) change is not a general CDW transition, and for example might be similar with that of the Ag/Si(111)-(6×1) $\leftrightarrow$ *c*(12×2) surface and the Si(001)-(2×1) $\leftrightarrow$ *c*(4×2) surface.

12.1.1.3 Initial stage of oxidation of the Si(111)-(7×7) surface

Adsorption and reaction of oxygen are important subjects of physical and chemical interest for the understanding of the oxidation processes of materials. Regarding Si, the metastable oxygen adsorbed on the Si(111)-(7×7) surface, whose lifetime was reported to be from approximately 10 min [50–53] to several hours [54–59], is one of the most important issues to understand the initial chemisorption stage. Especially, the determination of its bonding configuration is quite important to understand the oxidation process of Si on an atomic level. In the early studies, the metastable species was reported to be a molecular species, the so-called molecular precursor, that is adsorbed on top of an adatom of a clean Si(111)-(7×7) DAS [2] structure (the "paul" configuration shown in Fig. 12.5(A)). However, in studies based on density functional theory (DFT) calculations [60, 61], it was stated that the metastable oxygen has an atomic oxygen configuration (the "ad-ins" configuration in Fig. 12.5(A)). These DFT calculations [60, 61] reinterpreted the earlier valence band photoemission [52, 54, 55, 62] and O 1*s* core-level [52,58] results, in which the metastable oxygen was reported to be a molecular species. Nevertheless, as shown in Fig. 12.5 (B), the complex valence band electronic structure of the Si(111)-(7×7) surface, which is observed by the experimental condition used in the early studies, hinders the accurate information about the electronic structures of the oxygen adsorbed species. For example, only one state that originates from the metastable state is observed at a binding energy of 3.8 eV in Fig. 12.5(B). This means that even if the DFT calculations reinterpreted the earlier spectroscopic studies, the bonding configuration of the metastable oxygen is still unfixed at that point of time.

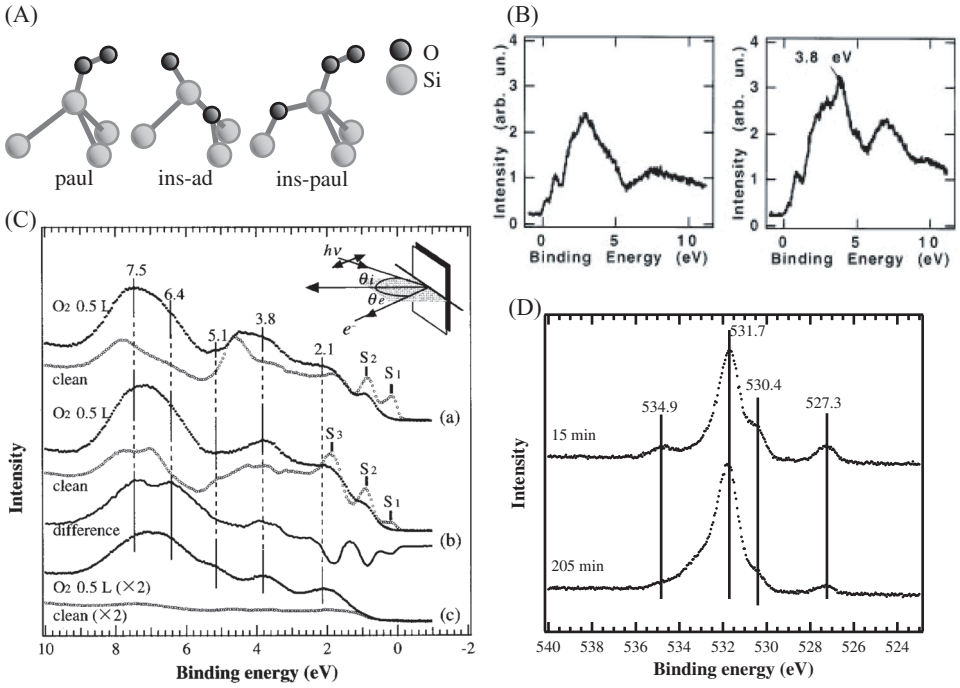

Figure 12.5: (A) Schematic illustrations of the bonding configurations for the metastable oxygen on a Si(111)-(7×7) surface. (B) Valence band spectra of a clean (left) and 0.15 L adsorbed (right) Si(111)-(7×7) surface obtained with $h\nu$ =40.8 eV (from ref. [62]). (C) Valence band spectra of a 0.5 L O_2 exposed Si(111)-(7×7) surface measured with $h\nu$ =21.2 eV (from Ref. [63]). (a) are recorded with geometry of ($\theta_i = 45°$, $\theta_e = 15°$), (b) ($\theta_i = 45°$, $\theta_e = 20°$), and (c) ($\theta_i = 0°$, $\theta_e = 60°$). (D) High-resolution O 1*s* core-level spectra recorded 15 min and 205 min after 20 L O_2 exposure on Si(111)-(7×7) surface (from Ref. [64].

Using a certain experimental condition, it is possible to minimize the intensity of the electronic structure of the Si(111)-(7×7) surface, and thus to enhance the electronic structure of the adsorbed oxygen species [63]. Figure 12.5(C) shows the valence band spectra of the clean (open circles) and 0.5 Langmuir (1 L=1×10^{-6} Torr × 1 sec) oxygen exposed Si(111)-(7×7) surfaces (filled circles) obtained at different experimental geometries. The spectra in (a) are recorded with a geometry of ($\theta_i = 45°$, $\theta_e = 15°$), (b) ($\theta_i = 45°$, $\theta_e = 20°$), and (c) ($\theta_i = 0°$, $\theta_e = 60°$), where θ_i is the incident photon angle and θ_e is the electron emission angle. As shown in Fig. 12.5(C), the spectra of the clean surface obtained by $\theta_i = 45°$ (the spectra in (a) and (b)) show complex electronic structures, whereas the spectrum of the clean surface obtained using a condition of ($\theta_i = 0°$, $\theta_e = 60°$) is structureless. According to the low intensity from the Si surface, five oxygen induced states, which are hardly recognized in Figs. 12.5(C)(a) and (b), are clearly observed in (c). Among the five oxygen induced states, the three at binding energies of 2.1, 3.8 and 5.1 eV disappear after annealing the sample at 600 K, and show the same oxygen dosage dependent-intensity. The disappearance at 600 K

indicates that they result from the metastable oxygen, and the same dosage dependent-intensity denotes that they originate from one and the same bonding configuration. Further, the dosage-dependent intensities of the three metastable states follow the dosage-dependent decrease in intensity of the back-bond states of adatoms of the DAS structure [2], and the dangling bond states of adatoms reappear after the 600 K annealing. These results denote that the adsorption of metastable species affects both the dangling bond and the back-bond of adatoms.

In the early O 1*s* core-level studies [52, 58], only two metastable components were observed at most. These early results suggest that the metastable oxygen consists of two oxygen atoms with different chemical environments. However, one has to notice that the poor resolution used in the early studies might hinder the determination of the accurate number of atoms, which constitute the metastable species. In fact, the high-resolution O 1*s* core-level study [64] reveals the presence of three metastable components. Figure 12.5(D) shows the high-resolution O 1*s* core-level spectra recorded (a) 15 min and (b) 205 min after exposing the Si(111)-(7×7) surface to 20 L of O_2. Among the structures observed in Fig. 12.5(D), the intensities of the 527.3-, 530.4-, and 534.9-eV peaks decrease with time, suggesting their origins to be the metastable oxygen. Moreover, their intensities show the same dosage dependence indicating that the three metastable components at 527.3, 530.4 and 534.9 eV result from one and the same bonding configuration, and therefore that three oxygen atoms with different chemical environments compose the metastable oxygen. Taking the symmetry of the bonding configurations into account, one realizes that it is impossible to reproduce three oxygen atoms with different chemical environments by the adsorption of atomic oxygen to the dangling bond and the back-bonds of one adatom, and therefore that the configuration of the metastable oxygen should be a molecular one. The valence band [63] and high-resolution 0 1*s* core-level [64] studies indicate that the metastable species does not adsorb on the clean surface, i.e., it is not a precursor, but has the "ins-paul" configuration shown in Fig. 12.5(A). Such result is hard to obtain by for example STM, and shows how powerful photoelectron spectroscopy is to determine the atomic geometric structure of a non-ordered surface.

12.2 Two-dimensional photoelectron spectroscopy

12.2.1 Two-dimensional photoelectron diffraction stereograph

Two-dimensional angular distribution (2DAD) of photoelectrons has full information in photoelectron spectroscopy, and recently applied to Fermi surface mapping or photoelectron diffraction, and holography. 2DAD can be obtained either by rotating sample, rotating analyzer, or by using display analyzer. The relation between the orientation of the sample and the direction of the electric vector of photon changes in the rotating-sample method. The information obtained in the rotating-analyzer method and in the display analyzer method is basically identical. Display-type spherical-mirror analyzer [65–67] can display 2DAD of photoelectrons of a specific kinetic energy at a time in a very wide acceptance angles without distortion. This advantage allows this analyzer to be used in a variety of applications. Recently it was modified so as to achieve higher energy resolution and even wider acceptance angles [68].

Here described are recent discovery and invention related to this analyzer, that is, "circular dichroism in photoelectron diffraction" [69], and "stereo microscopy of atomic arrangement"

[70]. The forward focusing peaks in a 2DAD pattern taken with left and right helicity light were found to shift azimuthally [69]. These shifts are the same as the parallaxes in a stereo view of atoms, and stereo photographs of atomic arrangement can be displayed directly on its screen without any computer-aided conversion process [70]. Stereoscopic recognition of three-dimensional atomic arrangement has become possible for the first time.

12.2.1.1 Display-type spherical mirror analyzer

A display-type spherical mirror analyzer (DIANA) (Fig. 12.6) was invented in 1988 [65] and gradually improved [66,67]. Comparing with Eastman-type display analyzer [71,72], this analyzer has two advantages. One is that the angles of emission and detection of photoelectrons are exactly parallel; hence the pattern displayed on its screen is not distorted. The other is that the acceptance angle can be made infinitely wide, because the convergence to the exit aperture is exact irrespective of the angle and has no higher order terms. Hence one can measure the angular distribution of particles of one particular kinetic energy up to about 2π steradian at a time.

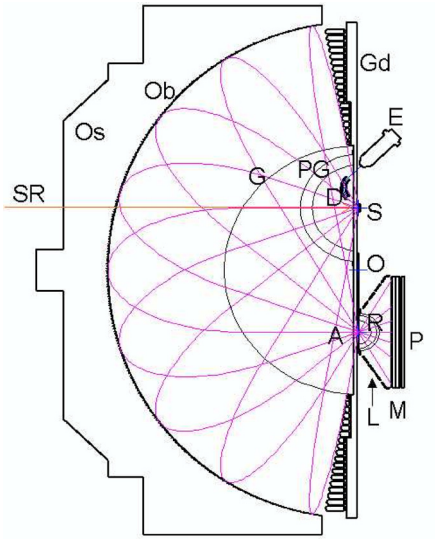

Figure 12.6: Display-type spherical mirror analyzer(DIANA)

The original analyzer has been applied to many surface studies, such as electron diffraction [73], two-dimensional photoelectron diffraction [74,75], photoelectron holography [76], electron stimulated desorption ion angular distribution (ESDIAD) [77–82], circularly polarized light photoelectron diffraction [69, 83–85], two-dimensional valence band analysis [86–95] etc. In the development of the analyzer, the energy analysis method has been changed from "focus-defocus" [65] to "high-pass and low-pass filter" [66, 67]. The energy resolution of the conventional DIANA has been about 1% of the pass energy.

Figure 12.6 shows a schematic view of the new display-type spherical mirror analyzer [68]. It consists of a hemispherical grid G, obstacle rings Ob and guard rings Gd. The number of

obstacle rings and guard rings are 260 and 20, respectively. The Ob's are axially symmetric with respect to the axis connecting the sample and the center O of the hemisphere, and their inner surfaces are a part of concentric spheres. G is usually grounded. The potential $V(r)$ of Ob's and guard rings are biased according to their radii r from O by a formula $V(r) = -2E_0(1 - a/r)$, where E_0 is the pass energy and a is the radius of the main grid G. The electrostatic field in the space surrounded by the electrodes G, Ob and Gd is thus made spherically symmetric with respect to the center O. The orbits of the emitted electrons from the sample are subjected to this field after passing through G, and their loci are ellipsoids obeying Kepler's law. Their trajectories inside G are straight lines.

The electrons converge exactly to the exit aperture A, which is located at the symmetric position of S with respect to O. Their incident angles are exactly parallel to their emission angles. Ob's play essential roles in energy analysis by cutting unnecessary electrons that have higher kinetic energies than the pass energy E_0 [2,3]. An electron having a little higher energy flies along a little outside locus and hit into the electrodes and absorbed or scattered, and hardly passes through the small aperture A. Thus the Ob's work as a "low-pass filter". On the other hand, retarding grid R works as a "high-pass filter" which retards the electrons having lower kinetic energies than the applied potential.

The electrons having passed through the retarding grid are amplified by a pair of microchannel plates (MCP) M and converted by a phosphor screen P to light pulses, which are detected from outside the vacuum chamber by a cooled CCD camera. The 2DAD on the screen is the same as the original angular distribution in front of the sample. An electron gun E is mounted for the purpose of LEED measurement. Synchrotron radiation SR is introduced through a hole. The acceptance cone covered by the MCP is $\pm 60^\circ$. This acceptance angle can be increased up to $\pm 80^\circ$ by using the lens L. The diameter of the main grid was two-times enlarged from 150 mm of the old analyzer to 300 mm. The shaping accuracy of Ob was intended to be within 50 μm. The energy resolution ($\Delta E/E_0$) of the present analyzer has been estimated to be 0.25% of the pass energy, which is four times higher than before. Angular resolution was estimated to be 0.6°.

12.2.1.2 Structure analysis by two-dimensional photoelectron diffraction, holography

The analysis of local atomic arrangements of surface and nano-materials is essential in understanding their microscopic phenomena. The development of the STM (scanning tunneling microscope) has made it possible to obtain atomic images easily, but it cannot indicate the relation between the top atom and the second layer atoms. An electron microscope can produce atomic images, but they are only two-dimensionally projected image. Usually, LEED (low-energy electron diffraction) or X-ray diffraction analysis is used to analyze detailed atomic positions on a surface, but they are complicated and indirect methods.

Recently, many direct methods for three-dimensional analysis using the technique of electron diffraction and holography have been developed, such as photoelectron holography [76, 96, 97], Kikuchi-electron holography [98–100] or correlated thermal diffuse scattering [101]. Holography analysis produces the three-dimensional atomic arrangement around the emitter atom by a Fourier transformation of the 2DAD pattern. Photoelectron holography is more powerful than Kikuchi-electron holography because it can specify an emitter by selecting the kinetic energy of photoelectrons. These holographic analyses are rather direct method be-

cause they do not need a trial model of atomic arrangement. Although its accuracy is not high (about 0.2 Å), it is useful for a distinction of various models or for making a first trial model for LEED analysis.

Figure 12.7 shows a various features in 2DAD pattern. The atom O produces a photoelectron wave Ψ^0 when it was excited by an X-ray. Ψ^0 produces a scattered wave Ψ^S when it hits a scatterer atom, for example A. The 2DAD pattern is described by a square of the sum of Ψ^0 and all Ψ^S's from nearby atoms. When the emitter atom is in the surface region, the characteristic features are "Forward focusing peaks" and "Interference rings". When the emitter atom is in the bulk they produce "Kikuchi bands" and "Kossel lines".

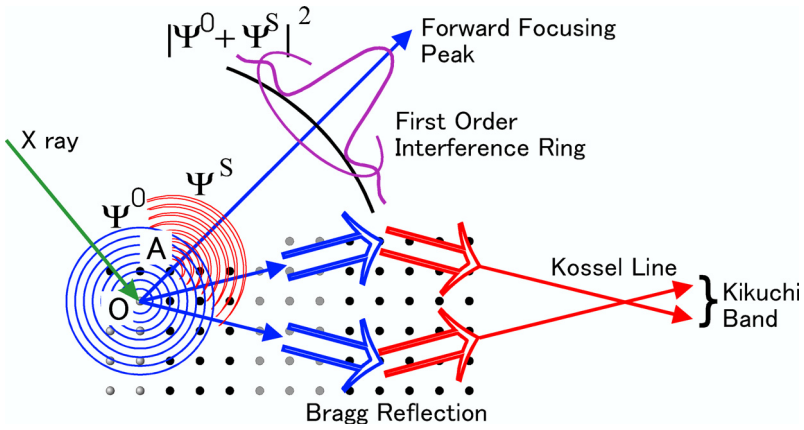

Figure 12.7: Various features in two-dimensional angular distribution (2DAD) pattern.

12.2.1.3 Surface photoelectron diffraction

Forward focusing peaks When the kinetic energy of a photoelectron is higher than several hundred eV, a strong forward focusing peak appears along the direction connecting the emitter and the scatterer. Figure 12.8 is an example of forward focusing peaks. It is a 2DAD pattern of the W 4f photoelectrons, from only the first-layer W atoms on W(110)1 × 12-O surface [102]. The photoelectrons from the first layer W atoms are easily distinguished from those of bulk W atoms utilizing a large chemical shift (0.73 eV). The 2DAD pattern of bulk photoelectrons will be shown later. Figure 12.8 is plotted by stereographic projection method. The center of the pattern corresponds to the surface normal direction and the edge corresponds to the polar angle of 90°. The excitation light is Al Kα.

We can see six strong forward focusing peaks. There are two domains on this surface, where O atoms are sitting at the middle of upward and downward triangles, as shown in Fig. 12.9. The directions of the peaks A, B, C, A′, B′, and C′ correspond to the direction of oxygen atoms seen from the first-layer W atoms.

The measurement of the directions of forward focusing peaks is sufficient for three-dimensional analysis when the structure is simple. In this case the position of adsorbed oxygen was determined directly from the directions of these peaks [102]. Usually, however, the pre-

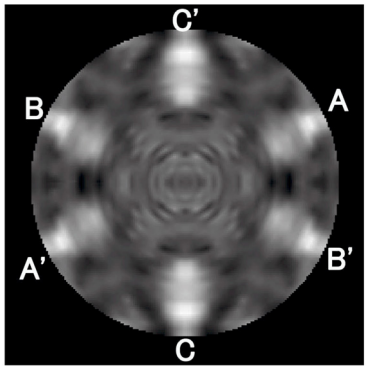

Figure 12.8: 2DAD of surface W4f XPD from W(110)1 $\times$ 12-O.

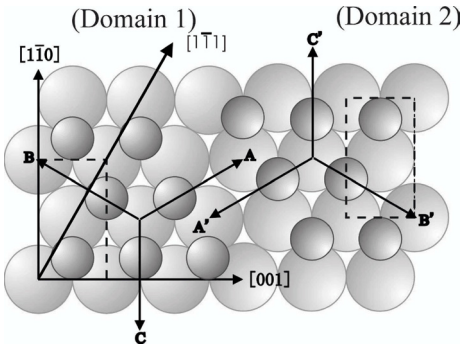

Figure 12.9: Structure of W(110)1 $\times$ 12-O surface.

cise structure can be obtained by comparing the observed pattern with the pattern calculated including multiple-scattering.

Interference Rings The interference rings are hardly seen in Fig. 12.8, because the forward focusing peaks are much stronger than them. Figure 12.10(a) shows an example of such rings. This pattern is the angular distribution of O 1s photoelectrons from adsorbed oxygen on W(110)1 $\times$ 12-O surface. We can see first, second, and even third order rings around the axes $\langle 1\bar{1}1\rangle$, $\langle 001\rangle$, and $\langle 1\bar{1}0\rangle$. Because the O atoms are sitting at the top of the surface, the forward focusing peaks must appear along the surface, which are out of the measurement area. Hence, we can see only diffraction rings. The fact that we can see these rings, whose center is at the polar angle of 90°, means that O atoms are sitting at the top of the surface. The order of the size of the ring is $\langle 1\bar{1}1\rangle$, $\langle 001\rangle$, and $\langle 1\bar{1}0\rangle$, which means that the nearest atoms are in $\langle 1\bar{1}1\rangle$ directions, and the second and the third nearest atoms are in $\langle 001\rangle$ and $\langle 1\bar{1}0\rangle$ directions, as shown in Fig. 12.9.

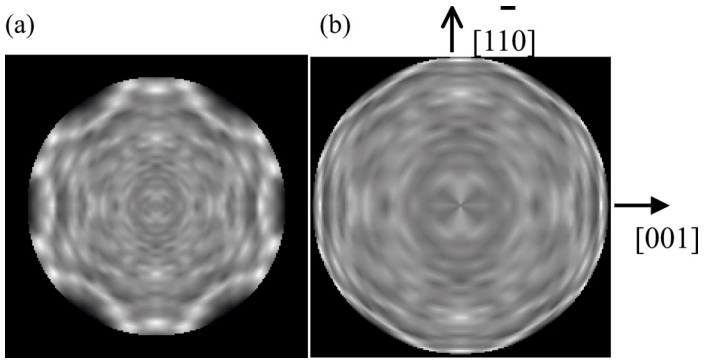

Figure 12.10: 2DAD of O1s photoelectrons from W(110)1 $\times$ 12-O surface.

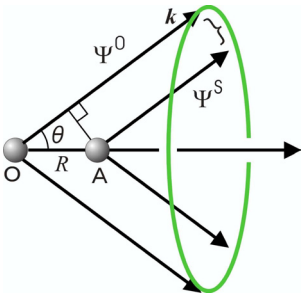

Figure 12.11: Geometry of the interference ring.

Figure 12.11 shows a diagram to show how these rings appear. Neglecting the phase of the scattering factor of atom A, the phase difference between Ψ_0 and Ψ_S is $kR - kR\cos\theta$. Hence the rings appear at θ satisfying

$$kR(1-\cos\theta) \quad = \quad 2\pi n \tag{12.1}$$

where n is an integer. In Fig. 12.10(b) the data of Fig. 12.10(a) is plotted so that the distance from the center is in proportion to $\cos\theta$, which is also proportional to the lateral momentum of the photoelectron. We can see that the rings in Fig. 12.10(a) became parallel lines in Fig. 12.10(b). This fact implies that Eq. (12.1) holds. The interatomic distance R can be calculated easily from the spacing $\delta(k\cos\theta)$ as $R = 2\pi/\delta(k\cos\theta)$.

12.2.1.4 Bulk photoelectron diffraction

Figure 12.12 shows an example of bulk photoelectron diffraction pattern. We can see strong peaks in [100] and [111] directions, which are forward focusing peaks along these crystallographic axes. The broad lines connecting these axes are called Kikuchi bands. The band edge is dark here, but it will be bright if the mean-free-path of photoelectrons become longer at higher kinetic energies. When these edges are strong, they are called Kossel lines. Original spherical photoelectron waves are considered as plane waves in a distance. The Bragg reflections of these plane waves produce the Kossel lines and Kikuchi bands as shown in Fig. 12.7. We can know the crystal orientation easily from Kikuchi pattern. The width of the band gives interlayer spacing.

12.2.1.5 Photoelectron holography

As described in another section in this book, it has been recognized that the holographic method (Fourier transformation) to obtain the real structure is not so straightforward. The difficulty in the photoelectron holography comes mainly from the strong forward focusing peaks in the 2DAD pattern, which always appear when the emitter atom is below the scatterer atoms. Many efforts have been made to eliminate the disturbance from these forward focusing peaks by means of SWIFT [98], SWEEP [103], energy extension [104], or differentiation [105].

Because the pattern of Fig. 12.10 consists of only interference pattern, it seems a good pattern for the holographic analysis, The Fourier reconstructed structure image of Fig. 12.10

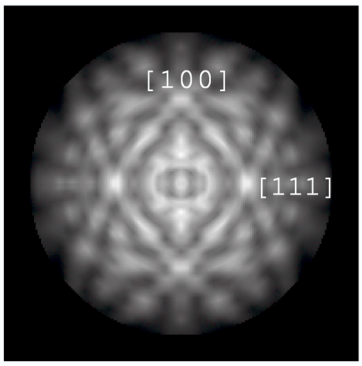

Figure 12.12: 2DAD of bulk W4f XPD from W(110)1 $\times$ 12-O.

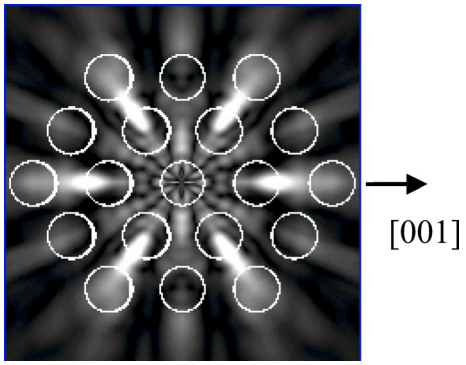

Figure 12.13: O1s holography from XPD of W(110)1 $\times$ 12-O.

is shown in Fig. 12.13 [106]. We can see strong peaks near the expected positions indicated by circles. The accuracy, however, is about 20% in this case.

12.2.1.6 Circularly polarized-light photoelectron diffraction

In general, a forward focusing peak has information about the direction from the emitter to the scatterer but does not have the information about the distance between them. Recently, it was found that the forward-focusing peak-positions in a 2DAD pattern excited by a circularly polarized light rotate in the same direction as the rotation of the electric vector of the light [69, 107]. This is a strong circular dichroism in photoelectron diffraction (CDPD) for non-chiral and non-magnetic materials

Figure 12.14(a) and (b) are examples of CDPD [107]. The six peaks are the same forward focusing peaks seen in XPD (Fig. 12.8). Here the photoelectron kinetic energy is 317 eV, the photon was incident normal to the surface, and the polar take-off angle range is from 61.0° to 73.5°.

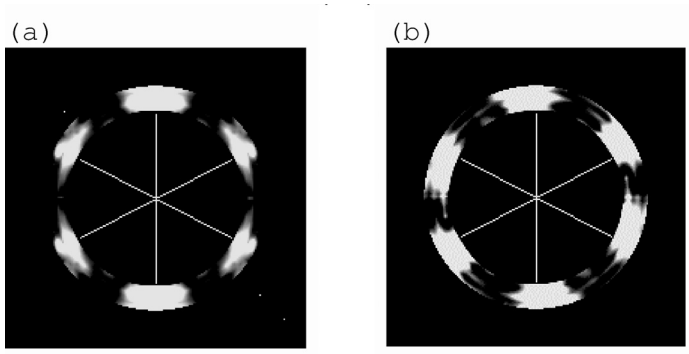

Figure 12.14: Rotation of forward focusing peaks excited by (a) LP and (b) LCP.

Figure 12.14(a) is the result of linearly polarized (LP) and (b) is of left circularly polarized (LCP) light. Here the definition of LCP is that the rotation direction of the electric vector of the photon in the plane of Fig. 12.14(b) is counter-clockwise (ccw). Because the emitter atom is the top layer W atom and there are only O atoms above it, these forward peaks in Fig. 12.14 are considered to be dominated by single scattering. It is clear that there is a tendency for the pattern to shift counterclockwise with LCP excitation in Fig. 12.14(b).

All these shifts are considered to be a rotation of the forward focusing peaks with respect to the photon incident direction ([110] axis). Such peak "rotations" are of the same qualitative type as seen for Si(001) [69], which was found recently by Daimon *et al.* in the photoelectron diffraction patterns from non-chiral and non-magnetic systems. This rotation has been explained as being due to the transfer of the angular momentum of photons to the photoelectrons, whose z component ratio has been biased while being excited by the circularly polarized light.

The rotation angle Δ of the peak around the photon incident axis is reproduced well by the simple formula [69]

$$\Delta \quad = \quad \tan^{-1} \frac{m}{kR\sin^2\theta} \simeq \frac{m}{kR\sin^2\theta} \tag{12.2}$$

Detailed theoretical works [83, 108, 109] support this formula. Here, m is the magnetic quantum number (z component angular momentum) of the photoelectron, k is its wave number, R is the internuclear distance between the emitter and the scatterer, and θ is the angle between the photon incident direction and the outgoing photoelectron direction, as shown in Fig. 12.15. When the position vector of the scatterer from the emitter is described as (R, θ, ϕ), the peak position observed by using cw and ccw circularly polarized light appears at (θ, $\phi \pm \Delta$). Using this formula we can construct three-dimensional atomic structure directly by measuring the azimuthal shift of the forward focusing peaks in the photoelectron diffraction patterns excited by the circularly polarized light [84, 85]. Hence, this method positively utilizes the forward focusing peaks for the structural analysis.

12.2.1.7 Peak rotation and the orbital angular momentum

The characteristic feature of the photoelectrons excited by a circularly-polarized light is that it has an orbital angular momentum around the incident light. We consider the photoelectrons from an initial core state Ψ_i with the quantum number of the angular momentum l' and its z-component m'. Its angular part can be described by a spherical harmonic $Y_{l'm'}(\theta, \phi)$. The quantum axis (z-axis) is the traveling direction of the incident circularly polarized light.

The transition operator $\mathbf{r} \cdot \mathbf{e}$ in photoexcitation process within the dipole approximation is conveniently expressed using the spherical harmonics.

$$\mathbf{r} \cdot \mathbf{e} \quad = \quad \sum_{\mu=-1}^{1} \sqrt{\frac{4\pi}{3}} e_\mu Y_1^\mu(\theta, \phi) r \tag{12.3}$$

where e is the electric vector of the photon. The transition operator for a circularly polarized light with the angular momentum of photon $\sigma_{h\nu}$ ($= \mu$) is expressed by the $\mu = \pm 1$ term. The transition matrix to the final state wave function Ψ_f with the quantum number l and m is

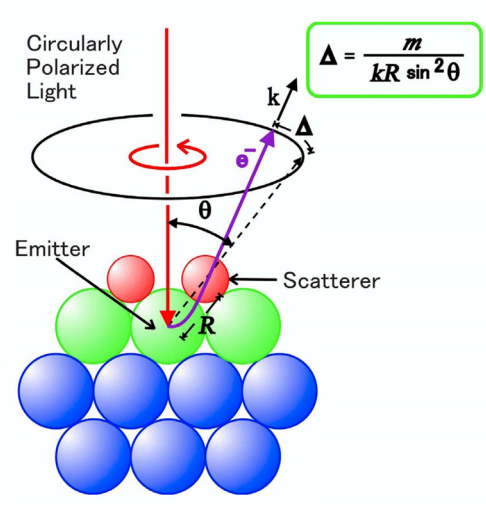

Figure 12.15: Azimuthal rotation of forward focusing peak.

written as [110]

$$\langle \Psi_f | \mathbf{r} \cdot \mathbf{e}_\pm \rangle \quad = \quad \sum_{l=l'\pm 1} R_{nl' \to kl} c^1(lm, l'm') \tag{12.4}$$

where $R_{nl' \to kl}$ is a radial matrix element, and $c^1(lm, l'm')$ is the Gaunt coefficient. This $c^1(lm, l'm')$ is not zero only when $m = m' \pm 1$. Hence, a circularly polarized light with the angular momentum of photon $\sigma_{h\nu}$ of ± 1 excites the ground state with the magnetic quantum number m' to the final state with $m = m' \pm 1$. In other words, the angular momentum that the electron gains by photoexcitation is ± 1.

First we consider a final state with only one m component. The final state wavefunction outside the emitting atom is expressed as

$$\begin{aligned} \Psi \quad &\propto \quad \frac{e^{ikr}}{r} Y_{lm}(\theta, \phi) \\ &\propto \quad \frac{e^{ikr}}{r} \Theta_{lm}(\theta) e^{im\phi} \end{aligned} \tag{12.5}$$

where $\Theta_{lm}(\theta)$ is the θ-function in the spherical harmonic.

The propagation direction of this final state wavefunction is intuitively calculated considering the wave front of Eq. (12.5) . The phase of the wave is expressed as

$$\exp[(kr + m\phi)] \tag{12.6}$$

The equation of constant phase surface is expressed as

$$r \quad = \quad -\frac{m\phi}{k} + C \tag{12.7}$$

where C is a constant. This curve is a spiral, and shown in Fig. 12.16 by solid and broken lines. The wave propagates perpendicular to these lines, which is the wave front, as shown by

thick arrow in Fig. 12.16. The shift of the forward direction Δ from OA direction is expressed as

$$\Delta = \tan^{-1}\frac{m}{kR\sin^2\theta} \simeq \frac{m}{kR\sin^2\theta} \tag{12.8}$$

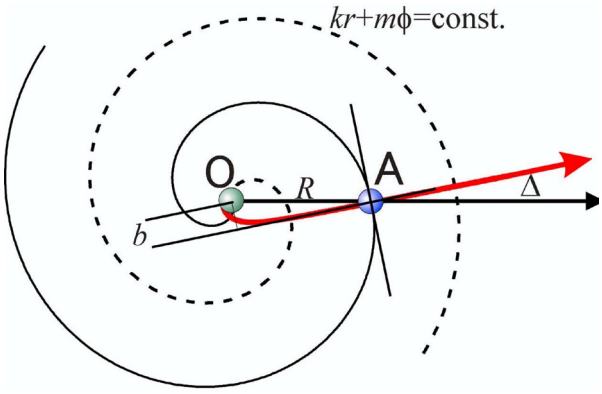

Figure 12.16: Constant phase surface of photoelectron wave with angular momentum m.

The physical base of the azimuthal shift is summarized as follows. The forward focusing peak appears because the phases of all wavelets on the wave front being scattered by each infinitesimal atomic potential coincide in the forward direction. This "forward direction" is perpendicular to the wave front of the wave. When the wave has as angular momentum, the wave front hit the scatterer at an angle. Hence the forward direction of the photoelectron wavefunction is inclined at the scatterer. In other words, the peak does not shift from the forward direction but the forward direction has shifted already before the scattering.

This formula for the direction of the forward focusing peak is exact when the photoelectron wavefunction can be expressed by only one component of angular momentum. This condition is satisfied in the excitation of s core, where final m should be ± 1. In the following, described is more general case of excitation.

The transition probability to the $l'+1$ final state is much higher than that to the $l'-1$ final state. In the case of the photoexcitation from the Si $2p$ ($l'=1$) core state by a photon of $\sigma_{h\nu}=+1$, which is the case of ref. [69], the final l is either 2 or 0, and the final (l,m) = (2,2), (2,1), (2,0) and (0,0). The probability of realizing these three $l=2$ final states is much higher than that for $l=0$, and is about 13:1 at the photon energy of around 350 eV [110].

The probabilities of realizing these three final m values are not equal because the Gaunt coefficients are different. For example, the probabilities for (l,m) = (2,2):(2,1):(2,0) are (6:3:1). When $\sigma_{h\nu}$ is -1, the ratio for m=(-2, -1, 0) is also (6:3:1). Even when the spin-orbit interaction of the core state is considered, this ratio is unchanged for each spin-orbit split component $P_{1/2}$ and $P_{3/2}$. This ratio, however, is that of the total cross section over 4π steradian and it depends on the emission angle θ (but does not depends on ϕ).

The effective m value as a function of θ, $m^*(\theta)$, has been derived considering the spin-orbit interaction [85]. When the small contribution of $l'-1$ component is neglected, the $m^*(\theta)$

for general l' initial state is expressed as

$$m^* = \frac{\sum_{m'=-l'}^{l'} m \left|c^1(l'+1,m,l',m')\Theta_{l'+1,m}\right|^2}{\sum_{m'=-l'}^{l'} \left|c^1(l'+1,m,l',m')\Theta_{l'+1,m}\right|^2} \tag{12.9}$$

where $m = m' + 1$ for $\sigma_{h\nu} = +1$. More general formula is written in [85].

The angular dependence of the contribution of each m state in the final state, which is $|c^1(l'+1,m,l',m')\Theta_{l'+1,m}|^2$, is shown in Fig. 12.18 for $l' = 3$. The effective m value $m^*(\theta)$ of Eq. (12.9) is also shown in Fig. 12.17. The neglect of $l-1$ channel causes an error of a few percent. Eq. (12.9) is convenient because it depends only on the initial angular momentum l' and does not depend on energy or atomic species.

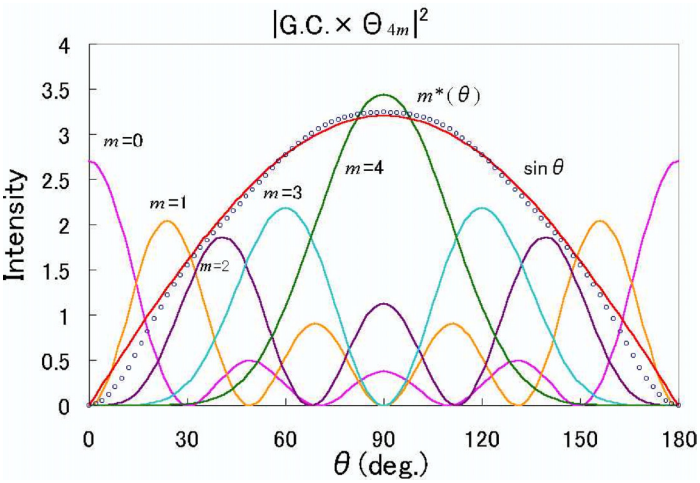

Figure 12.17: $m^*(\theta)$ for $l = 4$.

12.2.1.8 Stereograph by circular dichroism in photoelectron angular distribution

12.2.1.9 Stereoscopic photographs

A stereoscopic photograph consists of a pair of photographs; one is that to be seen by the left eye, and the other is to be seen by the right eye. The positions of an identical object in the two photographs differ by an amount of parallax, which is inversely proportional to the distance from the observer. Assume that you are facing the x direction and looking at an object A with your right and left eyes at E and F, respectively, as shown in Fig. 12.18. When the position of the object A is described as (R,θ, 0) in polar coordinates, the relation between the distance R and the azimuthal shift $\pm\Delta$ of the object A in the two photographs is described as

$$\Delta = \tan^{-1}\frac{b}{R\sin\theta} \tag{12.10}$$

where b is one half of the distance between the two eyes (OE and OF in Fig. 12.18).

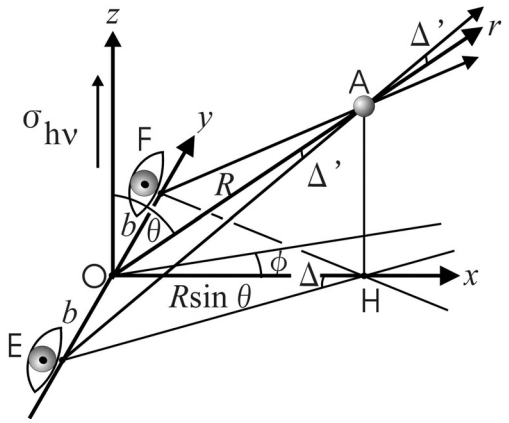

Figure 12.18: Stereo view of atom A with right and left eyes at E and F, respectively.

12.2.1.10 Stereo photograph of atomic arrangement

Two photographs of atomic arrangement satisfying the condition of Eq. (12.10) can be obtained by using a display-type spherical-mirror analyzer described above in the measurement of circular dichroism in two-dimensional photoelectron angular distribution (CDAD). For example, the CDAD pattern of W $4f$ photoelectrons from the W(110) surface at a kinetic energy of 800 eV is shown in Fig. 12.19(a) and (b) [70]. These patterns are observed on a flat screen of the analyzer. The angular range on the screen is about $\pm 60°$. Figure 12.19(a) and (b) were taken with cw and ccw circularly polarized light, respectively.

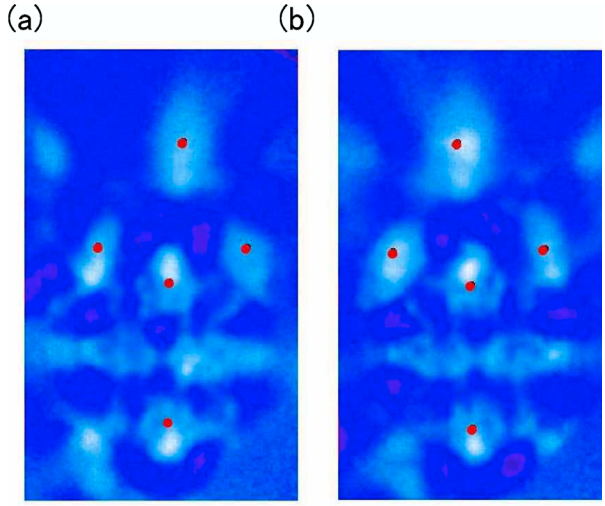

Figure 12.19: Stereo photograph of W crystal.

The center of the figure nearly corresponds to the surface normal direction, which is the [110] axis, and the horizontal direction is [001]. The ccw and cw excitation light is incident

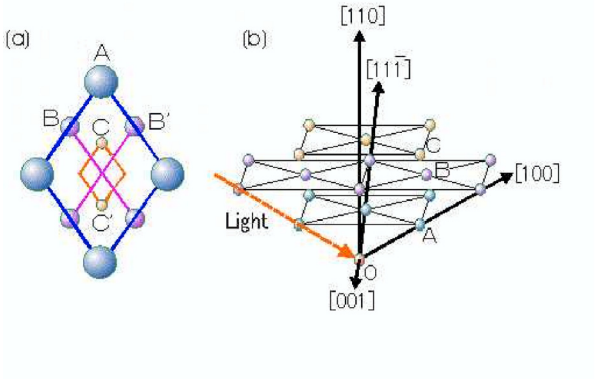

Figure 12.20: (a) Three-dimensional configuration of atoms imaged by stereo photograph of Fig. 12.19. (b) Structure of W crystal.

$45°$ inclined to the surface normal, which is the $[0\bar{1}0]$ direction, as shown in Fig. 12.20(b). We can see five forward focusing peaks, such as A, B, C, in the directions shown in Fig. 12.20(a). These forward peaks are produced by nearest neighbor atoms A, B, and C in Fig. 12.20(b). In XPD [102], the positions of these forward peaks are the same as these directions, but their positions in Fig. 12.19(a), (b) are slightly different from them. The patterns obtained by cw and ccw light are symmetric with each other with respect to the central vertical line. For example, the [100] peak A is slightly off the center to the right in (a) and left in (b), as shown by dots in the figure.

Because in both cases (Eqs. (12.8) and (12.10)) the angular shift Δ of the object is inversely proportional to the interatomic distance R from the emitter, these patterns can be considered as stereoscopic photographs. The necessary condition is that the direction of the photon be parallel to the z-axis in stereoscopic photography. Then, if we view the clockwise (cw) circularly polarized-light photoelectron diffraction pattern (Fig. 12.19(a)) with the left eye and the ccw pattern (Fig. 12.19(b)) with the right eye, we can image a three-dimensional arrangement of atoms in W(110) crystal as shown in Fig. 12.20(a). The A atom looks closer, the B and C atoms look farther, and others look the farthest. Moreover, near atoms look bigger and far atoms look smaller as in the case of real view. The elongation of atom A is due to the projection of the pattern to a flat screen.

To recognize the three-dimensional arrangement properly, it is necessary that the field of vision of both images should be the same as that in the measurement. The solid angle of these pictures is about $\pm 60°$ in the measurement whereas it is only $\pm 15°$ when these pictures are viewed by using usual stereo-viewer. Special projection method, such as a combination of polarized light projection and polarized glasses for individual image, is necessary to realize the field of vision of $\pm 60°$. If it is realized, the oval of atom A can be seen as a circle, and the inter-atomic relation is to be proportional to the real relation.

When Eq. (12.8) and Eq. (12.10) are identical, there is no distortion. The necessary condition is that $m/(k \sin\theta)$ be constant in Eq. (12.8). For the objects in the x-y plane, there is no distortion because $m/(k \sin\theta)$ is constant. In this case, the magnification ratio is bk/m. When $b = 3$ cm, k is 14 Å^{-1} (for the kinetic energy of 800 eV), and $m = 4$, the magnification ratio is about 10^9, which is 1000 times higher than usual electron microscope. When θ is not

90°, the sine function in the denominator of Eq. (12.8) would make the atoms closer to the viewer. However, this distortion is hardly present in the actual case because the value m in Eq. (12.8) is not constant, and the θ dependence of $m^*(\theta)$ is close to $\sin\theta$ [85], as shown in Fig. 12.17.

In this method the forward focusing peaks should be clearly seen in 2DAD pattern. This restriction implies that the emitter atom must lie under the scatterer atoms and that the kinetic energy of the photoelectron should be above several hundred eV. The photoelectron diffraction and the multiple-scattering effect could modify the forward focusing peaks, but these effects are order of magnitude smaller than the forward peaks. The peak positions have been reproduced well so far not only for the adsorbate single-scattering case [107] but also for the bulk multiple-scattering case when the forward focusing peaks are clearly seen [84]. Hence, this analysis is applicable not only to the molecules adsorbed on surfaces but also to the crystalline substances.

12.2.1.11 Stereo microscope

This stereoscopic photograph can be obtained directly on the screen of above mentioned display-type spherical-mirror analyzer [65–68] without any computer-aided conversion process. Rotatable analyzer method to measure photoelectrons two-dimensionally can also take this stereoscopic photograph with the aid of computer. However, rotating-sample method produces much-distorted image. Other types of display analyzers such as Eastman-type analyzer [71, 72] can also be used to take stereoscopic photographs. In this case, however, the pattern obtained on the screen is distorted, and computer processing is inevitably necessary to make the photograph. Because only the display-type spherical-mirror analyzer can obtain a distortion-free image in much wider solid angles than the Eastman-type one, it is the best analyzer to take the stereoscopic photographs.

Real-time observation will help understanding the dynamics of atoms. The problem in all the atomic-structure analysis methods so far (electron diffraction, X-ray diffraction, photoelectron diffraction and holography) is that the data obtained are that of reciprocal space, and a real-space structure cannot be imaged before conversion. It takes some time to calculate the atomic structure, and these methods are thus not suitable for real-time analysis. The situation is even worse for fluorescent X-ray holography [111] because the time for data collection is much longer than that for electron emission holography.

When the time required to switch the helicity of circularly polarized light is reduced and the signal intensity increases, this display analyzer will give an opportunity for real-time stereoscopic observation. On the screen of DIANA the stereo photographs for right eye and left eye will be displayed alternately by switching the helicity of the light. An alternate glasses can transmit each image to each eye by switching the transmittance of each glass with the same period. In this way one can image three-dimensional atomic arrangement as shown in Fig. 12.21 in real time. Although it takes about 30 min at present to obtain the photograph, the development of synchrotron radiation and measurement techniques will continue to shorten the measurement time. In the near future, measurement times at least as short as that of video rate “real time” will be achieved.

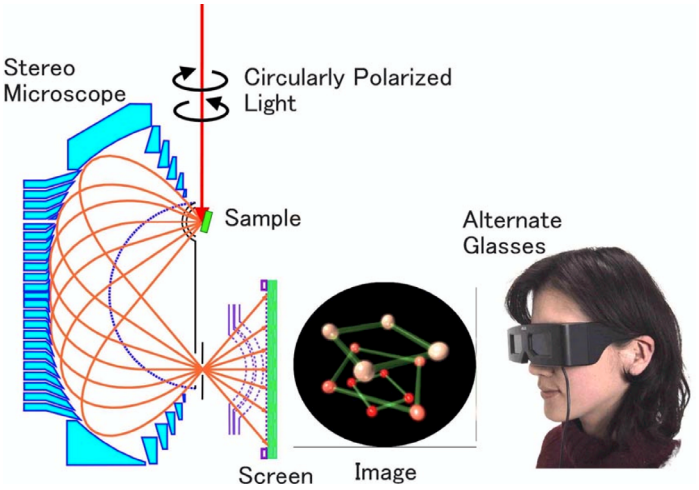

Figure 12.21: Stereo microscope. See also color figure on page 467.

12.2.2 Two-dimensional photoelectron spectroscopy of valence band

12.2.2.1 Photoelectron angular distribution from valence band

As the direct probe for the valence electrons, angle-resolved photoelectron spectroscopy (ARPES) has been the indispensable tool for elucidating the electronic nature of various solids [112]. ARPES gives the most detailed information about the band structure $E_{\mathrm{B}}(\mathbf{k})$ resolved in binding energy (E_{B}) and wave vector $\mathbf{k}$. Investigations of ARPES so far have been concentrated in a certain two-dimensional cross-section of the valence band structure. That is two-dimensional band dispersion $E_{\mathrm{B}}(k_x)$ at the high symmetry directions in reciprocal space or an iso-energetic line shape such as a cross-section of Fermi surface, $E_{\mathrm{F}}(k_x, k_y)$ [113]. However, most of information on the valence band structure in the full reciprocal space was not utilized.

The two-dimensional photoelectron angular distributions (PEAD) can be thought as a product of 1D-DOS, photoemission structure factor, and angular distribution from atomic orbitals (ADAO) [86]. By measuring PEAD obtained by using a linearly-polarized synchrotron radiation (SR), the analyses for not only the even/odd symmetry but also the component ratio among atomic orbitals, such as p_z or $d_{x^2-y^2}$, become possible.

12.2.2.2 Determination of atomic orbitals composing Fermi surface

The calculated ADAO from several orbitals are shown in Fig. 12.22. The stereo-projection method is used for the plot. The center is the polar angle of 0°, and the periphery of the circle correspond to the polar angle of 90°. In the calculation, the formula given by Goldberg *et al.* [110] was used for only $l+1$ shells because usually $l+1$ shell is excited much stronger than $l-1$ shell.

A two-dimensional display-type spherical mirror analyzer provides novel methods for such a measurement. This analysis has been justified by many observed data such as graphite

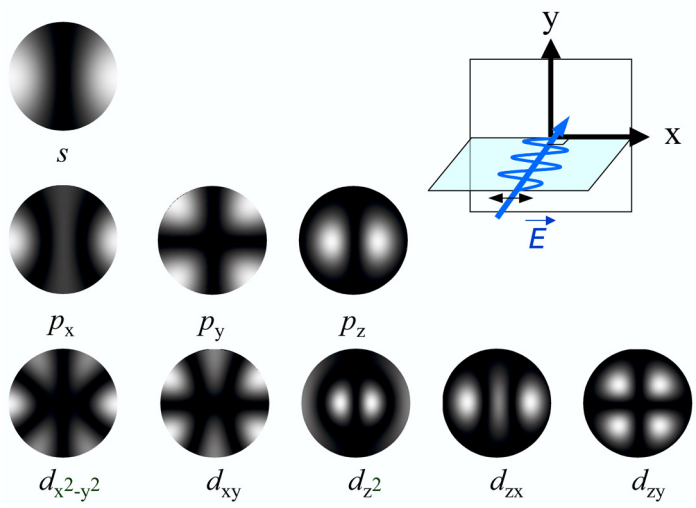

Figure 12.22: Calculated angular distribution from several atomic orbitals.

[87], TaS_2 [114], Sr_2RuO_4 and so on. In these cases, the atomic orbitals are determined among the orbitals with the same orbital angular momentum l. The discrimination of atomic orbitals among those in the same l shell was easily done by measuring the azimuthal angle dependence of the PEAD.

For example in the case of $Bi_2Sr_2CaCu_2O_8$ [91], the component ratio among five d orbitals has been revealed quantitatively. Figures 12.23(a)–(g) are the PEAD patterns from the Fermi surface of $Bi_2Sr_2CaCu_2O_8$. Brightness of the image is proportional to the intensity of the photoelectron. White line indicates the Brillouin zone, and black curves show the Fermi surface calculated by the FLAPW method [115]. The Fermi surface of $Bi_2Sr_2CaCu_2O_8$ are thought to be composed of the state in the Cu-O layer and the Bi-O layer [115]. The PEAD pattern changes gradually with rotating ϕ. The photoelectron intensity at point a in Fig. 12.23(a) is strong at $\phi = 0°$, and becomes weak at $\phi = 90°$ (Fig. 12.23(e)). The photoelectron intensity of point b is strong at $\phi = 45°$, and it becomes weak at $\phi = 135°$. The intensity of point c is weak at $\phi = 0°$, and it becomes strong at $\phi = 90°$. From quantitative analysis of the photoelectron intensity at points a, b and c, the symmetry of the atomic orbital constituting the Fermi surface was shown to be $d_{x^2-y^2}$.

12.2.2.3 Three dimensional band dispersion of graphite

The visualization of the curved surfaces of the valence band is obtained from the two-dimensional (k_x,k_y) ARPES measurement. These band dispersion "surfaces" contain fruitful information compared to the conventional band dispersion "curves" along a certain direction in k space. For instance, the angular dependence of the slope (the velocity) and the curvature (the mass) of local band structure can be derived. The integrated band energy over entire Brillouin zone, which can be thought as the electronic part of the condensation energy could also be obtained. When polarized light is used, the atomic orbitals composing each band

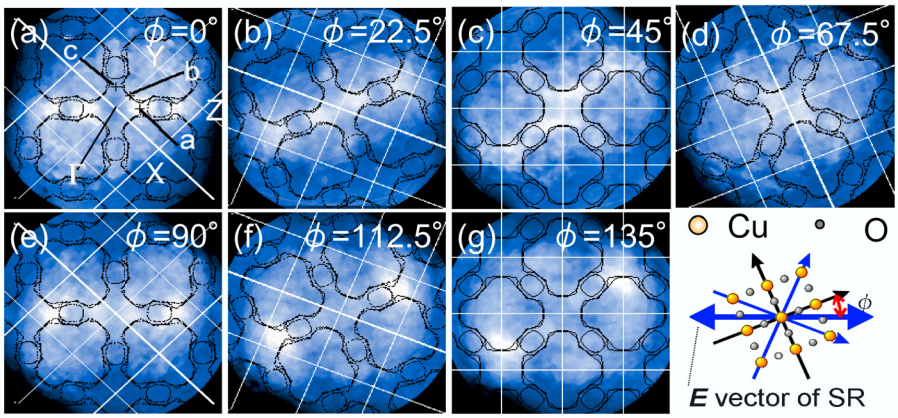

Figure 12.23: PEAD patterns of Fermi surface (a)-(g) with various azimuthal angle ϕ. Each PEAD images are plotted for polar angle $\theta = 0 \sim 60^\circ$ in reciprocal space. White line shows the Brillouin zone and black curves are the calculated Fermi surface.

can be determined from two-dimensional photoelectron intensity distribution. The display analyzer described in the previous section provides novel data acquisition method for two-dimensional photoelectron spectroscopy measurement. Here, three-dimensional (E,k$_x$,k$_y$) band dispersion measurement and atomic orbital analyses applied to single-crystalline graphite are presented.

The graphite π band has a parabolic dispersion with its bottom at the Γ point and the maxima at the six K points [116]. The PEAD patterns shown in Figures 12.24(a)–(d) correspond to the cross-section of the π band at the binding energy of 0.0, 1.0, 2.0 and 3.0 eV, respectively. Photon energy of 52.5 eV is used for the excitation. A synthesized single-crystalline graphite was used for the experiment. Sample was oriented so that one of the shortest C-C bond ($\Gamma - M$ direction) lies horizontally, which is along the electric vector of the normal incident SR. White hexagon indicates the first Brillouin zone of the graphite. All the PEAD patterns show two-fold symmetry due to the linear polarization of the incident light. For instance, at the Fermi level [Fig. 12.24(a)], bright spots appear at left and right four corners of the Brillouin zone, while the top and bottom two corners remain dark. As the binding energy increases, the size of these spots grows larger [Fig. 12.24(b)], and then starts to spread toward M and Γ points [Fig. 12.24(c)]. Finally the adjacent M points on the right- and left-hand sides are bridged as shown in Fig. 12.24(d). Note that these patterns show that photoelectrons predominantly appear in the first Brillouin zone. The M points outside the first Brillouin zone remain dark due to the 'photoemission structure factor' [86, 114].

As shown in Fig. 12.22, photoemission intensity is high along the central vertical line, in the case of $2p_x$. On the contrary, the same line is forbidden for the case of $2p_y$ and $2p_z$. The photoemissions from $2p_y$ and $2p_z$ can be distinguished from the azimuthal dependence of the PEAD patterns, since the former has another horizontal forbidden line. The ratio among atomic orbitals is obtained by fitting these calculated PEAD patterns to the observed patterns. The observed PEAD patterns at h$\nu = 52.5$ eV indicated that the π band consists of mainly C $2p_z$ atomic orbital [116].

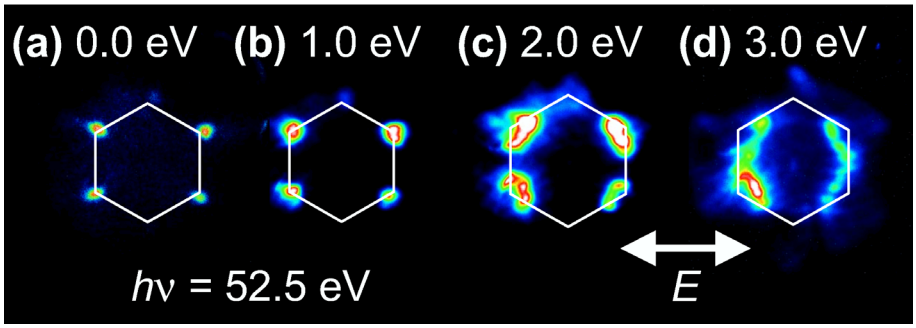

Figure 12.24: (a)-(d) The photoelectron angular distribution patterns from single crystal graphite valence band excited by a linearly polarized light corresponding to the cross-section of the π band at the binding energy of 0.0, 1.0, 2.0 and 3.0 eV, respectively. See also color figure on page 467.

By stacking PEAD patterns as a function of binding energy, the band dispersion of the entire Brillouin zone in $k_x - k_y$ plane can be obtained. The PEAD patterns for binding energies from -1.0 to 10.0 eV with respect to the Fermi level are taken with intervals of 0.2 eV. After stacking the PEAD patterns, spectra $E_{\rm B}(k_x, k_y)$ are picked up at each (k_x, k_y). This procedure is necessary to extract the band dispersions, by compensating the effect of 'photoemission structure factor'. The bird's-eye stereo-view of the three-dimensional band dispersion surfaces extracted is shown in Fig. 12.25. This method enables the visualization of the curved surface of the band dispersion, instead of curved line in the case of the conventional ARPES method. The bright areas are where the original photoemission intensity is high. The first Brillouin zone of the graphite is indicated as a green hexagonal prism with one-fourth of its volume cut away to indicate the Γ-K and Γ-M directions. The top of the prism corresponds to the Fermi level and the bottom to the binding energy of 10 eV. The patches of the hexagonal tiles underneath stand for the other Brillouin zones. The three-dimensional shape of the π band dispersion such as the saddle-like feature at the M points or vertices at the K points is easily recognized. As the band theory teaches us, the binding energy at the M point is lowered due to the periodic potentials in the C-C bond directions. The σ band dispersion colored yellow has maximum at the Γ point and saddle-like feature at the M points.

Figures 12.25(b) and (c) are the top views of the π and σ bands, respectively, which are two-dimensional distribution of excitation probabilities of these bands. The photoemission intensity of the π band is high at left and right sides, which corresponds to the simulated angular distribution pattern from a $2p_z$ atomic orbital as shown in Fig. 12.22. However, the fine structure of photoelectron intensity found around Γ point does not agree with this simulation. This suggests the hybridization with atomic orbitals other than $2p_z$. The energy of the π band averaged all over the Brillouin zone is 3.93 eV. The difference of this value and that of the initial p atomic orbital gives the electronic contribution of π band to the formation energy of graphite. This kind of information can only be obtained by three-dimensional measurement of band structure.

On the other hand, the σ band shows no photoemission intensity at horizontal direction. Its maximum intensity appears along upper and lower four $\Gamma - M$ directions. These trends also

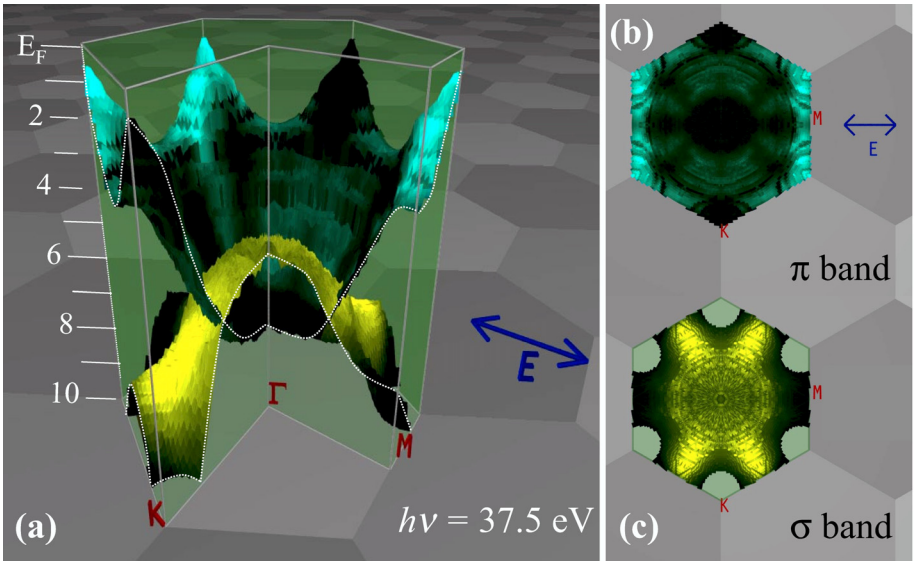

Figure 12.25: (a) Bird's-eye-view of three dimensional π (upper) and σ (lower) bands of graphite. Photon energy of 37.5 eV is used for the excitation. The patches of the hexagonal tiles underneath stand for the other Brillouin zones. (b,c) Photoemission intensity distributions of the π and σ bands, respectively. See also color figure on page 468.

appeared in the simulated angular distribution pattern from a $2p_y$ atomic orbital in Fig. 12.22. However the simulation indicates that the photoemission from $2p_y$ is forbidden along vertical and horizontal lines. The intensity observed at this area of the σ band in Fig. 12.25(c) can be attributed to the contribution from the overlapping C $2p_x$ orbital.

Figure 12.26 depicts the motion of electrons in the π band. Arrows indicates group velocity and direction for every momentum $\mathbf{k}$ obtained by differentiating the curved π band surface $\partial \mathrm{E}/\partial \mathbf{k}$. Note that arrows point radially around Γ point but focus to K point at edge of Brillouin zone [117].

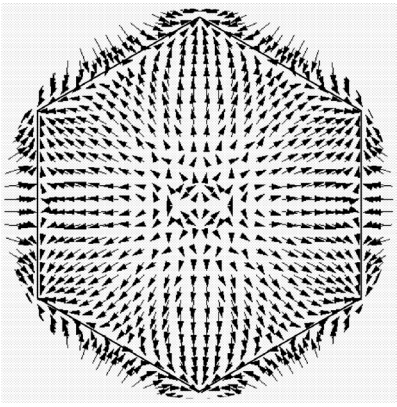

Figure 12.26: The motion of electrons in π band. The length, position and direction indicate the group velocity, wavevector $\mathbf{k}$ and direction of electrons. The Brillouin zone is indicated by a hexagon.

References

[1] K.C. Pandey, Phys. Rev. Lett. 1981, *47*, 1913.
[2] K. Takayanagi, Y. Tanishiro, M. Takahashi, S. Takahashi, Surf. Sci. 1985, *164*, 367.
[3] F.J. Himpsel, P. Heimann, D.E. Eastman, Phys. Rev. B 1981, *24*, 2003.
[4] R.I.G. Uhrberg, G.V. Hansson, J.M. Nicholls, S.A. Flodström, Phys. Rev. Lett. 1982, *48*, 1032.
[5] P. Mårtensson, W.-X. Ni, G.V. Hansson, J.M. Nicholls, B. Reihl, Phys. Rev. B 1987, *36*, 5974.
[6] R.I.G. Uhrberg, T. Kaurila, Y.-C. Chao, Phys. Rev. B 1998, *58*, R1730.
[7] R. Losio, K.N. Altmann, F.J. Himpsel, Phys. Rev. B 2000, *61*, 10 845.
[8] R.I.G. Uhrberg, G.V. Hansson, Critical Reviews in Solid State and Materials Sciences, 1991, *17(2)*, 133.
[9] H. Daimon, S. Ino, Surf. Sci. 1985, *164*, 320.
[10] T. Okuda, K. Sakamoto, H. Nishimoto, H. Daimon, S. Suga, T. Kinoshita, A. Kakizaki, Phys. Rev. B 1997, *55*, 6762.
[11] H.H. Weitering, X. Shi, S.C. Erwin, Phys. Rev. B 1996, *54*, 10 585.
[12] K. Sakamoto, T. Okuda, H. Nishimoto, H. Daimon, S. Suga, T. Kinoshita, A. Kakizaki, Phys. Rev. B 1994, *50*, 1725.
[13] H.H. Weitering, N.J. Dinardo, R. Párez-Dandoz, J. Chen, E.J. Mele, Phys. Rev. B 1994, *49*, 16837.
[14] S.C. Erwin, Phys. Rev. Lett. 1995, *75*, 1973.
[15] A.A. Saranin, A.V. Zotov, V.G. Lifshits, M. Katayama, K. Oura, Surf. Sci. 1999, *426*, 298.
[16] C. Collazo-Davila, D. Grozea, L.D. Marks, Phys. Rev. Lett. 1998, *80*, 1678.
[17] S.C. Erwin, H.H. Weitering, Phys. Rev. Lett. 1998, *81*, 2296.
[18] L. Lottermoser *et al.*, Phys. Rev. Lett. 1998, *80*, 3980.
[19] M.-H. Kang, J.-H. Kang, S. Jeong, Phys. Rev. B 1998, *58*, R13 359.
[20] Y. Gotoh, S. Ino, Jpn. J. Appl. Phys. 1978, *17*, 2097.
[21] T. Ichikawa, S. Ino, Surf. Sci. 1980, *97*, 489.
[22] W.C. Fan, A. Ignatiev, Phys. Rev. B 1990, *41*, 3592.
[23] J. Quinn, F. Jona, Surf. Sci. 1991, *249*, L307.
[24] K.J. Wan, X.F. Lin, J. Nogami, Phys. Rev. B 1992, *46*, 13 635; *ibid*. 1993, *47*, 13 700.
[25] D. Jeon, T. Hashizume, T. Sakurai, R.F. Willis, Phys. Rev. Lett. 1992, *69*, 1419.
[26] J.J. Paggel, G. Neuhold, H. Haak, K. Horn, Phys. Rev. B 1995, *52*, 5813.
[27] T. Okuda, H. Daimon, S. Suga, Y. Tezuka, S. Ino, Appl. Surf. Sci. 1997, *121/122*, 89.
[28] K. Sakamoto, H. Ashima, H.M. Zhang, R.I.G. Uhrberg, Phys. Rev. B 2002, *65*, 045305.
[29] E. Landemark, C.J. Karlsson, Y.-C. Chao, R.I.G. Uhrberg, Phys. Rev. Lett. 1992, *69*, 1588.
[30] R.J. Hamers, R.M. Tromp, J.E. Demuth, Phys. Rev. B 1986, *34*, 5343.
[31] Z.H. Zhang, S. Hasegawa, S. Ino, Phys. Rev. B 1995, *52*, 10 760.
[32] X. Tong, S. Hasegawa, S. Ino, Phys. Rev. B 1997, *55*, 1310.

[33] H.M. Zhang, K. Sakamoto, R.I.G. Uhrberg, Phys. Rev. B 2001, *64*, 245421.
[34] L.S.O. Johansson, E. Landemark, C.J. Karlsson, R.I.G. Uhrberg, Phys. Rev. Lett. 1989, *63*, 2092.
[35] X. Tong, C.S. Jiang, S. Hasegawa, Phys. Rev. B 1998, *57*, 9015.
[36] H. Aizawa, M. Tsukada, N. Sato, S. Hasegawa, Surf. Sci. 1999, *429*, L509.
[37] T. Takahashi, S. Nakatani, Surf. Sci. 1993, *282*, 17.
[38] Y.G. Ding, C.T. Chan, K.M. Ho, Phys. Rev. Lett. 1991, *67*, 1454; *ibid.* 1992, *69*, 2452.
[39] R.I.G. Uhrberg, H.M. Zhang, T. Balasubramanian, E. Landemark, H.W. Yeom, Phys. Rev. B *65*, will appear in the issue of Feb. 2002.
[40] J.E. Northrup, Phys. Rev. Lett. 1984, *53*, 683.
[41] J.M. Carpinelly, H.H. Weitering, E.W. Plummer, R. Stumpf, Nature (London) 1996, *381*, 398.
[42] J.M. Carpinelly, H.H. Weitering, M. Martkowiak, R. Stumpf, E.W. Plummer, Phys. Rev. Lett. 1997, *79*, 2859.
[43] A. Goldoni, S. Modesti, Phys. Rev. Lett. 1997, *79*, 3266.
[44] M. Göthelid, M. Björkqvist, T.M. Grehk, G. Le Lay, U.O. Karlsson, Phys. Rev. B 1995, *52*, 14 352.
[45] M. Göthelid, T.M. Grehk, M. Hammar, U.O. Karlsson, S.A. Flodström, Surf. Sci. 1995,*328*, 80.
[46] G. Le Lay, V. Ye. Aristov, O. Bostroöm, J.M. Layet, M.C. Asensio, J. Avila, Y. Huttel, A. Cricenti, Appl. Surf. Sci. 1998, *123/124*, 440.
[47] R.I.G. Uhrberg, T. Balasubramanian, Phys. Rev. Lett. 1998, *81*, 2108.
[48] J. Avila, A. Mascaraque, E.G. Michel, M.C. Asensio, G. Le Lay, J. Ortega, R. Pérez, F. Flores, Phys. Rev. Lett. 1999, *82*, 442.
[49] R.I.G. Uhrberg, H.M. Zhang, T. Balasubramanian, Phys. Rev. Lett. 2000, *85*, 1036.
[50] P. Bratu, K.L. Kompa, U. Höfer, Phys. Rev. B 1993, *49*, 14 070.
[51] F. Matsui, H.W. Yeom, K. Amemiya, K. Tono, T. Ohta, Phys. Rev. Lett. 2000, *85*, 630.
[52] U. Höfer, P. Morgen, W. Wurth, E. Umbach, Phys. Rev. Lett. 1985, *55*, 2979; Phys. Rev. B 1989, *40*,1130.
[53] P. Morgen, U. Höfer, W. Wurth, E. Umbach, Phys. Rev. B 1989, *39*, 3720.
[54] G. Dujardin, G. Comtet, L. Hellner, T. Hirayama, M. Rose, L. Philippe, M.J. Besnard-Ramage, Phys. Rev. Lett. 1994, *73*, 1727.
[55] G. Comtet *et al.*, Surf. Sci. 1995, *331-333*, 370.
[56] G. Comtet, L. Hellner, G. Dujardin, M.F. Ramage, Surf. Sci. 1996, *352-354*, 315.
[57] K. Sakamoto, K. Nakatsuji, H. Daimon, T. Yonezawa, S. Suga, Surf. Sci. 1994, *306*, 93.
[58] B. Lamontagne, D. Roy, R. Sporken, R. Caudano, Prog. Surf. Sci. 1995, *50*, 315.
[59] K. Sakamoto, S. Suto, W. Uchida, Surf. Sci. 1996, *357/358*, 514.
[60] S.-H. Lee, M.-H. Kang, Phys. Rev. Lett. 1999, *82*, 968; Phys. Rev. 2000, B *61*, 8250.
[61] S.-H. Lee, M.-H. Kang, Phys. Rev. Lett. 2000, *84*, 1724.
[62] G. Dujardin, A. Mayne, G. Comtet, L. Hellner, M. Jamet, E. Le Goff, P. Millet, Phys. Rev. Lett. 1996, *76*, 3782.

[63] K. Sakamoto, S. Doi, Y. Ushimi, K. Ohno, H.W. Yeom, T. Ohta, S. Suto, W. Uchida, Phys. Rev. B 1999, *60*, R8465.
[64] K. Sakamoto, F. Matsui, M. Hirano, H.W. Yeom, H.M. Zhang, R.I.G. Uhrberg, Phys. Rev. B 2002, *65*, 201309(R).
[65] H. Daimon, Rev. Sci. Instrum. 59, 545 (1988).
[66] H. Daimon and S. Ino, Rev. Sci. Instr. 61, 57 (1990).
[67] H. Nishimoto *et al.*, Rev. Sci. Instr. 64, 2857 (1993).
[68] M. Kotsugi *et al.*, Nuclear Instruments and Method in Physics Research A 467, 1493 (2001); T. Nohno *et al.*, Jpn. J. Appl. Phys. 42, (2003) in print.
[69] H. Daimon *et al.*, Jpn. J. Appl. Phys. 32, L1480 (1993).
[70] H. Daimon, Phys. Rev. Lett. 86, 2034 (2001).
[71] D.E. Eastman, J.J. Donelon, N.C. Hien, and F.J. Himpsel, Nucl. Instrum. Methods 172, 327 (1980).
[72] T. Dutemeyer *et al.*, Rev. Sci. Instrum. 72, 2638 (2001).
[73] H. Daimon and S. Ino, Surf. Sci. 222, 274 (1989).
[74] H. Daimon *et al.*, Surf. Sci. 242, 288 (1991).
[75] H. Daimon *et al.*, *Springer Series in Surface Science, 24 The Structure of Surfaces III ed. S.Y. Tong et al.* (Springer-Verlag, Berlin, 1991).
[76] T. Nakatani *et al.*, J. Synchrotron Rad. 3, 239 (1996).
[77] H. Daimon and S. Ino, Vacuum 41, 215 (1990).
[78] K. Sakamoto *et al.*, Surf. Sci. 306, 93 (1994).
[79] T. Yonezawa *et al.*, Appl. Surf. Sci. 79/80, 95 (1994).
[80] K. Sakamoto *et al.*, Surf. Sci. 359, 147 (1996).
[81] K. Nakatsuji *et al.*, Surf. Sci. 363, 321 (1996).
[82] T. Yonezawa *et al.*, Surf. Sci. 365, 489 (1996).
[83] P. Rennert *et al.*, J. Phys. Soc. Jpn. 66, 396 (1997).
[84] K. Enomoto *et al.*, Surf. Rev. Lett. 7, 643 (2000).
[85] H. Daimon, S. Imada, and S. Suga, Surf. Sci. 471, 143 (2001).
[86] H. Daimon, S. Imada, H. Nishimoto, and S. Suga, J. Electron Spectrosc. Relat. Phenom. 76, 487 (1995).
[87] H. Nishimoto *et al.*, J. Phys.: Condens. Matter 8, 2715 (1996).
[88] H. Nishimoto *et al.*, Solid State Commun. 98, 671 (1996).
[89] T. Matsushita *et al.*, J. Electron Spectrosc. Relat. Phenom. 78, 498 (1996).
[90] T. Matsushita *et al.*, Phys. Rev. B 56, 7687 (1997).
[91] M. Kotsugi *et al.*, J. Electron Spectrosc. Relat. Phenom. 88-91, 489 (1998).
[92] T. Okuda *et al.*, J. Electron Spectrosc. Relat. Phenom. 88-91, 287 (1998).
[93] T. Okuda *et al.*, J. Electron Spectrosc. Relat. Phenom. 88-91, 473 (1998).
[94] T. Okuda *et al.*, J. Electron Spectrosc. Relat. Phenom. 101-103, 355 (1999).
[95] T. Okuda *et al.*, J. Phys. Soc. Jpn. 68, 1398 (1999).
[96] A. Szöke, *AIP Conference Proceedings No.147* (American Institute of Physics, New York, 1986).

[97] J. Barton, Phys. Rev. Lett. 61, 1356 (1988).
[98] G.R. Harp, D.K. Saldin, and B.P. Tonner, Phys. Rev. Lett. 65, 1012 (1990).
[99] I.H. Hong, M. Jih, Y. Chou, and C. Wei, Surface Rev. Lett. 4, 733 (1997).
[100] C.Y. Chang, Y.C. Chou, and C.M. Wei, Phys. Rev. B 59, R10453 (1999).
[101] T. Abukawa, C.M. Wei, T. Hanano, and S. Kono, Phys. Rev. Lett. 82, 335 (1999).
[102] H. Daimon *et al.*, Surf. Sci. 408, 260 (1998).
[103] S. Tong, H. Li, and H. Huang, Phys. Rev. Lett. 67, 3102 (1991).
[104] J. Barton, Phys. Rev. Lett. 67, 3106 (1991).
[105] S. Ohmori, T. Kozaki, and Y. Nihei, Surf. Rev. and Lett. 6, 585 (1999).
[106] H. Takagi, H. Daimon, F.J. Palomares, and C.S. Fadley, Surf. Sci. 470, 189 (2001).
[107] H. Daimon *et al.*, Phys. Rev. B 58, 9662 (1998).
[108] A. Kaduwela *et al.*, Phys. Rev. B 52, 14297 (1995).
[109] A. Chasse and P. Rennert, Phys. Rev. B 55, 4120 (1997).
[110] S.M. Goldberg, C.S. Fadley, and S. Kono, J. Electron Spectr. Relat. Phenom. 21, 285 (1981).
[111] C.S. Fadley and P.M. Len, Nature 380, 27 (1996).
[112] S. Hüfner, *Photoelectron Spectroscopy* (Springer-Verlag, Berlin, 1995).
[113] J.C. Foo *et al.*, Phys. Rev. B 53, 9649 (1996).
[114] E. Shirley, L. Terminello, A. Santoni, and F. Himpsel, Phys. Rev. B 51, 13614 (1995).
[115] S. Massidda, J. YU, and A. Freeman, Physica C 152, 251 (1988).
[116] H. Nishimoto *et al.*, J. Phys. 8, 2715 (1996).
[117] F. Matsui *et al.*, Appl. Phys. Lett. 81, 2556 (2002).

Solid-State Photoemission and Related Methods
Wolfgang Schattke, Michel A. Van Hove (Eds.)

13 Holographic surface crystallography Substrate as reference

R.J. Harder and D.K. Saldin

We propose methods for solving the inverse problem in surface X-ray diffraction and low energy electron diffraction that might be termed holographic, in the sense that the structure factors may be written as a sum of a known part (a reference wave) and an unknown part (as object wave). By regarding the object wave as a linear combination of calculable independent elementary object waves, the coefficients of that expansion are determined from the experimental data by an iterative maximum entropy algorithm. The spatial distribution of these coefficients represents a solution to the surface structure in each case.

13.1 Introduction

Holography [1] is a technique for recovering a complete wavefield (an *object wave*) from a diffraction pattern formed by its interference with a known *reference wave*. Today, it is perhaps best known as the technique that produces ghostly three-dimensional images that appear on viewing illuminated developed photographic emulsions (*holograms*), created by recording the interference patterns of two or more beams of laser light.

Over the last fifteen years or so, holographic techniques [2] have also caught the imagination of surface crystallographers through techniques such as photoelectron holography [3], holographic low energy electron diffaction (LEED) [4], Auger holography [5] etc. that exploit the interference of electron waves generated at crystallographically equivalent atoms in a sample. The far-field diffraction pattern formed by the interference between the direct wave (the reference wave) from the atomic source, and that resulting from the scattering of this wave by neighboring atoms (the object wave) forms an electron hologram from which it is often possible to perform a computer reconstruction of the three-dimensional spatial configuration of the scattering atoms in relation to the source atom.

From a crystallographic standpoint, there have been several important successes of these techniques, for example the use of photoelectron holography to elucidate the structures of Al/Si(111) [6], and of acelylene and ethylene on Si(100) [7]. There is however one fundamental limitation of such techniques when using the low energy electrons that are necessary for surface sensitivity: due to the decay of the amplitude of a point-source reference wave with the inverse of the distance from the source, augmented by the short inelastic scattering length of electrons of such energy, significant object-wave contributions to the diffraction patterns come mainly from scattering atoms quite close to the source. Consequently, the relative positions of only such nearby atoms may be determined by holographic reconstruction. While this is a useful feature for structures containing only short-range order around the source atom,

Solid-State Photoemission and Related Methods: Theory and Experiment. Edited by Wolfgang Schattke, Michel A. Van Hove

ISBN: 3-527-40334-5

or when only such local structure is of interest, it is a handicap in determining the complete structure of a well-ordered surface with a large unit cell.

A case in point is the (3×3) surface reconstruction of SiC(111). This structure contains about 20 symmetrically-inequivalent atoms per surface unit cell whose positions need to be determined, and its structure solution would normally be beyond the capabilities of conventional methods of LEED that involve the trial-and-error matching of data simulations from model structures with experimental spectra [8]. Since scanning tunneling microscopy (STM) indicated the probable existence of a single protruding adatom in each surface unit cell [9–11], the structure seemed to be apt for an application of the technique of holographic LEED [12]. Indeed, application of this technique correctly revealed the structure of a local cluster of five atoms surrounding the adatom [13], but due to the limitations of its spatial range, alluded to above, the technique was unable to determine any more of the structure. It should be mentioned that the structure determination of this local cluster was quite rapid, taking no more than a few hours on a modern workstation. The determination of the rest of the structure by conventional LEED techniques required much greater effort (although the rapid determination of part of the structure undoubtedly reduced this considerably).

The rapid determination of structures as, or more complicated than, this one clearly requires the development of an alternative *direct* method for structure solution that does not involve trial-and-error search algorithms with their known practically insuperable barrier of non-polynomial (NP) scaling [8]. This paper suggests such a method that promises to overcome this problem and yet to enable the determination of the structure of an entire complicated unit cell. It represents an extension to LEED of the *maximum entropy* method previously developed for bulk protein X-ray crystallography [14], and also for surface X-ray crystallography [15]. We begin with a review of the theory for X-ray crystallography, which is not burdened by the extra complications of multiple scattering which are unavoidable in electron diffraction.

13.2 Surface crystallography as a structure completion problem

For diffraction from a single domain, the detected intensity in a surface X-ray diffraction (SXRD) experiment may be written

$$I_{\mathbf{q}} = |F_{\mathbf{q}}|^2, \tag{13.1}$$

where $F_{\mathbf{q}}$ is the structure factor of a unit cell of the entire structure (surface plus bulk), and the scattering vector $\mathbf{q}$ is defined as the difference between the wavevectors of the incident and scattered X-rays. In SXRD this may be taken to be

$$\mathbf{q} = H\mathbf{a}^* + K\mathbf{b}^* + L\mathbf{c}^* \tag{13.2}$$

where H, K, and L are Miller indices, $\mathbf{a}^*$ and $\mathbf{b}^*$ are reciprocal lattice vectors parallel to the surface, and $\mathbf{c}^*$ is one perpendicular to the surface. The periodicity of a crystal surface restricts H and K to integer values. The breaking of the periodicity perpendicular to the surface due to the crystal truncation allows a non-zero scattering amplitude over continuous range of L [15].

In general, the structure factor $F_{\mathbf{q}}$ may be written as the sum of two contributions, $R_{\mathbf{q}}$ due to scattering from the bulk (a *reference wave* in the holographic picture) and $O_{\mathbf{q}}$ from the surface layers (the *object wave*). Thus,

$$F_{\mathbf{q}} = R_{\mathbf{q}} + O_{\mathbf{q}}. \tag{13.3}$$

The surface contribution, $O_{\mathbf{q}}$ may be written as the Fourier transform of the electron distribution $\{u_j\}$, i.e.:

$$O_{\mathbf{q}} = \sum_j u_j \exp\left(i\mathbf{q} \cdot \mathbf{r}_j\right) \tag{13.4}$$

where $\{u_j\}$ is defined on a uniformly distributed grid of voxels at positions $\mathbf{r}_j$ within the surface unit cell. The structure of the surface can usually be deduced if it is possible to recover the distribution, $\{u_j\}$, of surface electrons.

It is important to realize that in surface crystallography the 2D unit cell of the surface atomic layers may be different (usually larger) than that of the bulk layers. Defining the reciprocal lattice vectors $\mathbf{a}^*$ and $\mathbf{b}^*$ with respect to the surface unit cell therefore, some of the reciprocal lattice rods (the so-called *superstructure rods*) corresponding to particular integer values of H and K exist solely due to scattering from the surface layers. Consequently, for those rods, $R_{\mathbf{q}} = 0$, and the structure factor $F_{\mathbf{q}}$ has only contributions $O_{\mathbf{q}}$ from the surface. Other reciprocal lattice rods corresponding to 2D reciprocal lattice vectors of the bulk, and known as *crystal truncation rods*, (CTRs) have contributions from both the bulk and surface regions according to Eq.(13.3).

If the set of amplitudes $\{O_{\mathbf{q}}\}$ may be found, the electron distribution $\{u_j\}$ follows by the inverse Fourier transform of (13.4). The recovery of $\{O_{\mathbf{q}}\}$ from the set $\{I_{\mathbf{q}}\}$ of measured intensities and the diffraction amplitudes $\{R_{\mathbf{q}}\}$ from the known part of the structure (the bulk) is akin to the recovery of an object wave from a hologram using a knowledge of a reference wave. The so-called *holographic* algorithm developed by Szöke and co-workers [16,17] seeks to find $\{u_j\}$ by solving the simultaneous equations relating that distribution to $\{I_{\mathbf{q}}\}$ and $\{R_{\mathbf{q}}\}$. In the following we will describe alternative algorithms for recovering $\{u_j\}$ from the same set of data, by using a knowledge of the reference wave $\{R_{\mathbf{q}}\}$ to *phase* the amplitudes $\{|F_{\mathbf{q}}|\}$ accessible from the experiment.

13.3 Maximum entropy algorithm for surface crystallography

13.3.1 Surface X-ray diffraction

The problem of obtaining stable and meaningful solutions from incomplete and noisy data has been addressed in a variety of fields by means of the principles of Bayesian statistics [24], and the maximum entropy method in particular [25, 26]. In X-ray crystallography, this idea has been used to develop an *exponential modeling* algorithm [27, 28] for improving the resolution of a pre-existing electron density map of a protein. A similar exponential modeling scheme has been used [29–32] as part of an iterative process of *phase extension* in which a knowledge

of the phases of some low-resolution structure factors is extended to those of higher resolution shells [33].

A maximum entropy algorithm, developed originally to improve the resolution of protein electron density maps [27], has been adapted to solve the problem of structure completion in protein crystallography [14] and surface X-ray diffraction [15]. The starting point of the theory is the fact that in Boltzmann's expression for the entropy, S, of a distribution $\{u_l\}$, namely

$$S[\{u_l\}] = k \ln\ \Omega[\{u_l\}] \tag{13.5}$$

where k is Boltzmann's constant, and the number of microstates per macrostate, Ω, is proportional to the probability (P) of the distribution. Consequently,

$$P[\{u_l\}] \propto \exp S[\{u_l\}]. \tag{13.6}$$

Thus the most probable distribution $\{u_l\}$ corresponds to that which maximizes S. A convenient form for the entropy, which is equivalent to Boltzmann's expression above, is Gibbs' form [34]:

$$S[\{u_l\}] = -\sum_l u_l \ln\left(u_l/(em_l)\right) \tag{13.7}$$

where e the base of the natural logarithms, and $\{m_l\}$ the best prior guess of the optimum distribution $\{u_l\}$ (which we could term the *measure* of the distribution). By differentiating S with respect to u_j (where j is a particular one of the set of indices $\{l\}$) it is easy to show that the distribution $\{u_l\}$ that maximizes S is the trivial one that is identical to $\{m_l\}$.

For our problem of finding the most probable electron distribution $\{u_l\}$ consistent with the experimental data, we need to constrain the distribution by the method of Lagrange multipliers. In the case of the structure completion problem, we identify $\{u_l\}$ with our best guess of the distribution $\{u_l^{(n)}\}$ of the unknown part of a unit cell at step n of an iterative algorithm. We identify the measure $\{m_l\}$ with our estimate $\{u_l^{(n-1)}\}$ of the electron distribution at the previous iteration. We seek to maximize the functional:

$$Q[\{u_l^{(n)}\}] = -\sum_l u_l^{(n)} \ln\ \left[\frac{u_l^{(n)}}{eu_l^{(n-1)}}\right] - \frac{\lambda}{2}\sum_{\mathbf{q}} \frac{|O_{\mathbf{q}}^{(n)} - T_{\mathbf{q}}^{(n-1)}|^2}{\sigma_{\mathbf{q}}^2} \tag{13.8}$$

where the first term on the right hand side (RHS) is Gibbs' expression for the entropy of the distribution $\{u_l^{(n)}\}$ with respect to the one $\{u_l^{(n-1)}\}$ from the previous iteration. The second term on the RHS constrains the structure factors $O_{\mathbf{q}}^{(n)}$, defined by

$$O_{\mathbf{q}}^{(n)} = \sum_j u_j^{(n)} \exp\left(i\mathbf{q}\cdot\mathbf{r}_j\right), \tag{13.9}$$

from the unknown part of the structure to be consistent with the experimental data, represented by a set of *target* structure factors $T_{\mathbf{q}}^{(n-1)}$ defined by

$$T_{\mathbf{q}}^{(n-1)} = |F_{\mathbf{q}}| \exp\left[\phi_{\mathbf{q}}^{(n-1)}\right] - R_{\mathbf{q}}, \tag{13.10}$$

and

$$\phi_{\mathbf{q}}^{(n-1)} = \arg[R_{\mathbf{q}} + O_{\mathbf{q}}^{(n-1)}] \tag{13.11}$$

is determined from the distribution $\{u_l^{(n-1)}\}$ at the previous iteration *via* (13.11) and (13.9). The quantity $\sigma_{\mathbf{q}}$ in (13.8) is the estimated uncertainty in the measured structure factor amplitude $|F_{\mathbf{q}}|$, and λ' is a Lagrange multiplier. Q may be maximized by requiring that

$$\frac{\partial Q}{\partial u_j^{(n)}} = 0 \qquad \forall j. \tag{13.12}$$

The differentiation of the entropy term in (13.8) is straightforward enough; that of the constraint term may be performed by writing $|O_{\mathbf{q}}^{(n)} - T_{\mathbf{q}}^{(n-1)}|^2$ as $\{O_{\mathbf{q}}^{(n)} - T_{\mathbf{q}}^{(n-1)}\}$ times its complex conjugate and noting that $O_{\mathbf{q}}^{(n)}$ depends on $u_i^{(n)}$, but not $T_{\mathbf{q}}^{(n-1)}$. After some algebra, we obtain

$$u_j^{(n)} = u_j^{(n-1)} \exp\left(-\lambda \,\mathrm{Re}\left[\sum_{\mathbf{q}} \{O_{\mathbf{q}}^{(n)} - T_{\mathbf{q}}^{(n-1)}\} \exp\left(-i\mathbf{q}\cdot\mathbf{r}_j\right) / \sigma_{\mathbf{q}}^2\right]\right). \tag{13.13}$$

It should be noted that if we may approximate all errors $\sigma_{\mathbf{q}}$ by their mean value, $< \sigma_{\mathbf{q}} >$, (13.13) can be written as a "single-voxel" equation

$$u_j^{(n)} = u_j^{(n-1)} \exp\left(-\lambda' \left[u_j^{(n)} - t_j^{(n-1)}\right]\right) \tag{13.14}$$

with the inverse Fourier transforms

$$u_j^{(n)} = \frac{1}{N} \sum_{\mathbf{q}} O_{\mathbf{q}}^{(n)} \exp\left(-i\mathbf{q}\cdot\mathbf{r}_j\right) \tag{13.15}$$

and

$$t_j^{(n)} = \frac{1}{N} \sum_{\mathbf{q}} T_{\mathbf{q}}^{(n)} \exp\left(-i\mathbf{q}\cdot\mathbf{r}_j\right) \tag{13.16}$$

where N is the number of voxels j, and $\lambda' = \lambda N / < \sigma_{\mathbf{q}} >^2$. Eq.(13.14) is an *implicit* relation for $u_j^{(n)}$ in terms of $u_j^{(n-1)}$. It can be written as an *explicit* equation for $u_j^{(n)}$ by substituting $u_j^{(n-1)}$ for $u_j^{(n)}$ on the RHS. This substitution would be justified if

$$|\delta u_j^{(n)}| \ll |u_j^{(n)} - t_j^{(n-1)}| \tag{13.17}$$

where

$$\delta u_j^{(n)} = u_j^{(n)} - u_j^{(n-1)}. \tag{13.18}$$

Note that if λ' were small enough it would be possible also to truncate the series expansion of the exponential on the RHS of (13.14) to approximate this equation by

$$\delta u_j^{(n)} = -\lambda' u_j^{(n-1)} \left\{u_j^{(n)} - t_j^{(n-1)}\right\} \tag{13.19}$$

from which it follows that condition (13.17) is equivalent to the requirement that $|\lambda' u_j^{(n-1)}| \ll 1$, or alternatively $\lambda' \ll 1/u_j^{(n-1)}\ \forall i$. This can be ensured by choosing

$$\lambda' \ll 1/u_{\max}^{(n-1)} \tag{13.20}$$

where $u_{\max}^{(n-1)}$ is the maximum value of the distribution $\{u_j^{(n-1)}\}$. It should be noted a λ' chosen according to this prescription would almost certainly also justify the truncation of the series expansion of the exponential in (13.13) that leads to (13.19) (since $u_j^{(n-1)}$, $u_j^{(n)}$ and $t_j^{(n-1)}$ are all similar in magnitude by construction), so the argument is self-consistent. Thus we may replace (13.13) by the following *explicit* recursion relation:

$$u_j^{(n)} = u_j^{(n-1)} \exp\left[-\lambda'\{u_j^{(n-1)} - t_j^{(n-1)}\}\right] \tag{13.21}$$

so long as λ'satisfies (13.20). This suggests that (13.13) may be replaced by the corresponding explicit recursion relation for $u_j^{(n)}$ in terms of $u_j^{(n-1)}$ using (13.9), namely,

$$u_j^{(n)} = u_j^{(n-1)} \exp\left(-\lambda \,\mathrm{Re}\left[\sum_{\mathbf{q}} \{O_{\mathbf{q}}^{(n-1)} - T_{\mathbf{q}}^{(n-1)}\} \exp\left(-i\mathbf{q}\cdot\mathbf{r}_j\right)/\sigma_{\mathbf{q}}^2\right]\right), \tag{13.22}$$

provided

$$\lambda \ll \frac{<\sigma_{\mathbf{q}}^2>}{N u_{\max}^{(n-1)}}. \tag{13.23}$$

Before each iteration, the input distribution is normalized by the condition

$$\sum_j u_j^{(n-1)} = \ N_{el}, \qquad \forall n > 0, \tag{13.24}$$

where N_{el} is the expected number of electrons in the surface unit cell. This algorithm has been tested successfully on simulated SXRD data from a model of the surface of O/Cu(104), where the superstructure has the same 2D periodicity parallel to the surface as the bulk, and hence all diffraction rods may be termed crystal truncation rods and have contributions from both the bulk crystal and the surface layers [15]. It has also convincingly generated the structure of reconstructed surface such as GaAs(111)-(2×2) from a dataset consisting of a mixture of superstructure and crystal truncation rods [15].

13.3.2 Low energy electron diffraction

Low energy electron diffraction (LEED) is an experiment in which electrons are directed into a sample from a distant source and the intensities of elastically backscattered electrons suffering different momentum transfers $\mathbf{g}$ parallel to the surface are monitored as a function of the energy E of the incident electrons. In the case of a crystal surface, non-zero diffracted intensities will be found only when $\mathbf{g}$ is a 2D reciprocal-lattice vector of the surface, i.e. when

$$\mathbf{g} = H\mathbf{a}^* + K\mathbf{b}^* \tag{13.25}$$

in the notation of section 2. Each diffraction data point may then be specified by an index ϵ representing a combination of diffracted beam $\mathbf{g}$ and electron energy E. The main difference between LEED and SXRD is that, due to the strong multiple scattering of LEED electrons, there exists no simple Fourier transform relationship between any characteristic of the structure and the diffraction amplitudes. Nevertheless, by identifying appropriate analogies, an adaptation of the maximum entropy theory above is able to determine the structure from LEED data also.

The first analogy is that, even in a case of strong multiple scattering, the dynamical (or multiple-scattering) structure factor of a unit cell (or repeat unit of the sample) may be written as the sum

$$F_\epsilon = R_\epsilon + S_\epsilon \tag{13.26}$$

where R_ϵ is the dynamical structure factor of the bulk crystal, which may be calculated exactly if the structure of the bulk is known. S_ϵ will then represent the effect of all multiple-scattering paths that include at least one scattering event from an atom in the surface unit cell. The second analogy we will draw on is that in LEED, to a very good approximation, it is possible to express S_ϵ in the form

$$S_\epsilon = \sum_j p_j O_{\epsilon j} \tag{13.27}$$

where $O_{\epsilon j}$ represents a *renormalized scattering matrix* (in a plane-wave representation) of a primitive 2D test superlattice, which includes an atom at a position j with respect to the substrate. The term *renormalization* implies that included in the calculation of this matrix is the dominant multiple-scattering between that layer and the substrate. It may be regarded as a form of *elementary object wave*, which may be calculated without a knowledge of the surface structure. The quantity S_ϵ is thus regarded as a linear combination of *calculable elementary object waves*, with a set of real and non-negative expansion coefficients p_j. This representation of S_ϵ is an approximation that neglects multiple scattering between the sublattices represented by the quantities $O_{\epsilon j}$. As we will see in the following, even in the rather severe test of LEED electrons normally incident on a surface containing normally oriented CO molecules this appears to be a good enough approximation. The important point is that writing the structure factor of the surface slab in the form (13.27) makes it formally similar to the corresponding expression (13.9) in surface X-ray diffraction. In both cases, the surface structure factor may be written as a linear combination of quantities calculable without a knowledge of the distribution of atoms in a surface unit cell. Thus the third analogy is that between the distribution $\{p_j\}$ of non-negative expansion coefficients and that $\{u_j\}$ of surface electrons in SXRD. This suggests that $\{p_j\}$ may be determined by a similar maximum entropy algorithm from the experimental data. Accordingly, we define an entropy of the distribution $\{p_j\}$ by the expression

$$S[\{p_l^{(n)}\}] = -\sum_l p_l^{(n)} \ln \left(p_l^{(n)}/e p_l^{(n-1)}\right) \tag{13.28}$$

of the unknown distribution $\{p_l^{(n)}\}$ at iteration n, relative to one $\{p_l^{(n-1)}\}$ at the previous

iteration, and a functional

$$Q[\{p_l^{(n)}\}] = -\sum_l p_l^{(n)} \ln\left[\frac{p_l^{(n)}}{ep_l^{(n-1)}}\right] - \frac{\lambda'}{2}\sum_\epsilon \frac{|S_\epsilon^{(n)} - T_\epsilon^{(n-1)}|^2}{\sigma_\epsilon^2} \tag{13.29}$$

in analogy with with (13.8), where the distribution $\{p_l^{(n)}\}$ substitutes for the electron density distribution $\{u_l^{(n)}\}$ at the n^{th} iteration,

$$S_\epsilon^{(n)} = \sum_l p_l^{(n)} O_{\epsilon l}, \tag{13.30}$$

$$T_\epsilon^{(n-1)} = |F_\epsilon| \exp\left[\phi_\epsilon^{(n-1)}\right] - R_\epsilon, \tag{13.31}$$

and,

$$\phi_\epsilon^{(n-1)} = \arg[R_\epsilon + S_\epsilon^{(n-1)}]. \tag{13.32}$$

The quantity $\sigma_{\mathbf{q}}$ in (13.29) is the estimated uncertainty in the measured structure factor amplitude $|F_{\mathbf{q}}|$, and λ is a Lagrange multiplier. Q may be maximized by requiring that

$$\frac{\partial Q}{\partial p_j^{(n)}} = 0 \qquad \forall j. \tag{13.33}$$

The differentiation of the entropy term in (13.29) is straightforward enough; that of the constraint term may be performed by writing $|O_\epsilon^{(n)} - T_\epsilon^{(n-1)}|^2$ as $\{O_\epsilon^{(n)} - T_\epsilon^{(n-1)}\}$ times its complex conjugate and noting that $O_\epsilon^{(n)}$ depends on $p_i^{(n)}$, but not $T_\epsilon^{(n-1)}$. After some algebra we obtain

$$\ln\left[\frac{p_j^{(n)}}{p_j^{(n-1)}}\right] = -\lambda\{\mu_j^{(n)} - \tau_j^{(n-1)}\} \tag{13.34}$$

where

$$\mu_j^{(n)} = \frac{1}{N}\sum_\epsilon \mathrm{Re}\{S_\epsilon^{(n)} O_{\epsilon j}^*\} \tag{13.35}$$

and

$$\tau_j^{(n-1)} = \frac{1}{N}\sum_\epsilon \mathrm{Re}\{T_\epsilon^{(n-1)} O_{\epsilon j}^*\} \tag{13.36}$$

and $\lambda = \lambda' N / < \sigma_\epsilon^2 >$, where the individual variances σ_ϵ^2 are replaced by their mean value $< \sigma_\epsilon^2 >$. Hence

$$p_j^{(n)} = p_j^{(n-1)} \exp\left[-\lambda\{\mu_j^{(n)} - \tau_j^{(n-1)}\}\right]. \tag{13.37}$$

Together with (13.35), (13.36), and (13.32), this consitututes an *implicit* relation for $p_j^{(n)}$ in terms of $\{p_i^{(n-1)}\}$. It can be written as an *explicit* equation for $p_j^{(n)}$ by substituting $\mu_j^{(n-1)}$ for $\mu_j^{(n)}$ on the RHS. By analogy with the case of X-ray diffraction, we would expect this to be valid if λ were chosen small enough. By the same analogy, it might be conjectured that the condition is approximately

$$\lambda \ll 1/p_{\max}^{(n-1)} \tag{13.38}$$

where $p_{\max}^{(n-1)}$ is the maximum value of the distribution $\{p_i^{(n-1)}\}$. Thus we argue that (13.37) may be replaced by the following *explicit* recursion relation:

$$p_j^{(n)} = p_j^{(n-1)} \exp\left[-\lambda\{\mu_j^{(n-1)} - \tau_j^{(n-1)}\}\right]. \tag{13.39}$$

so long as λ approximately satisfies (13.38).

The algorithm may be initiated at interation $n = 1$ by taking $\{p_j^{(0)}\}$ to be a uniform distribution normalized to the expected number N_{atom} of atoms in the surface unit cell. That is one may take

$$p_j^{(0)} = \frac{N_{atom}}{N_{vox}}, \qquad \forall j \tag{13.40}$$

where N_{vox} is the number of voxels at which the distributions $\{p_j^{(n)}\}$ are evaluated, and using this expression to evaluate $\mu_j^{(0)}$ and $\tau_j^{(0)}$ *via* (13.35) and (13.36), respectively, with $\phi_\epsilon^{(0)}$ found from (13.32). After completion of each iteration, the new distribution is re-normalized by the condition

$$\sum_j p_j^{(n)} = N_{atom}. \tag{13.41}$$

Form of reference and object waves for LEED

We now turn to the question of the form of R_ϵ and $O_{\epsilon j}$ for a workable algorithm for LEED. For a key to an understanding of this, consider first the evaluation of the scattering of a LEED electron from a surface consisting of an ordered 2D test layer of the periodicity of the superlattice above a crystal substrate. We assume that the structure of the substrate is known, and that thus it is possible to calculate exactly its reflection matrix $\mathbf{B}^{-+}$ in a plane wave basis. If the "in-out" scattering matrix of the test layer (in the same basis) is defined as $\mathbf{M}^{-+}$, the "in-in" matrix as $\mathbf{M}^{++}$, and the "out-out" matrix as $\mathbf{M}^{--}$ in the usual LEED notation, where the second superscipt denotes the direction from which a wave is incident on the layer or substrate, and the first one that of the scattered (or transmitted) wave. The superscript $+$ indicates a direction of flux from vacuum into the surface, and $-$ the reverse flux. Exploiting the weakness of back-scattering processes compared to forward-scattering ones, the scattering paths involving the adsorbate layer and substrate may be ordered by the number of back-scattering processes involved. Obviously, the minimum number of backscattering processes for the detection of a flux of backscattered LEED electrons above the surface is one. Also exploiting

the weakness of $\sim 90^\circ$ scattering of LEED electrons of normal incidence compared with either forward or back scattering, we approximate the scattering matrices $\mathbf{M}^{\pm\pm}$ by "kinematic" expressions [39], that neglect multiple scattering within the adlayer [40].

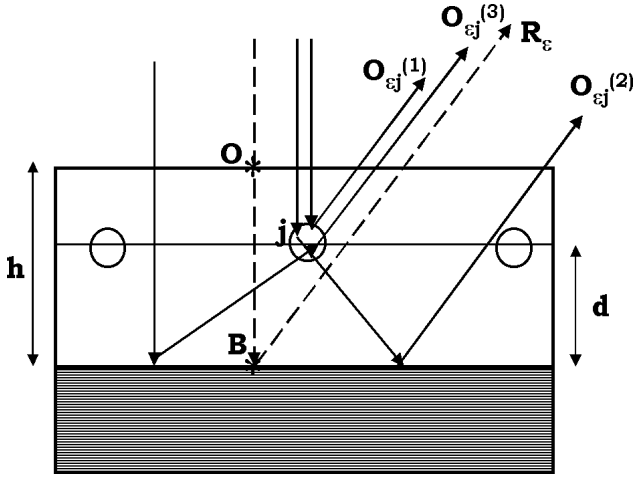

Figure 13.1: Representation of the electron propagation and scattering paths giving rise to the *reference wave* R_ϵ and three dominant contributions $O^{(1)}_{\epsilon j}$, $O^{(2)}_{\epsilon j}$, and $O^{(3)}_{\epsilon j}$ to the *object wave* $O_{\epsilon j}$ arising when the origin the surface atomic layer is at the point j at a height d above the outermost bulk atomic layer. The electron charge distribution of the surface is assumed to extend to a height h above the bulk. The plane parallel to the surface at this height contains the real-space origin O with respect to which all mutually coherent electron paths are referenced. The conventional origin for the calculation of the bulk reflection matrix $\mathbf{B}^{-+}$ is assumed to be at a point B just above the outermost bulk layer.

Suppose the electron cloud associated with the surface extends to a height h above the uppermost atomic layer of the substrate (see Fig. 13.1). The plane parallel to the surface at this height may then be regarded as the true interface between the sample and the vacuum. The propagation of electrons below this layer must take account of both refraction and absorption. It is thus convenient to define an origin, O, at some reference point in this interface plane, with respect to which is measured the phase of a plane wave of unit amplitude representing the incident LEED electron. Define also an origin j of the adsorbate layer, taken at the position of an atom in the test layer, and in a plane of height d above the outermost substrate layer. And define B to be the conventional origin assumed for the definition of the bulk reflection matrix $\mathbf{B}^{-+}$. Let the propagation matrix (also in the plane wave representation) of an electron from O to j be defined as $\mathbf{P}_{jO}$, that from j to B be $\mathbf{P}_{Bj}$, and the corresponding propagation matrices in the reverse directions be $\mathbf{P}_{Oj}$ and $\mathbf{P}_{jB}$, respectively. Then the total reflection matrix of the entire surface to first-order in backscattering may be written:

$$\begin{aligned}\mathbf{T} &= \mathbf{P}_{Oj}\mathbf{P}_{jB}\mathbf{B}^{-+}\mathbf{P}_{Bj}\mathbf{P}_{jO} + \mathbf{P}_{Oj}\mathbf{M}^{-+}\mathbf{P}_{jO}... \\ &\quad +\mathbf{P}_{Oj}(\mathbf{1}+\mathbf{M}^{--})\mathbf{P}_{jB}\mathbf{B}^{-+}\mathbf{P}_{Bj}(\mathbf{1}+\mathbf{M}^{++})\mathbf{P}_{jO} \qquad (13.42)\end{aligned}$$

where unit matrices $\mathbf{1}$ are added to the "in-in" and "out-out" matrices to take account of

unscattered transmission. Since the product of two free-space propagator matrices involving an intermediate point is independent of that intermediate point,

$$\mathbf{P}_{BO} = \mathbf{P}_{Bj}\mathbf{P}_{jO} \tag{13.43}$$

and

$$\mathbf{P}_{OB} = \mathbf{P}_{Oj}\mathbf{P}_{jB}. \tag{13.44}$$

From these relations, we see that the first term in (13.42) above is independent of the absorbate layer. One of its elements forms a suitable reference wave for our purposes, namely:

$$R_\epsilon = \left(\mathbf{P}_{OB}\mathbf{B}^{-+}\mathbf{P}_{BO}\right)_{\mathbf{g0}}, \tag{13.45}$$

where the indices **g0** specify the matrix element for scattering from an incident wave to the backscattered Bragg reflection labelled by the reciprocal lattice vector **g**. The remaining terms in (13.42) enable the calculation of the corresponding object wave *via*:

$$\begin{aligned} O_{\epsilon j} &= \left(\mathbf{P}_{Oj}\mathbf{M}^{-+}\mathbf{P}_{jO} + \mathbf{P}_{Oj}(\mathbf{1}+\mathbf{M}^{--})\mathbf{P}_{jB}\mathbf{B}^{-+}\mathbf{P}_{Bj}(\mathbf{1}+\mathbf{M}^{++})\mathbf{P}_{jO}\right)_{\mathbf{g0}} \\ &\simeq O_{\epsilon j}^{(1)} + O_{\epsilon j}^{(2)} + O_{\epsilon j}^{(3)}, \end{aligned} \tag{13.46}$$

where

$$O_{\epsilon j}^{(1)} = \left(\mathbf{P}_{Oj}\mathbf{M}^{-+}\mathbf{P}_{jO}\right)_{\mathbf{g0}}, \tag{13.47}$$

$$O_{\epsilon j}^{(2)} = \left(\mathbf{P}_{OB}\mathbf{B}^{-+}\mathbf{P}_{Bj}\mathbf{M}^{++}\mathbf{P}_{jO}\right)_{\mathbf{g0}}, \tag{13.48}$$

and

$$O_{\epsilon j}^{(3)} = \left(\mathbf{P}_{Oj}\mathbf{M}^{--}\mathbf{P}_{jB}\mathbf{B}^{-+}\mathbf{P}_{BO}\right)_{\mathbf{g0}}, \tag{13.49}$$

where a fourth term involving the product of the scattering matrices $\mathbf{M}^{--}$ and $\mathbf{M}^{++}$ has been neglected. Test computations [41] have shown this to be a reasonable approximation. Representative scattering paths followed by electrons contributing to R_ϵ, $O_{\epsilon j}^{(1)}$, $O_{\epsilon j}^{(2)}$, and $O_{\epsilon j}^{(3)}$ are illustrated in Fig. 13.1.

Taking the reference and elementary object waves to be of the form (13.45) and (13.46) respectively is justified if substitution of these expressions into (13.27) and (13.26) would give a reasonable approximation to the dynamical LEED structure factor F_ϵ for a distribution $\{p_j\}$ of atom positions within a surface unit cell, to be determined by the iterative algorithm of the last section. An assumption of this approximation is that multiple scattering between different adsorbate atoms may be neglected, and so the scattering. Again, due to the predominantly forward-scattering nature of atomic scattering factors for LEED electrons, this is usually a good approximation for normally incident electrons and adsorbates confined to a single layer parallel to the surface. What was therefore a little surprising, but very gratifying, the result described in the next section where we found that this approximation may even be used to determine the positions of both adsorbate atoms within the surface unit cell in the almost worst-case scenario of an assumed layer of CO with molecular axes perpendicular to the surface.

Test case for LEED

In this paper we will give only a very basic proof of principle of our proposed inverse method for LEED. We will aim to recover the height distribution of the C and O atoms above a Ni(001) surface from a single I/E curve of the (00), or specular, reflected intensities, as calculated by a standard and realistic computer program [42] over an experimentally accessible energy range from a hypothetical c(2×2)-CO/Ni(001) surface. Also required as input to the calculations of the reference waves, R_ϵ, are the dynamical structure factors, $\mathbf{B}^{-+}$, of a clean Ni(001) surface. The calculations of the propagation matrices, e.g. $\mathbf{P}_{jO}$, for the evaluation of R_ϵ and $O_{\epsilon j}$ from (13.45) and (13.46), respectively, require only the evaluation of complex exponentials with arguments containing the (complex) wavevectors of the plane-wave expansions between the atomic layers and the vectors relating the fixed reference positions O and B, and the test positions, j, of atoms within a surface unit cell.

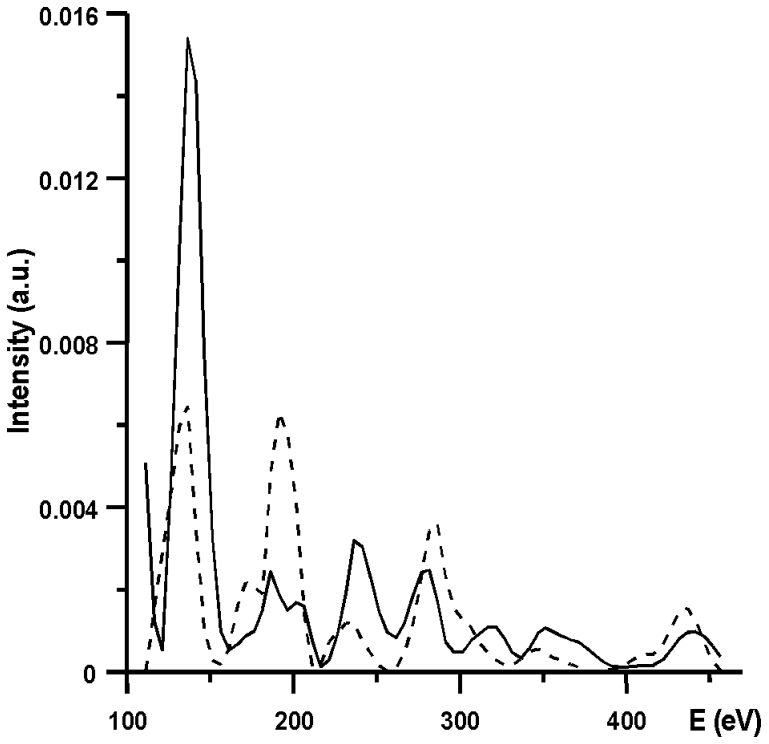

Figure 13.2: Solid line: calculated LEED intensity vs. energy for the specular, or (00) beam from a (1×1)-CO/Ni(001) surface from approximatey 100 to 450 eV. Dashed line: calculated LEED intensity vs. energy of the same beam over the same energy range from a clean Ni(001) surface with the same electron absorption parameters.

Figure 13.2 shows a calculated I/E curve (solid line) over an energy range from about 100 to 400 eV, of a c(2×2)-CO/Ni(001) surface, assuming atop adsorption of CO directly above each of the Ni atoms in the outermost substrate layer. The Ni-C distance was taken to be

1.7 Å, the C-O distance 1.5 Å, and the height h of the origin O above the outermost Ni layer taken to be 3.93 Å. The square roots of the elements of this distribution are the structure factor amplitudes $|F_\epsilon|$ used as input to the algorithm of Sec. 13.3.2. Also shown as a dashed line in Fig. 13.2 is the intensity from a clean Ni(001) surface for the same position of the origin O relative to the Ni atoms [43]. These intensities are equal to $|R_\epsilon|^2$, where the quantities R_ϵ are the calculated *complex* amplitudes representing the reference waves.

Since the specular beam for normal incidence in LEED is sensitive primarily to crystallographic structure in a direction perpendicular to the surface we attempt to recover only the distribution of the heights of the adsorbate atoms above the surface. That is, we specialize the general theory of Sec. 13.3.2 to that of a one-dimensional problem in which ϵ is represented by just the energy E of the specularly reflected LEED electrons (for which $\mathbf{g}=\mathbf{0}$) and $\{p_j^{(n)}\}$ is a one-dimensional distribution at iteration n of the algorithm, and j is an index representing the height above the Ni substrate.

One complication in the present case is that the two adsorbate atoms are of different chemical species, and in principle it might be imagined that the theory would need to be generalized for separate spatial distributions for the C and O atoms, with separate definitions of component object waves $O_{\epsilon j}$ for each chemical species. Yet, as we will see in the present example, it appears that the kinematic layer scattering matices $\mathbf{M}^{\pm\pm}$ of the same 2D unit cell size for C and O are sufficiently similar for the matrices $\mathbf{M}^{\pm\pm}$ in (13.46) to be defined for just one of the chemical species (just O for our present simulations).

We assumed an initial distribution $\{p_j^{(o)}\}$ to be the least-biased normalized one (13.40). The distribution $\{p_j^{(1)}\}$, after a single iteration, is shown in Fig. 13.3(a). That $\{p_j^{(500)}\}$ after 500 iterations already gives an approximate indication of the heights of the atoms of the adsorbed molecule, as seen in Fig. 13.3(b). The final result $\{p_j^{(3000)}\}$ after 3000 iterations, as shown in Fig. 13.3(c), gives a remarkably clear and accurate indication of the heights of both C and O atoms.

In practice, of course, data from all LEED beams available from an experiment (and not just the specular one) will be used as input to the algorithm. With the use of a number of these beams accesible from experiment, it is possible to recover the full 3D distribution of adsorbates on surfaces [44].

13.4 Discussion and conclusions

To date most surface crystal structures have been solved by a combination of chemical intuition, the pooling together of data from different physical probes, and by trial-and-error fitting to experimental diffraction data, of simulations of diffraction data from guessed models of the structure. The latter process invariably runs up against the exponential growth with complexity of the structure of the number of models that need to be tested. Consequently, more attention has been devoted in recent years to developing a reliable *direct* method for surface crystallography that may lead rapidly from the experimental diffraction data to the surface structure at the atomic scale. One of the ideas that has attracted attention in recent years is that of interpreting the diffraction patterns in some sense as an interference pattern between an assumed known spherical *reference wave* from an identifiable atom within a surface unit

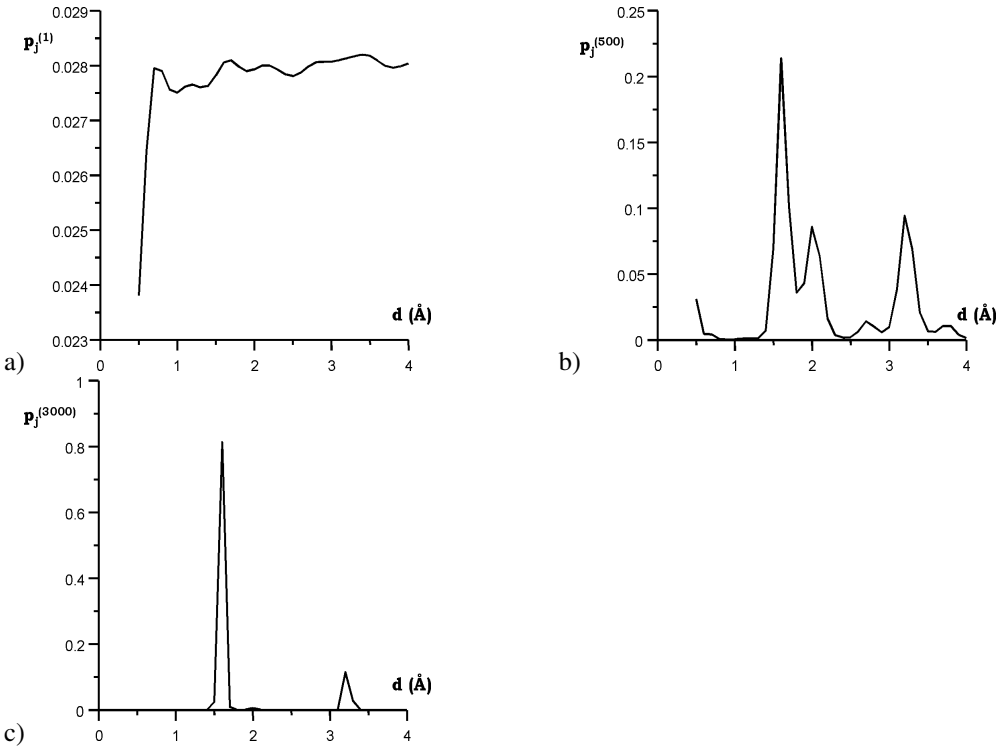

Figure 13.3: Evolution of the one-dimensional distribution of atomic scatterers as calculated by our algorithm as a function of height above the outermost layer of Ni atoms of the substrate. (a) The distribution $\{p_j^{(1)}\}$ after a single iteration (b) that $\{p_j^{(500)}\}$ after 500 iterations, and (c) that $\{p_j^{(3000)}\}$ after 3000 iterations. The final distribution correctly reproduces the heights of the C and O atoms at approximately 1.7 Å and 3.2 Å, respectively.

cell and the *object waves* formed by the scattering of this wave from its neighboring atoms. If such an interpretation is possible, *holographic* computer reconstruction algorithms are able to reveal the three-dimensional arrangement of the neighboring atoms relative to the reference wave source. When the hologram is formed by the interference of low energy electrons, the decay of the reference wave with the inverse of distance from the source, as well as its attenuation due to inelatic scattering, generally does not allow the recovery of more than just a few atoms in the vicinity of the source. Also the existence of more than one reference wave source could lead to the superposition of more than one local atomic environment, with a consequent difficulty of interpretation.

In this paper we develop an alternative holographic interpretation for surface crystallography that promises to overcome these problems. It is based on the idea that when an external beam of radiation is directed into a surface, the radiation detected outside the sample will have scattered from not just the outermost surface layers whose structure may need to be determined, but also from parts of the underlying bulk crystal, whose structure is generally

known. The calculable scattered radiation from this known part of the structure is thus identified with the reference wave and that scattered from the unknown part of the structure the object wave. A conventional holographic algorithm would be capable of recovering the object wave from the diffraction data and a knowledge of the reference wave (which may be calculated from a knowledge of the bulk structure). We go one step farther: by writing the object wave as a linear combination of calculated components associated with given positions on a uniform grid covering a 3D slab representing the surface unit cell, we develop an algorithm to recover the coefficients of that linear sum.

In the case of X-ray diffraction the calculated components are simple exponential functions, and the (non-negative) coefficients represent the electron density in the surface unit cell. In the case of LEED, the components may be regarded as elements of effective (or renormalized) scattering matrices of a primitive lattice of test atoms of the 2D periodicity of the superstructure *in a given geometrical relation to the substrate*. Such effective scattering matrices may be calculated rapidly from standard LEED programs, taking account of the dominant (first-order) multiple-scattering with the substrate. Only as many such scattering matrices need be calculated as there grid points within a symmetry-reduced sector of the surface unit cell multiplied by the number of energies at which LEED data are measured. This number is *independent of the structural complexity of the unit cell*. The coefficients of the expansion of these components of the object wave may be regarded as the elements of a non-negative distribution of atoms in the surface unit cell, to be determined.

In the cases of either X-ray diffraction or LEED the relevant distribution is determined by a maximum entropy algorithm, which iteratively satisfies the experimental constraints to the reciprocal-space data, while also ensuring the non-negativity of all elements of the sought distribution in real space at each iteration. The theory for X-ray diffraction has been given in an earlier paper [15], which also contains examples of the operation of the algorithm to recover the electron density of the surfaces of a number of structures from realistic simulations of surface X-ray diffraction data from a standard program. In the present paper, we extend the theory to LEED and demonstrate the algorithm for a very simple test case to determine from simulated LEED data just the height above a Ni(001) substrate of the atoms of a CO molecule with its molecular axis perpendicular to the surface. Future papers will show the effectiveness of this algorithm also for the determination of the full 3D superstructures of surface layers.

Acknowledgements

We acknowledge financial support for this work from the U.S. National Science Foundation (Grant No: DMR-9815092) and the U.S. Department of Energy (Grant Nos: DE-FG02-01ER45926 and DE-FG02-84ER45076).

References

[1] D. Gabor, Nature **161**, 777 (1948).

[2] A. Szöke, in *Short Wavelength Coherent Radiation: Generation and Applications*, edited by Attwood D J and Boker J, AIP Conf. Proc. No 147 (New York: AIP, 1986).

[3] J.J. Barton, Phys. Rev. Lett. **61**, 1356 (1988).

[4] D.K. Saldin and P.L. De Andres, Phys. Rev. Lett. **64**, 1270 (1990).
[5] G.R. Harp, D.K. Saldin, and B.P. Tonner, Phys. Rev. B **42**, 9199 (1990).
[6] D.-A. Luh, T. Miller, and T.-C. Chiang, Phys. Rev. Lett. **81**, 4160 (1998).
[7] S.H. Xu, M. Keeffe, Y. Yang, C. Chen, M. Yu, G.J. Lapeyre, E. Rotenberg, J. Denlinger, and J.T. Yates, Phys. Rev. Lett. **84**, 939 (2000).
[8] J.B. Pendry, K. Heinz, and W. Oed, Phys. Rev. Lett. **61**, 2953 (1988).
[9] M.A. Kulakov, G. Henn, and B. Bullemer, Surf. Sci. **346**, 49 (1996).
[10] L. Li and I.S.T. Tsong, Surf. Sci. **351**, 141 (1996).
[11] U. Starke, J. Schardt, and M. Franke, Appl. Phys. A **65**, 587 (1997).
[12] D.K. Saldin, X. Chen, J.A. Vamvakas, M. Ott, H. Wedler, K. Reuter, K. Heinz, and P.L. De Andres, Surf. Rev. Lett. **4**, 991 (1997).
[13] K. Reuter, J. Bernhardt, H. Wedler, J. Schardt, U. Starke, and K. Heinz, Phys. Rev. Lett. **79**, 4818 (1997).
[14] V.L. Shneerson, D.L. Wild, and D.K. Saldin, Acta Cryst. A**57**, 163 (2001).
[15] D.K. Saldin, R.J. Harder, H. Vogler, W. Moritz, and I.K. Robinson, Comput. Phys. Commun. **137**, 12 (2001).
[16] A. Szöke, Phys. Rev. B **47** 14044 (1993).
[17] A. Szöke, Acta Cryst. A**49** 853 (1993).
[18] W. Cochran, Acta Cryst. **4**, 408 (1951).
[19] G.A. Sim, Acta Cryst. **12** 813 (1959).
[20] G.A. Sim, Acta Cryst. **13** 511 (1960).
[21] R. Read, Acta Cryst. A**42** 140 (1986).
[22] J. Rius, C. Miravitlles, and R. Allmann, Acta Cryst. A**42**, 140 (1996).
[23] L. Marks, Phys. Rev. B **60**, 2771 (1999).
[24] D.S. Sivia, *Data Analysis: A Bayesian Tutorial* (Oxford University Press, Oxford, 1996).
[25] E.T. Jaynes, Phys. Rev. **106** 620 (1857).
[26] S.F. Gull and G.J. Daniell, Nature **272**, 686 (1978).
[27] D.M. Collins, Nature **298**, 49 (1982).
[28] D.M. Collins and M.C. Mahar, Acta Cryst. A**39** 252 (1983).
[29] G. Bricogne, Acta Cryst. A**40**, 410 (1984).
[30] G. Bricogne, Acta Cryst. A**44**, 517 (1988).
[31] G. Bricogne, in: *Maximum Entropy in Action*, edited by B Buck and V A Macaulay, p. 187 (Oxford University Press, Oxford, 1991).
[32] C.J. Gilmore, Acta Cryst. A**52**, 561 (1996).
[33] G. Bricogne, Acta Cryst. D**49**, 37 (1993).
[34] L.D. Landau and E.M. Lifshitz, *Statistical Physics* (Pergamon, New York, 1980).
[35] J.R. Fienup, Optics Lett. **3**, 27 (1978).
[36] J.R. Fienup, Appl. Optics, **21**, 2758 (1982).
[37] D.K. Saldin, R.J. Harder, V.L. Shneerson, and W. Moritz, J. Phys.: Condens. Matter **13**, 10689 (2001).

[38] D.K. Saldin, R.J. Harder, V.L. Shneerson, and W. Moritz, J. Phys: Condens. Matter **14**, 4087 (2002).

[39] J.B. Pendry, *Low Energy Electron Diffraction* (Academic, London, 1974).

[40] This *quasi-dynamical* approximation has also been employed successfully in conventional LEED analyses, see e.g. N. Bickel and K. Heinz, Surf. Sci. **163**, 435 (1985).

[41] A. Seubert, K. Heinz, and D. K. Saldin, Phys. Rev. B **67**, 125417 (2003).

[42] M.A. Van Hove and S.Y. Tong, *Surface Crystallography by LEED* (Springer, Berlin, 1979).

[43] This is necessary to ensure that the incident electrons are absorbed the same amount in propagating to the substrate.

[44] D.K. Saldin, A. Seubert, and K. Heinz, Phys. Rev. Lett. **88**, 115507 (2002).

Solid-State Photoemission and Related Methods
Wolfgang Schattke, Michel A. Van Hove (Eds.)

14 XAFS and related methods: Theoretical techniques

J.J. Rehr, R.C. Albers, and A.L. Ankudinov

Dramatic progress has been made over the past two decades in the development of the theory of X-ray absorption (XAS) and related spectroscopies, e.g., X-ray absorption fine structure (XAFS), X-ray photoelectron diffraction (XPD), etc. In this work we review the theoretical techniques and algorithmic developments needed for accurate calculations of these spectra. In particular real-space multiple scattering (RSMS) theory, which is based on Green's functions rather than wave functions and final state potentials turns out to be particularly well suited to calculate such spectra. This one-electron approach has become the standard model for most current XAS calculations and has led to efficient *ab initio* codes which permit a quantitative interpretation. The theory differs significantly from ground state calculations, since the spectroscopies of interest involve excited electronic states with a high energy photoelectron and a core-hole. However, it retains a close connection to excited state electronic structure, since X-ray spectra are directly related to a Green's function for the excited photoelectron in the presence of a core-hole. We also briefly discuss many-body corrections to this model.

14.1 Introduction

In this Chapter we review the theoretical techniques and algorithmic developments needed for accurate calculations of X-ray absorption and related spectra. We focus on algorithms and codes for practical calculations, rather than only on formal theory. In particular we discuss the development of a one-electron approach based on real space multiple-scattering (RSMS) theory and final state potentials, which has become a standard approach for such calculations. These developments are discussed in detail in a recent review [1].

Since they involve similar interactions between X-rays and condensed matter, all X-ray spectroscopies require similar theoretical treatments; that is, all can be described in terms of excited state electronic structure and the response of condensed matter to electromagnetic radiation at X-ray energies. The hard X-ray regime, with typical photon energies of order 10^2–10^4 eV, differs in many respects from the optical and UV. This regime generally involves high energy excited photoelectron states with typical photoelectron energies or order 10^1–10^3 eV and the sudden creation of a deep core hole. A crucial difference between excited state and conventional ground state electronic structure calculations is the need to include the effects of inelastic losses in excited states. That is, the photoelectron must be treated as a quasi-particle of finite lifetime, rather than as a stationary state. There is also a close connection between RSMS theory and excited state electronic structure, since X-ray spectra are directly related to a Green's function for the excited photoelectron in the presence of a core-hole.

Solid-State Photoemission and Related Methods: Theory and Experiment. Edited by Wolfgang Schattke, Michel A. Van Hove

ISBN: 3-527-40334-5

The development of X-ray spectroscopy theory has roughly paralleled that of modern synchrotron radiation X-ray sources over the past two decades. Advances in theory, particularly in the theory of excited states multiple-scattering (MS) theory have revolutionized techniques for local structure determinations such as extended X-ray absorption fine structure (EXAFS), X-ray photoelectron diffraction (XPD) and others. Indeed, modern theories of X-ray spectroscopies have essentially replaced the more phenomenological early theories. As a result of these advances, the basic theory of EXAFS and XPD can now be considered as well understood. A fully quantitative treatment has yet to be achieved, due to a number of complications, e.g., full potential corrections and many body effects such as core-hole effects and the screening of the X-ray field. However, significant progress has also been made in parallel with the development of the current series of high brilliance X-ray sources, such as the ALS and APS, as well as dramatically increased computational resources. This progress is largely aimed at understanding the physics of the near edge structure i.e., the structure within about 30 eV of threshold where strong chemical (and hence strong MS contributions) and excited state many-body effects such as the core-hole interaction and screening are most important.

Perhaps the most pervasive and important result of all improvements in theory has been the development of fast *ab initio* computer codes for the calculation of XAS and other X-ray spectroscopies. An example is the RSMS code FEFF8 developed by our group, which calculates both X-ray spectra and self-consistent electronic structure [2]. This code is highly automated and intended to be user friendly, requiring a minimum of input and few adjustable parameters. Such codes have now become quite sophisticated, and now include electronic and magnetic structure, many-electron excitations, and thermal vibrations. For example, FEFF8 yields results for electronic densities of states in good agreement with modern full-potential band-structure codes.

14.2 Standard one-electron theory of X-ray spectra

14.2.1 Theoretical considerations

As noted in the introduction, our primary focus in this Chapter is the theory of deep-core X-ray spectra, i.e., photoexcitation of core-levels by hard X-rays of energies between about 10^2 and 10^4 eV. Such photons create high energy excited photoelectron states with electron energies of order 10^1 and 10^3 eV, together with a deep and essentially structureless core hole at the absorption site. These characteristics demand theoretical treatments which differ significantly from those for the ground state. In particular at high energies, the photoelectron kinetic energy dominates and hence scattering due to the atomic potentials is comparatively weak. Thus to zeroth order, the photoelectron propagates in a uniform, lossy medium with a given electron density, and scattering can be treated as a perturbation. For this reason multiple-scattering (MS) theory [3] is well suited for practical calculations. Due to inelastic losses, the photoelectron must be treated as a quasi-particle of finite lifetime, rather than as a stationary state. Thus these losses give a photoelectron a finite mean-free path, so only a finite portion (typically a few tens of Å) of a system is typically probed by X-ray spectra. Thus long-range-order features seen in band-structure calculations [4] of the spectra (e.g., van Hove singularities) are smeared out by final state and lifetime broadening. Thus the theory of high energy excited

states is complementary to ground state techniques. For these reasons real space approaches within a finite cluster are advantageous [2]. Correspondingly Green's function rather than wave function based methods are more natural to handle effects of inelastic losses and self-energy effects. Finally the core-hole interaction is often crucial for accurate calculations; that is, a final state Hamiltonian is usually needed to describe the spectra [5]. In addition thermal vibrations and disorder must also be taken into account, since they lead to strong Debye-Waller damping effects on the spectra at high energies [6]. These considerations have led to the development of a real-space multiple scattering (RSMS) formalism [7], which has become the standard for most practical calculations of X-ray spectra.

14.2.2 Golden rule

Formal theories of X-ray spectra generally start from Fermi's Golden rule: i.e., the full many-body expression for X-ray absorption spectrum as a function of X-ray energy $\hbar\omega$ is given by

$$\mu \propto \sum_f \left| \left\langle \Psi_f^N \;\middle|\; \sum_{j=1}^{N} \mathbf{p}_j \cdot \mathbf{A}(\mathbf{r}_j) \;\middle|\; \Psi_i^N \right\rangle \right|^2 \delta(E_f - E_i - \hbar\omega), \tag{14.1}$$

where $|\Psi_i^N\rangle$ and $|\Psi_f^N\rangle$ denote N-particle initial and final states at energies E_f and E_i respectively, $\mathbf{p} \cdot \mathbf{A}$ is the electron-photon coupling with vector potential $\mathbf{A}$, and the sum is over all N-particle final states. However this formal expression is essentially useless for real calculations due to the difficulty of calculating many-body states. Thus practical calculations are usually based the reduction of the Golden rule to a one-electron approximation. Although the question of which one-electron states to use in a one-electron theory is not unambiguous, many current calculations are based on the *final state rule* [5]. This rule states that final states should be calculated in the presence of a screened core-hole. Also all many-body effects and inelastic losses are lumped into a complex valued self-energy or optical potential. In practice the final state rule appear to work well for highly excited photoelectrons and has become an important consideration in the *standard model* of XAS discussed in this Chapter. Various corrections, such as multi-electron excitations generally add broadening, but little if any additional structure.

Within this *standard*, one-electron model the Golden rule is simply

$$\mu(E) \sim \sum_f \left| \langle f | \mathbf{A} \cdot \mathbf{p} | i \rangle \right|^2 \delta(E - E_f), \tag{14.2}$$

where $E = \hbar\omega - E_i$ is the photoelectron energy and the damped quasi-particle final states $|f\rangle$ are calculated in the presence of an appropriately screened core-hole. The final states $|f\rangle$ are eigenstates of a lossy, non-Hermitian final state Hamiltonian,

$$H' = \frac{p^2}{2} + V'_{\mathrm{coul}}(\vec{r}) + \Sigma(E, \vec{r}), \tag{14.3}$$

where the prime denotes the potential in the presence of a screened core hole (e.g., a self-consistently determined core-hole potential), and $\Sigma(E)$ is the non-Hermitian, energy dependent self-energy operator, which replaces the exchange correlation potential of the ground state

density functional Hamiltonian. As discussed below, calculations of XAS from Eq. (14.2) can then be made from either one-particle wave-function or Green's function methods [8, 9]. For X-ray spectra, the Green's function approaches are generally preferable, since they are applicable over a wider energy regime.

14.2.3 Green's Function formalism

An important formal development in modern theories of X-ray spectra is the replacement of explicit calculations of wave functions or scattering states in the Golden Rule with a Green's function approach [8, 9]. Calculations of final states is usually a computational bottleneck, except possibly for symmetric molecules and periodic solids. However, many systems of interest lack such symmetry. Also k-space methods developed for periodic solids generally ignore important effects such as the core-hole and lattice vibrations, which spoil crystal translation symmetry. Moreover, inelastic losses are difficult to include in wave-function methods, except *a posteriori* through Lorentzian broadening; this broadening smears out detailed band structure features. Thus for excited states it is preferable to recast the Golden rule in terms of one-electron Green's function or photoelectron propagator in real space,

$$G(E) \equiv \frac{1}{E - H' + i\eta} = \sum_f |f\rangle \frac{1}{E - E_f + i\eta} \langle f| \tag{14.4}$$

which implicitly sums over all final states. The propagator $G(E)$ is the solution of an inhomogeneous Dyson equation $[E - H']G(E) = \delta(\mathbf{r} - \mathbf{r}')$, which is analogous to the Schrodinger equation. Thus in terms of $G(E)$ the XAS in Eq. (14.2) can equivalently be expressed as

$$\mu(E) \sim -\frac{1}{\pi} \mathrm{Im} \, \langle \mathrm{i}| \, \hat{\epsilon} \cdot \mathbf{r}' \, \mathrm{G}(\mathbf{r}', \mathbf{r}, \mathrm{E}) \, \hat{\epsilon} \cdot \mathbf{r} \, |\mathrm{i}\rangle. \tag{14.5}$$

Calculations of $G(E)$ at high energies are conveniently carried out using multiple-scattering (MS) theory [3]. Within MS theory the propagator near a given site (e.g., the origin) can be expanded as

$$G(\mathbf{r}, \mathbf{r}', E) = \sum_{L,L'} R_L(\mathbf{r}) G_{L0,L'0} R_{L'}(\mathbf{r}'). \tag{14.6}$$

Then the expression for μ can be reduced to a calculation of atomic dipole-matrix elements $M_L = \langle i|\hat{\epsilon} \cdot \mathbf{r}|L\rangle$ and a propagator matrix $G_{L0,L'0} \equiv G_{L,L'}$ in an angular momentum and site representation $|L, \mathbf{R}\rangle$. The relativistic generalization [10] is similar; however relativistic effects (e.g, spin-orbit effects) are biggest in the atomic cores and mostly affect the dipole matrix elements. Thus $L = (\kappa, m)$ denotes a relativistic angular momentum basis.

With the representation of the Green's function in Eq. (14.6), the Golden Rule for the XAS can be written as from a core level i can be expressed as

$$\mu(\omega) = \frac{4\pi e^2 \omega}{c} \sum_{i,LL'} M_{iL}(\omega) \rho_{L,L'}(E) M_{L'i}(\omega), \tag{14.7}$$

where $M_{iL}(\omega) = \langle R_L|\epsilon \cdot \hat{r}|i\rangle$, are dipole matrix elements, $\rho_{L,L'}(E) = (-1/\pi)\mathrm{Im}\, G_{L,L'}(E)$ are elements of the density matrix, and $E = \omega + E_i - E_F$ is the photoelectron energy (typically varying from about 10–1000 eV).

14.2.4 Multiple-scattering theory

To apply multiple-scattering theory [3] to EXAFS, it is necessary to separate the scattering potential into terms from individual sites i. Thus we define the final state potential as $V' = \Sigma_i v_i(\mathbf{r} - \mathbf{R_i})$. For high energy scattering a spherically symmetric muffin-tin model suffices. The scattering potentials v_i are implicitly contained in the scattering t-matrices which sum intra-atomic scattering at a given site to all orders. These are defined by the equation $t = v + vGt$ at each site, and can be represented in terms of partial wave phase shifts $t_l = \exp(i\delta_l)\sin(\delta_l)$. For XAS the usual procedure [8, 9] is to select out one site c as the absorber, so we can write $V' = v'_c + V^{sc}$ where V^{sc} is the scattering potential from all other scatterers. Then the Green's function propagator $G_{L,L'} = G^c_{L,L'} + G^{sc}_{L,L'}$ naturally separates into intra-atomic contributions from the central atom and from MS. Consequently XAS $\mu(E)$ can be separated into atomic and scattering parts as

$$\mu = \mu_0(1 + \chi). \tag{14.8}$$

Note that the behavior of μ depends both on an (embedded) atomic background μ_0 from the potential v'_c and on the MS or fine structure signal χ due to scattering from the environment, i.e., the scattering potentials in V^{sc}. This result is consistent with the experimental definition of XAFS

$$\chi = \frac{\mu - \mu_0}{\Delta\mu_0}, \tag{14.9}$$

where $\Delta\mu_0$ is the jump in the smooth atomic-like background at a given edge.

The matrix $G_{L,L'}(E)$ can be re-expressed formally as a sum over all MS paths that a photoelectron can take away from the absorbing atom and back [8]. For XANES, the MS expansion is often carried to all orders (full MS) by matrix inversion [11, 12],

$$G^{sc} = e^{i\delta}[\mathbf{1} - G^0T]^{-1}G^0e^{i\delta'}. \tag{14.10}$$

This approach is equivalent to *exact* treatments. e.g., the KKR band structure method [9]. However, as no symmetry is required it is particularly advantageous for calculations of complex, aperiodic systems.

For EXAFS, the expansion of the inverse matrix in a geometric series gives rise to a MS *path expansion* (discussed further below),

$$G^{sc} = e^{i\delta'}[G^0TG^0 + G^0TG^0TG^0 + \cdots]e^{i\delta}. \tag{14.11}$$

where matrix indices have been suppressed for simplicity. Here $T = t_{L,R}\delta_{L,L'}\delta R, R'$ is diagonal in a site-angular momentum basis, and only site-off diagonal elements of the free-electron propagator $G^0_{LR,L'R'}$ are included.

14.2.5 Scattering potentials

Calculations of the MS expansion require accurate potentials and phase shifts at each scattering site up to large angular momenta $l_{max} \sim kR/2$, where k is the electron wave number

$k \sim (2E)^{1/2}$ and R a near neighbor distance [7]. Thus l_{max} is typically about 25 for EXAFS energies $E \sim 1000$ eV. The calculation of scattering potentials simplifies for electrons of moderate energy since scattering depends largely on the density in the core of an atom, where spherical symmetry is a good approximation. Then the Coulomb part of these potentials are well described by an overlapped atomic charge density and the muffin-tin approximation (i.e., the Mattheiss prescription) [13], while the exchange term can be well approximated by a local self energy (see below). These approximations must be improved for XANES where chemical effects and charge transfer are important, in which case self-consistent (SCF) calculations are necessary. The SCF approach implemented in FEFF8 also yields an accurate estimate of the Fermi energy E_F. Muffin-tin corrections may also be important in XANES, especially in highly anisotropic systems, and hence the development of self-consistent, full-potential approaches remains an important challenge.

14.2.6 Self energy and mean free path

Since the self-energy operator $\Sigma(E)$ depends on both photoelectron energy E and position, and is generally non-local, an efficient algorithm for its calculation is essential [14]. FEFF and many other XAFS codes often use the GW electron gas self-energy of Hedin and Lundqvist [14] for such calculations, which is based on a local density approximation. However, this self-energy tends to overestimate losses at low energies. Alternatively the real Dirac-Hara exchange approximation is sometimes better. However, as these approximations are based on electron-gas theory, they can be inaccurate for XANES. One of the current challenges is to develop more realistic approximations.

From the complex valued self energy one can then obtain the effective electron mean free path [15]. For example, the XAFS mean free path is $\lambda_k \approx k/(|\mathrm{Im}\,\Sigma| + \Gamma/2)$, where Γ is the inverse core-hole lifetime. This mean free path differs from that in LEED, since it depends on the core-hole lifetime. The self-energy is essentially a dynamically screened exchange interaction, which is the analog of the exchange-correlation potential V_{xc} of ground state density functional theory. Since the self energy varies by about 10 eV over EXAFS energies, the variation leads to systematic shifts in energy of XAS peaks from their ground state positions. Indeed this shift can be represented at low energies by an approximately linear scaling with energy, i.e., $E_{\mathrm{exp}} = E_{\mathrm{th}}(1 + \alpha)$, where α is typically about 0.05 [16]. Although this effect is often ignored in phenomenological XAFS theories (e.g., theories only containing a mean-free path or an imaginary optical potential), it could have been anticipated, since the presence of a mean-free-path implies the existence of a real energy shift due to the dispersion relations satisfied by the self-energy operator.

14.3 Applications to X-ray spectroscopies

14.3.1 EXAFS

Curved-wave multiple scattering theory

One of the most successful theoretical developments in XAS is the theory of EXAFS. As discussed above the XAFS is given by the scattering part of the electron propagator. For

example the XAFS from a K shell can be written as $\chi(E) = -\mathrm{Im}\,\mathrm{Tr}_m\, G^{sc}$, i.e., as the trace of a matrix product

$$\chi(E) = -\mathrm{Im}\,\mathrm{Tr}_\mathrm{m}\, e^{i\delta_1'}[G^0TG^0 + G^0TG^0TG^0 + \cdots]_{1m,1m}e^{i\delta_1}, \tag{14.12}$$

where matrix indices have been suppressed for simplicity. For example, the single scattering terms come from the term $G^0TG^0_{1m,1m} = \Sigma_{LR}G^0_{1m,LR}t_{LR}G^0_{LR,1m}$. Because of curved wave effects, requiring increasingly higher angular momentum states with increasing energy, the matrices in the above have very large dimensions of order $l^2_{max}N$, where N is the number of sites. Thus exact MS calculations are extremely time-consuming and at high energies can only be carried out for low-order MS paths [17]. The same *angular momentum catastrophe* at high energies limits exact MS approaches and band structure techniques to energies below about 100 eV. Early treatments of XAFS used the plane wave approximation (PWA) to simplify this expression, however this led to unacceptable errors in the theory. However, Rehr *et al.* [18] showed how the dominant single scattering terms (G^0TG^0) could be recast in a form analogous to the PWA, but with an effective, curved wave scattering amplitude f_eff. Curved wave effects lead to phase shifts of order $\ell(\ell+1)/kR$ in each partial wave. Since f_eff has an expansion in partial waves analogous to the scattering amplitude in the PWA, it differs significantly from the plane wave back-scattering amplitude at all energies. This explains why the PWA is always a poor approximation even at the highest photoelectron energies observed in experiment (~ 1500 eV).

Although the single-scattering terms often dominate the EXAFS, multiple-scattering contributions are generally crucial beyond the nearest neighbor. Such MS contributions proliferate exponentially and are also harder to calculate, involving many more high order matrix multiplications. Thus one of the most important advances in XAS theory was the development of efficient approximations to treat curved wave effects both in single-scattering and multiple-scattering. Some of the first such approaches were developed by Barton and Shirley [19] for XPD. In an effort to improve on their approach, an efficient *scattering matrix formalism* was derived, based on a separable representation of the free propagator $G(E)$ [7]. This *Rehr-Albers* approach turned out to overcome all the computational difficulties of the MS expansion, namely the large angular-momentum basis, and the proliferation of MS paths. The approach also simplified the incorporation of correlated MS Debye-Waller factors in the theory to treat vibrations and disorder. The first difficulty was overcome in two steps. First, by using rotation matrices, successive bonds in a path are rotated to the z-axis, thus reducing the problem to a calculation of *z-axis propagators* [7]. Propagators along the z-axis have greatly simplified mathematical properties. Although the terminology "z-axis propagator" is recent, these quantities have a long history and have been rediscovered several times [20, 21]. However it has also been found that it is both stable and accurate to use the recursive calculations of the RA separable representation. A detailed discussion of the convergence of the RA approach has also been carried out [22]. The second step of the RA method is an exact, separable representation of the z-axis propagators. Together these steps yield the exact representation

$$G^0_{L\mathbf{R},L'\mathbf{R}'} = \frac{e^{ikR''}}{kR''}\Sigma_\lambda Y_{L,\lambda}\tilde{Y}_{\lambda,L'}, \tag{14.13}$$

where $\mathbf{R}'' = \mathbf{R}' - \mathbf{R}$. The coefficients Y and $\tilde{Y}$ depend on bond angles and converge rapidly in powers of $1/kR$, so the representation can be severely truncated. The approach

becomes exact at low energies or for single scattering, and typically $\lambda \sim 6$ suffices to within experimental precision over the full range of wave numbers in EXAFS experiment. The advantage of a separable representation is that it permits one to combine and then sum all the factors involving the angular momenta L at a given site into a low order scattering matrix $F_{\lambda',\lambda} = \sum_L \tilde{Y}_{\lambda',L} t_L Y_{L,\lambda}$. This matrix is the analog of the plane wave scattering amplitude and yields an accurate curved-wave XAFS formula analogous to the PWA, but with the usual scattering amplitudes $f(\theta)$ replaced by low-order (6×6) matrices. With such separable propagators, the MS expansion can then be calculated efficiently as a sum over MS paths. For EXAFS, for example, one then obtains the path expansion,

$$\chi(k) = S_0^2 \sum_{\text{paths}} \frac{|f_{\text{eff}}(k)|}{kR^2} \sin(2kR + \Phi_k) e^{-2R/\lambda_k} e^{-2\sigma^2 k^2}, \tag{14.14}$$

where $k = [2(E - E_0)]^{1/2}$ is the wavenumber measured from threshold E_0, λ_k is the XAFS mean-free path, and σ is the rms fluctuation in the effective path length $R = R_{\text{path}}/2$. This expression has the same form as the famous XAFS equation of Sayers, Stern and Lytle [23]. However, all quantities in Eq. (14.14) are redefined to include curved wave and many-body effects. For example, instead of the plane wave back-scattering amplitude, $f_{\text{eff}}(k)$ is the effective curved-wave scattering amplitude (from which the FEFF codes are named), and S_0^2 is a many-body amplitude reduction factor due to intrinsic losses, which was not in the original formula. Because of the path dependent phase shift Φ_k, theoretical calculations are essential to analyze experimental XAFS data beyond the nearest neighbors, due to the difficulty of obtaining suitable experimental MS EXAFS standards. With the RA approach, f_{eff} can be calculated efficiently and accurately as a product of low-order (typically 6×6) matrices for all XAFS energies, thus making high-order path expansions practicable. For XANES, however, exact propagators may be needed, but it turns out that the RA approach in Eq. (14.13) still provides a stable and efficient algorithm [24] for the propagator G^0, which is implemented in the FEFF codes for XANES calculations. At low energies only small angular momenta are involved, so the matrix dimensions are still relatively small.

The introduction of an automated path enumeration scheme and *path filters* which restrict the number of MS paths in the expansion [25] was another important development in EXAFS theory. It was also key to efficient EXAFS analysis techniques, permitting fits to the spectra in terms of a relatively small number of physical parameters, such as interatomic distances R. At high energies it turns out that the vast majority of MS paths are numerically insignificant, and the most important MS paths in EXAFS tend to be either linear and triangular. Although the PWA is inadequate for precise calculations, it can give quick estimates of path amplitudes for filtering purposes. With path filters only of order 10^2 distinguishable MS paths need to be calculated to yield XAFS to within experimental accuracy of a few percent. For the near edge, more paths (typically more than 10^3) are generally needed, but quite often, such a high order MS treatment suffices to describe most XANES features, sometimes including *white lines* and pre-edge structure [2, 26].

Thermal and configurational disorder

The effects of disorder are of crucial importance in XAFS, as the approximation of a static structure yields large overestimates of XAFS amplitudes at high energies. Indeed, it has been known since the earliest investigations that EXAFS *melts* with increasing temperature. This behavior turns out to be sensitive only to coarse details of the pair distribution function through a Debye-Waller-like factor. However, unlike the Debye-Waller factors in X-ray diffraction, those for EXAFS refer to correlated near-neighbor distance fluctuations. Thus a key theoretical development in in the theory was the use of the cumulant expansion of the Debye-Waller factor, $\exp[-W(k,T)] = \exp[-(2ik)^n \sigma^{(n)}(T)/n!]$. This expansion yields an efficient parameterization of such thermal and configurational disorder [6, 27] in terms of a few moments or cumulants $\sigma^{(n)}$ of the correlated vibrational distribution function. The most important (harmonic) term is the mean square variation in bond length, which leads to a gaussian Debye-Waller factor $\exp(-2\sigma^2 k^2)$ for each MS path. The thermal contributions to this factor can often be calculated in terms of a correlated Debye model [28]. The anharmonic corrections include the first cumulant $\sigma^{(1)}$, which is the thermal expansion, and the third cumulant $\sigma^{(3)}$, which characterizes the skew of the pair distribution function. Relations between the cumulants have been derived [29] which show that $\sigma^{(1)} \propto \sigma^2(T)$ and $\sigma^{(3)}$ is also related to $\sigma^2(T)$. If the third cumulant is neglected in the analysis, bond distances obtained from EXAFS appear too short. Additional cumulants are usually negligible. Improved treatments of XAFS Debye Waller factors have been developed that go beyond the Debye approximation [30] now permit fits of Debye-Waller factors to local spring constants. Another approach is to parameterize the N-particle distribution as in the GNXAS code [31]. Molecular-dynamics approaches are promising [32] as a less phenomenological approach, but accurate *ab initio* treatments require computationally intensive, total energy calculations and remain a challenge for the future. Another challenge is the need for better algorithms for treating disorder in full MS XANES calculations.

14.3.2 XANES

With the representation of the Green's function in Eq. (14.2) the XAS becomes

$$\mu(\omega) = \frac{4\pi e^2 \omega}{c} \sum_{i,LL'} M_{iL}(\omega) \rho_{L,L'}(E) M_{L'i}(\omega) = \mu_0(1+\chi). \tag{14.15}$$

Thus the calculations of XANES depend on both the fine structure χ and the dipole matrix elements $M_{iL}(\omega) = \langle R_L | \epsilon \cdot \hat{r} | i \rangle$ where $L = (\kappa, m)$ denotes a relativistic angular momentum basis. The density matrix elements $\rho_{L,L'}(E) = (-1/\pi)\mathrm{Im}\, G_{L,L'}(E)$ generally requires the inversion of a large matrix, Eq. (14.10) when the path expansion in Eq. (14.11) converges poorly.

Since the computational effort needed for matrix inversion in full MS calculations scales in time as the cube of system size, XANES calculations are usually much more time-consuming than EXAFS. Indeed, the matrix inversion approach becomes computationally intractable in the EXAFS regime or for cases (e.g., low Z atoms) where the mean free path is very long [12]. Thus one of the big challenges in XANES theory is to increase the computational speed.

Promising methods include the recursion method [33] repartitioning [34] and iterative approaches [35], which can provide substantial improvements on the conventional LU decomposition. However, much more dramatic reductions are obtained from parallel computational algorithms, which scale as $A + B/N$, where N is the number of processors, and hence can provide one–two orders of magnitude further improvement [36]. Parallelization has been implemented in FEFF8 with the MPI (message-passing-interface) protocol [37]. As a result XANES calculations even for very large systems of order 10^3 atoms can now be carried out in about one wall-clock hour on parallel computers with 32 processors.

14.3.3 Atomic-XAFS

As noted above [see Eq. (14.8)] the behavior of the XANES depends both on the fine structure χ and on the absorption μ_0 from the embedded atom at the absorption site with the scattering potential v_c. Although the behavior of atomic cross-sections are assumed to be structureless, there is now both theoretical and experimental evidence for weak oscillatory structure in μ_0 of atoms in condensed matter [38]. The origin of this atomic-XAFS or AXAFS [38, 39] is the scattering of a photoelectron at the periphery of an *embedded atom* due to intra-atomic charge contributed from neighboring atoms. This effect is important for the analysis of EXAFS, since if not removed by background subtraction, it would show up as a peak in the EXAFS Fourier transform at about 1/2 the near neighbor distance [40]. AXAFS may also be important for the interpretation of XANES since it is sensitive to the potential in the bonding region [41].

14.3.4 Photoelectron diffraction

The separable curved-wave multiple-scattering formalism of RA is also applicable to many other spectroscopies that depend on the final state of the photoelectron. For example, for XPD, the intensity at the detector is given by the RA expression [7]

$$\left(\frac{d\sigma}{d\Omega}\right) \propto \left|\sum_{L,N} G^{(N-1)}_{00,L} M_L(\hat{\epsilon}) e^{i\delta_l}\right|^2, \tag{14.16}$$

where the Green's function $G(E)$ propagates an electron from the origin to the detector at a large distance with N scatterings, $M_L(\hat{\epsilon}) = \langle R_L|\hat{\epsilon}\cdot\mathbf{r}|c\rangle$ is the dipole matrix element, and the sum is over all N-leg MS paths $\Gamma = [\mathbf{R}_\infty = \mathbf{R}_N, \mathbf{R}_{N-1}\ldots\mathbf{0}]$, $N = 1, 2, \ldots$, where $\mathbf{R}_\infty = \hat{k}R_\infty$ is the vector to the detector. For example, for the most important direct $(N = 1)$ and single-scattering $(N = 2)$ terms, the RA separable representation yields

$$\left(\frac{d\sigma}{d\Omega}\right) \propto \left|\sum_{L} m_{L,c}(\hat{\epsilon}) e^{i\delta^c_l}\left(Y_L(\hat{k}) + \frac{e^{ikR(1-\cos\theta)}}{R}\sum_{\lambda} F_{00,\lambda} M^{L,00}_{\lambda,00}\right)\right|^2. \tag{14.17}$$

where F is the RA scattering matrix in Eq. (14.13). This sum can be interpreted as an effective curved-wave single-scattering amplitude for XPD. These RSMS techniques have also been developed further for photoelectron diffraction (PD) [42]. Recently efficient Lanczos techniques have also been developed for summing additional terms in the MS series [43].

14.3.5 Other spectroscopies

Because the underlying physics is analogous, a similar RSMS approach can be applied to many other spectroscopies. Examples include electron energy loss spectra (EELS) [44], diffraction anomalous fine structure (DAFS) [45] and more recently for the the X-ray elastic scattering amplitude [46]. In this latter approach, both real and imaginary parts of the anomalous X-ray scattering amplitude are calculated simultaneously in the complex energy plane, without the necessity of a Kramers-Kronig transform. The presence of XAFS gives rise to very significant solid-state contributions in the anomalous scattering amplitudes, which have been ignored in standard tables [47]. This approach also includes dipole-quadrupole and quadrupole couplings and thus also allows calculations of X-ray natural circular dichroism (XNCD) and the X-ray anomalous cross scattering amplitude (XACS) $F_{\pi\sigma}$, which are both due entirely to solid state effects [48]. Similarly calculations of X-ray magnetic circular dichroism (XMCD) have be carried out with RSMS [49]. Calculations of XMCD for the K-shell emphasize the importance of spin-orbit relativistic effects in the final state.

14.4 Many-body effects

14.4.1 Inelastic losses

The standard one-electron model outlined above is essentially a quasiparticle treatment, with many-body effects incorporated into the photoelectron self-energy $\Sigma(E)$. However, it has long been known that this approximation is incomplete for XAS, since it ignores losses due to excitations like plasmons and shake-off excitations which lead to satellites in the spectra [50]. The photoelectron-core hole interaction also influences these contributions. In this Section we will briefly address the effects of these inelastic losses beyond the quasi-particle approximation. It is traditional to differentiate two types of inelastic losses in the photoabsorption, namely, *intrinsic* and *extrinsic* processes.

14.4.2 Extrinsic losses

Extrinsic effects refer to losses in propagation of the photoelectron and include excitations such as plasmons, electron-hole pairs, and inelastic scattering in which the photoelectron loses energy. As we have stressed, the inclusion of damping due to extrinsic losses is a key ingredient in modern short-range-order theory of XAFS. These losses give the final photoelectron state a finite lifetime and hence a decay of the final state, which has been accounted for phenomenologically by an energy dependent mean-free-path $\lambda(k)$ and hence a path-dependent decay factor $\exp(-2R/\lambda(k))$ of EXAFS amplitudes. As noted above, the extrinsic losses are more precisely described in terms of a complex, energy-dependent self-energy $\Sigma(E)$, which gives both a real energy shift and decay from the imaginary part.

14.4.3 Intrinsic losses

Intrinsic losses, on the other hand, refer to excitations in response to creation of the core hole. These losses are traditionally accounted for phenomenologically by a constant many-body

amplitude-reduction factor S_0^2. However, more precisely, the amplitude reduction is energy dependent and gives rise to a complex, path-dependent reduction factor. Although the theory of XAFS is often couched in one-electron language, where a single electron makes a transition from a core orbital to an excited state, the process is truly many body, as other electrons are generally excited as well. Examples of intrinsic processes are the well known shake-up and shake-off excitations in atoms. This secondary emission results from a relaxation of the $N-1$ electron Fermi sea in response to the creation of a core hole. Because both extrinsic and intrinsic processes involve the same final states, their quantum-mechanical amplitudes can in principle interfere, and hence one cannot simply add their transition rates. A treatment of such intrinsic effects in EXAFS was given by Rehr *et al.* [50]. This treatment ignores interference effects that can be important near the edge (as discussed below), but it appears to be adequate for most current EXAFS calculations.

To understand the origin of intrinsic losses, consider the full many-body expression for X-ray absorption spectrum in Eq. (14.1). In the Hartree-Fock approximation, for example, the initial and final states are Slater determinants of one-particle states, calculated with *different* self-consistent one-electron potentials, i.e., the ΔSCF approximation. The potential for the initial state is that of the ground state, while that for the final states include a core hole and a photoelectron. The calculations can be simplified if one assumes that the final state can be factored, i.e., $|\Psi_f\rangle = |{\Phi'_0}^{N-1}\rangle|\phi_f\rangle$, which is a reasonable approximation at high energies, when the *sudden approximation* is valid. Then the dominant contribution to the many-body dipole matrix element is given by

$$M_{fi} \cong \langle\phi'_f|\hat{\epsilon}\cdot\mathbf{r}|\phi_c\rangle\langle{\Phi'}_0^{N-1}|\Phi_0^{N-1}\rangle, \tag{14.18}$$

where the prime refers to states calculated in the presence of the core hole. Thus, the absorption in the lowest energy or *primary channel* is reduced in magnitude from the one-particle expression by a many-body overlap integral,

$$S_0^2 = \left|\left\langle {\Phi'}_0^{N-1} \;\middle|\; \Phi_0^{N-1}\right\rangle\right|^2. \tag{14.19}$$

In this approximation, the one-electron matrix element for the primary channel is consistent with the *final-state rule*, i.e., that the core orbital should be calculated with the initial ground-state Hamiltonian and the final state with a fully relaxed core hole [5].

However, one must also take into account the contributions from the excited states. Indeed, since $S_0^2 \neq 1$, there must be contributions from multi-electron transitions in which the $(N-1)$-electron *ion* is left in an excited state $|{\Phi'}_n^{N-1}\rangle$ with excitation energy E_n. The net absorption is then given by a sum over excited states or *channels* n,

$$\mu = \sum_n \mu_n = \sum_n \left|\left\langle \phi'_n \;\middle|\; \hat{\epsilon}\cdot\mathbf{r} \;\middle|\; \phi_c\right\rangle\right|^2 S_n^2, \tag{14.20}$$

where the many-body overlap integral $S_n = \langle{\Phi'}_n^{N-1}|\Phi_0^{N-1}\rangle$. Also, the energy of the photoelectron is reduced in accordance with energy conservation by the excitation energy E_n. The quantity S_n is usually small (for $n \neq 0$) and would vanish by orthogonality in the absence of

relaxation. Thus, the total absorption from all channels can be written as a convolution of the one-particle spectrum by a spectral function,

$$\mu(\omega) = \int_0^{\omega} d\omega' \mu^{(1)}(\omega - \omega') A(\omega'), \tag{14.21}$$

which is equivalent to a *broadened one-particle calculation*. Here $\mu^{(1)}$ is the one-electron spectrum and $A(\omega) = \sum_n S_n^2 \delta(\omega - E_n)$ is the intrinsic excitation spectrum.

14.4.4 Interference between extrinsic and intrinsic losses

Since the excitations of a system are indistinguishable, quantum *interference* between extrinsic and intrinsic losses is also possible. For photoemission spectroscopy, for example, it has been shown [51] that interference is strong near excitation thresholds, where the losses strongly cancel due to the opposite signs of the coupling between the photoelectron and the core-hole to excited states. A related treatment for XAFS has recently been developed by Campbell et al. [52] based on an extension of work by Hedin and Bardyszewski [51]. This theory is based on a quasi-boson (oscillator) model Hamiltonian, which includes couplings between photoelectron and valence electrons V_{pv}, photoelectron and core electrons V_{pc}, and valence electrons and core V_{vc} and only terms to second order in the coupling functions V^n are retained. The results can be formulated in terms of an effective one-particle propagator which includes both inelastic losses and interference effects. This approach is essentially a generalization of the GW approximation. However it is more general and also partly accounts for edge-singularity effects and corrections to the final state rule. More importantly the approach can provide semi-quantitative estimates of the XAFS amplitude reduction factor $S_0^2(\omega)$ within an electron gas model, which are in reasonable agreement with experiment. As in photoemission, there is appreciable cancellation of extrinsic and intrinsic losses by the interference terms near threshold, while the strength of the primary channel increases. Thus the theory explains the surprising weakness of multi-electron excitations in the observed XAS [52]. At sufficiently high energies both the extrinsic and the interference contributions become negligible, and the theory crosses over to the sudden-approximation limit [50]. The limiting cases of the theory are as follows: first, when the core-hole potential is neglected, one obtains an initial state one-electron theory with an additional complex, energy dependent one-electron potential $\Sigma(\omega)$, i.e., with only extrinsic losses; second, if there is no extrinsic scattering the interference terms vanish and the sudden-approximation limit is recovered. This theory also leads to an expression for the effects of inelastic losses in XAS as a convolution of the one-electron spectrum $\mu^{(1)}$ similar to Eq. (14.21) but with an energy dependent, asymmetric spectral function $A(\omega, \omega')$ and a slightly modified one-electron XAS, i.e.

$$\mu(\omega) = \int d\omega' \, A(\omega, \omega') \mu^{(1)}(\omega - \omega'). \tag{14.22}$$

where the single-particle XAS is given by

$$\mu^{(1)}(\omega) = \sum_{k' > k_F} \left| \langle k' \mid Pd \mid b \rangle \right|^2 \delta(\omega - \epsilon_k). \tag{14.23}$$

An important difference between $\mu^{(1)}$ and the usual one-electron XAS is the presence of the projection operator P in the dipole matrix element, which gives rise to edge singularity effects. Above the edge $P \approx 1$ and the *standard* one-electron expression for $\mu^{(1)}$ is obtained. Thus this theory provides a justification for the *standard model* of XAS, apart from many-body broadening effects implicit in the spectral function.

14.4.5 EXAFS amplitude reduction factor S_0^2

It is interesting to examine the effect of the losses and interference on the XAFS spectrum using the convolution in Eq. (14.22). Each term in the MS path expansion for χ contributes a rapidly oscillating energy dependent factor proportional to $\chi_R \sim f_{\rm eff} \sin(2kR + \Phi)$. The net effect of the convolution over a normalized, positive spectral amplitude $\tilde{A}_{\rm eff}(\omega, \omega')$ is clearly a decreased XAFS amplitude and a phase shifted oscillatory signal compared to the one-particle XAFS $\chi^{(1)}$. In particular, the effect on each multiple scattering path of effective length $2R$ can be expressed as a "phasor sum" over the effective normalized spectral function,

$$S_0^2(\omega, R) = \int_0^\omega d\omega' \tilde{A}_{\rm eff}(\omega, \omega') e^{i2[k(\omega-\omega')-k(\omega)]R}. \tag{14.24}$$

This result is similar in form to that derived and discussed earlier by Rehr *et al.* [50]. However, the effects of interference play a crucial role in the results, since the observed S_0^2 is closer to unity than in the intrinsic only model. Qualitatively the variation of S_0^2 can be understood as follows: At very low energies compared with the excitation energy the excitation terms strongly cancel so $A(\omega, \omega') \approx \delta(\omega - \omega')$ and hence, $S_0^2(\omega, R) \to 1$. At high energies the phase shift due to the excitation energy becomes negligible, and hence again $S_0^2(\omega, R) \to 1$. At intermediate energies, however, the value of $S_0^2(\omega, R)$ has a minimum.

14.4.6 Local field effects

The above theory implicitly assumes that the vector potential $\mathbf{A}$ is that of the external X-ray field. However, in general this external field will be screened by the dielectric response of the material. This screening effect is usually small for very deep levels, but becomes increasingly important for shallow levels. For example, it has been shown that such screening effects are partly responsible for the anomalous L_3/L_2 transition intensity *branching ratio* in transition metals, which differ markedly from the 2:1 value of one-electron theories. A useful approach for calculating this screening is the time-dependent local density approximation (TDLDA) [53]. As shown by Zangwill and Soven, the XAS including local field effects can be calculated with a straightforward modification of the usual expression for the XAS of Eq. (14.7), i.e.,

$$\mu(\omega) = \frac{4\pi e^2 \omega}{c} \sum_{v,LL'} \tilde{M}_{vL}(\omega) \rho_{L,L'}(E) \tilde{M}_{vL'}(\omega), \tag{14.25}$$

where $E = \omega + E_v - E_F$ is the photoelectron energy and $\tilde{M}_{vL}(\omega) = \langle R_L | \phi | v \rangle$ are renormalized dipole matrix elements. Here ϕ denotes the screened dipole interaction $\phi = \epsilon^{-1}(\omega)[\epsilon \cdot \mathbf{r}]$ where $\epsilon(\omega)$ is the non-local dielectric matrix in the system [53]. Thus the TDLDA approach can be straightforwardly incorporated the RSMS formalism used in FEFF8 with suitably modified dipole matrix elements.

14.5 Conclusions

RSMS theory make possible a general treatment of XAS, encompassing both XAFS and XANES as well as a number of other X-ray spectroscopies. The current state of XAFS is now highly quantitative and is widely used for theoretical simulations and experimental analysis. Significant progress has also been made in XANES theory. In particular a standard one electron model for XAS based on RSMS and a screened core hole is generally satisfactory for XAS spectra, except near the edge. Many-body corrections can be incorporated in terms of a convolution over an excitation spectral function. Improved treatments of the scattering potential going beyond the muffin-tin approximation and better many-body treatments which includes more accurate calculations of core-hole and excitation processes are still desirable; however, efforts along these lines are currently in progress.

Acknowledgements

We gratefully acknowledge the contributions to this work from our co-workers, students, and collaborators, especially K. Baberschke, G. Brown, L. Campbell, F. Farges, T. Fujikawa, L. Hedin, J. Mustre de Leon, C.R. Natoli, A. Nesvizhskii, M. Newville, B. Ravel, D. Sayers, E. Shirley, E.A. Stern, and J.W. Wilkins. This work was supported in part by the U.S. Department of Energy grant DE-FG06-97ER45623/A000 (JJR) and was facilitated by the DOE Computational Materials Science Network.

References

[1] J.J. Rehr and R.C. Albers, Rev. Mod. Phys. **72**, 721 (2000).
[2] A.L. Ankudinov, B. Ravel, J.J. Rehr, and S. Conradson, Phys. Rev. B **58** (1998) 7565; see also the FEFF URL http://leonardo.phys.washington.edu/feff/
[3] J.L. Beeby, Proc. Roy. Soc. A **279**, 82 (1964).
[4] J.E. Müller, O. Jepsen, and J.W. Wilkins, Solid State Comm. **42**, 365 (1982).
[5] U. von Barth, and G. Grossmann, Phys. Rev. B **25**, 5150 (1982).
[6] E.D. Crozier, J.J. Rehr, and R. Ingalls, *X-Ray Absorption: Principles, Applications, Techniques of EXAFS, SEXAFS, and XANES*, edited by D.C. Koningsberger, & R. Prins (Wiley, New York) 375 (1988).
[7] J.J. Rehr and R.C. Albers, Phys. Rev. B **41**, 8139 (1990).
[8] P.A. Lee, and J.B. Pendry, Phys. Rev. B **11**, 2795 (1975).
[9] W.L. Schaich Phys. Rev. B **8**, 4028 (1973).
[10] H. Ebert, Rep. Prog. Phys. **59**, 1665 (1996).
[11] C.R. Natoli, D.K. Misemer, S. Doniach, and F.W. Kutzler, Phys. Rev. A **22**, 1104 (1980).
[12] P.J. Durham, J.B. Pendry, and C.H. Hodges, Comp. Phys. Commun. **25**, 193 (1982).
[13] L.F. Mattheiss, Phys. Rev. **133 A**, 1399 (1964).
[14] B.I. Lundqvist, Phys. Kondens. Mater. **6**, 206 (1977).
[15] M.P. Seah, and W.A. Dench, Surf. Interf. Anal. **1**, 2 (1979).
[16] G. Materlik, J.E. Müller, and J.W. Wilkins, Phys. Rev. Lett. **50**, 267 (1983).

[17] S.J. Gurman, N. Binsted, and I. Ross, J. Phys. C **19**, 1845 (1986).
[18] J.J. Rehr, R.C. Albers, C.R. Natoli, and E.A. Stern, Phys. Rev. B **34**, 4350 (1986).
[19] J.J. Barton and D.A. Shirley, Phys Rev. B **32**, 1906 (1985).
[20] R. Nozawa J. Math. Phys. **7**, 1841 (1966).
[21] V. Fritzsche J. Electron Spectros. Relat. Phenomena **58**, 299 (1992).
[22] Y. Chen, F.J. García de Abajo, A. Chassé, R.X. Ynzunza, A.P. Kaduwela, M.A. Van Hove, and C.S. Fadley, Phys. Rev. B **58**, 13121 (1998).
[23] D.E. Sayers, E.A. Stern, and F.W. Lytle, Phys. Rev. Lett. **27**, 1204 (1971).
[24] F. Manar, and Ch. Brouder, Physica B **208&209**, 79 (1995).
[25] S.I. Zabinsky, J.J. Rehr, A.L. Ankudinov, R.C. Albers, and M.J. Eller, Phys. Rev. B **52**, 2995 (1995).
[26] F. Farges, G.E. Brown, Jr., and J.J. Rehr, Phys. Rev. B **56**, 1809 (1997).
[27] G. Dalba, and P. Fornasini, J. Synchrotron Rad. **4**, 243 (1997).
[28] G. Beni, and P.M. Platzman, Phys. Rev. B **14**, 9514 (1976).
[29] A.I. Frenkel, and J.J. Rehr, Phys. Rev. B **48**, 585 (1993).
[30] A.V. Poiarkova and J.J. Rehr, Phys. Rev. B **59**, 948 (1998).
[31] A. Filipponi, and A. Di Cicco, Phys. Rev. B **52**, 15122 (1995).
[32] M.I. McCarthy, G.I. Schenter, M.R. Chacon-Taylor, J.J. Rehr, and G.E. Brown, Jr. Phys Rev B **56**, 9925 (1997).
[33] A. Filipponi, J. Phys.: Condens Matter **3**, 6489 (1991).
[34] T. Fujikawa, J. Phys. Soc. Japan **62**, 2155 (1993); T. Fujikawa, K. Nakamura, S. Nagamatsu and J.J. Rehr, J. Phys. Soc. Jpn. **71**, 357 (2002).
[35] H. Wu and S.Y. Tong, Phys. Rev. B **57**, 1659 (1999).
[36] A.L. Ankudinov, C. Bouldin, J.J. Rehr, J. Sims, and H. Hung., Phys. Rev. B **65**, 104107 (2001).
[37] W. Gropp, E. Lusk, and A. Skjellum, *Using MPI: Portable Parallel Programming With The Message-Passing Interface* (MIT Press, Cambridge, Mass.) (1994).
[38] J.J. Rehr, C.H. Booth, F. Bridges, and S.I. Zabinsky, Phys. Rev. B **49**, 12347 (1994).
[39] B.W. Holland, J.B. Pendry, R.F. Pettifer, and J. Bordas, J. Phys. C **11**, 633 (1978).
[40] H. Wende, P. Srivastava, R. Chauvistre, F. May, K. Baberschke, D. Arvanitis, and J.J. Rehr, J. Phys. Condens. Matter **9**, L427 (1997).
[41] D. Koningsberger, B. Mojet, J. Miller and D. Ramaker, J. Synchrotron Rad. **6**, 135 (1999).
[42] M. Sagurton, E.L. Bullock, R. Saiki, A. Kaduwela, C.R. Brundle, C.S. Fadley, and J.J. Rehr, Phys. Rev. B **33**, 2207 (1986); C.S. Fadley, M.A. Van Hove, Z. Hussain, A.P. Kaduwela, R.E. Couch, Y.J. Kim, P.M. Len, I.J. Palomares, S. Ryce, S. Ruebush, E.D. Tober, Z. Wang, R.X. Ynzunza, H. Daimon, H. Galloway, M.B. Salmeron and W. Schattke, Surface Review and Letters **4**, 421 (1997).
[43] F.J. García de Abajo, M.A. Van Hove, and C.S. Fadley, Phys. Rev. B **63**, 075404 (2001).
[44] T. Sikora, G. Hug, M. Jaouen, and J.J. Rehr, Phys. Rev. B **62**, 1723 (2000).
[45] J.O. Cross, M.I. Bell, M. Newville, J.J. Rehr, L.B. Sorensen, C.E. Bouldin, G. Watson, T. Gouder, and G.H. Lander, Phys. Rev. B **58**, 11215 (1998).

[46] A.L. Ankudinov, and J.J. Rehr, Phys. Rev. B **62**, 2437 (2000).
[47] D.T. Cromer, and D. Liberman, J. Chem. Phys. **53**, 1891 (1970).
[48] C.R. Natoli, Ch. Brouder, P. Sainctavit, J. Goulon, C.H. Goulon-Ginet and A. Rogalev, Eur. Phys. J. B **4**, 1 (1998).
[49] A.L. Ankudinov and J.J. Rehr, Phys. Rev. B**52**, 10214 (1995).
[50] J.J. Rehr, E.A. Stern, R.L. Martin, and E.R. Davidson, Phys. Rev. B **17**, 560 (1978).
[51] W. Bardyszewski, and L. Hedin, Phys. Scripta **32**, 439 (1985).
[52] L. Campbell, L. Hedin, J.J. Rehr, and W. Bardyszewski, Phys. Rev. B **65**, 064107 (2002).
[53] A. Zangwill and P. Soven, Phys. Rev. A **21**, 1561 (1980).

Solid-State Photoemission and Related Methods
Wolfgang Schattke, Michel A. Van Hove (Eds.)

15 X-ray optics, standing waves, and interatomic effects in photoemission and X-ray emission

Charles S. Fadley, See-Hun Yang, Bongjin Simon Mun, and F.J. García de Abajo

15.1 Introduction

Optical effects in photoemission are discussed from a theoretical point of view elsewhere in this Handbook (Chapter 2, Section 2.8), but we here focus on the special case of soft X-rays in the energy range of approximately 200 eV to 1,500 eV incident on surfaces or other nanostructures so as to excite photoelectrons or secondary decay processes such as X-ray emission or X-ray inelastic scattering. The aim will be to consider ways in which these optical effects can be used at both non-resonant and resonant energies to more quantitatively probe surfaces, buried interfaces, and more complex nanoscale materials. We will begin with a brief review of the history of such studies, and then turn to recent examples of experimental results and theoretical simulations.

The theoretical calculations presented here will be mostly at the level of macroscopic optics, fundamentally based on the Fresnel equations as applied via a complex dielectric constant. However, at another extreme in discussing resonant interactions, a much more general and fully quantum mechanical picture will be used, with this one being reduceable to the first one in the limit of weak light-atom interaction, as is generally the case for soft X-rays, even at resonant energies.

We begin by considering non-resonant effects; that is, where the X-ray energy is not close to any sort of core-level absorption edge in any of the atoms present in the sample. Then we consider resonant effects.

15.2 Non-resonant X-ray optical effects in photoemission

15.2.1 Background and first applications in the total reflection geometry

The first discussions of X-ray optical effects on photoemission in the soft X-ray regime were by Henke [1]. In this seminal work, he pointed out that the penetration depths of X-rays in the 1 keV range are reduced to a few tens of Å when the incidence angle is lowered into the total reflection regime. The complex index of refraction n can be written as $n = \sqrt{\varepsilon} = 1 - \delta + i\beta$ [2], with ε equal to the dielectric constant and δ and β the small real and imaginary differences of n from unity, both assumed in the soft X-ray regime to be $\ll 1$ in magnitude. In this description, the onset of significant reflectivity occurs at a critical incidence angle

Solid-State Photoemission and Related Methods: Theory and Experiment. Edited by Wolfgang Schattke, Michel A. Van Hove

ISBN: 3-527-40334-5

of $\theta_{inc}^{c} = \sqrt{2\delta}$. Figure 15.1 shows some of the results of this first study. In Fig. 15.1(a), the penetration depth, which we shall take to be the exponential decay length perpendicular to the surface, is shown for three X-ray energies in the soft X-ray regime as the incidence angle goes into the total reflection regime. It is clear that the penetration depths decrease to values comparable to, or even smaller than, the X-ray wavelength, *and to typical photoelectron inelastic attenuation lengths*, and this immediately suggests using total reflection geometries to enhance surface sensitivity in photoemission or other related spectroscopies excited by soft X-rays. Jumping to the present time, we note that calculations of such depths for non-resonant energies can be conveniently carried out with the aid of online computer programs [3]. Henke went beyond this to note that the combined effects of reflection and refraction at the surface caused an enhancement of photoelectron intensity as one enters the total reflection regime, as shown in Fig. 15.1(b). This enhancement could be quantitatively predicted from optical theory via the Fresnel equations and the experimental curve in fact used to determine the optical constants δ and β, as shown in Fig. 15.1(c).

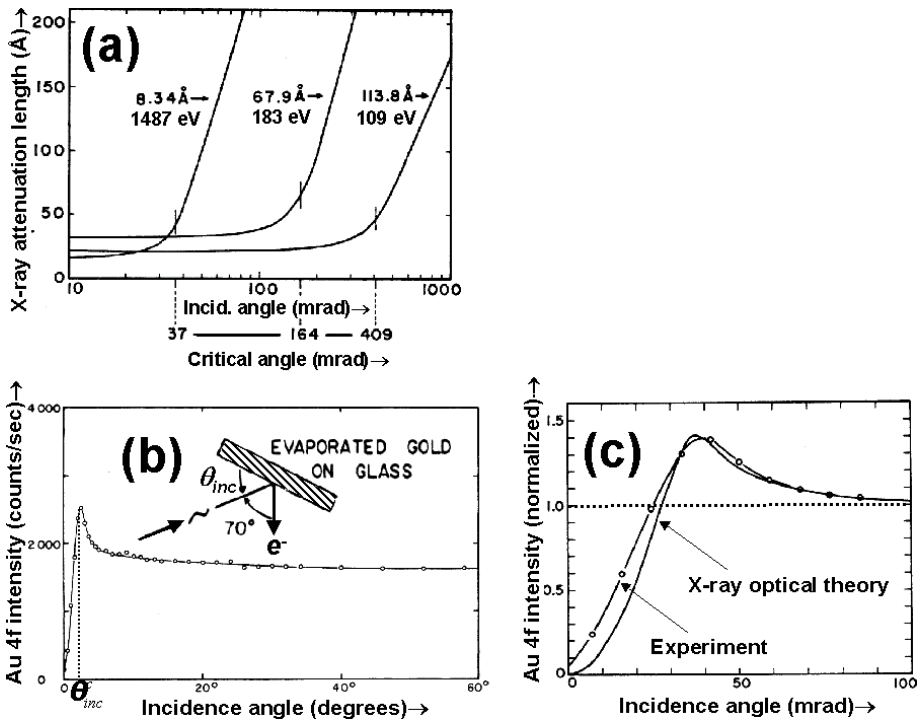

Figure 15.1: Results from the first study of non-resonant soft X-ray optical effects in photoemission by Henke. (a) The calculated variation of the exponential X-ray decay length (penetration depth) below the surface of Au for three different photon energies. (b) The variation in Au 4f photoelectron intensity as a function of X-ray incidence angle for a thick Au film deposited on glass. Note the increase in intensity in passing over the critical angle. (c) Comparison of experiment and X-ray optical theory for the intensity enhancement noted in (b). [From ref. [1].]

This work stimulated immediate interest in using such surface enhancements to characterize overlayers, and Fig. 15.2 summarizes some of these early results due to Mehta and Fadley [4, 5]. In Fig. 15.2(a), the sensitivity of the surface enhancement to even the small changes in photoelectron inelastic attenuation length from one kinetic energy to another are illustrated via the measurement of peak intensity ratios in photoemission from Au as the total reflection regime is approached. In Fig. 15.2(b), the ability to determine overlayer thicknesses is illustrated for an SiO_2 overlayer grown on a single-crystal Si substrate. Oscillatory scanned-angle X-ray photoelectron diffraction (XPD) effects are also evident in these data, due to photoelectron scattering in the substrate.

This work led sometime later to renewed interest in such effects as an adjunct in surface analytical studies, via work by Kawai and co-workers [6, 7] and Chester and Jach [8, 9]. In these studies, it was also pointed out that the concentration of X-ray flux near the surface for low incidence angles had the additional beneficial effect of significantly reducing the relative intensity of inelastically scattered electrons that underlies all photoelectron spectra. That is, since photoelectrons are preferentially created in a near-surface region of thickness comparable to their inelastic mean free paths, they will have less chance to inelastically scatter before escaping the surface. This effect is illustrated in Fig. 15.3 [10] for the case of a lightly oxidized Si surface. The overall benefits of being able to work in a total reflection geometry in laboratory XPS experiments has by now led to the availability of a commercial instrument specifically built for this purpose [10]. But beyond this, the inherently collimated nature of soft X-ray beams from any synchrotron radiation source and the ease with which most sample manipulators can vary the incidence angle through simple polar angle rotation make this type of experiment of obvious utility in many surface and interface studies.

15.2.2 Standing wave effects for probing buried interface and nanostructures

It is well known that, as soon as any significant reflectivity occurs at a solid surface, a standing wave will be set up as an interference between the incident plane wave and the outgoing reflected plane wave. The fundamental process is illustrated in Fig. 15.4(a), together with some fundamental relationships between incidence angle (= reflected angle) and standing wave period. Such standing wave effects have been used for some time in the hard X-ray regime of about 10 keV for studying surface structures and overlayers [11–13]. Here, the standing wave formed by X-rays with wavelength of about 1 Å via Bragg reflection from various low-index planes can be varied in position by rocking the incidence angle around the Bragg angle, thus yielding atomic positions with sub-Å accuracy [11, 12], or by going into total reflection, a simple standing wave of the type indicated in Fig. 15.4(a), but of longer wavelength due to the small incidence angle may be established and used to determine distances above a surface [13].

We will here consider similar experiments with soft X-rays of approximately 10–60 Å (1–6 nm) in wavelength, as this is the range most relevant to exciting typical photoemission or soft X-ray emission/inelastic scattering spectra. In this case, the use of grazing angles below the critical angle is always possible, but the standing wave in this case will have a very long wavelength, since from Figs. 15.1(a) and 15.4(a) the relationship $\lambda_{\mathrm{SW}} = \lambda_{\mathrm{x}}/2\sin\Theta_{inc}$ yields a standing wave period of roughly 3-10 times the X-ray wavelength, too large to probe

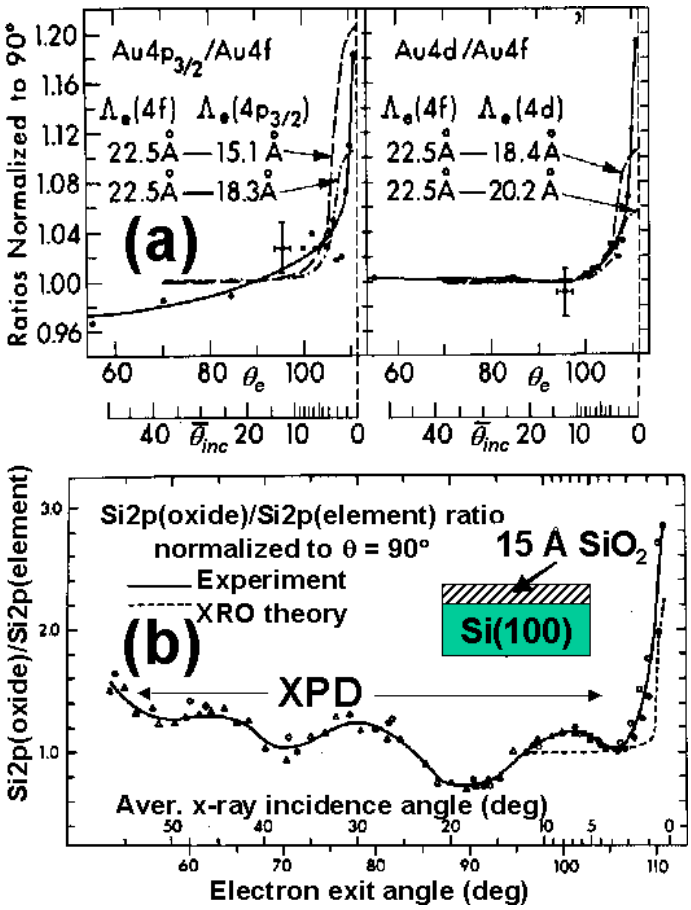

Figure 15.2: Some first applications of non-resonant X-ray optical effects. (a) Observation of the difference in inelastic attenuation lengths for different core-level photoelectron peaks from Au through the dependence of intensity ratios as a function of X-ray incidence angle. The observed change in these intensity ratios is due to the fact that the X-ray penetration depth decreases to values comparable to the electron inelastic attenuation lengths. Two different choices of attenuation lengths are shown for the theoretical simulations to indicate the sensitivity of these ratios to this parameter. [From ref. [4].] (b) Observation of the change in the ratio of two chemically-shifted peaks from an oxidized Si sample as X-ray incidence angle is decreased. Also evident are oscillatory scanned-angle photoelectron diffraction effects. [From ref. [5].]

on the nanometer scale that is most attractive. It has thus been proposed to use a synthetic multilayer mirror of suitable period to Bragg reflect soft X-rays so as to generate a strong standing wave with λ_{SW} of a few nanometers, and then to utilize the standing wave profile above the surface in both photoemission [14–17] and X-ray absorption spectroscopy [18]. This type of reflection is illustrated in Fig. 15.4(b), from which it is clear that the standing

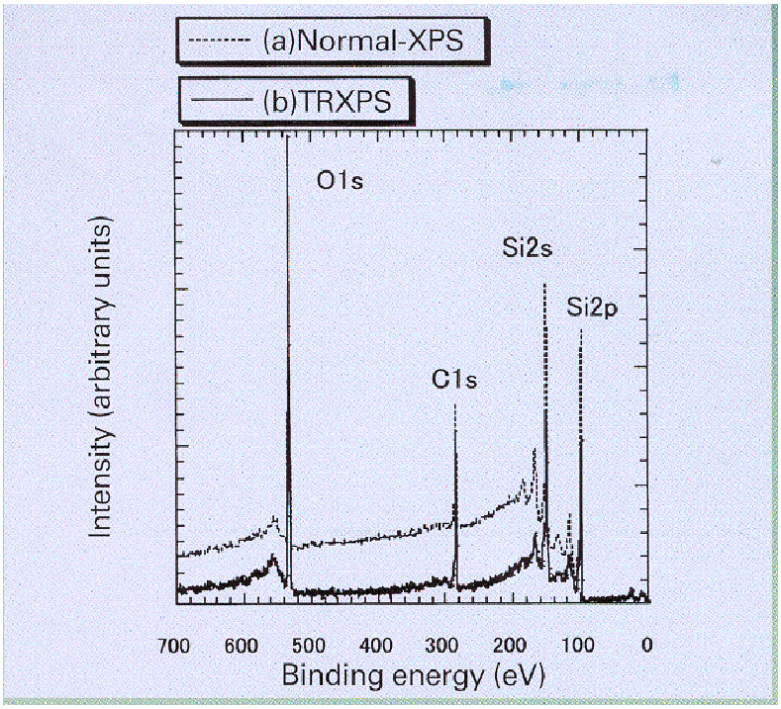

Figure 15.3: Reduction of inelastic background in XPS spectra with total reflection, from a slightly oxidized Si sample with a C-containing contaminant overlayer. [From ref. [10].]

wave period in first-order Bragg reflection is simply the periodicity of the multilayer d_{ML}. Present synthetic methods permit making such mirrors with periods down to about 3 nm, and with top-surface rms roughnesses of only 0.5 nm. Thus, they can be used as substrates of reasonably high quality on which to grow various types of samples for study. The multilayer mirror is in this context simply used as a standing wave generator (SWG).

Note also from Fig. 15.4(b) that, in the region of space above the surface in which the incident and reflected waves overlap and interfere to form the standing wave, the modulation strength of the standing wave goes roughly as the square root of the X-ray reflectivity R_x. Adding the incident and reflected waves in a more accurate mathematical way in fact shows that the maximum amplitude of the modulations in the standing wave should be $\pm 2\sqrt{R_x}$, or a full normalized modulation around a unit incident intensity of $4\sqrt{R_x}$. Thus, even a reflectivity of 5% can give a standing-wave modulation of something like 40%, provided the phase shift between incident and scattered waves is not too large (as is in fact found in realistic numerical calculations [19]). With the correct choice of materials, in particular one of lower electron density and X-ray scattering power (e.g. B_4C) and the other of higher density (e.g. W), 1^{st} order Bragg reflection can thus yield X-ray reflectivities R_x of 5-30% corresponding to standing wave modulation strengths of roughly 40-100% as measured relative to the incident wave, through the reasoning argument mentioned above.

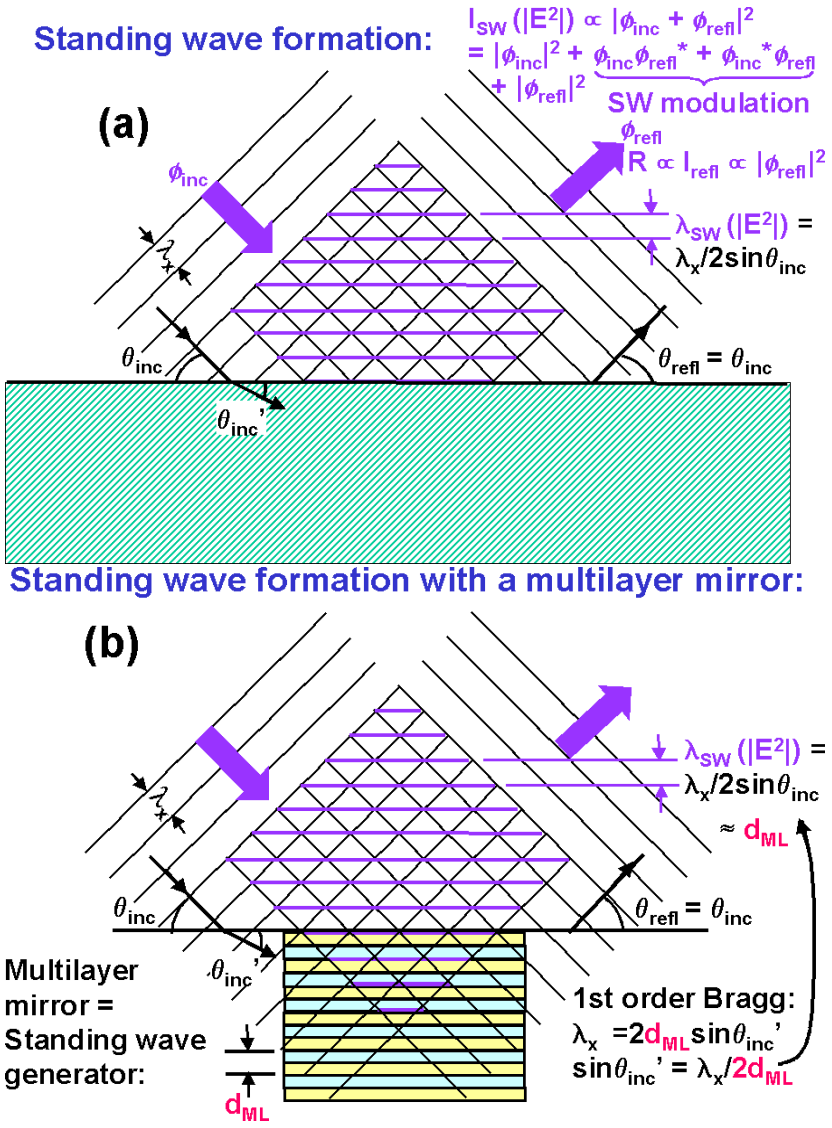

Figure 15.4: Basic geometry of standing wave formation. (a) General picture of standing wave formation, regardless of reflection type. (b) Standing wave formation in reflection from a multilayer mirror. Various key quantities and relationships are indicated in both panels.

Before considering some first experimental results of this type in photoemission, we briefly introduce the theoretical modeling of such non-resonant X-ray optical processes, as included in a computer program written by Yang [19]. The various ingredients necessary are illustrated in Fig. 15.5, here shown for a general multilayer system. Each layer is described by some

index of refraction n_i. Interfaces can have graded dielectric properties, with single and multiple reflection and refractive transmission at each interface gradation being included. Once the optical calculation is taken to convergence, the squared strength of the electric field appropriate to the excitation of photoemission is calculated at each depth z. $|E(z)|^2$ is then used to modulate the appropriate product of atomic density and photoelectric subshell cross section and inelastic attenuation factor on passing to the surface, with the end result being both the distribution of photoelectron intensity as a function of depth, and the total intensity as well by integration over depth. Refraction of the photoelectrons on crossing the barrier of the inner potential is also included. The same program can also be used to calculate soft X-ray emission intensities as a function of depth, with the only difference being the final inclusion of a different attenuation length due to absorption.

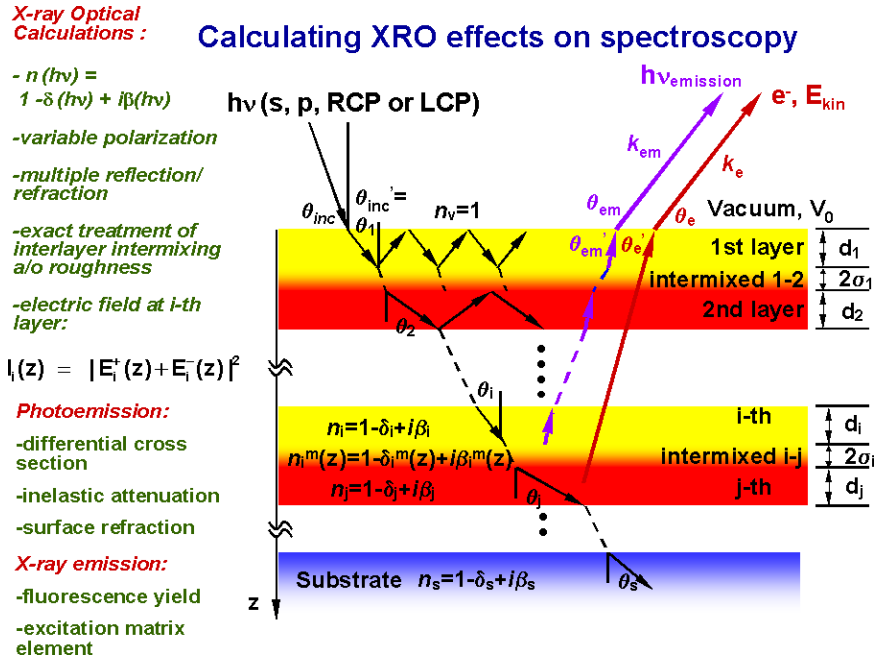

Figure 15.5: Calculation of X-ray optical effects on photoemission and soft X-ray emission. Various key ingredients are labelled. [From ref. [19].]

Some results from these calculations for a B_4C/W multilayer [19] are shown in Fig. 15.6. Note the strong standing wave modulation for incidence at the Bragg angle, and the change in the depth distributions of C 1s and W 4f photoelectron intensities on going from the situation with no standing wave at the right to the Bragg condition at left. The C 1s emission has its maximum in the center of the first B_4C layer with the standing wave, whereas it is a maximum at the surface without the standing wave. The W 4f distribution shows the opposite effect, being compressed nearer the B_4C/W interface with the standing wave. These results thus qualitatively indicate the kind of depth distribution modification that can be affected by using a soft X-ray standing wave for excitation.

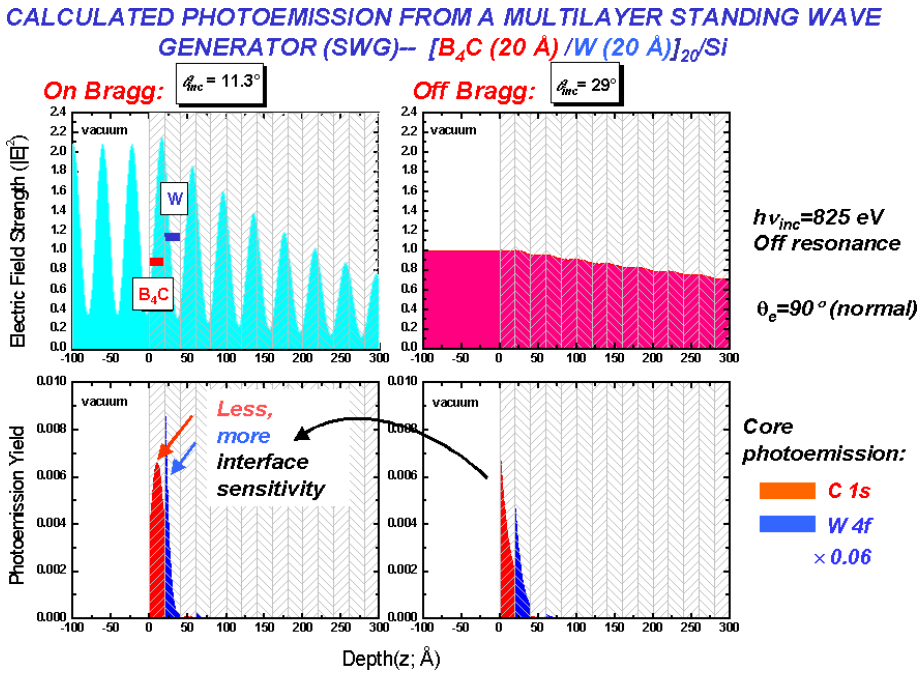

Figure 15.6: X-ray optical calculations of standing wave effects on the depth distributions of electric field strength and photoelectron intensity from a multilayer mirror composed of alternating layers of B_4C and W. The right panels show the depth distributions when the incidence angle is far from the multilayer Bragg angle, and the left panels the distributions at the Bragg angle. Note the strong standing wave created at the Bragg condition, and the influence on both the C 1s and W 4f depth distributions. [From ref. [19].]

As a recent first example of the application of this approach, we consider a study by Yang et al. [16] and by Mun [17] of the buried interface between Fe and Cr, a prototypical pair of ferromagnetic and non-magnetic metals, respectively, that has been much studied in connection with the giant magnetoresistance (GMR) effect. The basic configuration of the experiment is shown in Fig. 15.7. The sample to be studied, an Fe/Cr bilayer, was grown on top of a multilayer mirror consisting of 40 periods of B_4C/W bilayers, with a period of 4 nm each. Thus, the standing wave above the multilayer will have a period also of 4 nm (cf. Fig. 15.4(b)). Beyond working with X-ray incidence angles near the first-order reflection of the B_4C/W multilayer mirror, the Cr layer underneath a constant-thickness Fe overlayer was grown in a wedge form. As one key part of the experimental procedure, the variation of the wedge thickness from 38 Å to 116 Å over a sample width along the x direction in Fig. 15.7 of about 10 mm, together with the small X-ray spot size of 0.2 mm, permitted carrying out the experiment for a range of positions of the standing wave with respect to the buried interface. That is, as the sample is scanned along x, the standing wave is effectively scanned vertically with respect to the interface, provided that the Fe/Cr bilayer does not influence the position of

the standing wave. For a choice of photon energy that avoids any resonances in Fe or Cr, the desired "pinning" of the standing wave position by the multilayer mirror has been verified by direct calculations, as illustrated in Fig. 15.8. Even though the reflectivity is attenuated from about 9% to about 4% over the wedge, the Bragg position remains very constant at 11.15°, and this change in reflectivity would only change the estimated standing wave modulation (via the $4\sqrt{R_x}$ estimate mentioned above) from about 60% to about 40%.

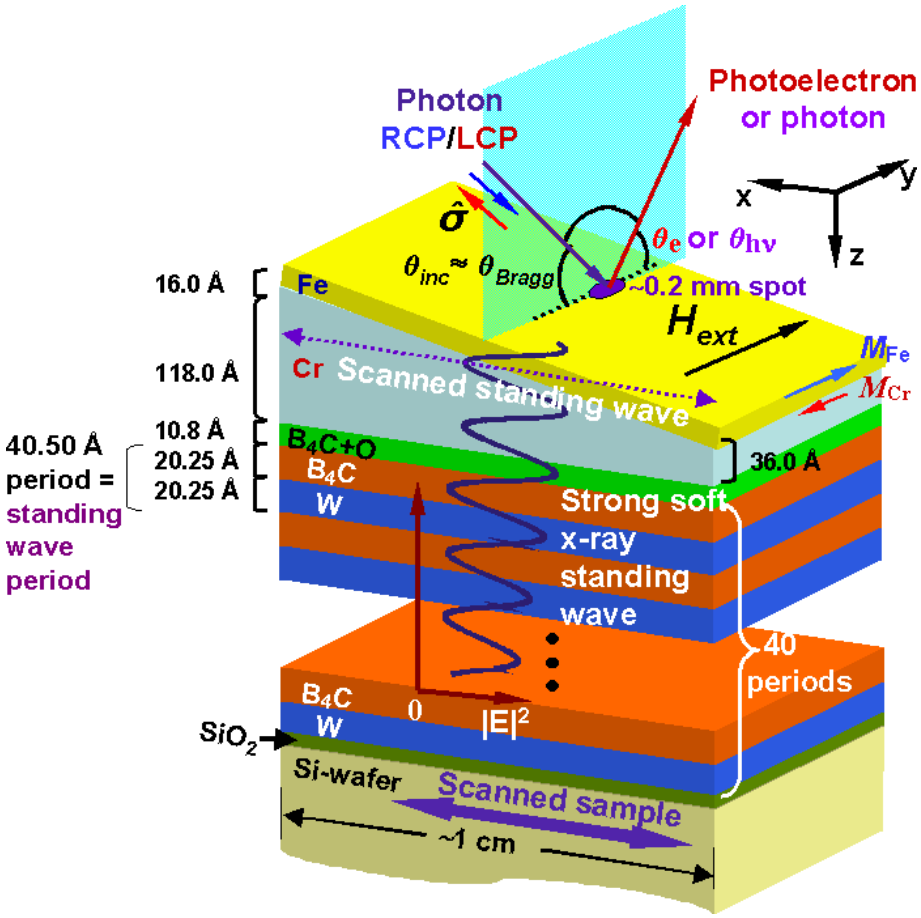

Figure 15.7: Basic geometry of an experiment combining soft X-ray excitation of photoemission with a wedge-shaped bilayer sample grown on a multilayer-mirror standing wave generator (SWG) so as to selectively study the buried interface between Fe and Cr. Scanning the sample position along the x axis effectively scans the standing wave through the interface. [From ref. [16].] See also color figure on page 469.

As in prior standing wave studies, it is also possible in such SWG+wedge experiments to scan the incidence angle around the Bragg angle, which is well known to both vary the position of the standing wave and to reduce its amplitude for angles away from the Bragg

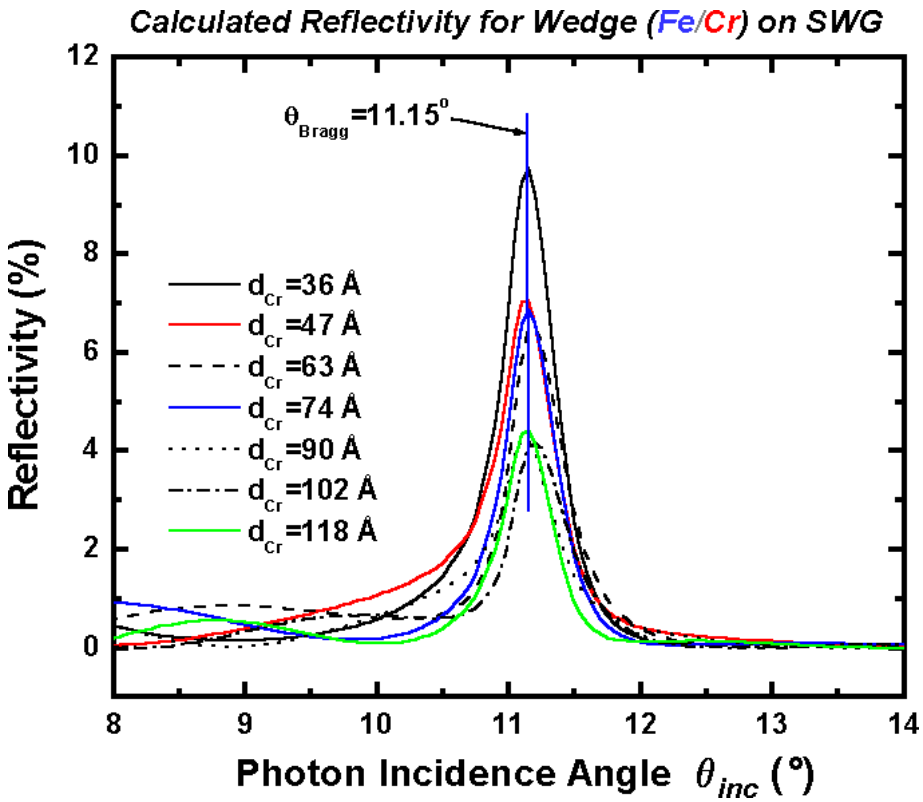

Figure 15.8: Calculated reflectivity for the sample geometry of Fig. 15.7: a wedge-shaped Fe/Cr bilayer on top of a 40-period multilayer mirror composed of bilayers of B_4C and W. Note that, although the reflectivity is attenuated by thicker Cr layers, the position of maximum reflectivity is pinned at the same angular position by reflection from the multilayer. [From refs. [16], [17], and [19].] See also color figure on page 470.

angle [18]. This provides a second method for varying the position of the standing wave with respect to the interface, which, together with scanning the sample in x (cf. Fig. 15.7), should yield an overdetermined set of data that can be analyzed in terms of models for composition and magnetization variation through the interface. We illustrate this complementarity of measurement schemes for the Fe/Cr case in Fig. 15.9, where the Cr3p/Fe3p intensity ratio is shown as a function of both incidence angle for various choices of Cr thickness (Fig. 15.9(a)) and Cr thickness for various choices of incidence angle. These results have been analyzed in terms of the simple model shown at left in Fig. 15.10(a) and they lead to a determination of the onset of the Fe/Cr interface at 12.8 $\pm$2 Å depth and an overall interface mixing or roughness of 6.8 $\pm$2 Å in thickness. The center of the interface is thus measured in this way to be at $12.8 + 3.4 = 16.2$ Å, in excellent agreement with the 15 Å expected from the quartz crystal thickness monitor used to deposit this layer.

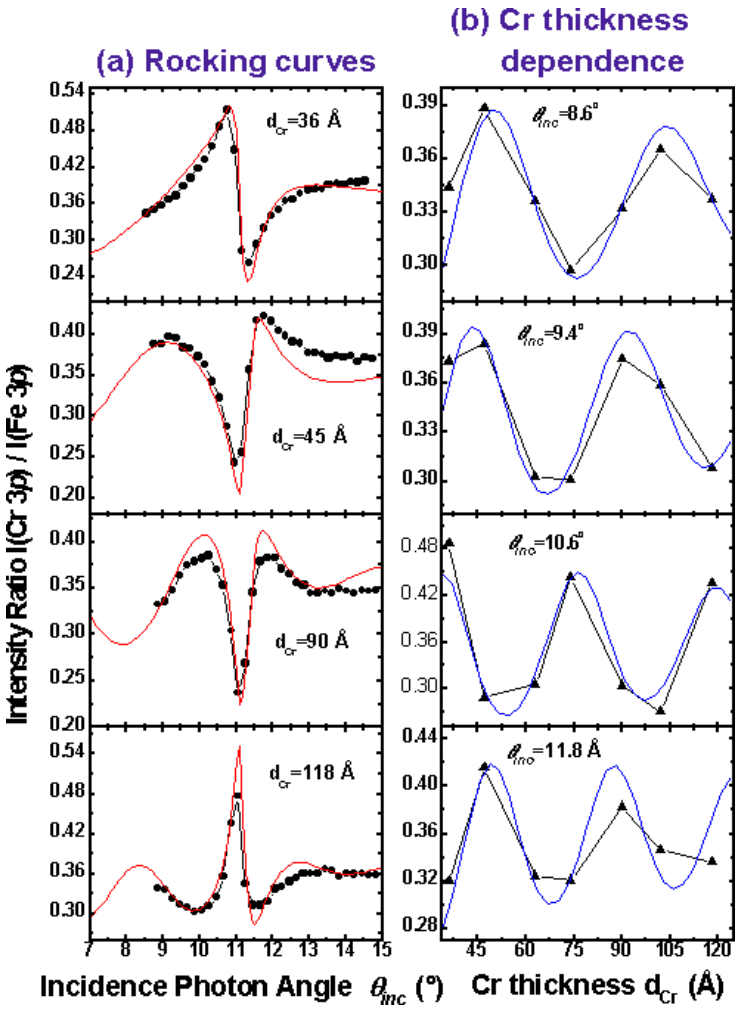

Figure 15.9: Experimental results for the Cr3p/Fe3p intensity ratio from the sample of Fig. 15.7 as a function of both (a) X-ray incidence angles centered on the Bragg angle (rocking curves) and (b) the thickness of the Cr layer. These data can be analyzed to determine the composition variation through the interface, via the simple two-parameter linear model at left in Fig. 15.10(a) and X-ray optical calculations of photoemission intensities as outlined in Fig. 15.5 and accompanying text, with the solid curves in (a) and (b) representing the final best fits. [From ref. [16].]

One can also measure magnetic circular dichroism for this Fe/Cr example by exciting core level Fe 2p and 3p and Cr 2p and 3p spectra with circularly polarized radiation. The nature of the MCD measurement means that ferromagnetic order will be detected only along the y direction in Fig. 15.7 that is nearly parallel to the light incidence direction due to the low Bragg angle of about 11^o. Some of this data for 2p emission and two Cr thicknesses

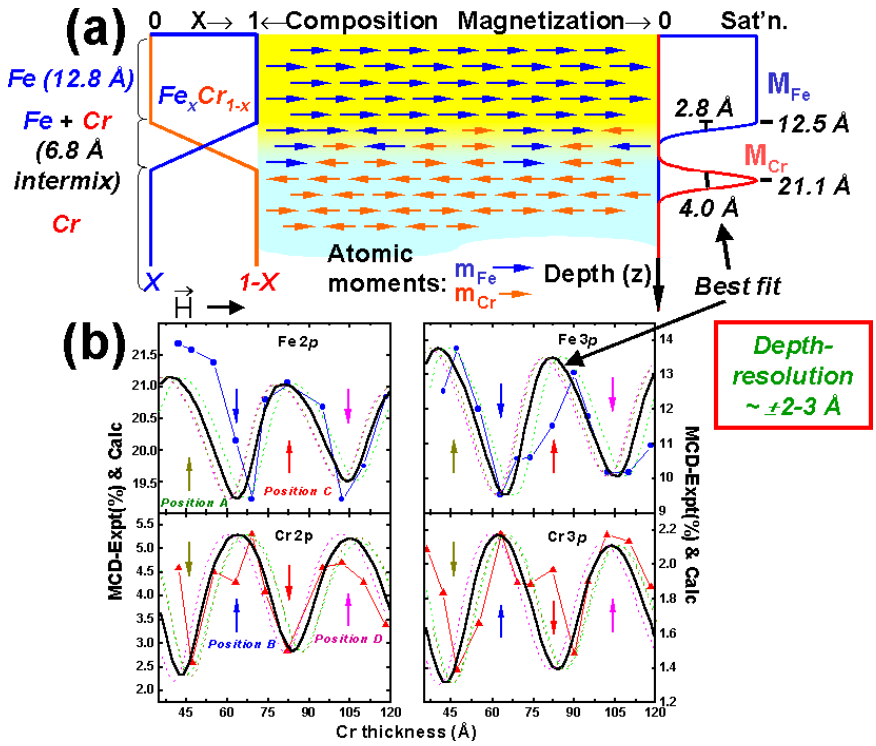

Figure 15.10: Non-destructive depth-resolved determination of composition and magnetization profiles via standing-wave excited photoemission. (a) Sample geometry together with the models used to fit both the Cr3p/Fe3p intensity ratio of Fig. 15.9 (left side–linear model) and the Fe 2p and 3p and Cr 2p and 3p magnetic circular dichroism (MCD) data of Fig. 15.11 (right side–gaussian or half-gaussian models) are shown, together with the final best fits to the MCD data. Note that only two parameters are used in the X-ray optical calculations for each set of data: a position and a width, and that the five sets of data (Cr3p/Fe3p, Fe 2p MCD, Fe 3p MCD, Cr 2p MCD, and Cr 3p MCD) have been analyzed independently. (b) Summary of the Fe 2p and 3p and Cr 2p and 3p MCD data, together with the best fits to experiment, and curves indicating how much the calculated curves change for 3 Å changes in the two parameters involved in each fit. [From ref. [16].]

denoted Positions B (standing wave a maximum at the Fe/Cr interface) and C (standing wave a minimum at the interface) is shown in Fig. 15.11. The right-circular-polarized (RCP) and left-circular-polarized (LCP) spectra are shown for both Fe and Cr, together with the difference as the magnetic circular dichroism (MCD) in %. Although the Cr dichroism is much smaller than that of Fe (a few % for Cr versus 10-15% for Fe) there is nonetheless clear evidence for some ferromagnetic ordering of Cr, even though it is normally not ordered in this way, but rather weakly antiferromagnetically ordered (with a transition temperature of 311 K near that at which these measurements were carried out), in which case the MCD should be zero.

The fact that the sign of the Cr dichroism is opposite to that of Fe also immediately indicates that the Cr ferromagnetic ordering induced by the Fe is opposite in direction to that of Fe, as qualitatively indicated in Fig. 15.10(a). It is also clear that varying the position of the standing wave (e.g. from Position B to Position C) affects the relative magnitudes of the MCD signal, with that of Fe increasing at C and that of Cr decreasing. Similar results were obtained for 3p emission from both Fe and Cr, and the overall experimental data are shown in Fig. 15.10(b), together with best-fit curves based on X-ray optical calculations in which the two parameters for each of the four sets of MCD data shown at right in Fig. 15.10(a) were varied. At right in Fig. 15.10(a) are also summarized the best-fit numbers, and it is interesting that the onset of reduction of the Fe ferromagnetism in approaching the interface occurs just where the Fe3p/Cr3p ratio analysis yields a reduction in the Fe atomic fraction. The Fe ferromagnetism also is found to go to zero at the point in the interface at which its atomic fraction drops to 0.5. The Cr by contrast shows its slight ferromagnetic ordering over only a narrow layer about one atomic layer in thickness, and about one atomic layer below the interface mixing region.

Further details concerning this standing wave study of the Fe/Cr interface can be found elsewhere [16, 17].

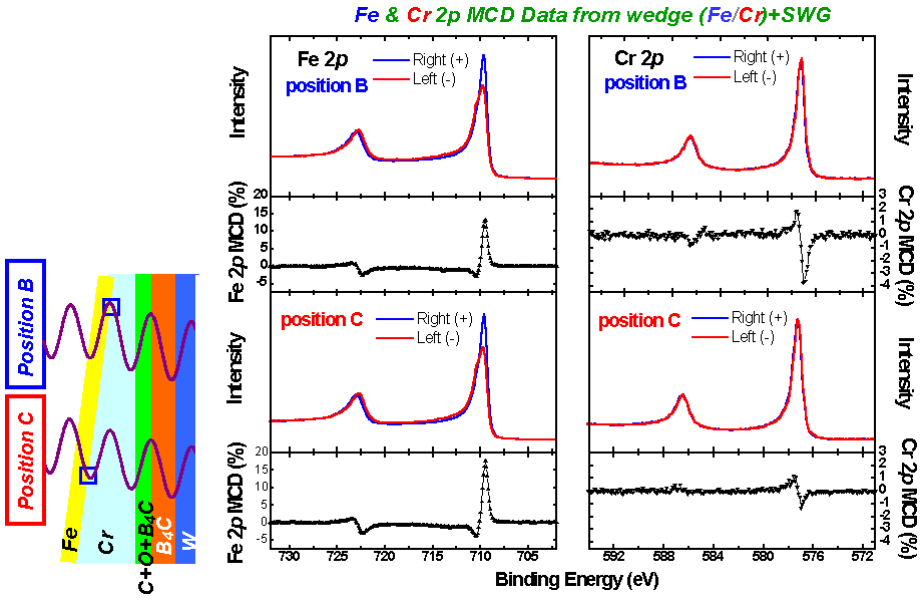

Figure 15.11: Magnetic circular dichroism measurements for Fe 2p and Cr 3p emission from the bilayer of Fig. 15.7, at two choices of Cr thickness that lead to having a standing wave maximum and a standing wave minimum at the buried interface (Positions B and C, respectively at left). [From ref. [16].]

Although these are at present the only published experimental data of their kind, they suggest some exciting future possibilities for selectively studying buried interfaces or other vertically heterogeneous nanostructures with photoemission or other soft X-ray excited spec-

troscopies such as soft X-ray emission. Soft X-ray emission (at least at non-resonant energies) has an advantage over photoemission in probing more deeply, thus being more sensitive to the standing wave modulation below the surface, and we return to consider it more specifically in a later section. Beyond studying multilayer structures of relevance to magnetism and semiconductor device technology, one can suggest looking at self-assembled monolayers or other nanocrystalline objects grown or somehow deposited on the top surface of a suitable SWG. Combining spectromicroscopy using soft X-rays, which at present yields two-dimensional in-plane information, with standing wave excitation by again growing the sample on an SWG, could yield information on the third dimension perpendicular to the sample surface plane, a topic to which we return below also.

15.3 Resonant X-ray optical effects and multi-atom resonant photoemission

15.3.1 General considerations

On passing through a core-level absorption edge or resonance, the absorption coefficient can increase dramatically, and this will be reflected also in the index of refraction via an increase in β and concomitant changes in δ that are derivable via a Kramers-Kronig analysis [3(b)]. As an example of this, we show in Fig. 15.12 the variation of β and δ which arise in crossing the Mn $L_{2,3}$ = Mn $2p_{1/2,3/2}$ absorption edges in MnO. Since X-ray absorption at the 2p resonances of the 3d transitions metals is much studied, especially in magnetism-related work with dichroism, this type of data is of high relevance. We can see that both β and δ increase by at least an order of magnitude in crossing these resonances, although they are still in magnitude always much less than unity, and in fact do not exceed 1% in magnitude, a fact which we will use later in making some simplifications in the optical analysis.

What effect will such resonant phenomena have on photoemission or other soft X-ray excited spectroscopies? In order to calculate this for a homogeneous, semi-infinite solid, we first follow the X-ray optical analysis of Yang [35] and Kay et al. [20], and then discuss the same phenomena in terms of a microscopic theory of multi-atom resonant photoemission [20–22].

15.3.2 Resonant X-ray optical theory

The resonant X-ray optical (RXRO) approach proceeds via the same basic ideas illustrated for a multilayer system in Fig. 15.5, except that we simplify to the homogeneous, semi-infinite solid with index of refraction n and a sharp vacuum-solid interface. The effect of the resonance is assumed to influence only the local electric field E at some depth z below the surface of the sample, with the associated differential photoelectric cross section $d\sigma/d\Omega$ varying only slowly through the resonance, as described by the usual one-electron theory [23]. The variation of photoemission intensity with photon energy $I(h\nu)$ is then obtained by integrating over the coordinate z perpendicular to the surface the product of the electric field strength $|E(h\nu, z)|^2$ at depths z relevant for photoemission, the energy-dependent differential photoelectron cross section $d\sigma/d\Omega$ appropriate to the experimental geometry (which may also in the experimental

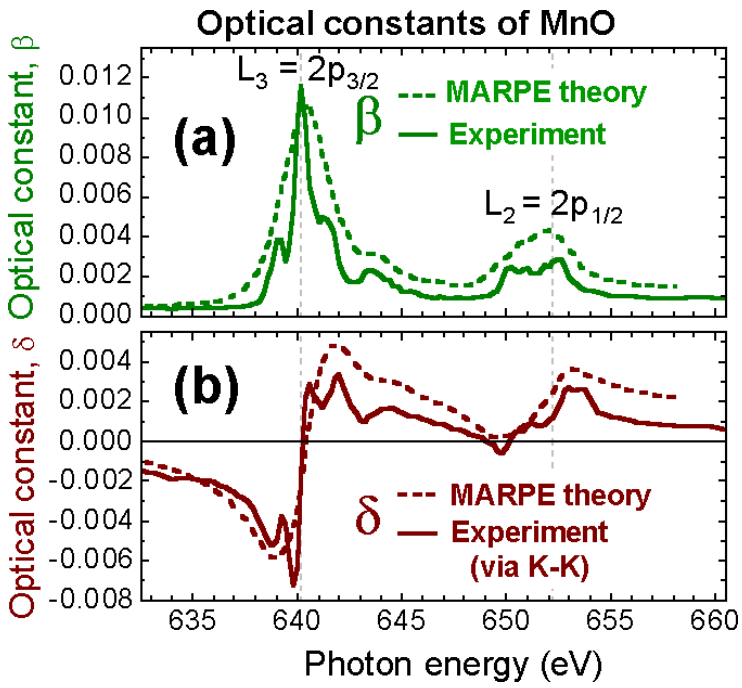

Figure 15.12: The optical constants β and δ of MnO as the Mn 2p absorption resonances are crossed, The solid experimental curves were derived from an experimental determination of the absorption coefficient and subsequent Kramers-Kronig transformation of the results. Also shown are dashed theoretical curves based on the microscopic theory of multiatom resonant photoemission (MARPE). [From refs. [20] and [22].]

data include the effects of photoelectron diffraction (PD) that result in modulations beyond the simple atomic cross section [24], as seen already in the scanned-angle data of Fig. 15.2(b)) and the kinetic-energy-dependent inelastic attenuation length for electrons Λ_e, as

$$I(h\nu) \propto \frac{d\sigma(\hat{E},h\nu)}{d\Omega} \int_0^\infty |\vec{E}(h\nu,z)|^2 \exp\left(-\frac{z}{\Lambda_e(E_{kin})\sin\theta'_e}\right) dz, \tag{15.1}$$

where $\hat{E}$ is a unit vector along $\vec{E}$ and accounts for the polarization dependence in the cross section, and we have not included factors of atomic density and the solid angle acceptance of the analyzer that will be constant over an energy scan. In scanning photon energy through a resonance, it is also possible that *scanned-energy* photoelectron diffraction effects will cause intensity modulations [24], and these we will in fact see below.

Via an analysis based on the Fresnel equations [19, 20], it can finally be shown that the integral in Eq. (15.1) reduces to

$$I(h\nu) \propto \frac{d\sigma}{d\Omega}(\hat{E},h\nu) \frac{|t(h\nu)|^2}{\frac{\mathrm{Im}\{4\pi n(h\nu)\sin\theta'_{inc}(h\nu)\}}{\lambda_x(h\nu)} + \frac{1}{\Lambda_e(E_{kin})\sin\theta'_e}}, \tag{15.2}$$

where the quantity t for p-polarized radiation incident on a planar surface from vacuum with $n_v = 1$, and for a conducting or non-conducting, but non-magnetic, reflective medium, is given by

$$t \equiv \frac{2 \sin \theta_{inc}}{\sin \theta'_{inc} + n_r \sin \theta_{inc}}, \tag{15.3}$$

with θ'_{inc} equal to the *complex* angle of propagation below the surface, again measured relative to the surface, θ'_e the real angle of propagation of the electron below the surface before allowing for possible refraction effects in crossing the inner potential barrier V_0, and λ_x the wavelength of the radiation. θ'_{inc} is further related to θ_{inc} via Snell's Law: $\cos \theta_{inc} = n_r \cos \theta'_{inc}$, with θ_{imc} real. Eqs. (15.2) and (15.3) are completely general formulas for calculating photoemission, with all dependences on energy explicitly indicated. Beyond optical constants such as those in Fig. 15.12, the only other inputs needed are radial matrix elements and phase shifts for calculating $d\sigma/d\Omega$ [23] and the electron inelastic attenuation length Λ_e, which we have evaluated for the O 1s photoelectrons leaving MnO using a well-established semi-empirical formula [25]. Henke [1] has carried out the same analysis using a somewhat different formalism, with simplifications going beyond the equivalents of Eqs. (15.2) and (15.3) that are reasonable in view of his dealing with non-resonant cases.

Figure 15.13 now presents results from using Eqs. (15.2) and (15.3) for the case of MnO with the optical constants of Fig. 15.12. The assumed experimental geometry is indicated in Fig. 15.13(a). In Fig. 15.13(b), it is obvious that the penetration depth is drastically decreased on going through the Mn 2p absorption resonances. In fact, its maximum for an energy just at the Mn $2p_{3/2}$ resonance is only approximately 130 Å for normal incidence, as illustrated in more detail by the solid curve in Fig. 15.14(a). On going to lower angles of incidence comparable to or below the critical angle at the Mn $2p_{3/2}$ resonance of $\sqrt{2\delta} \approx 7^\circ$, this decrease is even more dramatic, with X-ray penetration depths of only about 20 Å that are comparable to electron inelastic attenuation lengths [25]. Thus, the surface sensitivity of any soft X-ray spectroscopic measurement can be significantly affected in passing over such resonances. For comparison, we also show as the dashed curve in Fig. 15.14(a) a calculation from the Berkeley Center for X-ray Optics (CXRO) web program [3(a)] , which makes use of standard tabulations of the optical constants that do not fully include edge resonance effects [3(b)]. There is a dramatic difference between these two curves, making it clear that a proper allowance for the exact form of the absorption features is essential for properly estimating X-ray penetration depths. As a test of the accuracy of our calculation method, we compare our results off-resonance with those from the CXRO program off-resonance, and with the same optical constants, and the two curves are identical. Fig. 15.13(d) also shows that reflectivity is significantly enhanced on passing through these resonances, which from our previous discussion of course also implies an enhanced standing wave above the surface.

More interestingly from a spectroscopic point of view is the variation of the O 1s intensity on passing through these resonances, which is shown in Fig. 15.13(c). These calculations predict strong variations of photoelectron intensity as the X-ray incidence angle is decreased toward the total reflection regime, but which nonetheless persist to some degree up to incidence angles of 30–40° with respect to the surface. Such effects have in fact been observed for MnO, as illustrated in Fig. 15.15(a) and 15.15(b). Figure 15.15(a) first shows a broad scan

of the O 1s intensity over an energy region including the Mn 2p resonances, for an incidence angle of 20°. The most obvious feature here is a strong modulation of the intensity due to scanned-energy photoelectron diffraction effects [24], but on top of this at the position of the strongest $2p_{3/2}$ resonance at 640 eV is a modulation that is about 25% of the overall PD effect. Figure 15.15(b) shows similar data at an incidence angle of 10° and over a narrower energy window, and the resonance effects, measured as the overall + and - excursion are now considerably larger, being for example about 25% of the intensity just below the resonance, which has been set equal to unity in both Figs. 15.15(a) and 15.15(b). This marked increase is consistent with Fig. 15.13(d) in that the effects seen there also increase strongly on going to lower incidence angles, and we note that the 10° of Fig. 15.15(b) is furthermore not too far from the previously-estimated critical angle on the Mn $2p_{3/2}$ resonance of 7°. Also shown in Fig. 15.15(b) are the results of an X-ray optical calculation based on Eqs. (15.2) and (15.3) and, if allowance is made for the general curve in the experimental data due to PD effects, there is in general excellent agreement as to both the % effects (which have not been adjusted between experiment and theory) and the fine structure in the resonance-induced modulations for both the $2p_{3/2}$ and $2p_{1/2}$ features. Figure 15.15(c) shows the variation of the overall excursion with incidence angle, and compares the experimental data points with XRO calculations. Again, there is in general excellent agreement, together with a prediction that there will be effects of at least a few % even for normal X-ray incidence. Finally, in Fig. 15.15(d) we show similar results for O 1s emission from a NiO(001) surface [26], but at an even lower 5° incidence angle, and here the experimental and theoretical curves are nearly identical, with both leading to a modulation of about 86%. These data in fact show that an earlier search for such resonant effects in NiO [27] was done at too high an incidence angle and with insufficient statistical accuracy to resolve them.

As a final comment on the systematics of effects such as those seen in Figs. 15.15(c) and 15.15(d), it has been pointed out by Kay et al. [20] that the modulation of photoelectron intensity has a form very similar to the optical constant δ, and that, with certain simplifications reasonable in view of the small magnitudes of both δ and β, Eqs. (15.2) and (15.3) lead to a photoelectron intensity that is overall proportional to $1+\delta$, at least within the range of incidence angles under consideration here.

In summary up to this point, significant X-ray optical effects occur on passing through absorption resonances, especially for incidence angles close to the critical angle, but in fact also leading to a complex modulation of photoelectron intensities which in the low-incidence-angle limit are similar in form to the variation of δ.

15.3.3 An alternative viewpoint: multiatom resonant photoemission (MARPE)

We now look at resonant effects from a different viewpoint, treating them in a more general way as *interatomic* multiatom resonant photoemission (MARPE) [20–22]. This viewpoint is thus different from normal resonant photoemission, which involves only orbitals on a single atom [28, 29], and which can be termed single-atom resonant photoemission (SARPE) by comparison. This topic has also been introduced in Chap. 2 of this book (cf. Fig. 1.13), but we will amplify on it here.

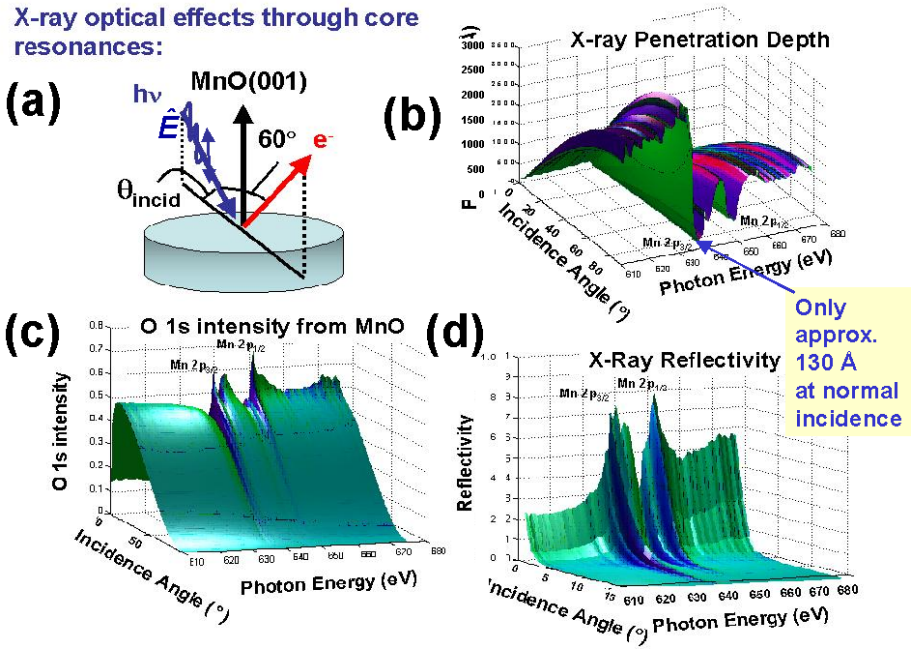

Figure 15.13: Resonant X-ray optical calculation for the experimental geometry in (a) of: (b) the X-ray penetration depth = exponential decay length Λ_x, (c) the O 1s photoelectron intensity, and (d) the reflectivity R_x. These calculations were carried out for p-polarized radiation incident on a flat MnO surface and photon energies were scanned through the Mn 2p absorption resonances. The plots in (a), (b), and (c) are all shown as a function of both photon energy and incidence angle. [From ref. [19].] See also color figure on page 471.

The basic process envisioned is shown in Fig. 15.16(a). A single photon absorption process involves both direct excitation of a photoelectron from the atom at left and a resonant excitation via a strong bound-to-bound absorption resonance on the atom at right. If the absorption resonance were on the atom at left, we would have normal SARPE, but for the case shown in Fig. 15.16(a), the resonances can occur on various atoms around a given emitter, and hence this becomes both interatomic and multiatom. We will also implicity consider that both of the excited levels involved are core in character, although similar effects can in principle occur between more weakly bound electronic levels situated on two different atoms, as we discuss below.

The theory of MARPE has been explored in detail elsewhere [20, 22], and for the case of O 1s emission from MnO dealt with in Figs. 15.13(c) and 15.15(a),(b),(c), the energy levels and basic matrix elements involved are as illustrated in Fig. 15.16(b). In brief summary, if the system is initially prepared in its many-body ground state $|g\rangle$, the contribution of the direct or unscattered wave function (that is, neglecting any sort of photoelectron diffraction effect) to

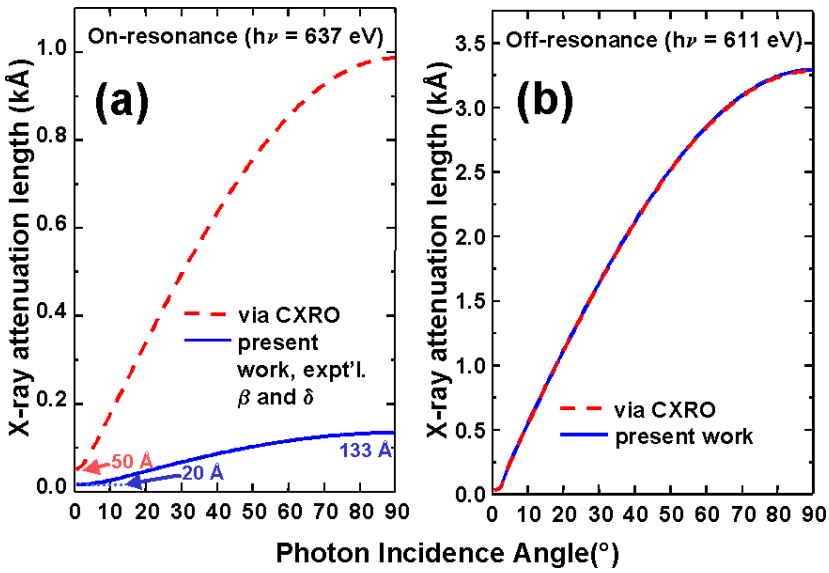

Figure 15.14: X-ray penetration depth in MnO as a function of incidence angle, for a photon energy (a) on the Mn $2p_{3/2}$ resonance of Fig. 15.12, and (b) below this resonance. The curve labelled CXRO is calculated using tabulated optical constants that do not allow for the full effect of the Mn $2p_{3/2}$ resonance [3(a)] . In (b), the two identical curves are from ref. [3(a)] and this work, and used identical optical constants. [From refs. [3(a)] and [19].]

the photoelectron intensity can be written

$$I\left(\vec{\mathbf{k}}_e\right) \propto \left|\phi^0_{\mathbf{k}}(\mathbf{r})\right|^2 \propto \left|\sum_{l\mu} Y_{l\mu}\left(\hat{\mathbf{k}}_e\right) i^l h_l^{(+)}\left(kr\right) M_{El\mu}\right|^2, \tag{15.4}$$

where $\vec{\mathbf{k}}_e$ is the photoelectron wave vector, $\phi^0_{\mathbf{k}}(\mathbf{r})$ is the wave function at the detector, $Y_{l\mu}$ is a spherical harmonic, $\hat{\mathbf{k}}_e$ is a unit vector along $\vec{\mathbf{k}}_e$, $h_l^{(+)}\left(kr\right)$ is a spherical Hankel function, and

$$M_{El\mu} = \langle El\mu, \underline{O1s}\,|T|\,g\rangle \tag{15.5}$$

is the matrix element describing the transition to the final state with a photoelectron $|El\mu\rangle$ of energy $E = \hbar^2k^2/2m$ and an O 1s hole. Final-state photoelectron diffraction effects can also be incorporated in this model by using $M_{El\mu}$ as input for self-consistent multiple-electron-scattering equations. If we keep only terms up to second order in in the perturbing potential V that is involved in T, it reduces to the well-known Kramers-Heisenberg formula for resonant photoemission [28, 29]

$$T = V^0_{\text{rad}} + \sum_{j,m} V^j_{\text{AI}} \frac{|m,j\rangle\langle m,j|}{\hbar\omega + E_g - E_m + i\Gamma_m/2} V^j_{\text{rad}}, \tag{15.6}$$

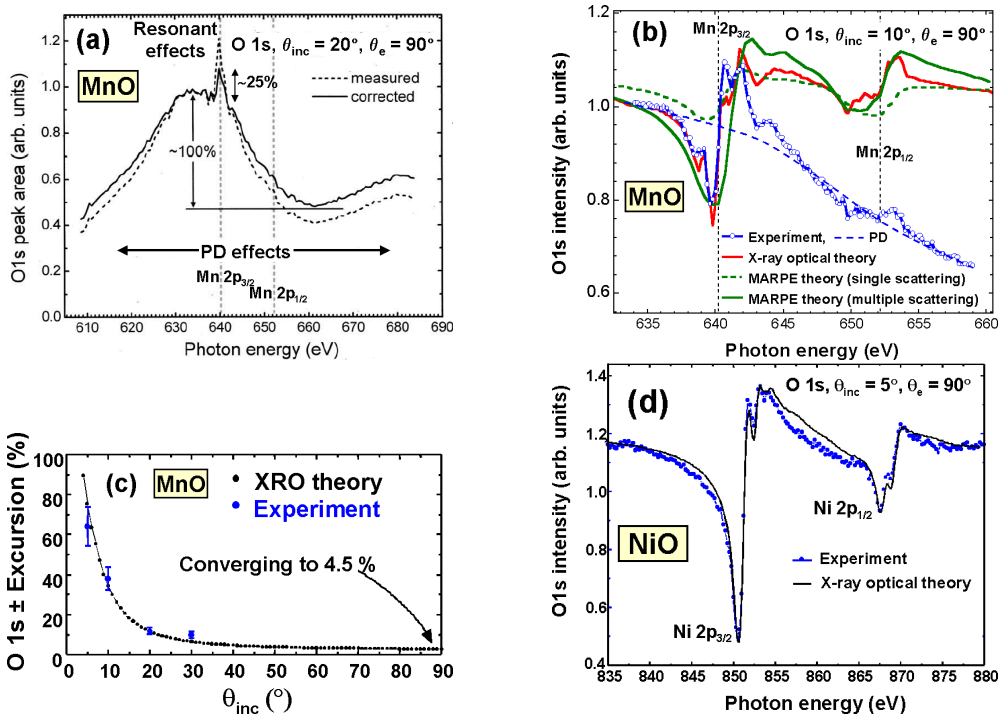

Figure 15.15: Resonant soft X-ray effects on O 1s emission from MnO and NiO on crossing the relevant transition-metal 2p absorption edges. (a) O 1s emission at a 10° exit angle from an MnO single crystal with (001) surface orientation, with photon energy scanned over a broad range which also reveals strong photoelectron diffraction (PD) effects. The dashed curve is as measured, and the solid curve is after correction for detector non-linearity. (b) As (a), but for a smaller energy range and with a 5° exit angle. Also shown are theoretical curves from the X-ray optical model and the microscopic MARPE theory with and without consideration of multiple scattering in the matrix elements. (c) The calculated variation of the overall $\pm$ excursion of the resonant effect in crossing the Mn $2p_{3/2}$ absorption edge as a function of X-ray incidence angle is compared to experimental data at four points. (d) As (b), but for O 1s emission from NiO(001) and with experiment corrected via the removal of a smooth PD curve and both curves renormalized to agree at the left and right ends. Note that the % variations in both experiment and theory have not been adjusted in any of the panels here. [From refs. [20] and [26].]

where $V^0_{\rm rad}$ is the interaction of the radiation with the emitter, $V^j_{\rm rad}$ is the interaction with the resonating atom j, $V^j_{\rm AI}$ is the autoionizing Coulomb interaction (cf. Fig. 15.16(b)) between the emitter and atom j, E_g is the ground state energy, and the sums are over both Mn atoms j and their intermediate many-body states $|m, j\rangle$ of energy E_m and width Γ_m. A fully general theory of MARPE should also include exchange effects in the matrix elements above, but we expect them to be negligible for the cases we are treating. There is also a formal connection between MARPE and interatomic Auger electron emission, since the same sorts of matrix elements are embedded in the expressions describing both. However, the overall processes are fundamentally different, since the interatomic Auger process can be viewed as a a two-step

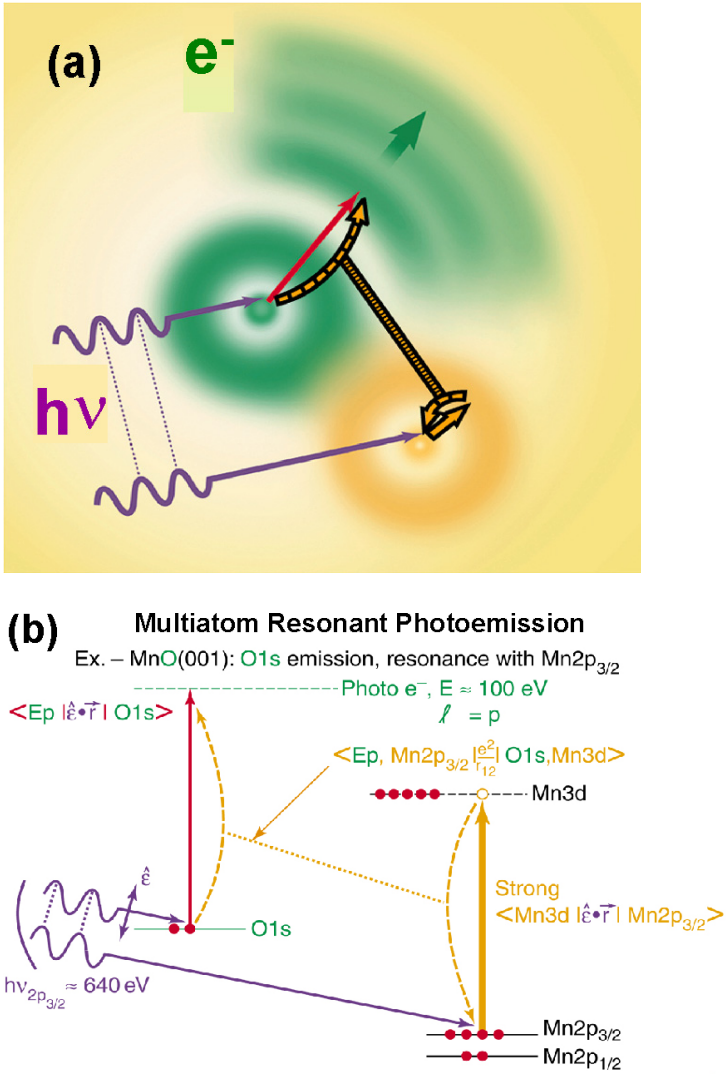

Figure 15.16: (a) Illustration of the basic process occurring in multiatom resonant photoemission (MARPE). (b) Additional diagram of the electronic transitions involved in the MARPE process, for the specific case of O 1s emission from MnO and with the photon energy passing over the Mn $2p_{3/2}$ absorption resonance. [After refs. [20] and [22].] See also color figure on page 472.

phenomenon: creation of the initial hole on a neighbor atom, and then decay of this hole so as to eject an electron from the central atom. A related process is interatomic excitation transfer following the formation of an inner valence hole (compared to a core hole in typical inter-

atomic Auger or MARPE), as recently discussed by Cederbaum and co-workers for atomic and molecular clusters, referred to as interatomic coulomb decay (ICD) [30] and for which experimental evidence has recently been published [31].

We now note two special points that have been considered previously and which make the theory of MARPE in the soft X-ray regime different from other processes occurring at lower excitation energies:

- the shorter wavelengths for soft X-ray excitation imply that retardation effects must be considered in the interaction with the external radiation and in the autoionization interaction, and
- the interatomic autoionization interaction must be generalized to the fully-relativistic Møller formula used previously in high-energy Auger theory [32].

In particular, retardation and relativistic effects lead to a dependence of the interatomic interactions on interatomic distance r_{12} as k^2/r_{12} (see Eq. (15.8) below). Here k is the momentum of the exchanged photon (dotted orange line in Fig. 15.16, which is sufficiently large in core-level MARPE to make this leading term significant (actually it is dominant at large separations in the MnO example discussed below). This is not the case in ICD [30,31], where the exchanged photon energy is small, so that the leading term in the interatomic interaction is provided by the non-retarded dipole-dipole expression, which behaves like $1/r_{12}^3$. A similar behavior in interatomic interactions at low-energy transfers is known as the Forster effect [33]. The transfer rate in the Forster effect is ruled by the square of the interatomic interaction, and therefore, it has been observed to decay like $1/r_{12}^6$ [33(b)]. A more detailed dicussion of the differences between MARPE and the Forster effect appears elswhere [34].

At the level of MARPE theory introduced here, the treatment should be capable of describing all many-electron interactions up to second order in the perturbation via Eq. (15.6), or up to arbitrary order via Eq. (15.5), including those for nearest-neighbors with the greatest overlap and thus enhanced many-electron interactions with the emitting atom.

The near-neighbor autoionization interaction can now be conveniently expanded in multipoles, and, with the further neglect of multipoles higher than dipoles, the effective interaction can be reduced to:

$$V_{\mathrm{AI}}^{j} \approx e^2 r_1 r_2 \sum_{\mu_1\mu_2} F_{\mu_1\mu_2}^{\mathbf{R}_j} Y_{1\mu_1}\left(\hat{\mathbf{r}}_1\right) Y_{1\mu_2}^{*}\left(\hat{\mathbf{r}}_2\right), \tag{15.7}$$

where

$$F_{\mu_1\mu_2}^{\mathbf{R}} = \frac{-4\pi k^3}{3}\left[\frac{\delta_{\mu_1\mu_2}}{2\pi} h_0^{(+)}(kR) + h_2^{(+)}(kR)\, Y_{2\mu_2-\mu_1}\left(\hat{\mathbf{R}}\right) \langle Y_{1\mu_2}|Y_{2\mu_2-\mu_1}Y_{1\mu_1}\rangle\right] \tag{15.8}$$

and the bracket represents a Gaunt integral with standard normalization. Eq. (15.8) is actually the retarded dipole-dipole interaction, which is retrieved from the Møller formula [32] under the assumption that the relevant electronic states have a spatial extension much smaller than both the wavelength and the inter-atomic separation. This is fully justified for the Mn2p and O1s states of our case.

Putting these results into a single expression now yields

$$\begin{aligned} M_{El\mu} &= A\langle E1\,|r|\,O1s\rangle\delta_{l,1}\sum_{\lambda}\varepsilon_{\lambda}^{\text{eff}}\,\langle Y_{1\mu}|Y_{1\lambda}Y_{00}\rangle \\ &= A\langle E1\,|r|\,O1s\rangle\delta_{l,1}\varepsilon_{\mu}^{\text{eff}}/\sqrt{4\pi}, \end{aligned} \tag{15.9}$$

where A is a light-intensity normalization constant,

$$\varepsilon_{\lambda}^{\text{eff}} = \varepsilon_{\lambda} - \sum_{\lambda'\mu_2} F_{\lambda\mu_2}\alpha_{\mu_2\lambda'}\varepsilon_{\lambda'} \tag{15.10}$$

is now the effective polarization vector that includes the effect of resonant X-ray scattering at the Mn sites, and the magnitude of the resonance is controlled by a product of a structure-factor type of sum over Mn sites

$$F_{\lambda\mu_2} = \sum_{j} F_{\lambda\mu_2}^{\mathbf{R}_j} e^{i\mathbf{k}_{inc}\cdot\mathbf{R_j}}, \tag{15.11}$$

and the Mn^{2+} polarizability tensor,

$$\alpha_{\mu_2\lambda'} = -\frac{4\pi e^2}{3}\sum_{m}\frac{\langle g\,|rY_{1\mu_2}^{*}|\,m\rangle\,\langle m\,|rY_{1\lambda'}|\,g\rangle}{\hbar\omega + E_g - E_m + i\Gamma_m/2}. \tag{15.12}$$

The form for the polarizability given here makes it clear that it is directly related to the usual description of resonant photoemission [29].

For the particular case of O 1s emission from MnO, this theoretical development predicts both the optical constants β and δ, and the O 1s intensity variation with reasonable accuracy, as seen in Figs. 15.12 and 15.15(b), respectively. It has furthermore been found by García de Abajo et al. [20, 22] that higher-order terms in the MARPE matrix elements, which can be considered to be multiple scattering of the radiation when resonantly scattered from one of the neighbors to the emitter, must be included in order to quantitatively describe these effects, as illustrated by two of the curves in Fig. 15.15(b). These higher-order contributions can be obtained by replacing epsilon in Eq. (15.10) by the self-consistent polarization vector derived from multiple scattering of the incoming photons at the Mn atoms of the crystal. The latter has been in turn derived from a layer-KKR description of photon scattering at the atomic planes parallel to the surface, yielding an equation similar to 15.10, but involving a dependence of the self-consistent polarization on atomic layer [20]

Although this quantum-mechanical treatment of MARPE effects is much more complex to deal with than the more macroscopic and empirically-linked resonant XRO picture, both have been shown to represent the same physical processes [20]. However, the proper MARPE theory outlined here obviously provides more insight into the nature of these interesting effects and it will also permit treating systems that go beyond what can be dealt with by RXRO, such as nanostructures localized in 1, 2, or 3 dimensions, or free molecules. We also note other treatments of such interatomic resonant photoemission processes, by Forster and later workers [33] and by Cederbaum et al. [30] with very low excitation energies assumed and by Fujikawa and Arai with direct relevance to the theoretical model discussed here [35].

As additional examples of experimental observations of related interatomic resonance effects in photoemission, we note that core-core MARPE effects analogous to those discussed here for MnO [20] and NiO [26, 27] have also been seen in CuO [27]. Similar core-core MARPE effects have also been seen in adsorbates on metals, specifically O on Ni(001) [36] and N_2 on Ru(111) [37]; for these cases also, it appears that the RXRO approach provides at least a semi-quantitative description of the phenomena. In addition, a few other groups have reported the enhancement of *valence* photoemission intensities primarily associated with emission from a certain atom upon tuning the photon energy through more weakly bound core-level or inner-valence absorption edges of a nearby atom, with this work including measurements near solid-solid interfaces [38, 39], on a free molecule [40] and on a free cluster, where the effect has been referred to as interatomic coulomb deday [31]. More recently, Guilleumin et al. appear to have seen core-core MARPE effects in free molecules through a more subtle avenue, specifically, the non-dipole parameter in a photoelectron angular distribution [41].

It is thus clear that such interatomic resonant effects will be seen in other systems in the future, and that they will not all be simply describable using an X-ray optical approach, which in any case does not provide a microscopic understanding of them. Effects going beyond a simple optical picture could provide interesting new information on the precise nature of X-ray interactions, including via the interatomic character, a method for uniquely identifying near-neighbor atoms in a complex sample, as originally proposed [21]. The microscopic theory outlined here, as well as other recent work [30, 35] should provide a sound basis for understanding and using these phenomena in surface and interfaces studies, nanostructure characterization, and molecular and cluster research. We also note the discussion of related optical effects in Chapter 2, Section 8 of this book, in which such phenomena are viewed in terms of screening and local fields.

15.4 X-ray optical effects in X-ray emission and resonant inelastic scattering

The two theoretical approaches outlined here, XRO calculations and microscopic MARPE theory, as well as the use of standing waves, can also be applied to soft X-ray emission (XES) and its close relative resonant inelastic X-ray scattering (RIXS), more bulk sensitive spectroscopic probes that are now coming into wider use [42] and which complement photoemission in the study of almost any system. As to bulk versus surface sensitivity, we point out again via Figs. 15.13(b) and 15.14(a) that, for the case of RIXS in which the incident energy is tuned to various points along an absorption curve like that in Fig. 15.12(a), the degree of bulk sensitivity may vary greatly from one energy to another.

The X-ray optical model can be simply modified to describe the overall intensity in such XES or RIXS experiments more quantitatively. For the case of a homogeneous flat surface, an emitted photon energy that is far from any resonance and with emission at an exit angle θ_{em} that is large enough to minimize refraction and reflection at the surface, this would involve replacing $\Lambda_e \sin\theta'_e$ with $\Lambda_{em} \sin\theta'_{em} \approx \Lambda_{em} \sin\theta_{em}$ in Eq. (15.2), with Λ_{em} equal to the fluorescent X-ray attenuation length along path length or $\lambda_{em}/[4\pi\beta(h\nu_{em})]$ in obvious

notation. With this replacement, Eq. (15.2) becomes

$$I(h\nu_{inc}, hv_{em}) \propto \left| M_{em}(\hat{E}, h\nu_{inc}, hv_{em}, \vec{k})_{em} \right|^2 \cdot \frac{|t(h\nu_{inc})|^2}{\frac{\mathrm{Im}\{4\pi n(h\nu_{inc}) \sin\theta'_{inc}(h\nu_{inc})\}}{\lambda_x(h\nu_{inc})} + \frac{1}{\Lambda_{em}(h\nu_{em}) \sin\theta'_{em}}} \tag{15.13}$$

where the matrix element M_{em} now allows for the precise X-ray transition involved, including the formation of the initial hole and subsequent decay processes, and t is evaluated again from Eq. (15.3), still at the incident wavelength. Equation (15.13) thus represents an accurate method for handling what essentially reduces to the well-known self-absorption effects in X-ray fluorescence that have been discussed previously in connection with MARPE [43, 44]. In fact, viewed in this light, MARPE in X-ray emission can be viewed as having self absorption as a key ingredient, but perhaps via specific near-neighbor effects described in the microscopic theory, not necessarily the only ingredient. This connection has not been recognized in some prior papers on MARPE in X-ray emission [44]. The microscopic model could also be similarly extended to predict fluorescence intensities, but we will not present these details here.

From the point of view of using standing waves to probe buried interfaces (cf. Figs. 15.6–15.11), the greater penetration depths of soft X-rays as compared to photoelectrons represents a significant advantage, since the depth-dependent distribution of intensity will much more closely follow the the standing wave strength $|\vec{E}|^2$, permitting the study of deeper interfaces and a simpler analysis of the data. This is illustrated by comparing Fig. 15.6 for photoelectron emission and Fig. 15.17 for X-ray emission, both based on calculations using the methodology introduced in Fig. 15.5 [19]. Note that the depth profile of X-ray emission from each layer almost exactly follows the standing wave strength, and that deeper layers can be probed if desired. Future experiments of this type using the SWG+wedge method should thus be very interesting.

15.5 Concluding remarks and future directions

In conclusion, soft X-ray optical effects, whether at non-resonant or resonant energies, can strongly influence photoemission intensities. Among these effects are marked decreases in X-ray penetration depth as the total reflection regime is approached, and significant decreases in the secondary electron background underlying photoemission spectra, both of which can be very useful for surface and interface studies. When incident energies are tuned to strong absorption resonances and the total reflection region is approached, these penetration depths can in fact be of the same magnitude as electron inelastic attenuation lengths, thus increasing surface sensitivity markedly.

There can also be significant negative and positive changes in intensity when the absorption edges of an atom neighboring the emitter are crossed, and this can be viewed as multiatom resonant photoemission (MARPE), with potential utility in identifying near-neighbor atoms in complex systems. Both X-ray optical theory and a microscopic theory of interatomic resonant photoemission have been succesfully used to describe these effects, which we expect to be ob-

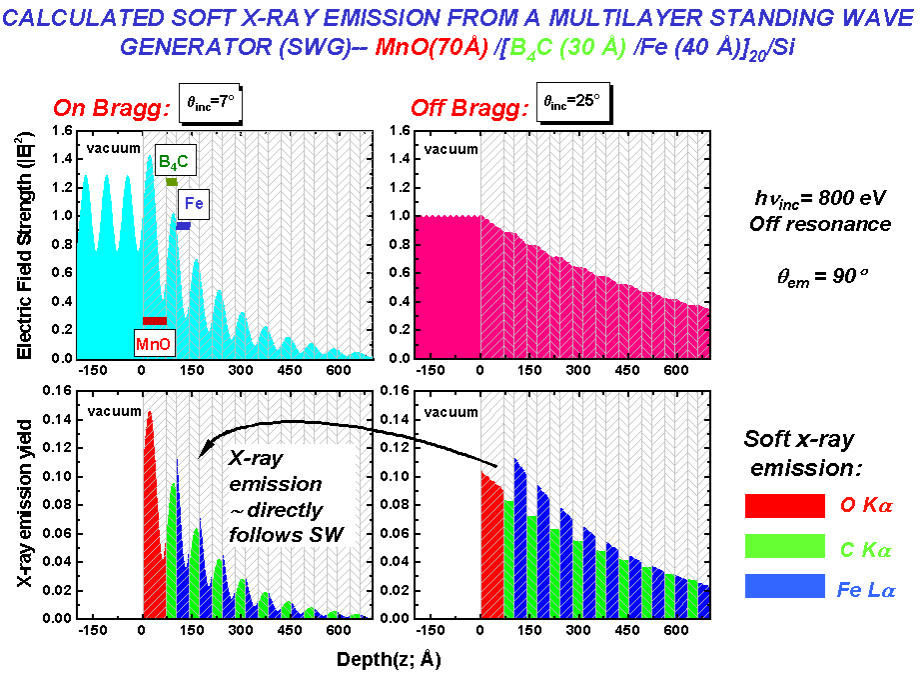

Figure 15.17: X-ray optical calculations of standing wave effects on the depth distributions of electric field strength and soft X-ray emission intensity from an MnO thin-film sample grown on a multilayer B_4C/W mirror. The right panels show the depth distributions when the incidence angle is far from the multilayer Bragg angle, and the left panels the distributions at the Bragg angle. Note the strong standing wave created at the Bragg condition, and the influence on the O Kα, C Kα, and Fe Lα X-ray depth distributions, whose intensity profiles with depth follow very closely the standing wave profile. To be compared with Fig. 15.6 for photoelectron emission. [From ref. [19].]

served in other systems beyond those discussed here in the future, including nanostructures, free molecules, and clusters.

The standing waves created due to reflection from a multilayer mirror can also be used to create a standing wave in the sample with period equal to the multilayer period, e.g. in the few-nanometer range. Photoemission excited by this standing wave can be used to non-destructively and selectively probe a buried interface, include magnetic order via circular dichroism. The multilayer mirror-plus-wedge sample technique discussed here should be applicable to a wide variety of studies of buried interfaces, including multilayer samples and other nanoscale objects that can be grown or deposited on top of a multilayer mirror. Future studies involving X-ray emission or inelastic scattering excited by such standing waves also look very promising. A final interesting potential application of such standing waves is in soft X-ray spectromicroscopy [45–47], which presently provides imaging only in the two dimensions lying in the sample surface plane, with some depth sensitivity in the third dimension

perpendicular to the surface through element- and chemical state-specific X-ray absorption processes. Being able to work at sufficiently low angles of incidence in microscopes making use of secondary electrons and an electron optical system for imaging [45] or in an X-ray reflection, rather than transmission, geometry for another type of microscope making use of Fresnel zone plates for imaging [46, 47], in combination with samples grown on a multilayer mirror, could add much more quantitative information on the perpendicular coordinate.

In summary, being able to thus "tailor" the radiation field in soft X-ray spectroscopic measurements should add considerably to the information derivable from photoemission and related techniques in the future.

References

[1] B.L. Henke, Phys. Rev. A **6**, 94 (1972)

[2] There are several conventions for the signs of δ and β, and we here use one that differs from that of Henke, which was $n = \sqrt{\varepsilon} = 1 - \delta - i\beta$.

[3] (a) One such is that written by E.M. Gullikson, Center for X-Ray Optics, Lawrence Berkeley National Laboratory, and available at: http://www.cxro.lbl.gov/optical_constants/, with related input data compilations in published form at (b) B.L. Henke, E.M. Gullikson, and J.C. Davis. Atomic Data and Nuclear Data Tables **54**, 181 (1993)

[4] M. Mehta and C.S. Fadley, Physics Lett. **55A**, 59 (1975)

[5] M. Mehta and C.S. Fadley, Chem. Phys. Lett. **46**, 225 (1977)

[6] J. Kawai, M. Takami, M. Fujinami, Y. Hashiguchi, S. Hayakawa, Y. Gohshi, Spectrochim. Acta Part B **47**, 983 (1992)

[7] J. Kawai, S. Hayakawa, Y. Kitajima, and Y. Gohshi, Anal. Sci. **11**, 519 (1995)

[8] M.J. Chester and T. Jach, J. Vac. Sci. Technol. B **11**,1609 (1993)

[9] M.J. Chester and T. Jach, Phys. Rev. B **48**, 17262 (1993)

[10] Information on a commercial XPS system making use of total reflection is available under "XPS" at http://www.jeoleuro.com/

[11] D.P. Woodruff, Prog. in Surf. Sci. **57**, 1 (1998)

[12] T. Jach and M.J. Bedzyk, Phys. Rev. B **42**, 5399 (1990)

[13] M.J. Bedzyk, D.H. Bilderback, G.M Bommarito, M. Caffrey, J.S. Schildkraut, Science **241**, 1788, (1988)

[14] K. Hayashi, S. Kawato, T. Horiuchi, K. Matsushige, Y. Kitajima, and Jun Kawai, Appl. Phys. Letters **68**, 1921 (1996)

[15] S.H. Yang, B.S. Mun, A.W. Kay, S-K. Kim, J.B. Kortright, J.H. Underwood, Z. Hussain, and C.S. Fadley, Surf. Sci. **461**, L557 (2000)

[16] S.H. Yang, B.S. Mun, N. Mannella, S-K. Kim, J.B. Kortright, J. Underwood, F. Salmassi, E. Arenholz, A. Young, Z. Hussain, M.A. Van Hove, and C.S. Fadley, J. Phys.-Cond. Matt. **14**, L407 (2002)

[17] B.S. Mun, Ph.D. thesis, University of California Davis, 2002.

[18] S.K. Kim, J.B. Kortright, Phys. Rev. Lett. **86**, 1347 (1999)

[19] S-H. Yang, to be published.

[20] A.W. Kay, F.J. Garcia de Abajo, S.-H. Yang, E. Arenholz, B.S. Mun, N. Mannella, Z. Hussain, M.A. Van Hove, and C.S. Fadley, Phys. Rev. B **63**, 115119 (2001)

[21] A. Kay, E. Arenholz, S. Mun, J. Garcia de Abajo, C.S. Fadley, R. Denecke, Z. Hussain, and M.A. Van Hove, Science **281,** 679 (1998)

[22] F.J. Garcia de Abajo, C.S. Fadley, and M.A. Van Hove, Phys. Rev. Letters **82**, 4126 (1999)

[23] S. M. Goldberg, C. S. Fadley, and S. Kono, Solid State Commun. **28**, 459 (1978); Y. Yeh and I. Lindau, At. and Nuc. Data Tables

[24] C. S. Fadley in *Synchrotron Radiation Research: Advances in Surface and Interface Science*, R. Z. Bachrach, Ed. (Plenum Press, New York, 1992)

[25] S. Tanuma, C.J. Powell, and D.R. Penn, Surf. and Interf. Anal. **35**, 268 (2003)

[26] N. Mannella et al., to be published.

[27] M. Finazzi, G. Ghiringhelli, O. Tjernberg, L. Duo, A. Tagliaferri, P. Ohresser, and N.B. Brookes, Phys. Rev. B **62**, R16215 (2000)

[28] M. Grioni, P. Weibel, M. Hengsberger, and Y. Baer, J. Electron Spectrosc. **103**, 713 (1999); S.L. Sorenson, and S. Svensson, J. Electron Spectrosc. **114**:1, (2001)

[29] A. Tanaka and T. Jo, J. Phys. Soc. Jpn. **63**, 2788 (1994)

[30] L. S. Cederbaum, J. Zobeley, and F. Tarantelli, Phys. Rev. Lett. **79**, 4778 (1997); R. Santra, J. Zobeley, L.S. Cederbaum, F. Tarantelli, Journal of Electron Spectroscopy and Related Phenomena 114–116, 41 (2001); R. Santra, J. Zobeley, and L. S. Cederbaum, Phys. Rev. B **64**, 245104 (2001)

[31] S. Marburger, O. Kugeler, U. Hergenhahn, and T. Moller, Phys. Rev. Letters **90**, 203401 (2003)

[32] J. P. Desclaux, in *Relativistic Effects in Atoms, Molecules, and Solids*, edited by G. L. Malli (Plenum Press, New York, 1981) pp. 115–143

[33] (a) T. Forster, Naturwissenschaften **6**, 166 (1946); Ann. Phys. (Leipzig) **2**, 55 (1948); (b) L. Stryer and R.P. Haugland, Proc. Natl. Acad. Sci. USA **58**, 719 (1967)

[34] C.S. Fadley, E. Ahrenholz, A.W. Kay, F.J. García de Abajo, B.S. Mun, S.-H. Yang, Z. Hussain, and M.A. Van Hove, in *X-ray and Inner Shell Processes*, AIP Conference Proceedings No. 506. R.W. Dunford et al., Eds. (AIP, New York, 2000), p. 251.

[35] T. Fujikawa and H. Arai, J. Electron Spectrosc. **123**, 19 (2002).

[36] D. Nordlund, M. G. Garnier, N. Witowsky, R. Denecke, A. Nilsson, M. Nagasono, N. Martensson, and A. Fohlisch, Phys. Rev. B **63**, 121402 (2001)

[37] P. Feulner, M. Ecker, P. Jakob, K. Kostov, R. Romberg, R. Weimar, and D. Menzel, S.-H. Yang, C.S. Fadley, R. Larciprete, S. Lizzit, A. Föhlisch, W. Wurth, private communication.

[38] K.L.I. Kobayashi, N. Watanabe, H. Nakashima, M. Kubota, H. Daimon, and Y. Murata, Phys. Rev. Lett. **52**, 160 (1984)

[39] P. Pervan, M. Milun, and D.P. Woodruff, Phys. Rev. Lett. **81**, 4995 (1999)

[40] Y.F. Hu, G.M. Bancroft, and K.H. Tan, Inorganic Chemistry 39, 1255-1264 (2000).

[41] . R. Guillemin, D. Rolles, S.W. Yu, A. Wolska, I. Tran, A. Hudson, J. Baker, O. Hemmers and D.W. Lindle, to be published.

[42] J. Nordgren, Ed., special issue on soft X-ray emission spectroscopy, J. Electron Spectrosc. **110,** nos. 1-3 (2000); E.Z. Kurmaev, A. Moewes, D.L. Ederer, X-Ray Spectrometry, **31**, 219 (2002)

[43] E. Arenholz, A.W. Kay, C.S. Fadley, M. Grush, T.A. Callcott, D.L. Ederer, C. Heske, and Z. Hussain, Phys. Rev. B **61**, 7183 (2000)

[44] A. Moewes, E.Z. Kurmaev, D.L. Ederer, T.A. Phys. Rev. B **62**, 15427 (2000); A. Moewes and E. Kurmaev, Nucl. Inst. & Meth. in Phys. Res. A **467** (Pt. 2):1529 (2001)

[45] A. Scholl, H. Ohldag, F. Nolting, J. Stohr, H.A. Padmore, Rev. Sci. Inst. **73**, 1362 (2002)

[46] G. Denbeaux, P. Fischer, G. Kusinski, M. Le Gros, A. Pearson, D. Attwood, IEEE Trans. on Magnetics **37**, 2761 (2001)

[47] A.P. Hitchcock, C. Morin, T. Tyliszczak, I.N. Koprinarov, H. Ikeura-Sekiguchi, Surf. Rev. and Lett. **9**, 193 (2002)

Solid-State Photoemission and Related Methods
Wolfgang Schattke, Michel A. Van Hove (Eds.)

16 Thermal vibrations at surfaces analyzed with LEED

W. Moritz and J. Landskron

16.1 Introduction

A detailed understanding of surface properties necessarily has to include the thermal vibrations. Thermal vibration at surfaces is usually assumed to be larger than in the bulk which follows from theoretical considerations (see for example: [1, 2]) and there are a number of experimental studies showing enhanced vibration amplitudes at surfaces [3–6]. There is further evidence for enhanced anharmonicity at surfaces [7]. A detailed knowledge of the anisotropy and anharmonicity of thermal vibrations at surfaces would allow a better understanding of numerous surface properties like phase transitions, surface reconstructions, adsorption and desorption phenomena and growth processes. The main experimental method to investigate thermal vibration at surfaces is HREELS [45], by which the frequencies of surface phonons and normal modes are measured. This technique has been developed to high accuracy. Why do we need to use a diffraction technique like LEED or surface X-ray diffraction, SXRD, for the analysis of thermal vibrations?

There are two reasons for doing this. The first is the improvement of accuracy of the LEED I/V analysis. A good agreement between experimental and calculated intensities and correspondingly a high accuracy of the structural parameters can only be reached including thermal vibrations. The second reason is that methods to measure vibration amplitudes at surfaces are rare and their determination from LEED intensities would therefore be highly desirable. There are also cases where the assignment of vibration modes to certain atoms is not unambiguous. The surface sensitivity of LEED offers a potential for studying vibration amplitudes at surfaces by temperature dependent measurements which has not been fully used up to now.

As far as the accuracy of the structure analysis is concerned, it is well known in X-ray structure analysis, that the accuracy of the atomic positions obtained with an overall temperature factor is usually improved by an order of magnitude when anisotropic thermal vibrations are considered [9]. In the multiple scattering case the situation will be certainly not better than in the single scattering case. It has been noticed also at the beginning of the development of the LEED theory that the thermal motion is an essential part of the theory [10] and also that LEED would be an adequate method to study thermal motion at surfaces as well [11]. In most of the LEED I/V analysis up to now only harmonic and isotropic vibrations have been considered, because these can be easily treated in the multiple scattering theory and are implemented in the existing programs. The reason why isotropic vibration is considered as sufficient is the following: the comparison between experimental and calculated I/V curves is done by comparing peak positions. A very common criterium for the agreement is Pendry's

Solid-State Photoemission and Related Methods: Theory and Experiment. Edited by Wolfgang Schattke, Michel A. Van Hove

ISBN: 3-527-40334-5

r-factor [12] which mainly compares the position of the peaks in the I/V curves. It is quite safe to argue that the peak positions are mainly determined by the atomic positions and the interatomic distances, while the thermal motion has in general more influence on the height of the peaks. Indeed, one of the reasons to use Pendry's R-factor is to eliminate uncertainties due to the insufficient the treatment of thermal vibrations in the multiple scattering theory, besides further experimental uncertainties. The peak positions therefore can be more reliably evaluated than the peak intensities.

Nevertheless, from the experience in X-ray diffraction we can expect that the extension of the multiple scattering theory to anisotropic and anharmonic vibrations should lead to a better agreement between calculated and measured I/V curves and that the accuracy obtained with LEED can be increased. In many cases, namely for complicated structures, the agreement which can be reached is not very satisfactory and thus the precision of the structure parameters is not as high as is routinely obtained in X-ray structure analysis. Though the isotropic temperature factors are certainly not the only cause of a misfit we can consider it as important factor which limits the accuracy of the structure parameters.

The theory described below [13] is an extension of the method used in current LEED programs by which isotropic vibration is included, namely the assumption of an uncorrelated motion of the surface atoms [14, 15]. As multiple scattering effects play a dominant role in LEED this approximation may be not sufficient. For an accurate description it would be required to include correlated motion in the multiple scattering paths. An applicable theory to include correlation effects has not yet been developed and its influence on the LEED intensities is unknown. Therefore the accuracy by which vibration amplitudes can determined from a LEED I/V analysis may be limited. Nevertheless, the inclusion of anisotropic and anharmonic vibration in the analysis provides an improvement compared to the isotropic case. Further improvement can be expected from a multiple scattering theory which includes correlated motion. The importance of this becomes obvious in RHEED and MEED experiments where the thermal diffuse scattering is strong enough to be measured without large effort. The analysis of the thermal diffuse scattering can be even used as an elegant method to determine directly the local environment of surface atoms, see for example a recent review article by Abukawa and Kono [8].

16.2 Thermal vibration in the kinematic theory of diffraction

We repeat in short the treatment of thermal vibrations in the kinematic theory in order to elucidate the way how anisotropic thermal motion can be included in the multiple scattering theory. A detailed description of the kinematic theory can be found, for example, in Willis & Pryor [16], a more recent review of theoretical and experimental methods to analyze atomic displacements has been given by Kuhs [17]. In the kinematic theory of diffraction the intensity of a reflection is given by

$$I(\vec{q}) = \sum_{i,j} f_i(q) f_j^*(q) e^{i\vec{q}(\vec{r}_i - \vec{r}_j)} \left\langle e^{i\vec{q}(\vec{u}_i - \vec{u}_j)} \right\rangle^2 \delta(\vec{q} - \vec{g}) \tag{16.1}$$

where $\vec{r}_i$,$\vec{r}_j$ are the equilibrium positions of atoms i and j, the sum is taken over all atoms of the crystal. $\vec{u}_i$ and $\vec{u}_j$ are the corresponding displacements at a given time, $\vec{q}$= $\vec{k}$'-$\vec{k}$ is the scattering vector. $f_i(q)$ are the atomic scattering factors. The brackets denote the average in space and time. In this description the displacements include static displacements due to defects like vacancies, interstitial atoms etc. as well as thermal vibrations. It has been therefore proposed to use the expression 'atomic displacement parameter' (ADP) (Kuhs [17] which we will follow here. Assuming a Gaussian distribution of displacements $\vec{u}_i, \vec{u}_j$ the average is given by:

$$\begin{aligned}\langle \exp\left[i\vec{q}(\vec{u}_i - \vec{u}_j)\right]\rangle &= 1 - \frac{1}{2}\left\langle \left[\vec{q}(\vec{u}_i - \vec{u}_j)\right]^2 \right\rangle + \cdots \\ &= \exp\left\{-\frac{1}{2}\left\langle \left[\vec{q}(\vec{u}_i - \vec{u}_j\right]^2 \right\rangle\right\} \\ &= \exp\left\{-\frac{1}{2}\left[\left\langle (\vec{q}\,\vec{u}_i)^2 \right\rangle + \left\langle (\vec{q}\,\vec{u}_j)^2 \right\rangle + \langle (\vec{q}\,\vec{u}_i)\,(\vec{q}\,\vec{u}_j)\rangle\right]\right\}\end{aligned} \tag{16.2}$$

It should be pointed out here that the assumption of a Gaussian distribution is an approximation, which is not in all cases justified, certainly not for static displacements around defects where the displacement depends on the distance from the defect [18]. A better description of the distribution may be even more important for LEED than for X-ray diffraction because in the multiple scattering case resonances may occur in the scattering paths between nearest neighbours. For the same reason a more detailed description of correlated motion should be included. Nevertheless, we use the approximation of a Gaussian distribution here to derive the expression for the kinematic temperature factor. In the following we may assume all atoms as equal for simplicity and obtain for the average

$$\left\langle (\vec{q}\,\vec{u}_i)^2 \right\rangle = \left\langle (\vec{q}\,\vec{u}_j)^2 \right\rangle = \left\langle (\vec{q}\,\vec{u})^2 \right\rangle \tag{16.3}$$

The intensity is obtained as

$$I = |f(q)|^2 \exp\left[-\left\langle (\vec{q}\,\vec{u})^2 \right\rangle\right] \sum_{i,j} \exp\left[i\vec{q}(\vec{r}_i - \vec{r}_j)\right]\left[1 + \langle (\vec{q}\,\vec{u}_i)\,(\vec{q}\,\vec{u}_j)\rangle + \cdots\right] \tag{16.4}$$

and thus can be separated into two terms. The first term is a sharp reflection I_{Bragg}, and second term the thermal diffuse scattering I_{TDS}

$$I = I_{\text{Bragg}} + I_{\text{TDS}} \tag{16.5}$$

The atomic displacements result in a reduction of the elastic scattered Bragg intensity by a factor $\exp(-2M)$

$$\begin{aligned}I_{\text{Bragg}} &= |F(q)|^2\,|T(\vec{q})|^2\,\delta(\vec{q} - \vec{g}) \\ &= |F(q)|^2\,e^{-2M}\delta(\vec{q} - \vec{g})\end{aligned} \tag{16.6}$$

with

$$M = \frac{1}{2}\left\langle (\vec{q}\,\vec{u})^2 \right\rangle \tag{16.7}$$

The intensity missing in the Bragg-peak is the thermal diffuse scattering (TDS). It is distributed over the Brillouin zone and is caused by correlated vibrations occurring in the term $\langle(\vec{q}\,\vec{u}_i)\,(\vec{q}\,\vec{u}_j)\rangle$ in Eq. (16.2). Though the TDS should not be neglected in the LEED I/V analysis their appropriate treatment in the multiple scattering theory is not solved. The treatment described in Section 16.4 neglects the thermal diffuse scattering. In the following only the Bragg intensity is described. Experimentally it has been found that the single phonon part is distributed as 1/q from the Bragg-peak, while the multiphonon part is more equally distributed in reciprocal space [19]. More recently the thermal diffuse scattering has been investigated by Henzler and coworkers with a high energy resolution combined with a SPA-LEED [20].

In LEED calculations frequently not the displacement parameter u but Debye temperature θ_D is used as parameter. In the high temperature limit the relation to the displacement parameter is given by:

$$\left\langle u^2 \right\rangle = \frac{3\hbar^2 T}{2mk_B\theta_D^2} \tag{16.8}$$

An alternative derivation of the temperature factor is obtained when the average in the left hand side of Eq. (16.2) is calculated from the distribution of the atomic displacements, the probability density function, PDF. The atomic Debye-Waller factor exp(-M) is then given

$$T(\vec{q}) = \int p(\vec{u}) e^{i\vec{q}\vec{u}} d\vec{u} \tag{16.9}$$

which is equivalent to

$$T(\vec{q}) = \exp(-\frac{1}{2}\left\langle(\vec{q}\,\vec{u})^2\right\rangle \tag{16.10}$$

in case the PDF is a Gaussian distribution. The probability density p(u) is in general not bound to a Gaussian distribution. When the temperature factor has been experimentally determined the corresponding probability density function can be obtained by the reverse Fourier transform of the temperature factor:

$$p(\vec{u}) = (2\pi)^{-3} \int T(\vec{q}) \exp(-i\vec{q}\,\vec{u})\; d\vec{q} \tag{16.11}$$

16.2.1 Harmonic vibrations

In the harmonic approximation the distribution of atomic displacements described by the probability density function PDF can be assumed as Gaussian distribution in the high temperature limit.

For isotropic vibrations the distribution is defined by a single parameter, the mean square displacement.

$$P(u) = \left(2\pi \left\langle u^2 \right\rangle\right)^{-3/2} \exp\left(-\frac{u^2}{2\left\langle u^2 \right\rangle}\right) \tag{16.12}$$

The atomic Debye-Waller factor is given by the Fourier transform of the probability density function

$$T(q) = \exp\left(-\frac{1}{2}q^2 \left\langle u^2 \right\rangle\right) \tag{16.13}$$

In case of anisotropic vibration, assuming mean square displacements in the directions of Cartesian coordinates, the atomic Debye-Waller factor is given by

$$T(\vec{q}) = \exp\left(-\frac{1}{2}q^T \left\langle u^T u \right\rangle q\right) \tag{16.14}$$

using the conventional crystallographic formulation, u^T denotes the transpose of a vector. The probability density function is given by

$$P(\vec{u}) = \left(\frac{\det B^{-1}}{8\pi^2}\right) \exp\left(-\frac{1}{2}u^T B^{-1} u\right) \tag{16.15}$$

with a symmetric matrix

$$B = \begin{pmatrix} \left\langle u_x^2 \right\rangle & \left\langle u_x u_y \right\rangle & \left\langle u_x u_z \right\rangle \\ \left\langle u_x u_y \right\rangle & \left\langle u_y^2 \right\rangle & \left\langle u_y u_z \right\rangle \\ \left\langle u_x u_z \right\rangle & \left\langle u_y u_z \right\rangle & \left\langle u_z^2 \right\rangle \end{pmatrix} \tag{16.16}$$

The exponent $\vec{u}^T B^{-1} \vec{u}$ is a quadratic function of the atomic displacements so that with $\vec{u}^T B^{-1} \vec{u} = const.$ an ellipsoid can be defined. Conventionally an ellipsoid is used such that the integral over the volume of the ellipsoid is 0.5. The six independent matrix elements describe the length of the axes and the orientation of the ellipsoid

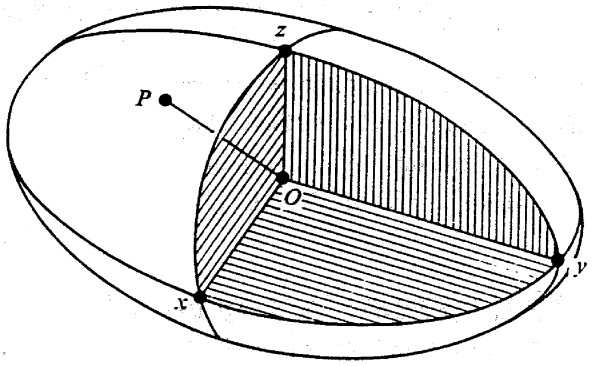

Figure 16.1: Ellipsoid of vibration amplitudes, the lengths Ox, Oy, Oz are proportional to the rms-displacements in the corresponding direction. $Ox \propto \sqrt{\langle u_x^2 \rangle} \equiv u_x$, $Oy \propto \sqrt{\langle u_y^2 \rangle} \equiv u_y$, $Oz \propto \sqrt{\langle u_z^2 \rangle} \equiv u_z$

16.2.2 Anharmonic vibrations

Deviations from the Gaussian distribution result from the movement of the atom in an anharmonic potential and lead in general to a deviation from the ellipsoid. For a theoretical calculation of anharmonic lattice vibrations the partition function of the atom in the one-particle potential is required [16]:

$$\langle \exp(i\vec{q}\,\vec{u})\rangle = \frac{\int \exp(i\vec{q}\,\vec{u}) \exp\left(\frac{-V}{k_B T}\right) dV}{\int \exp\left(\frac{-V}{k_B T}\right) dV} \tag{16.17}$$

The exact calculation of Eq. (16.16) is extremely complicated and has been done only in the case of simple metals. In surface structure determinations by LEED anharmonic thermal vibrations have not been considered up to now. On the other side, physical properties like the thermal expansion or temperature dependence of elastic constants can be explained only by anharmonic effects. Enhanced anharmonicity has been found for example on the Cu(110) surface by ion scattering [38]. It is therefore desirable to include anharmonic effects in the multiple scattering theory in addition to anisotropy.

Instead of calculating the one particle potential and the atomic movements there exist two possibilities to include anharmonic terms in the kinematic theory by a deformation of the thermal ellipsoid. The temperature factor can be expanded in moments [21]:

$$\langle \exp(i\vec{q}\,\vec{u})\rangle = \sum_{N=0}^{\infty} (1/N!) \left\langle (\vec{q}\,\vec{u})^N \right\rangle \tag{16.18}$$

or in cumulants [22]:

$$\langle \exp(i\vec{q}\,\vec{u})\rangle = \exp\left(\sum_{N=0}^{\infty} (1/N!) \left\langle (\vec{q}\,\vec{u})^N \right\rangle_{\text{kum}} \right) \tag{16.19}$$

The cumulant expansion has the advantage that in the harmonic case all cumulants with the order higher than 2 vanish, which helps to identify and separate anharmonicity effects. For LEED the application of these expansions in Cartesian coordinates is not quite appropriate as an expansion of the PDF in spherical harmonics is used.

Experiments on surfaces are rare, one example is the motion of Cs on Cu(110) determined by X-ray diffraction [23]

Anharmonicity occurs also in a number of special cases, e.g. libration modes and free rotation of molecules. Such cases can be considered in the kinematic theory, see for example Press [24] and require a treatment different from the conventional formalism described above and will be omitted here. The implementation of libration modes in the multiple scattering theory seems to be straightforward but has not yet been worked out.

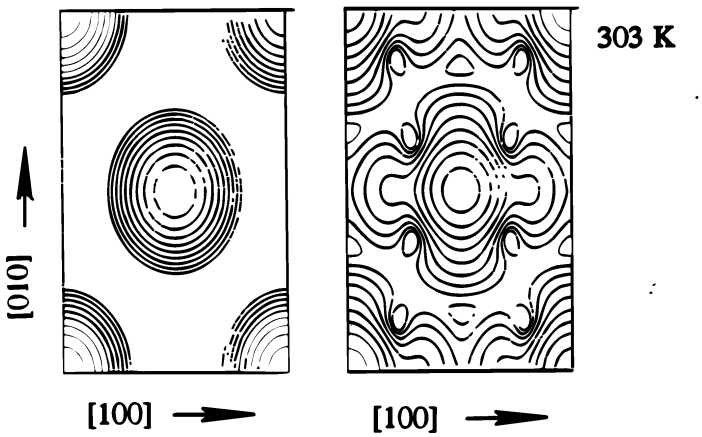

Figure 16.2: Example of anharmonic displacements at surfaces. The figure shows the PDF of Cs on Cu(110) at 303 K. The left panel shows the result of the analysis restricted to harmonic displacements, the right panel shows the result of the refinement allowing for anharmonic displacements (from Meyerheim et al., 1995 [23]).

16.3 Multiple scattering theory

In the multiple scattering theory the diffracted intensity is formally described in the same way as in the kinematic theory by summing up the scattering amplitudes:

$$I(\vec{k}', \vec{k}) = \left| \sum_{\nu} F_{\nu}(\overrightarrow{k'}, \overrightarrow{k}) \cdot e^{i(\overrightarrow{k'} - \overrightarrow{k})\vec{d}_{\nu}} \right|^2 \tag{16.20}$$

the only difference is that atomic scattering factors $F_{\nu}(\vec{k}', \vec{k})$ are generalized scattering factors which represent all scattering paths ending in atom and depend explicitly on the wave vectors $\vec{k}$ and $\vec{k}'$ of both, the incoming and diffracted beam. The generalized scattering factors depend also on the structure surrounding that atom in contrast to the kinematic theory where the atomic scattering factors depend on the scattering vector $\vec{q}$ = $\vec{k}$' - $\vec{k}$ and are independent of the structure. The generalized scattering factors are usually calculated in a spherical wave expansion as T-matrices and are given by:

$$F_{\nu}(\overrightarrow{k'}, \overrightarrow{k}) = \sum_{lm,lm} (-1)^m Y_{l-m}(\vartheta_k, \varphi_k) \cdot T_{v,lm,lm}(\overrightarrow{k}) \cdot Y_{lm}(\vartheta_{k'}, \varphi_{k'}) \tag{16.21}$$

$Y_{lm}(\vartheta_k, \varphi_k)$ are the spherical harmonics. The T-matrices result from the solution of a self-consistent equation which takes account of the multiple scattering processes:

$$T_{\nu}(\overrightarrow{k}) = t_{\nu}(E) + t_{\nu}(E) \cdot \sum_{\mu \neq \nu} G_{\nu\mu}(\overrightarrow{k}, \overrightarrow{P} + \overrightarrow{d}_{\mu} - \overrightarrow{d}_{\nu}) T_{\mu}(\overrightarrow{k}) \tag{16.22}$$

The indices lm,l'm' have been dropped here for convenience. The derivation of Eq. (16.22) and the definition of the matrices $T_{\nu}(\vec{k})$ and the electron propagator functions $G_{\nu\mu}(\overrightarrow{k}, \overrightarrow{P})$

can be found in text books (Pendry 1972 [15] and Van Hove 1986 [14]. The matrices $t_\nu(E)$ describe the single scattering processes and are diagonal in case of spherical symmetric potentials. Introducing the atomic displacement u of an atom the diffracted intensity is given by:

$$I(\overrightarrow{k}', \overrightarrow{k}) = \left\langle \left| \sum_\nu F_\nu(\overrightarrow{k}', \overrightarrow{k}, \overrightarrow{u}_\nu) e^{i(\overrightarrow{k}'-\overrightarrow{k})(\overrightarrow{d}_\nu+\overrightarrow{u}_\nu)} \right|^2 \right\rangle_T \tag{16.23}$$

By multiple scattering the generalized scattering factors depend now on the displacements and therefore the average cannot be restricted to the phase factors due to the displacements as in Eq. (16.1). We neglect correlations and the thermal diffuse scattering and average the scattering amplitudes. This corresponds to the approximation made in the kinematic theory when only the first term of Eq. (16.2) is considered. We obtain for the intensity of the Bragg-scattering:

$$\begin{aligned} I(\vec{k}', \vec{k}') &= \left| \sum_\nu \left\langle F_\nu(\vec{k}', \vec{k}, \vec{u}_\nu)\, e^{i(\vec{k}'-\vec{k})(\vec{d}_\upsilon+\vec{u}_\nu)} \right\rangle_T \right|^2 \\ &= \left| \left\langle F_\nu(\vec{k}', \vec{k}) \right\rangle_T \, e^{i(\vec{k}'-\vec{k})\vec{d}_\upsilon} \right|^2 \end{aligned} \tag{16.24}$$

with thermally averaged scattering factors:

$$\left\langle F_\nu(\vec{k}', \vec{k}) \right\rangle_T = \sum_{lm,l'm'} (-1)^m Y_{l-m}(\Omega_k) \left\langle \sum_\upsilon T_\upsilon \left(\vec{k}', \vec{k}\right) e^{i\left(\vec{k}'-\vec{k}\right)\vec{u}_\upsilon} \right\rangle_T Y_{l'm'}(\Omega_k) \tag{16.25}$$

The average in the right hand side of Eq. (16.26) can be defined as averaged T-matrix

$$\left\langle T_\nu(\overrightarrow{k}) \right\rangle_T = \left\langle T_\nu(\overrightarrow{k}, \overrightarrow{u}_\nu) e^{i(\overrightarrow{k}'-\overrightarrow{k})\overrightarrow{u}_\nu} \right\rangle_T \tag{16.26}$$

It has been shown first by Duke and Laramore [10], Holland [25] and by Pendry [15] that in the harmonic approximation the thermally averaged T-matrices are given by solving the multiple scattering equations using the thermally averaged single scattering t-matrices. Correlations between atomic displacements as well as correlations in the multiple scattering series are neglected here:

$$T_\nu(\vec{k}, \langle\vec{u}_\upsilon\rangle) = t_\nu(E, \langle\vec{u}_\upsilon\rangle) + t_\nu(E, \langle\vec{u}_\upsilon\rangle) \sum_{\mu\neq\upsilon} G_{\nu\mu}(\overrightarrow{k}, \overrightarrow{d}_\mu - \overrightarrow{d}_\nu)\, T_\mu(\overrightarrow{k}, \langle\vec{u}_\mu\rangle) \tag{16.27}$$

with

$$t_\nu(E, \langle\vec{u}_\nu\rangle) = \left\langle t_\nu(E) \cdot e^{i(\overrightarrow{k}'-\overrightarrow{k})\,\overrightarrow{u}_\upsilon} \right\rangle_T \tag{16.28}$$

Equation (16.28) means that the multiple scattering equations are solved with the thermally averaged atoms in a rigid lattice, in other words, the electron is scattered by a spherical symmetric potential which is displaced, the deformation of the electron density and the potential is

not considered. In the harmonic approximation and assuming a Gaussian distribution function the average in Eq. (16.29) can be replaced by

$$\left\langle e^{i(\vec{k}'-\vec{k})\vec{u}_\nu} \right\rangle = \exp\left(-\frac{1}{2}\left\langle \left[\left(\vec{k}'-\vec{k}\right)\vec{u}_\nu\right]^2 \right\rangle\right) \tag{16.29}$$

which can be expanded in spherical harmonics leading to a diagonal form of the t-matrices by which complex temperature dependent phase shifts are defined. This formulation makes the calculation of temperature effects especially easy.

Now, if we want to introduce anisotropic and anharmonic vibrations we start from the probability density of atomic displacements.

$$\left\langle e^{i(\vec{k}'-\vec{k})\vec{u}_\nu} \right\rangle = \int p(\vec{u}) e^{i(\vec{k}'-\vec{k})\vec{u}} d\vec{u} \tag{16.30}$$

We can use a multipole expansion of the probability density function $p(\vec{u})$:

$$p(\vec{u}) = \sum_{n,lm} R_n(u) \cdot c_{n,lm} \cdot Y_{lm}(\vartheta_u, \varphi_u) \tag{16.31}$$

where $c_{n,lm}$ are appropriate multipole expansion coefficients and $R_n(u)$ radial functions. It is convenient to derive the expansion coefficients and radial functions from the mean square displacements in different directions assuming Gaussian distributions. The calculation procedure is described below. The multipole expansion of the PDF is not restricted to harmonic vibrations and allows to include anharmonic terms as well. This case requires specific care to select the appropriate parameters, an example will be discussed in Section 16.5. The thermally averaged atomic scattering factor for single scattering is now given by

$$t(T, \overrightarrow{k}', \vec{k}) = t(0, \overrightarrow{k'}, \vec{k}) \cdot \int p(\overrightarrow{u}) \cdot e^{i(\overrightarrow{k}'-\overrightarrow{k})} \overrightarrow{u} d\vec{u} \tag{16.32}$$

where the atomic scattering factor at $T = 0$ is:

$$t(0, \vec{k}', \vec{k}) = \frac{-2\pi i}{k} \sum_l (2l+1) \cdot e^{i\eta_l} \cdot \sin(\eta_l) \cdot P_l(\cos\vartheta_{k,k'}) \tag{16.33}$$

l are the phase shifts. The scattering factors can be written as a diagonal matrix

$$t(0, \vec{k}', \vec{k}) = \frac{-8\pi^2}{k} \sum_{lm,lm} e^{i\eta_l} \cdot \sin(\eta_l) \cdot \delta_{ll} \cdot \delta_{mm} \cdot Y_{lm}(\vartheta_{k'}, \varphi_{k'}) \cdot Y_{l-m}(\vartheta_k, \varphi_k) \cdot (-1)^m \tag{16.34}$$

and for the phase factors a spherical wave expansion can be used.

$$e^{i\overrightarrow{k}\overrightarrow{r}} = \sum_{lm} 4\pi i l \; j_l(kr) Y_{lm}(\vartheta_r, \varphi_r) Y_{l-m}(\vartheta_k, \varphi_k)(-1)^m \tag{16.35}$$

Following the calculation for the isotropic case as given by Pendry [15] and using the same notation we define expansion coefficients for the Fourier transform of the probability density function:

$$\int p(\vec{u}) e^{i(\vec{k}'-\vec{k})\vec{u}} d\vec{u} = \sum_{L,M} \sum_{L',M'} W_{LM,L'M'}\, Y_{LM}(\vartheta_k, \varphi_k) Y_{L'-M'}(\vartheta_{k'}, \varphi_{k'}) (-1)^{M'} \quad (16.36)$$

After multiplying both sides with the spherical harmonics and integrating over the angles we obtain:

$$W_{LM,L'M'} = 16\pi^2 \sum_{n,lm} B_{LM,L'M',lm}\, c_{n,lm} \cdot \int R_n(u) (-1)^{L+L'}\, j_L(ku)\, j_{L'}(ku) u^2 du \quad (16.37)$$

We can now define temperature dependent expansion coefficients of the scattering factors:

$$t(T, \overrightarrow{k}', \overrightarrow{k}) = 8\pi^2 \sum_{lm} \sum_{lm} t_{lm,lm}(T)\, Y_{l,m}(\vartheta_{k'}, \varphi_{k'})\, Y_{l-m}(\vartheta_k, \varphi_k)\, (-1)^m \quad (16.38)$$

with

$$t_{lm,l'm'}(T) = \frac{1}{8\pi^2} \iint t\left(T, \vec{k}', \vec{k}\right) (-1)^m\, Y_{l-m}\left(\vartheta_k, \varphi_k\right) Y_{l'm'}\left(\vartheta_{k'}, \varphi_{k'}\right)\, d\Omega_k\, d\Omega_{k'} \quad (16.39)$$

where $d\Omega_k = \sin^2 \vartheta_k d\vartheta_k d\varphi_k$. Inserting Eq. (16.32), (16.34) and using the expansions in Eqs. (16.36) and (16.37) we obtain:

$$t_{lm,l'm'}(T) = \sum_{LM} \sum_{L'M'} W_{LM,L'M'}\, D_{LM,L'M',lm,l'm'} \quad (16.40)$$

where

$$D_{LM,L'M',lm,l'm'} = \frac{2\pi}{k} \sum_{l"m"} e^{i\eta_l}\, \sin \eta_l\, B_{LM,lm,l"m"}\, B_{LM,lm,l"m"} \quad (16.41)$$

are temperature independent factors and

$$B_{LM,L'M',lm} = \int Y_{LM}\left(\Omega\right) Y_{L'-M'}\left(\Omega\right) Y_{lm}\left(\Omega\right) d\Omega \quad (16.42)$$

with the conditions

$$M - M' + m = 0, \quad |L' - l| \leq L \leq |L' + l|, \quad L + L' + l = \text{even} \quad (16.43)$$

for non vanishing coefficients. Equations (16.40) and (16.41) define a temperature dependent atomic scattering matrix which now contains off-diagonal terms instead of the diagonal matrix, Eq. (16.34), for the case of isotropic displacements. The matrices can be inserted in the conventional LEED programs which requires only slight changes to take care of the non diagonal form.

The maximum number of angular momentum components in temperature dependent t-matrix, Eq. 40, result from the maximum number of phase shifts used ($\widetilde{l}_{\max}+1$) and the limits given in (16.43). It results in

$$l_{\max} = l'_{\max} = \widetilde{l}_{\max}, \qquad L_{\max} = L'_{\max} = 2\widetilde{l}_{\max}, \qquad l''_{\max} = 2L_{\max} \tag{16.44}$$

In the multipole expansion twice the number angular momentum components is required as in the partial wave expansion of the scattering amplitude, i.e. the number of phase shifts. Depending on the number of components in the multipole expansion the matrix of the expansion coefficients (Eq. (16.38)) gets off-diagonal terms. Care has to be taken that a sufficient number of phase shifts is used if large anisotropies occur.

In the case of isotropic and harmonic vibrations the result has to be consistent with the conventional derivation leading to a diagonal matrix. For spherical symmetric vibrations all coefficients $c_{n,lm}$ vanish unless $l, m = 0$ which leads to $L = L'$ and $M = M'$ in Eq. (16.38) and thus to a diagonal form of the matrix of expansion coefficients, see Fig. 16.3. The equivalence to the conventional form is best seen by performing the Fourier transform of the PDF prior to the expansion in spherical harmonics which immediately leads to the same derivation as given by Pendry [15].

16.3.1 Calculation of the multipole expansion coefficients

It is neither very convenient nor practically possible to optimize the expansion coefficients in Eq. (16.31) directly by fitting the experimental data. The appropriate way is to use the conventional parameters of the thermal ellipsoid as free parameters in the analysis. This requires the calculation of expansion coefficients as function of the vibration amplitudes and by this the number of free parameters is reduced as well. For anisotropic harmonic vibration there is a maximum number of 6 independent parameters which define the mean square displacements in three directions and the orientation of the ellipsoid. The multipole expansion in Eq. (16.32), on the other hand, requires the radial functions and a large number of expansion coefficients, their number depends on the ratio of the displacement parameters.

Harmonic vibrations

We assume an anisotropic probability density function

$$P(\vec{u}) = \frac{1}{\sqrt{8\pi^3 \langle u_x\rangle^2 \langle u_y\rangle^2 \langle u_z\rangle^2}} \exp(-\frac{1}{2}\left[\frac{u_x^2}{\langle u_x^2\rangle} + \frac{u_y^2}{\langle u_y^2\rangle} + \frac{u_z^2}{\langle u_z^2\rangle}\right] \tag{16.45}$$

where $\langle u_x^2\rangle$, $\langle u_z^2\rangle$ and $\langle u_z^2\rangle$ are the mean square displacements in x-,y-, and z-direction. For the moment we neglect a rotation of the ellipsoid. This is appropriate in cases where the site

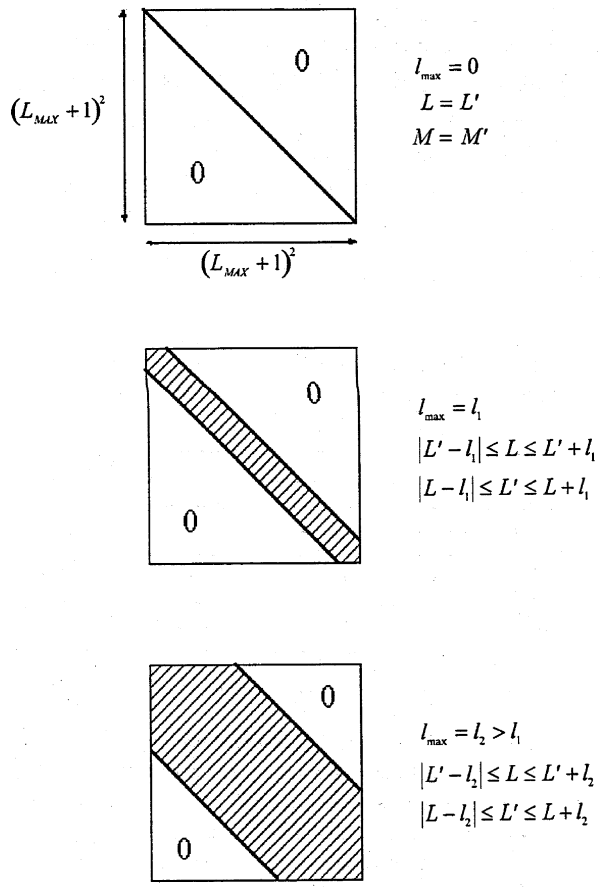

Figure 16.3: Off-diagonal terms in the matrix of the expansion coefficients $W_{LM,L'M'}$, which describe the Debye-Waller factor in angular momentum space, Eq. (16.38).

symmetry of the atom is mm2 and a matching choice of translation vectors parallel to the coordinate axes. For higher site symmetry only the components parallel and normal to the surface, $u_{||}$ and $u_{\perp}$, can be chosen as free parameters in the LEED calculations. The relation is then

$$u_{\shortparallel} = \sqrt{\langle u_x \rangle^2 + \langle u_y \rangle^2} \tag{16.46}$$

and $u_{\perp} = u_z$

We need to calculate the expansion coefficients and the radial functions such that the Gaussian shape of the probability density function is reproduced. The expansion of $P(\vec{u})$ in spherical harmonics can be written as

$$P(\vec{u}) = \sum_{n,lm} c_{n,lm} R_n(u) Y_{lm}(\Omega_u) \tag{16.47}$$

where appropriate radial functions

$$R_0(u) = (2\pi\sigma_0^2)^{-3/2} \exp\left(-\frac{u^2}{2\sigma_0^2}\right) \tag{16.48}$$

$$R_n(u) = u^2\ (2\pi\sigma_n^2)^{-3/2} \exp\left(-\frac{u^2}{2\sigma_n^2}\right), \qquad n \geq 1 \tag{16.49}$$

are used for a Gaussian distribution. The expansion of the ellipsoid in spherical harmonics requires in general high order coefficients, but there are symmetry restrictions. In the expansion in Eq. (16.47) all odd order terms in l vanish because of the centrosymmetry. As the probability distribution is a real quantity there are further general restrictions for the coefficients $c_{n,lm}$:

$$c_{n,l0} = \text{real} \tag{16.50}$$

$$c_{n,l-|m|} = c^*_{n,l|m|} \qquad m \text{ even} \tag{16.51}$$

$$c_{n,l-|m|} = -c^*_{n,l|m|} \qquad m \text{ odd} \tag{16.52}$$

and for harmonic distributions:

$$c_{n,lm} = 0 \qquad l \text{ and } m \text{ odd} \tag{16.53}$$

The number of expansion coefficients needed to match the Gaussian shape of the probability density function depends on the anisotropy of the vibration ellipsoid. The expansion coefficients $c_{n,lm}$ and the widths of the radial functions n are determined from the inverse relation

$$\sum_{n,lm} c_{n,lm} R_n(u) = \int d\Omega_u\ P(\vec{u})\ Y_{lm}(\Omega_u) \tag{16.54}$$

We start from the isotropic case where only one parameter exists, the mean square displacement $\langle u^2 \rangle$, the distribution function is Gaussian. In this case is

$$p(u) \propto e^{-\frac{u^2}{\langle u^2 \rangle}} \tag{16.55}$$

and all the expansion coefficients but $c_{0,00}$ vanish. To calculate the higher order coefficients we use the deviation from the isotropic average:

$$p'(\overrightarrow{u}) = p(\overrightarrow{u}) - e^{-\frac{u^2}{\langle u^2 \rangle}} \tag{16.56}$$

and calculate

$$c_{n,lm} R_{n,lm}\left(\langle u \rangle\right) = \int p'\left(\vec{u}\right) Y_{lm}\left(\Omega\right)\ d\Omega \tag{16.57}$$

The integral can be solved numerically. The validity of the expansion is shown in Fig. 16.4.

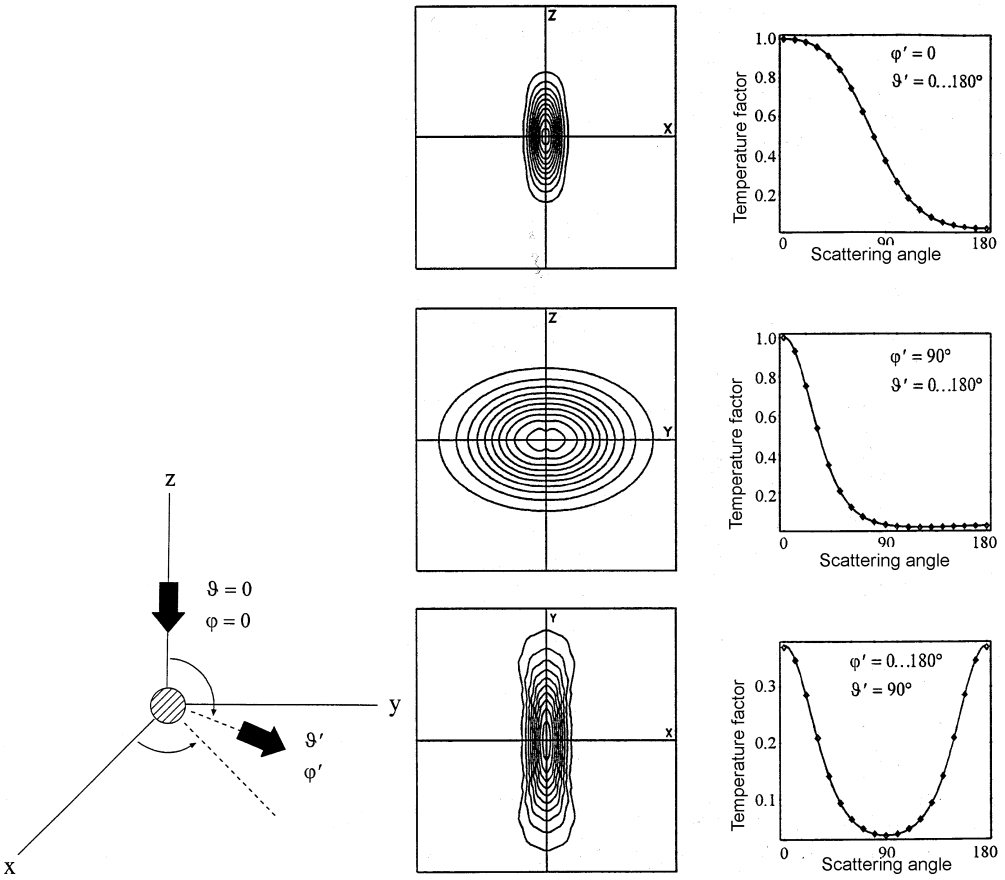

Figure 16.4: Comparison of the exact calculation of the temperature factor (solid line) with the multipole expansion for a thermal ellipsoid with the relation $u_x : u_y : u_z = 1 : 3 : 5$. In the multipole expansion $n = 2$ radial functions and $l_{\max} = 10$ in Eq. (16.30) has been used. The left panel shows the definition of the angles used in the right panel.

For an anisotropy of the vibration amplitudes up to $1 : 10$ two radial functions R_0 and R_1 and $\mathrm{l}_{\max} = 12$ have been found to be sufficient.

The orientation of the ellipsoid of the thermal vibration provides another three degrees of freedom. This is best considered by rotating the atomic t-matrix as has been shown by Nagano and Tong [26]:

$$t^{\mathrm{rot}}_{l_1 m_1, l_2 m_2} = \sum D^{l_1}_{m_1, m'} (\alpha\beta\gamma)\, t_{l_1 m', l_2 m''} D^{*l_2}_{m_2 m''} (\alpha\beta\gamma) \tag{16.58}$$

where appropriate rotation angles have to be defined.

The calculation of the rotation operator $D_{lmm'}(\alpha\beta\gamma)$ can be found in text books on quantum mechanics, see for example [27]. Care has to be taken to apply the sequence of rotations as shown in Fig. 16.6.

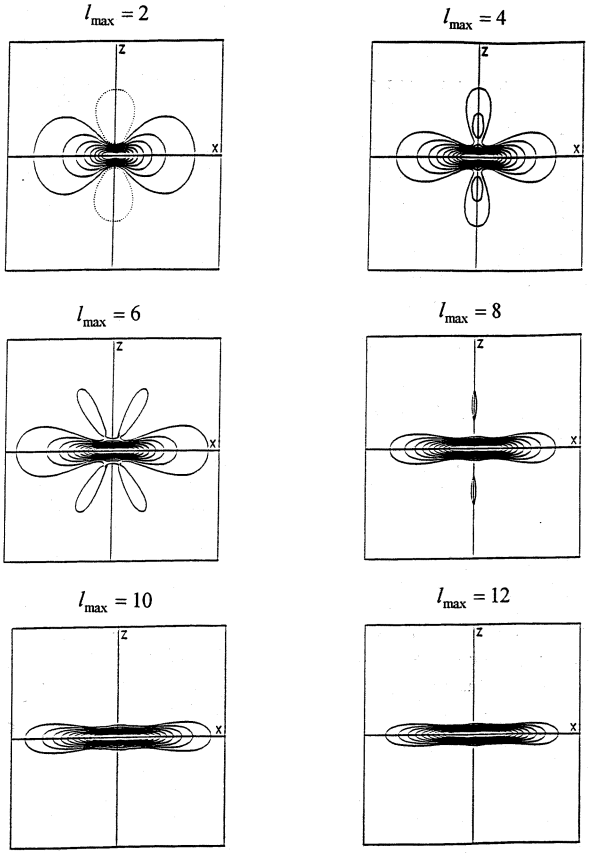

Figure 16.5: Shape of the probability density function obtained with a different number of angular momentum components included in Eq. (16.30). A rotational ellipsoid with a ratio $u_x : u_z = 10$ has been assumed. $l_{\max} = 12$ is required to match the ellipsoidal shape sufficiently close.

Anharmonic vibrations

The expansion in Eq. (16.31) allows to use non-Gaussian probability density functions, so that it is easily possible to treat anharmonic vibrations as well. In Fig. 16.5 it is also evident that the Gaussian shape requires high order coefficients. The number of terms increases with the anisotropy of the ellipsoid which has to be represented in the multipole expansion. An appropriate choice of the parameters allows also to describe static displacements by choosing the appropriate expansion coefficients in accordance with the local symmetry of the site.

Anharmonic vibrations produce a deviation of the PDF from a Gaussian. As the parity of the spherical harmonics is $(-1)^l$, i.e. $Y_{lm}(\pi-\vartheta, \varphi+\pi) = (-1)^l Y_{lm}(\vartheta, \varphi)$ a generalized, non-Gaussian PDF can be expanded as a sum of centrosymmetric and antisymmetric components

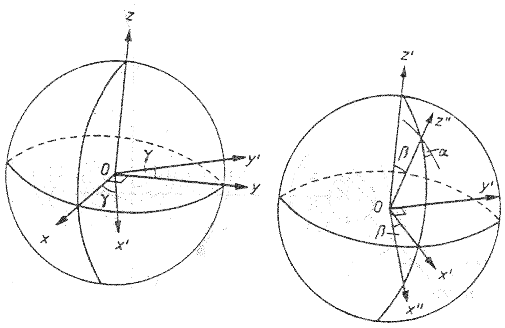

Figure 16.6: Definition of the Eulerian angles for the rotation of the atomic t-matrices.

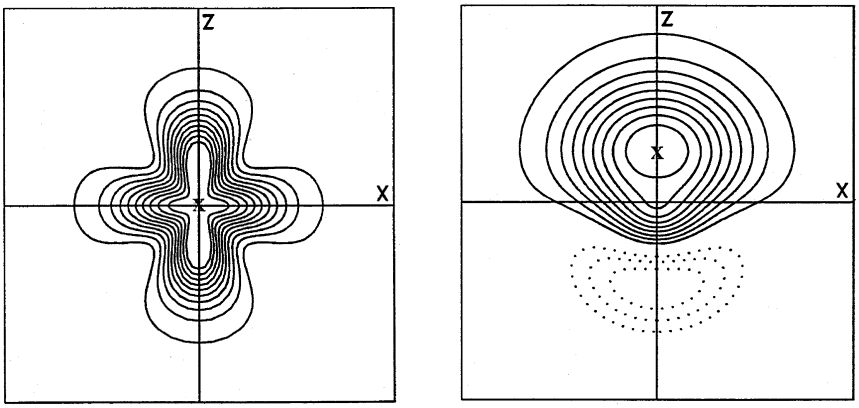

Figure 16.7: Examples of probability density functions resulting from an anharmonic potential. Left panel: PDF obtained from a quadrupol term, right panel: shift of the mean position resulting from odd order coefficients.

(the radial functions are always centrosymmetric):

$$p(\overrightarrow{u}) = \sum_n R_n(u) \left(\sum_{lm} c_{n,lm}\, Y_{lm}(\vartheta,\varphi) + \sum_{l'm'} c_{n,l'm'}\, Y_{l'm'}(\vartheta,\varphi) \right) \tag{16.59}$$

with l even and l' odd. The antisymmetric contributions represent an anharmonic distortion of the Gaussian and shift the first moment (mean) of the PDF which corresponds to the averaged position of the vibrating atom. Anharmonic deviations caused by the centrosymmetric components of the distribution function let the atomic position unchanged but affect the even moments of the distribution and therefore the mean square amplitude in a given direction. In this way the shape of the ellipsoid of thermal vibrations is modified e.g. with lobes constraint by local symmetry of the surface atom. By considering anharmonic effects the number of non-vanishing off-diagonal elements in the atomic t-matrix increases in comparison to the harmonic case.

16.4 Discussion

The multipole expansion of the probability density function provides an easy and obvious way to introduce anisotropic and anharmonic thermal vibration into the multiple scattering formalism. The averaged non-diagonal scattering matrices can be used in the current programs without large changes and also for XPD programs. The computing times become longer, but as large parts of the calculation needs to be done only once the computational effort remains bearable. The expansion coefficients are not appropriate parameters for the refinement, therefore the determination of the necessary number of expansion coefficients to represent a thermal ellipsoid turns out to be a necessary step. In case of anharmonic terms it is unavoidable to visualize the result and to control the calculated PDF.

The method is more appropriate than the previously developed method of split positions [5, 28] which can be even easier incorporated into existing LEED programs, but is limited in the application to special cases and in general requires a large computational effort. By split positions the distribution function is approximated by a small number of discrete positions. The expansion in spherical harmonics is, within the cutoff errors in the series expansion, equivalent to theories using an expansion in Cartesian coordinates [30]. The theory described here treats the multiple scattering effects correctly as long as the influence of correlated motion can be neglected. This is certainly not correct for nearest neighbours and it is just the multiple scattering between nearest neighbours (see Fig. 16.8, right panel) which makes the main contribution to the LEED intensities, next to the single scattering term. The correlation coefficient!of atomic displacements can be defined as:

$$C_{ij} = \frac{\langle (\vec{u}_i \vec{q})\,(\vec{u}_j \vec{q})\rangle}{\left\{\left\langle (\vec{u}_i \vec{q})^2\,(\vec{u}_j \vec{q})^2\right\rangle\right\}^{1/2}} \tag{16.60}$$

and has been calculated for the Debye model [14], as shown in Fig. 16.8 (left panel) as function of nearest neighbour distance. It is obvious that the atomic motion is strongly correlated for small distances. The correlated motion could be considered by distance dependent vibration amplitudes.

In the theory presented here anharmonic effects are introduced in a straightforward manner. The expansion coefficients of the PDF emerge directly from the fit procedure. There are no apriori assumptions whether the vibrating atoms move in a harmonic potential or not. As the PDF is determined by the atomic potential within which the atom vibrates anharmonic contributions to the one particle potential can be analyzed in terms of the resulting PDF itself. Possible applications are for example the determination of diffusion paths near an order-disorder transition or libration modes of molecules.

It is not likely that the determination of anisotropic thermal vibration is distorted by effects resulting from anisotropic atomic potentials. In the LEED calculation usually spherical muffin-tin potentials are used. There have been a few attempts to introduce more general potentials [26,31,32] where it has been found that the largest influence on the I/V curves appears at low energies. The anisotropy of the atomic potential occurs in the outer shell of the muffin tin sphere and this influences the scattering properties mainly at low energies, it becomes most important for VLEED. Anisotropic thermal motion, on the other hand, becomes important at

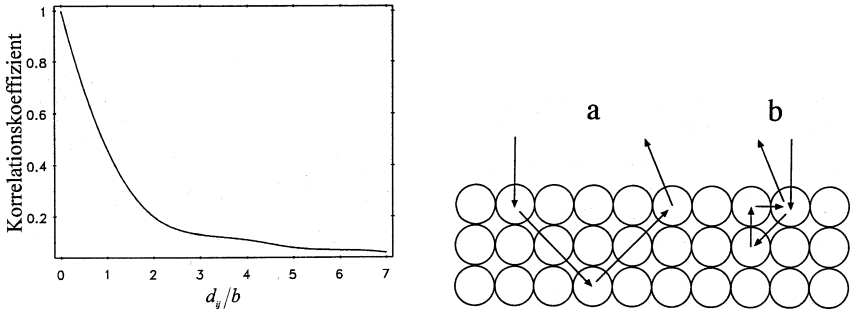

Figure 16.8: Left panel: Correlation coefficient as function of the nearest neighbour distance(after [15]). Right panel: Multiple scattering paths. The strong attenuation of the electron beam renders the multiple scattering between nearest neighbours the most important contribution to the diffracted intensity.

high energies, because of the product $\vec{k}\vec{u}$ in the exponential function. Therefore both effects should be separable.

16.5 Applications

Two examples are shown here where anisotropic vibration amplitudes have been determined in the LEED I/V analysis. For clean metal surfaces small anisotropies are expected and the analysis shows that even these can be detected by temperature dependent LEED measurements. In the second example the vibration amplitudes of CO adsorbed on Ru(0001) is analyzed. Here larger amplitudes are expected due to the bending mode, or libration mode, of the CO molecule.

16.5.1 Cu(110)

The structure and the vibration amplitudes of the Cu(110) surface have been investigated in the past by various methods [33–39]. Cu(110) is a model system where a measurable anisotropy of the vibration amplitudes can be expected due to the two-fold symmetry of the structure, see Fig. 16.9, and the surface has been studied in order to get better insight to the dynamics at surfaces and to understand related phenomena like anharmonicity, the roughening transition and surface melting on solid surfaces. Most of the experimental results agree in the geometry, the top layer spacing is contracted, the second layer spacing expanded. From ion scattering experiments and from theoretical calculations [35] enhanced vibration amplitudes in [001] direction are expected.

In order to analyze the vibration amplitudes with LEED temperature dependent I/V curves have been measured at nine temperatures in the range from 110 to 465 K. The intensities were measured with a video system. The I/V curves of two beams at different temperatures are shown in Fig. 16.10.

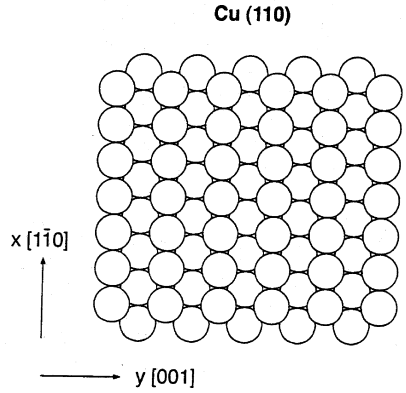

Figure 16.9: Model of the Cu(110) surface. The symmetry allows different vibration amplitudes in $[1\bar{1}0]$ and [001] direction.

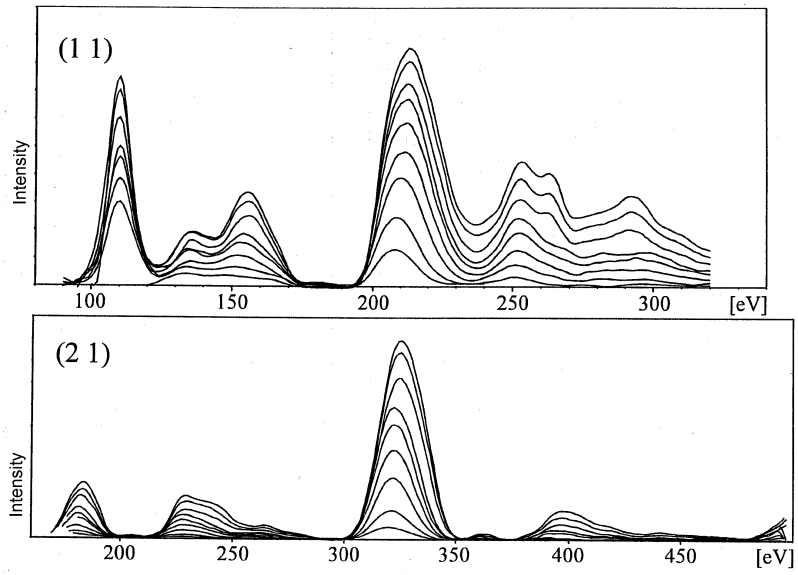

Figure 16.10: Experimental I/V curves from Cu(110) at temperatures between 110 and 465 K.

The main temperature effect is the reduction of the intensity, some of the peak positions shift slightly. In the analysis the comparison of experimental and calculated curves by Pendry's R-factor [12] turned out to be less suited. Therefore R_2, the mean square deviation between experimental and calculated intensities has been used instead.

At first the analysis was done assuming isotropic vibrations. The result is shown in Fig. 16.11.

In the analysis 4 layer spacings were optimized and the vibration amplitudes in the top three layers. In the next step anisotropic vibration amplitudes were introduced in the top layer only. It turned out to be important to use a common scale factor for all I/V curves. The result is shown in Fig. 16.12.

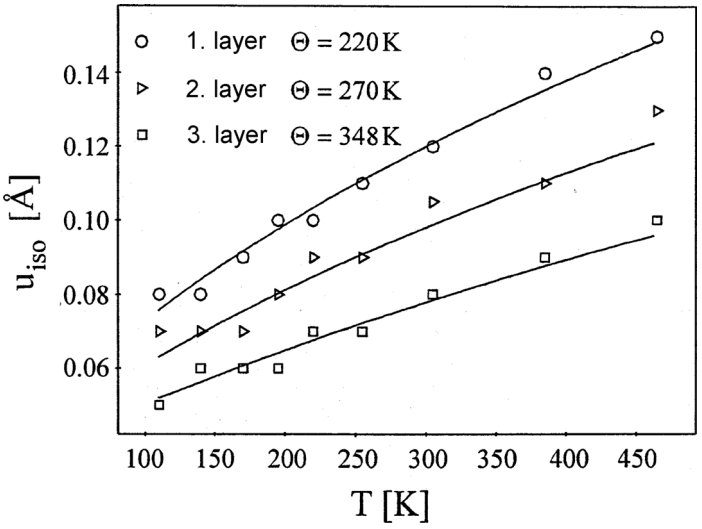

Figure 16.11: Vibration amplitudes for the top three layers in the Cu(110) surface.

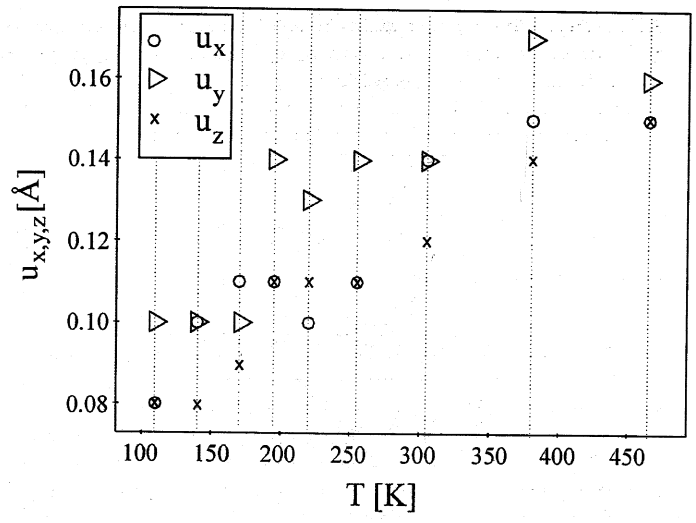

Figure 16.12: Vibration amplitudes in x-, y- and z-direction in the top layer of Cu(110) as a function of temperature.

The amplitudes normal to the surface are more or less the same as determined by assuming isotropic vibrations shown in Fig. 16.11. For the determination of isotropic vibrations the r-factors R_P and R_1 are used with individual scale factors for each beam. This is not appropriate for the determination of anisotropic vibrations, therefore here R_2 with the same scale factor for all beams is used. In the r-factor plot, Fig. 16.13, is clearly an enhancement of the vibration

amplitudes in y-direction, [001], visible. This is in agreement with theoretical calculations [35] and with ion scattering results [7].

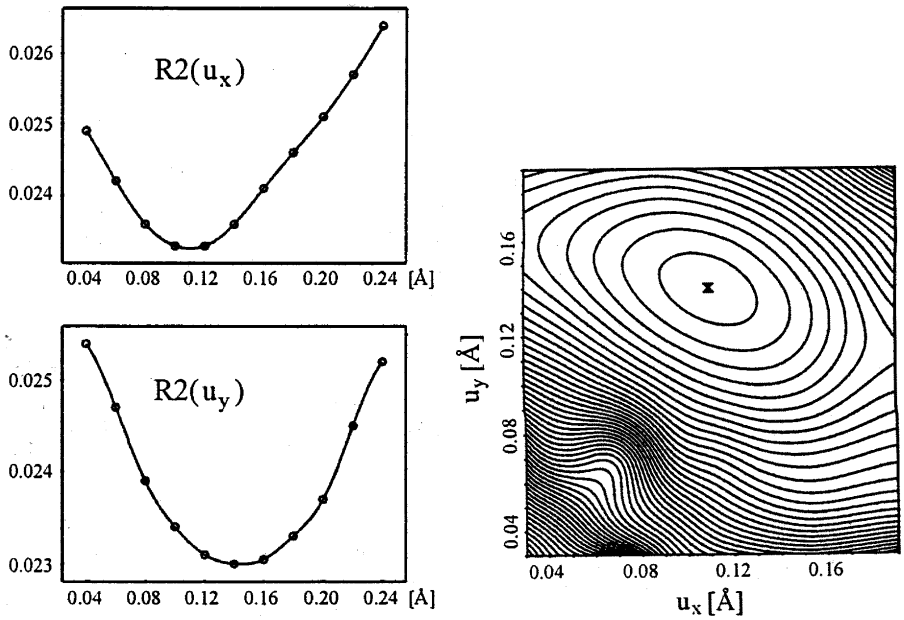

Figure 16.13: R-factors as function of the vibration amplitudes of the top layer in x and y-direction at T=255 K.

16.5.2 CO/Ru(001)

The adsorption of CO on Ru(001) has been extensively studied by various methods, the adsorption geometry has been determined by LEED, ESDIAD and ARUPS [40–42]. In the $\sqrt{3} \times \sqrt{3}$-structure CO occupies the top site and induces a slight buckling in the top Ru layer. The structure model and the notation of the parameters used in the present calculation are shown in Fig. 16.14.

The vibration of the CO molecule has been analyzed with temperature dependent LEED measurements. I/V curves were measured at six temperatures between 25 and 350 K and the anisotropy of the vibration amplitudes of C and O were analyzed using the multipole expansion formalism described above [43]. The same system has been analyzed independently using a coherent superposition of partially occupied positions to simulate anisotropic thermal vibration [5, 28]. The results were practically the same as those obtained with the multipole expansion. Starting from the structure as previously determined with isotropic vibrations [40] the analysis was performed with an optimization of the vertical and parallel vibration amplitudes for C and O together with the structural parameters for each temperature. Note that in this treatment the motions of C and O are independent of each other. As the variation of the vibration amplitude has quite a drastic influence on the superstructure beams, we have

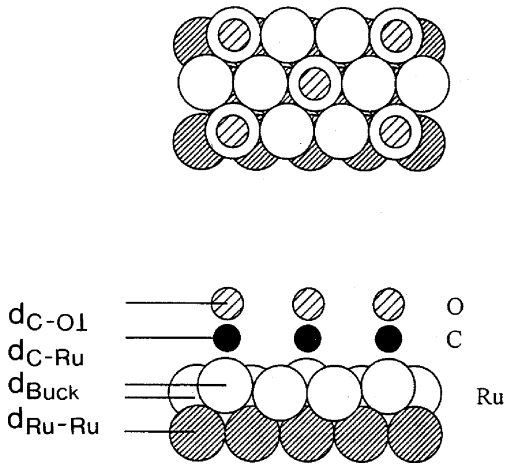

Figure 16.14: Model of the adsorption structure CO/Ru(0001)-$\sqrt{3} \times \sqrt{3}$, (from ref. [43]).

used Pendry's R-factor R_P [12], and a second r-factor R_{DE} [44], both leading to practically the same result. To show how sensitive the superstructure intensities are to the thermal parameters the I/V curves for the (0.67, 1.67) beam are shown in Fig. 16.15, together with the corresponding R-factors for this particular beam, Fig. 16.16.

The R-factors show also a noticeably better agreement between experimental and calculated data with anisotropic than with isotropic vibrations. With isotropic vibrations the R-Factors are $R_P = 0.29$ at 25 K and increase to 0.39 at 350 K, while with anisotropic vibrations the optimum values for RP are 0.26 at 25 K and 0.34 at 350 K. The increase of the R-factors with temperature is commonly observed in LEED-I/V analyses and could be the result of anharmonicity, i.e. non-Gaussian probability density or a dependence of the lateral vibrational amplitude on the azimuthal direction in-plane. In this case a triangular shape of the in-plane PDF is compatible with the symmetry but this cannot be described within the harmonic approximation. Therefore we have tested anharmonic models by including higher terms in the multipole expansion. A deviation from the lateral isotropy in the probability density function could be detected, no improvement of the fit was found. It is indeed not expected from the previous ESDIAD results [41] that preferential directions for the vibration parallel to the surface exist. It is, nevertheless, conceivable that actually the correlated motion of the C and O atoms is important. This cannot be considered in the present formulation of the multiple scattering theory where only uncorrelated motions are possible, as mentioned above. The remaining deviation from ideal fit could also result from defects, whose number increases with temperature.

The results for the temperature dependence of the vibration amplitudes are shown in Fig. 16.17. All amplitudes increase with temperature. The parallel displacement for the oxygen atom is noticeable larger than that for the carbon atom except for the lowest temperature where both amplitudes are equal. Both parallel components are larger than the vertical components. After optimizing the thermal vibrations the structural parameters have been optimized again, but no deviations were detectable within the error limits.

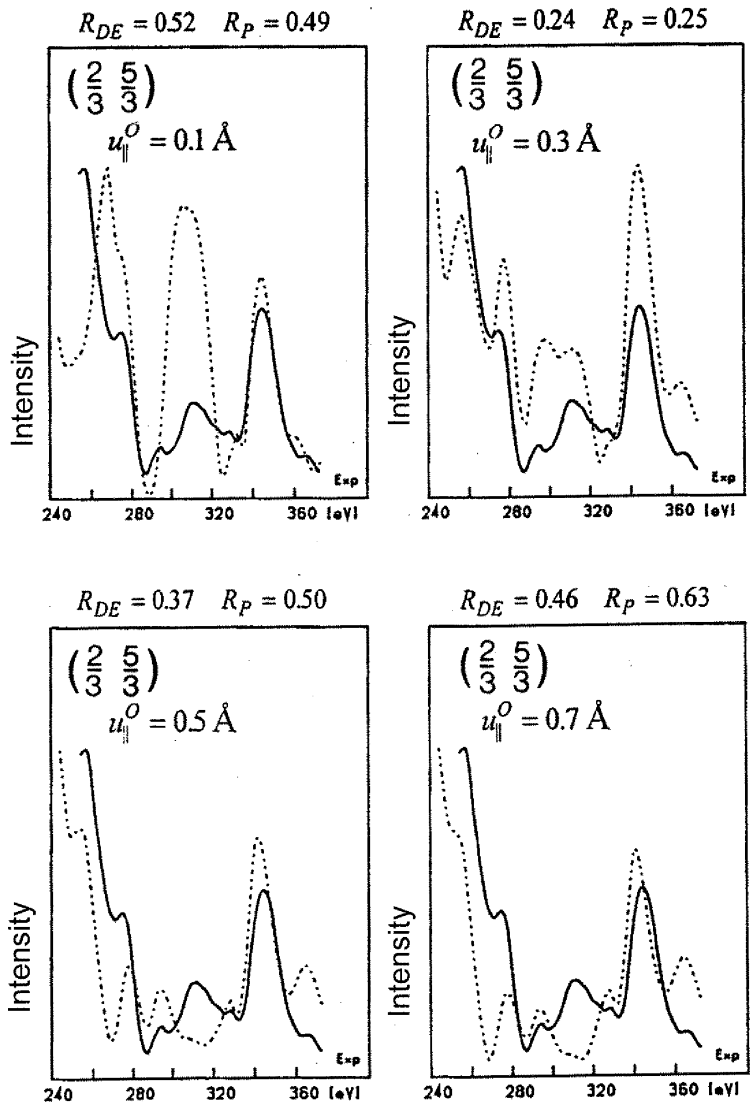

Figure 16.15: I/V curves of the (2/3,5/3) superstructure beam of CO/Ru(001)-$\sqrt{3} \times \sqrt{3}$ illustrating the importance of the temperature factor in the calculation. Full line: experimental curve, dotted line: calculated curves with different vibration amplitudes of the O atom parallel to the surface as indicated in each panel,(from ref. [43]).

16.6 Summary

There have been a number of studies performed where the vibration amplitudes of surface atoms have been determined by LEED. Without intending to give a complete list we just men-

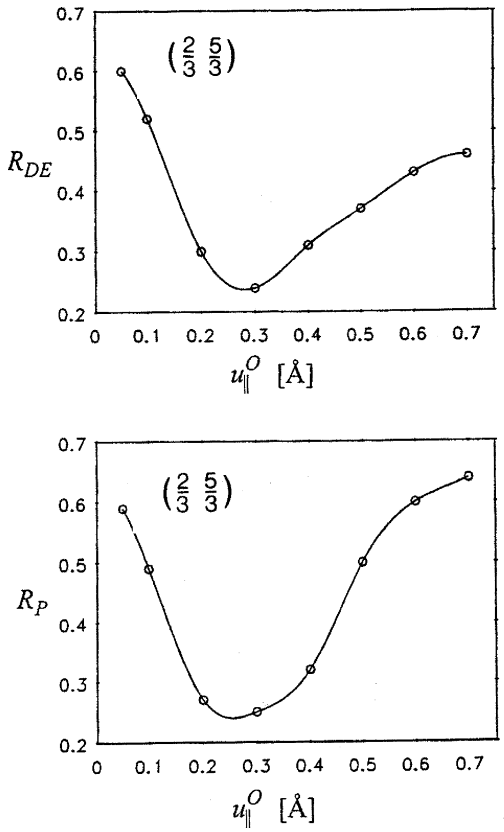

Figure 16.16: R-factors of the (2/3,5/3) superstructure beam of CO/Ru(001)-$\sqrt{3} \times \sqrt{3}$ as function of the parallel component of the vibration amplitude of the oxygen atom, (from ref. [43]).

tion some recent examples, Al_2O_3(0001) [3], Rb/Al(111) [6], K/Cu(100) [4] where enhanced vibration amplitudes have been found. The comparison of the results of different methods has shown the reliability of LEED I/V analyses not only of the geometry but also of thermal vibrations. Further improvement can be obtained by low temperature measurements and inclusion of anisotropic vibrations in the LEED I/V analysis.

The analysis of anisotropic vibration amplitudes has been demonstrated for two cases, the clean Cu(110) surface and an adsorbate system CO/Ru(0001). For the clean metal surfaces the anisotropy of the thermal vibration is small, the anisotropy is small and the clean metal surfaces are certainly a limiting case. Nevertheless, it is shown that a measurable effect exists and the anisotropy can be determined and is comparable with results from other methods, namely, ion scattering and theoretical calculations. It is also obvious that precise measurements are required where all I/V curves can be put on the same scale. The lateral anisotropy of thermal vibration influences the relative intensities between the different beams. For each I/V curve the momentum transfer parallel to the surface is constant. Allowing different scale factors for

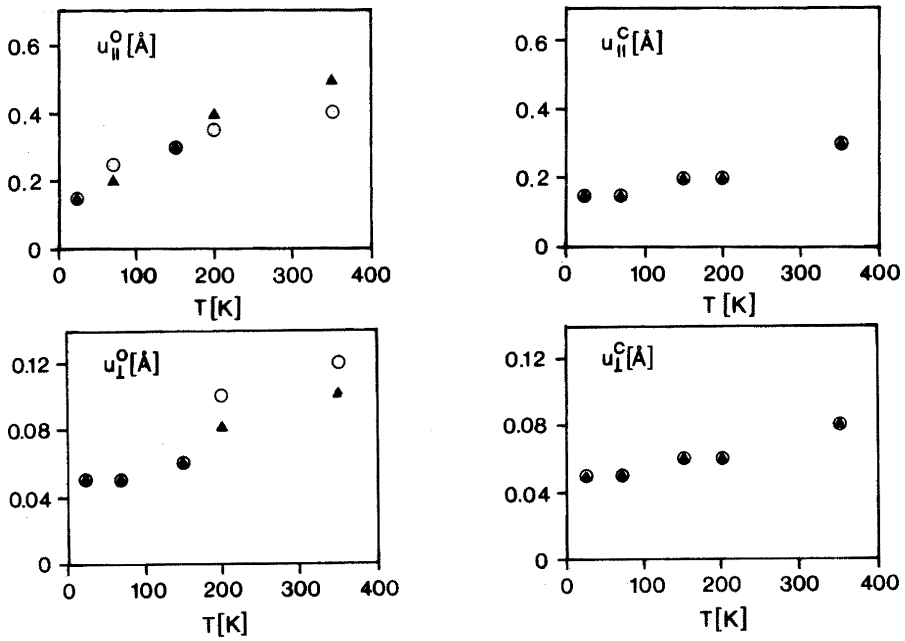

Figure 16.17: Vibration amplitudes of C and O in the CO/Ru(0001)-$\sqrt{3} \times \sqrt{3}$ structure as a function of temperature. The open circles refer to the fit using Pendry's r-factor R_P [12] and the triangles refer to the fit using R_{DE} [44]. $u_{\parallel}^{\mathrm{O}}$ and $u_{\perp}^{\mathrm{O}}$ represent the vibration amplitudes of the O-atom parallel and normal to the surface, $u_{\parallel}^{\mathrm{C}}$ and $u_{\perp}^{\mathrm{C}}$ of the C atom, respectively, (from ref. [43]).

each beam, or eliminating the common scale factor by comparing mainly the peak positions, neglects the most important effect of the temperature factor. The CO/Ru(001)-$\sqrt{3}\times\sqrt{3}$ adsorbat structure represents a case where larger amplitudes occur, where the influence on the I/V curves is larger, especially for weak superstructure beams of higher order. The agreement between experimental and theoretical curves is substantially improved by including anisotropic thermal vibrations.

References

[1] M.C. Desjonquères, D. Spanjaard, Concepts in Surface Physics, Springer Verlag, Berlin, Heidelberg, (1993).

[2] A.A. Maradudin, J. Melnagailis, Phys. Rev 133, A1188 (1964)

[3] C.F. Walters, K.F. McCarty, E.A. Soares, M.A. Van Hove, Surf. Sci. 464 (2000) L732–L738.

[4] U. Löffler, U. Muschiol, P. Bayer, K. Heinz, V. Fritzsche, J.B. Pendry, Surf. Sci. 331, 1435 (1995)

[5] H. Over, W. Moritz, G. Ertl, Phys. Rev. Lett. 70, 315 (1993)

[6] M.M. Nielsen, J. Burchhardt, D.L. Adams, Phys. Rev. B 50, 7851 (1994).
[7] H. Dürr, R. Schneider, Th. Fauster, Vacuum 41, 376 (1990)
[8] T. Abukawa, S. Kono, Progress in Surface Science 72, 19-51 (2003)
[9] C. Giacovazzo, H.L. Monaco, D. Viterbo, F. Scordari, G. Gilli, G. Zanotti and M. Catti, Fundamentals of crystallography, Oxford University Press, 1992,
[10] C.B. Duke, G.E. Laramore, Phys. Rev. B 2, 4765 (1970)
[11] M.G. Lagally, M.B. Webb, in G.A. Somorjai : The Structure and Chemistry of solid Surfaces, Wiley, New York (1969)
[12] J.B. Pendry, J. Phys. C 13, 937 (1980).
[13] W. Moritz, J. Landskron, Surf. Sci. 337, 278 (1995)].
[14] M.A. Van Hove, W.H. Weinberg, C.M. Chan, Low-Energy Electron Diffraction: Experiment, Theory and Surface Determination, Springer-Verlag, Berlin, Heidelberg (1986)
[15] J.B. Pendry, Low Energy Electron Diffraction, Academic Press, 1974
[16] B.T.M. Willis, A.W. Pryor, Thermal vibrations in crystallography, Cambridge University Press, London, (1975)
[17] W.F. Kuhs, Acta Cryst. A 48, 80 (1992)
[18] M.A. Krivoglaz, The theory of X-ray and thermal neutron diffraction by real crystals, Plenum Press, London, (1969)
[19] J.T. McKinney, E.R. Jones, M.B. Webb, Phys. Rev. 160, 532, (1967)
[20] V. Zielasek, A. Büssenschütt, and M. Henzler, Phys. Rev. B 55 (1997) 5398.
[21] P.I. Kuznetsov, R. Stratonovich, V.I. Tikhonov, Theory Probab. Its Appl. 5, 80 (1960)
[22] C.K. Johnson, Thermal neutron diffraction, ed. B.T.M. Willis, Oxford University Press (1970).
[23] H.L. Meyerheim, W. Moritz, H. Schulz, P.J. Eng, I.K. Robinson, Surf. Sci. 331, 1422 (1995).
[24] W. Press, Springer Tracts in Modern Physics Vol. 92 (Springer, NewYork, 1981).
[25] B.W. Holland, Surf. Sci. 28, 258 (1971)
[26] S. Nagano, S.Y. Tong, Phys. Rev. B 32, 6562 (1985)
[27] A. Messiah, Quantum mechanics Vol.II, Walter de Gruyter, Berlin, New York, (1976)
[28] M. Gierer, H. Bludau, H. Over, G. Ertl, Surf. Sci. 346, 64 (1996)
[29] M. Ulehla, H.L. Davis, J. Vac. Sci. Technol. 15, 642 (1978)
[30] V. Fritzsche, Phys. Rev. B 50, 1922 (1994) 301, 346 (1994)
[31] Y. Joly, Phys. Rev. Lett. 68, 950 (1992)
[32] J.-V. Peetz, W. Schattke, J. Electron Spectrosc. (1996).
[33] D. Gorse, J. Lapujoulade, Surf. Sci. 162, 847 (1985)
[34] C.S. Jayanthi, E. Tosatti, L. Pietronero, Phys. Rev. B31, 3456 (1985)
[35] L. Yang, T.S. Rahman, Phys. Rev. Lett. 67, 2327 (1991)
[36] M. Copel, T. Gustafsson, W.R. Graham, S.M. Yalisove, Phys. Rev. B33, 8110 (1986)
[37] I. Steensgaard, R. Feidenhans′l, J.E. Sorensen, Surf. Sci. 128, 281 (1983)
[38] H. Dürr, Th. Fauster, R. Schneider, Surf. Sci. 244, 237 (1991)
[39] D.L. Adams, H.B. Nielsen, J.N. Andersen, Surf. Sci. 128, 281 (1983)

[40] G. Michalk, W. Moritz, H. Pfnür, D. Menzel, Surf. Sci. 129, 92 (1983)
[41] W. Riedl, D. Menzel, Surf. Sci. 163, 39 (1985)
[42] T.E. Madey, Surf. Sci. 79, 575 (1979)
[43] J. Landskron, W. Moritz, B. Narloch, G. Held and D. Menzel, Surf. Sci. 441 (1999) 91.
[44] G. Kleinle, W. Moritz and G. Ertl, Surf. Sci. 238 (1990) 119.
[45] see for example: H. Ibach, Surf. Sci. 299-300 (1994) 116-128.

Solid-State Photoemission and Related Methods
Wolfgang Schattke, Michel A. Van Hove (Eds.)

Color figures

Chapter 2

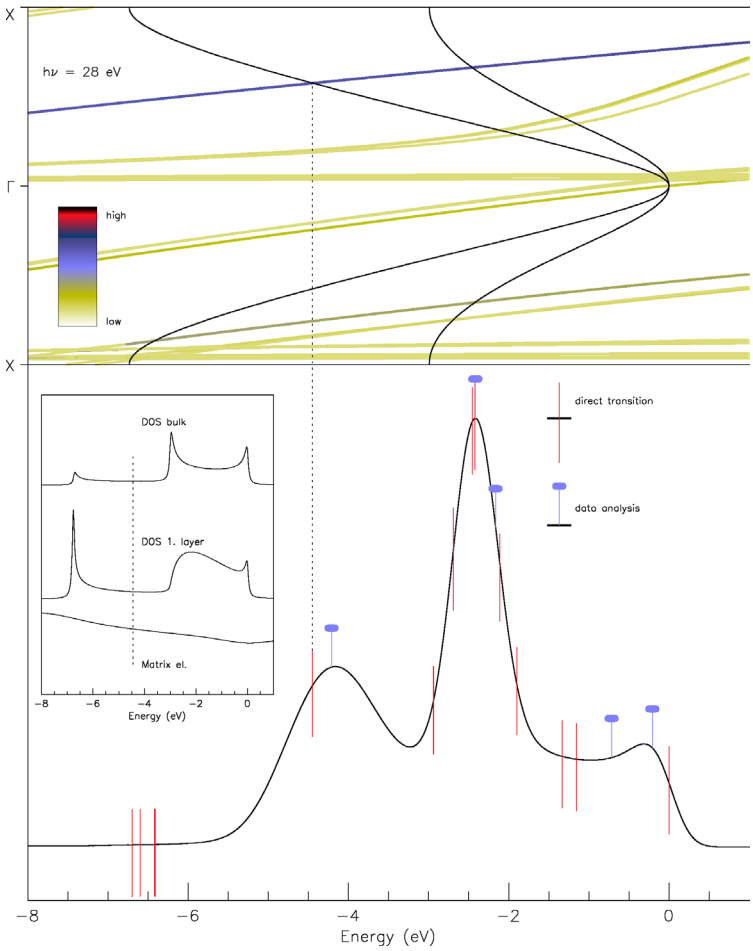

Figure 2.7: Ab initio computed spectrum of GaAs(001) for photon energy 28 eV (lower part) deconvoluted to yield peaks at energies marked by bars with full dots, compared with bare bars mapped from intersections of initial bands (black lines) with final bands (flat curves) shifted by photon energy down to binding energy scale (upper part), one example shown by dotted line; insert shows density of states and a matrix element, position of direct transition near -4.5 eV indicated.

Solid-State Photoemission and Related Methods: Theory and Experiment. Edited by Wolfgang Schattke, Michel A. Van Hove

ISBN: 3-527-40334-5

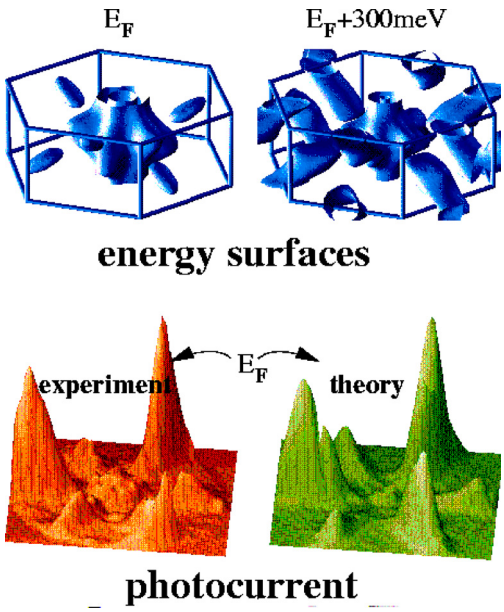

Figure 2.8: Theoretical and experimental pattern of photocurrent into emission hemisphere with $h\nu = 26$ eV from Fermi energy for $TiTe_2(0001)$ (bottom); Fermi surface plot (top left) compared with energy surface slightly above E_F (top right) .

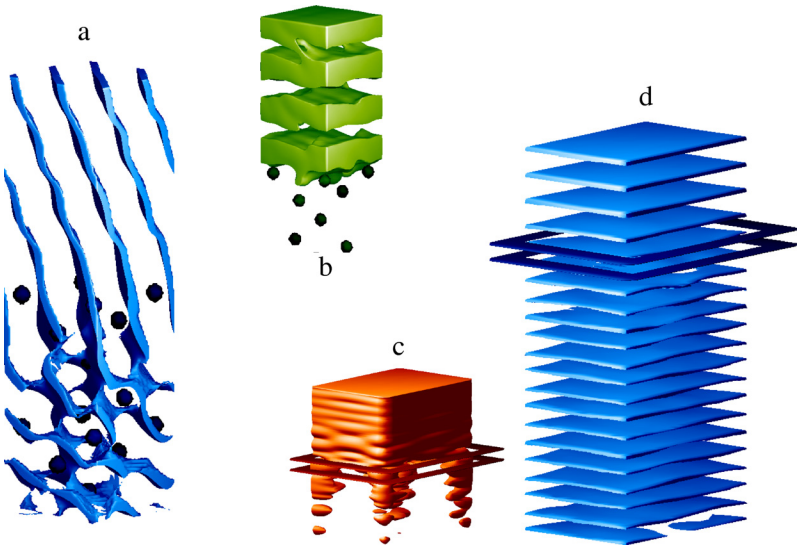

Figure 2.10: Plot of phase, a and d, and modulus, b and c, of wavefunction for Si(001) entering surface from vacuum (top) to solid (bottom), inclied electron escape (a,b), normal escape (c,d); dots show nuclei positions, frame indicates interface.

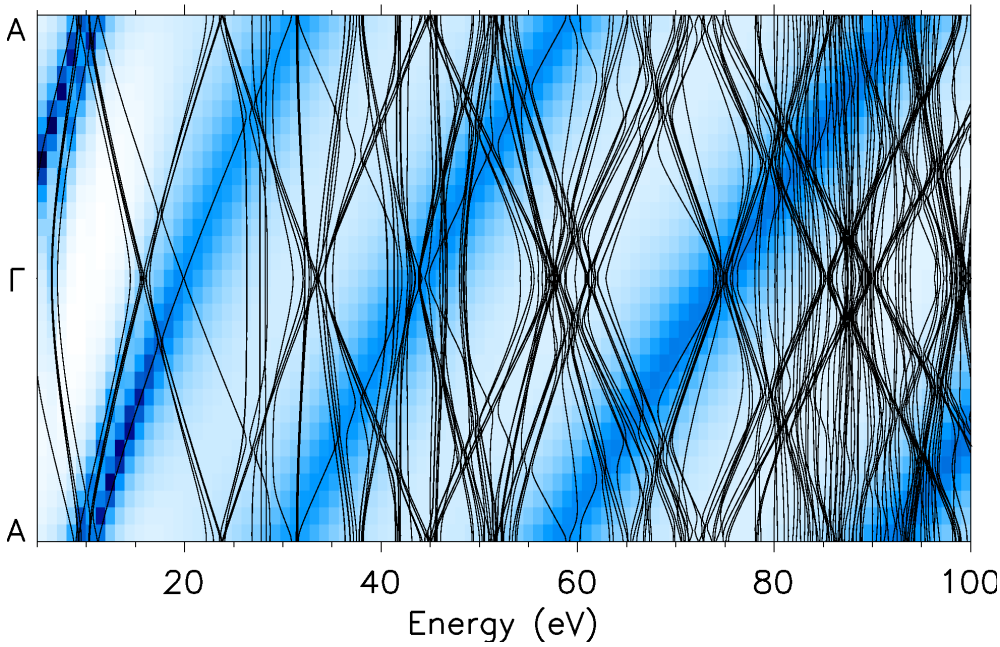

Figure 2.11: Wave functions Fourier transformed along (0001) direction ($A\Gamma A$) of $TiTe_2$(0001), for each energy intensity of shading represents modulus of Fourier coefficient vs. wave vector; real band-structure (black lines)is underlaid.

Chapter 4

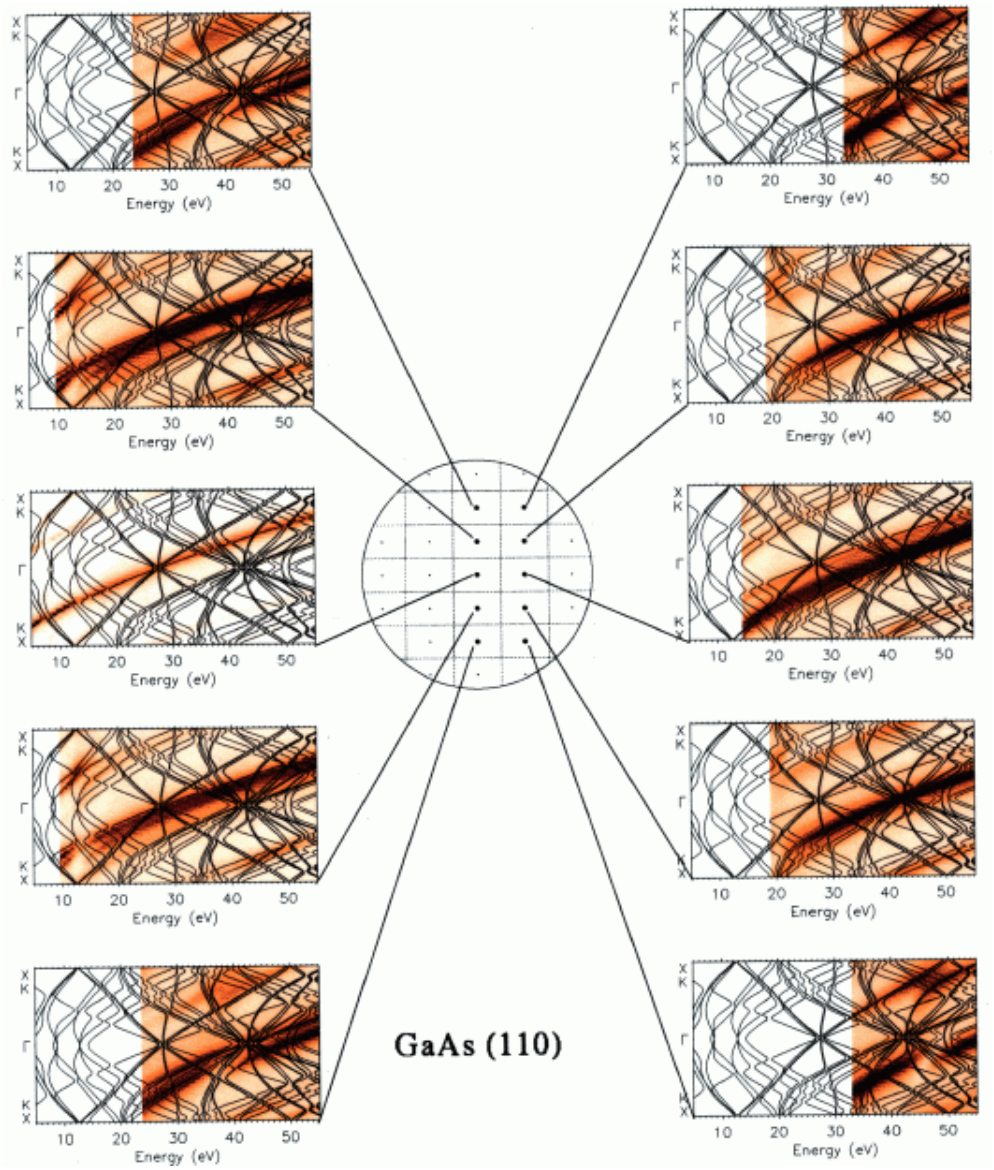

Figure 4.1: Wave vector Fourier decomposition of the inverse LEED state (brown shaded) for several $\bar{\Gamma}$ points with normal emission in center of circle and underlaid pseudopotential band structure (black lines).

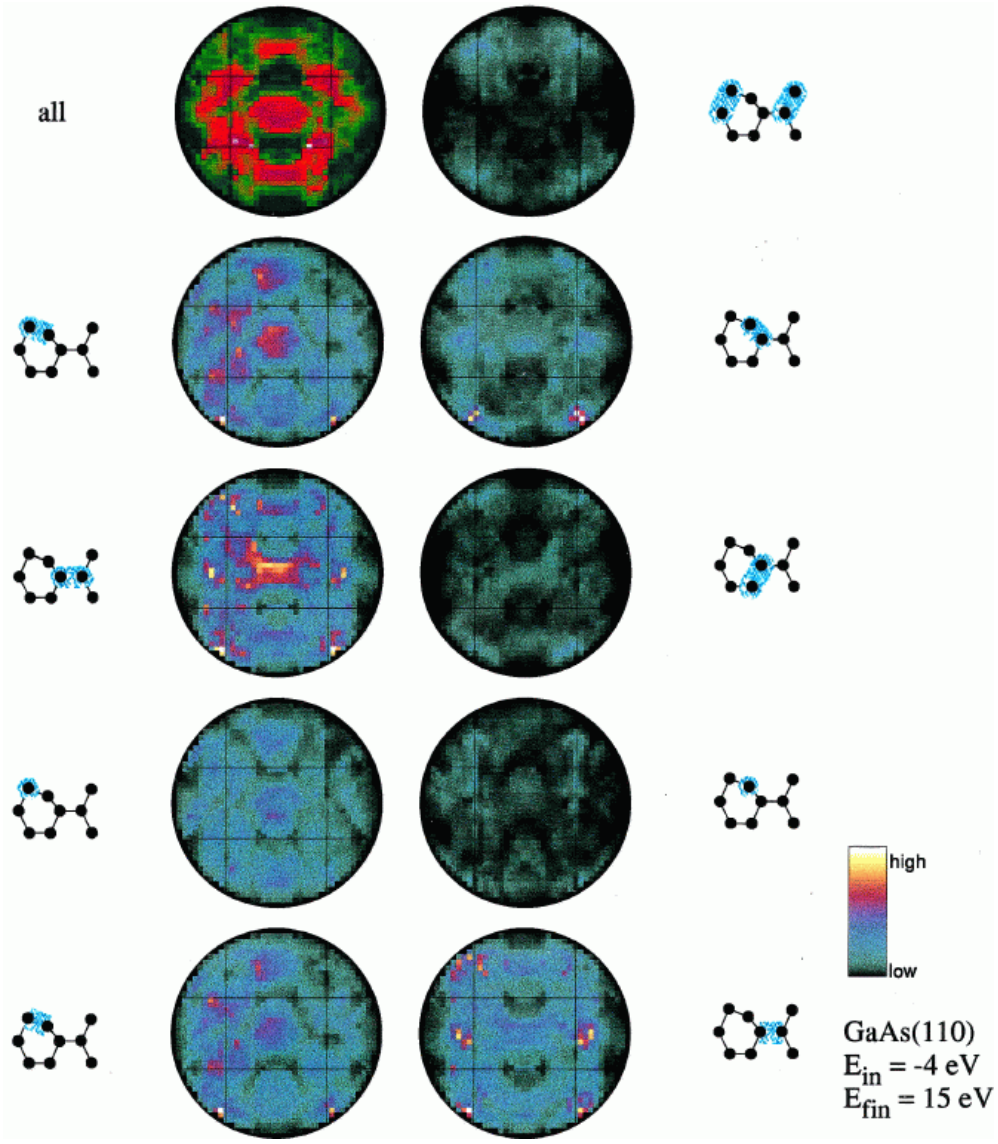

Figure 4.6: Local emissivity of extended initial states: hemispherical photocurrent plotted for selected spatial areas cutted out of the whole volume as depicted by the blue region in side view scheme of GaAs(110) surface aside each pattern; note that additionally interference between these areas exists and has to be taken into account.

Chapter 5

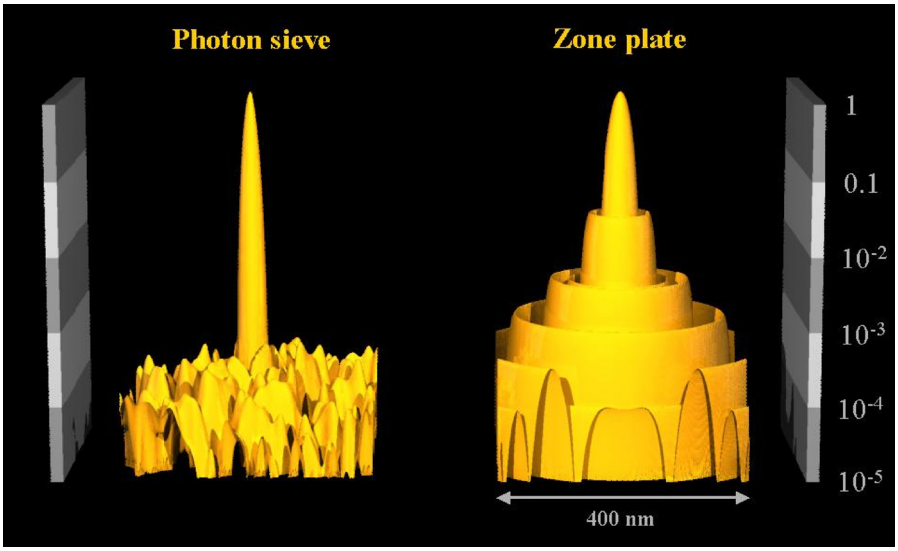

Figure 5.11: Intensity distribution on the focal plane of a photon sieve compared to a zone plate. Smallest structure size for both optical elements is 30 nm. For the photon sieve, the suppression of the secondary maxima is evident. This provides sharper images.

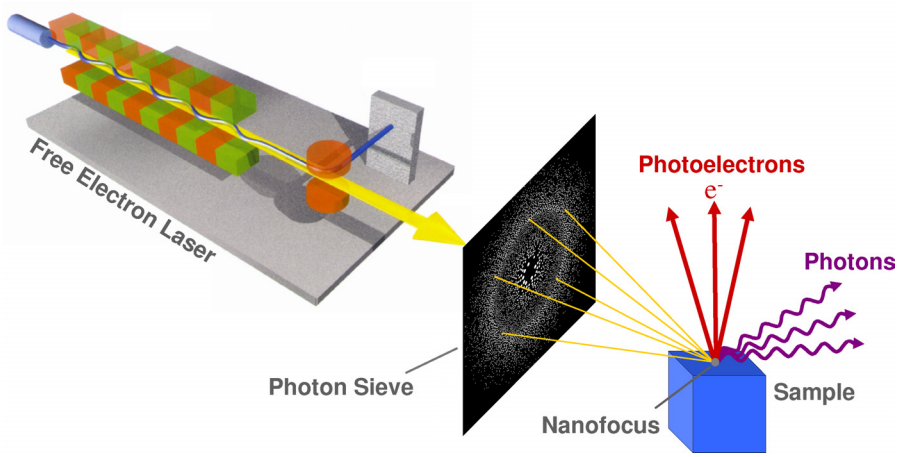

Figure 5.12: Schematic of a nanospectroscope capable of recording high-resolution images revealing chemical composition, morphology, and the electronic properties of materials in the nanometer regime.

Chapter 12

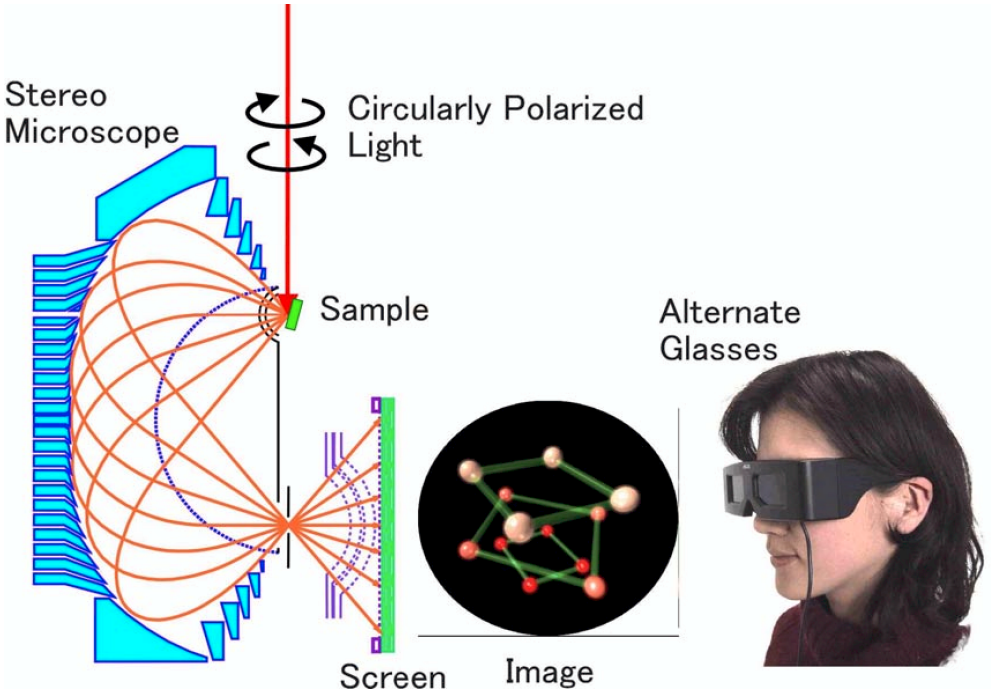

Figure 12.21: Stereo microscope.

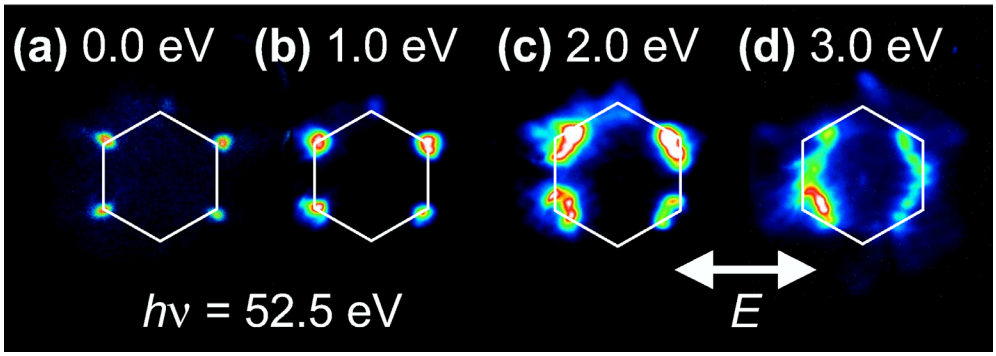

Figure 12.24: (a)-(d) The photoelectron angular distribution patterns from single crystal graphite valence band excited by a linearly polarized light corresponding to the cross-section of the π band at the binding energy of 0.0, 1.0, 2.0 and 3.0 eV, respectively.

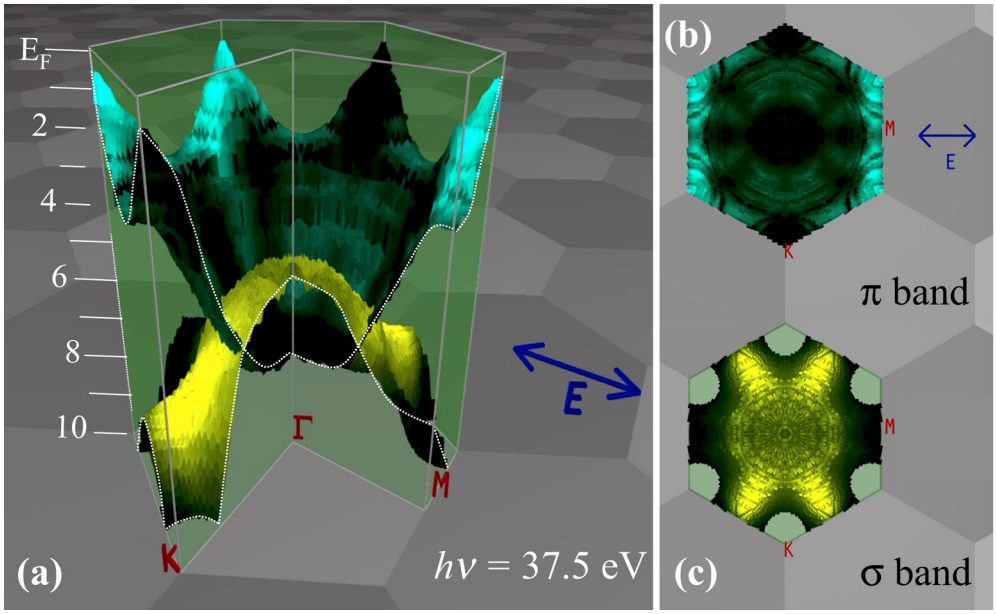

Figure 12.25: (a) Bird's-eye-view of three dimensional π (upper) and σ (lower) bands of graphite. Photon energy of 37.5 eV is used for the excitation. The patches of the hexagonal tiles underneath stand for the other Brillouin zones. (b,c) Photoemission intensity distributions of the π and σ bands, respectively.

Chapter 15

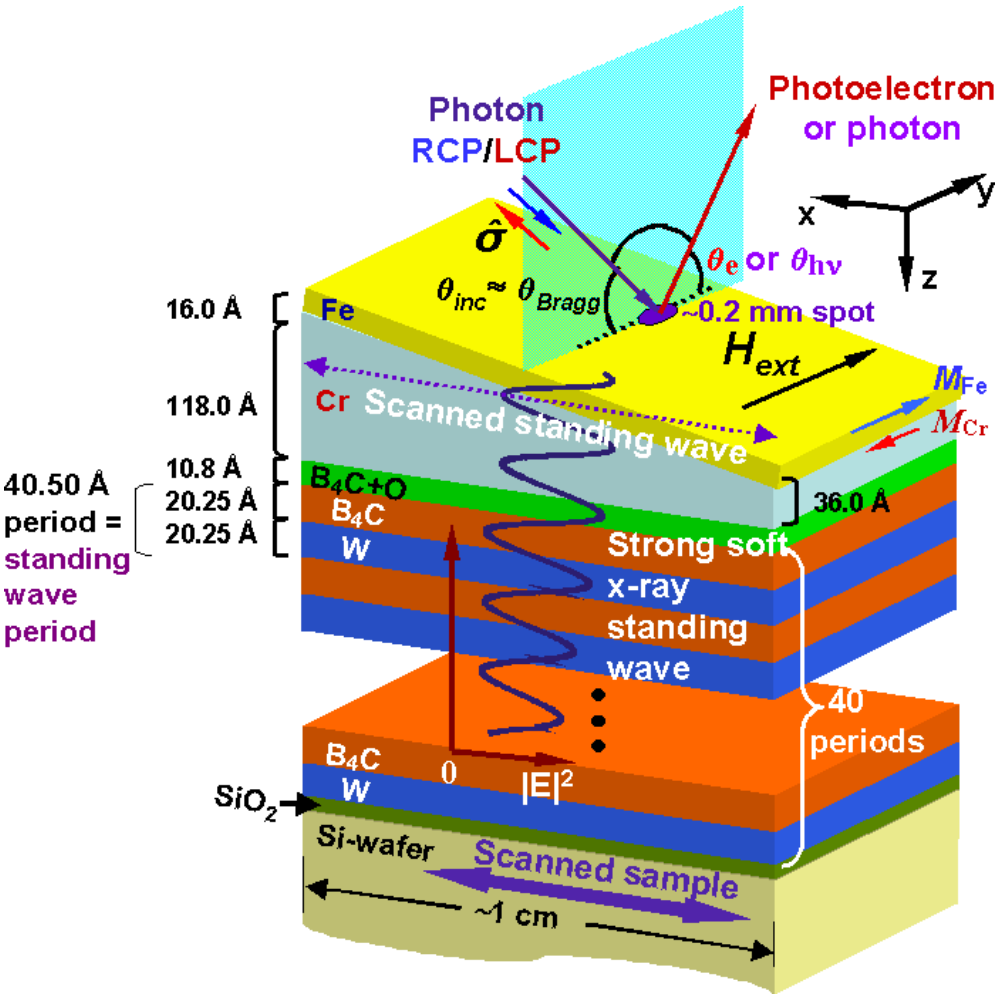

Figure 15.7: Basic geometry of an experiment combining soft X-ray excitation of photoemission with a wedge-shaped bilayer sample grown on a multilayer-mirror standing wave generator (SWG) so as to selectively study the buried interface between Fe and Cr. Scanning the sample position along the x axis effectively scans the standing wave through the interface. [From ref. [16].]

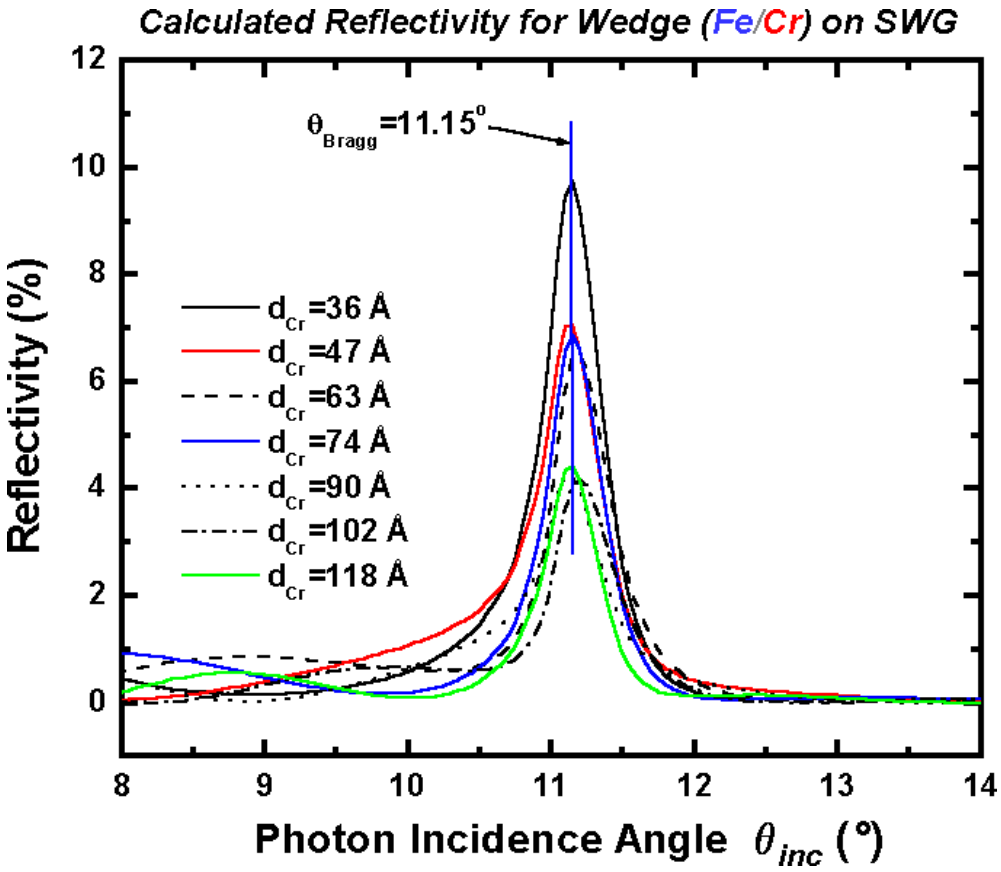

Figure 15.8: Calculated reflectivity for the sample geometry of Fig. 15.7: a wedge-shaped Fe/Cr bilayer on top of a 40-period multilayer mirror composed of bilayers of B_4C and W. Note that, although the reflectivity is attenuated by thicker Cr layers, the position of maximum reflectivity is pinned at the same angular position by reflection from the multilayer. [From refs. [16], [17], and [19].]

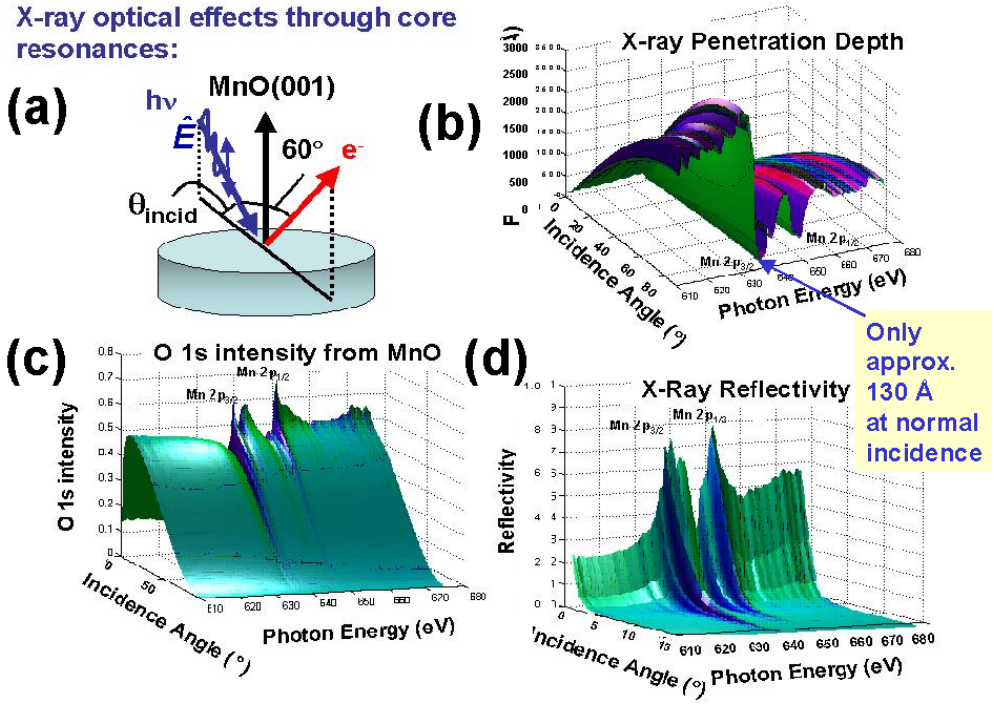

Figure 15.13: Resonant X-ray optical calculation for the experimental geometry in (a) of: (b) the X-ray penetration depth = exponential decay length Λ_x, (c) the O 1s photoelectron intensity, and (d) the reflectivity R_x. These calculations were carried out for p-polarized radiation incident on a flat MnO surface and photon energies were scanned through the Mn 2p absorption resonances. The plots in (a), (b), and (c) are all shown as a function of both photon energy and incidence angle. [From ref. [19].]

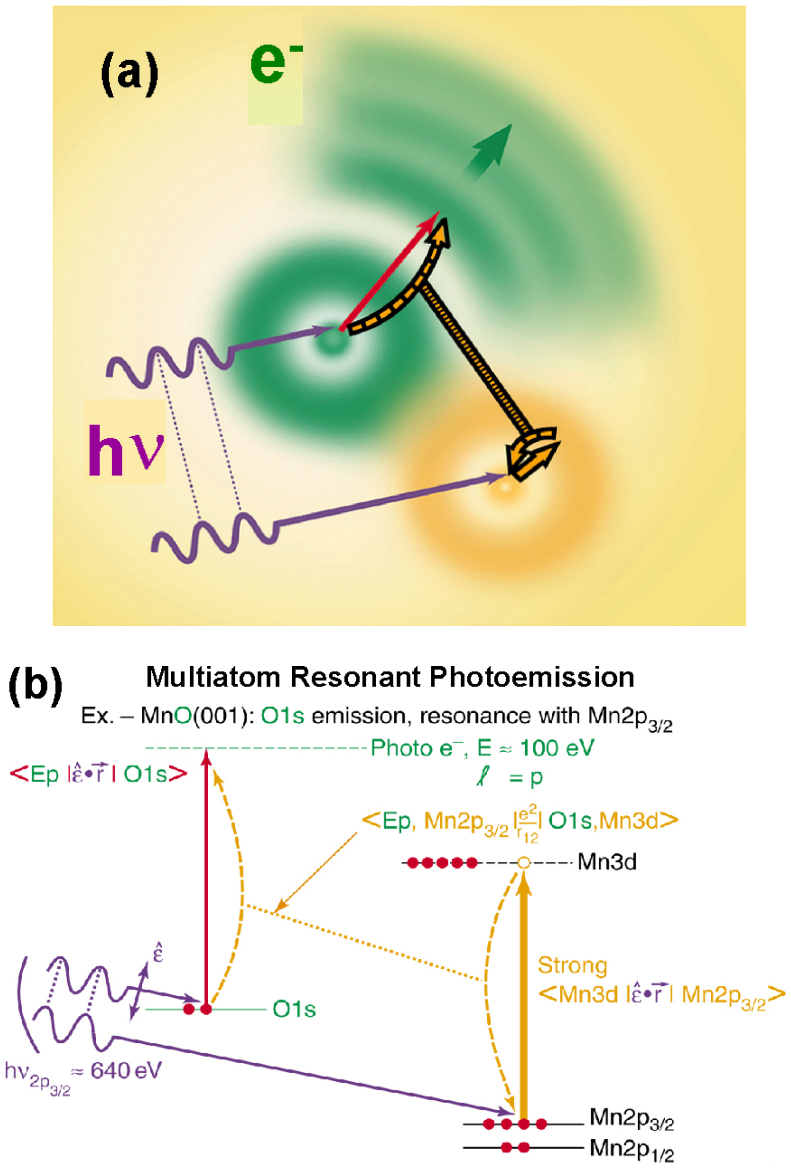

Figure 15.16: (a) Illustration of the basic process occurring in multiatom resonant photoemission (MARPE). (b) Additional diagram of the electronic transitions involved in the MARPE process, for the specific case of O 1s emission from MnO and with the photon energy passing over the Mn $2p_{3/2}$ absorption resonance. [After refs. [20] and [22].]

Solid-State Photoemission and Related Methods
Wolfgang Schattke, Michel A. Van Hove (Eds.)

Index